Deciphering the Complex Alteration Recorded in Primitive Asteroids

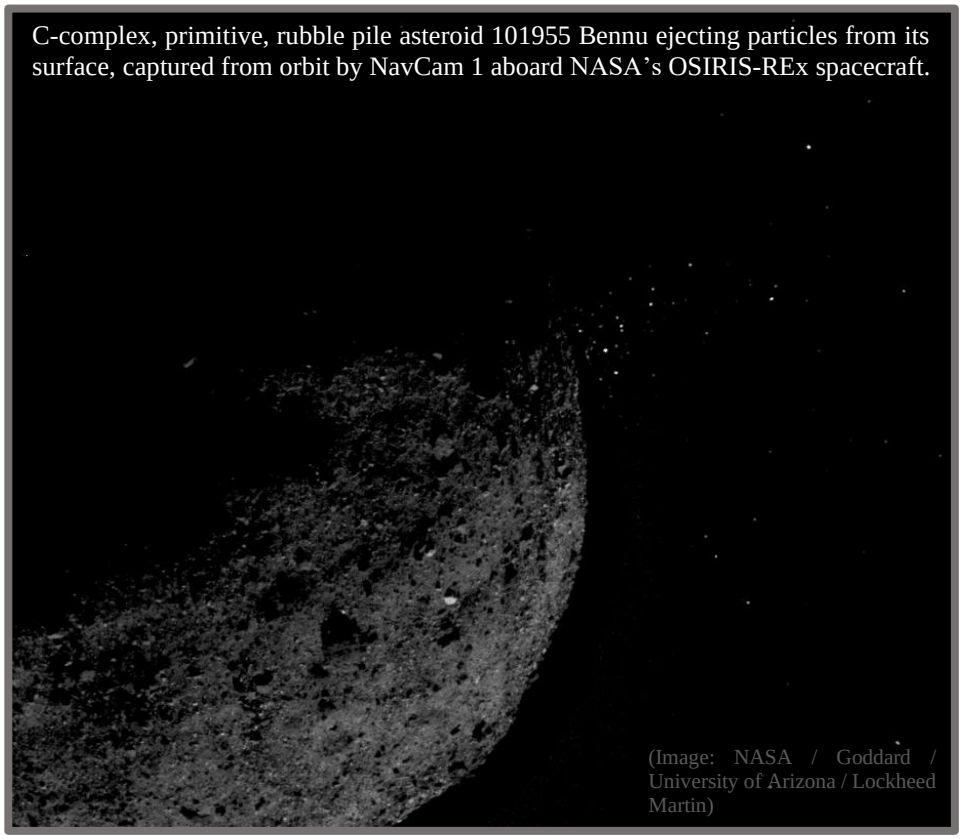
C-complex, primitive, rubble pile asteroid 101955 Bennu ejecting particles from its surface, captured from orbit by NavCam 1 aboard NASA's OSIRIS-REx spacecraft.

(Image: NASA / Goddard / University of Arizona / Lockheed Martin)

Ross Findlay

A thesis submitted for the degree of Doctor of Philosophy

The Open University

School of Physical Sciences

July 2023

Abstract

CM chondrites are unequilibrated breccias sampling primitive asteroids altered by water-rock interactions. While much research has focused on bulk measurements, only tentative attempts have been made to elucidate the complex petrographic and O-isotopic heterogeneity at the clast and component scale utilising this high precision approach.

Clasts of petrologic subtype CM1/2.0 – 2.8 were found in four falls and one very diverse find, LON 94101, the latter of which strengthens the case of a discrete parent body source for CM chondrites. The petrologic subtype of moderately altered clasts ranging from 2.2-2.6 appear to correlate well with variable 'FeO'/SiO_2 and Mg# compositions within their phyllosilicates, though this is poorly matched from meteorite to meteorite. Fully altered clasts (CM1/CM2.0) host an array of diverse textures ranging from dark, Mg-dominated matrix-rich clasts to those containing abundant chondrule pseudomorphs, comparable in large part to the diversity seen in CM2 material. An array of rarer, petrographically distinct lithologies, including incipiently altered, predominantly anhydrous examples, attest to the diversity of CM material in the meteorite record.

Matrix phyllosilicates from 30 petrographically characterised CM lithologies and 4 cataclastic matrix fractions were micro-sampled to investigate lithology-specific aqueous alteration phenomena through their O-isotopes, obtained via a revised laser fluorination protocol for small, phyllosilicate-rich samples. The exclusion of a significant anhydrous precursor component within these fractions reveals a novel, apparently mass-dependent trend: the CM matrix fractionation line (CMF) at ~ $\Delta^{17}O$ = -2.35 ± 0.46‰ (2σ), indicating the CM lithologies were altered within a narrow range of water to rock (WR) ratios and that historical O-isotope variation primarily just reflects variable amounts of anhydrous precursor. This weakens the case for a closed system style of alteration, where variable WR ratios may be expected; indeed, an open system may provide a better explanation where equilibration of water is achieved over a mineralogically diverse area on the CM asteroid.

Declaration

I declare that the work presented herein is my own original work and does not contain any material submitted for any other qualification at The Open University, or any other academic institution.

As of July 2023, most of the work in this thesis is unpublished with the exception of minor contributions to collaborative publications:

Chapter 3 builds upon the foundations of a technique called the laser-fluorination single-shot procedure, pioneered at the Open University, and first reported in Schrader *et al.* (2014). During this work I revised the procedure, and it was used both in the analysis of micromilled fractions from Winchcombe and of asteroid Ryugu particles as part of Team Kochi of the larger Hayabusa2 initial analysis effort. Details of this procedure were published in the journals *Nature* (Greenwood *et al.,* 2022; Ito *et al.,* 2022) and *Meteoritics and Planetary Science* (Greenwood *et al.,* 2023).

I collected the initial oxygen isotope measurements of the Winchcombe meteorite which were published in *Science* (King *et al.,* 2022) in addition to micromilled measurements that were published alongside lithological descriptions of WC-01-A (NHM number BM.2022, M1-85): and WC-01-A (NHM number BM.2022, M1-123), in *Meteoritics and Planetary Science* (Greenwood *et al.,* 2023).

References:

Greenwood, R., **Findlay, R**., Martins, R., Steele, R., Shaw, K., Morton, E., Savage, P., Murphy, M., Rehkämper, M. & Franchi, I. 2023. The formation and aqueous alteration of CM2 chondrites and their relationship to CO3 chondrites: A fresh isotopic (O, Cd, Cr, Si, Te, Ti, and Zn) perspective from the Winchcombe CM2 fall. *Meteoritics & Planetary Science*.

Greenwood, R. C., Franchi, I. A., **Findlay, R**., Malley, J. A., Ito, M., Yamaguchi, A., Kimura, M., Tomioka, N., Uesugi, M., Imae, N., Shirai, N., Ohigashi, T., Liu, M.-C., Mccain, K. A., Matsuda, N., Mckeegan, K. D., Uesugi, K., Nakato, A., Yogata, K., Yuzawa, H., Kodama, Y., Tsuchiyama, A., Yasutake, M., Hirahara, K., Tekeuchi, A., Sekimoto, S., Sakurai, I., Okada, I., Karouji, Y., Nakazawa, S., Okada, T., Saiki, T., Tanaka, S., Terui, F., Yoshikawa, M., Miyazaki, A., Nishimura, M., Yada, T., Abe, M., Usui, T., Watanabe, S.-I. & Tsuda, Y. 2022. Oxygen isotope evidence from Ryugu samples for early water delivery to Earth by CI chondrites. *Nature Astronomy*. 29-38.

Ito, M., Tomioka, N., Uesugi, M., Yamaguchi, A., Shirai, N., Ohigashi, T., Liu, M.-C., Greenwood, R. C., Kimura, M. & Imae, N. et al. 2022. A pristine record of outer Solar System materials from asteroid Ryugu's returned sample. *Nature Astronomy***,** 1-9.

King, A. J., Daly, L., Rowe, J., Joy, K. H., Greenwood, R. C., Devillepoix, H. a. R., Suttle, M. D., Chan, Q. H. S., Russell, S. S., Bates, H. C., Bryson, J. F. J., Clay, P. L., Vida, D., Lee, M. R., O'brien, Á., Hallis, L. J., Stephen, N. R., Tartèse, R., Sansom, E. K., Towner, M. C., Cupak, M., Shober, P. M., Bland, P. A., **Findlay, R**., Franchi, I. A., Verchovsky, A. B., Abernethy, F. a. J., Grady, M. M., Floyd, C. J., Van Ginneken, M., Bridges, J., Hicks, L. J., Jones, R. H., Mitchell, J. T., Genge, M. J., Jenkins, L., Martin, P.-E., Sephton, M. A., Watson, J. S., Salge, T., Shirley, K. A., Curtis, R. J., Warren, T. J., Bowles, N. E., Stuart, F. M., Di Nicola, L., Györe, D., Boyce, A. J., Shaw, K. M. M., Elliott, T., Steele, R. C. J., Povinec, P., Laubenstein, M., Sanderson, D., Cresswell, A., Jull, A. J. T., Sýkora, I., Sridhar, S., Harrison, R. J., Willcocks, F. M., Harrison, C. S., Hallatt, D., Wozniakiewicz, P. J., Burchell, M. J., Alesbrook, L. S., Dignam, A., Almeida, N. V., Smith, C. L., Clark, B., Humphreys-Williams, E. R., Schofield, P. F., Cornwell, L. T., Spathis, V., Morgan, G. H., Perkins, M. J., Kacerek, R., Campbell-Burns, P., Colas, F., Zanda, B., Vernazza, P., Bouley, S., Jeanne, S., Hankey, M., Collins, G. S., Young, J. S., Shaw, C., Horak, J., Jones, D., James, N., Bosley, S., Shuttleworth, A., Dickinson, P., Mcmullan, I., Robson, D., Smedley, A. R. D., Stanley, B., Bassom, R., Mcintyre, M., Suttle, A. A., Fleet, R., et al. 2022. The Winchcombe meteorite, a unique and pristine witness from the outer solar system. *Science Advances*, 8**.**

Schrader, D. L., Davidson, J., Greenwood, R. C., Franchi, I. A. & Gibson, J. M. 2014. A water–ice rich minor body from the early Solar System: The CR chondrite parent asteroid. *Earth and Planetary Science Letters*, 407**,** 48-60.

Acknowledgements

Foremost, I must express heartfelt thanks to my supervisors, with the lion's share to Ian, for both possessing an otherworldly degree of empathy and persisting with me through my self-imposed writing sabotage during one of the more challenging times in my life. Unfortunately, I made writing this thesis — for the lack of any other gracious phrase — comparable to expelling a pineapple backwards. Coming to terms with my academic limitations in between both personal and health-related crises has been an excruciating journey, yet I stand here at last upon on the shoulders of giants. Thank you, Ian, Richard, and Mahesh, for your support and time over the years and especially Ian (and Martin) for the atrociously last-minute comments on my chapters. Thanks are extended to Sally and Robert, for being the catalyst to get my butt in gear; to the OU for their patience and trust considering the numerous extensions I needed to get this through the door; and to STFC for funding my work and being equally understanding when further time was needed.

Scientific writing is always such a serious business and I relish this once-in-a-thesis chance to write light-heartedly. Subversively, and perhaps ironically when considering my tumultuous write-up stage, this PhD was genuinely a pleasure to undertake. Nothing less than a cocktail of fascination, challenge, elation, late nights, and rhythmically banging my head against a wall.

Bizarre co-incidences can occur during any given moment. I started this PhD with the intent of analysing a rather spectacular block of CM2 chondrite recovered from Antarctica called LON 94101. It is (was? It's full of holes now) a pretty, behemoth of a block with a smorgasbord of meteorites sandwiched in it. It seemed impossible that the limelight could have ever been stolen from it. As it happens, this happened. Why? Well! It was because a brand spanking new meteorite (or two) fell from the heavens every year of my PhD. It all started off with the Mukundpura fall in India, followed by the Aguas Zarcas fall in Costa Rica, then Kolang in Indonesia and last (but certainly not least) Winchcombe in

Gloucestershire, UK. The latter fall is nothing short of miraculous. Not only did it shoot directly over my childhood home, but it was also the rare meteorite type (out of > 40 possible groups) that I was studying. To this end, thanks must go to Mahesh and Ian for grabbing pieces of the first three of these samples and for teaming up with Richard and the NHM to acquire some Winchcombe in record time, something I will never forgive them for. In all seriousness I owe them a lot for providing me with the most spectacular CM chondrite sample set on the planet (no mean feat!).

A project of such an interdisciplinary nature demanded a wide network of technical support and guidance: Giulia, Rich, Feargus, James Mo, Simona, Tom W, Pete, Ashley and Martin, in addition to being good friends, deserve special mention in this regard. Moreover, gratitude is extended across the various ponds to Dr Mike Zolensky for entrusting me with LON; and Dr Motoo Ito for allowing me the once in a lifetime opportunity to partake in the initial analysis of asteroid Ryugu as part of Team Kochi.

In receipt of the technician's medal of honour, enter Jam. In between the bouts of philosophical, political, and musical discussion, Jam and I sometimes found ourselves analysing meteorites. It was during a cold March morning in 2021, while dilly dallying around with our reinvented version of the infamous 'single shot' procedure, that we were put in the fortuitous position of obtaining the first oxygen isotopic measurements of Winchcombe, possibly setting the word record for 'asteroid belt to mass spectrometer' at the time. A mere 6 months later and in a freakish turn of events, we were breaking the record yet again when particles of asteroid Ryugu ethereally appeared on our doorstep! Jam and Richard, thank you for being excellent mentors and for trusting me to 'freeze' Ryugu onto two molecular sieves. I will never forget those moments, particularly when Ryugu was tweezed into the well inside the glove box. Those minutes just before the first measurement came in…the atmosphere was palpable.

Everyone else inside the Robert Hooke ‘pig pen’ and K-block have been great. To start with, most of you laughed at me, then you realised you were sharing and office with me for four years. Sorry about that, though it’s been a privilege to know and work alongside you all. We work in the dark to serve the light, we are... Hooke Soc!

To Mum and Dad and Mae, who have supported me throughout this PhD without the burden of financial worry and have been pretty much abandoned over the past four years, thank you. Without the childhood nurturing of curiosity, I would have never made it this far.

Finally, my dear partner Morgane, with whom I shared the burden of analysis, writing and interpretation with blood, sweat and tears: I couldn’t have asked for a better companion who so enthusiastically accepts all aspects of my truly peculiar attitude to life. Everything you did for me in those final four months glued me together and made this thesis possible.

"Deep inside the ruin, was a single stone that would change the course of our history forever"

- Bentusi Narrator, Homeworld (1999)

Table of Contents

List of Figures

List of Tables

List of Plates

'Plate' refers to the table / figure composites in Chapter 4, specifically made to ease the observations and interpretations of individual CM lithologies

List of abbreviations

AOA – Amoeboid Olivine Aggregates

AU – Astronomical Unit

BSE – Backscatter Electron

CAI – Calcium-Aluminium-Rich inclusions

CC – Carbonaceous Chondrite

CRE – Cosmic Ray Exposure

CMF – CM chondrite matrix fractionation line

EDS – Energy Dispersive Spectroscopy

EDX – Energy Dispersive X-ray

EPMA – Electron probe micro analyser

Ga – Giga annum. Specifically referring to one billion years *before* present

GEMS – Glass with Embedded Metal and Sulphide

IR – Infrared

IRMS – Isotope Ratio Mass Spectrometer

Ma – Mega annum. Specifically referring to one million years *before* present

MDF – Mass-dependent fractionation

MIF – Mass-independent fractionation

MQ – MilliQ Water

NanoSIMS – Nano Secondary Ion Mass Spectrometry

NEA – Near Earth Asteroid

OU – The Open University

PCP – ‘Poorly Characterised Phase’

SE – Secondary Electron

SEM – Scanning Electron Microscope / Microscopy

SIMS – Secondary Ion Mass Spectrometry

SLAP – Standard Light Antarctic Precipitation

SMOW – Standard Mean Ocean Water

TCI – Tochilinite-Cronstedtite Intergrowths

TEM – Transmission Electron Microscopy

TOFSIMS – Time of Flight Secondary Ion Mass Spectrometry

UV – Ultraviolet

VSMOW – Vienna Standard Mean Ocean Water

WDS – Wavelength Dispersive Spectroscopy

WR – water/rock ratio

Chapter 1 – Introduction

1.1 Project introduction and literature review

The planets of the present-day Solar System were built by the accretion of precursor planetesimals during the evolution of the protoplanetary disk (*e.g.*, Morbidelli *et al.*, 2012). Today, fragmentary remnants of these planetesimals reside in the main asteroid belt between Mars and Jupiter (*e.g.*, Burbine, 2016; Greenwood *et al.*, 2020). Amongst the population of original asteroids, those that formed small or late escaped the homogenising effects of radiogenic heating and are the only known objects to inherit the near-original composition of the Solar System, and thus, retain information about the original 'building blocks' of the planets (e.g. Drake and Righter, 2002; Fitoussi *et al.*, 2016; Moynier and Fegley Jr, 2015; Valdes *et al.*, 2014; Walker *et al.*, 2015). Despite the lack of physical differentiation, these primitive bodies did not escape modification entirely. Indeed, many endured low-temperature aqueous alteration through the melting of accreted water ice, partially or fully transforming the precursor mineralogy into a range of secondary minerals (Brearley, 2006; Suttle *et al.*, 2021). The subsequent ~4.5 billion years, laden with impact and reassembly, rearranged these primary asteroids into secondary rubble piles of accretionary debris (Michel *et al.*, 2020; Michel and Richardson, 2013) where fortuitous impacts send fragments of these asteroids on an intercept course with Earth; if they survive atmospheric entry, they are recovered as chondritic meteorites.

A shown in Fig 1.1, the CM 'Mighei-type' carbonaceous chondrites are a group of aqueously altered meteorites that spectrally resemble the C-complex asteroids (Bates *et al.*, 2020; Clark *et al.*, 2011; Cloutis *et al.*, 2012; DeMeo *et al.*, 2022; Hamilton *et al.*, 2019; Hanna *et al.*, 2020; Hiroi *et al.*, 1996; Vernazza *et al.*, 2017), the most abundant group of primitive planetesimals in the main belt (DeMeo *et al.*, 2015; Masiero *et al.*, 2015; Morbidelli *et al.*, 2015). A phyllosilicate-rich mineralogy — indicative of the interaction of water and rock at low temperatures (Brearley, 2006) — provide the potential to shed light on the nature and evolution of the silicate, water, and organic reservoirs in the protoplanetary disk, including

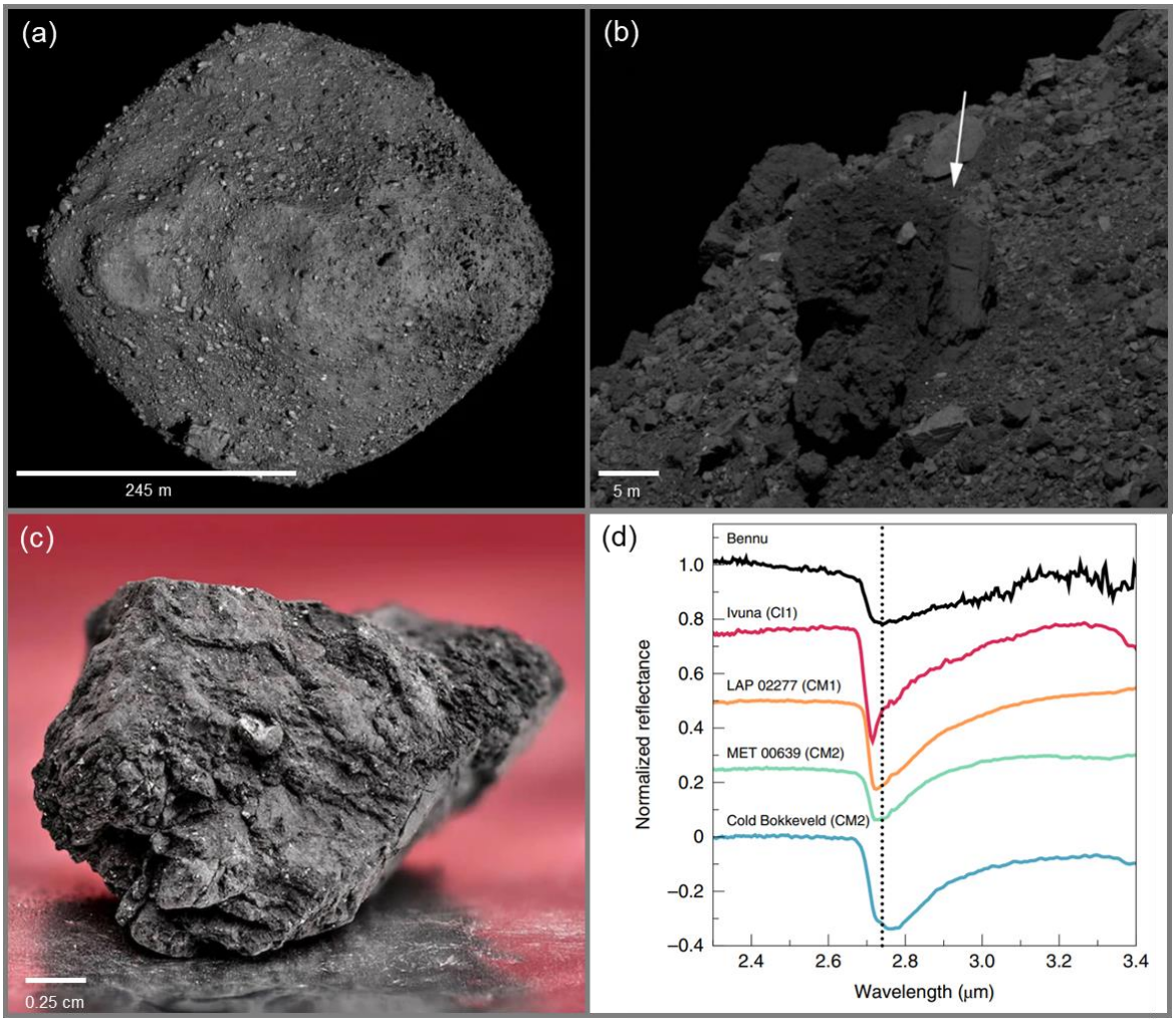

Figure 1.1- Comparison of primitive asteroidal material at multiple scales. (a), Orbital image of C-complex rubble-pile asteroid 101955 Bennu, the target of NASA's sample return mission OSIRIS-REx. (b), Fragmented boulders on the surface of Bennu showing a brecciated texture, the white arrow points towards a boundary between two lithologies. (c) a chunk of the Winchcombe meteorite, showing a similar brecciated texture with abundant clasts. Size of the specimen is an estimate. (d), Normalised visible to near-infrared reflectance / emission spectrum of Bennu in comparison to various, OH-rich carbonaceous chondrites, which all have a pronounced 2.7 μm feature reflective of OH in clay minerals. Sources: (a) NASA/Goddard/University of Arizona; (b) Ishimaru *et al.* (2021); (c) Trustees of The Natural History Museum, UK; (d) Hamilton *et al.* (2019).

a possible contribution to Earth's volatile budget through the late delivery of water (Drake and Righter, 2002; Newcombe *et al.*, 2023; O'Brien *et al.*, 2014; Raymond and Izidoro, 2017; Raymond *et al.*, 2009; Sarafian *et al.*, 2014b and references therein). This tantalising promise has seen CMs become one of the most widely studied chondrite groups, further heightened by the return of regolith samples from asteroids 162173 Ryugu (Ito *et al.*, 2022;

Nakamura *et al.,* 2022) and 101955 Bennu (*e.g.,* Righter *et al.* 2023) via space missions Hayabusa2 and OSIRIS-REx, respectively.

A C-complex rubble-pile heritage is plausible (Fig 1.1), as shown by a highly brecciated petrography containing clasts of variable lithologic character with very different levels of aqueous alteration (Bischoff *et al.,* 2006; Lentfort *et al.,* 2021). However, this vital petrographic observation is often overlooked and poorly correlated with respect to the geochemistry, despite significant geochemical and isotopic heterogeneity in and between samples (*e.g.,* Lee *et al.* 2019), limiting the conclusions that can be drawn from such data (Clayton and Mayeda, 1999; Findlay *et al.,* 2022; Franchi *et al.,* 2001; Franchi, 2008; Greenwood *et al.,* 2023a). How the CM parent asteroid was structured, and/or if the CM meteorites sample multiple asteroids remain open questions (Clayton and Mayeda, 1999; Greenwood *et al.,* 2019; King *et al.,* 2020; King *et al.,* 2017; Lee *et al.,* 2019; Lee *et al.,* 2023; Vernazza *et al.,* 2016; Young, 2001).

The purpose of this thesis is to further elucidate the structure and evolution of primitive C-complex asteroids through coupled investigation of the aqueous alteration phenomena in CM chondrite clasts. This is achieved by pairing high resolution petrography with spatially resolved triple oxygen isotope measurements from multiple clasts in a number of different meteorites, providing constraints on the possible nature and even number of CM parent bodies. This introductory chapter establishes context and rationale through a review of past and present literature. Chapter 2 outlines analytical techniques with a focus on petrographic tools, including microscopy and micro-sampling. Chapter 3 concerns oxygen isotope analysis via laser-assisted fluorination and the challenges associated with fluorinating small samples of CM chondrites. Chapter 4 outlines classification and petrography, while 5 and 6 detail the oxygen isotope systematics of CM falls and finds, respectively. Chapter 7, synthesis, will systematically compare the results to CM parent body models in the literature, specifically those concerning either open and closed systems of aqueous alteration, to refresh

current insights and assess the feasibility of both approaches. A summary of the findings and suggestions for further work will be reported in Chapter 8.

1.2 Early Solar System processes

CM chondrites are a complex, heterogeneous amalgam of processes and chemical signatures inherited from the molecular cloud, the protoplanetary disk and from parent body processing. Deciphering the relationship between geochemistry and petrography requires a basic understanding of a broad range of planetary science topics from the protoplanetary disk to meteorite arrival on Earth; however, to be exhaustive is beyond the scope of this Chapter and so this Introduction aims to be more general, covering the early Solar System processes relevant to the discussion of CM chondrites and the triple oxygen isotope system.

1.2.1 Molecular cloud collapse

The Solar System formed from a concentration of the interstellar medium, a molecular cloud of predominantly hydrogen, helium, and dust; held together by electrostatic forces (Ballesteros-Paredes *et al.*, 2020; Caselli and Ceccarelli, 2012). The composition of the Sun indicates that this cloud was a product of multiple stellar cycles, owed to the existence of elements that are only produced via multiple generations of nucleosynthesis (Forbes *et al.*, 2021; Gounelle, 2015; Koll *et al.*, 2019; Vasileiadis *et al.*, 2013). Disruption of the electrostatic equilibrium occurred in a localised region, possibly by a nearby supernova shockwave (Gritschneder *et al.*, 2011) or collision with an adjacent cloud (Inoue and Fukui, 2013). Isothermal followed by adiabatic collapse ensued, generating enough heat and pressure in the centre to kickstart nuclear fusion and the birth of a protostar 4.6 billion years ago (McKeegan and Davis, 2003). Continued collapse caused the protostar to gain mass from the molecular cloud, increasing the star's gravitational field and exhibiting a greater pull on the adjacent sphere of dust and gas. As the gas contracted, the conservation of angular momentum caused the sphere to flatten into a rotating protoplanetary disk (*e.g.*, Williams and Cieza, 2011).

Few geochemical remnants of the molecular cloud stage persist in meteorites today, a result of extensive homogenisation during collapse; however, it is noted that signatures in many elements may have been inherited in discrete phases or regions within the protoplanetary disk by physical or chemical processes. Of important relevance are the isotopes of oxygen that through the processes of photochemical self-shielding, may be enriched or depleted in certain regions relative to others (Clayton, 2002).

1.2.2 Accretion

Broadly, protoplanetary disks span 10s - 100s of AU and consist of 99% gas and 1% dust (Carmona, 2010). Dust, centred around the midplane of the disk, orbits the sun at Keplerian speed, while the gas orbits at slower rate as it experiences an outward, pressure gradient force (Morbidelli, 2018; Weidenschilling, 1980). The gas therefore imposes headwind or drag on the suspended dust. The dust is slowed, and as a consequence radially drifts into the central star (Fig 1.2, (b)). The distribution of radiation from the star outwards produces a volatility gradient in the disk, with the 'snowline' representing the condensation point of water, ammonia, and methane (*e.g.*, Lecar *et al.,* 2006; Martin and Livio, 2012). A similar line exists for organics, the 'tar line' (Nakano *et al.,* 2003; Piani *et al.,* 2018). In addition, there will also be temporal and spatial gradients exhibited by any condensed solid phases including silicate and metal dust that has condensed out of the nebula, for example forsterite (Sturm *et al.,* 2013). As the disk evolves through viscous spreading and eventual gas-dissipation, the radial distance of these lines will increase as the opacity of the protoplanetary disk decreases (Williams and Cieza, 2011). The composition of any accreted body therefore depends on the spatial and temporal region in which it formed.

The earliest stages of accretion remain enigmatic (Morbidelli and Raymond, 2016). Current research suggests that the formation of particles on the scale of 1 mm requires a layer of amorphous ice to promote Van-der-Waals coagulation of sub-micron dust to overcome the

(a)

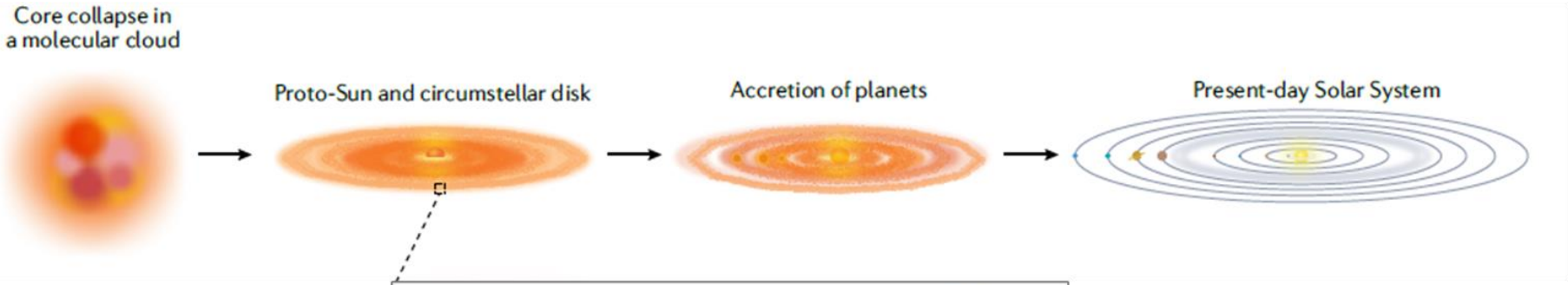

(b)

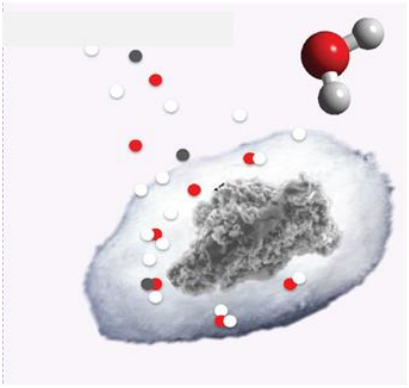

Dust grains ~0.1 μm with 0.05 μm thick icy mantle stick and agglomerate together

(c)

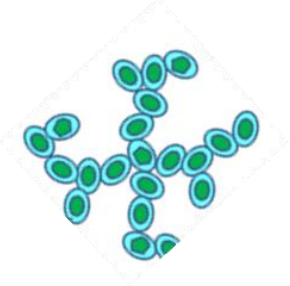

(d)

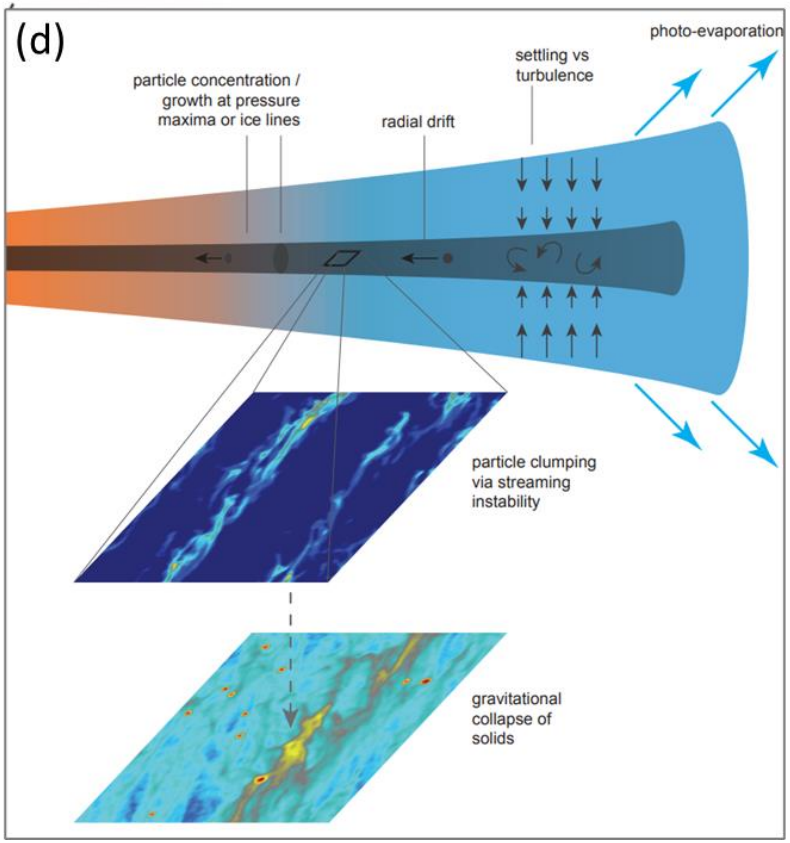

(e)

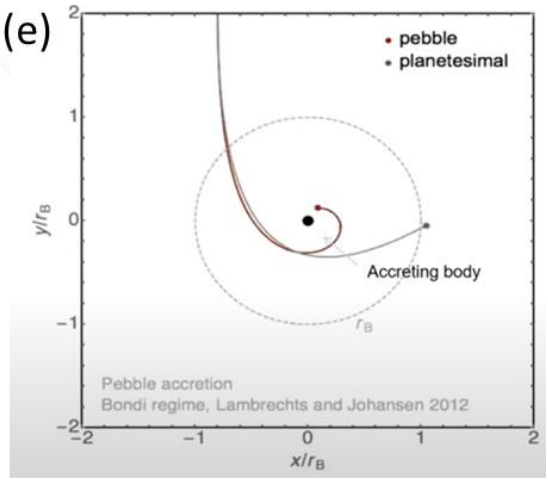

Figure 1.2 - A combined schematic overview of important accretionary processes. (a) the temporal evolution of the disk. (b) the growth of ice on sub-micron dust grains. (c) the agglomeration of dust grains via their icy surfaces. (d) important disk processes governing the earliest stages of accretion, including turbulence, settling, and streaming instability at the mid plane. (e) Impact parameters for a planetesimal vs a pebble, pebbles are more likely to accrete onto larger bodies. This figure is a collage from many sources: (a) Halliday and Canup (2023); (b) Ceccarelli and Du (2022); (c) Matsumoto *et al*. (2019); (d) Armitage (2019); (e) Lambrechts and Johansen (2012); Morbidelli (2021).

effects of the ‘bouncing barrier’ (Fig 1.2 (b) and (c)), where small particles collide and ricochet as opposed to agglomerating, limiting the initial accretion region to beyond the snow line where volatiles can condense (Blum, 2018; Dominik and Tielens, 1997; Zsom *et al.,* 2010). A further ‘metre-sized barrier’ is imposed upon larger objects that must overcome radial drift into the Sun by accreting to a size of the order of 1 km, but this is problematic as high velocity impacts are more likely to break these objects apart than combine them (Morbidelli and Raymond, 2016; Zsom *et al.,* 2010). Recent models suggest the gravitational collapse of dense disk filaments, induced by settling and streaming instabilities caused by dust (Fig 1.2, (d)), could form planetesimals of the order of 10s – 100s km within turbulent vortices (Johansen *et al.,* 2006; Johansen and Youdin, 2007; Schäfer *et al.,* 2020; Yang *et al.,* 2017; Youdin and Johansen, 2007). In the classical accretion model, runaway growth is expected to follow, producing thousands of planetary embryos of the scale of ~500km (Kokubo and Ida, 1996). This is succeeded by oligarchic growth, where the largest embryos accrete the remaining planetesimals followed by a final period of giant impact between the surviving ‘Mars-sized’ oligarchs (Kokubo and Ida, 1998).

The formation of Jupiter and Saturn require cores of ~20 Earth masses to initiate the accretion of gas from the disk (Lambrechts *et al.,* 2014; Morbidelli and Nesvorny, 2012; Weber *et al.,* 2018). Critics suggest classic accretion is not rapid enough (Pollack *et al.,* 1996), or indeed too difficult (Levison *et al.,* 2010), to form these cores as disk neighbourhoods will rapidly deplete their population of planetesimals (Johansen and Lambrechts, 2017). The new paradigm of ‘pebble accretion’ was proposed as an alternative (Ormel, 2017 for a detailed review). In this case, a self-gravitating Moon-sized body will begin to rapidly accrete radially drifting pebbles from the outer Solar System (Morbidelli, 2020), which are both abundant and have favourable impact parameters compared to a planetesimal (Fig 1.2, (e)), resulting in rapid growth (Ida *et al.,* 2016; Johansen and Lacerda, 2010; Lambrechts and Johansen, 2012; Ormel and Klahr, 2010).

1.2.3 Planetary migration

A recent, but significant discovery is that many exoplanetary star systems contain 'Hot' and 'warm' Jupiters — gas giants orbiting within ~0.05 and 1 AU of their star — in addition to 'super Earths' / 'mini-Neptunes' (Dawson and Johnson, 2018; Fogg and Nelson, 2007; Hatzes, 2016). It has been suggested that the root cause of this exoplanetary setup is the progressive inward migration of gas giants towards the central star, a consequence of the gas-induced torque from the outer disk pushing a rapidly accreting gas-giant planet inwards during the early stages of planetary formation. Another interesting observation is that many exoplanets have very elliptical orbits, suggestive of a later episode of giant planet instability and interaction through outward migration after the supportive gas budget of the disk has been depleted (Hatzes, 2016 for a review).

If Jupiter migrated in the Solar System, the gravitational effect of its ~300 Earth masses (~2.5 times all other planets combined) would have profound implications on the orbits of forming planets and planetesimals (Morbidelli and Raymond, 2016). This likely happened as the main asteroid belt, for example, is populated with outer and inner Solar System asteroidal material, which is only possible through gravitational disturbance (DeMeo and Carry, 2014). The Moon too, in tandem with other planets, shows widespread crater evidence for a Late Heavy Bombardment (LHB) approximately 600 Myr after the birth of the Solar System, suggesting the destabilisation of a previously stable population of planetesimals (Bottke and Norman, 2017; Wetherill, 1975). However, oddities exist that posit our Solar System's migration history differed slightly to that experienced by many extrasolar systems. At 5 AU from the Sun, Jupiter is certainly not 'hot'; Mars is in apparent mass-deficit assuming static Solar System formation models (Izidoro *et al.,* 2015); the Jupiter trojan asteroids (mostly D-type) suggest 3:2 resonance with the largest planet (Morbidelli *et al.,* 2005); and the orbits of the giant planets are also only mildly elliptical. Why then, does the Solar System not corroborate the apparently common extrasolar outcome? One explanation

could simply be a bias in detection capability, as smaller, distant planets in systems resembling our own may pose a greater challenge for detection. Alternatively, the Solar System could have endured a unique set of circumstances that prevented the common outcome. This latter argument formed the foundation of two scenarios that explain the current configuration: The 'Nice' and 'Grand Tack' models.

The Grand Tack requires the early formation of Jupiter's core, probably by pebble (Fig 1.3, (e)) then gas accretion, opening a disk-gap within 100,000 years following molecular cloud collapse (Walsh *et al.,* 2012; Walsh *et al.,* 2011). Due to the large torque from the gas-rich outer disk, Jupiter migrates to approximately 1.5 AU and is of sufficient size to create a pressure maximum (*e.g.,* Brasser and Mojzsis, 2020) that acts as a barrier for radial drift of pebbles, 'fossilising' the snowline and starving the inner Solar System of fine material (Morbidelli *et al.,* 2016). Simultaneously, large planets (including 'super-Earths') forming exterior to Jupiter cannot easily pass the giant planet. By fortuitous co-incidence, the core of Saturn formed not long after Jupiter's, and due to the temporal change in the relative conditions of accretion (essentially, Saturn forming later and being 'pushed' in the inward direction of the gas-depleted void left in the wake of Jupiter) migrates 10 times faster than and intercepts the giant planet (Walsh *et al.,* 2012; Walsh *et al.,* 2011). The result is a 2:3 motion resonance with very low torque between Jupiter and Saturn, causing both to then migrate outwards as a unit. A consequence of this outward migration is truncation of planetesimals and oligarchs in the inner disk, scattering and depleting the 1.5 AU Martian orbit (Walsh *et al.,* 2011). Another side effect is the mobilisation of outer planetesimals inwards and inner planetesimals outwards, populating the main belt with both inner and outer (including CM chondrite) Solar System material. The Grand Tack provides robust explanations for the configuration of the Solar System, the Mars mass deficit, and the main belt heterogeneity; however, its rapid execution (< 1Myr) cannot explain the Late Heavy

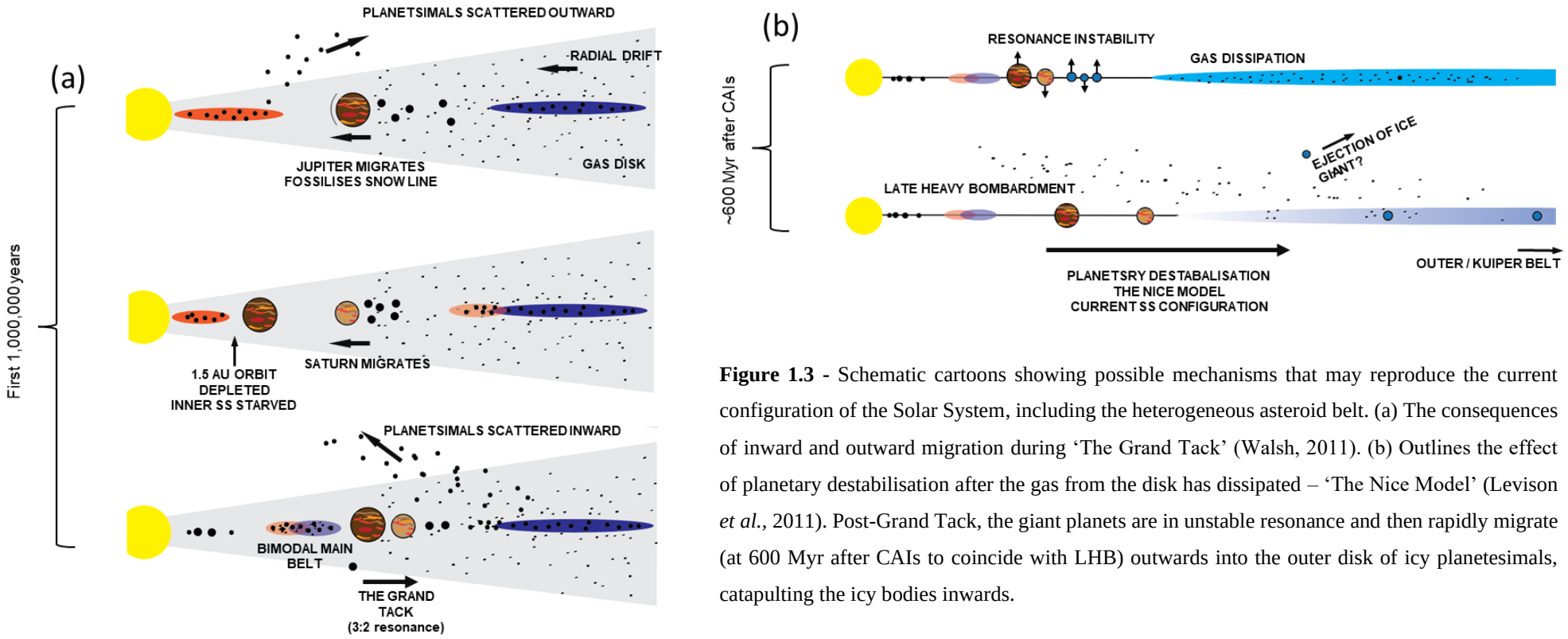

Figure 1.3 - Schematic cartoons showing possible mechanisms that may reproduce the current configuration of the Solar System, including the heterogeneous asteroid belt. (a) The consequences of inward and outward migration during 'The Grand Tack' (Walsh, 2011). (b) Outlines the effect of planetary destabilisation after the gas from the disk has dissipated – 'The Nice Model' (Levison *et al.*, 2011). Post-Grand Tack, the giant planets are in unstable resonance and then rapidly migrate (at 600 Myr after CAIs to coincide with LHB) outwards into the outer disk of icy planetesimals, catapulting the icy bodies inwards.

Bombardment. Furthermore, for the Solar System at this primordial stage, Jupiter, Saturn, and the other gas giant planets were likely in resonance, closer to the Sun than the present (Izidoro *et al.*, 2017). Another episode of later planetary disturbance is therefore required.

Originally independent of the Grand Tack but now considered as a follow-on process, the Nice Model (Levison *et al.*, 2011; Morbidelli *et al.*, 2007) suggests that after gas dissipation (*e.g.*, Ogihara and Ida, 2009), the resonances of Jupiter, Saturn, Uranus, and Neptune become dynamically unstable without gas support. The result is rapid outward migration into the trans-Neptunian disk of surviving planetesimals, scattering them inwards (Late Heavy Bombardment), while also explaining the unusual distribution of trojan asteroids, the present-day Kuiper belt, and the current orbits of the planets. The time of instability is dependent on the location of the original trans-Neptunian belt. To reproduce the present day, mildly elliptical orbits of the gas giants, it is requisite that Jupiter and Saturn by chance did not interact during planetary destabilisation (Levison *et al.*, 2011; Morbidelli *et al.*, 2007).

A significant consequence of the planetary destabilisation is the possibility that water-rich material such as comets or even CI and CM chondrite material (as C-complex asteroids) were delivered late from the outer to the inner Solar System, including the early formed Earth (*e.g.*, Morbidelli and Wood, 2015). This may explain the origins of Earth's water. While this topic and its likelihood is hotly debated (Drake, 2005; Greenwood *et al.*, 2018; Greenwood *et al.*, 2023b; Marty, 2012; Morbidelli *et al.*, 2000; Piani *et al.*, 2020; Sarafian *et al.*, 2014a; Vattuone *et al.*, 2013; Wu *et al.*, 2018), it nevertheless highlights the importance of understanding the temporal evolution of CM chondrite material — including its relationship with migration —from the earliest stages to its present location in the main belt.

1.2.4 The greater influence of Jupiter

Warren (2011) recognised a compositional 'gap' between the inner and outer Solar System recorded in the isotopic signatures of certain elements, such as titanium, chromium, and

oxygen in meteorites (Fig 1.4) In the wake of this observation, numerous studies have reproduced a similar dichotomy in other elements (Kleine *et al.*, 2020; Kruijer *et al.*, 2020).

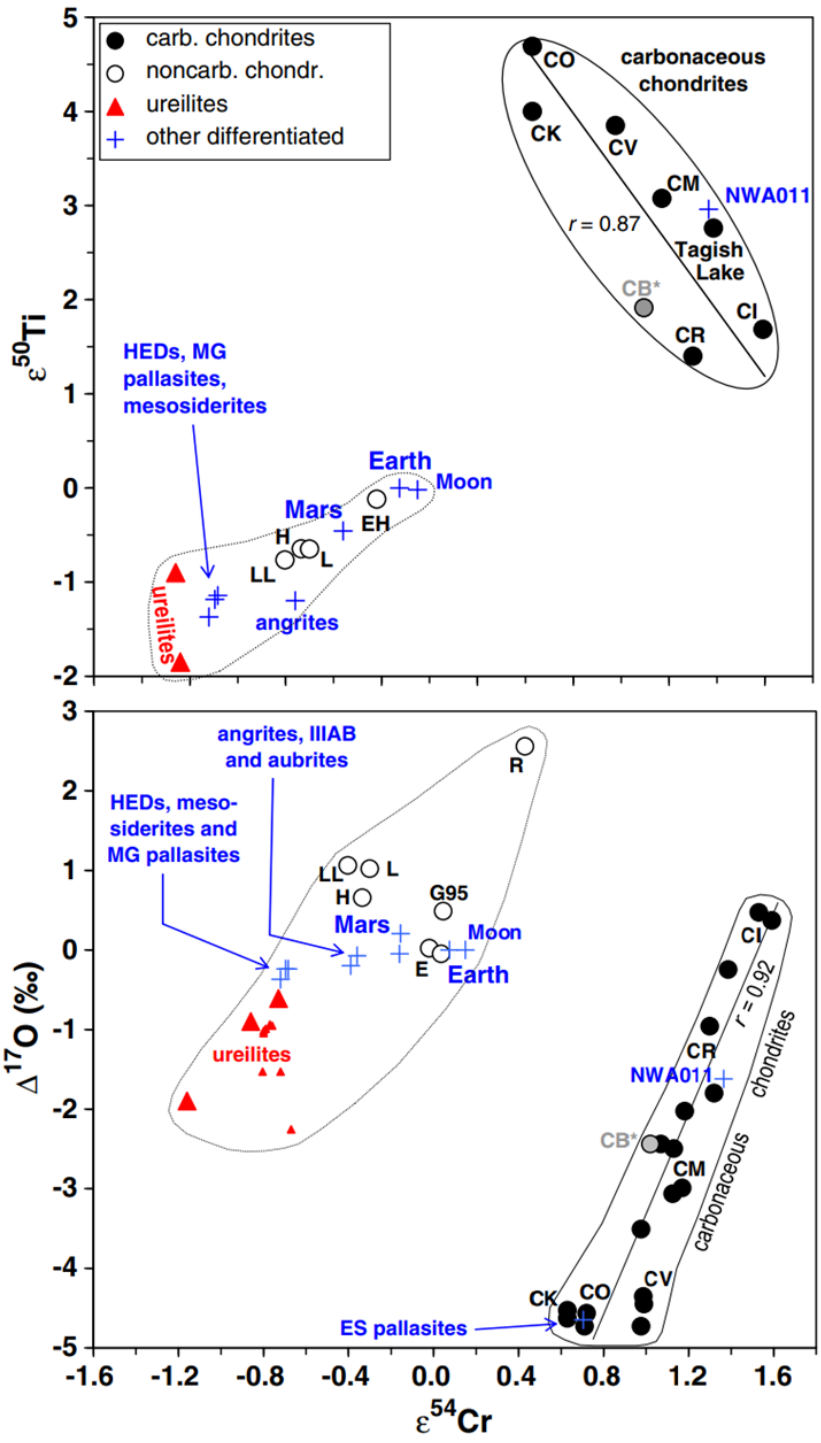

Figure 1.4 – The isotopic dichotomy of the Solar System from Warren (2011). Inner and outer Solar System materials are clearly separate from one another and form distinct arrays. The influence of Jupiter upon the radial drift of material to the inner Solar System (essentially, starving it of dust) is a popular explanation for this pattern. Smaller red triangles represent diverse ureilitic clasts in the Almahatta Sitta polymict meteorite.

The current paradigm postulates that Jupiter, by inhibiting the radial drift of dust and planetesimals interior to its orbit, caused a prolonged spatial separation of inner and outer Solar System materials (Morbidelli *et al.,* 2016). In tandem with starving the inner Solar System of material, this also produced an isotopic dichotomy as the outer disk evolved independently of the inner disk.

1.3 Meteorite taxonomy

Meteorites are naturally delivered objects from a broad range of planetary bodies, that, with the exception of the small cache of mission returned material to date, remain the only direct and plentiful sample set of the early Solar System. A meteorite *fall* is where stones are rapidly recovered after landfall and are associated with a witnessed fireball event or actually observed to fall, and as such are usually minimally weathered. Falls are rather rare, but recent advances fireball monitoring (*e.g.,* The UK Fireball Alliance; UKFall) have increased the likelihood of recovering stones (Daly *et al.,* 2020). A meteorite *find* is a stone recovered without association to an observed fireball, and often have resided on the Earth's surface for an extended period prior to collection. Many such samples have been collected from systematic searches in hot and cold deserts where the conditions are favourable for preservation and discovery (Krot *et al.,* 2014; Weisberg *et al.,* 2006).

The meteorite record can be broadly subdivided into those that experienced melting and differentiation (achondrites, irons and stony irons) and those that did not (chondrites) (Weisberg *et al.,* 2006). The latter are important caches of information about the dust in the early Solar System and primitive asteroids. Within their texture, mineralogy and chemistry is a record of the ~4.5 Ga processes that formed the planets and asteroids, permitting critical comparison between numerical models and extant ground based, telescopic and mission observations.

Normally, meteorites are grouped according to their similarities. As outlined in detail in Krot *et al.* (2014) and Weisberg *et al.* (2006), but briefly summarised here: chondrites consist of

three major *classes*: Ordinary, Enstatite and Carbonaceous. Each is subdivided into *groups* based on 5 or more specimens sharing similar petrography, mineralogy, and bulk chemical / isotopic properties (Krot *et al.,* 2014). There are ten groups of recognised carbonaceous chondrites: CI, CY, CM, CO, CV, CR, CH, CB, CL and CK, and one suggested group, the CTs, with the first letter C denoting the term carbonaceous and the second the name of the first discovered meteorite (usually fall) of that group. A group is commonly interpreted to represent a single planetesimal of origin, called a *parent body*. Chondrite *clan* is used as a higher order of classification than group, but lower than class, implying potential petrologic kinship. Most chondrites are prescribed a 'petrologic type' (Van Schmus and Wood, 1967), providing a measure of alteration from 1-7 (Fig. 1.5). Type 1 meteorites are entirely altered by water-rock interactions, whereas the highest, type 6, sometimes 7, are recrystallised due to thermal metamorphism. Type 3 is considered the most 'pristine' and unmodified by either process (though the existence of any truly unmodified material is exceptionally rare, or even debated), possibly representing 'starting materials' from which other petrologic types are derived (Abreu, 2018). Some meteorite groups, including as the CM chondrites, are subdivided at the 0.1 scale to provide increased resolution (Browning *et al.,* 1996; Howard *et al.,* 2015; Rubin, 2015; Rubin *et al.,* 2007). This is due to the combination of very variable degrees of thermal and/or aqueous processing between different members of the same group, and the plenitude of material displayed by that group (which offers a larger selection of material to identify different alteration grades).

1.3.1 The chondritic components

Chondrites are essentially cosmic sediments, consisting of two major components, chondrules and matrix, together with minor instances of Calcium Aluminium Inclusions (CAIs), Amoeboid Olivine Aggregates (AOAs), metal and sulphide. Collectively, these form an accretionary texture known as the chondrite assemblage (Brearley and Jones, 1998;

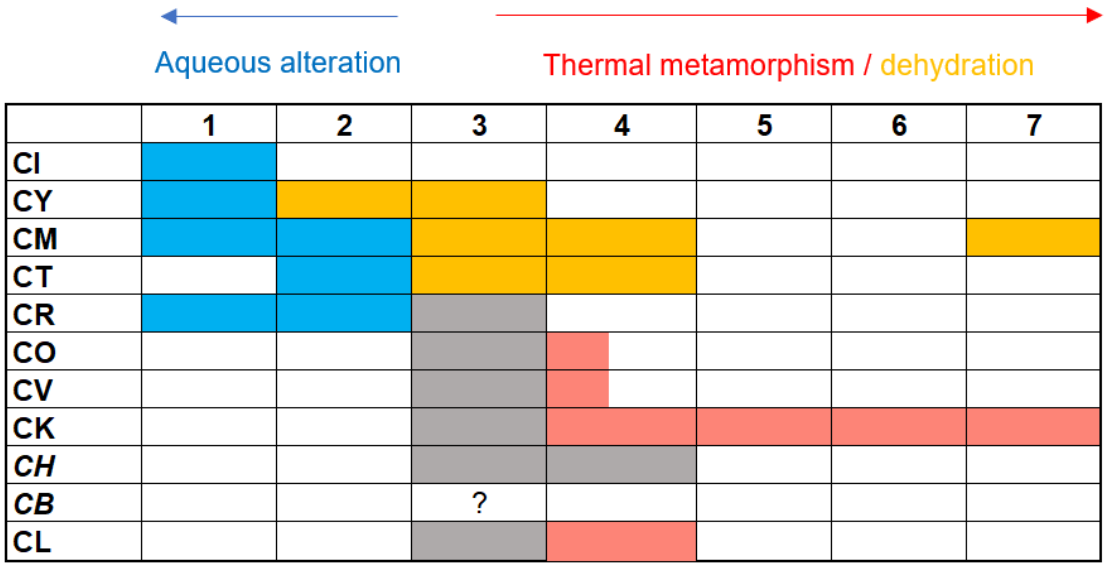

Figure 1.5 – The known carbonaceous chondrite groups and their petrologic types, modified after Van Schmus and Wood (1967). Some chondrite groups (the CIs, CYs, CMs, CTs and CRs) underwent a stage of aqueous alteration to varying extents (King *et al.*, 2019; Krot *et al.*, 2014). In opposition, the CK chondrites underwent high levels of metamorphism (Krot *et al.*, 2014). The COs, CVs, CHs and CL chondrites are nearly all petrologic type 3, but most experienced mild aqueo-thermal alteration, but not enough to move beyond petrologic type 4 (Krot *et al.*, 2014). The CY meteorite group is very similar to the CIs, though it apparent that this group underwent an additional stage of dehydration after aqueous alteration (King *et al.*, 2019). The CMs and 'CTs' (yet to be formally recognised) likewise underwent aqueous alteration followed by dehydration (Irving *et al.*, 2022; King *et al.*, 2021; Suttle *et al.*, 2021). There is one reported metamorphic CM7 clast in Murchison (Kerraouch *et al.*, 2019).

Weisberg *et al.*, 2006). The CAIs are high temperature, rapidly formed (within 700,000 years) super-refractory nebula gas condensates (*e.g.*, anorthite, hibonite, spinel, melilite) dated at 4.568 billion years old (for the lastest re-evaluation of this number, see Piralla *et al.* 2023), accepted as the 'time-zero' anchor for the start of the Solar System (McKeegan and Davis, 2003). CAIs have ^{16}O-rich O-isotope compositions (Clayton *et al.*, 1973) in agreement with published O-isotope data of the solar wind and photosphere (Lyons *et al.*, 2018; McKeegan *et al.*, 2011), and therefore broadly represent the composition of the bulk Solar System.

Chondrules are small, igneous spherules typically ~ 1 mm in diameter but with a range from 20 μm in CH chondrites to 1 cm in CB chondrites (Friedrich *et al.*, 2015). They are ubiquitous (with rare exception in the CI chondrites), formed by ephemeral flash-heating

events in the protoplanetary disk (Krot and Nagashima, 2017). The exact cause of heating remains a salient, unanswered question, but the timescales of such events were brief, as evidenced by rapid cooling rates (Desch and Connolly Jr, 2002; Pape *et al.,* 2019; Stockdale, 2020), and numerous over several million years, apparent by the large spread of chondrule radiometric ages overlapping the initial stages of CAI formation and extending up to 5 Myr post CAI formation (Krot *et al.,* 2009). Olivine, pyroxene, metal, sulphide, and glassy mesostasis dominate the mineral budget with a variety of crystalline textures (Brearley and Jones, 1998).

Fine-grained, dusty matrix accreted alongside chondrules and CAIs to form the dominant 'groundmass', although the constituent proportions of the chondritic assemblage — including chondrule and CAI size — are very different from one chondrite group to another, indicating an apparent variation in matrix-chondrule availability with heliocentric distance (Krot *et al.,* 2009). In more pristine type 3 examples (Greshake, 1997), the matrix is a roughly proportional mixture of micron scale amorphous glass, metal, and sulphide (GEMS-like) and micron / sub-micron crystalline fragments of olivine and pyroxene similar in composition to chondrules, with a complement organic matter for meteorites sourced beyond the tar line (Krot *et al.,* 2009; Yurimoto *et al.,* 2008). Water ice would have originally been present but has long since evaporated or sublimated from the asteroids, though rare, fossilised remnants of water ice crystals have been reported in porous meteorites (Matsumoto *et al.,* 2019). This pristine fine-grained matrix (type 3.0) is susceptible to modification by heating and aqueous alteration reflected in the various chondrite groups by recrystallisation and replacement by phyllosilicates, respectively (Van Schmus and Wood, 1967).

1.4 The CM chondrites

The CM carbonaceous chondrites are the central foci of this thesis. A unique trait of this group is that they provide the only extensive, albeit incomplete, sample set of aqueous

alteration phenomena (Velbel and Palmer, 2011). The cause of this variation is innately linked to the disruption and re-accumulation mechanisms occurring the breakup of the original CM parent body (Michel *et al.*, 2020; Michel and Richardson, 2013), and most, if not all CM chondrites are breccias (Bischoff *et al.,* 2006; Lentfort *et al.,* 2021). For this reason, information regarding the geological history of the CM parent body(ies), is recorded not only between different CMs, but within individual meteorites. All CMs contain clasts to some degree or another, each exhibiting a different degree of alteration indicative of a unique environment of formation.

Correlating meteorites to a parent body is a process that requires the combination of ground-based telescopic and orbital observation with laboratory analyses of material (Greenwood *et al.,* 2020), and at present the nature, number and source location of the original CM parent body(ies) remains poorly constrained. Unusually short CM cosmic ray exposure ages of < 20 Ma, with a large grouplet spanning < 1 Ma (Nishiizumi *et al.,* 2014; Suttle *et al.,* 2021; Zolensky *et al.,* 2021) indicate that fragile CM material may not survive long in space as small fragments (Rubin, 2018), and / or that the latest breakup event occurred relatively recently compared to many other meteorites. It is possible that a plenitude of CM materials lies on favourable Earth-crossing orbits (Lee *et al.,* 2020), as they are the most plentiful group among carbonaceous chondrites with 21 CM chondrite falls and 704 finds listed on the Meteoritical Bulletin as of 2023 (*e.g.,* Gattacceca *et al.,* 2022). The common explanation is that they sample an asteroid breakup event, reflected by a primitive C-complex asteroid family in the main belt (Jenniskens, 2013; Jenniskens, 2018). As shown by Fig 1.6, recent CM and CM-like falls Maribo, Sutter's Mill, Flensburg and Winchcombe were fortuitously captured on camera (Bischoff *et al.,* 2021; Haack *et al.,* 2012; Jenniskens *et al.,* 2012; King *et al.,* 2022), and their flight trajectories define pre-atmospheric orbits close to the 3:1 resonance Kirkwood gap of the inner main belt (Fig 1.7). Asteroid families

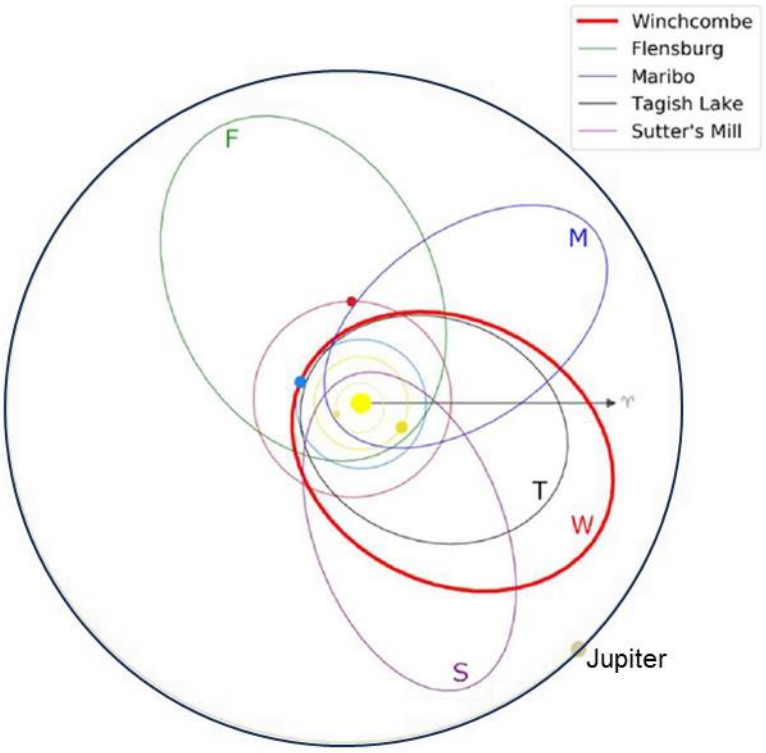

Figure 1.6 – Pre-atmospheric orbits of recent CM and CM-like falls Winchcombe (W) (King *et al.*, 2022), Sutter's Mill (S) (Jenniskens *et al.*, 2012), Maribo (M) (Haack *et al.*, 2012) Tagish Lake (T) (Brown *et al.*, 2000) and Flensburg (F) (Bischoff *et al.*, 2021). Planets are in the configuration at the time of the Winchcombe fall. Figure from King *et al.* (2022).

that lie close to this resonance band include the Eulelia, Polana, Clarissa, Erigone or Sulamitis families (Arredondo *et al.*, 2021; Jenniskens, 2013; Jenniskens, 2018; King *et al.*, 2022; Morate *et al.*, 2018; Nesvorný *et al.*, 2015; Walsh *et al.*, 2013), populated by C-complex asteroids that bear spectral resemblance to the CM chondrites (see Fig 1.1 and 1.7). During breakup and subsequent impact, material may be destabilised into the Kirkwood gap, sending fragmentary debris on trajectories to Earth or into near-Earth orbit. However, there has been some pushback regarding the feasibility of asteroid family breakup as a delivery mechanism, as none of the past 70 asteroid breakup events (Terfelt and Schmitz, 2021) appear to translate to an increased flux on material on Earth through deep time bar two, the L-chondrite parent body disruption during the Ordovician (Schmitz *et al.*, 2001), and possibly the Veritas family asteroid breakup during the Miocene (Farley *et al.*, 2006). This lead Terfelt and Schmitz (2021) to suggest that the delivery mechanism remains unknown

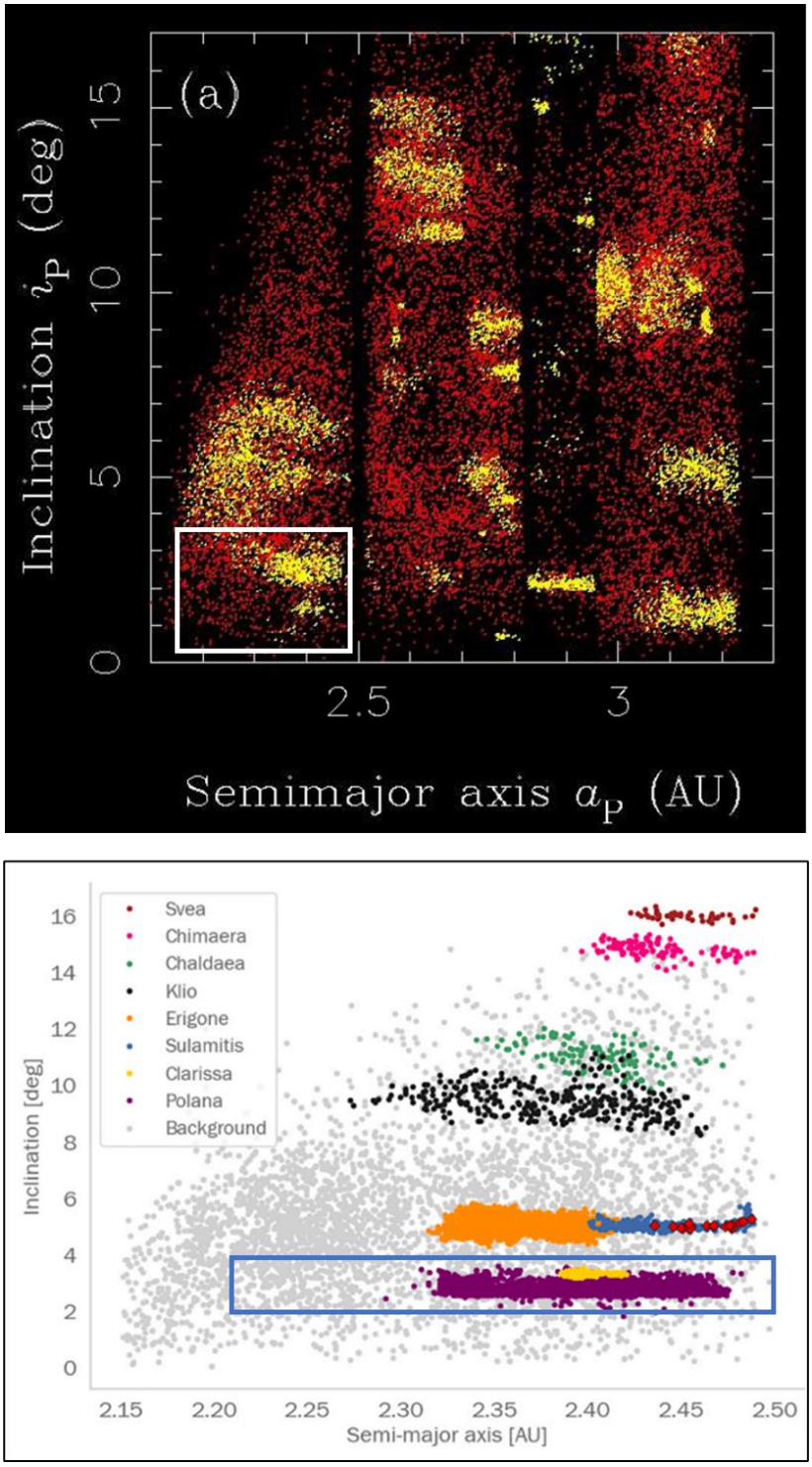

Figure 1.7 – Asteroid families within the main belt. (a) proper orbital parameters (semi-major axis and inclination) of the whole asteroid belt. Points in yellow outline clusters of asteroid families. The inner main belt is separated from the middle and outer belt by the 3:1 resonance Kirkwood gap at approx. 2.5 AU, from Nesvorný et al. (2015). (b) a higher resolution representation of the inner main belt from Arredondo et al. (2021). Likely candidates for a CM parent family are the Sulamitis, Erigone, Clarissa, Polana and Eulelia asteroid families (Eulelia is shown by the blue square after Walsh *et al.*, (2013), that both bear spectral resemblance to CMs and lie close to the Kirkwood gap.

but is highly specific. To suggest an alternative in addition to impacts: CM chondrites may have a delivery mechanism endemic to the asteroid itself. The work of Lauretta *et al.* (2019) and Melikyan *et al.* (2021) shows that Near Earth Asteroid Bennu is an active asteroid, experiencing surface mass loss via the ejection of 1-10 cm sized particles (the reader is referred to the front-page thesis image), possibly caused by thermal fracturing and volatile release. Particularly active asteroids in the main belt may periodically release material during episodes of particle ejection, and the plenitude of CM material may be linked to the continuous liberation of material during one such event.

1.4.1 Mineralogy and physical characteristics

Sample heterogeneity precludes a precise account of the general characteristics of CM chondrites. Very generally, CM bulk compositions are broadly solar, with a mild depletion in the most volatile elements with respect to CI chondrites, considered to be the closest match to the bulk solar composition (Braukmüller *et al.,* 2018). Surviving chondrule silicates are smaller than most chondrites at <0.5 mm in the longest dimension (Abreu, 2018) dominated by type I PO/POP chondrule fragments, and common, but minor constituents include whole or fragmental type II chondrules, metal and refractory inclusions, commonly spinel (Brearley and Jones, 1998). These coarse constituents reside in a fine grained, serpentine-rich matrix of variable Fe content (Metzler *et al.,* 1992; Suttle *et al.,* 2021). Uniquely, the silica-free iron hydroxy sulphide mineral tochilinite is common as an alteration product, rare in terrestrial environments but common in CMs (Brearley and Jones, 1998; Palmer and Lauretta, 2011; Pignatelli *et al.,* 2017; Pignatelli *et al.,* 2016; Zolensky and Mackinnon, 1986). Other minor minerals include secondary pyrrhotite, pentlandite, trace phosphides, phosphates, sulphates and smectites. The quantity of phyllosilicates is variable between meteorites from ~50-95 % as shown by X-ray diffraction data (Howard *et al.,* 2015; Howard *et al.,* 2009; Howard *et al.,* 2011b). Most CMs contain matrix mantles surrounding coarse phases as ‘accretionary rims’, widely considered a nebular feature (Bischoff, 1998; Metzler, 2004; Zanetta *et al.,*

2021; Zega and Buseck, 2003; Zolensky *et al.*, 1993) with potential for modification in a parent body environment. Preferentially orientated, sometimes flattened chondrules and phyllosilicate clumps form heterogeneously distributed petrofabrics within some lithologies,

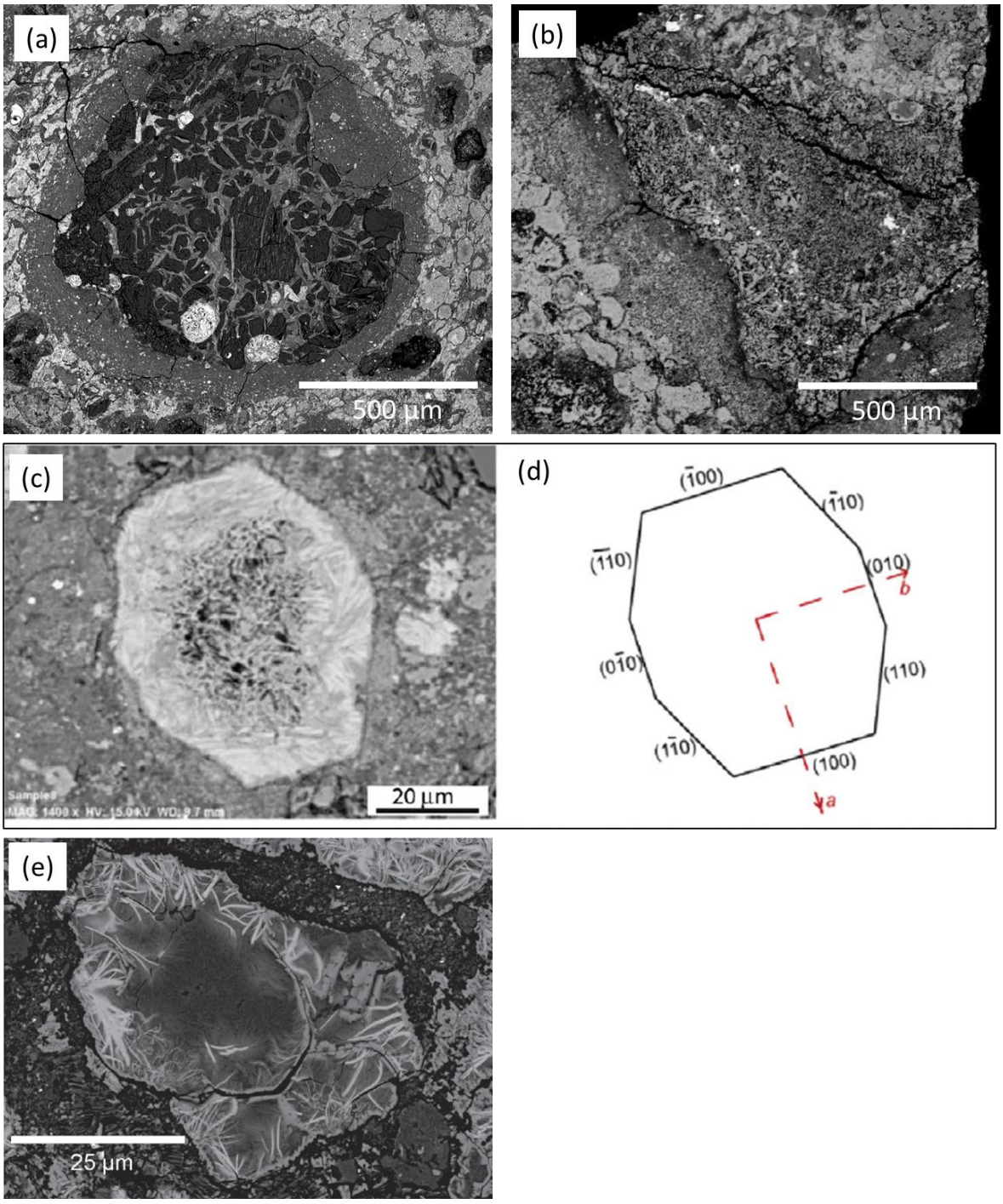

Figure 1.8 – Chondritic assemblage components with some CM specific minerals. (a) A chondrule from the Aguas Zarcas CM (this study) surrounded by a rim of fine grained, dark matrix. Interstitial to the chondrule and matrix rims are Tochilinite-Cronstedtite intergrowths (TCIs). (b) A heavily altered Calcium Aluminium Inclusion (CAI) in Winchcombe, also surrounded by dark matrix and TCI (Suttle *et al.*, 2023). (c) and (d) a TCI replaced after a euhedral pyroxene grain (Pignatelli *et al.*, 2016). (e) a TCI replaced after carbonate or a chondrule fragment. An accretionary rim of matrix surrounds this replacement product (Suttle et al., 2022).

indicative of repeated, low velocity impact (Floyd *et al.*, 2023; Hanna *et al.*, 2015; Lindgren *et al.*, 2014; Lindgren *et al.*, 2015; Tomeoka *et al.*, 1999). Recently, Bland and Travis (2017) suggested such textures could be the result of asteroid-scale convective mud flow, though this process is not (yet) widely accepted. Bulk densities are low compared to the chondrite average (Abreu, 2018; Macke *et al.*, 2011), owed in part to the serpentinization of olivine and pyroxene which causes a ~52 % volume increase (Malvoisin *et al.*, 2020). Measured porosities are high but variable (Corrigan *et al.*, 1997) and permeabilities low, with a study by Bland *et al.* (2009) showing porosity and permeability are not linked. Observed porosity and permeability are poor reflections of original asteroid characteristics, as the unconsolidated matter experienced gradual lithostatic compaction through accretion and impact (Hanna *et al.*, 2015) alongside serpentinization and cementation of pore space during aqueous alteration, further complicated by the fact that the most fragile regolith will not often survive atmospheric entry (Borovička *et al.*, 2019; Sears, 1998). Recent, orbital analysis of C-complex asteroids Ryugu and Bennu indicate very high porosities in the observable surface boulders (DellaGiustina *et al.*, 2019; Michel *et al.*, 2020; Sakatani *et al.*, 2021; Tricarico *et al.*, 2021), which has recently been corroborated by laboratory analysis of Ryugu particles (Yada *et al.*, 2022). High porosity in CM material may therefore be commonplace, but not well sampled by the meteorite record.

1.4.2 The aqueous alteration process

Aqueous alteration is a ubiquitous feature of CMs, evidenced by a complex assemblage of OH-bearing replacement products (Table 1.1) with clumpy, fibrous and pseudomorphic textures, chiefly composed of serpentine group phyllosilicates. As partially altered rocks, the alteration is mostly confined to the matrix and the smaller coarse phases, only extending to the largest chondrules in lithologies suffering the most pervasive alteration. Because of this, the hypothetical CM3 precursor has been a long-sought ‘holy grail’ in meteoritics, as identification of this subtype opens up the possibility of characterising the CM matrices

Table 1.1 – The most common secondary minerals in CM chondrites formed during the aqueous alteration process. The budget is dominated by the serpentine group minerals. Note this is not an exhaustive table, many other minerals exist in minor quantities or await discovery. Adapted from Abreu (2018) and Zolensky *et al.* (1988).

Group	Name	Formula
Serpentine	Chrysotile	$Mg_3Si_2O_5(OH)_4$
	Cronstedtite	$Fe^{2+}{}_2Fe^{3+}(Si,Fe^{3+})O_5(OH)_4$
	Greenalite	$(Fe^{2+}{}_2Fe^{3+}{}_2)_{2-3}(Si,Al)_2O_5(OH)_4$
	Berthierine	$(Fe^{2+}{}_2Fe^{3+}, Mg)_{2-3)}\,(Si,Al)_2O_5(OH)_4$
Hydroxysulphides	Tochilinite	$6Fe_{0.9}S.5(Fe, Mg)(OH)_2$
Sulphides	Pyrrhotite	$Fe_{1-0.17}S$
	Pentlandite	$(Fe,Ni)_9S_8$
Carbonates	Calcite	$CaCO_3$
	Dolomite	$MgCa(CO_3)_2$
Oxides	Magnetite	$Fe^{2+}Fe^{3+}O_4$

before alteration. Several recently recovered Antarctic CMs have closely met this criterion but lack a detailed evaluation of the matrix phases by TEM (Kimura *et al.*, 2020). Here, the matrix of Acfer 094, a uniquely primitive 'CM-like', is used as an approximation of the original CM3 matrix, containing: 40 % amorphous 'GEMS-like' silicate glass (sub-micron), and 60 % micron-scale crystalline silicates of 30 % olivine, 20 % pyroxene and 10 % other (Greshake, 1997; Yurimoto *et al.*, 2008), plus trace pre-solar grains, organics, and an undefined quantity of water ice (at the time of accretion).

1.4.2.1 Serpentinisation

Asteroidal aqueous alteration is analogous to terrestrial serpentinisation, a complex phenomenon with many reaction pathways and products. Mg serpentines are 1:1 layered

trioctahedral silicates built from repeat 0.72 nm thick structural unit cells (Carmignano *et al.*, 2020) each composed of a 'brucite-like' octahedral sheet of Mg—(O,OH) that shares an oxygen on one side with the apices of a 'tridymite-like' sheet of Si-O tetrahedra. Each 1:1 unit cell is linked to another by hydrogen bonding (Deer *et al.,* 2013). As the lateral dimensions of the octahedral and tetrahedral sites are not well matched, the sheets distort to accommodate the charge counterbalance (Fig 1.9), causing polymorphism as lizardite, chrysotile and antigorite (Deer *et al.,* 2013). In reality, the composition of the reactants and the conditions of alteration may vary, and serpentine responds by being multivalent and chemically diverse. Approximately 20 serpentine subtypes exist in terrestrial settings (Carmignano *et al.*, 2020), in contrast to the ~6 that are reported in CM chondrites (Abreu *et al.*, 2018; Table 1.1). Indeed, the scope for the discovery of new phyllosilicates in CMs is large as the unique, microgravity environments of asteroidal alteration are rarely comparable to terrestrial settings (*e.g.,* Bridges *et al.*, 2022; Suttle *et al.,* 2021; Topping *et al.,* 2023).

CMs are assigned petrologic type 2 with a few examples of complete, or near complete alteration assigned as CM1 and CM1/2 meteorites respectively (King *et al.,* 2017; Suttle *et al.,* 2021; Zolensky *et al.*, 1997). The variable degrees of aqueous alteration were recognised early (Bunch and Chang, 1980; McSween Jr, 1979; Tomeoka and Buseck, 1985; Zolensky *et al.,* 1997) by correlating progressive alteration with enrichment of Mg in matrix phyllosilicates. Fe-rich precursor phases such as kamacite, primary sulphide, glass and fayalitic olivine have higher dissolution rates than Mg-rich silicates (Velbel and Palmer, 2011; Velbel *et al.,* 2012; Velbel *et al.,* 2015); consequently, early formed matrix phyllosilicates are Fe-rich and late-formed Mg-rich (Browning *et al.,* 1996). Furthermore, the solar abundances of chondrites provide a plenitude of diverse cations, so a more holistic, formula for CM serpentines by Velbel and Palmer (2011) after Browning *et al.* (1999) is:

$$((\mathbf{Fe^{2+}},\mathrm{Mg,Mn,Ca,\ldots})_{3-x}(\mathbf{Al,Fe^{3+}})_x)(\mathrm{Si}_{2-x}(\mathbf{Al,Fe^{3+}})_x)\mathrm{O}_5(\mathrm{OH})_4$$

M-site (octahedral) T-site (tetrahedral)

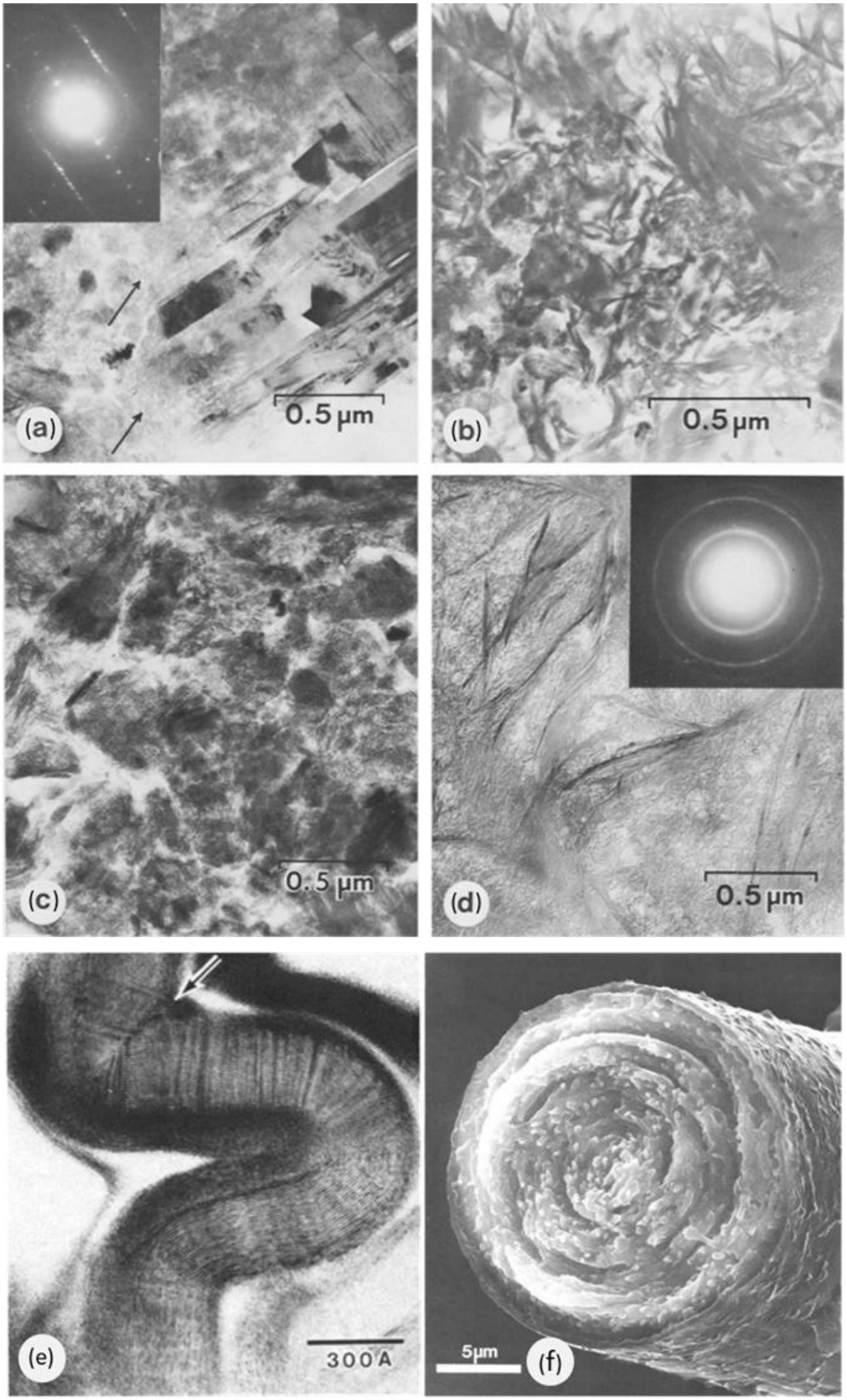

Figure 1.9 – The highly variable and disordered nature of serpentine and related minerals in CM chondrites. (a), (b), (c) and (d) are transmission electron micrographs showing coarse-grained platy, fine-grained platy, 'sponge-like' and fern-like morphologies (Barber, 1981). (e) a TEM micrograph of contorted cylindrical tochilinite (Tomeoka and Buseck 1989) and (f) A SE image of cylindrical tochilinite (Zolensky *et al.*, 1986).

Where $0 < x < 1$. Fe-rich solutions promote the substitution of Fe^{2+} and/or Fe^{3+} into the octahedral M-site to create greenalite, an Fe-rich serpentine. Furthermore, if the greenalite formation process is accompanied by coupled substitutions of trivalent Al or Fe^{3+} into the tetrahedral T site, berthierine and cronstedtite can crystallise, so long as the redox conditions are optimal (Pignatelli *et al.,* 2016; Pignatelli *et al.,* 2017; Vacher *et al.,* 2019b). Substitution of larger Fe for Mg worsens the serpentine structural mismatch creating additional crystalline disorder. In CMs, cronstedtite, greenalite and chrysotile are in solid solution.

1.4.2.2 Phyllosilicates and TCIs

As discussed above, differing alteration environments lead to a wide range of disordered serpentine structures (Fig 1.9), and this is a characteristic observed at the nanoscale in CMs (*e.g.,* Pignatelli *et al.,* 2018). Generally, these alteration products can be split into two categories:

The first category is the altered matrix interstitial to the coarse phases as well as accretionary rims. This material is typically low contrast in SEM BSE, Mg-rich, 'dark' and nearly always containing serpentine, tochilinite, sulphide and rare surviving 'GEMS-like' material (Bischoff, 1998; Metzler, 2004; Suttle *et al.,* 2021; Zolensky *et al.,* 1993). This represents a replaced version of the original, pristine matrix. Accretionary rim material, while similar, has been reported to differ in porosity and level of alteration when compared to the inter-chondrule material, suggesting a discrete formation region and perhaps pre-accretionary alteration (Metzler, 2004; Zanetta *et al.,* 2021; Zega and Buseck, 2003).

The second category encompasses isolated phyllosilicate clumps of intergrown Fe and Mg-serpentine with the mineral tochilinite (Zolensky and Mackinnon, 1986), an Fe-rich hydroxy sulphide mineral common in CMs but rare in terrestrial settings with the general formula (Vacher *et al.,* 2019b):

$$2Fe_{1-x}S \cdot n(Fe,Mg,Al,Ca)(OH)_2$$

Where $0.08 < x < 0.28$ and $1.58 < n < 1.75$. Tochilinite is composed of nanoscale alternating brucite and amakinite-like layers (Mackinnon and Zolensky, 1984). Collectively, these clumps were referred to as Poorly Characterised Phases (PCP) (Fuchs *et al.,* 1973; Mackinnon and Zolensky, 1984; Nakamura and Nakamuta, 1996; Ramdohr, 1963; Tomeoka and Buseck, 1985), now called Tochilinite-Cronstedtite Intergrowths (TCIs) (Palmer and Lauretta, 2011), and display a large range of pseudomorphic and chemical compositions seemingly dependent on the products they are replacing (Fig 1.10) (Pignatelli *et al.,* 2016). The amount of TCI can be variable from lithology to lithology; indeed, the phyllosilicate budget of some lithologies constitute up to 80 % TCI (Suttle *et al.,* 2023). Type I TCIs are found in association with kamacite beads distributed throughout the matrix, and around and within chondrules (Fig 1.10). The replacement products are tochilinite with minor cronstedtite and goethite (Palmer and Lauretta, 2011; Pignatelli *et al.,* 2017). *Bona fide* tochilinite is rare but has been reported in in Winchcombe (Fig 1.10) and possibly Aguas Zarcas (Kerraouch *et al.,* 2021; Suttle *et al.,* 2023). Type II TCIs are centripetal replacement products which appear to show inward crystallisation from core to rim (Fig 1.10). The precursors are euhedral olivine, pyroxene and carbonate grains, evidenced by the existence of these minerals in the core of some type II TCIs and the occurrence of convincing mono- and polycrystalline pseudomorphic geometry (Fig 1.8) (Pignatelli *et al.,* 2016; Suttle *et al.,* 2023). Many Type II TCIs are mantled by fine grained accretionary rims that resemble those around chondrules, suggesting the type II TCI precursors were suspended in the nebular gas during their history (Haack *et al.,* 2012). Type II TCIs vary between meteorites in both morphology and composition (Fig 1.10): in weakly altered lithologies they appear platy, with lath-like intergrowths of tochilinite, cronstedtite and sometimes pentlandite; in moderately altered lithologies they are often compositionally zoned with an Fe-rich rim and a fibrous, Mg-rich core often in association with carbonate, indicating a changing aqueous environment; in heavily altered lithologies the TCIs become progressively Mg-rich, fibrous, homogenous, and begin to lose coherent shape; and in completely replaced lithologies type

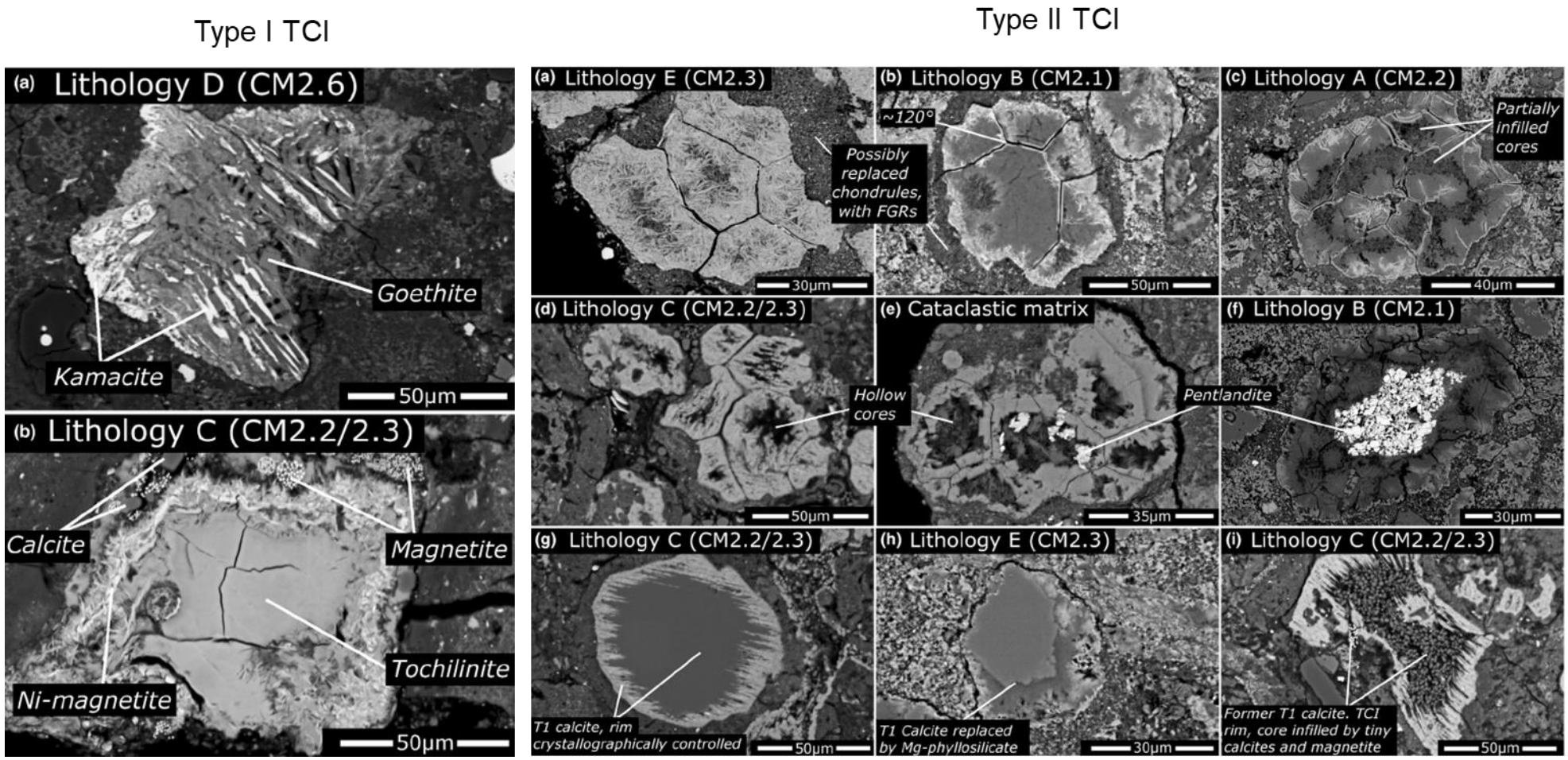

Figure 1.10 – Examples of both type I and type II TCIs as evidenced from the Winchcombe meteorite. Lithology designations strictly refer to the Winchcombe meteorite. Figures are slightly modified after Suttle *et al.* (2023).

II TCIs are absent, but matrix domains of elevated iron content in between Mg-rich, pseudomorphed chondrules may represent the final stage of TCI evolution (Suttle *et al.*, 2023). TCIs have a wide compositional range, notably with respect to 'FeO'/SiO_2 and S/SiO_2 ratios and both Rubin *et al.* (2007) and Lentfort *et al.* (2020) conclude this is correlated to the degree of aqueous alteration. As alteration proceeds, Fe and S concentration in the altering fluid is reduced and the TCI replacement products become more Mg-rich.

For all CM phyllosilicates, nanoscale diversity poses a challenge for *in situ* petrography due to the lack of matrix matched standards, coupled with the unavoidable risk of targeting multiple minerals with a single SEM or EPMA spot analysis. As such, mineral identification by typical stoichiometric methods is limited. Recent TEM work on Winchcombe suggests the existence of undiscovered, S rich serpentines, which may be one of many new meteoritic phyllosilicate minerals yet to be recognised (Bridges *et al.*, 2022, Topping *et al.*, 2023)).

1.4.2.3 Carbonate, magnetite, and sulphide

Carbonates are ubiquitous within CM matrices (Fig 1.11). Aragonite, calcite, breunnerite, and dolomite are present with monocrystalline and polycrystalline habits (Lee *et al.*, 2014), often intergrown with sulphide, tochilinite or magnetite (Tyra *et al.*, 2007; Tyra *et al.*, 2012; Vacher *et al.*, 2017). Detailed petrographic examination reveals complex relationships and isotopic characteristics, indicative of discrete pulses of fluid evolution (Farsang *et al.*, 2021) (Fig. 1.11). Calcite typically dominates CM2s and CM1s, although dolomite has been reported in the most altered CM chondrites (King *et al.*, 2017, Zolensky *et al.*, 1997, Lee *et al.*, 2014, Tyra *et al.*, 2016). Carbonates are typically divided into early formed (T0 and T1) and late-formed (T2) as evidenced by their ^{16}O-poor and ^{16}O-rich oxygen isotope compositions, respectively (Tyra *et al.*, 2012). Early formed carbonates are T0, T1a, T1b and T1c varieties and are mostly monocrystalline (Fig 1.11), but occasionally polycrystalline individuals. T0 calcites are solitary (Vacher *et al.*, 2017), often aragonite, while T1a, T1b and T1c are associated with serpentine/tochilinite; Fe-Ni metal and sulphide; and magnetite

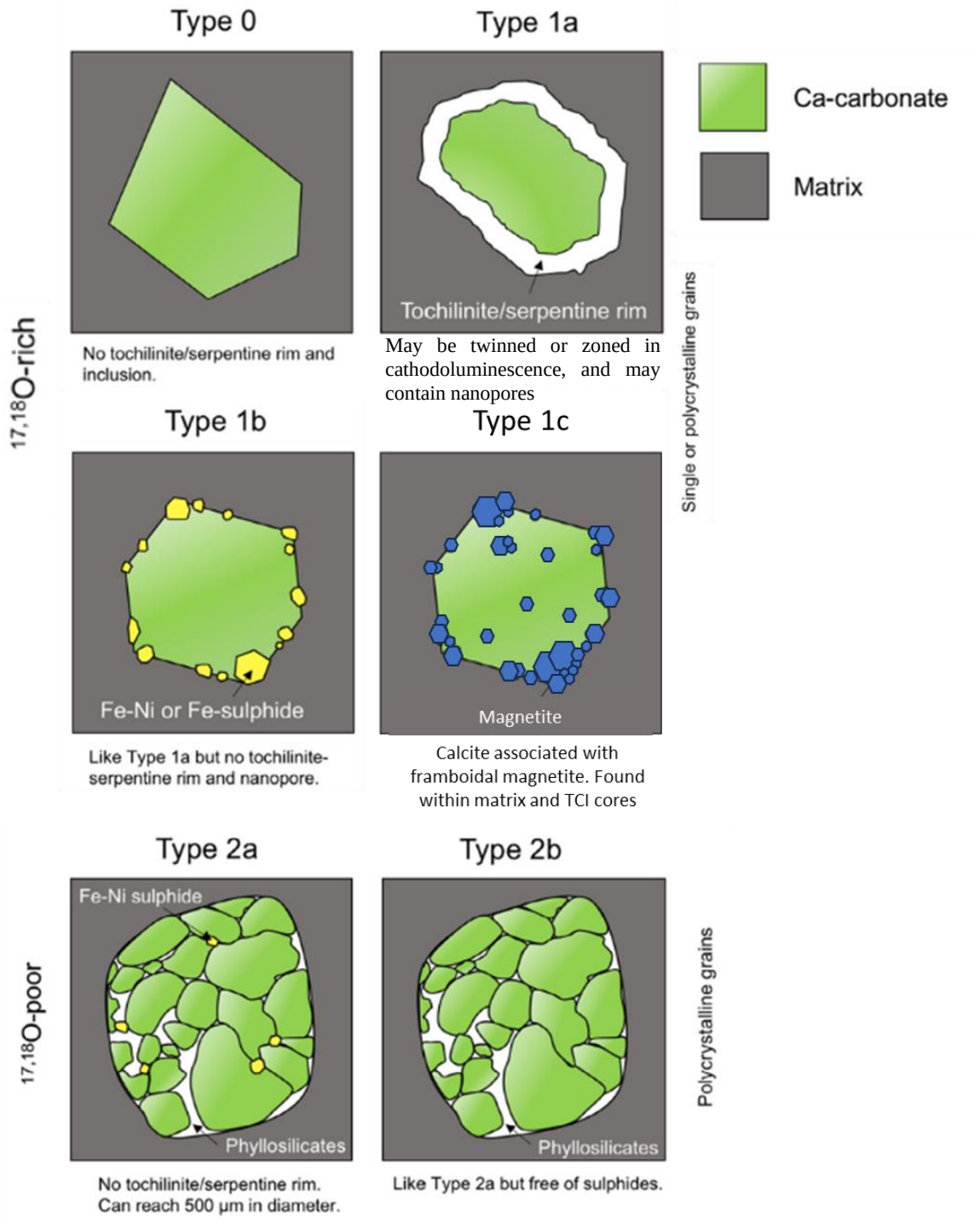

Figure 1.11 – The morphology of different carbonate grains in CMs (Lee *et al.*, 2014; Tyra *et al.*, 2007; Tyra *et al.*, 2012), modified after Vacher *et al.* (2017) to include the type 1c grains reported in Farsang *et al.* (2021). Differing crystal morphologies are a consequence of discrete fluid pulses occurring under variable conditions and fluid chemistry.

respectively (Farsang *et al.*, 2021; Lee *et al.*, 2014; Tyra *et al.*, 2007; Tyra *et al.*, 2012). Late formed carbonates are named T2a and T2b, exhibiting polycrystalline masses of calcite or dolomite in association with phyllosilicates and commonly replacing chondrules (Lee *et al.*, 2014). T2a are also associated with sulphide (Fig 1.11). Magnetite is normally absent or

minor in CM2 meteorites, but occasionally present in highly altered CM2s and CM1 and CM1/2 meteorites as massive, platy and framboidal habits (Farsang *et al.*, 2021; Suttle *et al.*, 2023) suggesting a direct precipitation from a fluid as the predominant formation mechanism (potentially syn- carbonate precipitation).

Primary sulphides are rare, usually occurring as troilite / Ni-bearing pyrrhotite grains in surviving chondrules (Singerling and Brearley, 2018), otherwise the majority of the S budget is sequestered into tochilinite, S-bearing serpentine or secondary Fe-depleted pyrrhotite and pentlandite. The Fe/S ratio of pyrrhotite appears to trace the degree of oxidation and sulphidation but necessitates high-precision EPMA data (Schrader *et al.*, 2021). Highly altered CMs and CM-like meteorites, such as Kolang and Flensburg, contain large, ~100 μm laths of recrystallised pyrrhotite (Bischoff *et al.*, 2021; Schrader *et al.*, 2021), indicating prolonged alteration and redistribution of sulphur, potentially at elevated temperatures (> 100 °C).

1.4.2.3 Alteration conditions and timescales

Radioactive ^{26}Al is the currently favoured canonical source of parent body heating in early planetesimals. As the half-life of ^{26}Al is very short at 7.17 x 10^5 years, its source must have been coincident with the collapse of the molecular cloud *e.g.*, injected by a nearby supernova (*e.g.*, Gounelle, 2015) or synthesized by the young Sun (Gaches *et al.*, 2020). The degree of heating experienced by a parent body is a function of both the availability of ^{26}Al, which is linked to formation time, and the potential for heat regulation (Fu *et al.*, 2017). Incorporation of this radioisotope caused the melting of water ice, reacting first with the most vulnerable GEMS-like amorphous phases, kamacite and chondrule mesostasis to produce the first saturated fluids, likely Ca, Na, Cl, S, and CO_2-rich brines (Nakamura *et al.*, 2022). Precipitation of first generation (T0 and T1) carbonates and the formation of tochilinite-cronstedtite intergrowths soon followed the melting of water ice (Suttle *et al.*, 2021; Tyra *et al.*, 2012; Vacher *et al.*, 2017) as shown by the mineralogy of incipiently altered lithologies

and fossilised ‘voids’ remnant of former ice pockets in Acfer 094 (Matsumoto *et al.*, 2019). Protracted alteration resulted in the dissolution of small Mg-rich silicates, increasing the Mg-activity of solution, replacing TCI material with Mg-rich serpentines and precipitating T2 calcites, dolomite, and magnetite. The final stages of alteration are defined by complete pseudomorphic replacement of large, crystalline silicates (King *et al.*, 2017; Suttle *et al.*, 2021).

The conditions of aqueous alteration are inferable from the stability fields of minerals, petrographic relationships, and isotopic compositions (Suttle *et al.*, 2021). The preponderance of evidence, particularly in carbonate, shows that the temperature evolution was prograde, rising throughout the course of aqueous alteration (*e.g.*, Vacher *et al.*, 2019b). Furthermore, experimental petrology has shown the co-precipitation of tochilinite and cronstedtite requires restrictive conditions: mildly alkaline, S-bearing fluids (pH 7-8) at temperatures of 80-150 °C (Suttle *et al.*, 2021; Vacher *et al.*, 2019b). Overall, published temperature estimates are in broad agreement from 0-300 °C, with the vast majority falling between ~20-200 °C; however, these estimates seldom show fine-scale agreement within these boundaries (Suttle *et al.*, 2021). This is due to the different methods employed to infer temperature (Fig 1.12). Molar water/rock (WR) ratios may be extrapolated from oxygen isotope data using mass balance calculations. Assuming a closed system of alteration (which may not be precisely correct –the reader is referred to section 1.7), estimates for volumetric WR ratios fall between 0.2-0.7, in the realm of ‘wet sand’.

The timing of aqueous alteration can be inferred from SIMS analysis of carbonates — the only quantitatively datable phases within CM chondrites — as sequestration of manganese into the carbonate structure permits analysis via the Mn-Cr decay system. As the initial

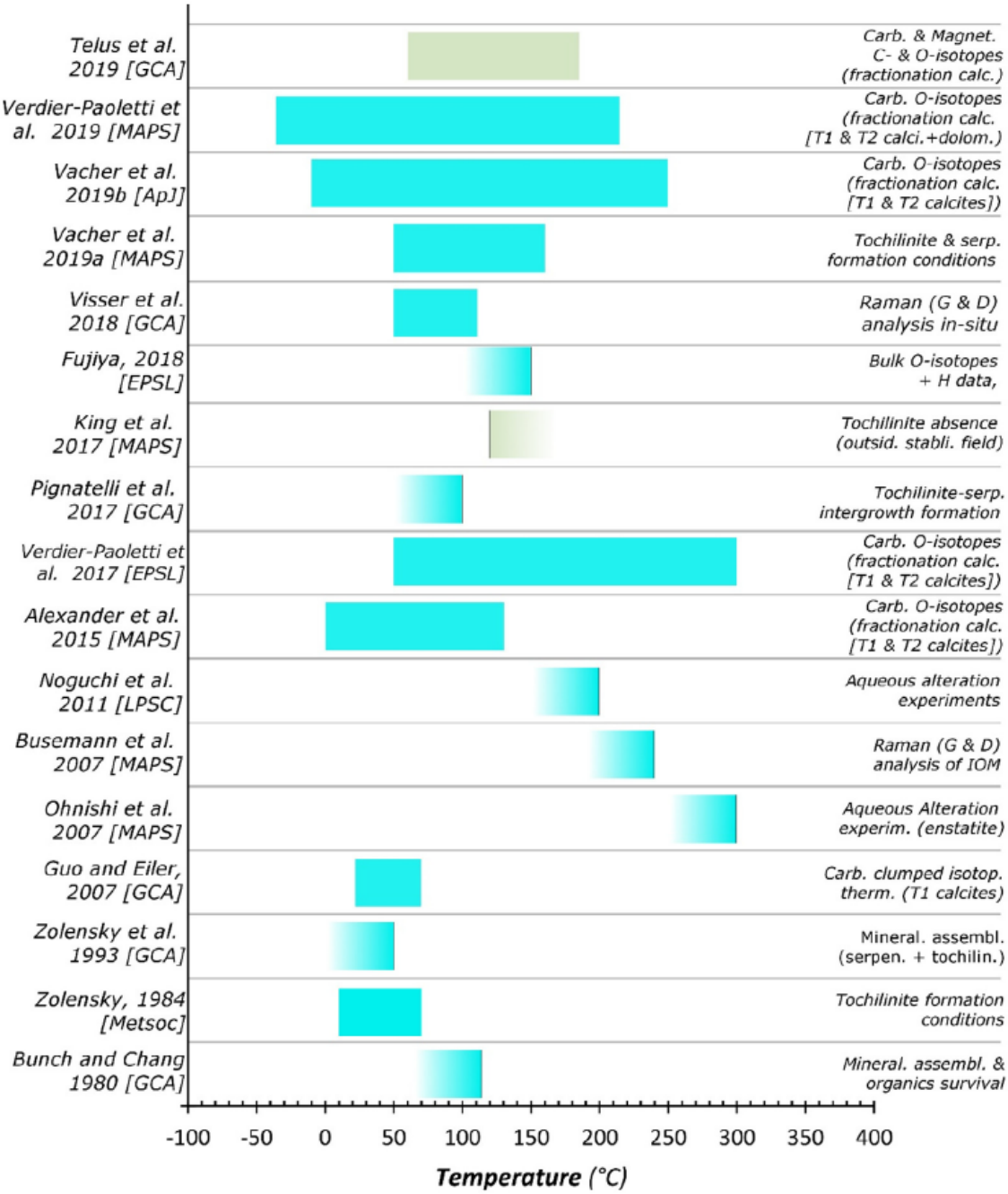

Figure 1.12 – A compilation of temperature estimates for CM chondrite alteration. Figure from Suttle *et al.* (2021).

$^{53}Mn/^{55}Mn$ of the Solar System is unconstrained, the Mn-Cr system is relative and requires anchoring to a time-zero, Pb-Pb age such as the angrite D'Orbigny or CAIs to produce absolute ages. These dates represent the crystallisation age of carbonate from water, assuming the Mn budget was not remobilised post-crystallisation (Vacher *et al.*, 2019a). There is sparse age data for CMs, but the range is consistent with alteration occurring ~4-6 Ma after CAIs (Fujiya *et al.*, 2012; Fujiya *et al.*, 2013; Jilly *et al.*, 2014; Visser *et al.*, 2020),

supporting the notion that water-bearing asteroids accreted late, had a deficit of ^{26}Al and did not reach ambient temperatures of above 300 °C. They were therefore probably quite large, on the order of several 10s -100s of km radius. However, McCain *et al.* (2023) highlighted the importance of using true matrix-matched standards for dolomites and calcites and stated that the lack thereof in previous studies (except for Fujiya *et al.*, 2012) may have produced younger ages in error. Matrix-matched dolomite ages in Ryugu particles (McCain *et al.*, 2023) and matrix-corrected ages in Flensburg (Bischoff *et al.*, 2021) are significantly older than CMs at ~1.8 and ~2.5 Ma after CAIs, respectively. Both Ryugu and Flensburg may represent different parent bodies (CI and C1-ungrouped), however Flensburg has convincing CM affinities, including an identical O-isotope composition to CM1 chondrites. An older alteration age than the current canonical estimates should therefore not be dismissed.

1.4.3 Sub-classification

Conventional meteorite classification is too 'low resolution' to accommodate CMs through designation of a type 1 or type 2 petrologic type; further subdivision, *i.e.*, a new, preferably single digit parameter is needed to better resolve incipiently altered CMs from moderately and heavily altered versions. Many have been developed (Table 1.2).

1.4.3.1 The 'MAI'

The first attempt to design a CM scaling procedure was the Mineralogical Alteration Index (MAI) as outlined by Browning *et al.* (1996). The MAI is quite innovative in its approach, representing alteration by the degree of Fe^{3+} enrichment in cronstedtite and serpentine, tracking coupled substitutions of trivalent (Fe^{3+}, Al) ions in the T1 site, and the resultant charge balance through divalent ion substitution (Fe^{2+}, Mg) in the M1 site (Browning *et al.*, 1996, Velbel and Palmer, 2011). The full MAI procedure is outlined in the appendix of Browning *et al.* (1997), but ultimately represents the amount of Fe-cronstedtite (MAI = 0) to Mg-serpentine (MAI = 2). The MAI has been criticised for its use of a non-intuitive algorithm with multiple screening steps applied to EPMA data (Rubin *et al.*, 2007) and the

Table 1.2 – The various classification schemes developed over the years for CM and CM-related meteorites. Meteorites are only included if one or more scales have been used (published) to classify degree of alteration. As can be seen, the approach varies significantly between each, though there are broad correlations between the Howard and Alexander schemes. Table is modified after Abreu (2018). References: [1]Hanowski and Brearley (2001). [2]Velbel *et al.* (2012). [3]Browning *et al.* (1996). [4]Rubin *et al.* (2007). [5]Howard *et al.* (2015). [6]Alexander *et al.* (2013). *Bells and Essebi are not classified as CM meteorites, but C2 ungrouped, and so are not equally comparable to the other classification schemes.

Meteorite	Stage[1, 2]	MAI[3]	Rubin subtype [-[4]	Phyl fraction [5]	Howard subtype[5]	Water/OH H (wt %) [6]	Alexander subtype [6]
Paris	0	-	2.7-2.9	-	-	-	-
QUE 97990	-	-	2.6	0.69	1.6	0.93	1.7
Y 791198	-	-	2.4	0.72	1.6	1.08	1.5
Bells*	-	0.46	-	0.82	1.4	0.46	2.3
Murchison	1	0.43	2.5	0.76	1.6	0.96	1.6
Pollen	-	0.53	-	-	-	-	-
Erakot	-	-	-	-	-	-	-
Boriskino	-	0.73	-	-	-	-	-
Murray	1	0.57	2.4-2.5	0.76	1.5	1.03	1.5
LEW 90500	3	-	-	0.78	1.6	0.99	1.6
Mighei	2	0.77	-	-	-	0.99	1.6
ALH 81002	4	-	-	-	-	1.21	1.3
Haripura	-	-	-	-	-	-	-
Nogoya	5	0.97	2.2	-	-	1.31	1.1
MAC 88101	-	0.81	-	-	-	1.11	1.4
Essebi*	-	0.82	-	-	-	0.77	1.9
Cold Bokkeveld	-	1.03	2.2	-	1.4	1.22	1.3
QUE 93005	6	-	2.1	-	-	-	-
MET 01070	-	-	2.0	-	-	-	-

limitation of the targeting of intergrown serpentines, among other reasons, and has not been reproduced for any additional CMs outside of the original Browning *et al.* (1997) publication, with the exception of the Paris meteorite (Marrocchi *et al.*, 2014). Despite its oversights, the MAI is the only CM scaling method to attempt to quantitatively track a specific alteration process (Fe^{3+} substitution), and modification / development of this procedure could be a powerful tracer of oxidation state in TCIs, for example.

1.4.3.2 Petrologic subtype

Petrologic criteria can be a useful semi-quantitative tool to assess degree of alteration, as most planetary institutions have access to a scanning electron microscope. The first comprehensive attempt to utilise a petrographic criterion was suggested by Hanowski and Brearley (2001), who correlated alteration to the extent aqueous attack on chondrules,

defining four stages of progressive phenocryst replacement. This was later expanded by (Velbel *et al.,* 2012) who extended this to a fifth stage. Later, Rubin *et al.* (2007) improved upon Browning's MAI by removing the need for a complex algorithm, instead outlining multiple petrologic criteria, including Hanowski and Brearley's suggestion of chondrule phenocryst replacement; the replacement of chondrule mesostasis; abundance of metallic Fe-Ni; and the volume percentage and composition of TCI (formerly PCP). Equal weighting is applied to all criteria and the alteration is expressed as a petrologic subtype between 2.0 (most altered) – 2.6 (least altered). The scale was later expanded to 2.7 (Rubin, 2015), then 2.9 (possibly 3.0, but this has yet to be formally agreed in the meteorite community) after the discovery of the Paris and 'Asuka' CM chondrites (Kimura *et al.,* 2020). Further modifications by Lentfort *et al.* (2021) suggested slight adjustments to the interpretation of TCI data. The Rubin *et al*. (2007) scale remains the most widely accepted scale, and indeed, the easiest to quickly apply to CM chondrites, though it is noted that this scale poorly reflects the most altered CM1 material.

1.4.3.3 Modal mineralogy

Breaking with the tradition of basing petrographic scales on SEM or EPMA data, Howard *et al.,* (2015) proposed a scale based on the modal abundance of minerals determined by calibrated, position sensitive X-ray diffraction. In contrast to the Rubin method, this scale is linear from 1.0-3.0, determined by the ratios of 'phyllosilicate' to anhydrous material and equally considers both CM1 and CM2 material. The notable advantage to this approach is the discrimination between Fe and Mg rich phyllosilicates which is a powerful tracer for the Fe/Mg activity of the reacting fluids. Disadvantages include the requirement of less commonly available instrumentation and the removal of petrographic context if complementary SEM data is missing. As such, there is a risk of ambiguity through sample heterogeneity and bulk 'phyllosilicate' abundances are often highly variable. Coupling a micro-XRD technique, as outlined in Bland *et al.* (2007), with micro fractions of

characterised powder mitigates this issue, but has yet to be successfully deployed on fine, micromilled powder. An expansion to the Howard *et al*. (2015) approach, and perhaps representing the best combination of the latter with Rubin's scale, is that proposed by Zanetta *et al.* (2019). ACADEMY (Analysing the Composition, modal Abundance, and the Density using Electron MicroscopY) is an advanced model applied to SEM and EPMA data to overcome the challenges associated with fine grained matrices. The method is promising but requires both SEM and probe contribution, plus commitment to understanding the exhaustive and detailed data reduction models.

1.4.3.4 C, N, H

Alexander *et al.* (2013) proposed two scaling procedures. The first, from 2.0-3.0, was intended to complement Rubin's scale, calculating petrologic subtypes based on bulk C, N and H isotopic compositions. However, this was found to scale poorly with respect to the least altered CMs when extrapolated upwards towards higher (*i.e.,* 2.6 and above) petrologic subtypes. In addition, the approach was incompatible with the CR chondrite group and other aqueously altered meteorites, including Bells and Essebi. Instead, a second scale of 1.0-3.0 was suggested based on the wt % H in water and OH, defining a statistically significant correlation with the reported phyllosilicate abundance as determined by Howard *et al.* (2015), and as such, the two have often been used in tandem. Interpretation of this scale preferably requires correction for the contribution of H from organics, but this is not always considered, introducing scatter and artificial inflation of the H content. Again, this scale is vulnerable to sample heterogeneity.

1.4.3.5 Heating

Some CM chondrites experienced post-alteration heating, likely through repeated, low intensity impacts, resulting in progressive dehydration and recrystallisation of phyllosilicates Several reviews have established classification schemes to quantify the degree of post-alteration metamorphism through XRD, infrared spectroscopy, and the thermal maturity of

organics (Chan *et al.,* 2019; King *et al.,* 2021; Tonui et a., 2014). This thesis did not encounter any obvious petrographic indicators for intense heating among the samples studied, such as shrinkage cracks in chondrule accretionary rims or recrystallised phyllosilicate matrix and metal, and so the reader is referred to the studies by King *et al.* (2021) and Tonui *et al.* (2014) for a detailed account of thermal effects in CM chondrites.

1.4.3.6 Brecciation

There is little doubt that the immediate, secondary parent body(ies) of the CM chondrites are, or were, diverse; C-complex asteroids Ryugu and Bennu, much to the surprise of many planetary scientist at the time, revealed a gravity-bound pile of accretionary debris with a spinning top structure (Fig 1.1), indicative of a long history of impact and reassembly through regolith processing. Panel (a) of Figure 1.13 shows the severity of a catastrophic asteroidal disruption event on a large, 100 km-scale planetesimal to produce smaller rubble piles of accretionary debris. CMs reflect these processes on the hand specimen and microscopic scale (Fig 1.1, 1.13). The highly complex, and sometimes paradoxical petrographic features of CMs are reflected in accretionary textures around chondrules and chondrule fragments (Metzler *et al.,* 1992), secondary minerals (Haack *et al.,* 2012), and sometimes even around clasts from pre-altered regions (Lee *et al.,* 2023), indicative of repeat processing and re-accumulation disruption both early and during the aqueous alteration process and long after such processes were active (Figure 1.13, (a)). The rubble pile structure of Ryugu and Bennu represents the culmination of this process from the beginning of the Solar System to the present day (Michel *et al.,* 2020). In thin section, clasts of surviving undisturbed CM lithologies are termed ‘primary accretionary rock’ after Metzler *et al.* (1992), juxtaposed with sharp or gradational boundaries between highly disturbed material, herein called ‘cataclastic matrix’ (Metzler *et al.,* 1992; Suttle *et al.,* 2023), the former representing distinct CM lithologies and the latter heterogeneous contribution from

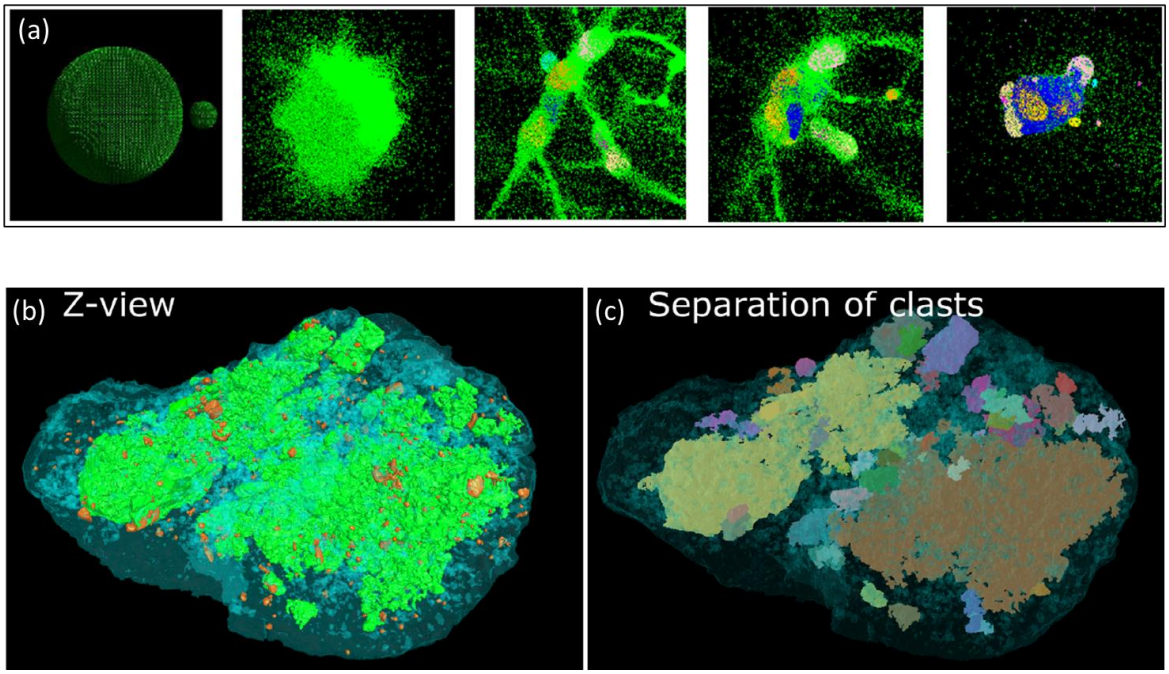

Figure 1.13 – (a) The breakup and reassembly of a 100 km parent body into a rubble pile asteroid. In this case the 1 km wide Near-Earth asteroid Itokawa (Michel and Richardson, 2013). (b) A µCT scan of a hand-specimen chunk of Winchcombe with different colours representing different phases: green represents clasts, orange represents high density phases, and blue represents cataclastic matrix. (c) a colour coded version of the µCT scan where lithologically unique clasts are highlighted in different shades (Suttle *et al.,* 2023). It can be observed that the effect of parent body disruption is reflected in brecciation from the asteroid to the hand specimen scale.

brecciated, impact derived, clastic material (Fig 1.13 (b)). Only the former confidently represents a specific alteration environment.

Of all the sub-classification systems discussed above, the Rubin *et al.* (2007) scale remains the most entrenched in the literature. Lentfort *et al.* (2021) has expanded this scale to assess primary accretionary lithologies within individual CMs breccias, encouraging new work to report any CM sample a 'petrologic range' (*e.g.,* Cold Bokkeveld CM2.0 - 2.7).

1.5 Oxygen isotopes

Oxygen isotope analysis is a well-established method for understanding asteroidal parent body provenance and can be used to great effect to trace water-rock interactions, providing insight into the specific formation environment (Clayton, 2003; Franchi, 2008). As such, they form the core of the coupled isotopic-petrography approach in this work.

1.5.1 Overview

Isotopes of all elements may vary in concentration from one phase to another by the process of isotopic fractionation. The extent of these variations is controlled by chemical and physical processes and are typically (but not always) small, requiring high precision measurement by a mass spectrometer.

Oxygen has many favourable characteristics for isotope geochemistry (Criss and Farquhar, 2008):

- As the third most abundant element in the cosmos, there is seldom too little oxygen for high-precision analyses.
- As a low mass element, isotope mass differences are relatively large and reflected in large fractionation factors.
- Oxygen is a multiphase element, readily reacting to form solids (*e.g.*, H_2O, SiO_2, Fe_3O_4), liquids (H_2O and organic compounds), and gases (CO_2, CO, H_2O).
- Oxygen has three stable isotopes (Table 1.3: ^{16}O, ^{17}O and ^{18}O), allowing systematic comparisons to be made in a 3-isotope plot (Clayton *et al.*, 1973) to explore both mass-dependent and mass-independent fractionation effects, a particularly important capability for the study of extra-terrestrial samples.

Table 1.3 - The three stable oxygen isotopes (Bao *et al.*, 2016)

Isotope	Symbol	Isotopic mass (u)	Solar System abundance (%)
Oxygen - 16	^{16}O	15.994	99.76
Oxygen - 17	^{17}O	16.999	0.038
Oxygen - 18	^{18}O	17.999	0.200

These points explain why O-isotope analysis is a fundamental cosmochemical tool to understand the origin of planets and asteroids. The Solar System is spatially heterogeneous

with respect to the three isotopes of oxygen (Clayton *et al.*, 1973) as recorded by the diverse spectrum of oxygen isotope data across all meteorites and returned samples (Franchi, 2008). By understanding why oxygen isotopes fractionate on a theoretical level, one can apply this understanding to the signatures expressed in meteorites to probe the processes and environments of formation at the beginning of the Solar System.

1.5.2 Mass-dependent fractionation in meteorites

While the chemical behaviour is identical between isotopes of one element, the difference in the relative mass manifests subtle variations in both kinetic behaviour and bond environment causing the phenomenon of mass-dependent isotopic fractionation (Criss, 1999; Criss and Farquhar, 2008). As the delta notation (the common form of showing variation in O-isotope composition) is an expression of ^{17}O and ^{18}O relative to ^{16}O (a difference 1 and 2 neutrons, respectively), any mass-dependent effects in the $^{17}O/^{16}O$ ratio are nearly always half that of $^{18}O/^{16}O$. This can be visually expressed as a slope of gradient ~0.52 on a 3-isotope graph (Clayton, 1973) with $\delta^{17}O$ as the abscissa and $\delta^{17}O$ as the ordinate (Fig 1.14). The line is called a fractionation line with a slope λ, known as the fractionation exponent (Matsuhisa *et al.*, 1978). A particularly convenient fractionation line is that of the Earth, called the terrestrial fractionation line (TFL), whereby almost all terrestrial rock samples fall along a single mass fractionation line (Fig 1.14) (Greenwood *et al.*, 2018).

Kinetic fractionation effects are rapid, incomplete, and unidirectional, reflecting the energy required to move isotopes from one region to another (Young *et al.*, 2002; White, 2015). Examples such as diffusion and evaporation favour lighter isotopes as they move faster and are commonly paired with open systems where the moving species is either sequestered away or lost from the main reservoir.

Equilibrium fractionation effects are bidirectional and occur when components in a system are in thermodynamic equilibrium (White, 2015). In this scenario, the mass-dependent effect is produced from differences in bond energies, specifically the vibrational frequencies of a

bond, which are lower for heavier isotopes (Criss and Farquar, 2008). Generally, heavier isotopes prefer to partition into the phase where the bonds are the shortest and strongest, or 'stiffest', which are associated with features such as high charge (oxidation state), low coordination number, and ordered crystal structure (Schauble, 2004). As an example, the small highly charged C^{4+} ion has a high ionic potential compared to H^{+}. It is for this reason that calcium carbonate is often enriched in ^{18}O and ^{17}O relative to the water it is precipitated from (*e.g.*, Zheng, 1999). The isotopic fractionation between two phases (a and b) in equilibrium is called the fractionation factor α, which can be directly related to the measured isotopic composition by:

Equation 1.1

$$1000 \ln \alpha_{a-b} \approx \delta_a - \delta_b$$

The fractionation factor broadly conforms to a temperature-dependent (T^{-1}) relationship with the extent of isotopic fractionation greatest at low temperatures (Criss and Farquhar, 2008). Experimental derivation of fractionation factors can therefore be used for palaeothermometry if the isotopes of the two phases in equilibrium are measured in a sample and α is known (Beaudoin and Therrien, 2009).

Another useful parameter is $\Delta^{17}O$ (Clayton and Mayeda, 1988) which is the expression of the relative excess or depletion in ^{17}O between a sample and the TFL (as defined by VSMOW):

Equation 1.2

$$\Delta^{17}O = \delta^{17}O-(\lambda \times \delta^{18}O)$$

With a λ of 0.52. Plotting this value as the ordinate on a 3-isotope plot rotates any mass-dependent fractionation line to the horizontal with the TFL as the abscissa, useful for assessing any deviance from mass-dependency and for identifying parent-body relationships (Fig 1.14). It is worth noting that nuances exist with respect to the fractionation exponent λ.

While a good approximation is 0.52 as defined by (Matsuhisa *et al.*, 1978), the relationship in Equation 1.2 actually approximates a power law (Miller *et al.*, 2002) and for most equilibrium fractionation effects λ is temperature-dependent, and can be process-dependent

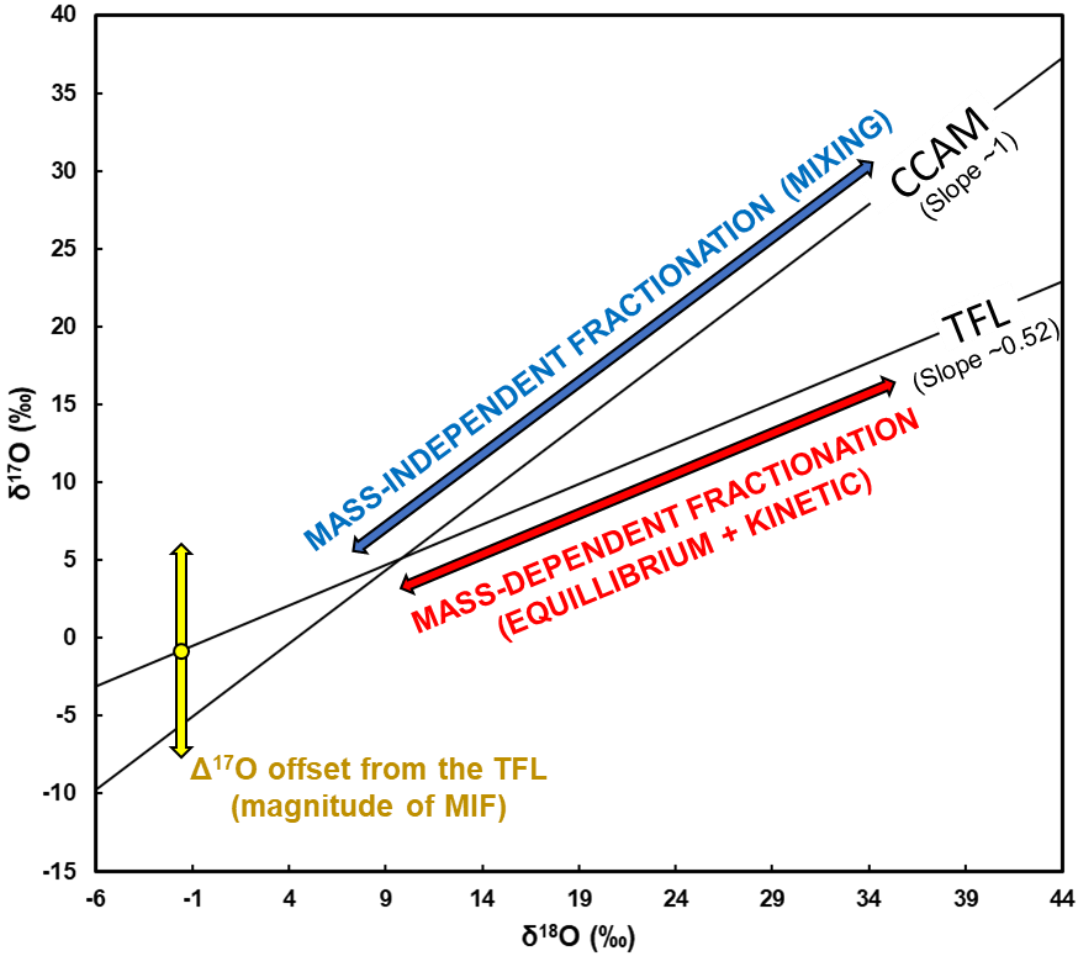

Figure 1.14 – Schematic demonstrating the relationships between mass-dependent and mass-independent fractionation effects. In this case, the terrestrial fractionation line (TFL) is plotted as an example of a slope ~0.52 line. The CCAM line, as defined by refractory minerals in Allende (Clayton, 1973), is an example of mass-independent fractionation with a slope of ~1. The $\Delta^{17}O$ value measures this mass-independent effect as an offset compared to the TFL

for kinetic effects (Young *et al.*, 2002). Linearisation coupled with careful consideration for λ is critically important for systems where small variations in $\Delta^{17}O$ are observed alongside large variations in $\delta^{18}O$. For that reason, this approach is not used here in line with the vast

majority of CM literature. CMs are a heterogeneous mix of high and low temperature components formed in different environments, rarely 100 % equilibrated, and as such any real deviations due to λ will be swamped by sample heterogeneity. The 'classical' expression in Equation 1.2 is therefore appropriate.

1.5.3 Mass-independent fractionation in meteorites

Early investigation into the oxygen isotope compositions of meteorites revealed unusual patterns (Clayton *et al.,* 1973); in particular, CAIs in the CV3 meteorite Allende had ^{16}O-rich compositions that did not obey the laws of mass-dependent fractionation and manifested as a slope ~1 line on a 3-isotope plot (Figure 1.14). This 'slope ~1 effect' is responsible for much of the O-isotopic heterogeneity in the Solar System (Fig 1.15). Mass-dependent fractionation lines are also observed within specific groups of related samples, often offset from one another, necessitating inheritance of an isotopic fingerprint not produced by mass-dependent processes (Franchi, 2008). Further investigation has revealed that all solar nebula anhydrous silicates — including chondrules from unequilibrated meteorites (Krot *et al.,* 2006), unaltered matrix (Sakamoto *et al.,* 2007; Starkey *et al.,* 2014; Vacher *et al.,* 2020) and even organics (Tartèse *et al.,* 2018) — inherit a slope ~1 signature, to varying enrichments or depletions, and the relative abundance of these components dictate the region in 3-isotope space that a particular planetary body resides (Yurimoto *et al.,* 2008). The principal slope ~1 line is the Carbonaceous Chondrite Anhydrous Mineral line (CCAM), first defined by Clayton *et al.* (1973). Other slightly offset slope ~1 lines have also been discovered through analysing refractory minerals in other meteorites using different techniques, including the Young and Russel (Y & R) and Primitive Chondrule Mineral (PCM) lines (Ushikubo *et al.,* 2012; Young and Russell, 1998). At present there is little consensus if the offset between these lines represent variation in the causal process in the disk or a mineralogical / analytical artifact. Three main theories have been proposed to explain the slope ~1 effect.

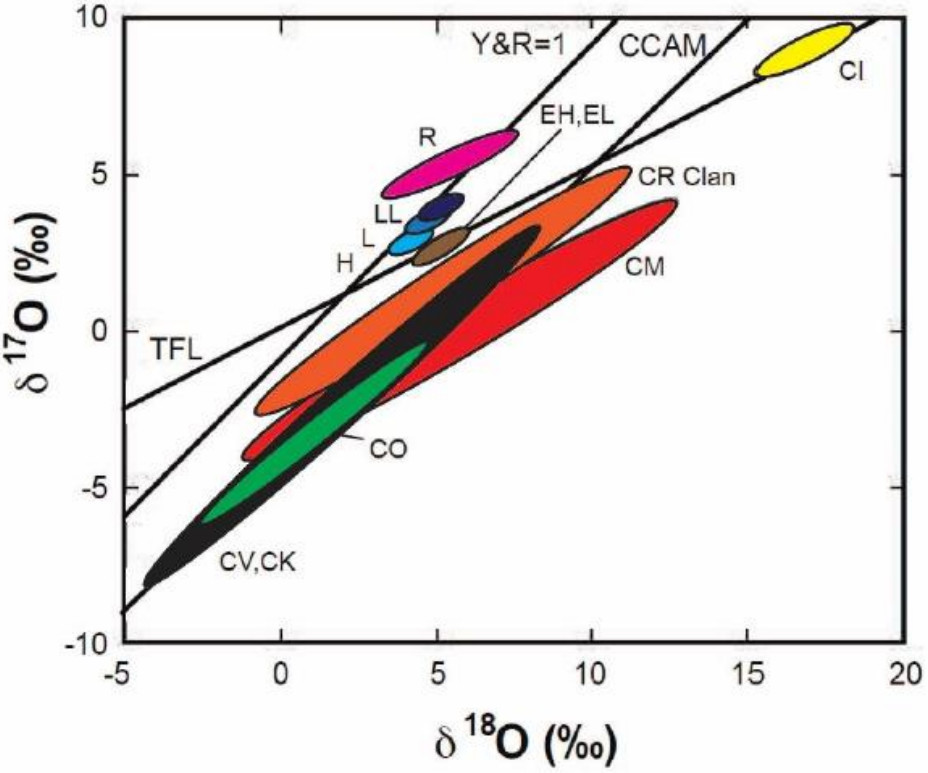

Figure 1.15 - 3 isotope plot of the chondritic meteorites, including ordinary, enstatite and carbonaceous. Both mass-dependent lines of slope ~0.52 (as shown by the individual ordinary chondrite groups H, L and LL) and mass-independent fractionation lines (such as the CM line in red, with a slope of ~0.7) are visible. The offset of each line is a result of variable quantities of components with an O-isotopic composition reflective of the ~slope 1 effect. Modified (coloured) after Franchi (2008)

1.5.3.1 Galactic evolution

The first proposed solution was the concept of continued injection of oxygen into the interstellar medium through repeat supernova explosions as the galaxy evolves. ^{16}O is a primary nuclide produced by the burning of helium and carbon; all stars produce this nuclide, so the concentration of ^{16}O will increase linearly with time through subsequent star deaths (Young *et al.,* 2008). Initially, Clayton (1973) suggested the ^{17}O and ^{18}O compositions of the Solar System were relatively 'set', and the heterogeneous insertion of a pure ^{16}O carrier by a nearby supernova could explain the slope ~1 line; although to date, there has been no meteoritic or observable evidence for such a pure ^{16}O carrier. Consequently, this concept

was expanded into the Galactic Evolution Model by considering that both ^{17}O and ^{18}O are products of secondary nucleosynthesis. These isotopes require extant nuclides inherited from dead stars, such as ^{16}O, ^{17}F, and ^{14}N, to allow their formation in supernovae. The result is that while ^{16}O increases linearly with time in the interstellar medium (ISM), ^{17}O and ^{18}O increase linearly together with the square of time (Jacobsen *et al.*, 2007; Young *et al.*, 2008). These signatures may be inherited in dust grains, which form from the ISM gas at a specific point and remain stable up to 1100 Myr. While the gas phase continues to evolve, the dust will hold on to these 'older', relatively ^{16}O-rich signatures. A key testable aspect of this hypothesis is the oxygen isotope composition of the Sun. As it mostly represents the gas phase, the Sun should be enriched in the isotopes of ^{17}O and ^{18}O relative to the orbiting planets which were mostly formed from dust. Measurements of the solar wind by Genesis and measurements of the ^{18}O composition of the solar photosphere (Lyons *et al.*, 2018; McKeegan *et al.*, 2011) suggest the sun is ^{16}O enriched at $\delta^{18}O$ of roughly -50 ‰, similar to CAIs, and so the Galactic Evolution Model has not gained traction as an accepted explanation.

1.5.3.2 Photochemical self-shielding of CO

The second theory is that of isotope-selective photochemical self-shielding of carbon monoxide (CO) in the protoplanetary disk (Clayton, 2002; Thiemens and Heidenreich III, 1983). This effect is dependent upon the fact that each isotopologue of CO dissociates after absorbing a UV photon of a specific wavelength. In a protoplanetary disk with the UV source (*e.g.*, a T-Tauri stage star) at its core, wavelengths of UV radiation will be radiated outwards through the cloud where they will dissociate CO (Fig 1.15). As $C^{16}O$ is by far the most abundant isotopologue, the specific UV wavelength required for its dissociation will rapidly

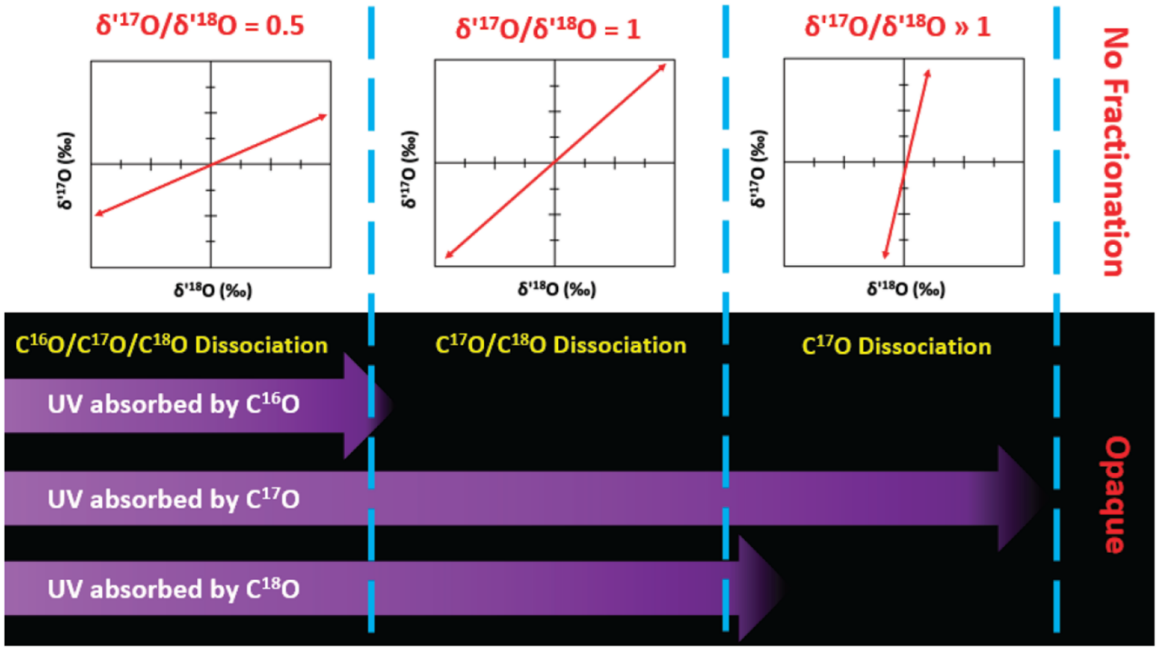

Figure 1.16 – The effect of photochemical self-shielding in the protoplanetary disk as a function of heliocentric distance from left (Sun) to right (outer Solar System). Opacity is the major control. A slope~1 effect will occur in the region where both $C^{17}O$ and $C^{18}O$ will dissociate but $C^{16}O$ will not. Figure from (Thiemens and Lin, 2021).

become attenuated, shielding distant $C^{16}O$ from further dissociation as heliocentric distance increases. In opposition, the wavelengths required to dissociate the less abundant $C^{17}O$ and $C^{18}O$ will penetrate further into the cloud and any liberated oxygen will be comparatively, and equally enriched in ^{17}O and ^{18}O, producing a slope~1 effect (Fig 1.16). As distance increases, the second most abundant isotopologue, $C^{18}O$, will also eventually attenuate, or self-shield its dissociation wavelength, and the only dissociated oxygen will be ^{17}O, leading to a slope >1, or a ^{17}O 'pure effect' in the very farthest reaches (Fig 1.16). Once dissociated, the free oxygen will then be available for condensation into solid phases such as silicate and water ice. It is thought that water ice formed beyond the snow line in the region where there was equal dissociation of ^{17}O and ^{18}O, and the radial drift of this material towards the inner disk contributed to the oxygen budget of the forming chondrules and CAIs and therefore, directly causes the extension of the slope~1 effect from the inferred solar values reported by Genesis (McKeegan *et al.*, 2011), to more positive values shown by the CAIs, chondrules and dust (Lyons and Young, 2005).

There are some issues with the self-shielding model. The most prominent is the inevitable back-reaction of dissociated oxygen with the CO gas reservoir, eliminating any self-shielding heterogeneity. The condensation and freezing of water ice, followed by radial drift is a suitable workaround but requires self-shielding to occur beyond the snow line. This necessitates a low disk opacity for the UV radiation to penetrate to heliocentric distances cold enough to promote condensation, which is highly unlikely at the midplane. Two models account for this issue, the first is that shielding occurs in the placental molecular cloud and the signature is inherited via infall of material (Yurimoto and Kuramoto, 2004), whereas the second occurs at the more diffuse edges of the protoplanetary disk either from the Sun at an angle from the centre outwards (Fig 1.17) or from an outside far-UV source, irradiating the outer edges of the disk (Lyons and Young, 2005). Such scenarios have been elegantly modelled, producing very good matches for the observed slope ~1 effect.

Despite this workaround, the self-shielding model has been subject to criticism by a group of researchers at the San Diego group. Specifically, the review by Thiemens and Lin (2021) that states that while self-shielding is a real phenomenon, the signatures it produces are unlikely to be transferred to meteorites due to a plethora of potential back-reaction mechanisms and the current gaps in understanding the physical chemistry of dissociation, including the likelihood of undiscovered isotope effects. This is evident in the failure to reproduce the mass-independent variations in the laboratory under the specific conditions (1.5-107 nm) required to dissociate CO by self-shielding. Furthermore, other oversights are proposed by Thiemens and Lin (2021), including the reliance of self-shielding on the measured isotopic composition of the Sun by Genesis (McKeegan *et al.,* 2011) which requires a large correction factor, and the assumption that the photochemical absorption cross sections of the dissociating species accounts for the entirety of the isotopic variation; however, as the cross sections of minor isotopes are difficult to measure this may propagate large errors (1000s ‰) into self-shielding models, which to date have been mostly ignored.

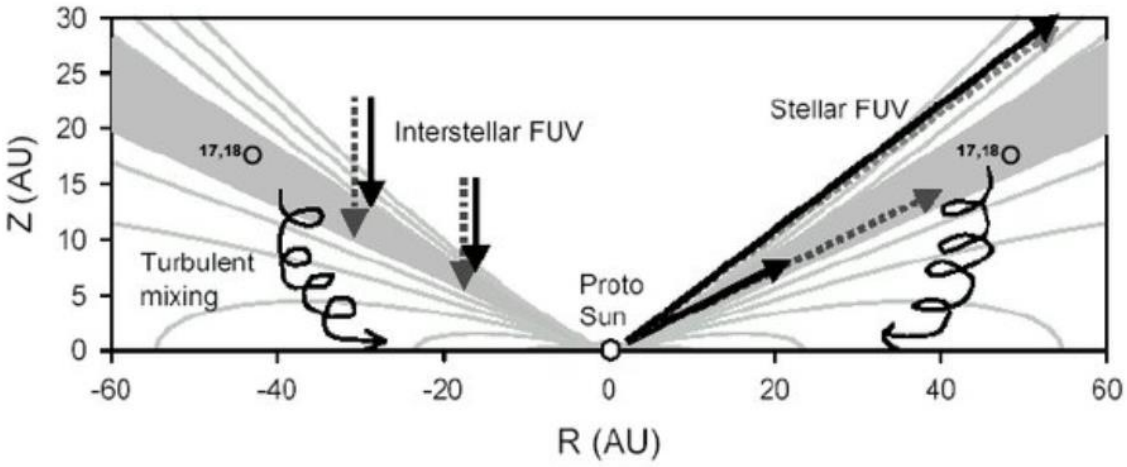

Figure 1.17 – A mechanism where self-shielding occurs in the diffuse edges of the protoplanetary disk, were dissociated ^{17}O and ^{18}O then falls down into the midplane via turbulent mixing. It will freeze into water, and then be transported into the inner solar system. Figure from Lyons *et al.* (2005)

The reader is referred to the detailed review by Thiemens and Lin (2021) for a comprehensive account of these issues.

1.5.3.3 Symmetry-based chemical effects

The third theory posits that the slope ~1 effect is the result of molecular symmetry. The root cause of this effect is quantum mechanical, related to the stability of vibrationally excited symmetrical molecules relative to their asymmetric counterparts (Young *et al.*, 2008). Essentially, if a molecule forms through collision or dissociation it will be vibrationally excited. The molecule then has two options: it either re-dissociates or is stabilised by loss of energy in a subsequent collision, where the likelihood of stabilisation is dependent on the lifespan of the molecule. Symmetrical molecules typically have shorter lifespans than their asymmetric counterparts, and the likelihood that a symmetrical molecule will be stabilised by a collision is lower. The quantum mechanical mechanisms behind this are far beyond the scope of this chapter to explain, but can be summarised by Young *et al.* (2008) as symmetrical molecules containing 'fewer intramolecular dynamical couplings' or less 'phase space'. It is therefore possible that stabilised and re-dissociated molecules could be incorporated into different components. Many elements form molecules with potential symmetry, the most well-known being O_3 (Thiemens and Heidenreich III, 1983; Thiemens

and Lin, 2021). The formation of ozone by photodissociation produces a natural mass-independent effect in Earth's stratosphere that is double the magnitude of that observed in CAIs (Thiemens and Lin, 2021). This effect has been experimentally determined as a symmetry-based reaction. This has prompted laboratory investigation into other isotopic systems such as sulphur and titanium which also show mass-independent fractionation due to symmetry (Bains-Sahota and Thiemens, 1989; Robert *et al.*, 2020).

A similar scenario may occur for SiO_2 in the solar nebula, while adsorbed on the surface of dust grains (Chakraborty *et al.*, 2013), for example:

$$O + SiO \rightarrow SiO_2$$

Or

$$OH + SiO \rightarrow SiO_2 + H$$

The adsorbed SiO_2 molecule could be $^{16}OSi^{16}O$, $^{17}OSi^{16}O$ or $^{18}OSi^{16}O$. The symmetrical isotopologue, $^{16}OSi^{16}O$, has a higher chance of re-dissociation, the consequence of which is an increase in ^{16}O availability for incorporation into the forming dust grain (a chondrule or CAI) it was adsorbed onto (Young *et al.*, 2008). Conversely, the asymmetrical isotopologue may be stabilised and then over time evaporate into the gas phase, causing ^{17}O and ^{18}O enrichment of the nebula gas where it will contribute towards the formation of new minerals, for example, chondrules. In reality, the formation mechanism of CAIs and chondrules remain poorly understood, and this may be one of multiple potential avenues for symmetry-based reactions to influence the composition of early formed silicates in the disk.

Critically, progress towards empirical proof of concept has been steadily increasing in recent years. Reproduction of the slope ~1 effect in the laboratory by Chakraborty *et al.* (2013) provides convincing evidence that SiO_2 symmetry reactions could reproduce the observed variations in CAI material. Because of this potential, Thiemens and Lin (2021) propose that the range of symmetry effects occurring in the early Solar System may be broader than the

few that are currently known. This has been used as a strong argument against the simplicity of the self-shielding model as a mechanism to produce ^{17}O and ^{18}O enriched water ice; notably, the most profound evidence for self-shielding has been the very large enrichments in ^{17}O and ^{18}O measured in cosmic symplectites in Acfer 094 (Sakamoto *et al.,* 2007), in addition to those reported in interplanetary dust particles (Starkey *et al.,* 2014). Thiemens and Lin (2021) provide a counterargument that this may be caused by a symmetry-based isotope effect during the formation of magnetite, which could be plausible within the micron scale minerals where these signatures are typically found. It must be noted that as of 2023, symmetry as a mechanism for mass-independent fractionation is not universally accepted in the cosmochemical literature due to the popularity of the self-shielding model.

1.5.3.4 Summary

The cause of the mass-independent anomaly is not resolved. Self-shielding remains the popular paradigm and has been observed in extrasolar disks and molecular clouds. It has also been successfully modelled in a range of cosmochemical settings; however, it lacks empirical, experimental evidence to support it. Symmetry based effects remain a plausible mechanism to fractionate oxygen mass-independently and is subject to a growing body of research but has yet to be accepted by the wider cosmochemistry community. Further studies on the possible symmetry effects during gas to particle conversion (CAI formation) and the aqueous alteration process, in addition to high resolution data of molecular clouds and protoplanetary disks via the new James Webb telescope will shed light on which scenario is more likely.

1.6 Oxygen isotope systematics of CMs

While the larger, differentiated planetary bodies sampled by the differentiated meteorites define mass-dependent fractionation lines in 3-isotope space, the chondrites instead show complex patterns spanning ~20‰ in $\delta^{18}O$ that deviate from slopes of ~0.52 (Franchi, 2008). This is due to the fact that chondrites are mostly unequilibrated assemblages, having not

experienced enough homogenisation to eliminate the distinct, mass-independent O-isotopic composition of their primordial components. For the aqueously altered chondrites, the resultant trends are mixing lines linking unaltered assemblages with secondary products formed by water-rock interactions (Fig 1.15). As the largest carbonaceous chondrite meteorite group, CMs offer the opportunity for O-isotopic investigation at the bulk and component scale. The latter is particularly useful in understanding the former and so will be covered first.

1.6.1 Components

The key to deciphering the origin and evolution of any planetesimal is to forge an understanding of the reservoirs from which they formed, and how they subsequently interacted over time.

1.6.1.1 Chondrules and CAIs

The surviving anhydrous components in CMs retain their oxygen isotopic compositions from their time of formation and accretion. CAIs and AOAs are pervasively altered and relatively rare compared to chondrules (Brearley and Jones, 1998; Greenwood *et al.*, 1994). Of the CAI minerals, spinel alone is very resistant to alteration (Greenwood *et al.*, 1994) and has been measured as a bulk density separate by Clayton and Mayeda (1984), with a ^{16}O-rich composition at a δ^{18}O value of approximately -50 ‰, in agreement with CAIs from other meteorites (Fig 1.18). Further SIMS measurements of CAIs (Liu *et al.*, 2009) and AOAs (Chaumard *et al.*, 2021; Ushikubo *et al.*, 2017) in other CMs corroborates these compositions, which lie close to the inferred Genesis measurement of the solar wind and therefore, the bulk solar nebula (McKeegan *et al.*, 2011), indicating these minerals condensed out of the very first nebula gases (Fig 1.18).

Chondrules and chondrule fragments in CMs are the most volumetrically abundant surviving anhydrous precursor assemblages, dominated by Mg-rich forsteritic olivine. Density separates of olivine from Murchison define a mean composition of -7.4 (δ^{17}O) and -5.2

($\delta^{18}O$) ‰ (Clayton and Mayeda 1984; Clayton and Mayeda, 1999) which is largely matched by SIMS measurements (*e.g.,* Chaumard *et al.,* 2021; Chaumard *et al.,* 2018). The fine details of the chondrule SIMS data as shown by Fig 1.18 displays a larger spread than the Clayton and Mayeda (1984) average, owed to heterogeneities in the chondrule population, including Fe and Mg-rich members which formed during discrete events (Krot *et al.,* 2006), and the measurement of relict grains. The canonical explanation as to why chondrules are ^{16}O-poor compared to CAIs is tied directly to a component of ^{17}O and ^{18}O-rich water ice produced by self-shielding in the outer Solar System. This ice radially drifts into the inner Solar System where it contributes to the chondrule forming events before the chondrules are redistributed into the outer disk, probably by gravitational disturbances (see section 1.2.3).

1.6.1.2 Water ice

The isotopic composition of the original water ice phase is unknown but can be estimated by mass balance and stoichiometry calculations (Suttle *et al.,* 2021). An issue is the reciprocal nature of water/rock ratio and water composition in these calculations; as neither are directly measurable, one must always be assumed to calculate the other (Clayton *et al.,* 1999). Therefore, attempts to decipher the composition of the primordial water by mass balance is plagued by circular problems, and as shown by Fig 1.18, different studies have produced very different estimates (Clayton and Mayeda, 1984; Clayton and Mayeda, 1999; Fujiya, 2018; Guo and Eiler, 2007; Verdier-Paoletti *et al.,* 2017; Young *et al.,* 1999). Nevertheless, the preponderance of support for the self-shielding model, in addition to the very ^{16}O-poor O-isotope measurements of cosmic symplectites in Acfer 094 (Sakamoto *et al.,* 2007), supports the notion that the water must have been ^{16}O poor near to the TFL.

1.6.1.3 Matrix

Phyllosilicate matrix poses a challenge for *in situ* isotopic measurement and as of 2023, no corrected SIMS values have been reported in the literature. However, bulk O-isotope compositions of matrix phyllosilicates from several CMs have been measured as matrix

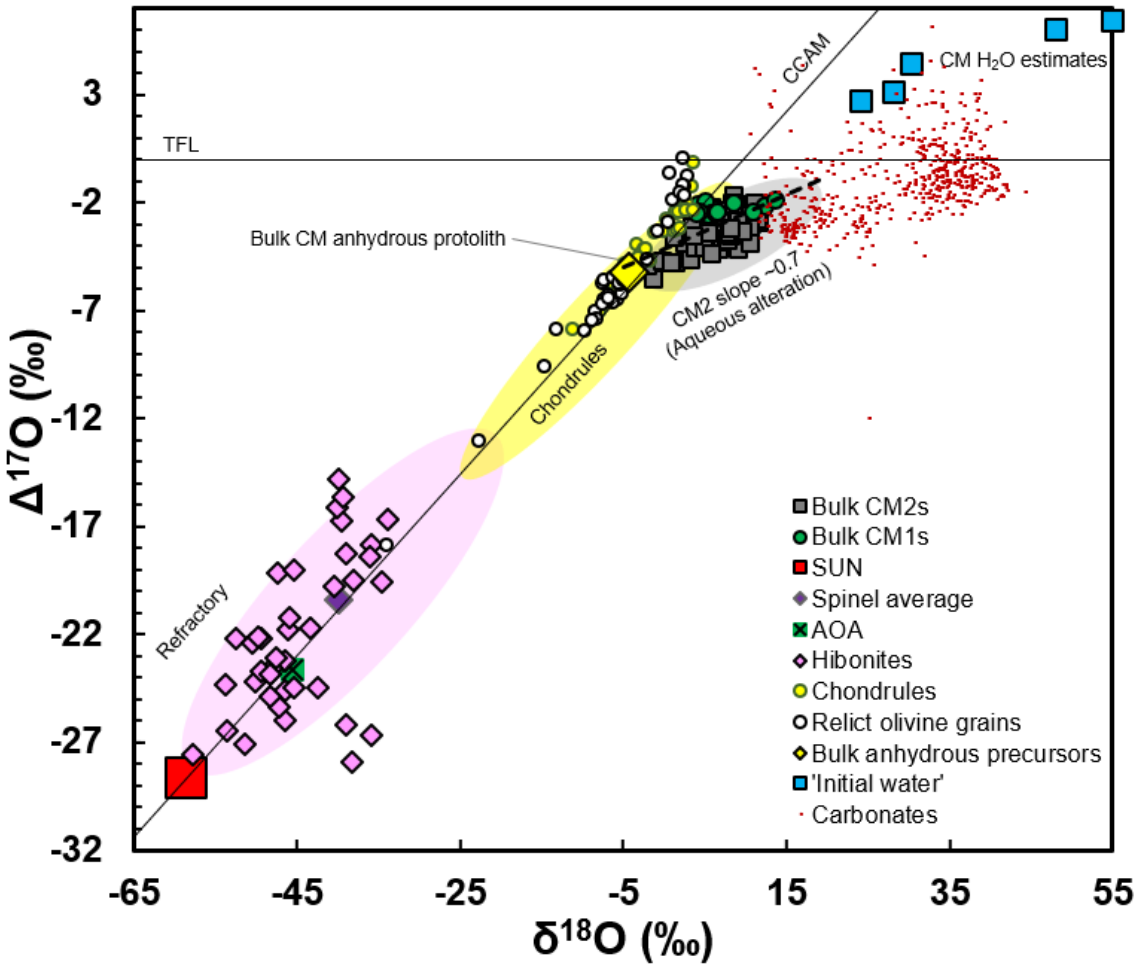

Figure 1.18 – The oxygen isotopic composition of various CM components. The Sun: (McKeegan *et al.*, 2011). Data from a range of sources. Spinel average and bulk anhydrous precursors: (Clayton and Mayeda 1999). Chondrules and AOA: (Chaumard *et al.*, 2018; Chaumard *et al.*, 2021). CAI: (Liu *et al.*, 2009). Initial water estimates (Clayton and Mayeda, 1984; Clayton and Mayeda, 1999; Fujiya, 2018; Guo and Eiler, 2007; Verdier-Paoletti *et al.*, 2017). See Fig 1.20 for CM2 and CM1 data.

density separates (Clayton and Mayeda, 1984; Clayton and Mayeda, 1999; Rowe *et al.*, 1994). These measurements plot above chondrules and CAI in a limited region of isotope space (Fig 1.19 and 1.20) reflecting the serpentinisation reaction between the anhydrous precursors and a significant fraction of ^{17}O- and ^{18}O-rich water ice, indicating the parent asteroids of the CM chondrites accreted beyond the snow line. The scatter exhibited by the limited data precludes any determination of mass-dependent or mass-independent relationships between these phyllosilicates. Density separation has been noted as a potentially unreliable technique as residual, nanoscale precursor fragments may reside in the matrix density separate if the process is not 100 % efficient (Franchi, 2001).

Meteoritic matrix tochilinite has only been measured once as an isotopographic NanoSIMS measurement on a Murchison thin section (Sakamoto *et al.,* 2007). It has a very high uncertainty (Fig 1.19, 1.20), but a statistically resolvable, isotopically light composition compared to the matrix density separates by Clayton and Mayeda (1999). Neither cronstedtite, greenalite, berthierine or S-rich serpentine have been measured for their O-isotope composition.

Finally, the original, pristine CM matrix would have likely been composed of amorphous glass with embedded metal and sulphides (GEMS) alongside nanoscale silicate fragments and organics (Yurimoto *et al.*, 2008). Very little of this phase survives, and because of this these components have not yet been exhaustively measured for their O-isotopic composition.

1.6.1.4 Carbonates

The O-isotopic composition of carbonates in CM chondrites are excellent tracers of water evolution because oxygen self-diffusion in this mineral is very slow at the temperatures predicted for CM chondrite alteration (Farver, 1994; Vacher *et al.,* 2019a). Therefore, once formed, they retain the O-isotopic composition of the fluid phase they precipitated from (Lee *et al.*, 2014; Lee *et al.*, 2013).

Prior to the report of *in situ* O-isotope measurements, bulk carbonates were measured as CO_2 gas through acid dissolution (Benedix *et al.*, 2003). Clayton and Mayeda (1999) noted that the bulk carbonate compositions appear to be in isotopic equilibrium with the matrix phyllosilicate density separates, and that they could be used to infer temperatures of alteration. Later work by Benedix *et al.* (2003) revealed the limitation of such an assumption as the measured carbonates revealed variable O-isotopic compositions, plotting on an apparent slope of 0.6 in 3-isotope space, in agreement with CM bulk rock data. This trend potentially reflects the progressive reaction / equilibration of the initially ^{16}O-poor water reservoir with the surrounding rock. Further information was gleaned yet again by coupling the *in-situ* O-isotopic composition with petrographic context, revealing the aforementioned

slope 0.6 may be an artefact caused by several generations of carbonates occupying different and offset mass-dependent fractionation lines (Tyra *et al.,* 2012, Vacher *et al.,* 2019). The current consensus posits the O-isotope compositions of specific carbonates generations reflect episodic precipitation, and that aqueous alteration occurred in discrete pulses as opposed to a progressive reaction (*e.g.,* Farsang *et al.,* 2021).

Figure 1.19 is a relatively exhaustive plot of published carbonate analyses. The first-generation of carbonates to crystallise in CM chondrites are the monocrystalline T1 calcites often found in association with TCIs (Tyra *et al.,* 2012; Vacher *et al.,* 2017; Vacher *et al.,* 2019a). These carbonates on average have ^{16}O-poor compositions straddling the terrestrial fractionation line, or in the case of aragonite (sometimes called T0 aragonite), residing slightly above (Vacher *et al.,* 2017). T1/0 calcites broadly indicate crystallisation from a fluid with a composition residing near the terrestrial fractionation line ($\Delta^{17}O \approx 0$). It has been suggested that these carbonates represent the onset of aqueous alteration, where the ^{16}O-poor water ice melted, and the fluid had not yet equilibrated with the rock. The later generation, polycrystalline T2 calcites have $\Delta^{17}O$ O-isotopic compositions similar to the matrix density separates, suggesting they may have formed coevally with the Mg-serpentines during an event where the water had begun to equilibrate with the rock and take on an intermediate composition (*e.g.,* Vacher *et al.,* 2017; Vacher *et al.,* 2019a). As such, these compositions have been used to some effect to calculate temperatures of alteration (Vacher *et al.,* 2019a). In most cases, T2 calcites precipitated as a higher temperature than T1 calcites.

Many other O-isotopic compositions of carbonate grains are reported from multiple CMs (Fig 1.19), including those that have been very altered such as the CM1s. Most of these measurements lack detailed petrographic context, but very generally, the isotopic compositions reside within the boundaries defined by T1 and T2 calcites. Nevertheless, the scatter is considerable, suggestive of additional carbonate generations than simply T1 and T2 calcites and the importance of petrographic context (Vacher *et al.,* 2019). Dolomites from

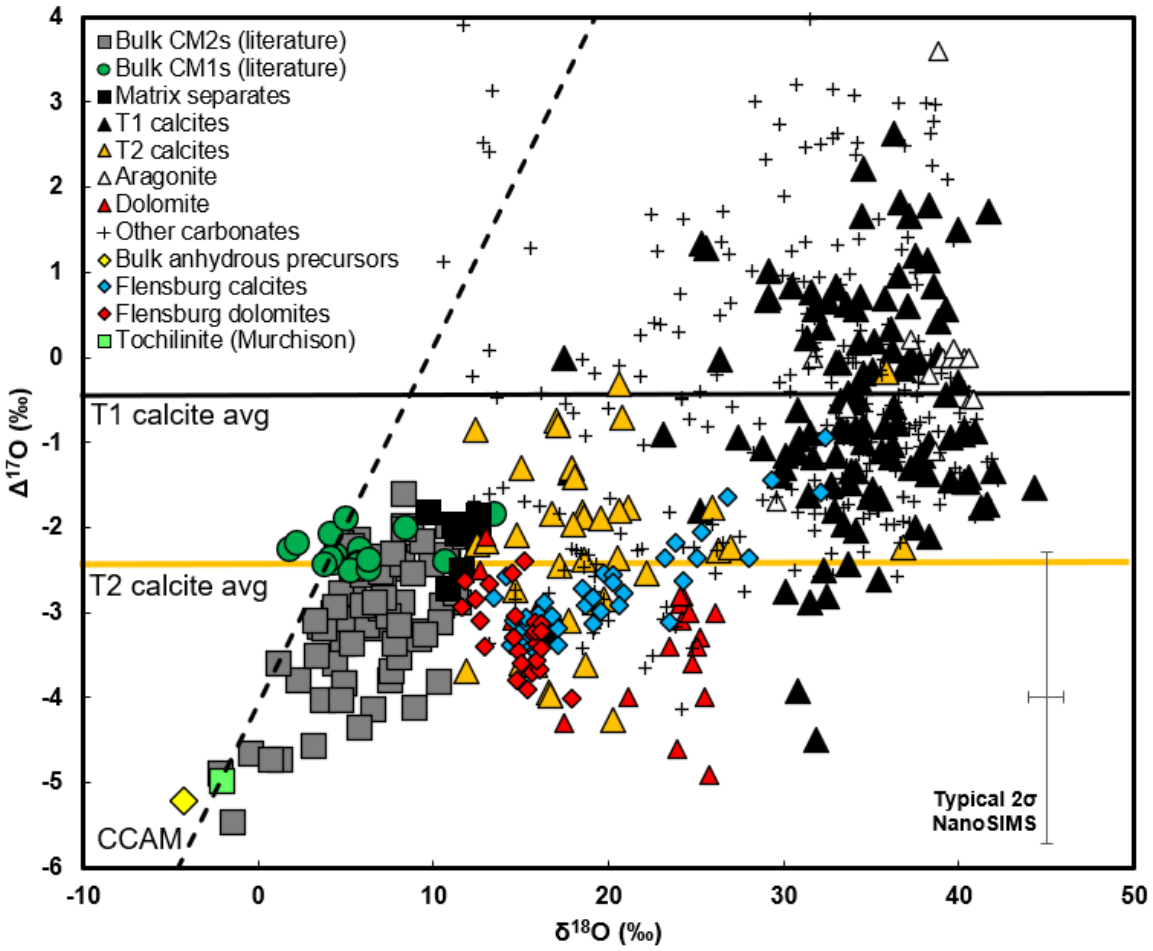

Figure 1.19 – O-isotopic composition of published carbonates compared to bulk data. CM matrix density separates, anhydrous precursors and tochilinite are also included. The matrix separates may be in isotopic equilibrium with the T2 calcites, which are resolvable (within error) from the T1 calcites. Data from a range of sources (Bischoff *et al.*, 2021; Farsang *et al.*, 2021; Fujiya *et al.*, 2015; Jenniskens *et al.*, 2012; Kerraouch *et al.*, 2021; Lee *et al.*, 2013; Lindgren *et al.*, 2017; Tyra *et al.*, 2012; Vacher *et al.*, 2019a; Verdier-Paoletti *et al.*, 2017; Verdier-Paoletti *et al.*, 2019). See Fig 1.20 for CM2 and CM1 data sources. 2σ uncertainty of bulk measurements are smaller than symbols.

the most altered CMs — including the potentially CM-like, C1-ungrouped chondrite Flensburg — are also isotopically variable with many exhibiting ^{16}O-rich compositions (Bischoff *et al.*, 2021; Telus *et al.*, 2019). Akin to how the T1 calcites represent the onset of aqueous alteration or an early alteration event, carbonates formed during late-stage events could reflect protracted alteration with the rock, resulting in carbonate compositions that are pulled further down towards the O-isotopic composition of the precursors.

1.6.2 Bulk measurements

There is a sizable literature compilation of bulk CM2 measurements spanning a large range of falls and finds. The pioneering, nickel-bomb CM2 chondrite dataset by Clayton and Mayeda (1999) defines a slope 0.7 array in 3-isotope space with considerable scatter (Fig 1.20). In the years following the publication of this dataset, measurements obtained via laser fluorination produced similar results spanning slopes of 0.7-0.8 to a higher precision among the samples analysed (*e.g.*, Greenwood *et al.*, 2022). In all cases, this relationship is very generally explained by the mixing of different unequilibrated components, namely the secondary phyllosilicates formed by the incomplete interaction of ^{16}O-poor water and ^{16}O-rich anhydrous precursors. Most of these measurements were undertaken using large aliquots of homogenised powder and have been used to good effect to estimate the overall level of alteration experienced by an individual CM (Greenwood *et al.*, 2023). The least altered CM chondrites typically have isotopic compositions closer to that of the anhydrous precursor phases as their relative proportion of unaltered chondrule fragments is high (Fig 1.20), whereas the more altered CMs have heavier compositions as they contain a larger proportion of phyllosilicates. This is not always steadfast, however, and many CM O-isotope measurements suffer from heterogeneity issues owed to the lithological diversity, for example, LEW 85311 (Lee *et al.*, 2019). Interestingly, with the identification of more CM1 and CM1/2 samples, these pervasively altered members of the CM family do not appear to obey the aforementioned trend either, in that they are isotopically light compared to the most altered CM2 chondrites and occupy a shallower slope in 3-isotope space (Bouvier *et al.*, 2017; Greenwood *et al.*, 2019; Howard *et al.*, 2011a; Howard *et al.*, 2010; King *et al.*, 2018; King *et al.*, 2017; Ruzicka *et al.*, 2017; Zolensky *et al.*, 1997). This has raised a number of interesting points including whether or not the CM1s were altered at higher temperatures than the CM2s or if they are derived from a different asteroid entirely. A lack of convincing petrologic kinship to date, *i.e.*, finding CM1 material juxtaposed next to CM2 material in

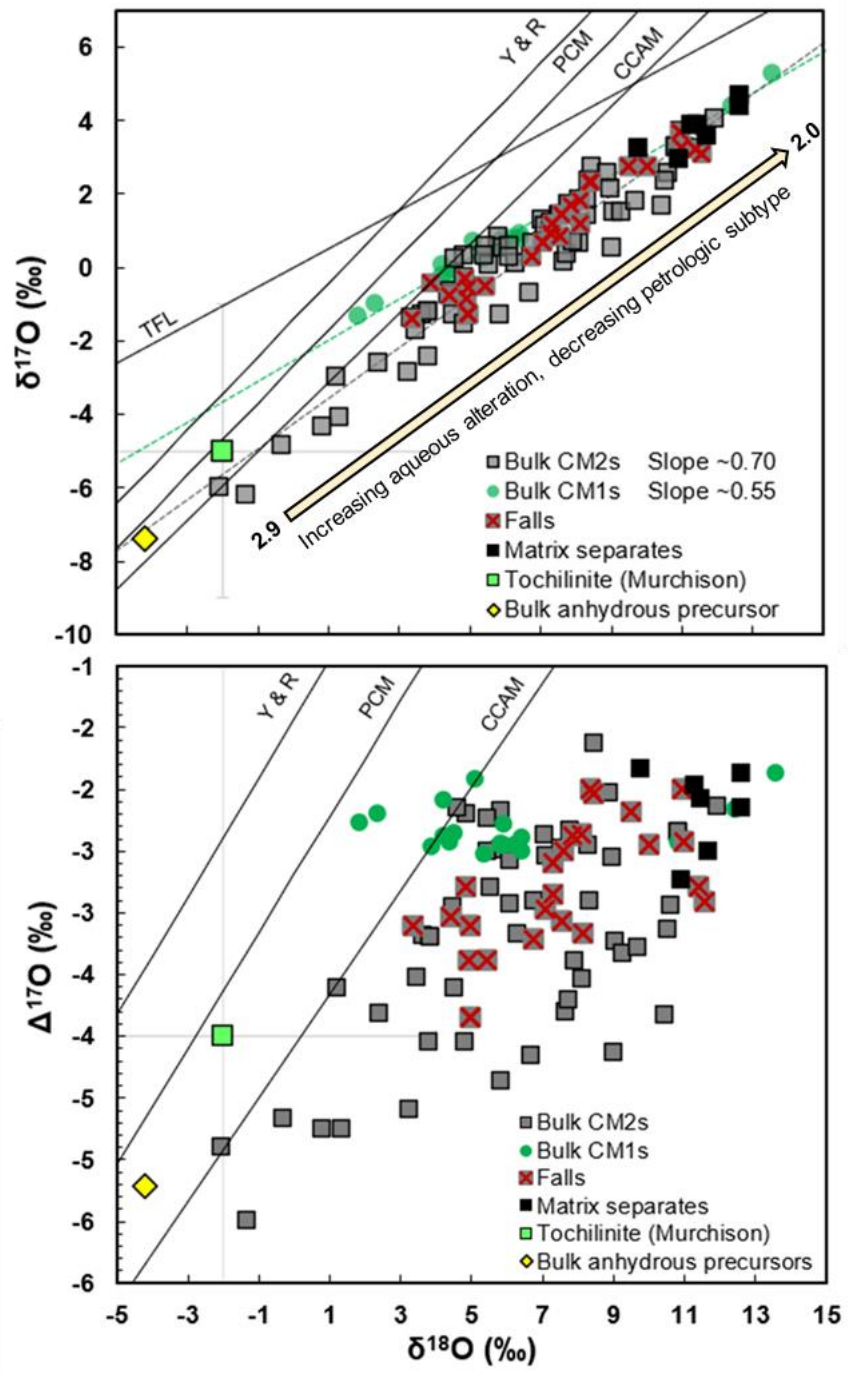

Figure 1.20 – O-isotope composition of bulk CMs. CM2s reflect the progressive hydration of the anhydrous precursors, which can be partially traced by petrologic type. CM2s and CM1s appear to define different grouplets, although CM1s may be contaminated by Antarctic weathering. Falls define less scatter than the larger CM2 data. Included are the PCM (Ushikubo *et al.*, 2012) and Y & R (Young and Russel, 1998) lines for completeness. Average CM anhydrous precursors (Clayton and Mayeda, 1999) lie between the PCM and CCAM lines. CM2 data from a range of sources (Bischoff *et al.*, 2021; Clayton and Mayeda, 1999; Fan *et al.*, 2022; Greenwood *et al.*, 2023; Haack *et al.*, 2012; Hewins *et al.*, 2014; Kerraouch *et al.*, 2021; Kimura *et al.*, 2020; King *et al.*, 2022; Lee *et al.*, 2019; Lee and Lindgren, 2016; Tyra *et al.*, 2007; Verdier-Paoletti *et al.*, 2019). CM1 data (Bouvier *et al.*, 2017; Howard *et al.*, 2011a; Howard *et al.*, 2010; Irving *et al.*, 2009; King *et al.*, 2017; Ruzicka *et al.*, 2017; Zolensky *et al.*, 1997). 2σ uncertainty smaller than symbols unless plotted.

thin section has limited the formation of hypotheses suggesting a common parent body origin for both (King *et al.*, 2020).

Scatter around the CM2 and CM1 lines is attributed to unidentified mass-dependent effects during aqueous alteration, uncertainty in the volume of anhydrous precursor, and terrestrial weathering effects (Findlay *et al.*, 2022; Franchi, 2008; Franchi *et al.*, 2001; Greenwood *et al.*, 2019; King *et al.*, 2018). The latter point is of particular relevance to the CM1 and CM1/2 chondrites as many have been recovered from Antarctica. Interaction of these phyllosilicate-rich samples with isotopically light Antarctic precipitation may have skewed the composition to lighter values (Greenwood *et al.*, 2019; King *et al.*, 2018).

1.6.3 The CM-C2-ung-CO relationship

It has been suggested that the CO 'Ornans-type' carbonaceous chondrites share a genetic relationship with the CM group. This is owed to their clan heritage, similar chondrule sizes, and, as initially highlighted by Clayton and Mayeda (1999) and by other publications since (*e.g.*, Greenwood *et al.*, 2023), occupation of the same slope ~0.7 mixing line (Fig 1.21). In this sense, the major difference between the two groups is reflected in the abundance of water ice accreted, with the COs being essentially dry while the CMs contained larger quantities of water ice, promoting aqueous alteration. This has led to the suggestion that the COs and CMs do not sample the same parent body, but different parent bodies occupying a narrow region in the protoplanetary disk (Schrader and Davidson, 2017; Torrano *et al.*, 2021); consequently, it has been proposed that the COs and CMs formed just interior and exterior to the snowline, respectively, or that they represent the temporal evolution of the snow line throughout the lifetime of the disk (Chaumard *et al.*, 2021). It is also noted that a compositional 'gap' exists between the two groups in 3-isotope space, that is conveniently filled (Fig 1.21) by a number of C2 ungrouped meteorites (Clayton *et al.*, 1999; Franchi *et al.*, 2008; Greenwood *et al.*, 2019). Many of these meteorites exhibit primitive CM characteristics, *i.e.*, they are CM-like in terms of their chondrule sizes and matrix abundance

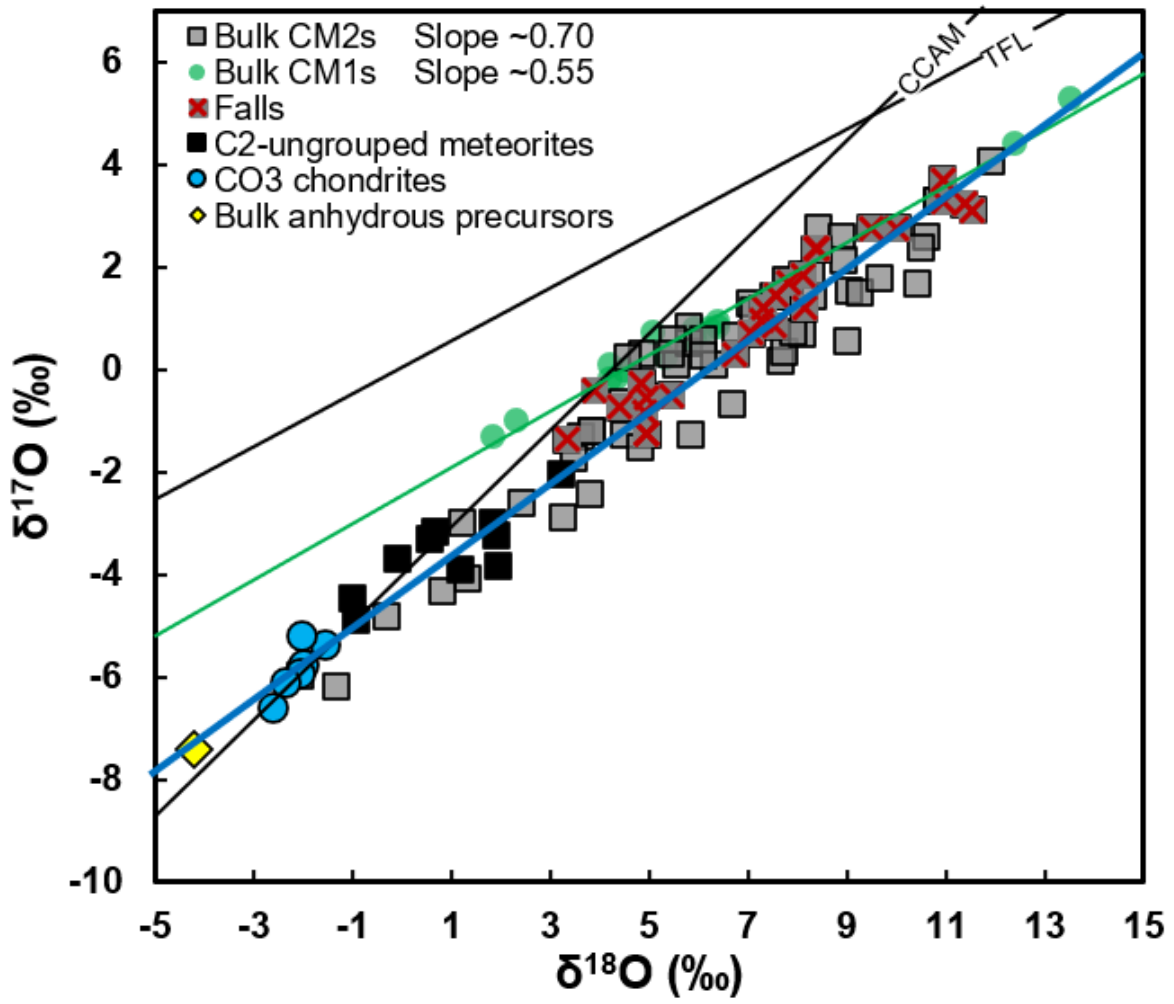

Figure 1.21 – The relationship between CO chondrites, C2-ungrouped chondrites, and CM chondrites. The blue line plots through all three groups, including the anhydrous precursors measured by Clayton and Mayeda (1984), suggesting a genetic link between the three groups with CO chondrite-like material possibly representing possible CM-starting materials. See Fig 1.20 for CM1 and CM2 data sources. C2-ung data (Greenwood *et al.*, 2019). CO chondrite data (Alexander *et al.*, 2018), only CO falls are plotted.

but lack strong evidence for pervasive alteration — prompting classifiers to argue for an ungrouped classification. Many of these meteorites may be primitive, CM2.9 -CM3.0 specimens that have been misclassified, as they occupy the same region as the recently identified Asuka CM2.8-CM3.0 meteorites (Greenwood *et al.*, 2019; Kimura *et al.*, 2020; Torrano *et al.*, 2021), and now overlap with a number of incipiently altered CMs, such as LEW 85331 and some Paris lithologies. As these C2-ungrouped meteorites lie close or on the CCAM and PCM lines, it is probable they directly represent the CM precursor assemblage, or if not, provide the most plausible candidates to understand what the original CM3 looked like.

1.7 Candidate aqueous alteration environments for CMs

It is now widely accepted that aqueous alteration was predominantly a parent body and not a nebular process (Brearley, 2006). Therefore, the aim of any published O-isotope model, simple or complex, is to suggest a parent body alteration regime that is capable of reproducing the measured O-isotope compositions of bulk CMs.

Within the CM chondrite parent asteroids, water interacts with rock to form secondary minerals, undergoing oxygen isotopic exchange over time (Castillo-Rogez and Young, 2017). Although the O-isotope kinematics associated with serpentine crystallisation are poorly known, it can be confidently assumed that to produce it, a part of the oxygen within the water is exchanged with the silicate lattice of the precursor during crystallisation of the phyllosilicate (Saccocia *et al.*, 2009). For this reason, the phyllosilicates are partial proxies for the isotopic composition of the fluid phase. The isotopic composition of these minerals, specifically the $\Delta^{17}O$, are controlled by the capacity of the rock to exchange with the fluid, which itself is dictated by several variables (Franchi, 2008):

1) Higher temperatures lead to higher rates of reaction;

2) The length of time that the asteroid reacted with water;

3) The water/rock ratio (WR): The amount of water compared to the amount of rock that interacted to form secondary minerals. The WR ratio can be expressed in molar or volumetric terms. The molar ratio is plainly:

$$Molar\ WR\ ratio = \frac{Moles\ of\ O\ in\ water}{Moles\ of\ O\ in\ rock}$$

Which depends upon the minerals used to infer the composition of the rock. In the literature, this is simply expressed as the interaction of olivine and pyroxene to form magnesium serpentine (Clayton and Mayeda, 1999; Fujiya, 2018):

$$Mg_2SiO_4 + MgSiO_3 + 2H_2O \rightarrow Mg_3Si_2O_5(OH)_4$$

Forsterite + Enstatite + Water → Magnesium serpentine

(4 moles) + (3 moles) + (2 moles) → (9 moles)

This reaction is appropriate as the majority of CM secondary products are serpentine that regardless of composition, possess the same number of oxygens (Table 1.1). Seven moles of oxygen in the precursor silicates are required to combine with 2 moles of oxygen in the water to produce the 9 moles of oxygen in the serpentine. The minimum molar WR ratio, expressed as a ratio of oxygen atoms is therefore 2/7, or 0.29 to fully produce serpentine (Clayton and Mayeda, 1999). To convert this to a volumetric ratio, one must first multiply the moles of the material by their respective molecular weights to retrieve mass. The mass can then be divided by the density of the material to produce the volume of each. The volumetric WR ratio is 0.49 in this case, comparable to 'water saturated sand' (Clayton and Mayeda, 1999).

4) And finally: if alteration occurred in a closed or open system (Clayton and Mayeda, 1999; Young *et al.*, 1999)

1.7.1 Closed system

In a closed system, water is static and not permitted to enter, leave, or 'evolve' from one part of the asteroid to another, and the water residing in the pore spaces reacts directly with the rock to form secondary phyllosilicates (Fu *et al.*, 2017). The reaction will be progressive (Fig 1.22), with the earliest formed products having a $\Delta^{17}O$ composition reflective of the pore water, whereas the later formed products will reflect the bulk rock as the system undergoes isotopic exchange as alteration proceeds (Clayton and Mayeda, 1999). In the final stage, the isotopic composition of the final drop of water will occupy a spot in 3-isotope space between the composition of the initial water and the initial rock, dependent on the water/rock ratio (Fig 1.22). As a result, minerals precipitated along a reaction path in a closed system will lie on mixing lines linking unaltered and altered rock.

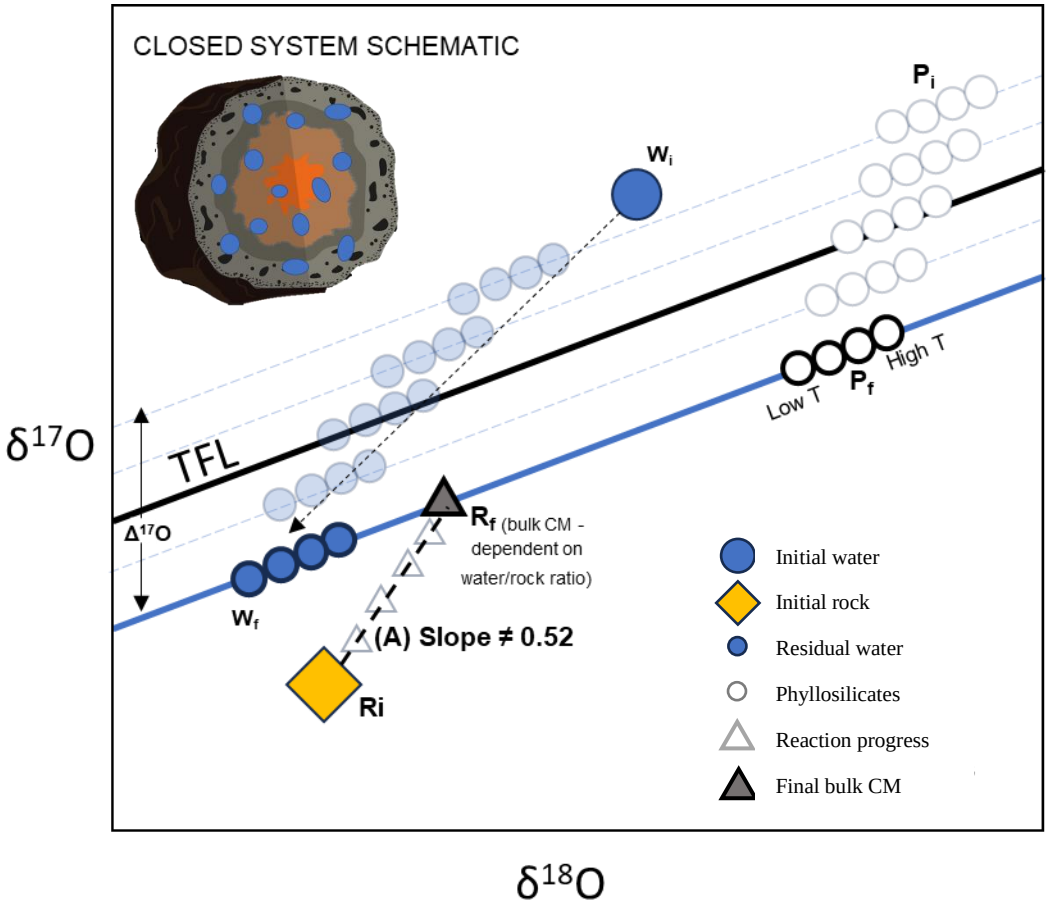

Figure 1.22 - In a closed system asteroid, water is stagnant. There is a progressive reaction of an initial reservoir water (W_i) and rock (R_i) Initially, the first phyllosilicate products (P_i) in the progress of reaction will have a $\Delta^{17}O$ composition close to the initial water, and a $\delta^{18}O$ offset depending on the magnitude of mass-dependent fractionation between water and phyllosilicate (temperature dependent). As the water exchanges further with the rock, the phyllosilicate and the pore water will begin to take on the composition of the rock. The final isotopic composition of the bulk CM will lie in a region in between W_i and R_i with distinct $\Delta^{17}O$, which is dictated by the water/rock ratio. The final phyllosilicates, P_f, will lie on a mass-dependent fractionation line with the altered rock. In CM chondrites, there is very rarely 100 % alteration; therefore, in a closed system, CM chondrites halted at different stages in the alteration process will have a bulk composition reflective of the amount of rock reacted with the water. Lines such as (A) linking unaltered rock with rocks of partial alteration will always deviate from slopes of ~0.52. Note that this schematic does not use accurate locations for the composition of starting water and rock – and the degree of mass-dependent fractionation illustrated here is arbitrary and could vary to much greater extents during the reaction path.

The $\delta^{17}O$ and $\delta^{18}O$ will also be influenced by the water/rock ratio in the same manner as $\Delta^{17}O$; however, where these parameters differ is that the $\delta^{17}O$ and $\delta^{18}O$ values are also affected by mineral and temperature dependent, equilibrium mass-dependent processes during serpentine precipitation. Therefore, whereas $\Delta^{17}O$ traces the water/rock ratio, $\delta^{17}O$ and $\delta^{18}O$ may also trace the precipitation and temperature conditions of alteration. In a case

where the water/rock ratio was sufficiently high enough to promote local scale equilibration at points during the reaction path, there may be minerals such as carbonates and different serpentines lying on mass-dependent fractionation lines that depart from the mixing line, causing apparent scatter (Fig 1.22).

Clayton and Mayeda (1999) express a closed system as an isotopic mass balance equation under the following assumptions:

- The system is closed, and the water is consumed in the reaction
- Serpentine is in isotopic equilibrium with water
- The fractionation between serpentine and water is consistent
- The isotopic composition of the original precursors is consistent.

While the mass balance equation appears quite involved, the function is simplistic:

Equation 1.3

$$7x\delta_w^i + 7\delta_r^i = (7x - 2f)\delta_w^f + 7(1-f)\delta_r^i + 9f\delta_s^f$$

Where:

δ^i_w = the O-isotopic composition of the initial water

δ^i_r = the O-isotopic composition of the initial rock

δ^f_w = the O-isotopic composition of the final water

δ^f_s = the O-isotopic composition of the measured serpentine

f = the fraction altered (0-1), determined in thin section

x = the WR ratio

This equation demonstrates that the O-isotopic composition of any bulk CM chondrite can be explained by the *in situ* (closed system) alteration of ferromagnesian silicates by stagnant pore water. To break down the terms: the left-hand side of the equation is essentially the

starting reactants and their molar quantities, where 7 moles of oxygen in the rock (olivine + pyroxene) react with a set amount of moles of oxygen in the water, determined by multiplying the initial water by the WR ratio, x. The right-hand side of the equation is the composition of the final products, which consist of final water, leftover initial rock, and serpentine. The moles of each term on the right are both a function of the WR ratio and the fraction rock that has been altered. The initial isotopic composition of the water in the model was taken to be the result of a calculation by Clayton and Mayeda (1984), which assumed the isotopic variations exhibited by high temperature minerals were due to exchange with a nebular gas, which partially condensed to produce water. The calculation yielded a δ^{i}_{w} of 28.1 ($\delta^{18}O$), 17.7 ($\delta^{17}O$) and 3.1 ($\Delta^{17}O$) ‰ (to note, this is probably no longer the best estimate for water, but represent one of many possible compositions).

Furthermore, as the final isotopic composition of the water, δ^{f}_{w}, is unknown, it has to be approximated by assuming a fractionation factor, Δ_{sw}, between the final water and serpentine. Clayton and Mayeda used 12 ‰ at 0 °C:

Equation 1.4

$$\delta_w^f = \delta_s^f - \Delta_{sw}$$

Equation 1.4 can be substituted into equation 1.3, and rearranged (please see the Appendix A6 for this rearrangement, as it is simple but quite long):

Equation 1.5

$$\delta_s^f = \frac{\delta_w^i + \Delta_{SW} + \left(\delta_r^i - \frac{2}{7}\Delta_{SW}\right)\frac{f}{x}}{1 + \frac{f}{x}}$$

There are two equations to produce final serpentine, one for $\delta^{17}O$ and one for $\delta^{18}O$. The terms on the right-hand side of the equation can be manipulated to produce final serpentine values that are congruent with the CM2 data, or the equation can be rearranged to reveal information about the WR ratio.

Clayton and Mayeda (1999) stated that provided the degree of alteration 'f' is successfully determined in thin section, and a set value for the initial water is assumed (Clayton and Mayeda, 1984), the equation can be re-arranged to produce values for the WR ratio for a given CM chondrite. The results of the model showed that the distribution of bulk CM2 oxygen isotope data is very influenced by changes in WR ratio, but not so much by degree of alteration (f) (Fig 1.23). This can be visually expressed as a graph of the modelled data. If the WR ratio is assumed to be constant, and the altered fraction 'f' is varied from 0-1, the range of modelled whole rock compositions varies little between f = 0.6 – 1.0 (reflective of the majority of aqueously altered CMs), from 7-8 ‰ in $\delta^{18}O$. Conversely, if the alteration fraction, f, is arbitrarily set to 1 (100% alteration), the modelled serpentine compositions recreate the slope ~0.7 CM2 array between WR ratios of 0.3 and 0.7.

However, the model did not test the effects of temperature, and the chosen Δ_{sw} of 12 ‰ is not in line with recently calculated serpentine-water fractionation factors (Zheng, 1993). Variation in Δ_{sw} may therefore shift the modelled serpentine and whole rock data to higher values.

Ultimately, the Clayton model predicts that the range in bulk CM O-isotopic compositions, and therefore the range of CM lithologies can be explained by different WR ratios by discrete regions sampling of a statically altered parent body, or perhaps more likely, multiple, statically altered precursor bodies.

1.7.2 Open system

The open vs closed system debate is heavily influenced by the observation of isochemical alteration in the most altered chondrites. Paradoxically, these chondrites are the most pristine geochemically, with a budget of volatile elements that are within a 10 % match of the solar photosphere (Bland *et al.,* 2009; Braukmüller *et al.,* 2018; Lodders, 2003). As volatility is correlated to solubility, any mass transport of water through an asteroid is expected to leach

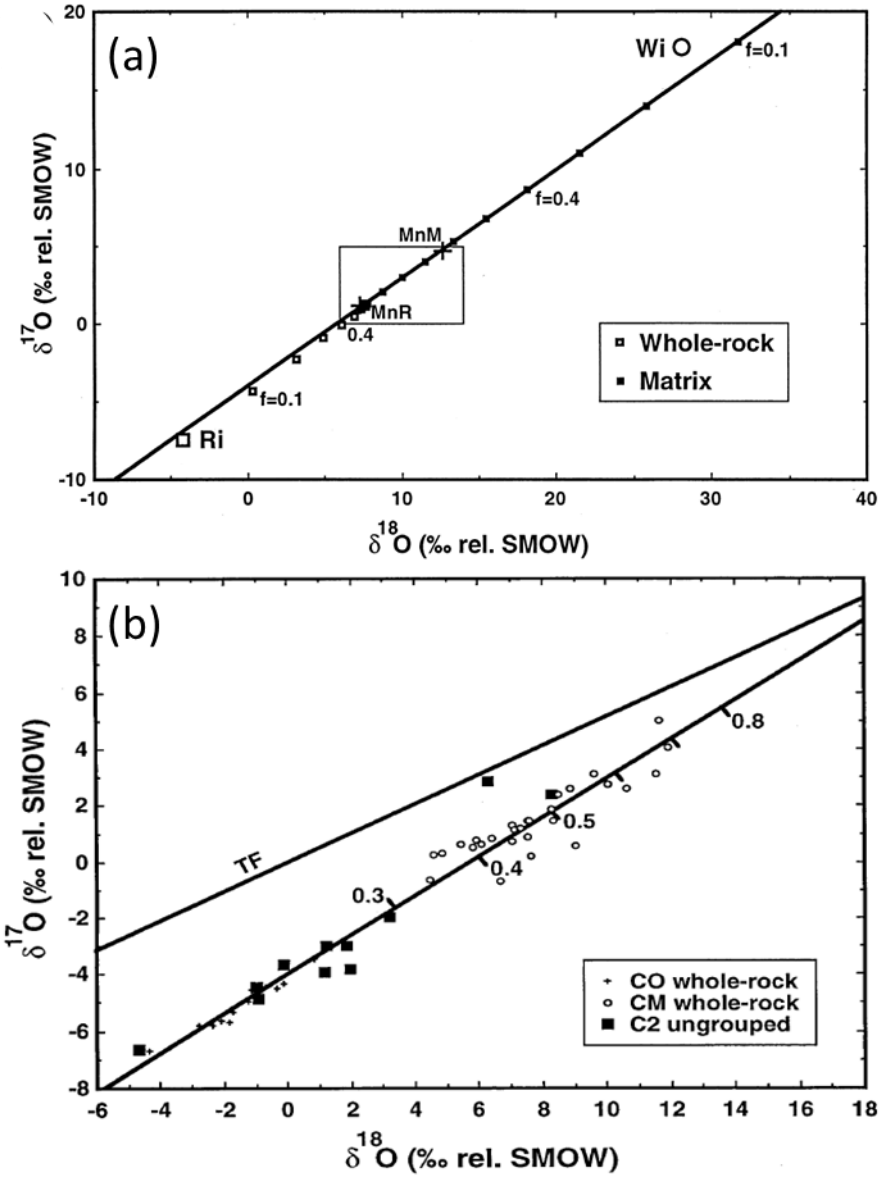

Figure 1.23 – Modelled, closed system O -isotopic compositions from Clayton and Mayeda (1999). (a) Tests the effect of variable levels of alteration ('f') with a consistent WR ratio of 0.47. Compositions of the water and rock reservoirs are given in Clayton and Mayeda (1999). Modelled whole rock compositions are initially affected by the onset of aqueous alteration (f = 0.1) but this effect diminishes dramatically once f = 0.6. The rectangle encompasses a region where there is very little change in $\delta^{18}O$ from f = 0.6 to f = 1.0. (b) Tests the effect of variable WR ratios with the same reactants as before and a consistent level of alteration (f = 1). WR ratios from 0.3-0.8 appear to reproduce the majority of the CM bulk measurements that were measured at the time of publication.

these fluid mobile elements and reprecipitate them elsewhere, potentially as asteroidal salt deposits. As this is not directly observed, Bland *et al.* (2009) has suggested that fluid was not transported beyond 100s of μm at most because the permeability of CM chondrites and their fine-grained starting materials were modelled to be extremely small, on the order of 10^{-19} – 10^{-17} m^2. The tight match of the modelled O-isotope data produced by the Clayton model

— which also requires minimal mobilisation of water — to bulk CM2 O-isotopic compositions has added weight to the theory of isochemical alteration.

In contrast, open systems with fluid flow are an outcome that is always predicted by numerical simulations of water-rich asteroids. This is in part due to the fact that they employ higher permeabilities in their models (10^{-15} – 10^{-11} m^2) compared to those reported by Bland *et al.* (2009), justified by the existence of large fracture networks that can increase permeability through the rock by several orders of magnitude. The cause is serpentinisation and the oxidation of Fe which produces H_2 gas as a by-product, in addition to the later production of CH_4 as the hydrogen reacts with the CO_2 in solution. Furthermore, asteroids inevitably accrete a budget of ^{26}Al and therefore generate heat. If the asteroids reached 200 °C or above, the pressure of water vapour within the body (in combination with the release H_2 and CH_4) would produce pressure in the realm of 10s of MPa, which would rapidly overcome the tensile strength of intact basalts, and most definitely chondritic material (Fu *et al.,* 2017). This would create an interconnected, asteroid-wide fracture network for fluid migration. The effect of surface tension can also contribute to flow. Unfortunately, existence of such a large fracture network has not been observed directly in the meteorite record but has been observed on the surface of asteroid Bennu in the form of large, cm-scale carbonate veins, suggesting these features rarely survive atmospheric entry to Earth as a meteorite (Kaplan *et al.,* 2020).

1.7.2.1 Rock and fluid dominated regimes

With respect to oxygen isotopes, the amount of water in any given location within the open system dictates the alteration regime (Fu *et al.,* 2017). Where the WR ratios are low, the system could be considered ‘rock dominated’ (Fig 1.24). As the water permeates through the rock, the O-isotopic composition of the water begins to change as it undergoes isotopic exchange and takes on the characteristics of the rock (Fu *et al.,* 2017). The rock buffers the fluid, and the O-isotopic composition of any products will lie on a near mass-dependent

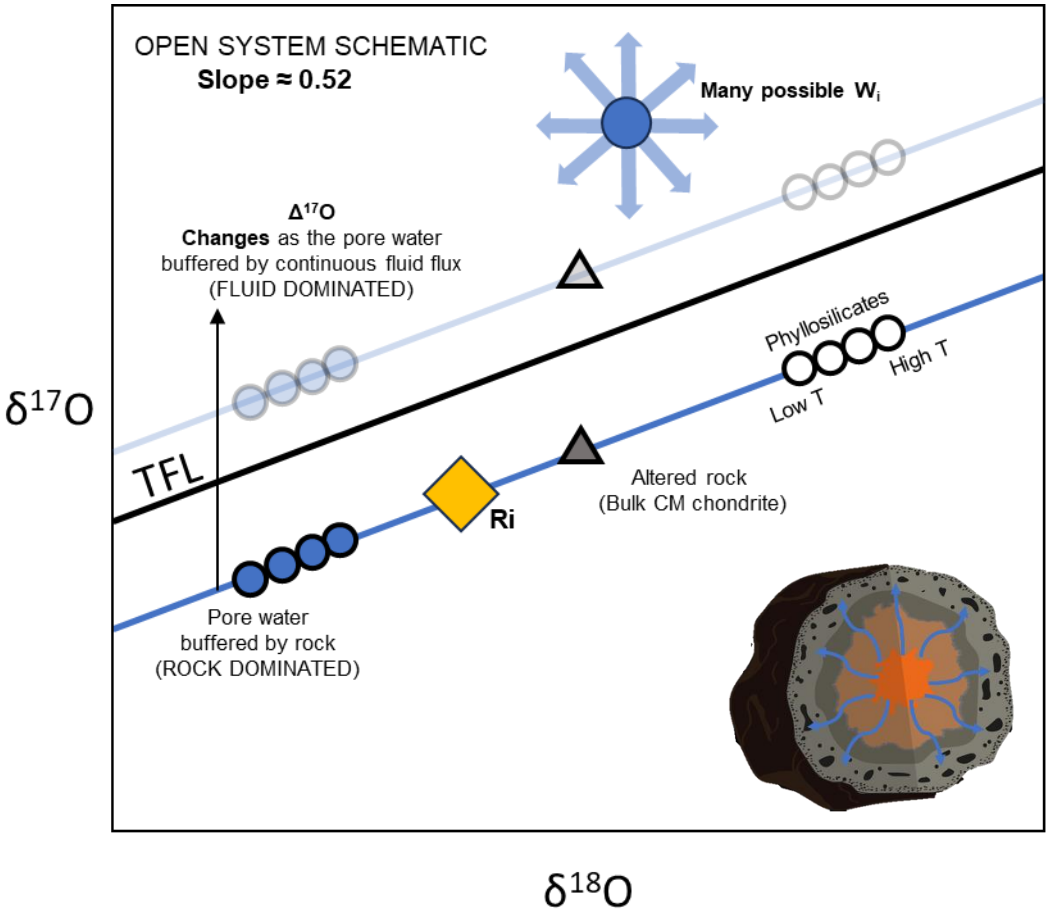

Figure 1.24 - In an open system water is able to flow and there may be both rock-dominated and fluid-dominated regimes. While any mass-dependent effects will be similar to that in a closed system, the $\Delta^{17}O$ of the system will not be as straightforward. This is because fluid can be transported, and indeed, evolve from one region to another. In rock dominated systems, the rock will buffer the fluid composition so that it is nearly the same as the rock itself. Therefore, any secondary products formed will lie on a slope ~0.52 line with the initial rock (R_i). In systems where fluid flow and volume is pervasive, the system will be fluid dominated. In this case the $\Delta^{17}O$ can change as the rock loses its capacity to exchange with the rock. The magnitude of this change is dependent on the quantity of water moving through the system, and the location of the altering rock, whether it is downstream or upstream. For this reason, there are a multitude of possible starting water (W_i) compositions for each distinct location in the open system as water flows from one regime to the other (and perhaps back again, depending on the model), *i.e.,* W_i is time integrated (Young *et al.*, 1999). The compositions of the rock, water and degree of mass-dependent fractionation is arbitrary in this cartoon.

fractionation line close to the $\Delta^{17}O$ of the original rock (Fig 1.24). This has been used to explain why dark inclusions in Allende are mass fractionated from the Y&R line (Young *et al.*, 2002; Young and Russell, 1998), as the WR ratios were very low on the CV3 parent body. In open regimes of higher WR ratio the fluid dominates the system and the anhydrous precursors exchange with the water until the rock loses its buffering capacity (Fu *et al.*, 2017;

Young *et al.,* 1999). Thereafter, the $\Delta^{17}O$ of the products will migrate towards equilibrium closer to the composition of the moving water (Fig 1.24). Within open systems, mass-dependent fractionation lines are attainable in areas of consistent fluid flux (Franchi *et al.*, 2001; Young, 2001; Young *et al.,* 1999), where the water acts as a buffer. In between these regions, the O-isotope composition of the fluid may evolve from one region to another, producing the effect of mixing as the $\Delta^{17}O$ of the water begins to change (Fig 1.25). The nature of fluid flow is a function of the asteroid's size, heat budget, and its permeability (Castillo-Rogez and Young, 2017), and in all models the O-isotopic composition of the fluid and rock is is time integrated due to the multitude of possibilities regarding continuous evoltion of fluid as it passes from one region to another (Fig 1.25).

1.7.2.2 Single pass 'exhalative' fluid flow

Small <10 km radius asteroids may have experienced 'single pass' flow (Bayron, 2021; Young, 2001; Young *et al.,* 1999). In this regime, water moves from the warm centre of the asteroid to the surface in one pass down a temperature gradient, where it is frozen and potentially sublimed into space (Fig 1.25). Finite difference models have reproduced the O-isotopic trends of CM whole rock and carbonates by modelling them as part of a diverse asteroid that experienced single pass flow and produced areas similar to CV, CM and CI chondrites from core to surface (Fig 1.25, 1.26). In this model, an alteration front forms in the asteroid where fluid flux is very high, and just exterior to the front represents the domain of highest aqueous alteration. Progression between different fluid environments is presented as a series of shallow and steep vectors from left to right on a 3-isotope plot (Fig 1.26). Shallow vectors are consistent with mass-dependent fractionation lines in line with regions of consistent, rock or fluid dominated fluid flux. Steep vectors represent the transition between regimes of fluid flux, giving the appearance of mixing. The zone of highest fluid flux, and therefore greatest aqueous alteration, occurs in regions of lowest temperature.

Young *et al.* (2001) postulated that the CM chondrites sample a region intermediate between the alteration front and the core of the body (Fig 1.25, 1.26).

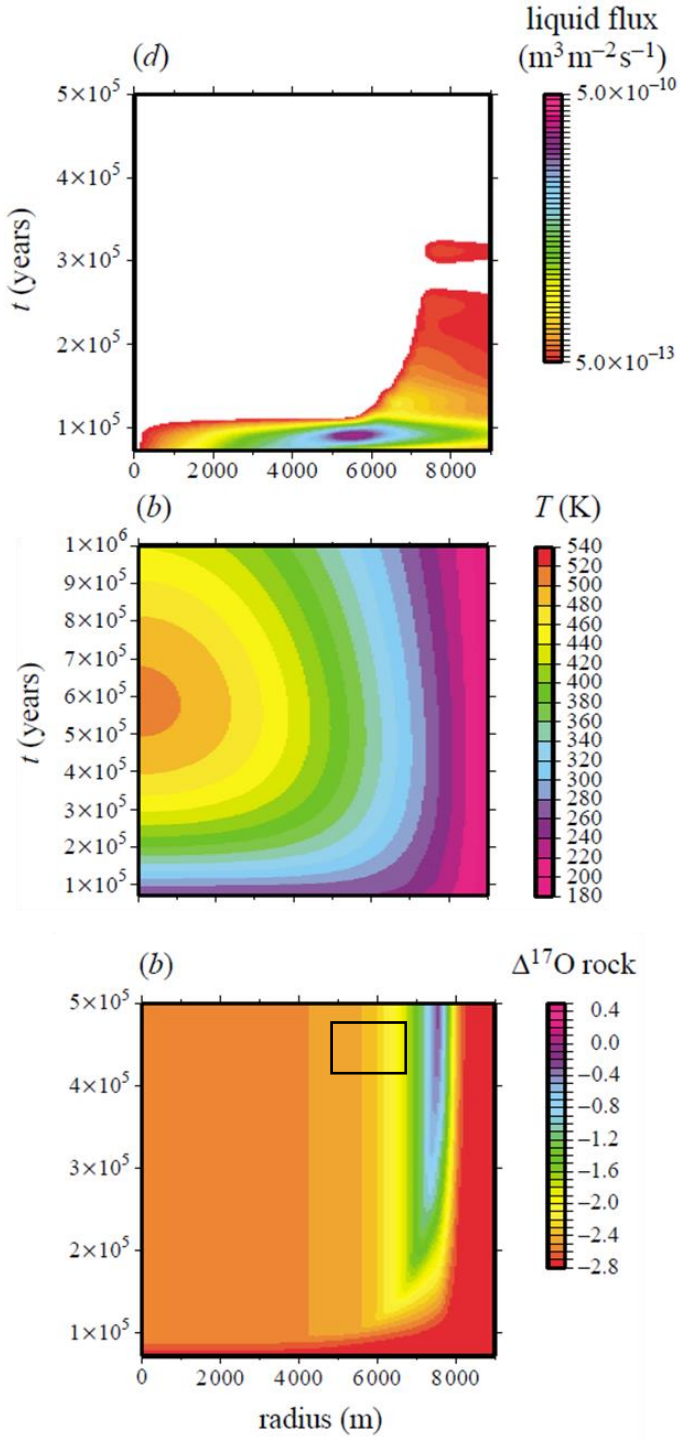

Figure 1.25 – Finite element models by Young *et al.* (2001) for a 9 km radius asteroid 500,000 years after accretion undergoing exhalative flow. The flux of liquid water varies throughout time as it moves from the centre of the body outwards down a temperature gradient. An alteration front forms within the body just exterior to the region of highest fluid flux. The area delineated by the small black box is congruent with the composition of CM chondrites.

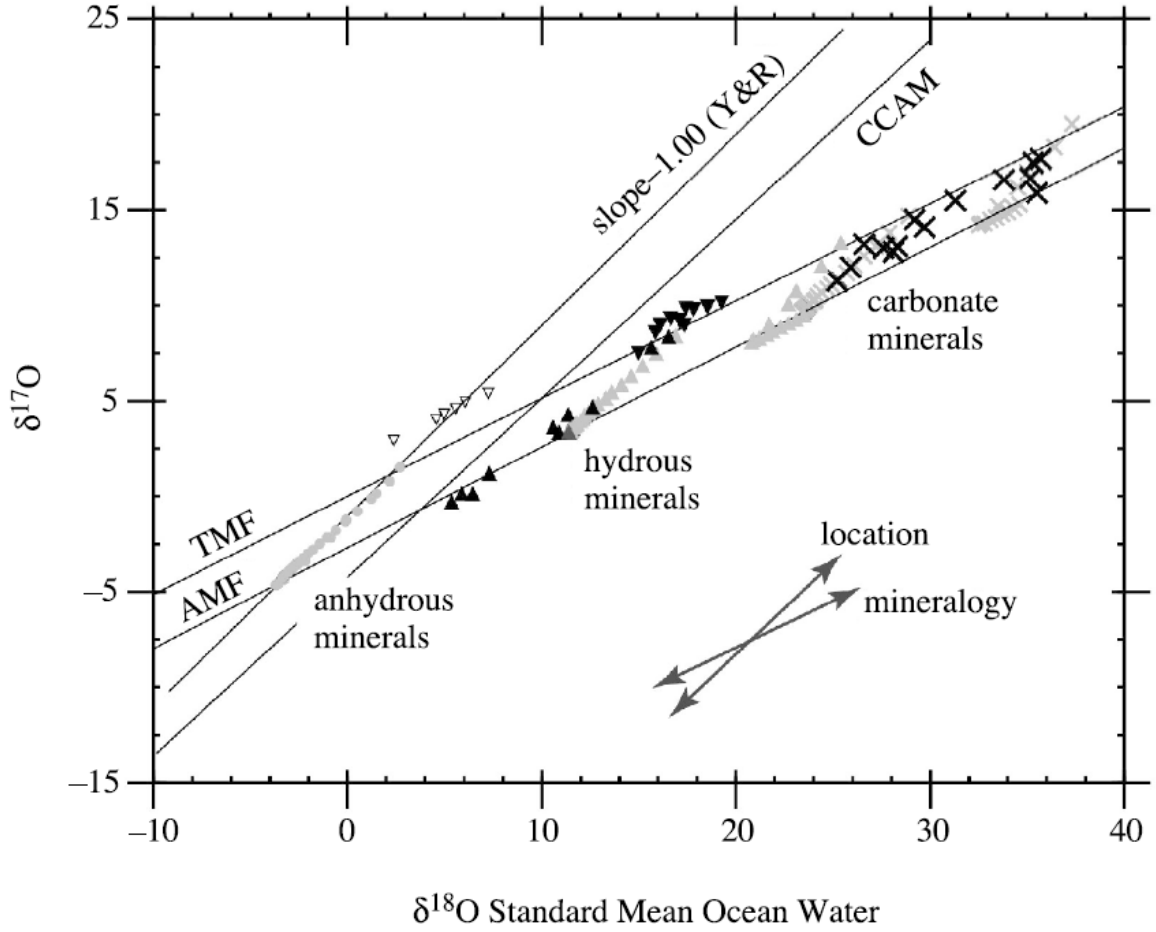

Figure 1.26 – Finite difference model results from Young (2001) (Fig 1.25) showing the variety of modelled products (grey triangles and crosses) that could be produced in a 9 km radius, parent body within a single-pass flow regime with an initial $^{26}Al/^{27}Al$ ratio of 1×10^{-5}. Included are bulk values from the literature (Clayton and Mayeda, 1999; Rowe *et al.*, 1994). Downward facing triangles are literature compositions for CI chondrites. Upward triangles are for CM chondrites. Light grey symbols are modelled values. As can be seen, consistent fluid flux in regions of either rock or water dominated alteration produce mass-dependent fractionation lines, indicative of changing mineralogy (shallow vector). Transitioning from one region of fluid flux to another causes a steepening of the modelled data (steep vector), indicating a change in location in the parent body. As stated by Young (2001), this does not explicitly suggest that CI and CM chondrites sample one asteroid, only it is possible that a common geological evolution encompassing fluid flow could have affected many chondrite parent bodies.

Mineral compositions in between these areas of constant fluid flux represent a transition in location from one region to another, at varying depths within a parent body.

1.7.2.3 Convection

Larger asteroids, upwards of 50-100 km may undergo multi-pass via convection, where upwelling hot water is cooled at the frozen surface before being transported back to the centre of the asteroid (Bland and Travis, 2017; Cohen and Coker, 2000; Grimm and

McSween Jr, 1989; McSween Jr *et al.*, 2002; Palguta *et al.*, 2010; Travis and Schubert, 2005). Convection differs from single pass in that the oxygen isotopic composition of the rock is not as strictly coupled to the temperature gradient, as convective cells regulate the heat from the top to the bottom of the asteroid and vice versa, producing large zones of fluid flux within the body as upwellings and downwellings (Palguta *et al.*, 2010; Travis and Schubert, 2005). The temperature may vary slightly across a convective plume of consistent fluid flux as a result. The results in O-isotope space would be like that of Young (2001) but less extreme, and the domains alteration would be spatially heterogeneous, not radial.

Bland and Travis (2017) suggested that a combination of convection and isochemical alteration could occur if the flowing medium was not water, but mud. In this, it is argued that upon accretion, the CM parent asteroids would have not had time to lithify before being saturated in water. As such, water and rock would move together as a giant, convecting mud ball, producing a well-mixed asteroid where net transport of volatile elements was severely limited. However, support for this model remains tentative to date.

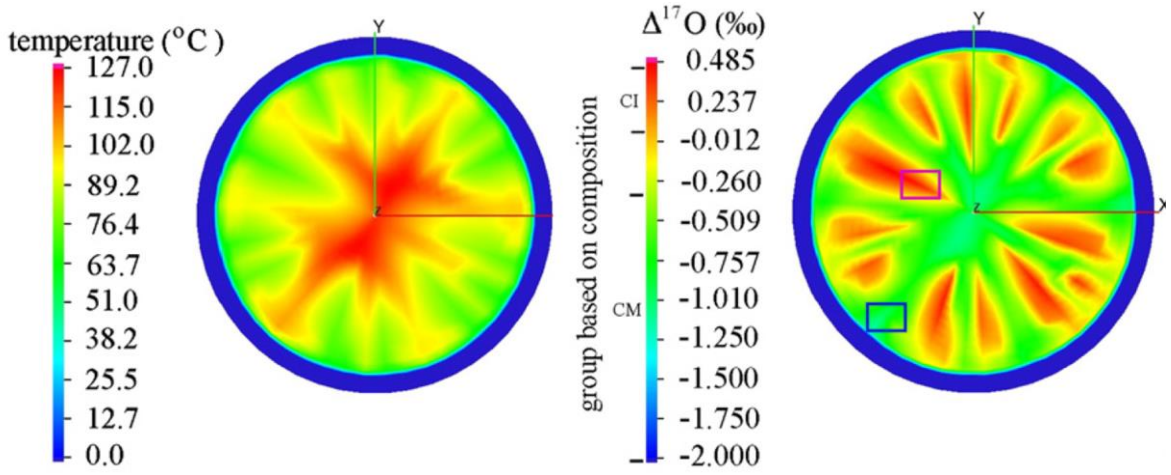

Figure 1.27 – Results of a convection model by Palguta *et al.* (2010) in an asteroid of 50 km radius with an initial $^{26}Al/^{27}Al$ ratio of 4.5×10^{-8}. Results are 2.7 million years after accretion. Convective movement of water causes upwellings and downwellings of water and an efficient mechanism for heat regulation, producing a highly heterogeneous parent body. The black square overlain by Palguta *et al.* (2010) represents the most 'CM-like' region with respect to O-isotope composition.

1.8 Challenges in CM meteoritics

"One of the other things that has occurred is the change of emphasis within extra-terrestrial science. As I said, my first exposure to extra-terrestrial things was through Anders and Urey and Harrison Brown. They were doing everything really as 'chemists', without any geological or petrological context. I mean, you got a sample vial with some powder in it. You analysed it, and you analysed it exquisitely well, and you could draw some broad conclusions, say, about the role of volatility in fractionation within the solar nebula, and so on. But you didn't think about meteorite parent bodies as actual places with actual processes going on. I think that really came along later."

Robert N. Clayton (Marvin, 2001)

The closed and open system models are heavily reliant on bulk O-isotope data. However, O-isotope analysis often utilises the homogenisation technique, wherein a large chip of CM chondrite (typically 100s mg) is finely ground to reflect a bulk composition. This is done with the underlying assumption that the petrography of that sample is known, presumably drawn from investigation of a small number of sections. A likely reason for this rationale is conservative sampling owed to sample rarity, which is understandably justified as many CMs — despite the considerable range of now-recognised petrologic subtypes — appear chemically homogeneous with respect to most elements (Braukmüller *et al.*, 2018; Lee *et al.*, 2020; Lodders, 2003). However, with the realisation that most, if not all CM chondrites are complex breccias (Bischoff *et al.*, 2006), it is apparent that chondrule and CAI abundances vary considerably within and between lithologies. Different measurements of even single CM chondrites can vary along the slope ~0.7 array (Lee *et al.*, 2019) – resulting in different estimations of WR ratio within and between individual CM chondrites assuming a closed system model (Clayton and Mayeda, 1999). Estimation of the degree of alteration in thin section to aid these models may also not be translatable to the region sampled for O-

isotope analysis. The magnitude of contamination by anhydrous precursors is therefore intimately mixed with any potential variance caused by parent body effects.

With this information, the homogenisation approach becomes difficult to rationalise when uncharacterised chips may contain a random assortment of diverse clasts reflecting a wide range of alteration histories. Higher resolution O-isotope analyses of the aqueously altered products, particularly phyllosilicates, are desperately needed to complement the ever-growing repertoire of carbonate data and reveal any as of yet unknown O-isotope patterns caused by the alteration process. The core motivation of this work is to resolve this ambiguity problem for O-isotopes in recognition of the exceptional CM diversity.

1.8.1 Thesis aims

The research objectives of this thesis are summarised by a single question:

What is the nature of the complex alteration in CM chondrites?

To provide an answer, the following objectives will be sought:

- To robustly assess the lithological diversity within a suite of CM falls and finds. Petrographic context will be established through investigation of polished blocks with a high surface area via scanning electron microscopy. The aim will be to elucidate the boundaries, and the differences in mineralogy and chemistry between primary lithologies.
- To measure precise O-isotope ratios of the 'bulk' aqueous alteration products (matrix and TCI) in characterised lithologies, away from the contaminating influence of anhydrous precursors. This will aid in elucidating the lithology-specific conditions of aqueous alteration.
- To marry petrographic context with O-isotopes to relate the differences in mineralogy to any systematic, mass-dependent, or mass-independent isotopic

variations, and if these can be accommodated by current models of closed or open system alteration.

By achieving these objectives, further questions can be considered:

2) *Can different lithologies in CMs have a common parent body origin?*

The extent of lithologic heterogeneity between CMs is not uniformly distributed in thin section. Meteoritic kinship is strongly reinforced by the presence of petrographic relationships, *i.e.,* if two clasts are juxtaposed then they probably sampled the same source body, which necessitates two asteroids interacting in a discrete area of space. It is equally possible that the clasts within CM chondrites could represent a diverse, single parent body. Spatially resolved O-isotope data will aid in identifying any xenolithic or foreign fragments. Clear aims in this regard would be to actively search for unusual xenoliths; the 'CM3' precursor; 'regolith-like' material and CM1 material juxtaposed against CM2 material.

3) *What is the extent of terrestrial weathering?*

The very porous, poorly crystalline CM chondrites are vulnerable to contamination by atmospheric moisture (Lee *et al.,* 2020). Making use of a diverse a sample set containing both pristine falls and weathered finds will resolve any O-isotope effects owed to terrestrial weathering. Analysis of minimally weathered CM1 material in particular would go far in confirming if CM1 Antarctic finds are weathered to lighter O-isotope compositions.

4) *Are the CM chondrites in our meteorite collections representative of the whole CM asteroid?*

The meteorite record is a poor reflection of the diversity, and relative abundance of asteroidal material as only the most robust material survives entry into Earth's atmosphere to be recovered as a meteorite. Surveying a large surface area of CM material increases the likelihood of identifying rare, or fragile lithologies that may represent more unusual areas of the CM asteroid that have not yet been examined

Chapter 2 - Material and Methods

2.1 Sample selection

Several samples were selected and made into polished blocks to fulfil the thesis objectives (Table 2.1). Blocks with a large surface area are desirable to maximise the probability of finding multiple CM lithologies. An important sample studied in this thesis is LON 94101, an exceptionally diverse CM chondrite from which a large, resin block (7 cm in the longest dimension) was made and provided for this work by the Meteorite Working Group (Zolensky *et al.*, 2022). Initially, the project planned to compare any results obtained from LON 94101 with the recent, pre-rain fall, Mukundpura to assess any terrestrial weathering effects. Fortuitously, three more CM falls, Aguas Zarcas, Kolang and Winchcombe, fell over the course of this PhD, amounting to 30 kg of recovered stones. As a result, material was more freely available and samples of each were purchased to expand the sample set.

Table 2.1 – Meteorite falls and finds investigated in this work. LON 94101 was recovered in the Antarctic Search for Meteorites Program (ANSMET) in 1994. All meteorite nomenclature, including recovered mass and classification, is sourced from the Meteoritical Bulletin Database (*e.g.*, Gattacceca *et al.*, 2020).

Name	Year	Location	Mass (kg)	Classification[#]
Falls				
Mukundpura	2017	Mukundpura, India	2	CM2
Aguas Zarcas	2019	Alajuela, Costa Rica	27	CM2
Kolang	2020	Sumatera Utara, Indonesia	2.5	CM1-2
Winchcombe	2021	Gloucestershire, UK	~0.8	CM2
Finds				
LON 94101	1994	Antarctica, Lonewolf Nunataks	2.8	CM2

2.1.1 Carbonaceous chondrite falls

2.1.1.1 Mukundpura

Despite falling in 2017, Mukundpura has seen little published work. Debate continues over its petrologic classification, with initial reports suggesting a CM2.7, whereas later publications argue for it being a CM2.0 or even a CM1 evidenced by a wide distribution of heavily altered lithologies (Pizzarello and Yarnes, 2018; Potin *et al.*, 2020; Ray and Shukla, 2018; Rudraswami *et al.*, 2019). Analysis of its organic content and carbonate O-isotopic

compositions agree with the meteorite having experienced intense alteration (Pizzarello and Yarnes, 2018; Potin *et al.*, 2020; Vacher *et al.*, 2019b).

A large, 8 g pre-rain chunk of Mukundpura and a ~8 g vial of small post-rain chips were sourced from a private collector and examined for potential sampling opportunities. Prior to sampling, it was noted the 8g pre-rain chunk was lithologically diverse, and so it was scanned using X-ray computed microtomography by Brett Clark and Dr Sara Russell at the Natural History Museum, which revealed the extent of the approximately 5 x 11 mm featureless inclusion within. The inclusion is unique, appearing compact, featureless, fractured, and lighter grey in hand specimen. The host is brecciated but appears consistent with highly disturbed, comminated material, commonly called 'cataclastic matrix'. Small, ~50 mg chips of the host and clast were mounted into 10 mm rounds respectively (MP-03 and MP-05). In addition, a total of five small (10-20 mg) post-rain fragments were mounted adjacent to each other in a 24.5 mm aluminium round (MP-01).

2.1.1.2 Aguas Zarcas

Falling in Costa Rica in 2019, the ~27 kg Aguas Zarcas is the largest recovered CM fall since Murchison. A number of papers have been published since its arrival, revealing the meteorite predominantly hosts moderately altered lithologies from CM2.4 – 2.7 (Kerraouch *et al.*, 2021; Kerraouch *et al.*, 2022; Pizzarello *et al.*, 2020; Yang *et al.*, 2022). Unusual clasts, including C1, CM1/2 and two metal-rich lithologies have been reported by Kerraouch *et al.* 2021 and Kerraouch *et al.* 2022, further corroborated by Dionnet *et al.* (2022). The metal-rich lithologies are out of place compared to the typical, aqueously altered characteristics of altered CM2s as metal is one of the most vulnerable phases during aqueous alteration. As a result, these clasts have been hypothesised to represent impactor fragments from a discrete accretionary environment separate from the typical CM2 area (Kerraouch *et al.*, 2021).

The sample of Aguas Zarcas in this study is from a large 16 g pre-rain fragment acquired from the reputable meteorite collector Graham Ensor. A proximal lobe of the fragment was removed using a manual rock press to exploit an existing fracture, and a 900 mg chunk was selected from the debris after observing acute clast boundaries under the binocular microscope. Two slices were cut from the chip and made into blocks AZ-03 and AZ-04, respectively, which contained identical clasts; therefore, only AZ-04 was used. A smaller chip, weighing approximately 50 mg, was recovered from a vial of cutting fragments from a previous sampling attempt unrelated to this project. This chip exhibited interesting hand-specimen characteristics (appearing compact, and chondrule-poor) and was subsequently mounted into a 10 mm brass ring, AZ-02.

2.1.1.3 Kolang

Kolang fell in Indonesia in 2020 and is officially classified as a CM1/2, the sole example of a fall in this subgroup of meteorites and the most altered of any CM chondrite fall to date, at least when considering modern CM classification methods (Alexander *et al.,* 2013; Howard *et al.,* 2015; Rubin *et al.,* 2007). Few papers delve into detail regarding the petrography of Kolang though all corroborate its highly altered nature (*e.g.,* Schrader *et al.,* 2021). The sparsity of published data is compensated by a detailed entry on the Meteoritical Bulletin, describing numerous, predominantly CM lithology types (chondrule-poor and chondrule-rich, respectively) in addition to metal-rich and 'green-gray breccias' that have peculiar ^{16}O-rich O-isotopic compositions, though the absence of petrography limits any conclusions that can be drawn from this data (Gattacceca *et al.,* 2021).

Five chips of Kolang were purchased from meteorite collector Graham Ensor, amounting to approximately 6 g. From these chips, several lithologies were identified for subsampling. One chip, weighing ~400 mg contained a sharply delineated clast, and the entire chip was mounted into a 1-inch brass round, KO-01. A second chip contained two lithologies: a

cataclastic host (KO-02) and a pea sized, polygonal clast (KO-03) standing proud from the surface. 50 mg samples of each were mounted into 10-mm brass rounds.

2.1.1.4 Winchcombe

The response to the 2021 Winchcombe fall was rapid and an initial paper was quickly published in Science Advances (King *et al.,* 2022). Further papers have since been published in a special issue in Meteoritics and Planetary Science, comprising a wide range of topics and analytical approaches including meteorite recovery, coarse- and fine-grained mineralogy, isotopes, weathering and insights into the nature of the fusion crust (Daly *et al.,* 2021; Genge *et al.,* 2023; Greenwood *et al.,* 2023; Jenkins *et al.,* 2023; McMullan *et al.,* 2023; Russell *et al.,* 2023; Sephton *et al.,* 2023; Suttle *et al.,* 2023). Eight lithologies have been reported spanning a petrologic range of 2.0-2.6, with a dominance in the lower petrologic subtypes, indicating Winchcombe is a highly altered CM chondrite like Mukundpura, but probably less altered than Kolang (Suttle *et al.,* 2023).

Two, ~ 8.5 g chunks (BM.2022, M1-85, 86) of Winchcombe are on long term loan from the Natural History Museum and stored under nitrogen at the Open University (Greenwood *et al.,* 2023). Approx 100 mg from each chunk was removed prior to storage and mounted into two 10 mm brass rings. As these chunks are the property of the NHM, the subsequent 10 mm brass round blocks adopt their nomenclature and are named BM.2022, M1-117 and BM.2022, M1-123 respectively. In addition, a 1-inch resin NHM round block, P30424 was loaned from the NHM for microsampling.

2.1.2 Lonewolf Nunataks 94101

LON 94101 and its pairing mate LON 94102 are two of the largest CM finds recovered from Antarctica. This meteorite is well known for its exceptional lithological diversity, with every thin section analysed over the years appearing completely different with lithologies spanning the entire CM petrologic range from CM1-CM3.0 (Gregory *et al.,* 2015; Lee *et al.,* 2013; Lindgren *et al.,* 2011; Lindgren *et al.,* 2013; Zolensky *et al.,* 2022). A 42 g mass of LON

was obtained from the Meteorite Working Group where it was scanned using XRCT at the UT High-resolution X-ray CT Facility (Fig 2.1), identifying at least 20 lithologic clasts up to ranging from 100 mm – 1 cm in the longest dimension. At the Johnson Space Centre, an optimal plane was chosen that would expose the greatest number of clast surfaces and the stone was vacuum impregnated entirely into a large block of epoxy to prevent the sample from falling apart during the sectioning process. The block was then and slowly cut without water using a thin, isomet saw blade. One half was used for an LPI summer internship in 2015, wherein space exposure ages were determined on individual clasts (Gregory *et al.*, 2015). The sister half was shipped to The Open University, where it underwent additional surface preparation and is described here.

2.2 Polished block preparation

All polished blocks are listed in Table 2.2. Electron microscopy applications (SEM, EPMA) have demanding sample requirements and necessitate well prepared, topographically flat samples achieved by polishing (*e.g.*, Harrington and Righter, 2017). However, phyllosilicate-rich carbonaceous chondrites pose challenges for the polishing process. The variation in hardness between refractory grains and soft, friable matrix causes plucking, scratching and preferential erosion of soft regions, inducing topographic variations through the recession of sample into resin. The consequences of topography include charging effects under the SEM, as well as undesirable electron scattering, resulting in poor images and low analytical totals.

2.2.1 Vacuum assisted resin impregnation

One possible solution for the polishing of challenging terrestrial samples (*e.g.*, mudstones) is vacuum-assisted resin impregnation of the sample surface (Bonato, 2020; Harrington and Righter, 2017). While this approach produces a desirable sample surface for chondrites, it percolates the upper layers of the sample creating the potential for significant resin contamination (Fig 2.3). Resin impregnation was not attempted in-house to avoid this issue,

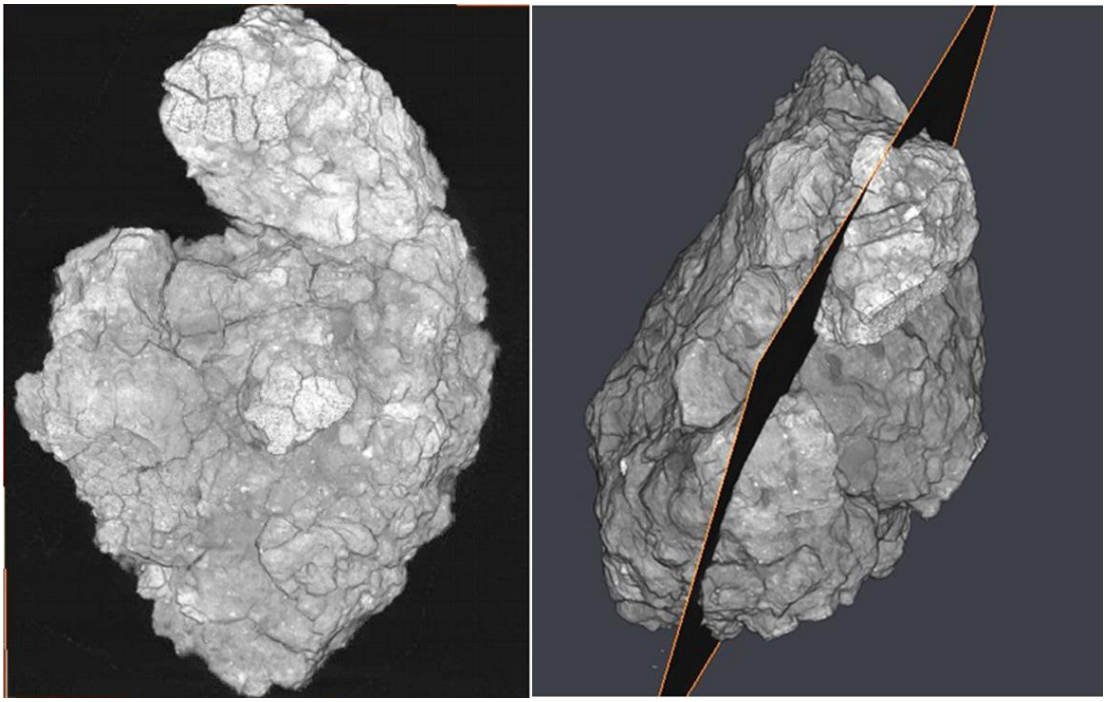

Figure 2.1 - X-ray computed tomography of LON 94101-4, Undertaken at the UT High-resolution X-Ray CT Facility at the University of Texas. Image courtesy of Dr Mike Zolensky (Zolensky *et al.*, 2022).

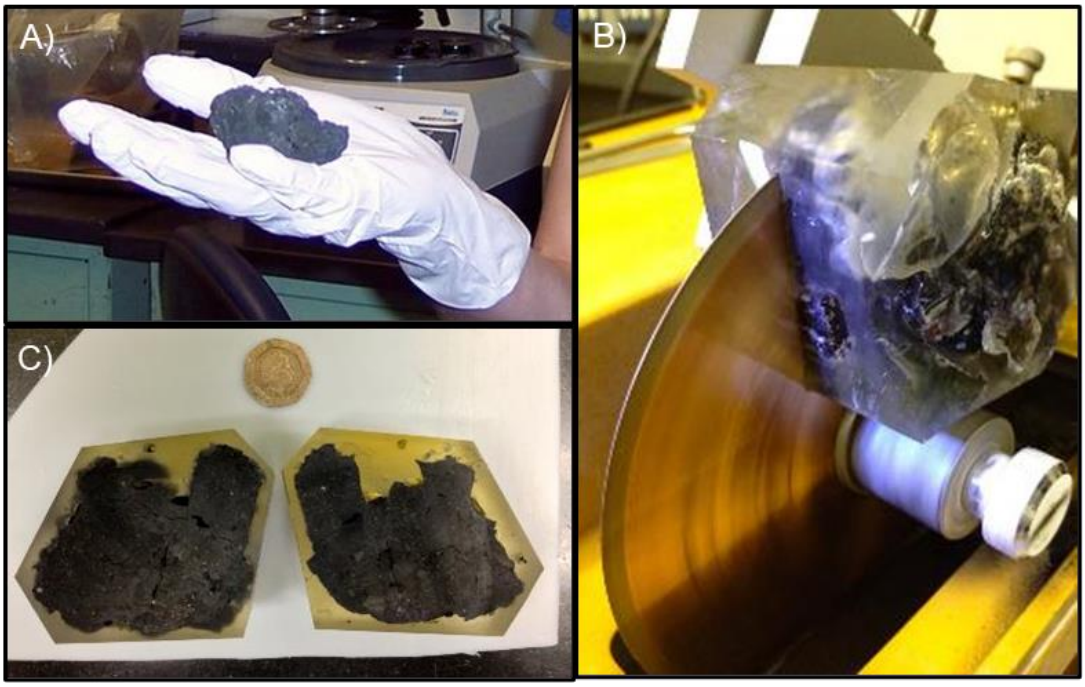

Figure 2.2 - Preparation images of LON 94101 at the Johnson Space Centre, 2015; A) The original. ~100 g hand specimen before mounting in resin. B) Halving of the specimen using an ultra-thin, isomet saw blade to minimise sample loss (Gregory *et al.*, 2015). C) Both 'sister-halves', of which the specimen on the right-hand side (LON-04) was used in this project, contain mirror images of some lithologies. The size of the twenty pence piece is 24.1 mm. Images courtesy of Dr Mike Zolensky and Dr Tim Gregory.

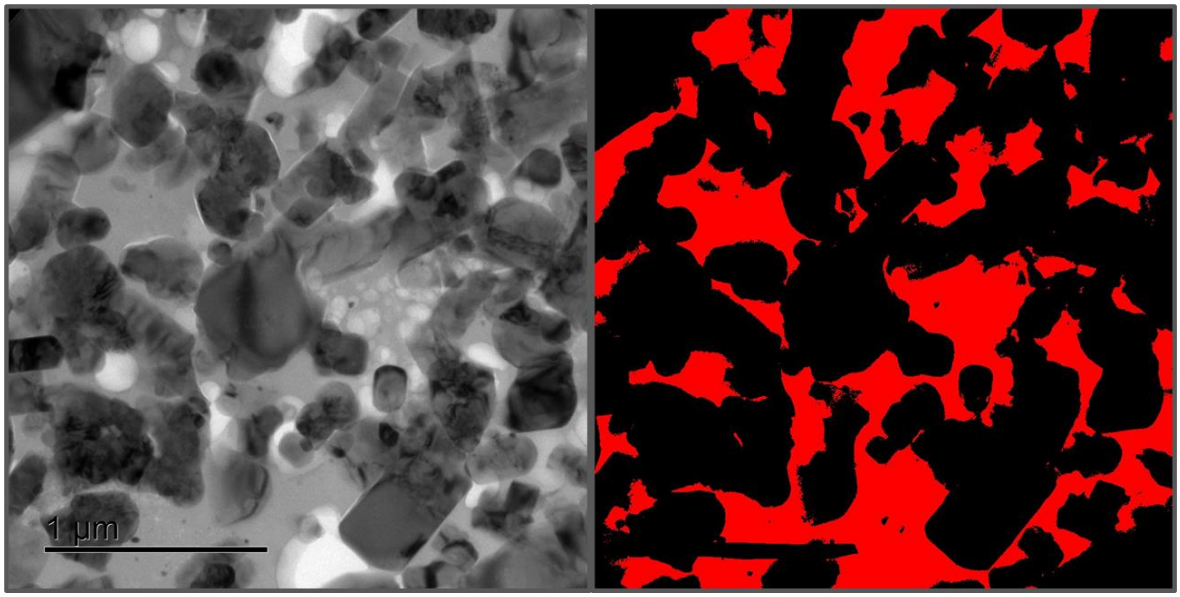

Figure 2.3 - TEM lamella of a vacuum-assisted resin impregnated thin section of CO3.6 chondite Moss with resin percolation between anhydrous grains at the nanometre scale. The red colour in the right-hand image is epoxy resin. Figure courtesy of Dr Enrica Bonato (Bonato, 2020).

as the small surface area of the 1 inch and 10 mm round polished blocks permitted careful polishing without impregnation. The exception was LON-04, which had a very large surface which was challenging to flatten / polish without disastrous scratching of the sample surface owed to plucking. Early attempts to image the raw surface revealed extensive saw marks across the sample that made obtaining good quality images impossible. Subsequently, the block was treated by Dr Enrica Bonato at the Natural History Museum to stabilise the very large surface before minimal hand polishing. The resin used was low viscosity Struers Specifix which was vacuum impregnated into the surface of the block and left to cure for two days. The sample was ground by hand using coarse diamond fixed abrasive then followed by finer SiC abrasive, ranging from 100 – 4000 grit. The problem of resin contamination in this case can be mitigated as the large sample size permits milling away the first 50 µm of material to access uncontaminated material beneath.

2.2.2 Mounting

In house, meteorite chips were mounted in a 25.4 mm or 10 mm round brass rings (Table 2.2). Each ring was placed on a Parafilm coated glass slide and firmly pressed to create a

Table 2.2 - Polished rounds. A, B, R designate Al ring, brass ring, and resin rounds respectively. All polished blocks of Winchcombe were analysed as part of the Winchcombe consortium and represent a contribution towards published work (Greenwood *et al.*, 2023; King et al, 2022; Suttle *et al.*, 2023) *LON-04 has a greater surface area than all other blocks combined and dominates the sample set. Samples described as 'brecciated' contain multiple lithologies, but most are too small to sub sample. Light grey boxes indicate sections that were made but not sub-sampled

Polished block	Size (mm)	Chips	Notes
Mukundpura			
MP-01	25.4 [A]	5 small	2 lithologies (made prior to project – 2017)
MP-02	25.4 [A]	3 small	1 lithology (made prior to project – 2017)
MP-03	10 [B]	1 small	2-3 lithologies - moderately brecciated
MP-04	10 [B]	1 small	Multiple lithologies – highly brecciated
MP-05	10 [B]	1 small	1 CM1 lithology
Aguas Zarcas			
AZ-01	10 [B]	1 small	1 CM2 lithology - mostly fusion crust
AZ-02	10 [B]	1 small	1 CM2 lithology
AZ-03	25.4 [B]	1 large	4 CM2 lithologies. One chip cut in half, both mounted in separate blocks.
AZ-04	25.4 [B]	1 large	
Kolang			
KO-01	25.4 [B]	1 large	3 lithologies
KO-02	10 [B]	1 small	2-3 lithologies - moderately brecciated
KO-03	10 [B]	1 small	1 lithology – C1 inclusion
Winchcombe			
BM.2022, M1-117	10[B]	1 small	1 lithology 'B'
BM.2022, M1-123	10[B]	1 small	Multiple lithologies
P30424	25.4[R]	1 small	1 lithology 'B'
Lonewolf Nunataks 94101			
LON-01	25.4 [R]	1 large	Multiple lithologies - highly brecciated
LON-02	25.4 [B]	1 large	Multiple lithologies - One chip cut in half, both mounted in separate blocks.
LON-03	25.4 [B]	1 large	
LON-04[*]	25.4 [R]	1 very large	Multiple lithologies - highly brecciated

hermetic seal. A two-part epoxy resin / hardener mixture with low outgassing for vacuum systems (Epoxicure2 by MetPrep) was mixed for 3 minutes by hand in a foil bucket, slowly, to prevent air bubbles. Then, the meteorite chip was placed inside the brass ring and the resin was syringed on top. The slide was tapped to liberate air bubbles and left to cure at room temperature for three days. Afterwards, the parafilm was peeled off and the sample was ready for primary stock removal.

2.2.3 Stock removal and polishing

The primary stock removal of the larger, 25.4 mm rounds were carried out by machine by the laboratory technicians in the thin section laboratory, whereas 10 mm brass rounds were flattened by hand. All the polishing procedures after initial flattening were undertaken by hand with materials supplied by MetPrep. First, the sample was ground on the rear side to clean and flatten using 180 grit followed by 1200 grit SiC paper. The sample side was then progressively ground with 1200 SiC paper followed by 2400. Primary polishing was undertaken using a Nylap polishing cloth charged with 9 µm diamond paste. Final polishing was undertaken using a Durasilk polishing cloth with 6 µm followed by 3 and 1 µm stages (Fig 2.4 for overview). Durasilk is a soft, silk cloth that can 'smear-polish' and flatten the phyllosilicates without rounding the edges of harder grains or plucking them loose. The Nylap and Durasilk cloths are napless and host the polish grades without accumulation or rolling of paste. All other standard cloths, especially those with a nap (*e.g.* Multicloth, Alphacloth, Truenoire) were not used to avoid abrasion of the carefully prepared surface. The polishing was essentially dry, *i.e.*, with no lubricant, to mitigate the inherent hygroscopic nature of CMs, as water-based solvents will cause any smectites (if present), and phyllosilicates to swell and damage the sample surface. All trialled solvents, including IPA and non-polar options such as hexane or ethylene-glycol caused detrimental damage to the surface of the section, possibly as a result of the variable pressure associated with hand polishing, and the absence of any surface stabilisation through resin impregnation. Further experimentation to improve the polish is needed for any future work on *in situ* isotopic analysis of these polished blocks. Light charging of paste, followed by at least 1 hour hand polishing at the 9, and 6 µm stages and 3-4 hours on the 3 µm and 1 µm stages appeared to produce the most optically flat surface with minimal plucking, scratching and chip recession. The most effective polishing action appeared to be vertical lines, from back to front (Fig 2.4), rotating the sample every 5 strokes. Circular movement caused plucking, smearing and disruption of the surface.

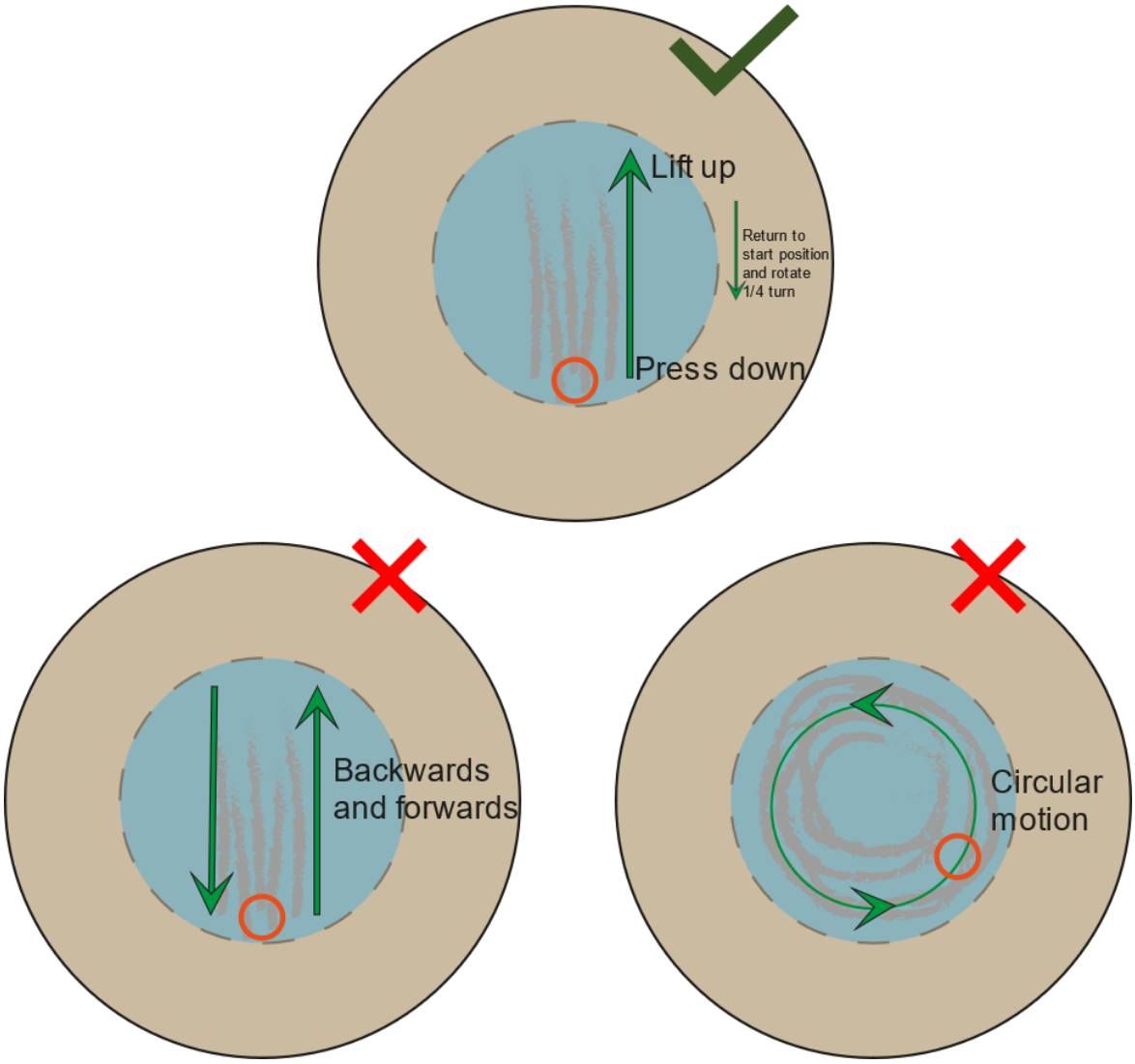

Figure 2.4 - Dry hand-polishing techniques for fragile carbonaceous chondrites. The beige circle represents the polishing cloth. The blue circle represents area charged with polishing paste. The small orange circle represents the sample. The best approach is to use a gentle linear motion from the bottom to the top, lifting the sample at the top and then bringing it back to the original spot, rotating ¼ turn every 5 strokes, and repeating (top). Forwards and backwards action and/or circular motions appear to pluck the surface (bottom). No lubricant was used, gentle pressure applied using fingers.

2.2.3.1 Cleaning

Cleaning between each polishing stage was undertaken as follows: First the resin surrounding the sample surface was gently wiped with a non-linting cloth wetted with IPA. A beaker was filled with electronic grade (99.9 %) IPA and lowered using a wire basket into an ultrasonic bath. The sample was then ultrasonicated for 2-3 seconds to minimise risk of sample surface disruption. During ultrasonication the sample remained in the column of fluid

and did not touch the bottom of the glass to prevent rattling. The ultrasonic cleaning can damage fragile samples if care is not taken - chondrules and larger fragments of matrix may fall out. If the sample surface was significantly disrupted, the polishing procedure was restarted. If the sample was particularly friable, it was only wiped and no ultrasonication was attempted.

2.3 Scanning Electron Microscopy

Analysis of backscattered electrons and X-rays through energy dispersive spectroscopy is a fast, time effective method achievable on a scanning electron microscope, and so was utilised extensively during this work. All samples were carbon coated with a ~20 nm carbon coat before investigation.

2.3.1 Large Area Mapping

Preliminary mapping was undertaken on a tungsten filament, FEI Quanta 200 3D FIBSEM at the OU. This machine was exploited for its AutoMate feature which permitted high-resolution large area mapping (LAM) of backscattered electrons (BSE). Backscattered electrons have larger interaction volumes than topography sensitive, secondary electrons (SE), and are therefore more forgiving of the poor polish often accompanying CM sections. The BSE output greyscales reflect variation in atomic number in the minerals contained in the area of interest (higher atomic number = lighter greyscales). A qualitative snapshot of meteorite chemistry can thus be inferred if a user has a basic knowledge of the samples they are investigating, *e.g.*, Mg (dark) vs Fe (light) rich domains (Fig 2.5). For preliminary mapping, the working conditions were 20 kV, 0.6 nA and a working distance of 15 mm. The maps were undertaken using 200x magnification with an image resolution of 1204 x 896 pixels for BSE. Individual BSE frames were then stitched in Image Composite Editor to remove the resolution caps imposed on exports by the Oxford Instruments INCA software.

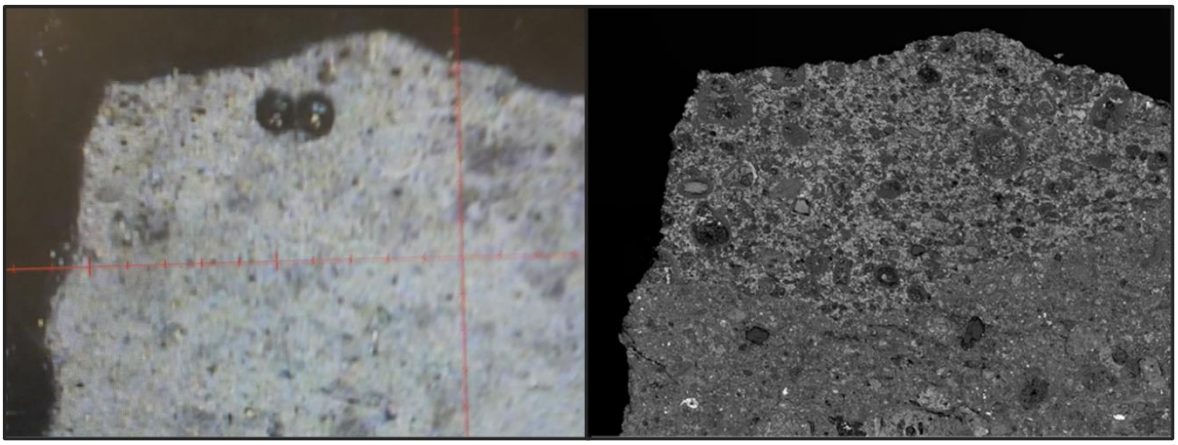

Figure 2.5 - A comparison of a reflected light image (left) obtained using the micromill camera and BSE image (right) of the CM1-2 meteorite Kolang. Note the difficulty in identifying clast boundaries in the reflected light image when compared to the ease of identification in the BSE image. The clast is a lozenge-shaped inclusion which encompasses 50 % of the top field of view. SEM imaging is therefore essential for identifying different lithologies. Black circles are micromilled holes 500 μm wide.

2.3.2 Spot analyses

After preliminary mapping, quantitative investigation was undertaken using field emission scanning electron microscopes over two analytical campaigns. Initially, representative areas of each CM lithology were mapped at a much higher BSE and EDS resolution (variable dependent on machine used – see below). After assessment of the maps, spot analyses were then undertaken. Due to time constraints, spot analyses of all the lithologies in LON-04 were not possible; therefore, in these cases, super-high-resolution EDS area maps were used to create 'regions of interest' where the EDS data per pixel was averaged over a chosen area, done using the Aztec software provided by Oxford Instruments.

2.3.2.1 Zeiss Supra 55 VP

The first campaign involved investigation of the polished blocks encompassing all the meteorite falls in addition to the small 1-inch round sections of LON, and was undertaken on a Zeiss Supra 55 VP FEGSEM using the following working conditions: 20 Kv, 0.5 nA and 8.5 mm working distance. EDS analyses were undertaken using an Oxford Instruments, 80mm^2 X-max Energy Dispersive X-ray detector. Overview BSE images were acquired

between 150-200 x magnification with a resolution of 2048 x 1536 pixels, with a dwell time of 20µs per pixel. Overlay EDS maps were acquired at the same resolution with a dwell time of 200 µm per pixel. Owed to difficulties with the instrument, the EDS maps from this campaign suffered from inconsistency issues owed to multiple detector failures over the course of the project, and as such, some maps are of lower resolution due to the consequence of acquisition during a limited time frame. Spot analyses were acquired with a spot size of 1 µm and an acquisition time of 1 minute.

2.3.2.2 Zeiss Crossbeam 550 FIB/FEGSEM

The Zeiss Supra 55 VP was sold halfway through this project and replaced with a state of the art Zeiss Crossbeam 550 outfitted with an Oxford Instruments 170mm^2 Ultim Max EDS detector. This new detector setup was used to undertake the second analytical campaign on the clasts identified in the large block, LON-04. The conditions used were 15 Kv, 0.5 nA and 10 mm working distance. High resolution BSE and EDS maps were acquired at a resolution of 4096 x 3092 pixels with dwell times of 20 µs (BSE) and 500 µs (EDS) respectively; furthermore, this SEM also had the required stage movement (~10 cm) to accommodate the large (7 cm long) LON sample. Spot analyses were acquired with a spot size of 1 µm and acquisition times of 1 minute.

2.3.2.3 Calibration, detection limits and quantification.

Both the Zeiss Supra and the Zeiss Crossbeam were calibrated using built-in factory defaults as provided by Oxford Instruments (the Factory Standard Extended Set). This modern calibration set was obtained in-factory using a set of pure elements under strict measuring conditions. Deviation from these factory standards is typically not needed if there is only interest in major element analysis under typical working conditions.

Detection limits are dependent on the acquisition time, accelerating voltage, the element concerned and the vulnerability of its elemental spectrum to peak overlaps and pulse pile up corrections. This is because the detection limit is determined by the number of counts

recorded at a certain X-ray wavelength relative to the instrument background. Typical detection limits for most elements are between 0.1 and 0.2 wt % when using a 1-minute acquisition time. The Aztec software will also reject any element where the peak to background ratio is less than 10:1.

Beam optimisation was undertaken prior to each session using a cobalt or copper standard. Quantification fell between 98-102 % elemental totals for in-house standard peridot. The totals from sample serpentine, phyllosilicate, and tochilinite are typically lower than that for anhydrous silicates. This is due to the existence of undetectable hydrogen and hydroxyl, and totals typically fall between 75-90 %. This is not uncommon for serpentines which suffer from beam damage, poor polish, often contain porosity, and in the case of CM chondrites, contain appreciable organic content often close to phyllosilicates. The nanoscale intergrowths of different serpentines also cause difficulty in normalising for variations in mineral-specific X-ray intensity, also known as ZAF corrections (atomic number, X-ray absorption and fluorescence effects, respectively), which introduces another layer of unknown uncertainty. The primary elements of interest were Fe, Mg, Si, Ni, S, Al, Na, Ca, Cr, Ti and P.

2.3.3 Regarding classification

The combination of large area maps and spot analyses permit evaluation of the petrologic type and hence the degree of aqueous alteration a CM lithology has experienced. The SEM work here follows the protocols from several published classification schemes (Browning *et al.,* 1996; Lentfort *et al.,* 2021; Rubin *et al.,* 2007), as outlined in detail in Chapter 4.

Wavelength Dispersive Spectroscopy (WDS) has been the method of choice for CM classification in the literature (Browning *et al.,* 1996; Lentfort *et al.,* 2021; Rubin *et al.,* 2007), though some recent work on the Winchcombe meteorite used EDS (King *et al.,* 2022; Suttle *et al.,* 2023). Here, EDS was favoured over the more precise WDS because at present, modern CM classification systems utilise variations in the major element compositions of

Fe, Mg, Si and S only. The EDS detection limits for most elements range from 0.1-1 %, which is within the smallest variations seen between the major elements listed above in most CM phyllosilicate phases.

2.4 The MicroMill

As outlined in the thesis aims, the objective of this work is to better understand the aqueous alteration process on primitive asteroids by O-isotope measurement of lithology specific, secondary alteration products. As these products are distributed in between the large chondrules and CAI fragments, 100-500 µm scale spatial resolution was required to permit specific targeting of the phyllosilicate-rich matrix. A micromill provides 50 µm – 1 mm spatial resolution which, subject to the density of material drilled, can recover µg – mg fractions of powder from a polished section for analysis. This method is most useful where heterogeneities are limited to the mm scale *i.e.*, 'imprisoned' within a polished block where hand sampling is not easily possible, provided the geological context of the targeted surface is well-characterised by SEM. If larger, cm sized inclusions or clasts ('macro-scale' lithologies) exist, it makes more sense to sub-sample these by hand through scraping or cutting. In this case, there must be enough material for an aliquot of homogenised powder and a polished block so the destructive analyses can be correlated with petrography.

2.4.1 Instrument description

The OU micromill is a first-generation New Wave Research Micro-Mill (Fig 2.6) purchased through Elemental Scientific Lasers. The instrument consists of a low eccentricity, high speed (1200-35000 rpm) chuck mounted above an automated X, Y and Z stage with sub-micron step resolution The stock drill bit provided with the instrument is a conically shaped, scriber tip that is capable of 50 µm scale spatial resolution at the apex. A microscope equipped with two CCD cameras permit live, top-down observation for allocation of drill 'scans' on the sample surface and live viewing of the micro-drill bit. A motorised stage with an accurate, Y offset facilitates manual site selection followed by automated drilling (Fig

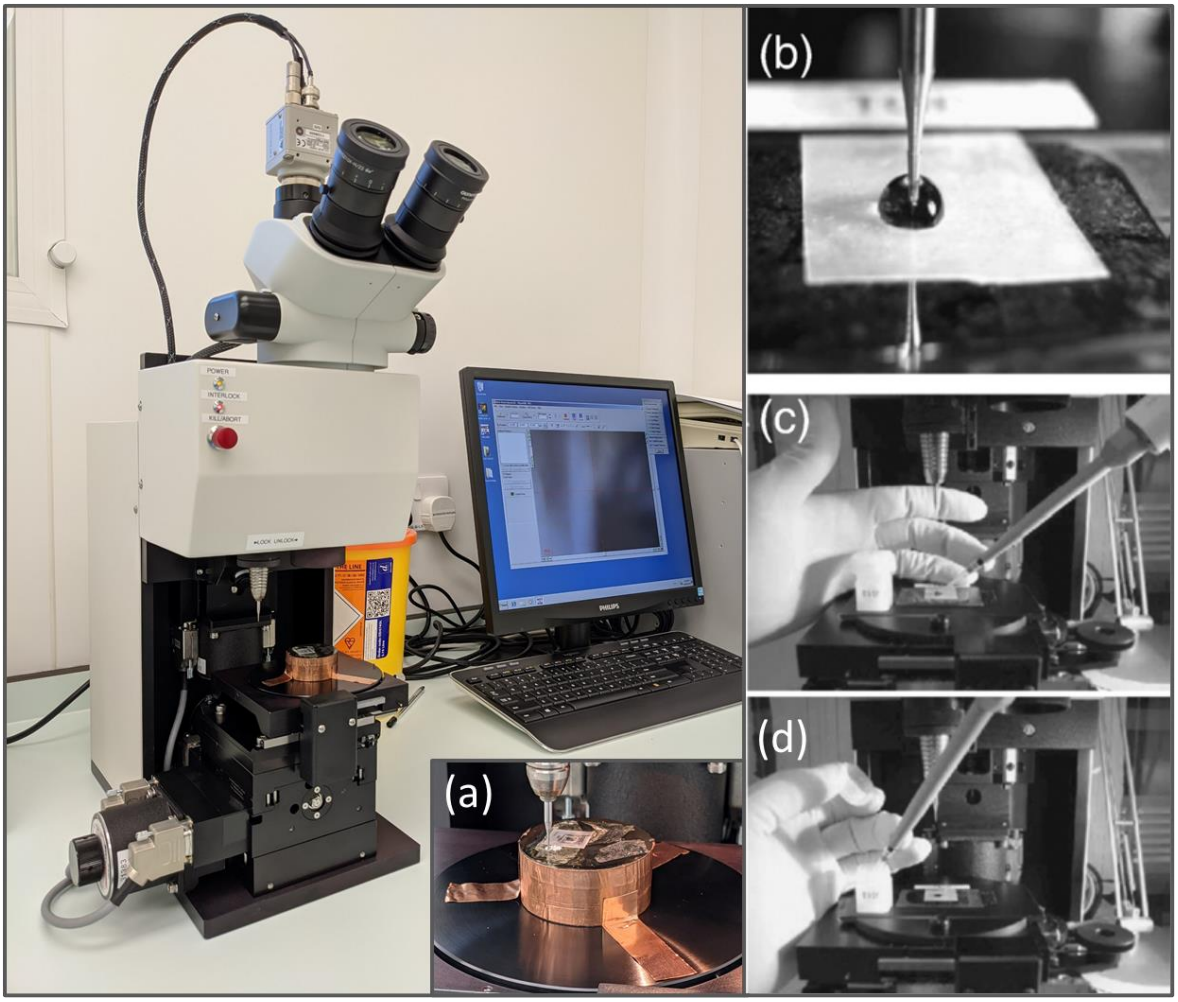

Figure 2.6 – Left) The New Wave Instruments MicroMill in 'scope mode'. (a) a serpentine sample is mounted using copper tape and is drilled dry in 'drill mode' though a parafilm square remains from a previous wet drilling experiment. (b), (c) and (d). the process of wet milling extraction using a droplet of MilliQ and a square of Parafilm (modified after Charlier *et al.* 2006). In this project, the droplet is transferred to a microcentrifuge tube and not a Teflon beaker as shown in the figure. The red interlock button is pressed in the case of emergency.

2.6). The micromill is operated using software provided with the instrument. Up/down and lateral movement is controlled using a fast or slow nudge feature on the scroll bars on the perimeter of the screen (Fig 2.6). Drill parameters are input in 'scope' mode, including desired drill sites which are called 'scans', *i.e.,* a single point, a series of holes, or a raster. Once the sample is attached and all the correct calibration parameters are set at the start of the day, 'drill mode' is selected, deactivating the built-in interlock, and permitting activation of the drill. Once complete, reselection of 'scope' mode is needed to remove the sample. An overview of the most important functions is outlined in Fig 2.7, further elaborated on in the

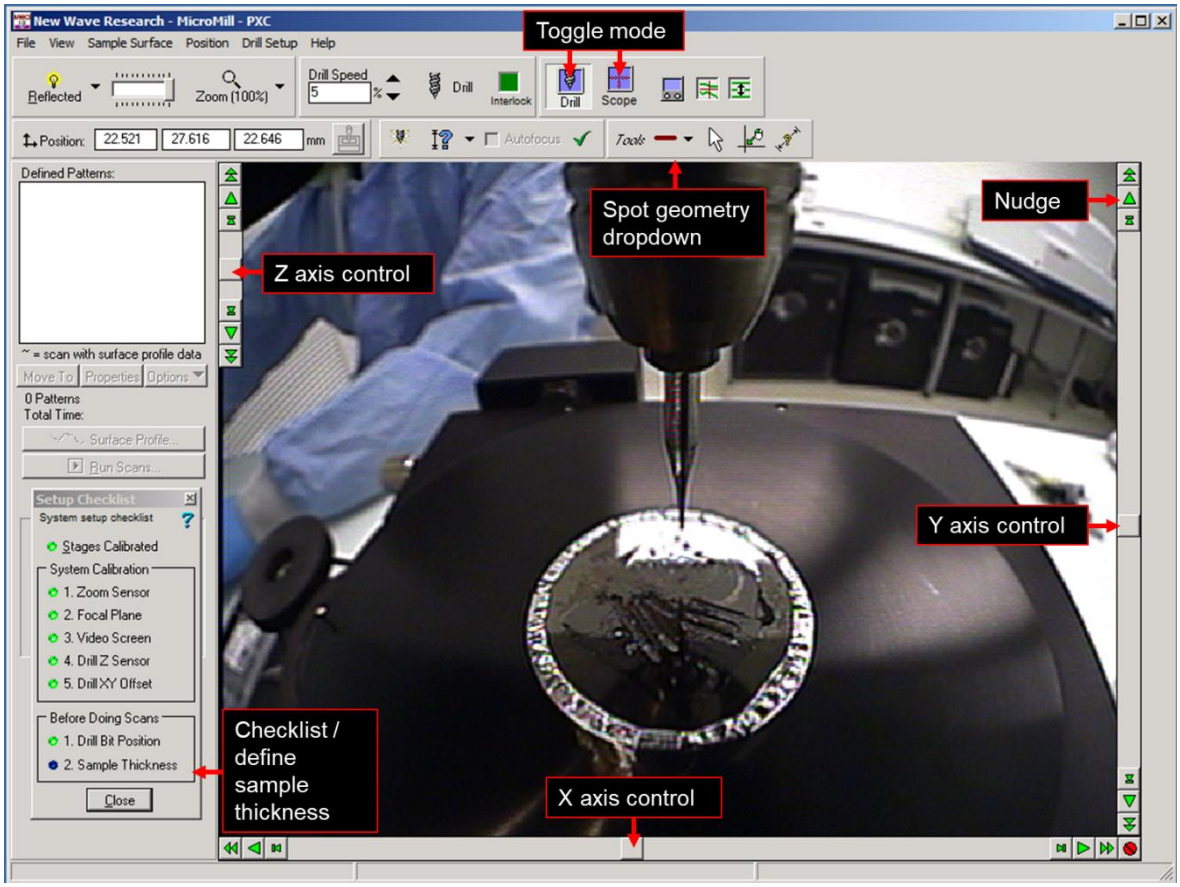

Figure 2.7 – Screen snap of the MicroMill software, encompassing a live view of the milling process in 'drill mode'. Important functions are labelled. The sample is a polished slab of the departmental obsidian standard and the drill bit is the diamond impregnated tip.

Appendix A1. Standard micromill procedures use a 10 µl droplet of MilliQ water — held in place by Parafilm — on the surface of the thin section to lubricate the drill tip and mitigate heating (*e.g.*, Charlier *et al.*, 2006). To summarise: the slurry is removed from the polished surface of the section / block using a pipette tip cut at 45° and transferred to a micro centrifuge tube. As described in Charlier *et al.* (2006), typically a washing step is undertaken with an additional 10 µl of water where the pipette tip is gently moved in a circular motion on the polished surface while 'slurping' the water in and out to maximise recovery. This droplet is also transferred to the microcentrifuge tube, which is then spun and 90 % of the supernatant removed before the residual slurry is then pipetted onto a pre weighed foil boat (Charlier *et al.*, 2006).

2.4.2 Micromill method development

There was some concern that the micromill procedure as described in the literature (Charlier *et al.,* 2006) may pose some challenges for the extraction of CM chondrite material. This is primarily because phyllosilicates possess a high water adsorption potential (*e.g.,* Hatch *et al.,* 2012) and may have a higher capacity for isotopic exchange with the liquid water during exposure and drilling (evidenced by labelled experiments undertaken by Morris (2008)). It was decided that wherever water was used in the CM extraction process, the powder most certainly required extended baking step to remove the adsorbed moisture, similar to the degassing step required to remove residual moisture from CM chondrites prior to bulk hydrogen analysis (Vacher *et al.,* 2020). This was done at 150 ℃ for 48 hours in an oven prior to analysis. The rationale for choosing these conditions are as follows: TGA analyses of CM chondrites by King *et al.* (2020) reveal that most terrestrial water is removed from the sample between the 0 – 200 ℃ step; furthermore, Vacher *et al.* (2020) degassed their samples under vacuum prior to hydrogen isotopic analysis for 48 hours at 120 ℃ and noted minimal contribution from residual adsorbed water. As there was no access to a vacuum oven during the timescales of this project, a slightly higher temperature of 150 ℃ was chosen to degas the wet drilled samples over 48 hours. The residue is then scraped off the foil, weighed and placed into the Ni tray for fluorination. The remaining challenges included:

- Isotopic exchange effects during drilling
- Physical challenges associated with the recovery and transport of micromilled powder (static electricity and fine grain size), and any associated isotopic exchange effects
- Selection of appropriate drill tips to extract the desired quantity of powder.

In this work, these challenges were each tackled in turn, using the laser fluorination system where required to measure the O-isotopic composition of any samples that were influenced

by undesirable isotope effects. A summary of the laser fluorination procedure is given in section 2.5.4.

2.4.3 Isotope exchange effects during drilling

The micromill chuck rotates at a speed of 1000-35000 rpm which poses a large risk of heating the sample; however, the approach wherein a MilliQ droplet is used for cooling was considered potentially unsuitable for CM chondrites as their phyllosilicate and organic-rich mineralogy is vulnerable to isotopic exchange with water. To investigate, a terrestrial serpentine, S1 was used as a CM-chondrite analogue and prepared as a polished block. S1 is a serpentinised nodule from the Oman ophiolite and contains large crystals of green lizardite, alongside minor occurrences of talc, magnetite and residual olivine. A lizardite-rich fragment was handpicked for bulk analyses and sectioning.

The following experiments were undertaken on the lizardite (S1) sample:

- Drilling dry
- Drilling in MilliQ H_2O
- Drilling in isotopically labelled water of composition: $\Delta^{17}O$ = 66.5 ‰; $\delta^{18}O$ = -3.9 ‰ (Morris, 2008). The extreme composition of this water would cause a $\Delta^{17}O$ offset if it exchanged with the serpentine powder during drilling.

The results are presented in Table 2.3 and plotted in Fig 2.8

2.4.3.1 Results

Four bulk measurements of the S1 lizardite sample exhibit a 1 ‰ range in $\delta^{18}O$ (Table 2.3), a not unexpected level of sample heterogeneity given its polymineralic nature and the lower temperatures typically associated with terrestrial serpentinisation, resulting in a high $\delta^{18}O$ 2σ uncertainty for bulk S1. While every effort was made to sample only homogeneous serpentine crystals, accessory magnetite or talc may have been included in the powder. However, the mean $\Delta^{17}O$ of 0.01 ‰ plots close to the TFL, as expected. Drilling dry and in

Table 2.3 - O-isotopic composition of serpentine drilled in a variety of mediums. *Liberated 166 µg of O_2 upon analysis.

Sample	$\delta^{17}O$ (‰)	$\delta^{18}O$(‰)	$\Delta^{17}O$ (‰)
Bulk			
S1 average	4.3	8.3	0.01
Drilled dry			
S1	4.5	8.7	-0.01
S1	4.6	8.8	0.02
Drilled in MilliQ H_2O			
S1	4.5	8.6	-0.01
Drilled in labelled H_2O			
S1	4.7	8.8	0.09
S1	4.6	8.7	0.11

regular MilliQ H_2O does not appear to affect the isotopic composition of the serpentine, however it should be noted that as terrestrial samples, the $\Delta^{17}O$ of the MilliQ H_2O and the serpentine should be indistinguishable and therefore no mass independent ^{17}O effect is expected. The water may therefore be influencing the $\delta^{18}O$, but as the $\delta^{18}O$ composition of the MilliQ is unknown the magnitude of such an effect is also unknown. However, drilling in isotopically labelled water influences the $\Delta^{17}O$ of the serpentine, enriching the $\Delta^{17}O$ by approximately 0.1 ‰, while the $\delta^{18}O$ remains unaffected (Fig 2.8). This contribution can be assessed using simple mass balance equation:

Equation 2.1

$$M_E = \frac{(\Delta^{17}O_{CS} - \Delta^{17}O_s) \times M_{CS}}{\Delta^{17}O_{LW} - \Delta^{17}O_{CS}}$$

Where:

M_E = the amount (mass) of exchanged /adsorbed oxygen

M_{CS} = the amount of oxygen liberated from the contaminated serpentine (166 µg)

$\Delta^{17}O_S$ = the average composition of uncontaminated serpentine (0.01 ‰)

$\Delta^{17}O_{CS}$ = the composition of the contaminated serpentine (0.108 ‰)

$\Delta^{17}O_{LW}$ = the composition of the labelled water (66.5 ‰)

The O_2 contribution required from labelled water to achieve this small enrichment is 0.25 µg in a total sample size of 166 µg liberated O_2 (an example taken from one of the analyses in Table 2.3, highlighted in Fig 2.7). This extent of isotopic exchange is slight, given the extremity of the labelled water $\Delta^{17}O$ composition, and would be negligible if the water had terrestrial composition. However, this may not be the case of CM chondrites, which have a $\Delta^{17}O$, of approximately -3 ‰. This fact, coupled with the possibility that CMs have a higher capacity for isotope exchange owed to their diverse mineralogy, rendered wet drilling an unsuitable method for extracting material.

An additional complication of wet drilling that discounted it from use was the adherence of the serpentine slurry to the drill tip, which caused migration up the bit shaft due to capillary action and consequential spattering of the sample over the workstation. Furthermore, liberation of the residue from the pre-weighed foil boats proved challenging due to stubborn drying (essentially, very thin pancake-like residues), ultimately resulting in low net-recovery. Ultimately, wet drilling wasn't pursued.

2.4.4 Dry drilling and associated challenges

It was decided the best course of action was to drill the sample dry. However, this can cause frictional heating and oxygen isotope exchange with the atmosphere. A low drill speed (20 %) and a high plunge rate (24 µm/s) was used to ensure the shortest possible drill time. As serpentines (and by extension CMs) are soft, this method excavated the material as a small

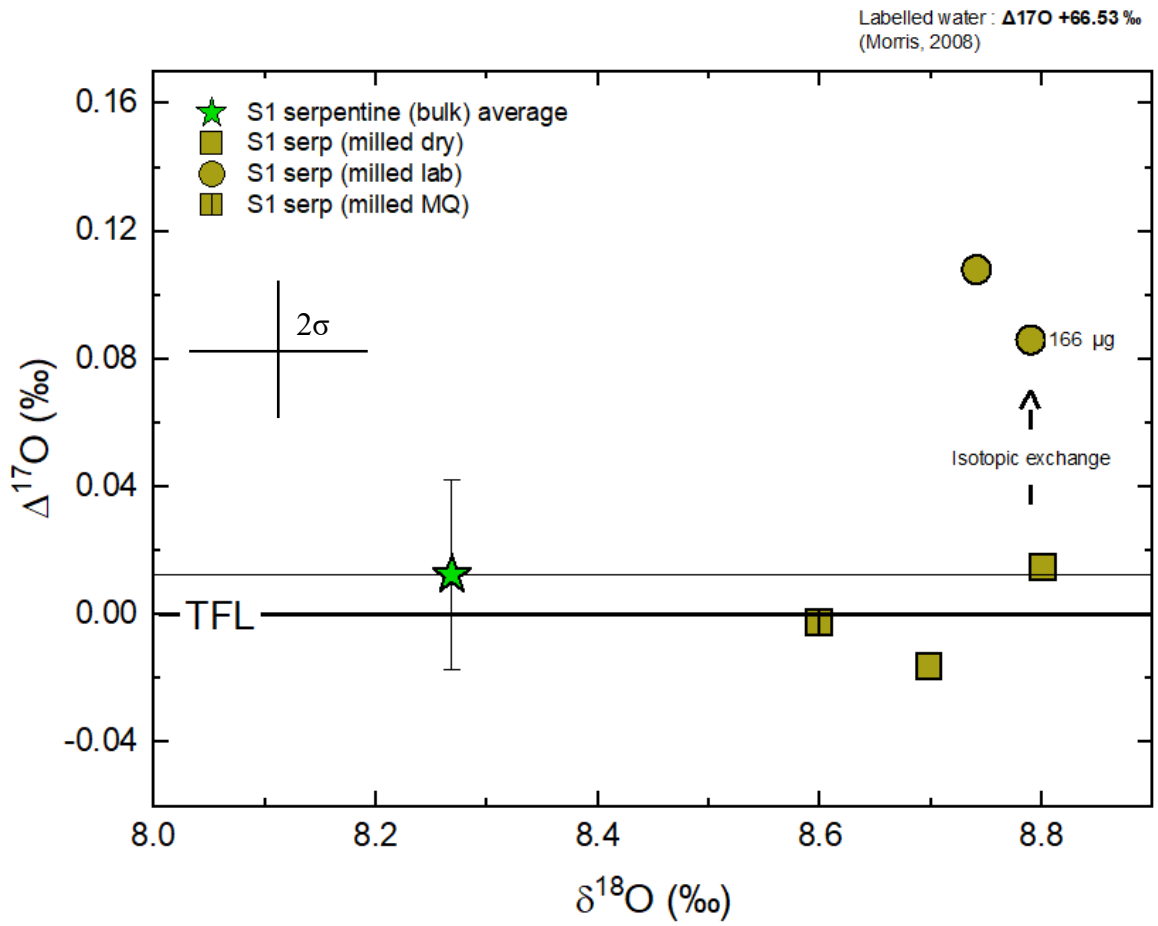

Figure 2.8 - Isotopic exchange effects while drilling serpentine in a variety of mediums. Drilling in isotopically labelled water shifts the $\Delta^{17}O$ composition upwards. Error on the bulk measurement is the 2σ uncertainty from 4 homogenised bulk measurements). The stated 2 σ error below the legend is the published uncertainty for oxygen line (Windmill *et al.*, 2022).

molehill which was easily recovered by removing the sample from the stage and tapping over a piece of foil.

Problems were encountered with static as the micromilled powder is a µm - sub-µm, fluffy powder (Appendix, A3) with a high surface area to volume ratio and material was easily, often entirely lost; therefore, great care was needed to ensure that static was mitigated, including wearing an anti-static bracelet and through regular discharging through a grounded object. A small, foil transport container was constructed to recover the powder to the clean room for weighing (see Appendix A3). The largest issue with static was during sample loading into the nickel analysis tray where the powder would scatter, or eject entirely from the well, contaminating the entire sample tray. A solution was devised wherein water was used to wet the sample into the well, causing the fine powder to clump at the bottom,

followed by a 48-hr drying of the whole tray at 150 °C. This also had the advantage of permitting larger fractions of powder to be loaded on top if a larger sample mass was desired. As in section 2.4.3, wetting of the sample may cause isotopic exchange effects simply through exposure, or contamination through adsorption. To test if this occurred, three sample types were wetted into the tray with both MilliQ and $\Delta^{17}O$ +65.5 ‰ labelled water (each a separate single-shot analysis – see section 2.5): another terrestrial serpentine (S2), the PSSRI obsidian standard, and a bulk CM powder (Aguas Zarcas).

S2 was proposed as an alternative to S1 after the observation that the latter was isotopically heterogeneous. S2 is a homogenous lump of flaky antigorite talc, sourced from the Oman ophiolite. This sample was deemed asbestos free via bulk fibre analysis, undertaken by Santia Asbestos Management. It is a very soft, porous sample that did not polish well, and may better reflect interaction of CM chondrites during ambient exposure to water. In addition, a polished chunk of the PSSRI Obsidian standard was prepared for micromilling. It was chosen because its oxygen isotopic composition is well constrained, and as a silicate glass it is less likely to undergo isotopic exchange compared to serpentine as it does not contain OH. The obsidian may therefore provide insight into any adsorption effects on silicate powder. In addition, several aliquots of a homogenised, 200 mg vial of CM chondrite cutting tailings (Aguas Zarcas) were also wetted to see if the CM mineralogy is more vulnerable to exchange than pure serpentine.

The results are presented in Table 2.4, Fig 2.9 and 2.10.

Table 2.4 - O-isotope results using water as a wetting medium to pack the powder into the well.

Sample	$\delta^{17}O$ (‰)	$\delta^{18}O$ (‰)	$\Delta^{17}O$ (‰)
Drilled dry			
Obsidian	3.8	7.2	0.02
Obsidian	3.8	7.3	0.03
Obsidian	3.8	7.2	0.01
Obsidian	3.6	7.0	-0.01
Obsidian	3.6	6.9	-0.01
Obsidian	3.7	7.1	-0.01
Obsidian	4.1	7.8	0.02
Obsidian	3.9	7.5	0.01
Obsidian	3.8	7.3	0.02
S2	3.3	6.4	0.01
S2	3.2	6.2	0.01
Aguas Zarcas	0.9	7.3	-2.94
Aguas Zarcas	1.1	7.8	-2.92
Aguas Zarcas	0.9	7.4	-2.90
Aguas Zarcas	0.7	7.1	-2.93
Wetted with MilliQ H_2O			
Obsidian	4.1	7.8	0.00
Obsidian	3.6	6.8	0.04
Wetted with Labelled H_2O			
Obsidian	3.7	7.1	0.02
Obsidian	3.7	6.9	0.09
S2	4.1	7.8	0.00
S2	4.0	7.6	0.05
Aguas Zarcas	1.6	7.8	-2.45
Aguas Zarcas	2.0	8.5	-2.45

2.4.4.1 Results

One obsidian wetted using labelled water shows an elevation to higher $\Delta^{17}O$, which is probably a residual adsorption effect (Fig 2.9) owed to heterogeneous crusting of the sample during drying and causing the formation of a protective barrier; as a result, drying powder from subsequent samples were disturbed several times with a fine needle to break this crust. Alternatively, the obsidian standard may be more heterogeneous on the mm scale than the average bulk composition determined from replicate, 2 mg measurements of the >1g homogenised chunk used for internal standardisation, as evidenced by a much larger spread in $\delta^{18}O$ among the micromilled samples. The later obsidian results, including one replicate drilled in labelled water, and one in MilliQ, show that there is no interaction with water when used as a wetting medium, as expected. Similarly, S2 does not show any effect after being wetted with MilliQ H_2O but does show slight enrichment in $\Delta^{17}O$ after being wetted with labelled water, though the magnitude of this offset is much less than that which occurs when using water as a drilling lubricant (Fig 2.8 and 2.9). However, wetting the CM powder with labelled water has a much larger effect with a deviation of ~ 0.45 ‰, indicating the CM mineralogy is highly susceptible to ambient exposure of liquid water (Fig 2.10). Using equation 2.1, the required contribution of labelled water to generate the +0.45 ‰ enrichment in $\Delta^{17}O$ is 2 µg O_2. Consequently, wetting the sample into the well was also deemed inappropriate for this work. While the observed interaction is primarily due to the extreme composition of the labelled water, it is nevertheless an avoidable outcome that would only worsen with decreasing sample size. Dry drilling and dry loading were therefore considered the best approaches to minimise modification of the CM-isotope signature.

The issue of sample ejection due to static was mitigated by avoiding the use of nitrile gloves, which appeared to be the prime cause of persistent charge. Constructing the foil transport container with tweezers using clean room wipes to cover the fingers appeared to solve the problem. Furthermore, gentle tapping of the crimped foil container with the loaded sample

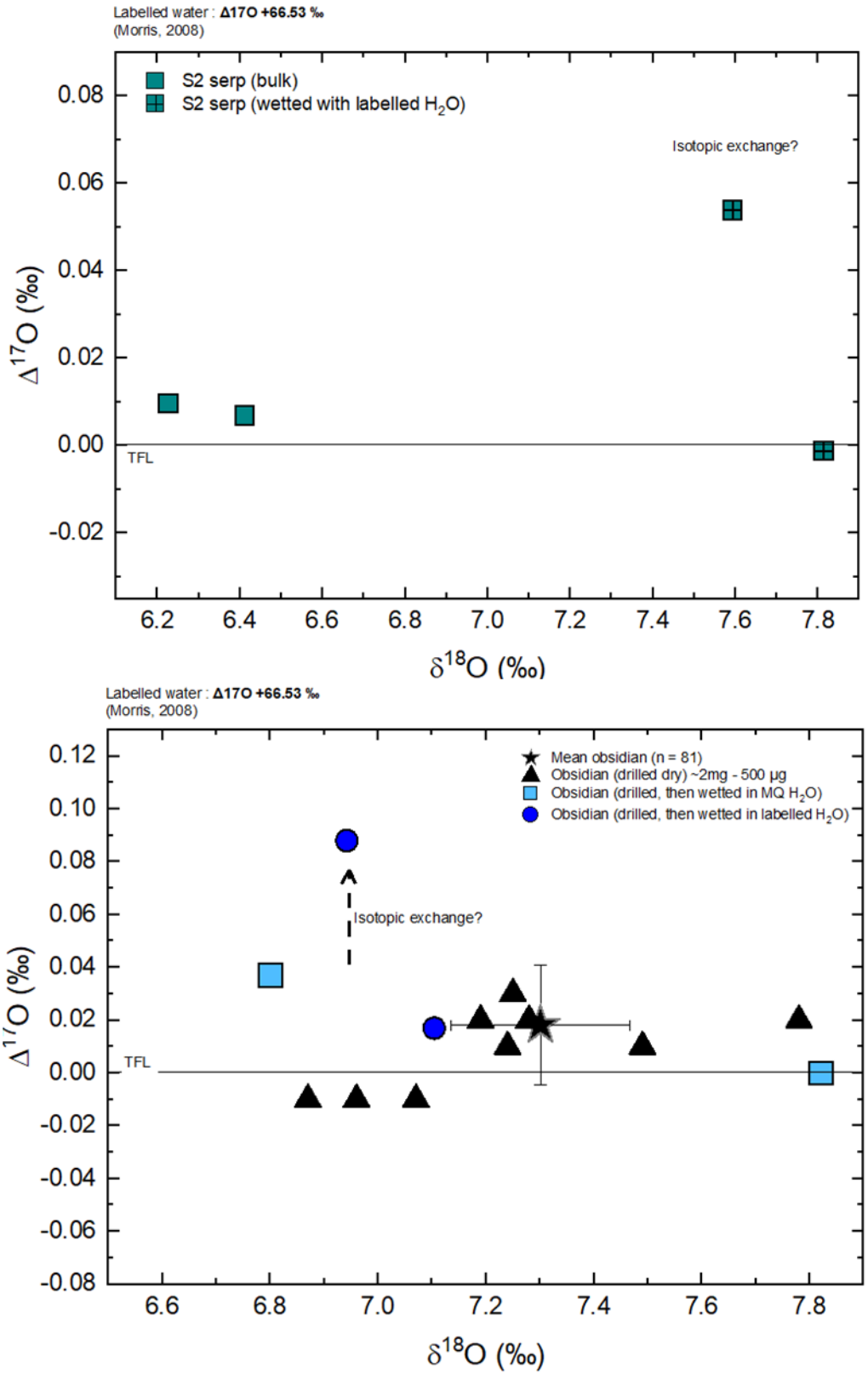

Figure 2.9 – The effect of using water to wet, or pack the sample into the well, on the oxygen isotopic composition of obsidian and serpentine.

inside (using two sets of tweezers, one to grip the package, and the other to tap the back of the gripping tweezers) caused the fluffy powder to coagulate and clump together. The sample was then transported between labs in a small plastic container lined with foil, and then loaded

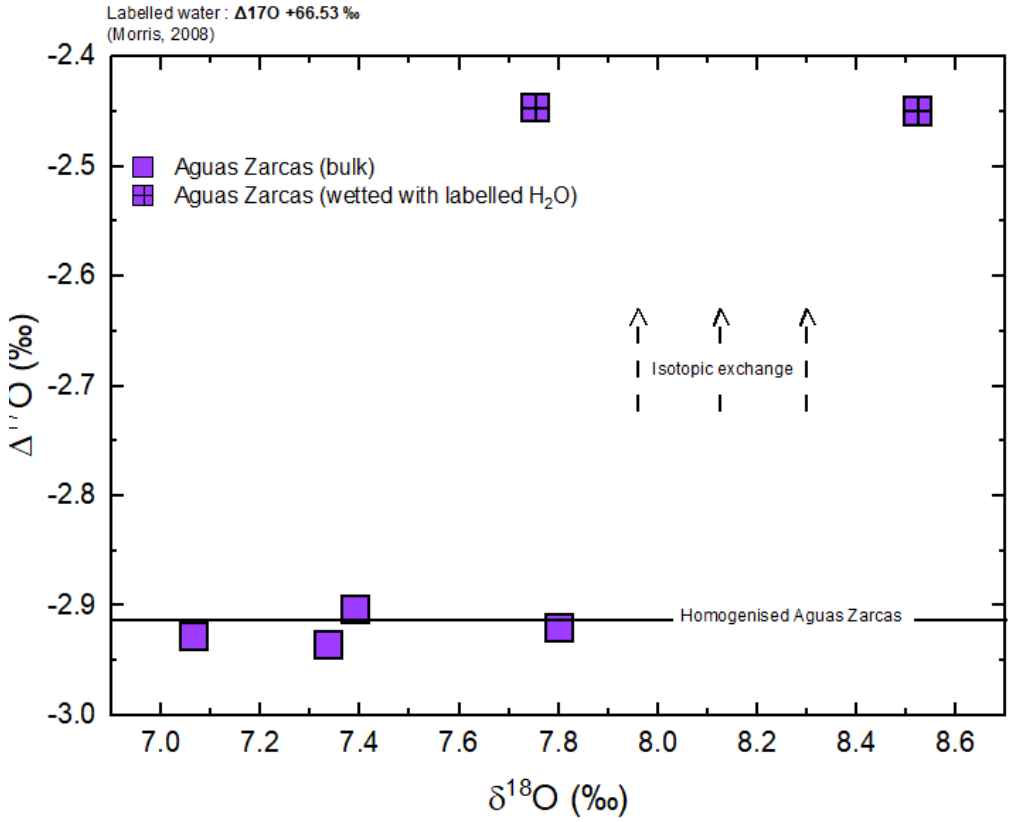

Figure 2.10 – The effect of using water to wet or pack a CM sample. There is significant $\Delta^{17}O$ enrichment.

Without nitrile gloves, again using clean wipes as improvised hand protection. Drilling and loading the sample in a short time frame (<1hr) appeared to minimise any build-up of ambient static.

2.4.5 Drill bit selection

Historically, micromills have been used for TIMS and ICP-MS applications such as Rb and Sr isotopes (Charlier *et al.*, 2006), where very small quantities of powder are removed from thin sections for spatially resolved isotope analysis. This is highlighted by the stock drill bit that is supplied with the instrument which is a conical scriber with 50µm resolution at the tip. In the paper by Charlier *et al.* (2006) samples are extracted from domains of high Sr concentration and range in size from <10 to >100 µg, requiring anywhere from 10 – 140 drilled holes depending on the sample requirements of the isotope of interest. O-isotope measurements typically necessitate a higher relative sample mass to achieve the level of

precision afforded by a small-sample laser-assisted fluorination procedure. The aim was to extract between 200 and 300 µg of matrix from each lithology, which at an approximate yield of 25 % oxygen (the average yield of oxygen from a CM chondrite), would provide approximately 40-60 µg of oxygen gas to be analysed to excellent precision on the microvolume facility on the MAT 253 mass spectrometer (see section 2.5 for further information).

An important consideration is the depth of drilling. A maximum depth of 300 µm was chosen to minimise the uncertainty associated with sampling undesirable precursors at depth, while maximising the recovery of sample powder. As large chondrules are on the scale of 100 µm and above, quick SEM examination of the excavated holes post-drilling permits evaluation of any significant contamination.

Assuming an average bulk CM chondrite density of 2.2 g/cm^3 (Abreu, 2018; Macke *et al.*, 2011), a drill depth of 100 µm, and using the volume of a cone to calculate the recovered mass, The stock scriber tip supplied with the drill would need to scan ~20 – 30 holes to recover the desired sample mass (~11 µg per hole), or to drill deeper into the section which would increase the likelihood of contamination from chondrules below. A selection of larger drill bits were purchased to increase the time efficiency of extraction and reduce the requirement for the number of holes (Fig 2.11). A ball-point carbide tip was chosen as the geometry facilitates efficient, gentle excavation of serpentine and CM lithologies at low drill speed, forming cylindrical holes. As the tip is 500 µm wide at the largest circumference, it significantly reduced the number of holes required to extract the 200-300 µg sample mass. Assuming the volume of a cylinder is reflective of the geometry of the milled holes, the expected recovery of CM powder per 500 µm wide, 300 µm deep hole is 130 µg, ten times that of the scriber tip, thus necessitating only 2-3 holes. 30 CM lithologies were drilled in total over the duration of the project, and each sample yielded between 80-110 % of the expected yields (average = 91.7±9.7% (1 SD)) assuming a bulk CM chondrite density of 2.2

g/cm^3 (Table 2.5 for results). As the bulk density of the extracted matrix phases is likely to contribute to a lower density, the true value is likely closer to 100 % in all cases, ignoring any sample loss due to fine-grain size.

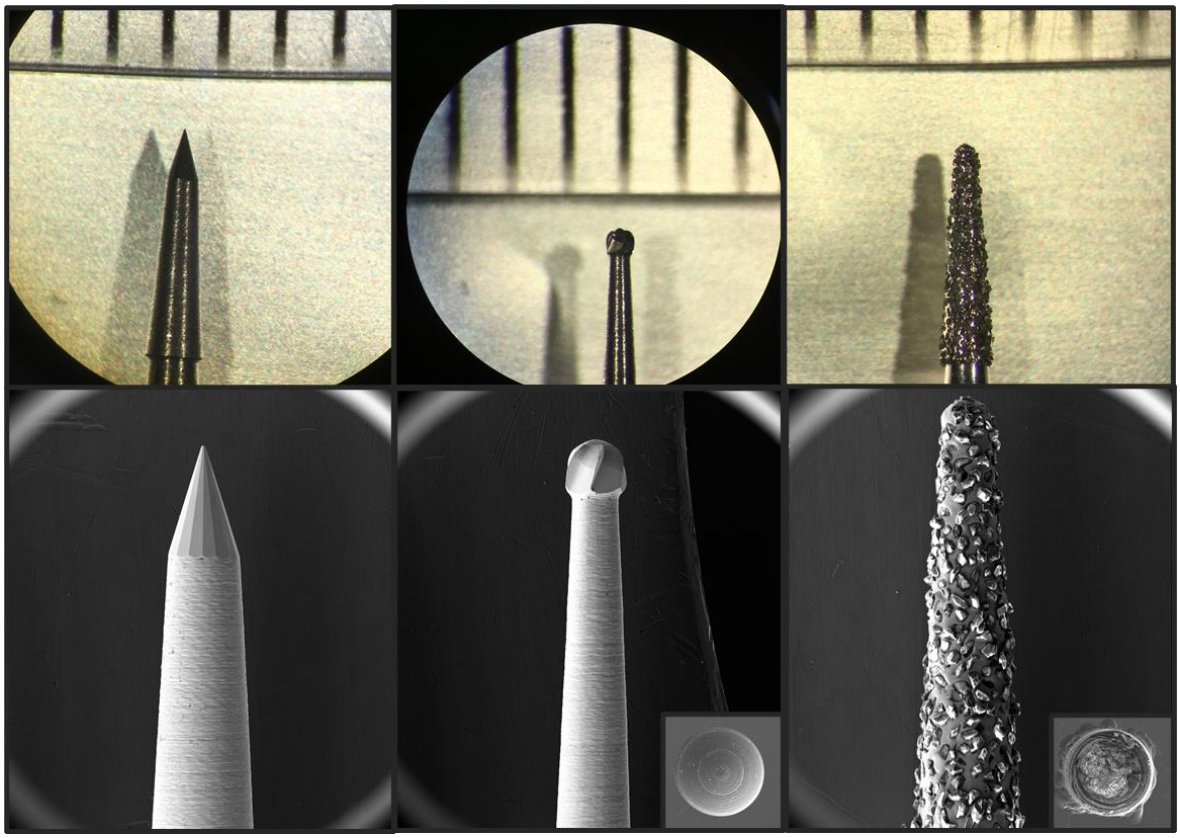

Figure 2.11 - The selection of the various tungsten carbide micro drill bits used in this project. The top images are binocular images with a 1 mm increment scale bar in the field of view, the bottom images are secondary electron images. From left to right: scriber tip; ball point carbide; diamond impregnated. The ball point carbide and diamond impregnated tips excavate, round, cylindrical holes with good potential for improved recovery over the very precise scriber tip.

For soft samples, the 500 µm ball point bit was used at 20 % drill speed, a plunge time of 24 µm/s and a dwell time of 5 s. Each hole was drilled over three passes to a total depth of 300 µm per hole. For obsidian – which as a hard silicate glass presents a challenge for the micromill - the 1 mm diamond tip was used at 100 % drill speed.

2.4.6 Summary

A micromill was used to microsample the CM aqueous alteration products in line with the thesis objectives. Several challenges were overcome with respect to the powder geometry

Table 2.5 - Expected vs measured mass for the ball point carbide for 30 CM chondrite examples drilled during this study, considering the expected mass per 300 μm deep hole. In all cases, the expected / measured percentage is above 75 %. The ball point carbide is therefore an efficient extractor which preserves the integrity of the sample, precluding the need for deeper excavations.

Holes	Expected (mg)	Measured (mg)	Expected / Measured (%)
3	0.360	**0.357**	99.2
3	0.360	**0.323**	89.7
3	0.360	**0.337**	93.6
2	0.240	**0.224**	93.3
2	0.240	**0.198**	82.5
2	0.240	**0.228**	95.1
3	0.360	**0.345**	95.8
1.5	0.180	**0.170**	94.5
3	0.360	**0.317**	88.1
2	0.240	**0.209**	87.0
2	0.240	**0.192**	79.8
2	0.240	**0.181**	75.3
3	0.360	**0.291**	80.7
3	0.360	**0.287**	79.6
2	0.240	**0.217**	90.4
2	0.240	**0.233**	97.0
3	0.360	**0.291**	80.9
2	0.240	**0.189**	78.6
2	0.240	**0.220**	91.5
3	0.360	**0.348**	96.6
2	0.240	**0.265**	110.3
3	0.360	**0.385**	106.9
2	0.240	**0.216**	90.1
2	0.240	**0.257**	107.0
2	0.240	**0.204**	85.0
2	0.240	**0.204**	85.0
2	0.240	**0.201**	83.8
2	0.240	**0.258**	107.3
2	0.240	**0.234**	97.6
2	0.240	**0.257**	107.0
Average			91.7 ± 9.7 (1σ)

(principally static) and the possibility of adsorption of water and isotopic exchange during the drilling process. Terrestrial serpentines, the PSSRI Obsidian standard, and a bulk CM powder were used to investigate these issues. The literature-favoured approach of using a MilliQ water droplet to lubricate the drill tip and catch the sample during milling was deemed unsuitable as experiments showed labelled water it produced a $\Delta^{17}O$ enrichment of ~ 0.1 ‰ from the terrestrial value (~0 ‰) in S1 serpentine. Furthermore, drilling dry and then using

labelled water to transport the sample produced $\Delta^{17}O$ enrichments of 0.5-0.45 ‰ in S2 serpentine, obsidian, and CM powder. These observations indicate that both adsorption and isotopic exchange effects during drilling are pathways for contamination via moisture. The favoured approach was to drill the sample dry and transport it with great care, avoiding the use of nitrile gloves to mitigate static. In between scans, the drill bit was cleaned by spinning it at maximum rpm in a vial of isopropanol. If the tip appeared stubbornly dirty, a 30 second ultrasonication sufficed to clean it.

2.5 Laser-assisted fluorination

The following section outlines a brief history of laser-assisted fluorination followed by the Open University protocols that were in place at the start of this project.

2.5.1 A brief history

Liberating oxygen from silicates is a tricky business due to the strength of the Si-O bond. The halogen compound bromine pentafluoride (BrF_5) — a straw-coloured liquid at room temperature and a powerful fluorinating agent — can break this bond (Greenwood *et al.*, 2017). The liquid state of BrF_5 permits it to be cryofocussed, aliquoted and manipulated on a vacuum line, making it a preferable choice over molecular fluorine gas, F_2. As the most electronegative element, fluorine is more oxidising than oxygen itself, and when heated reacts aggressively with silicates and oxides to form fluorides and salts, releasing the oxygen from the mineral structure. Decomposition of silicates in the presence of BrF_5 was first tried by Clayton and co-workers who achieved liberation of the oxygen gas by reacting the sample in a reaction tube (‘bomb’) of nickel baked at high temperature (Clayton and Mayeda, 1963). This technique increased the analytical yields compared to previous attempts, for example, those that utilised chlorinating agents (Clayton, 1955; Manian *et al.*, 1934).

These earlier studies converted the O_2 gas to CO_2 by passing the gas over a bed of hot carbon (Clayton and Mayeda, 1963; Matsuhisa *et al.*, 1971; Taylor Jr and Epstein, 1962). The

justification of using CO_2 as the analyte as opposed to O_2 was that the former produced a mass spectrum far away from the contaminating products in air (Clayton, 1955). However, during these earlier days, the importance of ^{17}O measurements was only just being realised. Later, the popularity of using O_2 gas as the analyte increased (Clayton and Mayeda, 1983; Kusakabe *et al.,* 2004), as conversion to CO_2 resulted in undesirable isobaric effects on the ^{17}O measurement due to the unavoidable presence of ^{13}C ($^{12}C^{16}O^{17}O$ being to all intents identical in mass to $^{13}C^{16}O^{16}O$). Molecular oxygen as the analyte is now preferred, so long as the products CF_4 and NF_3 are removed in clean-up (Clayton and Mayeda, 1983) as they generate fragment ions interfering with the O_2 measurement.

It became apparent that the Ni bomb technique, while a significant improvement over the preceding methods (Clayton and Mayeda, 1963; Matsuhisa *et al.,* 1971; Taylor Jr and Epstein, 1962), still suffered issues of incomplete reaction and consequently, isotopic mass fractionation (Greenwood *et al.,* 2017). The major setback was the inability to reach higher temperatures (>1000 °C) and the large sample requirements (5-30 mg), which also encouraged a high analytical blank (Greenwood *et al.,* 2017). A necessary development was the introduction of high power, CO_2 lasers to heat the sample in the presence of BrF_5 in excess of 1000 °C (*e.g.,* Franchi *et al.,* 1999). The rapid liberation of oxygen gas reliably produced 100 % oxygen yields, affording the most efficient method for quantitatively recovering O_2 gas from a silicate or oxide sample. Another benefit was the reduction in analysis time, allowing multiple measurements to be obtained in one day (Greenwood *et al.,* 2017). However, a common misconception is that laser-assisted fluorination can be used *in-situ* on a polished section. It cannot, because as a bulk analysis technique, the relatively slow reaction rates achieved with a CO_2 laser makes *in situ* analyses with this technique impossible. An alternative is ultraviolet laser ablation. Historically there has been success in utilising this method on a polished block *in situ*, bathed in fluorine gas, to resolve the isotopic composition of components to useful levels of precision (*e.g.,* Young and Russell, 1998). As

this project is concerned with analysis of spatially resolved material from CM chondrites, this could be a viable method; however, the high reactivity of CM chondrite matrices — which react with the fluorinating reagent at room temperature even without the influence of a laser — coupled with the small amounts of gas liberated by the spot analysis would ultimately offset any advantage from the spatial resolution (Greenwood *et al.*, 2017; Young and Russel, 1998). Furthermore, the amount of gas liberated by UV ablation is at the microgram to sub microgram level, far too small to be analysed to high precision by a dual inlet system, instead relying on a continuous flow inlet and a subsequent loss of precision compared to laser-assisted fluorination by about an order of magnitude.

The challenge is to utilise a sampling technique that can provide spatially constrained samples at a size large enough that permits laser fluorination and analysis via a dual inlet, where a sample and reference volume of gas are balanced using a pair of bellows. The bellows maintain an identical pressure to negate any pressure-mass-dependent effects and permit multiple sample-standard comparisons, offering the highest precision available for O-isotope analysis (Greenwood *et al.*, 2017). Such measurements form the core of this project. Introducing a micromill to the back end of the process reclaims a high degree of spatial resolution, permitting the retrieval of µg scale samples from SEM characterised polished blocks.

2.5.2 Sample requirements

A typical laser fluorination measurement requires 500-1000 µg liberated O_2 to produce a suitable bellows signal on the dual inlet IRMS spectrometer for high precision. Sample masses typically range from 1-2.5 mg, with CMs at the higher end to compensate for lower O_2 yields (20-25 %) invoked by its diverse mineralogy (which includes a proportion of sulphide that contributes substantially towards the weight of the sample but not the O_2 budget). For small samples, the preferred amount of liberated oxygen is between 10 – 120 µg, ideally around 60 µg, to utilise the microvolume facility on the MAT 253 IRMS (Goderis

et al., 2020; Suttle *et al.,* 2020). Correct sample weights are imperative for calculating percent yield of oxygen, necessitating the use of a Radwag UYA 6.4Y ultramicrobalance capable of weighing to 0.1 μg. Samples and standards are then loaded into a Ni tray in an ISO class 5 clean room using tweezers and foil boats.

Silicates and oxides can be loaded adjacent to each other as a typical multi-sample tray (up to 22 samples) and run over several days (Miller *et al.,* 1999). Included are aliquots of the internal PSSRI Obsidian standard. This is to monitor the long-term reproducibility of the O_2-line and check for any errors or significant drift in the instrument over the course of the analytical day. The number of obsidian standards are scaled to the number of samples. Ideally an obsidian should be analysed after every 2-3 unknowns.

2.5.3 Outline of procedure

A photograph and schematic cartoon overview of The Open University laser fluorination system is shown in Figs 2.12 and 2.13. A detailed, step-by-step procedure including all valve configurations is outlined in detail in Windmill (2021).

The OU fluorination system consists of four fundamental parts:

1) A reaction chamber, where the sample is fluorinated with the laser
2) A gas clean-up line, where waste products are removed from the sample gas
3) A molecular sieve, where the gas is cryofocussed
4) A mass spectrometer, where the isotope ratios are measured.

2.5.3.1 Loading

A prepared sample tray is transported from the clean room to the O_2 laboratory to be loaded into the sample chamber. The chamber is sealed using a KFX clamp with a copper gasket between two knife edges. The top of the chamber consists of a large BaF_2 window 38 mm wide and 3 mm thick, with a vacuum seal achieved with a Viton O-ring. The Swagelok VCR gasket that leads into the gas clean up section contains a frit to trap any fluorinated debris

(Fig 2.2, c)). Once the chamber is fully sealed, the chamber vacuum is roughed out to a pressure of 10^{-4} mbar using a rotary pump. After a few minutes, the rotary pump is sealed from the chamber and the vacuum was improved to 10^{-7} mbar using a turbo pump backed by the rotary. To aid pumping, the sample chamber is enveloped in heater tape and Al foil and baked overnight at a temperature of 80 ˚C to remove adsorbed moisture. The next day, the heater tape is removed, and the chamber is cooled to room temperature. The PSRRI obsidian standards are then fused under vacuum with a Photon Machines Inc. CO_2 50 W fusion laser at low laser power. This causes the obsidian to release lingering moisture.

2.5.3.2 BrF_5 refluxing

Before BrF_5 can be used for any purpose on the O_2 line, it must first be cleaned. To do this, an aliquot of BrF_5 is sequestered from the main reservoir into the volume of Trap 1 (approximately 410 mbar) and frozen onto a cold trap at liquid nitrogen temperature. The small aliquot is then cleaned by repeated reflux (heating and freezing), with any outgassed contaminants pumped away.

2.5.3.3 Pre-fluorination

A critical preparatory step is to pre-fluorinate the sample chamber to remove any lingering adsorbed moisture from the chamber and exposed sample surfaces. This is typically done over two ambient exposures of the chamber to BrF_5. A duration of 2 x 20 minutes has been determined as an appropriate length of time to reduce the blank of the system to below 6 µg of O_2 (*e.g.,* Windmill *et al.,* 2021).

2.5.3.4 Lasering and cleaning up a sample

All samples are fluorinated in the presence of a refluxed BrF_5 aliquot at a pressure of 225 mbar, using a Photon Machines Inc. CO_2 50 W fusion laser. A continuous laser beam of 3 mm diameter, slowly increased to 25 % power (12 W) is used to react the sample. Once the sample reduces in size to ~1 mm, a 1 mm diameter laser beam is selected and quickly increased to 15 % laser output (7.5 W) to react the remaining bead. The fluorination reaction

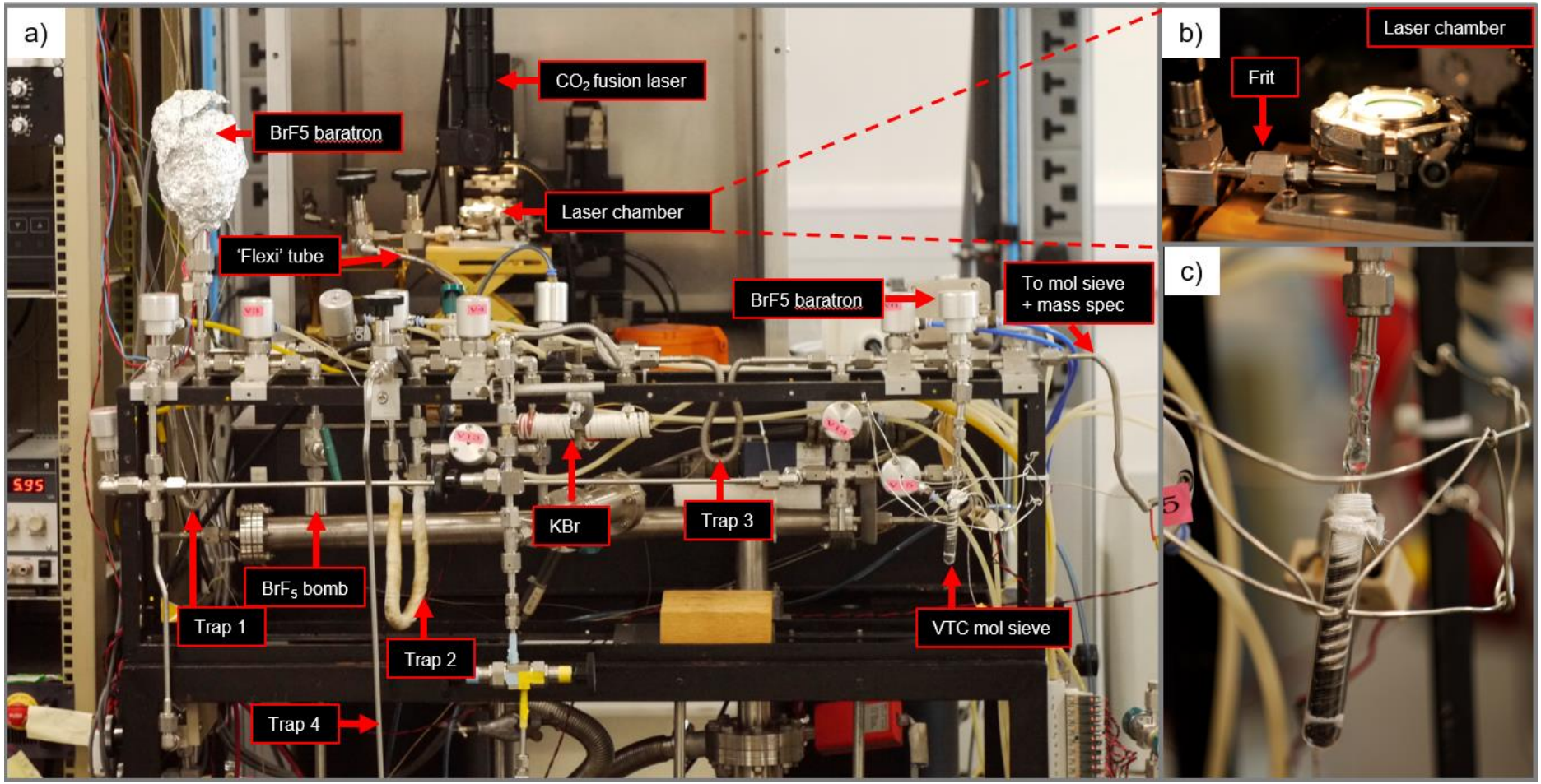

Figure 2.12 – Photographic plates of: a) the OU gas clean-up line; b) the sample chamber, including KFX clamp and frit; c) VTC molecular sieve finger used for cryogenic transfer. The main molecular sieve and mass spectrometer are not included in the picture but are connected to the flexi tube shown on the far right.

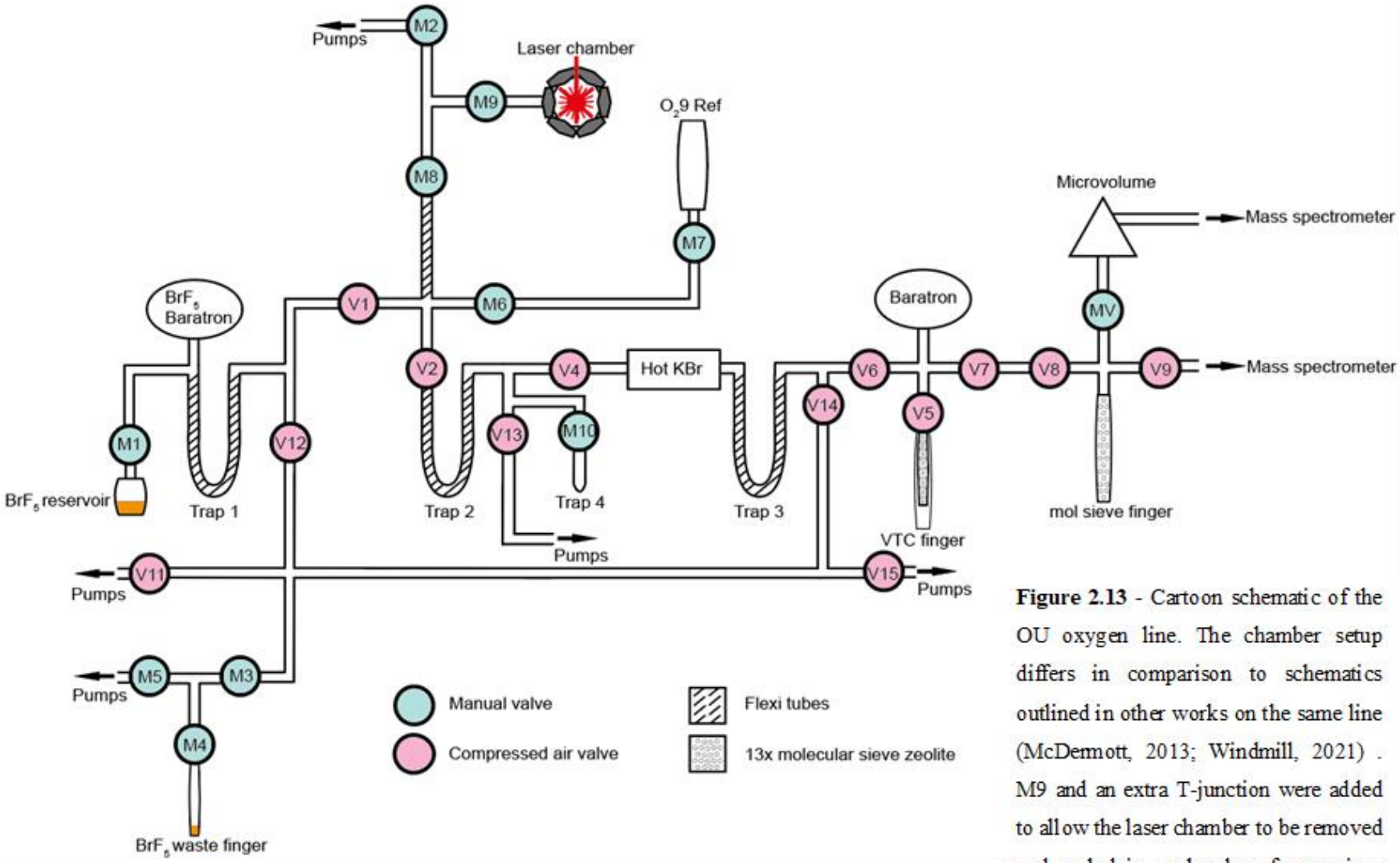

Figure 2.13 - Cartoon schematic of the OU oxygen line. The chamber setup differs in comparison to schematics outlined in other works on the same line (McDermott, 2013; Windmill, 2021) . M9 and an extra T-junction were added to allow the laser chamber to be removed and sealed in a glovebox for precious sample return material (Hayabusa-2).

liberates the oxygen gas which is strategically passed through a stainless-steel vacuum line controlled with manual and air actuated, pneumatic valves. The gas clean-up section of the vacuum line consists of a series of two cryogenic traps (Traps 2 and 3) at LN_2 temperature (-196 °C) and a heated bed of KBr (110˚C) to remove excess BrF_5 and reaction products other than O_2. At this stage, the gas in-line can be measured as a pressure at the baratron (Fig 2.13). The pressure is converted into a mass unit (µg O_2) by multiplying by a conversion factor of 209. The conversion factor of 209 is an experimentally derived calibration using a set of international standard measurements (UWG2 Garnet and NBS 28 quartz) with a known yield of oxygen. The conversion factor was then determined to be [baratron measurement (mbar) x 209] when it was observed that 100 % of a sample had been reacted from the calibration samples. To record an accurate measurement of pressure, any LN_2 traps needed to be topped up to the exact height each time due to variations in pressure induced by the ideal gas law.

2.5.3.5 Isotope ratio mass spectrometry

The molecular oxygen gas is then expanded into a Thermo Scientific MAT 253 IRMS which has a mass resolving power of 200. All method files were then executed using Isodat 2.0 software. Mass 32 ($^{16}O^{16}O$), 33 ($^{16}O^{17}O$) and 34 ($^{16}O^{18}O$) were measured simultaneously on Faraday cups with resistivities suitably matching the natural abundances of the isotopes concerned: 3×10^8 Ω for mass 32, 3×10^{10} Ω for mass 34, and 1×10^{11} Ω for mass 33. All method files analysed the sample gas against the O_2-8 working reference gas, which in turn is calibrated to VSMOW.

2.5.3.6 Bellows mode

Regular-sized (~2.0 mg) samples permit analysis using the conventional dual inlet methodology because the amount of liberated gas is sufficient to maintain laminar flow through the capillaries. The sample gas is expanded into the bellows where it is compressed to achieve the desired signal (ideally $1.5 – 4.0 \times 10^{-8}$ A for m/z=32). The gas is bled into the

mass spectrometer, using the volume of the bellows as the reservoir to provide the most stable beam conditions. Although the sample and reference sides may have different volumes, the decay in pressure during an analysis is negligible and therefore the beams remain balanced within tight tolerance during an analysis.

2.5.3.7 Microvolume mode

Mass spectrometry via microvolume cryofocuses smaller quantities of sample gas onto a miniature volume, generating comparable signal intensity as the bellows. It is a small volume and leads to significant decay in signal intensity as the sample gas bleeds into the instrument through the capillary. To facilitate accurate sample-reference comparison a comparable volume is achieved on the reference side of the dual inlet by closing off the bellows volume. The resultant signal, approximately 2×10^{-8} A at m/z=32, will be on par with high precision measurements obtained using the bellows on the dual inlet system, at the cost of only being able to analyse the gas once.

Where the microvolume will be used for more than one sample (which is always the case, as each analysis requires at least a standard measurement in addition to the unknown), the BrF_5 used for fluorination is removed and frozen onto a trap that is isolated from the rest of the line (Trap 4 – Fig 2.13), to remove any possibility of blank contamination from the dirty BrF_5 clathrates present on Trap 2 (McDermott, 2013).

2.5.3.8 Notation and reproducibility

Triple oxygen isotopes are reported in the delta notation (McKinney *et al.,* 1950), which cleverly exploits the ability for a mass spectrometer to determine the difference between two substances to a much greater accuracy than the absolute ratios themselves. If one substance is an internationally recognised standard, then the results can also be compared between laboratories. The standard is Vienna Standard Mean Ocean Water (VSMOW):

Equation 2.2

$$\delta^{18}\mathrm{O}_{\mathrm{sample}} = \frac{R_{sample} - R_{VSMOW}}{R_{VSMOW}}$$

This equation demonstrates the basic idea of a relative difference in ratios (Railsback, 2007). Subtracting the ratio in the standard from that in the sample, and then dividing by the ratio in the standard expresses the degree to which the sample differs from the standard. An algebraic transformation of equation 2.2 is as follows:

Equation 2.3

$$\delta^{18}\mathrm{O}_{\mathrm{sample}} = \frac{R_{sample}}{R_{VSMOW}} - 1$$

In this transformation, the purpose of the delta symbol becomes more apparent (Railsback, 2007). The difference between the sample and standard is a 'ratio of ratios'. As the variations between the isotopes in R_{sample} and R_{VSMOW} is very small (Table 1.3), the ratio is close to unity (*e.g.*, 1.0010 or 0.9990) subtracting 1 gives an absolute value identical to equation 2.2 (*e.g.*, 0.001 or -0.001). Because these values are also small, simply multiplying by 100 to give 'difference in per cent' is not enough. Multiplication by 1000 is required:

Equation 2.4

$$\delta^{18}\mathrm{O}_{\mathrm{sample}} = \left(\frac{R_{sample}}{R_{VSMOW}} - 1\right) \times 1000$$

The result is the difference in ^{18}O relative to ^{16}O between the sample and VSMOW, in units of per mil (‰). Values can be positive or negative, reflecting the sample ratio relative to the VSMOW standard.

Calculation of the $\delta^{17}O$ and $\delta^{18}O$ values to VSMOW was done in-software. As each volume of sample gas is a single population, uncertainty is calculated as two standard errors of the mean of the block of cycles (40 or 10, depending on procedure).

$\Delta^{17}O$ is calculated as follows:

Equation 2.5

$$\Delta^{17}O = \delta^{17}O - 0.52 \times \delta^{18}O$$

Uncertainty on the $\Delta^{17}O$ is calculated according to the long-term reproducibility of the O-line. The reader is referred to Chapter 1, section 1.5.1, for the justification on using the classical approximation of $\Delta^{17}O$ as opposed to the linearised version in this work.

The most up to date, published long term reproducibility of the Open University fluorination line is ± 0.09 ‰ for $\delta^{17}O$, ± 0.16 ‰ for $\delta^{18}O$, and ± 0.021 ‰ for $\Delta^{17}O$ based on 52 analyses of the PSSRI Obsidian (Windmill *et al.,* 2022).

2.5.4 Summary of previous CM chondrite analytical techniques

The above description of the Open University laser-assisted fluorination system concerns the daily, general operation applicable to all types of rock samples; however, where certain samples do not meet the typical operating requirements of the system and are therefore incompatible and / or challenging to analyse, certain aspects of the operation can be amended to accommodate them. Small samples of volatile-rich CM material are arguably some of the most challenging types of samples that have been analysed to date on the Open University setup (Greenwood *et al.,* 2023) and to facilitate their analysis, two modifications to the system have been utilised previously.

2.5.4.1 Modification 1: The single shot method

Firstly, a ‘single shot’ method has been deployed whereby only one sample and standard is loaded at a time into a bespoke Ni tray specifically designed to tackle several problems arising during lasering, as shown in Fig. 2.14 (Greenwood et al., 2023; Schrader et al., 2014). The tray contains round-bottomed, 3 mm wide wells as opposed to the more conical, wells present in ‘normal’ sample trays, which decreased the risk of an aggressive eruption of the sample once laser power is increased by optimising the surface area of the

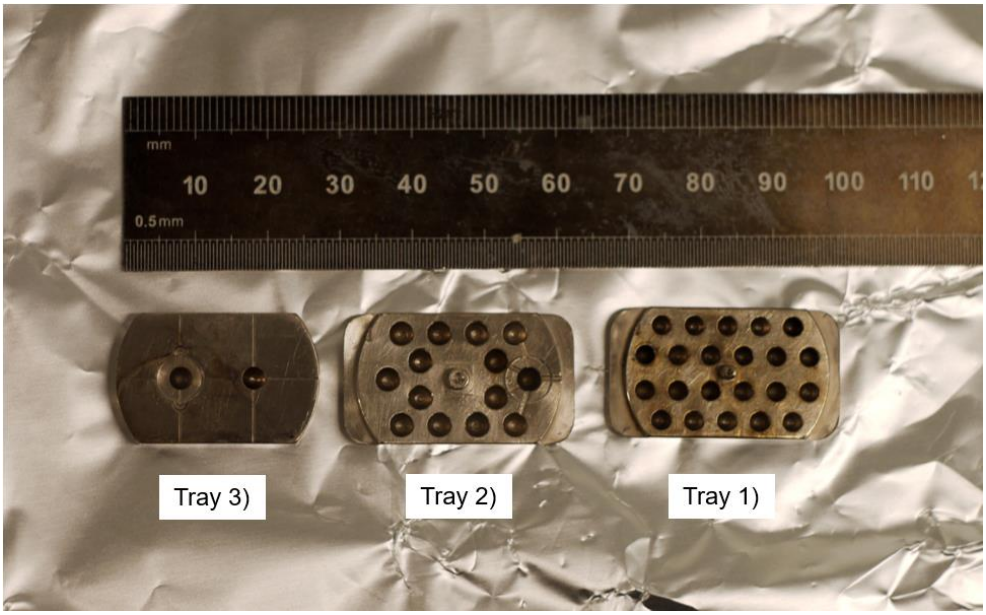

Figure 2.14 – The evolution of the nickel single shot- tray. Tray 1 is a standard 22-hole fluorination tray. Tray 2 is a modification of the original design with wider wells and a smaller BaF_2 window on top of the right-hand sample well. Note the scribed valleys under the small window to allow BrF_5 to circulate. Tray 3, the Hayabusa-2 tray, only features 2 holes but also a depression for the BaF_2 window to sit in. This is the most optimised design but would require an extra hole to fulfil the minimal analytical requirements for a small sample single shot (1 sample + 2 standards) – scheduled for machining in 2024.

sample that is exposed to the 3 mm laser during the first ramping steps of the protocol. Shallow, 300 µm deep grooves were also scribed into the surface of the tray, allowing an additional, 5 mm wide, 1.5 mm thick BaF_2 window to be placed on top of the CM sample well, maintaining good flow of BrF_5 underneath the window. This acted as a containment cover, preventing any sample loss due to ejection and inhibiting spatter during the lasering process which would otherwise contaminate nearby wells. During this work, an optimised, prototype tray was machined, containing a 1.5 mm deep, circular indentation for the small BaF_2 window to slot into (Fig 2.14). This prevented the issue of the small window 'wandering' across the surface of the tray during sample reaction, which often resulted in shattering of the small window as the beam was attenuated by the window edge and allowed each little window to be utilised multiple times. Furthermore, the single shot procedure overcame a significant pre-reaction issue that occurred when multiple legacy CM samples were analysed in one tray, causing the isotopic composition of sequential unknowns to become compromised (Fig 2.15, 2.16). The phyllosilicate-rich nature of the samples

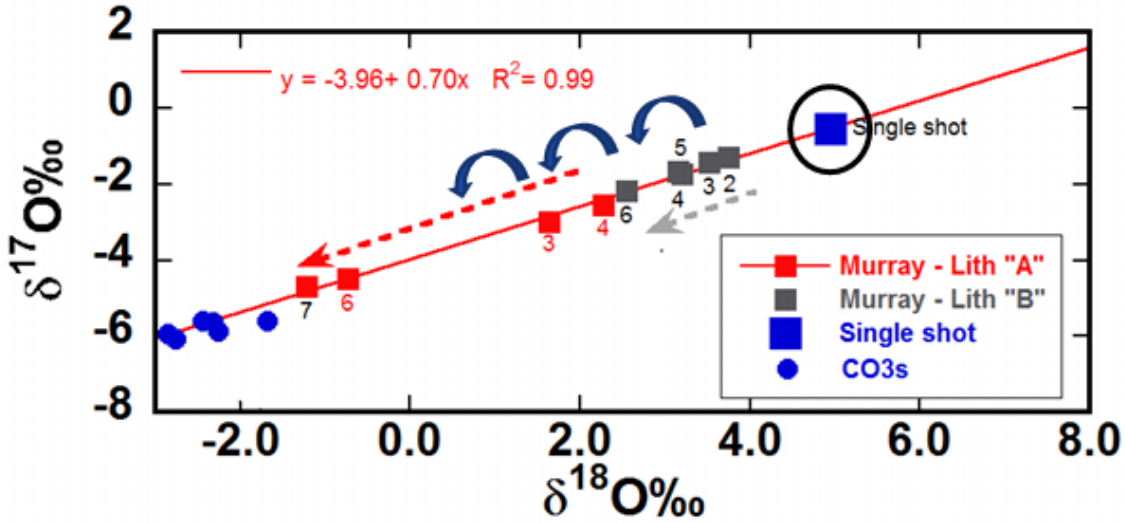

Figure 2.15– Graphical representation of the gradual removal of an isotopically heavy component when multiple CM chondrites are reacted in a single tray. The ambient exposure and heating of neighbouring wells by the laser in the presence of BrF_5 is the cause of this effect. As the numbers of shots (shown by digits next o the symbols) increase, the samples become progressively 'enriched' in ^{16}O. This effect cannot be solely because to sample heterogeneity as the powders were homogenised. Figure courtesy of Dr Richard Greenwood. Data unpublished. Uncertainties are within symbols.

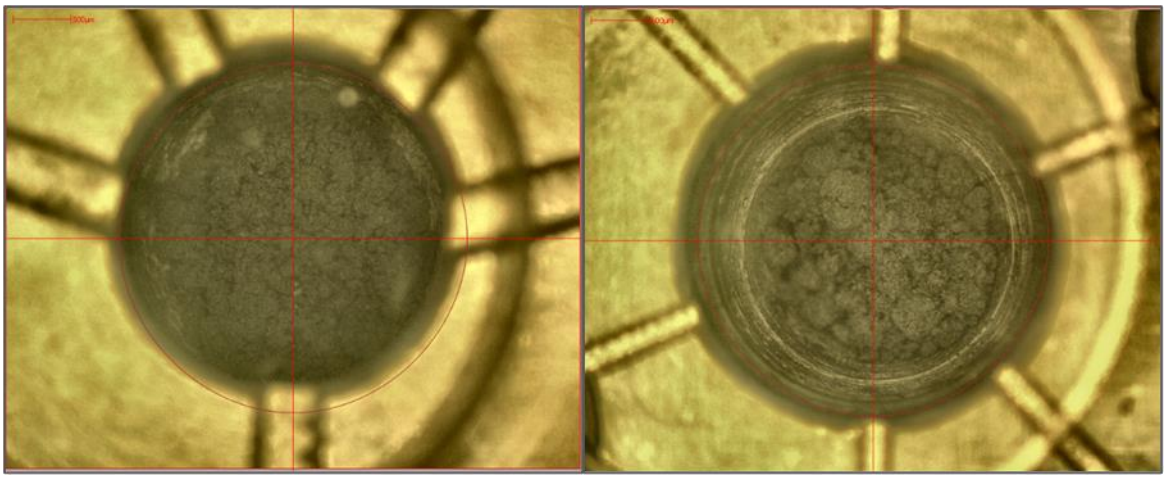

Figure 2.16 – A visual representation of pre-reaction of the CM1-2 chondrite Kolang. Left: A sample before any pre-fluorination of the sample chamber. Right: a sample after 5 minutes of pre-fluorination, made visually evident by the white ring of fluorides surrounding the sample which was actively observed to appear by the author. This is an extreme example, as most CMs do not visually show pre-reaction. This sample of Kolang (KO-03-A) had a high proportion of cronstedtite.

(Howard *et al.*, 2015), variable as a function of the degree of aqueous alteration, in addition to a plethora of organic molecules reflected as 1-2 total wt. % hydrogen (Alexander *et al.*, 2013), render them particularly vulnerable to the influence of BrF_5 even at room temperature (Fig 2.16). This caused the sample, or samples to pre-react during the pre-fluorination step

(to clean the chamber, see section 2.5.3.3) and in the case of a multi sample tray, each sequential BrF_5 exposure, essentially removing an isotopically heavy component from the unreacted samples during each exposure of BrF_5 (Fig 2.15).

2.5.4.2 Modification 2: Backfreezing to remove NF^+

CM chondrites contain significant levels of nitrogen, typically >1000 ppm (Pearson *et al.*, 2006), and therefore during laser fluorination of such samples, nitrogen trifluoride, NF_3, can be generated (*e.g.,* Miller *et al.,* 1999). It is typically synthesised via the fluorination of nitrogen-rich organics. NF_3 will fragment in the electron source as follows:

Equation 2.6

$$NF_3 \rightarrow NF_2^+ + NF^+$$

NF^+, m/z=33, is therefore a mass interference to the $^{17}O^{16}O$ ion measured on the mass spectrometer (used to determine the $^{17}O/^{16}O$ ratio). With a freezing temperature of 66 K some NF_3 remains in the gas phase and un-reactive with the warm KBr and therefore can enter the mass spectrometer along with the O_2 analyte, causing an artificial inflation of the $\Delta^{17}O$ value.

Previously, the procedure at the OU involved monitoring for NF_3 via the mass 52 NF_2^+ fragment ion during an analysis (Miller *et al.,* 1999). As this peak is dominant in the NF_3 fragmentation spectrum, it is more easily detected and was used to infer the presence of interfering NF^+. If a significant amount of mass 52 is detected, the sample was backfrozen onto a variable temperature cryotrap (VTC) filled with 13x molecular sieve zeolite and then re-released at -120 °C while being transferred to a second molecular sieve cold finger at -196 °C (Abe, 2008; Ahn *et al.,* 2014; Miller *et al.,* 1999). This retains all the detected NF^+ onto the VTC while the pure oxygen is transferred successfully and the now NF^+-free O_2 gas can be remeasured. However, the efficacy of this approach is questionable, and this is addressed in section 3.1.2.

2.5.4.3 Small samples

Finally, while 2 mg is nominally the preferred sample size equating to approximately 1000 µg of liberated O_2 gas, smaller aliquots of material approximating 20-120 µg can be readily measured by the microvolume setup on the MAT 253 mass spectrometer (section 2.5.3.7). Oxygen isotope analysis of small samples at the OU was pioneered by Greenwood *et al,* (2007) and McDermott (2013) and used in recent years for the analysis of micrometeorites (*e.g.,* Goderis *et al.,* 2020; Suttle *et al.,* 2020). However, accuracy issues affecting the known isotopic composition of standards occurred in all campaigns. This phenomenon has also been reported in other laboratories attempting similar types of analyses (*e.g.,* Cordier *et al.,* 2011; Suavet *et al.,* 2010) and is not a minor problem. Although decreasing sample size has little impact on precision, there is a progressive decrease in the measured $\delta^{18}O$ of increasingly smaller samples (Goderis *et al.,* 2020; McDermott, 2013; Suavet *et al.,* 2010; Suttle *et al.,* 2020), although two early studies report the opposite effect, tending towards more positive oxygen isotopic compositions (Cordier *et al.,* 2011; Greenwood *et al.,* 2007).

Deciphering the nature of this issue is complex and has previously only been partly resolved. Significant efforts by McDermott (2013) sought to investigate if the fractionation was induced within a specific part of the Open University gas handling line by expanding reference gas from the mass spectrometer back through parts of the clean-up and laser fluorination system. McDermott (2013) measured the isotopic composition of the gas each time it interacted with each part of the vacuum line and found that only once it was expanded into the sample chamber with an aliquot of BrF_5 was an isotopic shift detected. The cause of the isotopic shift was unclear but interpreted by McDermott (2013) as the result of an analytical blank caused by the BrF_5 itself, either by retaining a contaminant O_2 component, or by fractionating the gas during cleanup. A third alternative was the BrF_5 itself was interacting with the sample chamber (McDermott, 2013). If the culprit is indeed a blank, it is likely to be far too small to be accurately measured and must instead be inferred.

Chapter 3 - Laser Fluorination and Small Sample Method Development

3.1 Fluorination of small CM chondrites: challenges and solutions

To fulfil the thesis aims, it is requisite that the apparatus at the Open University can measure, precisely and accurately, smaller sample sizes than is traditional, as the micromilling procedure reduces the typical sample size by an order of magnitude from ~2mg ~200 μg. The OU 'small sample' procedure (section 2.5.3.7) that was used prior to this thesis work sacrificed little in terms of instrumental precision (Goderis *et al.,* 2020; Suttle *et al.,* 2020) when compared with the nominal procedure for larger samples of silicate (*e.g.,* Miller *et al.,* 2002; Starkey *et al.,* 2016) but suffered from issues with accuracy due to several potential contamination and blank problems affecting the smaller volumes of oxygen gas liberated (McDermott, 2013). Its application therefore had been limited to samples displaying large variations in oxygen isotope composition — like micrometeorites (Goderis *et al.,* 2020; Suttle *et al.,* 2020) — where such effects are unlikely to significantly impact the interpretation of the results.

This chapter outlines the contribution of the author to improving the previously published 'single-shot' procedure for analysing CM chondrites (Greenwood *et al.,* 2023; Schrader *et al.,* 2014). The two outstanding challenges with CM analyses as outlined in the previous chapter are:

- Interferences generated by the high nitrogen content of CMs
- Challenges associated the small amount of O_2 liberated, and the potential for blank contamination. To define the term blank: During an analysis, the system (or analytical) background is a contribution to the analysed sample gas that is not derived from the sample. The amount and isotopic composition of this system or analytical background is determined by running 'blanks'. This will be discussed in further detail in section 3.1.3.

While these issues were acknowledged prior to this work, only partial solutions were devised to counteract their effect, greatly limiting their application to the most challenging, volatile-rich meteorite material.

3.1.2 Challenge 1: The generation of nitrogen trifluoride

There are several drawbacks to the backfreezing NF_3 mitigation technique (section 2.5.4.2). Firstly, relying on the mass 52 (NF_2^+) peak to detect NF^+ by proxy is limited by the background and sensitivity of the detectors on the mass spectrometer. The NF_2^+ signal required to detect a $\Delta^{17}O$ displacement of 10 ppm (0.01 ‰) on the centre faraday cup is 0.6 mV (resistivity of 3×10^{11} Ω), a level approaching the noise on the detector and the analytical precision which can normally be achieved and therefore not practically detectable (Kohl *et al.,* 2016; Rumble *et al.,* 1997). Further hampering the detection of NF_2^+ fragment ions is the potential presence of other molecules with mass 52 (Fig 3.1). During this work, these isobars persisted through mass scans of reference gas and O_2 gas from the laser fluorination of obsidian glass, and their nature is unknown. Consequently, the effect of NF^+ upon the $\Delta^{17}O$ will have surpassed 0.1 ‰ before a signal is noticed as anomalous compared to these background signals. Secondly, it has been shown in the OU laboratory that backfreezing onto a molecular sieve can induce significant mass-dependent isotopic fractionation of the oxygen gas, an effect that has also been reported in the literature when manipulating O_2 gas between cold fingers using molecular sieve (Ahn *et al.,* 2014). This means that while the residual effect on the $\Delta^{17}O$ measurement is corrected, the $\delta^{17}O$ and $\delta^{18}O$ values may be compromised. There are also considerable memory effects due to the 'stickiness' of NF_3 which can reside in the inner workings of the mass spectrometer for many hours after organic-rich chondrite analyses, for example affecting the subsequent obsidian standard measurements.

In this study many of the samples will be too small to perform repeated analyses before the sample signal decays, and so can only be analysed once rendering backfreezing unfeasible.

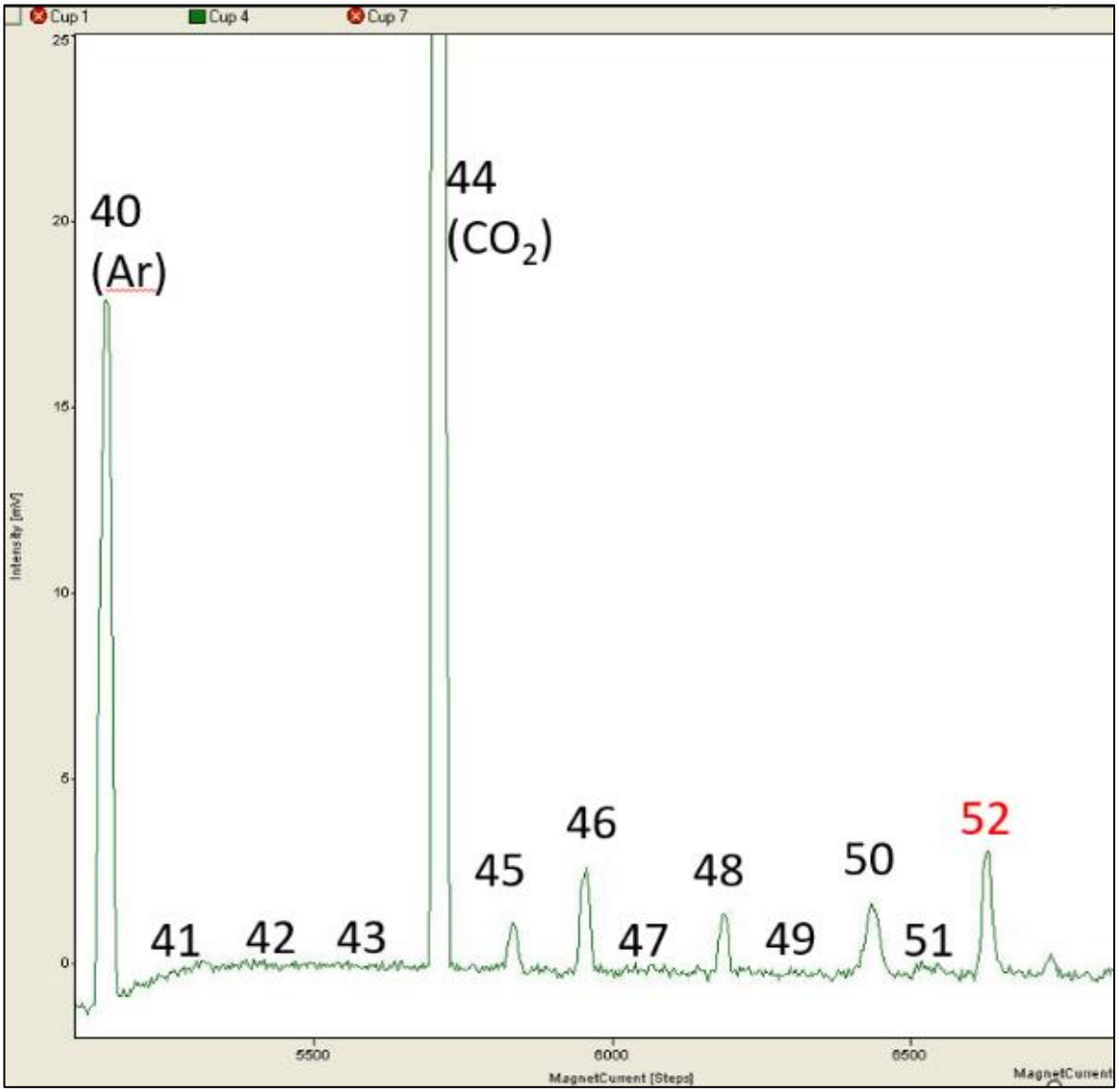

Figure 3.1 - Mass scan from 40 – 54 extracted from Isodat InstrumentControl software. The sample gas is an obsidian standard ran after a CM chondrite. There is 4 mV signal on the 52 peak, which would correspond to an NF^+ enrichment of ~ +0.05 ‰ on the average $\Delta^{17}O$ value of obsidian (Kohl *et al.*, 2016). No such effect was observed on this measurement and the $\Delta^{17}O$ is within the expected range (0.005 ± 0.02 ‰ [Windmill *et al.*, 2022). Therefore, the 52 peak is attributed to an unidentified isobar produced during the fluorination of the CM.

However, as the samples also contain significant amount of nitrogen it is paramount to adapt the technique to ensure NF_3 is quantitatively removed before admittance into the mass spectrometer to begin with.

Table 3.1 – O-isotope results demonstrating the effect of temperature upon O_2-10 reference gas while being 'backfrozen' from the inlet followed by cryogenic transfer between two 13x molecular sieves. The average measurement of the reference gas, taken as the mean of 20 measurements, is: 4.38 ± 0.03 ‰ ($\delta^{17}O$), 9.03 ± 0.04 ‰ ($\delta^{18}O$).

'Backfrozen' O2-10 Ref gas		
$\delta^{17}O$ (‰)	**$\delta^{18}O$ (‰)**	**$\Delta^{17}O$ (‰)**
	-100 °C	
4.44	9.12	-0.30
4.44	9.14	-0.31
	-110 °C	
4.44	9.14	-0.32
4.44	9.15	-0.32
4.45	9.16	-0.31
	-120 °C	
4.45	9.15	-0.31
4.46	9.17	-0.31
4.43	9.16	-0.33
	-130 °C	
4.38	9.00	-0.31
	-135 °C	
4.27	8.81	-0.31
	-140 °C	
4.32	8.90	-0.31

3.1.2.1 The 'freeze-first' method.

A work around was devised inspired by the dual cold finger setup by Ahn *et al.* (2014). Here, the gas is first frozen onto a VTC cold finger filled with 13x molecular sieve zeolite at -196 °C. Then, the VTC is warmed to a chosen temperature and the gas is transferred to a second molecular sieve finger at -196 °C. This means no NF_3 containing gas will ever be present inside the dual inlet. Here, this procedure is named 'freeze-first'.

Ahn *et al*. (2014) states that up to 0.2 ‰ fractionation of the $\delta^{18}O$ value can occur during transfer between two molecular sieves from -114 to -196 °C. However, no transfer times were published so it is unclear if this fractionation was caused by incomplete transference or by prolonged transfer. For this work, a transfer time of 12 minutes was chosen, adding an extra two minutes to the usual freezing time for small samples (e.g., Goderis *et al.*, 2020; Suttle *et al.*, 2020). After 10 minutes have passed, the baratron typically registered

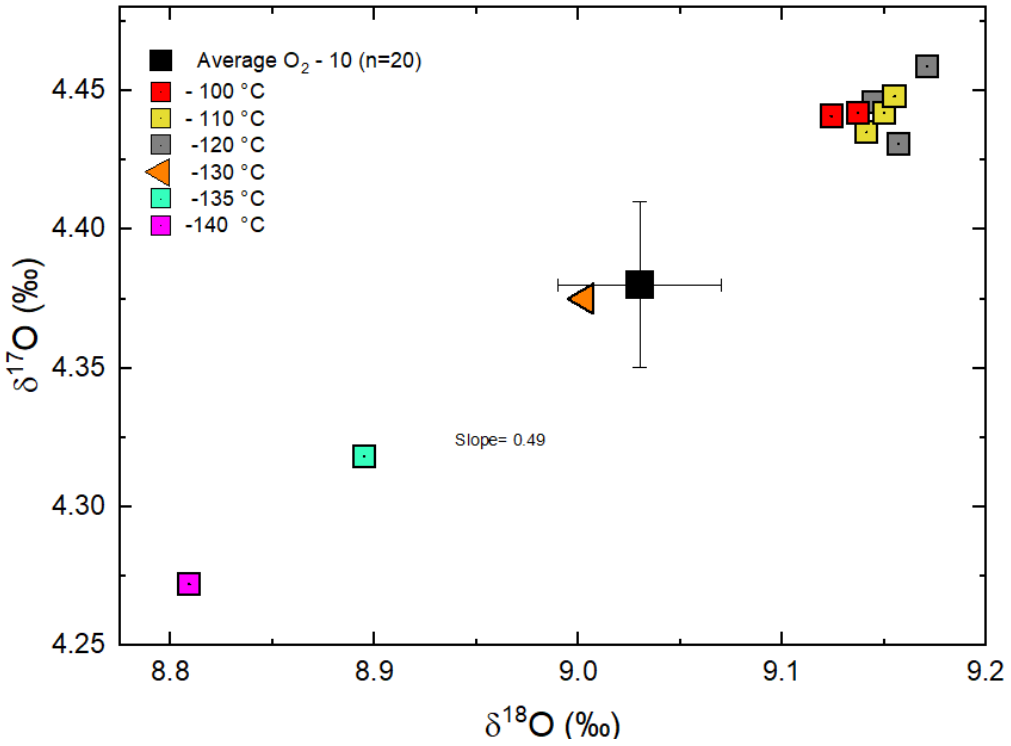

Figure 3.2 – 3-isotope plot of different 'backfrozen' cryogenic transfer temperatures between two 13x molecular sieves for O2-10 reference gas. The average measurement of the reference gas, taken as the mean of 20 measurements, is: 4.38 ± 0.03 ‰ (δ17O), 9.03 ± 0.04 ‰ (δ18O). Backfreezing the gas at temperatures > -130 degrees appears to induce a ~0.2 enrichment in $\delta^{18}O$, whereas temperatures colder than -130 degrees produce the opposite effect. There appears to be a balance between fractionation to heavier values occurring within the inlet of the mass spectrometer at warmer temperatures, and fractionation by retention of lighter isotopes on the molecular sieve at colder temperatures. Neither is desirable, so this technique is sub-optimal.

background levels indicating that essentially all of the gas was cryogenically transferred. The further two minutes guaranteed that any minute quantities of gas still transferring between the two fingers is collected.

Extensive tests were then performed on both obsidian standards and O2-9 reference gases to trial different 'freeze-first' release temperatures to check for any residual fractionation effects, such as those reported by Ahn *et al.* (2014). Temperatures of -115 °C have been used to retain NF_3 by other laboratories (Abe, 2008; Ahn *et al.*, 2014; Clayton and Mayeda, 1963), though this value was historically set by using an ethanol slush. Colder release temperatures of -120, -125, -130 and -140 °C were trialled to guarantee the retention of NF_3 in the case of slight human error when warming the sieve (*i.e.*, ± 2 °C). No O-isotope fractionation is observed (within 2σ error of the sample average) for all release temperatures except for -140

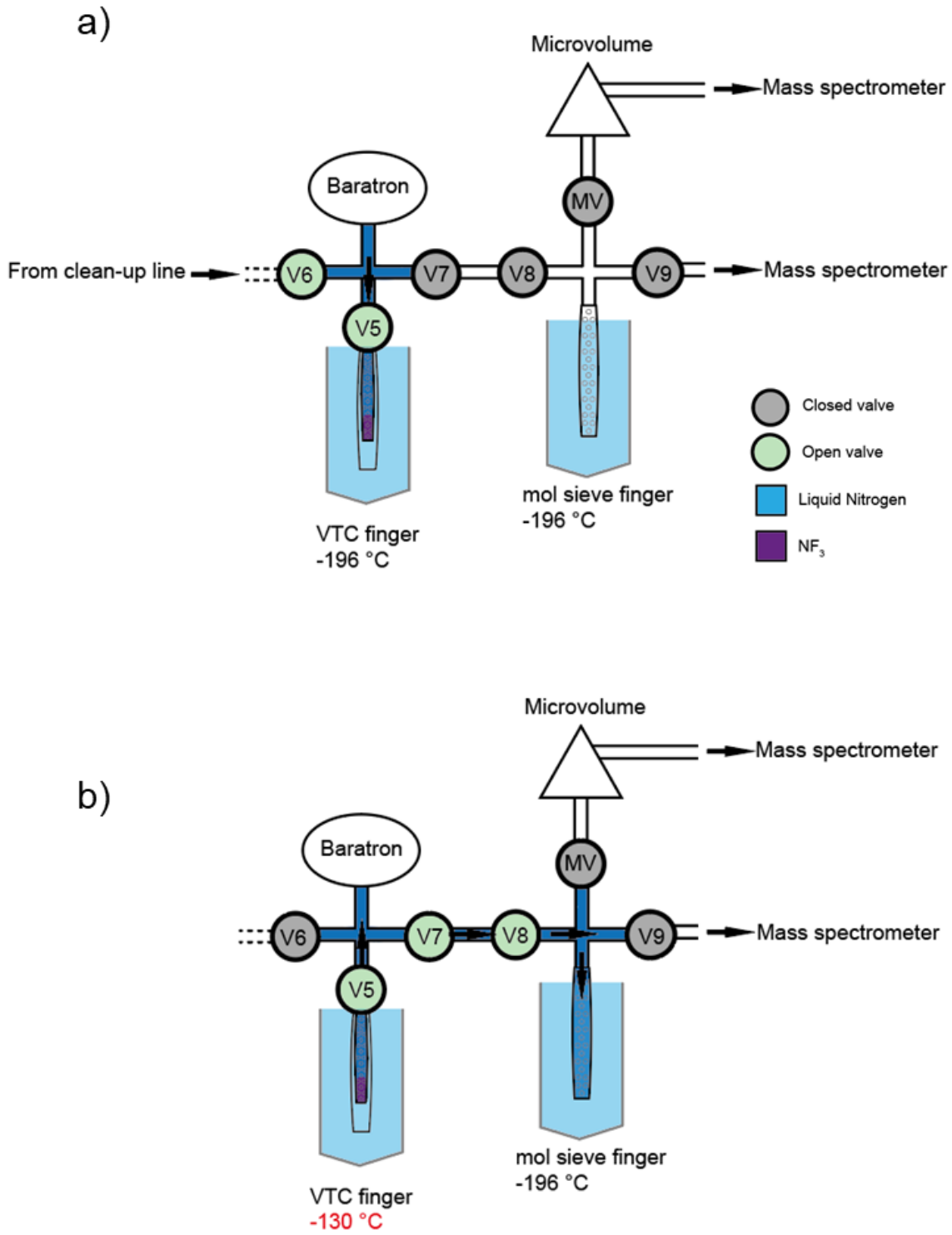

Figure 3.3 – A schematic cartoon outlining the 'freeze-first' method: a) The sample was initially frozen onto the VTC finger at -196 over 10 minutes, trapping any NF_3. Once transfer was complete, V6 was closed, and the VTC warmed to -130 ° C by turning the heater jacket to 4.75-4.90 V while the main molecular sieve cooled to -196°C. b) Once the desired temperature was reached, V7 and V8 were opened which initiated the transfer to the main mol sieve finger. Cryogenic transfer took 12 minutes and any contaminant NF_3 remained on the VTC. After 12 minutes, V8 and V5 are closed and the gas can either be expanded directly into the bellows of the mass spectrometer, or in the case of a small sample, frozen onto the microvolume.

°C, where significant isotopic fractionation occurs. This indicated retention of an O_2 gas component in addition to NF_3 between -130 and -140 °C. A temperature of between -125 and -130 °C was therefore chosen to guarantee retention of NF_3, ensuring 99.9% of the oxygen is released during molecular sieve transfer, thus preventing isotopic fractionation. Fortuitously, no significant isotopic fractionation of the gas is observed, demonstrating this procedure is effective at mitigating NF_3 with no consequences for the isotopic composition. The isotopic fractionation reported in the study of Ahn *et al.*, (2014) must be a feature of their setup or the amount of molecular sieve used (here, each cold finger was filled with many 13x pellets, compared with Ahn *et al.* (2014) who only used one, 95 mg pellet), and so the results are not comparable with those obtained here.

After choosing a release temperature, several samples of Orgueil (a CI chondrite) were reacted very slowly for 30 minutes to deliberately induce an NF_3 effect that would compromise the system. This effect was tracked by analysis of a departmental PSSRI obsidian standard after the Orgueil was reacted. As can be seen (Table 3.2, Fig 3.4), the obsidian samples were severely compromised from the average, enriched by 0.2 - 0.4 ‰ ($\Delta^{17}O$). Initially, the established method of back-freezing was attempted (Miller *et al.*, 1999) onto a molecular sieve, followed by re-releasing at -125 - -130°C and reanalysing the gas. As expected, this method reduces the influence of NF_3, however memory effects persist within the mass spectrometer and an enrichment to 0.1 ‰ is still observed (turquoise symbol on Fig 3.4) in the treated gas. On the other hand, ‘freezing first’ the sample and standard onto the VTC, followed by release at a temperature between -125 and -130 °C, removed any influence of NF_3, and the obsidians fell within the $\Delta^{17}O$ range of the PSSRI obsidian average (Fig 3.4).

Table 3.2 – O-isotope results for compromised obsidian analyses; back frozen obsidian using a traditional clean-up technique, and obsidians 'Frozen First' onto the VCT as shown in Fig 3.4.

$\delta^{17}O$ (‰)	$\delta^{18}O$ (‰)	$\Delta^{17}O$ (‰)
Compromised obsidian (post Orgueil analysis)		
3.96	7.51	0.05
4.06	7.10	0.37
3.93	7.46	0.05
3.99	7.34	0.17
3.93	7.31	0.13
'Backfrozen' obsidian		
3.89	7.35	0.07
'Freeze-First' obsidian		
3.85	7.37	0.02
3.83	7.35	0.01
3.84	7.37	0.01

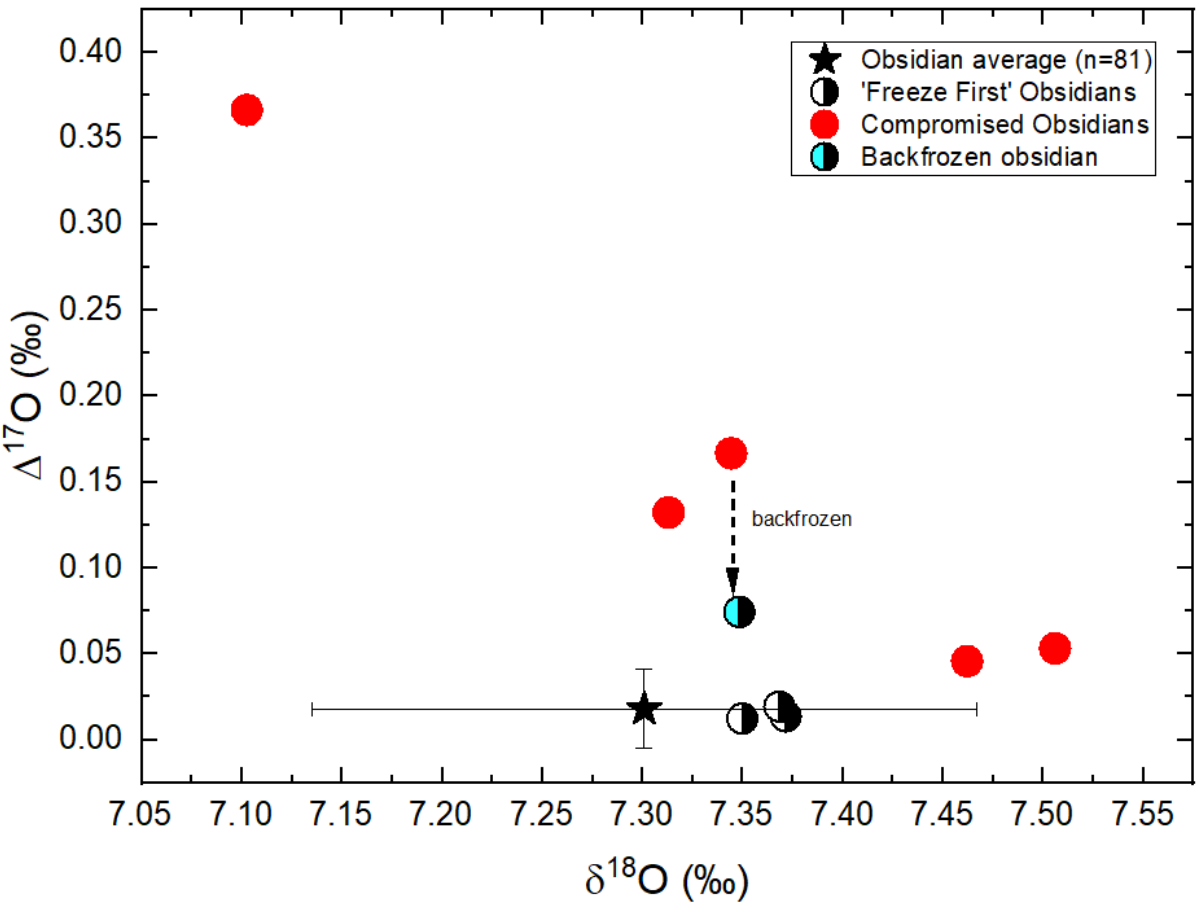

Figure 3.4 – The effect of NF_3 upon the standard obsidian measurement after reacting a sample of Orgueil for 30 minutes. The compromised obsidian measurements have an elevated $\Delta^{17}O$

Table 3.3 – O-isotope results demonstrating the effect of temperature upon O_2-9 reference gas while undergoing cryogenic transfer between two 13x molecular sieves. The average measurement of the reference gas, taken as the mean of 5 measurements, is: 4.29± 0.04 ‰ ($\delta^{17}O$), 8.87 ± 0.07 ‰ ($\delta^{18}O$).

'Freeze First' Ref gas (O_2-9)		
$\delta^{17}O$ (‰)	**$\delta^{18}O$ (‰)**	**$\Delta^{17}O$ (‰)**
	-120 °C	
4.29	8.88	-0.33
4.30	8.87	-0.31
	-125 °C	
4.30	8.89	-0.32
4.27	8.89	-0.35
	-130 °C	
4.29	8.90	-0.34
4.32	8.86	-0.29
	-140 °C	
4.05	8.35	-0.29
4.01	8.29	-0.30

Table 3.4 - O-isotope results demonstrating the effect of temperature upon obsidian glass while undergoing cryogenic transfer between two 13x molecular sieves, *i.e.*, 'freeze-first'. The average measurement of the obsidian, taken as the mean of 81 measurements, is: 3.81± 0.09 ‰ ($\delta^{17}O$), 7.30 ± 0.17 ‰ ($\delta^{18}O$).

Additional 'Freeze First' Obsidians		
$\delta^{17}O$ (‰)	**$\delta^{18}O$ (‰)**	**$\Delta^{17}O$ (‰)**
	-120 °C	
3.79	7.29	0.00
3.80	7.30	0.01
3.79	7.25	0.02
	-125 °C	
3.80	7.32	-0.01
3.82	7.33	0.01
	-130 °C	
3.78	7.27	0.00
3.84	7.31	0.04
3.79	7.24	0.02
3.82	7.28	0.03
	-140 °C	
3.58	6.82	0.03
3.62	6.91	0.01

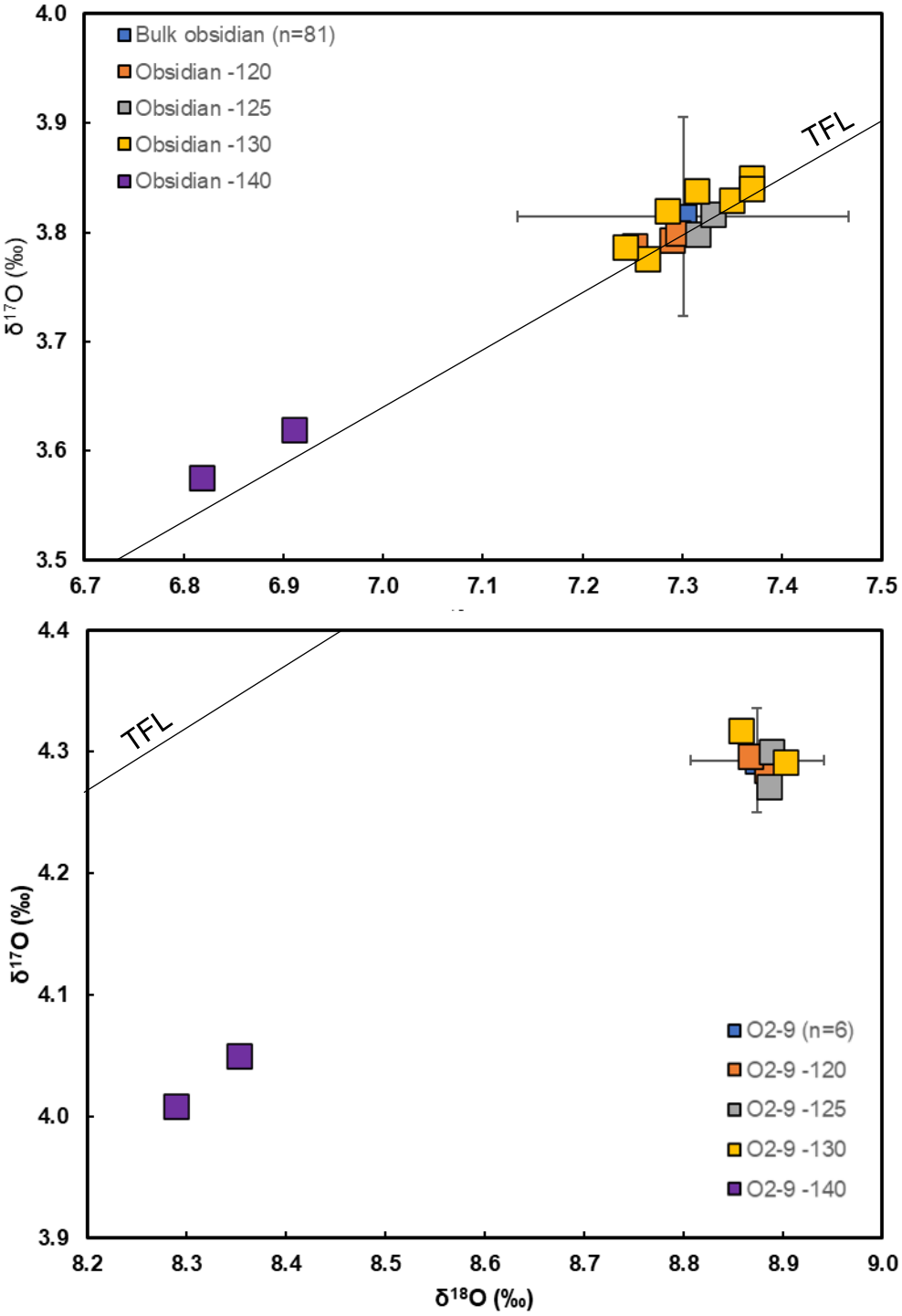

Figure 3.5 – 3-isotope plot of different 'Freeze-First' cryogenic transfer temperatures between two 13x molecular sieves for obsidian (top) and O2-9 ref gas (bottom). Temperatures between -120 and -130 produce no visible fractionation of the sample gas within 2σ uncertainty of the long-term sample mean. 'Freeze-first' obsidians are included from both Table 3.1 and 3.3.

3.1.3 Challenge 2: Accuracy of isotopic measurements of small samples

To complement the work of McDermott (2013) and to decipher the cause of isotopic fractionation with decreasing sample size, it was decided to fully characterise the analytical background that may be present explicitly at the moment of analysis. Several types of blanks have been measured on the microvolume on the MAT 253 IRMS, where possible, during the CM single shot procedures undertaken over the course of this work. These included:

- The amount and isotopic composition of the gas released during a 5-minute pre-fluorination step of the procedure (2.5.4.3). This step has been significantly shortened from the original 2 x 20 minutes as the pre-reaction potential of CMs also significantly impacts the opportunity to undertake extensive pre-fluorination. Any gas released during the pre-fluorination is henceforth called the 'pre-reaction blank'. This step has been attempted previously by Schrader *et al.* (2014) during the analysis of 'big' ~2 mg samples of CR chondrites; however, the 5-minute pre-reaction blanks in Schrader's study were very large (50-170 µg) and dominated by atmospheric contribution (Schrader *et al.*, 2014), and therefore unlikely to be representative of the true blank during a small sample analysis. Here, the pre-reaction blanks were much smaller, and were measured prior to each small sample measurement to home in the isotopic composition of the blank during analysis where possible (see section 3.1.3.3). However, the presence of O_2 from reaction of BrF_5 with the sample itself complicates interpretation.
- The amount and isotopic composition (where measurable) of the gas released during an additional, ambient chamber fluorination after the sample has been analysed, henceforth called the 'post-reaction blank'. The purpose of this blank was to determine if the system had returned to typical background levels after the reaction and has historically been a 2-minute exposure (Schrader *et al.*, 2014), though rarely measured for its isotopic composition. In this work, the post-reaction blank exposure

was increased to 10 minutes, to allow for any residual O_2 gas to be captured. If this blank was elevated, then this warranted measurement and comparison with data to determine if there was an incomplete reaction or contamination within the sample chamber. In almost all circumstances, the sizes of these blanks are far too small to maintain laminar flow in the capillaries of the mass spec, leading to significant isotopic fractionation if a measurement was attempted, limiting any conclusions that can be drawn from the data.

By assessing the pre- and — if needed — post- reaction blanks, estimations can be made regarding the amount of blank contributing to the sample at the time of analysis. On the other hand, making inferences regarding its O-isotopic composition is much more difficult without many data points; however, there is a large legacy dataset in the OU data repository that includes the isotopic composition of 5-minute pre-reaction blanks from many OH-bearing meteorites, here described as legacy blanks, including: CM, CR and C2-ung (Appendix A4), analysed over the last decade. The author extracted and tabulated these results, which are plotted in Fig 3.6. There does not appear to be any systematic correlation between the isotopic composition of the samples analysed and the composition of the blanks. As these data points span almost a decade of analytical improvements, they are not necessarily directly comparable to the pre-fluorination blanks obtained during the present 'small sample' study; they are typically large, often more than 50 μg O_2, occasionally as large as 200 μg O_2 (appendix A4). In 2017, the culprit was identified as a dirty VCR frit gasket that had accumulated fluorination debris over several years and was acting as a moisture trap. Nevertheless, the size of the dataset allows information about which components are dominating to be revealed. To a first order most of the gas released from the sample during the pre-fluorination step is indeed terrestrial and displays a wide range in isotopic compositions along a line (A-B on Fig 3.6) close to the TFL. The pre-reaction blank is therefore a result of the mixing of different gas reservoirs, including that released during pre-

reaction of the CM chondrite (line C-D on Fig 3.6), terrestrial air, and terrestrial moisture, the latter of which may be severely fractionated to heavier compositions during baking of the sample chamber. The isotopic composition of terrestrial air has $\Delta'^{17}O$ of -0.410 ‰ (λ = 0.5262) (Barkan and Luz, 2005). It is probable a proportion of the pre-reaction blank is air. Meteoric waters (moisture) generally possess slight $\Delta'^{17}O$ excesses of ~0.035 ‰ relative to VSMOW, and negative isotopic composition of roughly -5 to -25 ‰ ($\delta^{18}O$) (Luz and Barkan, 2010). A portion of this terrestrial contaminant probably lingers in the system, contributing towards the gas released during analysis of the unknown. However, it is unlikely to be the sole cause for the shift to lighter $\delta^{18}O$ values as sample size decreases, as the $\delta^{18}O$ compositions are predominantly positive, not negative. There must be other causal effects.

McDermott (2013) noted: "The analytical blank produced by the interaction between the BrF_5 and the fluorination system cannot be negated". While true, the effects of the analytical blank can be minimised and corrected either by direct measurement or by taking an assumed value and subtracting this influence from the measured unknown. Unravelling the composition of the analytical blank was a large focal point of method development in this work. Firstly, this required a revision of current loading and cleaning protocols to observe if the blank could be decreased and any further information revealed as blank levels drop.

3.1.3.1 Cleaning the sample chamber

Analysis of many meteorites using the multi-sample trays meant that the sample chamber required frequent cleaning, potentially building up moisture and oxide layers that could contribute to the blank. Therefore, an approach that minimised sample chamber cleaning and exposure to atmosphere was developed by the author to further reduce the blank. Before an analytical campaign, the sample chamber was removed from the line and ultrasonicated in deionised water for 30 minutes, then baked at 150 °C overnight in air. New components were installed, including a the external BaF_2 window, Viton O ring, copper gasket and VCR frit. The following day the empty sample chamber was baked overnight under vacuum at 80°C,

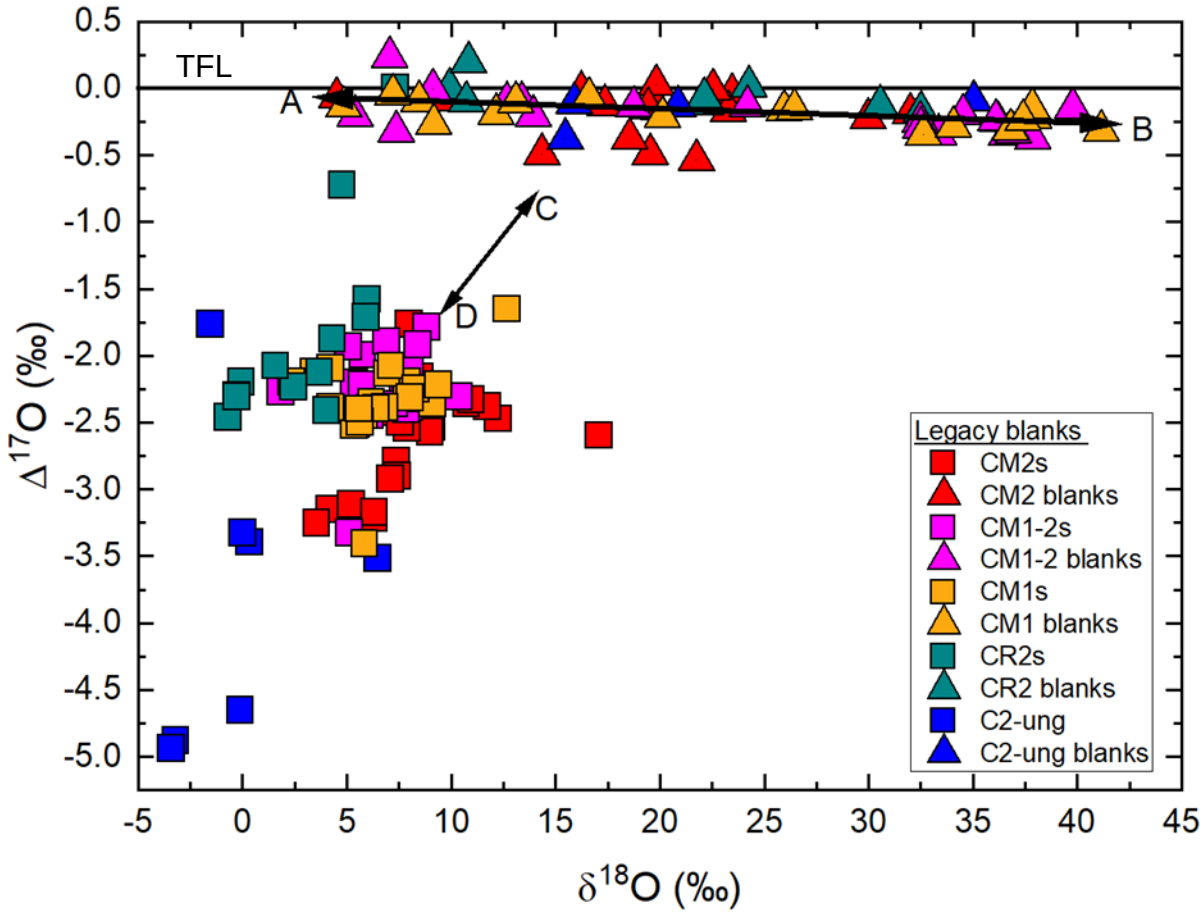

Figure 3.6 - A plot of all legacy blanks and their respective samples. The arrow A-B defines a low temperature fractionation line of terrestrial composition as exhibited by the pre-reaction blanks. The arrow C-D is an arbitrary direction for potential pre-reaction towards the hydrous meteorite field. Uncertainties are well within symbols.

and subsequently pre-fluorinated three times for twenty minutes until any gases released registered below 2 µg O_2 on the baratron. After this preparation the system was deemed ready to start analysing samples.

Each single shot sample and associated standard(s) was loaded into a clean sample tray, which was then loaded into the sample chamber within 1 minute of venting the chamber, with only the copper gasket being replaced if required. This minimised the exposure of the chamber to contaminating atmospheric moisture. No compressed gas or isopropanol was used to clean the chamber between analyses, which risks adding O-bearing propellants that may elevate the blank levels. Using the small BaF_2 windows to contain the CM2 during

analysis largely prevented significant build-up of fluorination waste in the chamber, as such it stays clean for 10 + single shot analyses.

Back-to-back single shots were facilitated by cleaning of the previous tray in parallel to the on-going analysis over a course of two 30-minute ultrasonications; one in Mega Clean non-ferrous detergent, and the other in MilliQ water, before baking for at least 6 hours at 150 °C before loading the next sample. Trays were not left overnight in detergent to minimise any effect this may potentially have on the blank.

An additional measure was implemented to minimise any influence from adsorbed moisture, which was to independently pre-fluorinate the stainless steel 'flexi' tube that is present between M8 and V2 (Fig 2.12 & 2.13 for valve configurations). This area is a moisture trap for adsorbed atmospheric H_2O that is driven off during baking. The BrF_5 aliquot is expanded into the flexi line for 10 minutes to pre-fluorinate. The gas liberated is cleaned up and the amount of O_2 generated determined from the pressure measured on the baratron. The mostly clean BrF_5 aliquot, now on Trap 2, will be recycled (*i.e.*, expanded back into the flexi line) multiple times until the background reaches baseline, < 2 μg on the baratron.

The final measure was to ensure that every single 'shot' of BrF_5 entering the system was fresh and adequately refluxed. Any BrF_5 from a prior analysis was therefore removed from Trap 2 and frozen onto Trap 4, which was shut using a manual valve and isolated from the rest of the line. This ensured no residual oxygen from prior analyses residing in the dirty BrF_5 was able to compromise the measurement.

As a result of this extensive cleaning, all small sample 5-minute pre-fluorination blanks were lowered to < 15 μg O_2, with the majority falling below 10 μg (Table 3.5 and Fig 3.7). Plotting these data alongside the legacy blanks reveal that isotopic compositions are increasingly negative with decreasing amount of blank, an amount that is much more comparable to the background during an unknown. It was decided that each small CM had should have an

Table 3.5 – O-isotopic composition of pre-reaction blanks throughout this work.

µg O_2	**$\delta^{17}O$ (‰)**	**$\delta^{18}O$ (‰)**	**$\Delta^{17}O$ (‰)**
Pre reaction blanks			
48.9	12.9	25.1	-0.1
46.6	9.9	19.4	-0.2
35.1	-1.4	-2.6	0.0
30.8	8.2	15.5	0.2
28.4	8.9	17.1	0.0
22.6	10.9	20.8	0.1
22.0	2.8	5.2	0.1
21.8	1.8	3.6	-0.1
21.0	5.7	11.1	0.0
20.5	9.1	17.8	-0.2
20.1	2.4	4.7	0.0
19.8	9.2	18.2	-0.3
19.8	4.6	8.2	0.3
15.7	-0.2	-0.3	-0.1
14.8	-1.9	-3.4	-0.1
14.5	3.4	6.8	-0.2
14.2	1.4	2.6	0.1
13.5	-1.5	-2.7	-0.1
13.5	1.1	2.2	0.0
13.4	2.8	5.8	-0.2
12.5	-2.2	-4.5	0.1
12.3	4.5	8.9	-0.1
11.9	0.6	1.4	-0.1
11.5	4.9	9.5	-0.1
11.4	4.5	8.7	0.0
10.7	2.3	4.5	-0.1
10.5	-3.6	-6.7	-0.1
9.4	-2.8	-5.3	0.0
9.2	-1.0	-1.8	0.0
8.4	-2.1	-3.8	-0.1
8.2	-4.6	-8.6	-0.2
8.2	-4.8	-8.8	-0.2
7.6	-3.9	-7.4	-0.1
7.6	-1.5	-2.8	-0.1
7.1	-3.1	-6.0	0.0
6.4	-2.5	-4.7	-0.1
6.4	-1.7	-3.1	-0.1
5.4	-1.9	-3.5	-0.1
4.9	-6.0	-11.2	-0.1
4.5	-3.5	-6.2	-0.2
4.5	-7.0	-13.2	-0.2
4.3	-4.3	-7.9	-0.2
3.5	-3.8	-7.0	-0.1
2.8	-0.7	-0.9	-0.2

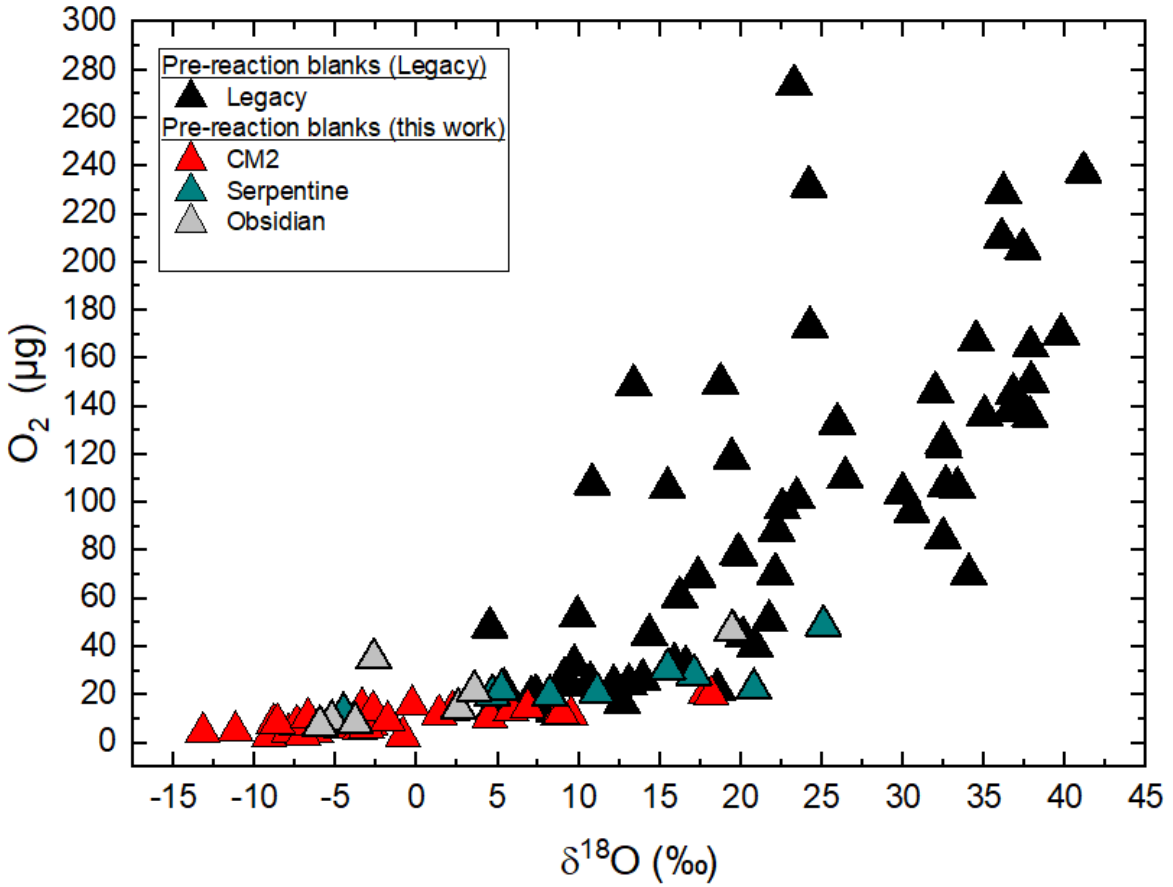

Figure 3.7 – 3-Isotope plot comparing the size and isotopic composition of the single-shot pre-reaction blanks measured in this study with those obtained during legacy analyses. As the amount of blank decreases, the composition tends towards more ^{16}O-rich compositions. Uncertainty lie within the symbol size.

accompanying small obsidian measurement, comparable to the oxygen liberated during a small CM analysis (~ 50 µg O_2), to trace the effect of the blank. All single small obsidian analyses are isotopically lighter than the average for large obsidian samples, falling along a mass fractionation line, indicating either some fractionation of the sample gas, or mixing with a blank with a terrestrial $\Delta^{17}O$ signature and a negative $\delta^{18}O$ composition, possibly with a composition lower than the most isotopically negative pre-reaction blanks. Assuming this effect is due to a terrestrial blank, the next logical step was to determine how much of this blank was influencing the sample at the time of fluorination.

3.1.3.2 'Dummy' trays

To establish the precise amount of blank at the time at which a sample is lasered, a revised protocol was developed consisting of five shots of BrF_5 (Fig 3.8).

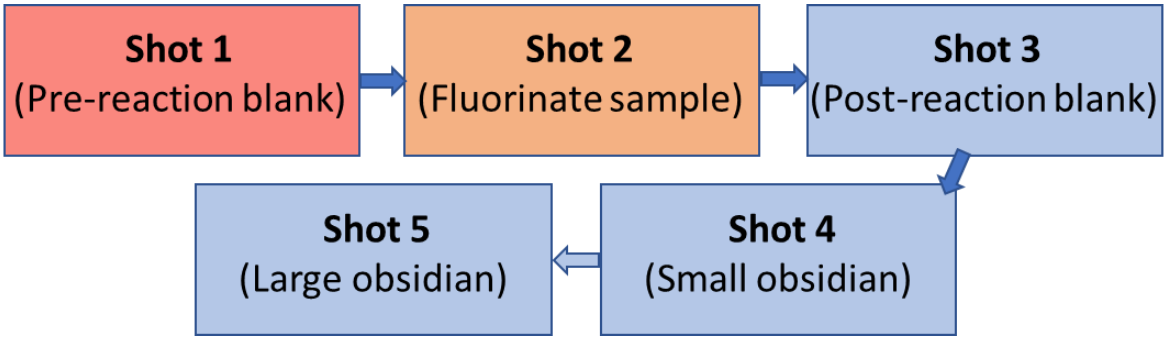

Figure 3.8 - Flow chart outlining the single-shot procedure. The blank is highest during shot 1, but rapidly decreases throughout the run. The amount of blank during shot 2 — where the unknown is measured is not directly measurable and must be inferred — is combined with the sample gas.

Table 3.6 – Dummy trays analysed throughout this work in chronological order. Each tray was loaded with a large and a small, fused obsidian, a small BaF_2 window, and no CM sample. Three shots of BrF_5 were sequentially loaded into the system. Shot 1 represents the 5-minute pre-reaction blank. Shot 2 represents the analysis shot, during this time an empty well was lasered for a few minutes to simulate any effects induced by heating of the windows and well during lasering. Shot 3 is a post-reaction blank to check the oxygen levels have dropped to small, background levels. No further shots were attempted, as the purpose of the dummy tray was to constrain the amount of blank at the time analysis of the unknown (Shot 2 in Figure 3.9.)

Dummy trays (µg O_2)			
Date	**Shot 1**	**Shot 2**	**Shot 3**
27/11/2020	12	5	2
01/12/2020	56	12	5
02/12/2020	8	2	2
06/12/2020	7.7	2.2	1.2
08/12/2020	12.1	3.5	2.3
25/02/2021	15.2	3.7	3.9
26/02/2021	8.7	2.6	1.8
05/08/2021	24.0	5.0	5.0
22/11/2021	12.2	3.0	2.0
23/11/2021	6.1	2.3	2.3
10/01/2022	10.0	4.3	3.3
22/06/2022	17.2	4.0	3.8
23/06/2022	17.5	5.6	4.7
Average	16	4	3
1σ	13	2.6	1.3

Several empty trays, loaded with all components (including fused standards) but without the sample were analysed as normal except no sample was lasered. Instead, the single shot was simulated by lasering an empty well overlain by small BaF_2 window. These are ‘dummy’

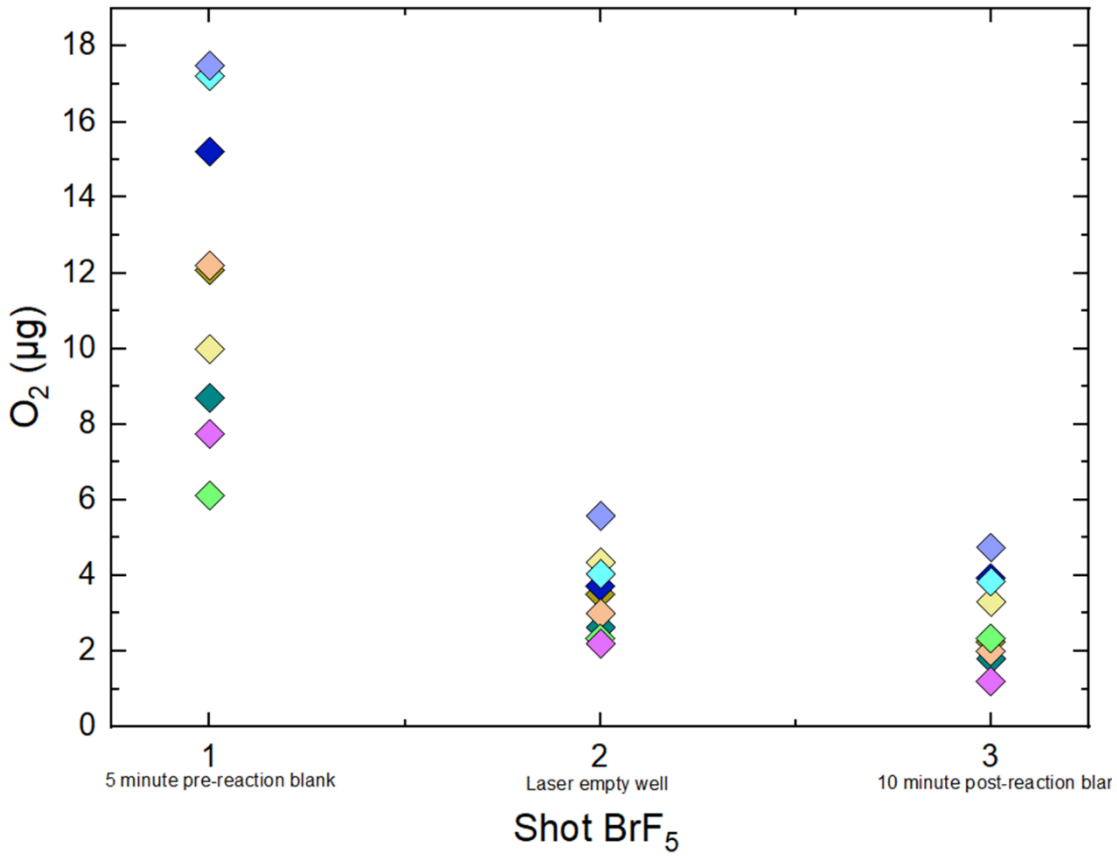

Figure 3.9 The amount of blank vs shots of BrF_5 for all dummy trays. Each dummy tray is designated a different colour for ease of tracing. The amount of blank falls quite rapidly to 3-4 ug O with successive shots, as long as the first blank is below ~20 µg O_2.

trays that record the amount of blank released by the system at each step. The results show if the volume of gas liberated by the first shot is below 20 µg O_2, the second and third and subsequent shots decrease consistently to a baseline of between 2-3 µg (Table 3.6 and Fig 3.9). To assess the evolution of the system blank, a dummy tray was run before, during and after each campaign. The average of the gas liberated during shot 2 permits evaluation of a sensible mass of oxygen to use for blank correction. The mass is between 2 and 4 µg O_2.

3.1.3.3 Blank correction

The true isotopic composition of the blank at 'shot 2' (analysis shot) is unable to be determined directly as the amount of gas is too small to allow accurate measurement in the mass spectrometer as laminar flow through the capillaries could not be ensured, but it must at least be towards the most negative isotopic composition of the pre-fluorination blanks to account for the isotopically light obsidian measurements. The composition can therefore be

determined by indirect methods through investigation of its effect on the small obsidians. A correction was devised by experimenting with the amount of blank released during shot 2 the dummy trays (2-4 µg), and the most negative isotopic compositions released during the 5-minute pre-reaction blanks in order to cause the isotopic compositions of the small obsidians to converge on the true value with a minimum amount of scatter. The best outcomes were produced when approximately 2.4 µg of blank with a terrestrial isotopic $\delta^{18}O$ composition of roughly -10 ‰ The following blank correction equation is used after Ohlsson (2013):

Equation 2.7

$$\delta s = \frac{n_T \delta_T - n_b \delta_b}{n_T - n\_b}$$

Where δ_s represents the blank corrected value; δ_T is the measured isotopic composition of the sample; n_T is the total amount of O_2 gas liberated from the reaction; n_b is the amount of blank inferred; δ_b is the inferred isotopic composition for the blank.

The compositions are listed in Table 3.7 and the small obsidians were corrected using these values (Table 3.8 and Figure 3.10). The resultant accuracy and 2σ reproducibility for $\delta^{17}O$ is 3.79 ± 0.11 ‰, for $\delta^{18}O$, 7.30 ± 0.20 ‰ and for $\Delta^{17}O$, -0.01 ± 0.04 ‰ (n=23). This is comparable to the published precision for regular samples, at 3.81 ± 0.09, 7.30 ± 0.16 and 0.02 ± 0.02 ‰ respectively (section 3.3). Considering the sample size is an order of magnitude less, this shows the single shot and blank correction protocol outlined here has considerable merit. Although the system blank isotopic compositions are inferred, they are consistent with the smallest/lightest measured pre-fluorination blanks and display remarkably consistent results between individual trays across three sessions providing good confidence that it is mitigating the effect of the system blank effectively.

Table 3.7 - The amount and isotopic compositions of the analytical blank for each small sample campaign. Campaign 1 & 2 used the same composition as the same batch of BrF_5 was used for both. Campaign 3 used a different batch of BrF_5 and was undertaken 6 months later and a slightly different composition works in favour of stabilising the reproducibility.

	µg O_2	**$\delta^{17}O$ (‰)**	**$\delta^{18}O$ (‰)**
Campaign 1	**2.4**	-5.2	-10.0
Campaign 2			
Campaign 3	**2.4**	-4.7	-9.0

Table 3.8 – Uncorrected and corrected obsidian measurements

	Small obsidians					
	Uncorrected			*Corrected*		
µg O_2	**$\delta^{17}O$ (‰)**	**$\delta^{18}O$ (‰)**	**$\Delta^{17}O$ (‰)**	**$\delta^{17}O$ (‰)**	**$\delta^{18}O$ (‰)**	**$\Delta^{17}O$ (‰)**
64	3.42	6.57	0.01	3.76	7.21	0.01
74	3.46	6.69	-0.02	3.75	7.25	-0.02
96	3.52	6.85	-0.05	3.74	7.28	-0.05
61	3.43	6.57	0.01	3.79	7.25	0.01
62	3.51	6.76	0.00	3.87	7.44	0.00
67	3.44	6.60	0.00	3.75	7.21	0.00
72	3.57	6.82	0.03	3.87	7.39	0.03
60	3.40	6.54	0.00	3.76	7.22	0.00
85	3.49	6.79	-0.04	3.75	7.28	-0.04
45	3.36	6.49	-0.02	3.81	7.36	-0.02
82	3.57	6.89	-0.01	3.83	7.37	-0.01
58	3.54	6.81	0.00	3.90	7.49	0.01
94	3.53	6.78	0.00	3.74	7.19	0.00
50	3.31	6.34	0.02	3.72	7.12	0.02
57	3.42	6.60	-0.01	3.78	7.28	-0.01
62	3.42	6.61	-0.02	3.75	7.24	-0.02
51	3.35	6.49	-0.02	3.75	7.25	-0.02
54	3.47	6.71	-0.02	3.85	7.44	-0.02
65	3.42	6.56	0.01	3.73	7.15	0.01
41	3.37	6.50	-0.01	3.88	7.46	-0.01
50	3.37	6.54	-0.04	3.77	7.32	-0.04
73	3.45	6.68	-0.02	3.73	7.22	-0.02
77	3.54	6.87	-0.03	3.81	7.38	-0.03
Average	3.45	6.65	-0.01	3.79	7.30	-0.01
2σ	0.15	0.29	0.04	0.11	0.20	0.04

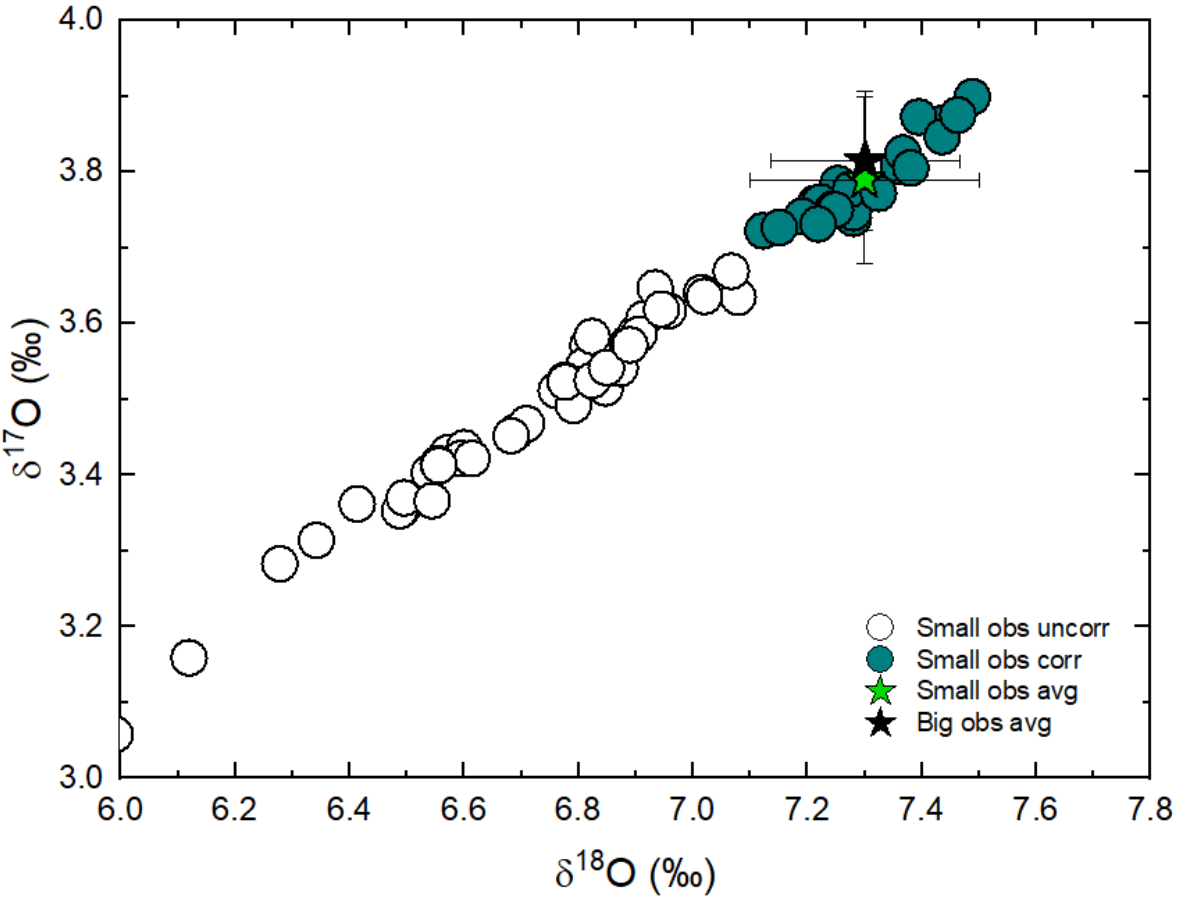

Figure 3.10 – A 3-isotope plot demonstrating the effectiveness of the blank correction upon small obsidian measurements. The uncorrected measurements define a large spread towards lighter values, whereas the corrected measurements cluster around the big obsidian (~2 mg) average. The reproducibility of both approaches are nearly comparable, with the small obsidian average defining a slightly larger spread.

3.2 Blank or mass fractionation?

It is important to know if the effect of the blank is purely a contamination effect, or if mass-fractionation is also playing a role. McDermott (2013) suggested the BrF_5 may have a fractionating effect upon the sample gas through the formation of BrF_5 clathrates on Trap 2. To determine whether the isotopic shift to ^{16}O-rich compositions is caused by a blank effect or by mass fractionation, a sample of known, and extreme $\Delta^{17}O$ can be used. Eagle Station is a pallasite with a $\Delta^{17}O$ of ~ -5 ‰. As all blanks would be composed of sources close to the terrestrial fractionation line ($\Delta^{17}O$ = 0 ‰), we would expect the $\Delta^{17}O$ of small Eagle Station samples to be pulled towards the TFL if a blank effect is predominant. Alternatively, if mass fractionation is the cause, the $\Delta^{17}O$ should stay consistent, but $\delta^{17}O$ and $\delta^{18}O$ would

change. Four, 120 μg, acid washed samples of Eagle Station were loaded in a single tray and ran one after the other. The blank correction procedure is the same as that outlined above for the small obsidians, with compositions used from Campaign 1 and 2. The results show that the issue is predominantly blank related as the $\Delta^{17}O$ is pulled towards the TFL (Table 3.9, Fig 3.11) and not as a result of any resolvable mass fractionation. The corrected Eagle Station values have lower 2σ precision compared to the average reproducibility for small obsidian (Fig 3.13). The bulk corrected values still fall within reasonable proximity of 2σ of the small obsidian, but nevertheless still scatter outside this boundary. This indicates that the blank correction procedure is very good for samples close to the TFL but may introduce errors of approximately 0.1 ‰ in $\Delta^{17}O$ for samples that lie far away from the TFL at -5 ‰. By extrapolation, this may indicate an error in the blank correction at the $\Delta^{17}O$ for CM chondrites ($\Delta^{17}O$ -2 to - 3 ‰) of approximately half this value, at 0.05‰. This was not propagated into the uncertainty as more measurements of Eagle station olivine are needed to corroborate this level of correction.

3.3 Reproducibility

Throughout the campaign, the OU internal obsidian standard was used to monitor the quality of the data being generated by the system (Fig 3.12, Appendix A5). The overall precision (2σ, n=81) of the single-shot method, as defined by repeat analyses of regularly sized (~2 mg) obsidian standards over the duration of this project for $\delta^{17}O$ is 0.091 ‰, for $\delta^{18}O$ is 0.166 ‰ and for $\Delta^{17}O$ is 0.023 ‰. For small samples this is slightly lower precision as follows: $\delta^{17}O$ is 0.11 ‰, for $\delta^{18}O$, 0.20 ‰ and for $\Delta^{17}O$, 0.04 ‰ (2σ n=23). Both small and large samples are in excellent agreement with each other. It is noted the small obsidians may be slightly mis-corrected, either through variation in the true blank amount or its composition, resulting in a marginally negative $\Delta^{17}O$ compared to large obsidian, however the error bars between these two averages overlap and the values are essentially identical.

Table 3.9 – Uncorrected and corrected small Eagle Station olivines. Also included are large Eagle Station olivines to provide a bulk composition.

	Small Eagle Station (~100 µg)					
	Uncorrected			*Corrected*		
	$\delta^{17}O$ (‰)	**$\delta^{18}O$ (‰)**	**$\Delta^{17}O$ (‰)**	**$\delta^{17}O$ (‰)**	**$\delta^{18}O$ (‰)**	**$\Delta^{17}O$ (‰)**
	-6.37	-3.36	-4.62	-6.43	-3.03	-4.86
	-6.46	-3.65	-4.56	-6.55	-3.24	-4.86
	-6.57	-3.43	-4.79	-6.64	-3.09	-5.04
	-6.56	-3.31	-4.84	-6.63	-3.00	-5.07
Average	-6.49	-3.44	-4.70	-6.56	-3.09	-4.96
2σ	0.19	0.30	0.26	0.20	0.21	0.23
	Large Eagle station (~2 mg)					
	-6.55	-2.99	-5.00			
	-6.49	-2.93	-4.97			
	-6.55	-3.05	-4.97			
Average	-6.53	-2.99	-4.98			
2σ	0.07	0.12	0.04			

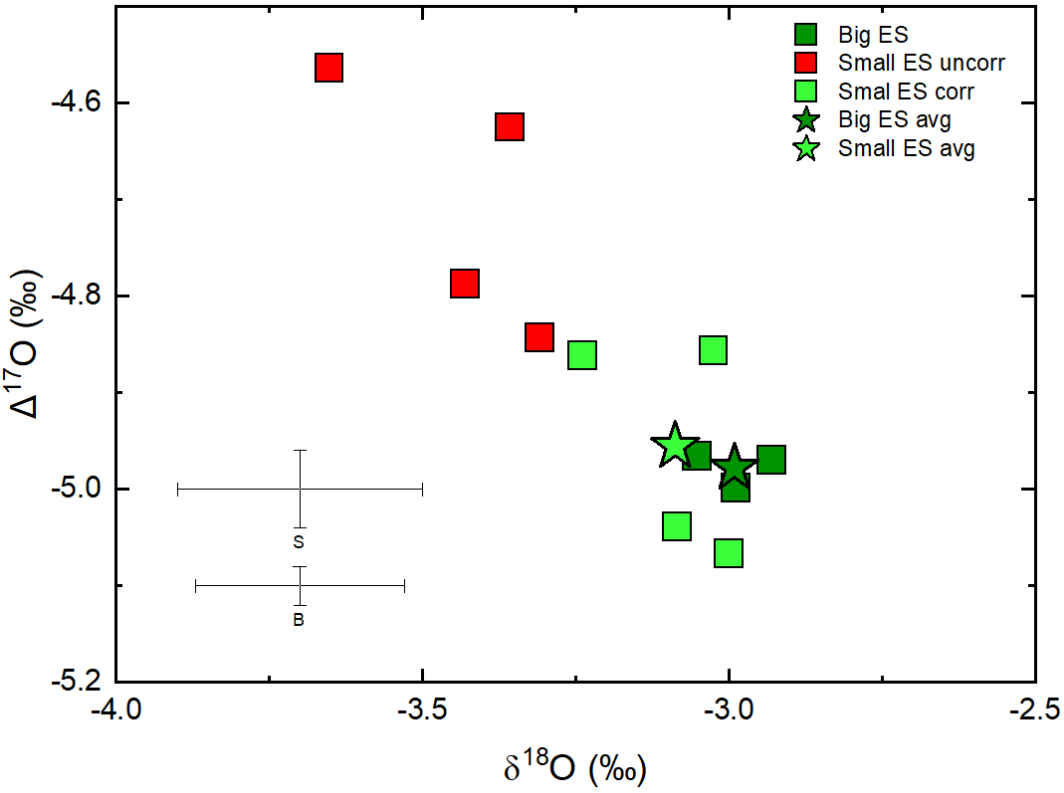

Figure 3.11 - The influence of the blank on the $\Delta^{17}O$ composition of Eagle Station. Uncorrected values fall well outside 2 standard deviations of high precision samples, shown by 'S', the uncertainty defined by small, corrected obsidian standard replicates confirming that the isotopic lightening is indeed a blank issue of terrestrial nature. Also of note is the isotopic shift of $\delta^{18}O$ still prevails even on a sample with negative isotopic composition, like Eagle Station, which provides a lower limit to the potential composition of the assumed analytical blank. The two error bars shown are the long-term reproducibility defined by large ~2 mg obsidian standards (B) and small, corrected obsidian standards (S).

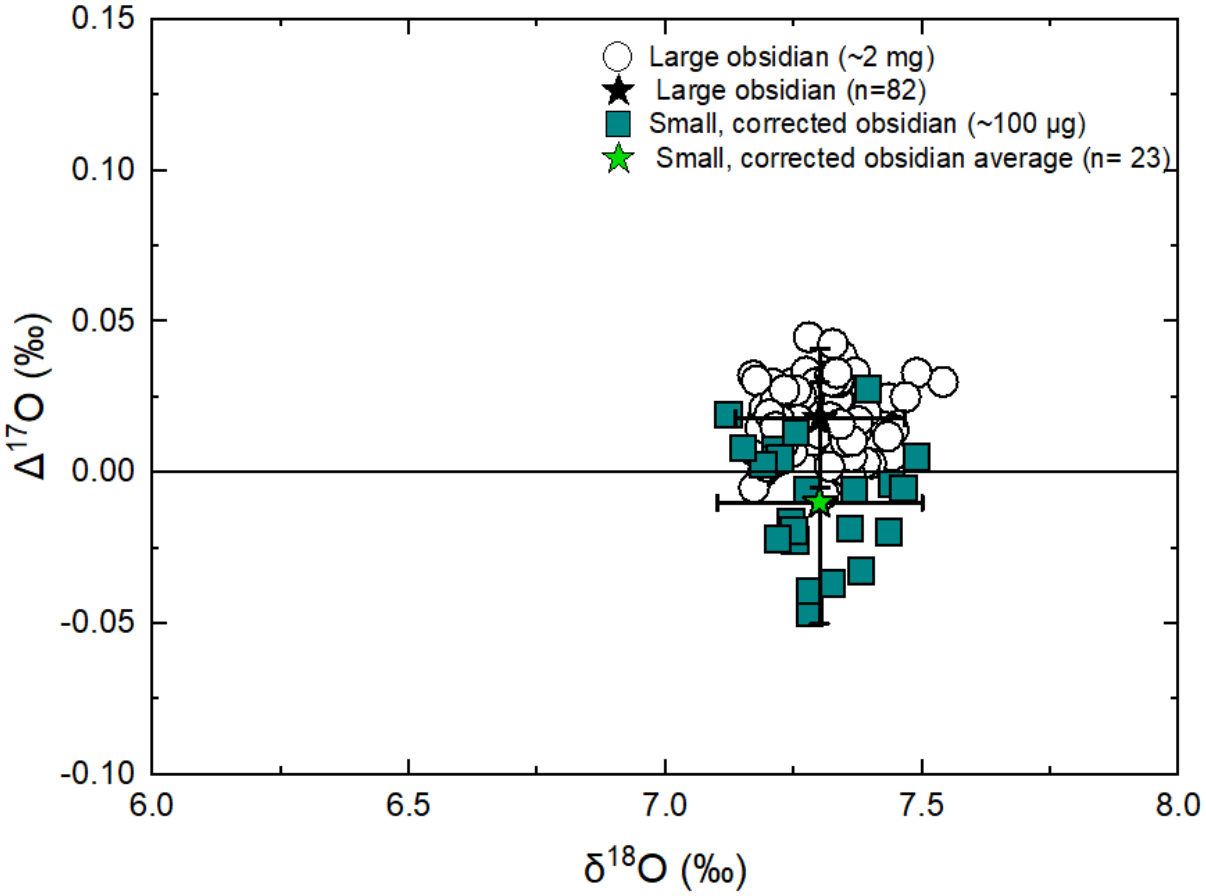

Figure 3.12 – The reproducibility of the single shot method as defined by large, repeat analyses of the obsidian standard, and repeat, small, corrected analyses of the obsidian standard. Both are in good agreement, with good overlap between the averages and their associated 2σ uncertainty.

3.4 Final comments on the modified single shot procedure

This chapter outlines several problems associated with the single shot procedure and its application for small CM samples. Several solutions are proposed to counter the effects of pre-reaction, sample ejection, NF_3 contamination and system blank contribution, and were applied to the analyses of samples of CM material studied in this thesis. The procedure is summarised here:

1) A single CM is loaded into a cleaned, pre-fluorinated nickel tray, alongside a large obsidian standard, and 1 or 2 small standards (nominally obsidian). A small BaF_2 window is placed on top of the reactive sample to contain it
2) The flexi line is pre-fluorinated 2-3 times to remove any moisture until a baseline of < 2 µg is reached

3) The chamber is then pre-fluorinated ambiently for 5 minutes, and the isotopic composition of the gas is measured on the microvolume. This is called ‘the pre reaction blank’
4) The small sample is then fluorinated and transferred between two molecular sieves from -130 to -196 ° C to remove the influence of NF_3, then measured on the microvolume
5) The chamber is fluorinated ambiently for 10 minutes, and the amount and isotopic composition of the gas is measured on the microvolume if desired. This is called the ‘post-reaction blank’
6) The small obsidian is fluorinated and measured on the microvolume
7) The additional standard (if loaded) is fluorinated, and measured on the microvolume
8) The large obsidian is fluorinated and measured using the bellows
9) The sample measurement is then post-processed to correct for the effects of the blank, including any residual mass fractionation, until the small obsidian is within acceptable uncertainty. The correction is then extrapolated to the sample.

This technique allows for the analysis of samples of CM2-like material with sample masses down to ~ 200 μg with a precision of ±0.17 ‰ for $\delta^{18}O$ and ±0.023 ‰ for $\Delta^{17}O$, and comparable levels of accuracy.

Chapter 4 - Classification and Petrography of CM Clasts

4.1 Determining petrologic subtype

Petrologic criteria, which are easily obtainable with an SEM if the polish is acceptable, are the simplest way to unravel the level of alteration experienced by a CM chondrite. It is for this reason that the sub-classification approach used herein is inspired by the widely cited, criterion-based Rubin method, to facilitate meaningful comparisons to the literature (Rubin, 2015; Rubin *et al.,* 2007). Details regarding each of the Rubin criteria are outlined in Chapter 1 (1.4.4.2).

4.1.1 Compositional criteria

The salient petrologic features associated with both incipiently (2.7-3.0) and heavily altered (2.1-1.0) CM material provide reliable criteria for classifying such grades of alteration (Rubin, 2015; Rubin *et al.,* 2007). However, these become somewhat mixed in the intermediate stages (2.6-2.2) (Rubin *et al.,* 2007). For this reason, compositional data from key phases are useful in identifying transitional stages between these two end member scenarios (Rubin, 2015).

Tochilinite-Cronstedtite Intergrowths (TCIs), formerly Poorly Characterised Phases (PCPs) are exclusive to CM lithologies (Suttle *et al.,* 2021) and the composition of these phases has become a conventional metric for moderate alteration (2.6-2.2) (*e.g.,* Lentfort *et al.,* 2021; Rubin, 2015; Suttle *et al.,* 2023). This has mostly been directed at type II TCIs (Chapter 1, section 1.4), which are radially replaced products after grains of olivine, pyroxene and carbonate. While the origins, precursors and alteration mechanisms of these phases have been, and are currently being investigated by numerous laboratories (Mackinnon and Zolensky, 1984; Nakamura and Nakamuta, 1996; Pignatelli *et al.,* 2017; Pignatelli *et al.,* 2016; Tomeoka and Buseck, 1985; Vacher *et al.,* 2020; Zolensky and Mackinnon, 1986) it was Rubin *et al.,* (2007) that initially observed that TCIs in the more altered CM chondrites tend towards higher concentrations of Mg and Si and lower concentration of Fe and S . Both the ‘FeO’/SiO_2 and S/SiO_2 compositions show statistically significant positive correlations

with increasing subtype (Rubin *et al.,* 2007; Lentfort *et al.,* 2021; Suttle *et al.,* 2023). Similarly, the matrix of CM chondrites, whether it be present interstitial to the coarse phases, or as mantles surrounding them, becomes consistently Mg-rich and S-poor with increasing alteration (Browning *et al.,* 1991; Bunch and Chang, 1980; McSween Jr, 1979; McSween Jr, 1987; Zolensky *et al.,* 1993; Zolensky *et al.,* 1997). Both observations can be coupled to the broad-scale mobilisation of Fe and S through the dissolution of Fe-Ni metal, troilite, amorphous matrix and mesostasis, through to the later dissolution of Mg-rich mafics as alteration proceeds (Suttle *et al.,* 2021 and references therein). Rubin *et al.,* (2007) proposed thresholds for the 'FeO'/SiO_2 and S/SiO_2 composition of TCIs and later the MgO/'FeO' and S/SiO_2 of matrix (Rubin *et al.,* 2015), for subtypes 2.6-2.0, albeit with ample overlap between each, subsequently extended to 2.7-2.0 upon analysis of the Paris meteorite (Rubin, 2015).

Following the two initial publications, two further modifications were suggested. First, Kimura *et al.* (2020) analysed the mildly altered Asuka CMs and proposed criteria for subtypes 2.8, 2.9 and 3.0, though no TCIs were present in any of their samples so the aforementioned compositional data is lacking. Later, Lentfort *et al.* (2021) put sole emphasis on the 'FeO'/SiO_2 composition of TCIs, expanding the compositional range to 2.9 with stricter thresholds than Rubin *et al.* (2007), removing overlap between subtypes, but did not include other criteria as essential. In light of the data in this thesis, Kimura *et al.* (2020) certainly analysed CM3.0 – CM2.9 material, though whether this is as low as 2.8 as they propose is debatable due the apparent absence of any early generation TCI in their CM2.8, as observed in other meteorites like Paris (Hewins *et al.,* 2014; Marrocchi *et al.,* 2014). More likely is that all three have alteration indices between 2.9-3.0. It appears both Kimura *et al.,* (2020) and Lentfort *et al.* (2021) disagree on what constitutes highly altered material, for example CM2.9, as investigation of the BSE maps in both publications show different structures with Lentfort's CM2.9s having clear TCI and phyllosilicate clumps. It is possible

that Lentfort *et al.* (2021), while analysing an impressive 75 lithic clasts across 22 meteorites, perhaps did not discover any truly incipiently altered lithologies, and in an effort to extend the gauge to CM2.9 lead to an artificial stretching of the scale. In agreement, Suttle *et al.* (2023) analysed 8 lithologies within the Winchcombe meteorite and found the criteria suggested by Lentfort *et al.* (2021) would have resulted in artificially inflated subtypes relative to the true level of alteration.

How to classify fully altered material remains a moot point. The most recent published work attempting to subdivide type 1 material (to same level of detail as that in CM2s) have been undertaken at the Natural History Museum, London (Bates *et al.,* 2020; King *et al.,* 2019; King *et al.,* 2017; Russell *et al.,* 2022). These studies are influenced by alternative classification approaches (Alexander *et al.,* 2013; Howard *et al.,* 2015; King *et al.,* 2017) that support an alteration index between 1.0-3.0 using different metrics to the Rubin method. As these schemes are based on bulk techniques it would be a necessity that petrographic context is established before analysis, in part due to the lack of petrographic study so far and the scarcity of C1 material (Russell *et al.,* 2022). Even so, many petrologic criteria used to subdivide CM2 material become obsolete when considering the most altered CM chondrites. For example, TCIs rarely exist in such material (*e.g.,* King *et al.,* 2017; Rubin *et al.,* 2007; Suttle *et al.,* 2023), so the composition parameter of this phase cannot be used. In addition, features may imply the existence of a pre-existing phase without explicitly being that phase, *e.g.,* the occurrence or absence of chondrule pseudomorphs (King *et al.,* 2017). The Rubin scale accommodates this level of aqueous alteration as CM2.0, at odds with the official Meteoritical Bulletin (MetBul) (*e.g.,* Gattacceca *et al.,* 2022) which has yet to agree on a formal subclassification nomenclature for CMs. Instead, the MetBul opts for the 'CM1' designation, largely on the two sole criteria of CM-like oxygen isotope compositions partnered with the observation of 'complete secondary replacement'; however, again, these meteorites are rarely petrographically examined; consequently, the descriptions of the 54 (as

of 2023) CM1s or CM1/2s within the MetBul vary in their content and petrographic details, but suggest more complex variations in mineralogy than perhaps first considered (Gattacceca *et al.,* 2022). To further muddy the waters, CM1/2 meteorites such as Kolang are classified based on transitional characteristics, namely small quantities of anhydrous precursors at a quantity transitionary between CM2s and CM1s. This by requirement places them as a 2.1 on the Rubin scale and so the CM1/2 petrographic designation could be considered obsolete.

4.1.2 Approach

The criteria used to classify the lithologies in this work are presented in Table 4.1. The thresholds for the 'FeO'/SiO_2 and S/SiO_2 composition of TCIs; and the Mg# and S/SiO_2 of matrix remain faithful to Rubin *et al*. (2007) but have been modified in light of the data in this work (the Mg number ((Mg/Mg + Fe)*100) [at %] of phyllosilicates was favoured by Suttle *et al.* (2023) instead of MgO/'FeO', so the same approach is used here for comparison). In addition, new thresholds for the 'FeO'/SiO_2 of fine-grained matrix are added as they appear to be a useful classification metric (see section 4.7.2). These modifications aim to provide enhanced precision over Rubin (2015) and be more inclusive than Lentfort *et al.* (2021). This naturally requires some overlap of compositional thresholds and extension to higher and lower values. Approximately equal weighting is given to each of the Rubin criteria to establish an alteration grade (Suttle *et al.,* 2023), in contrast to Lentfort *et al*. (2021) who only use TCI composition. I agree with the comments of Suttle *et al*. (2023) that TCI shape, composition and indeed, abundance, can vary considerably from meteorite to meteorite.

Incipiently to heavily altered, chondrule-bearing material will be classified CM3.0-CM2.1, as is the favoured paradigm (Rubin *et al.,* 2007). While the Rubin subtype of 2.0 is, by design, applicable to any fully altered CM material, the author chose to use CM1, again to ease comparison with published work. In the absence of an exhaustive assessment of fine-grained clasts, it was decided to add an additional designation of 'm' *e.g.,* CM1**m**; which

implies a phyllosilicate mineralogy dominated by a modal area of >80 % fine grained matrix, congruent with the matrix content of CI1-like material such as Ryugu (Greenwood *et al.,* 2022; Ito *et al.,* 2022; Nakamura *et al.,* 2022), Orgueil or fine-grained clasts observed in other meteorites (*e.g.,* Greenwood *et al.,* 1994; Patzek *et al.,* 2018; Patzek *et al.,* 2020; Russell *et al.,* 2022). It must be noted that this 'm' designation is not limited to CM1 material or any aqueous alteration state and can be extended to include moderately – incipiently altered CM2 material if it fulfils the matrix requirement. This allows more unusual CM materials to be included within the index as opposed to being rejected on the grounds of being exogenous or anomalous xenoliths (*e.g.,* as in Lentfort *et al.,* 2021 supplementary information). The CM1/2 subclassification will not be used except when reporting literature data.

There is a considerable 'ambiguity region', as denoted by the grey box in Table 4.1, where the differences between subtypes 2.6 to 2.4 are determined by a restricted range in compositional TCI and matrix data. Therefore, the Rubin-inspired classification only serves as a partial guide; indeed, many CM lithologies fulfil criteria spanning multiple subtypes. It is appropriate that a lithology should ideally satisfy the essential criteria of mesostasis alteration, phenocryst alteration and matrix phyllosilicate abundance appropriate for that subtype (red text in Table 4.1), because it is these criteria that best represent irrefutable interaction with water. The compositional thresholds for anhydrous silicate alteration have been extended from subtypes 1.0, 2.1-2.3 (Rubin, 2015) to include the higher subtypes of 2.4, 2.5 and 2.6. Subtle alteration of phenocrysts is frequently observed in such material, albeit heterogeneously, and should be considered to avoid dumping of lithologies into the <2.3 subgroups. In addition to these essential criteria, a preferable requirement of three or more diagnostic compositional criteria within the chosen column are also desired (Table 4.1). If a CM spans criteria from different subtype(s) in an equal fashion, for example, it contains highly altered phenocrysts, but no phyllosilicates in the matrix, this should prompt

the classifier to consider if the lithology is anomalous, as such a diversity in characteristics renders the lithology essentially unclassifiable (in confidence) by current means. Each meteorite will be presented in the order of their year of fall: Mukundpura (2017), Aguas Zarcas (2019), Kolang (2020), Winchcombe (2021), followed by the Antarctic find, LON 94101, with their respective lithologies listed, as best as can be assessed, from least altered to most altered, although in some cases the differences are not sufficient to provide definite ordering. For each polished block, a navigation pane containing an overarching BSE image will prompt where the lithologies are located for context. Then, the lithologies will be briefly described alongside a higher-mag plate consisting of a BSE image and complementary EDS map with regions of interest (ROIs). Quantitative geochemical data will be listed underneath as part of the plate and summarised in the latter part of this Chapter. The naming convention for the samples is in the form X-Y-Z. Where:

X = an abbreviation of the official meteorite name: Aguas Zarcas = AZ; Mukundpura = MP; Kolang = KO; Winchcombe = WC; LON 94101 = LON.

Y = a number representing a specific polished block

Z= A letter from A-Z representing a lithology

E.g., AZ-01-A refers to Aguas Zarcas, polished block 1, lithology A. Only relevant blocks are listed. As there are many lithologies, any blocks with replicate clasts are excluded from specific mention. Only 'primary accretionary rocks', *i.e.,* discrete lithologies with no evidence of regolith processing are presented as they represent individual environments of accretion and alteration (Bischoff *et al.,* 2006; Metzler *et al.,* 1992). Highly disturbed 'cataclastic matrix' (Bischoff *et al.,* 2006; Metzler *et al.,* 1992; Suttle *et al.,* 2023), consisting of brecciated clast, chondrule fragments, and disturbed regolith, is discussed only briefly as the reprocessed nature of this material, while interesting, reflects complex post-alteration impact gardening (*e.g.,* Michel and Richardson, 2013) and is beyond the scope of examination for the purposes of this thesis.

Table 4.1 – Rubin inspired criteria for chondrule-bearing CM lithology classification.

CHONDRULES, MATRIX AND MINOR MINERALS											
If combined TCI and chondrule abundance < 20 % apply suffix 'm' to indicate 'matrix-dominated'											
Subtype	**CM3.0**	**CM2.9**	**CM2.8**	**CM2.7**	**CM2.6**	**CM2.5**	**CM2.4**	**CM2.3**	**CM2.2**	**CM2.1**	**CM1**
Mesostasis in chondrules	Glass > phyl.	Glass = phyl.	Phyl > glass	Phyl	Phyl	Phyl	Phyl	Phyl	Phyl	Phyl	Phyl
Alteration of phenocrysts[&]	Unaltered	Unaltered	Unaltered	Unaltered	0-5 % altered	0-5 % altered	0-5 % altered	5-15 % altered	15-85% altered	85 – 99% altered	99-100 % altered
Matrix phyllosilicate[&]	Rare / absent	Rare	Minor	Abundant	Abundant	Abundant	Abundant	Abundant	Abundant	Abundant	Abundant
Matrix Mg# [&]	30-40	40-50	45-55	45-55	55-60	55-60	60-65	60-65	60-65	65-75	>65
Matrix 'FeO'/SiO_2[&]	>1.0	>1.0	0.9-1.0	0.9-1.0	0.8-0.9	0.8-0.9	0.6-0.8	0.6-0.8	0.6-0.8	0.5-0.6	0.4-0.55
Matrix S/SiO_2[&]	>0.18	0.14-0.18	0.14-0.18	0.14-0.18	0.10-0.18	0.08-0.16	0.07-0.14	0.07-0.12	0.07-0.12	0.05-0.10	<0.05
Fe-Ni metal host	Matrix + chondrules	Matrix + chondrules	chondrules	In mafic phenocrysts	In mafic phenocrysts	In mafic phenocrysts	In mafic phenocrysts	Rare / Absent	Rare / Absent	Absent	Absent
Carbonate[&]	Absent	Absent	Minor	T1 Ca carbonate	T1 Ca carbonate	T1/T2 Ca carbonate	T1/T2 Ca carbonate	T1/T2 Ca carbonate	T1 /T2 Ca/Mg carbonate	T1 / T2 Ca/Mg carbonate	Ca/Mg carbonate
Sulphide	Tro > po + Pn	Tro > po + Pn	Tro > Po + Pn	Po + Pn	Po + Pn > int	Po + Pn > int	Po + Pn + int	Po + Pn + int	Pn + int > Po	Pn + int > Po	Pn + int > Po

Mg# = (Mg/Mg + Fe) * 100 (at %).

If the CM lithology is matrix dominated 'm', most of these criteria are rendered obsolete. Use [&] to assist subclassification.

Po = Pyrrhotite; Pn = Pentlandite; Tr = Troilite. Pn can be present as a product of aqueous alteration, but also as a primary product via the initial sulphidation process in the least altered lithologies (Lauretta *et al.,* 1996) Int = intermediate sulphides (Ni/Fe + Ni) showing solid solution between Po – Pn and are most common in the intermediate CM stages of alteration (Chokai *et al.,* 2004; Rubin *et al.,* 2007).

The grey box delineates a compositional 'ambiguity zone'. The items in red text represent essential criteria, of which a chondrule-rich CM lithology should ideally fulfil all three to be designated a subtype. In addition, three or more additional criteria from each column are preferred. The thresholds for the alteration of chondrule phenocrysts have been expanded from Rubin, (2015) to include 5-15 % alteration for subtype 2.4 and 0-5 % alteration for subtypes 2.5 and 2.6. This was implemented after observing alteration in phenocrysts within clasts that clearly show less alteration. The thresholds for Matrix Mg# and Matrix S/SiO_2 have been modified in light of new data in this thesis combined with that from Lentfort *et al.* (2021) and Suttle *et al.* (2023).

Table 4.1 continued – Thresholds for TCI composition in chondrule-bearing CM lithologies

TOCHILINITE-CRONSTEDTITE INTERGROWTHS (FORMERLY PCP)[#]											
Petrologic subtype	**CM3.0**	**CM2.9**	**CM2.8**	**CM2.7**	**CM2.6**	**CM2.5**	**CM2.4**	**CM2.3**	**CM2.2**	**CM2.1**	**CM1**
BSE Contrast	-	High contrast	High contrast	Moderate contrast	Moderate contrast	Moderate contrast	Moderate contrast	Moderate contrast	Low contrast	Low contrast	Low contrast
Appearance	-	Off-white	Light grey	Light grey	Light grey	Grey	Grey	Grey	Dark grey	Dark grey	Dark grey
Habit	-	Micro- lenses, granular	Micro- lenses, granular	Platy laths of toch + phyl	Needles, phyl core[*]	Needles, phyl core[*]	Fibrous, phyl core[*]	Fibrous, phyl core[*]	Phyl Core thin rim*, mesh	Core and thin rim*, mesh	Incoherent mesh pervasive
TCI type	-	Type I	Type I	Type 1 + Type II	Type II > Type I	Type II > Type I	Type II > Type I	Type II > Type I	Type II	Type II or absent	Type II or absent
TCI 'Feo' / SiO_2	-	>15.0	7.0-15	4.0-7.0	2.6-4.0	2.0-2.6	1.5-2.0	1.5-2.0	1.0-1.7	0-1.7	0-1.7
TCI S/SiO_2	-	>5	3.0-5.0	1.0-3.0	0.6-1.0	0.4-0.6	0.3-0.4	0.2-0.3	0.1-0.3	0.1-0.2	0.1-0.2

Grey box delineates ambiguity zone. The thresholds for TCI 'FeO'/SiO_2 ratio and TCI S/SiO_2 have been modified in light of new data in this thesis combined with that from Lentfort *et al.* (2021) and Suttle *et al.* (2023). TCI appearance and contrast thresholds have been added from Lentfort *et al.* (2021). The addition of TCI habit follows observation of different crystal structures in TCIs from different subtypes.

[#] Each TCI may have multiple zones of differing contrast. For consistency, EDS measurements are taken strictly from the most prevalent Fe- and / or S- rich phyllosilicates exhibiting high contrast, typically laths or fibrous rims. Where TCIs have Mg-serpentine cores, these compositions are also measured but are not counted towards the TCI measurement for classification but are considered within the wider scale interpretations of the data.

[*] While the nature and habit of TCIs follow the stated descriptions *sensu-lato*, in reality these textures can be quite variable and there are many exceptions to the trend. Plates, laths, needles, fibres and meshwork fabrics may present themselves in TCIs at any petrologic subtype, and so these metrics should always be used in tandem with the other criteria to establish an appropriate subtype.

4.2 Mukundpura (2017)

The lithologies described below are sourced from two polished blocks (Fig 4.1 and 4.2)

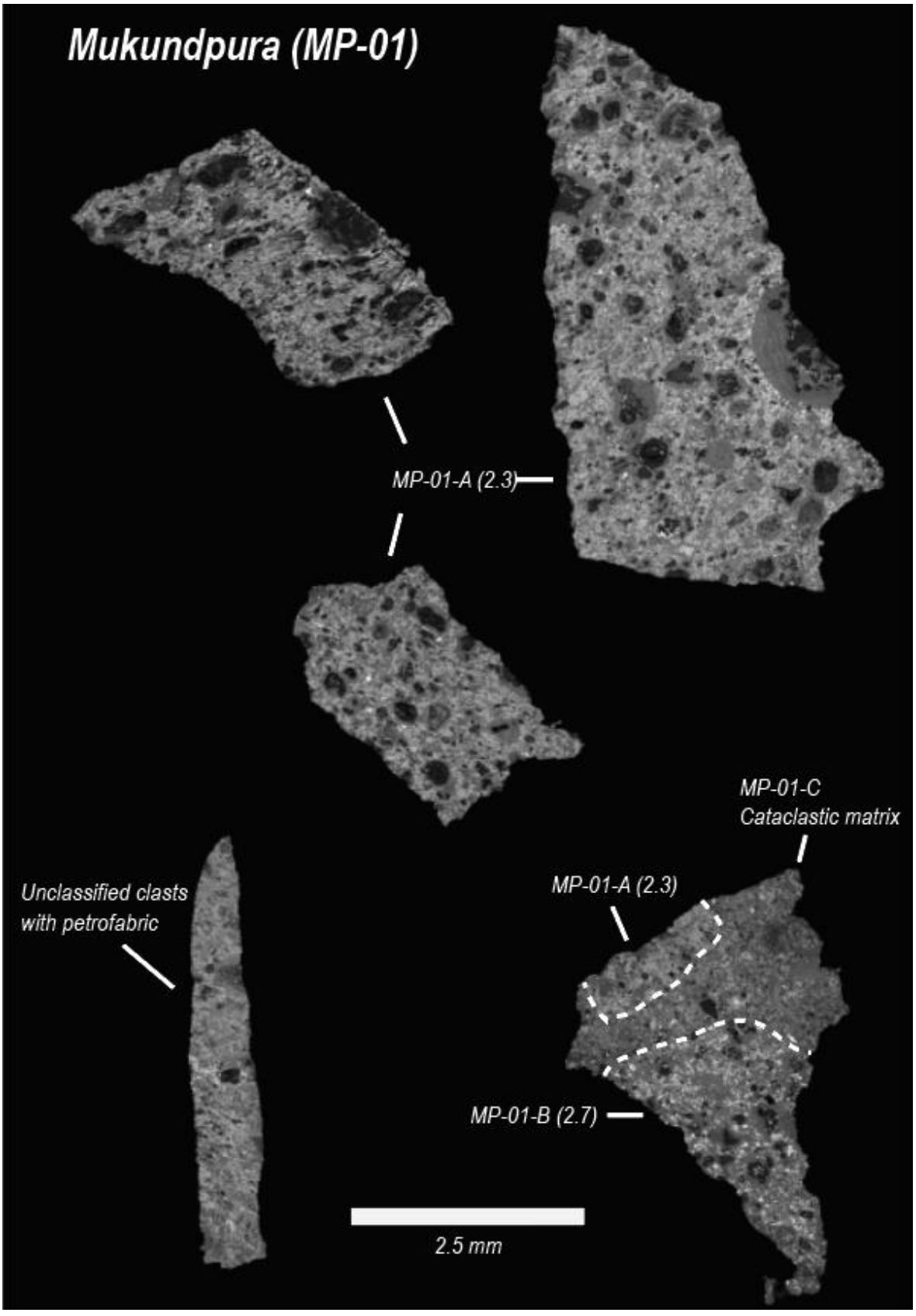

Figure 4.1 - Navigation pane for the polished block MP-01. Five chips are mounted in this section.

4.2.1 MP-01-B

MP-01-B outcrops as 50 % of the surface area of a single chip in the section (Fig. 4.1). Chondrule phenocrysts are unaltered yet mesostasis has been replaced by phyllosilicate and TCI (Plate 4.1, ROI 1). Numerous, pristine chondrule fragments of forsterite and fayalite are embedded alongside whole, mantled chondrules in a low contrast matrix of both accretionary rim and interstitial material. TCIs are widespread with sharp delineated boundaries and show very high contrast. Magnified images of the TCIs reveal three principal components making up their structure – the dominant is high contrast lath-like growths of tochilinite, cronstedtite and sulphide (Plate 4.1, ROI 2), with lower contrast phyllosilicate interstitial. The 'FeO'/SiO_2 composition of the TCI laths and interstitial material are on average very high, but extremely variable with a 2SE uncertainty of 7. Clearly, this this lithology is partially altered due to the high modal abundance of phyllosilicate matrix. Carbonates are uncommon (< 0.5 area %), but where present are calcite. Sulphides are pyrrhotite and pentlandite, no intermediate compositions were identified. Compositional data for the matrix agrees with a 2.7 classification.

4.2.2 MP-01-A

MP-01-A appears in numerous post-rain chips (Fig 4.1). This lithology is TCI dominant with an absence of interstitial fine-grained matrix except for accretionary rim material (Plate 4.2, ROI 1 & 2). The TCIs are moderately sized and heterogeneously distributed (between 50 and 100 μm) and geometric, retaining the crystal habit of their pseudomorphed precursors, appearing heterogeneous with a needle-like habit as alternating high and low contrast domains. The total TCI coverage averages at 46 area % in all occurrences, though in separate chips the TCIs can show similar but subtly different variations in contrast and habit (Plate

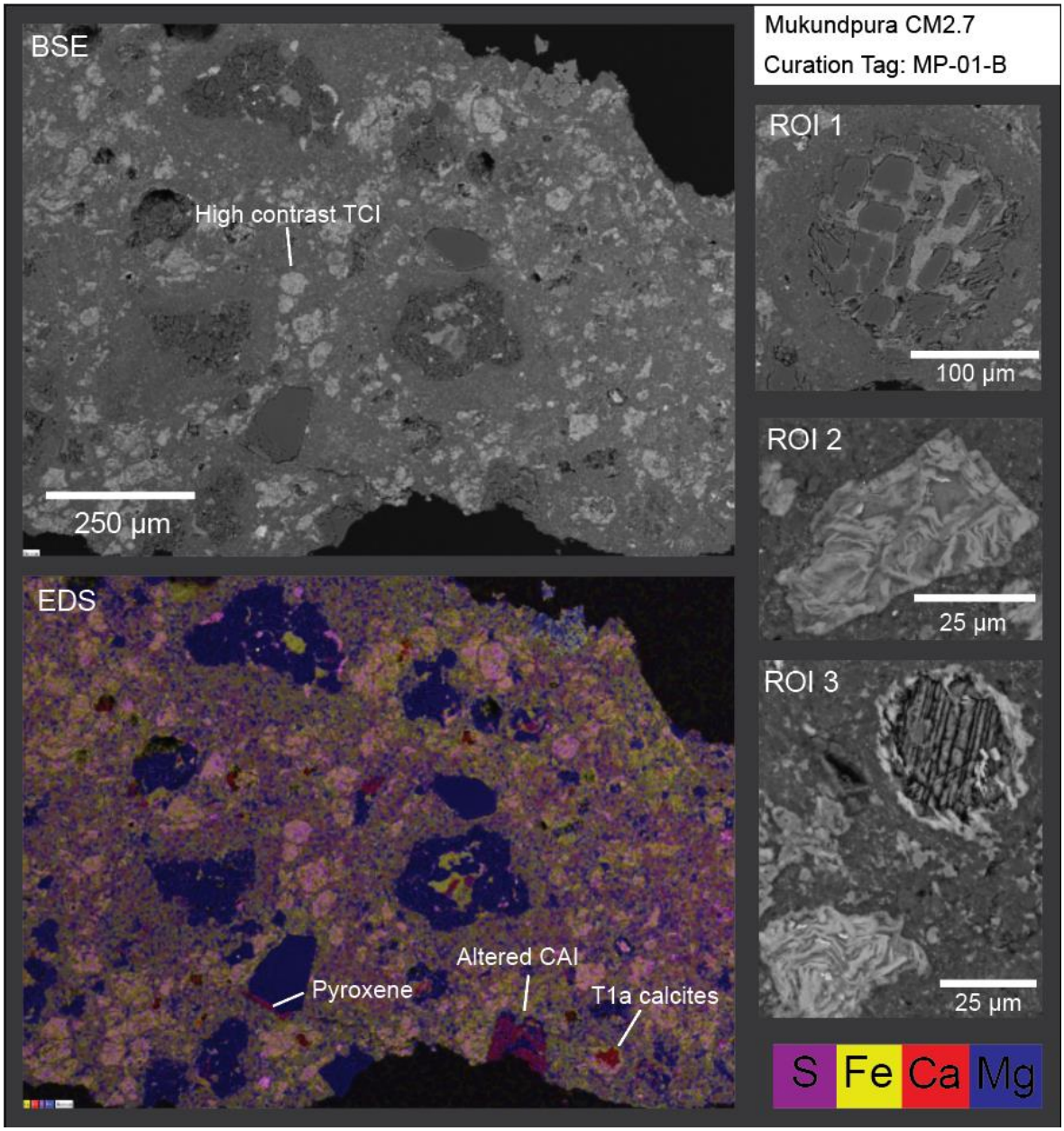

Phyllosilicates	**n**	**Area %**	**'FeO'/ SiO_2**	**S/SiO_2**	**Mg #**	**Totals**
TCI	8	21.16	12.95 ± 7.13	1.79 ± 0.58	21.17 ± 6.58	90.73 ± 5.02
Matrix	9	63.01	0.90 ± 0.08	0.11 ± 0.02	53.35 ± 2.53	74.88 ± 2.59
Accessory minerals		**Area %**	**Form**			
Surviving precursors[#]		14.02	Small chondrules and mafic phenocrysts			
Carbonates		0.33	Sparse T1a			
Sulphides		1.48	Po + Pn			
Chondrules						
Mesostasis	Phyllosilicate					
Phenocryst replacement	Negligible					
Rubin Subtype:	CM2.7					

Plate 4.1 - MP-01-B. Area % = threshold estimates from polished block. [#]Evenly distributed within matrix (*i.e.,* not large chondrules). Totals are EDS oxide wt %. ROI 1 - TCI bearing chondrule; ROI 2 – TCI with platy, lath-like structure; ROI 3; TCI and highly fractured, T1a calcite. Uncertainties are 2SE

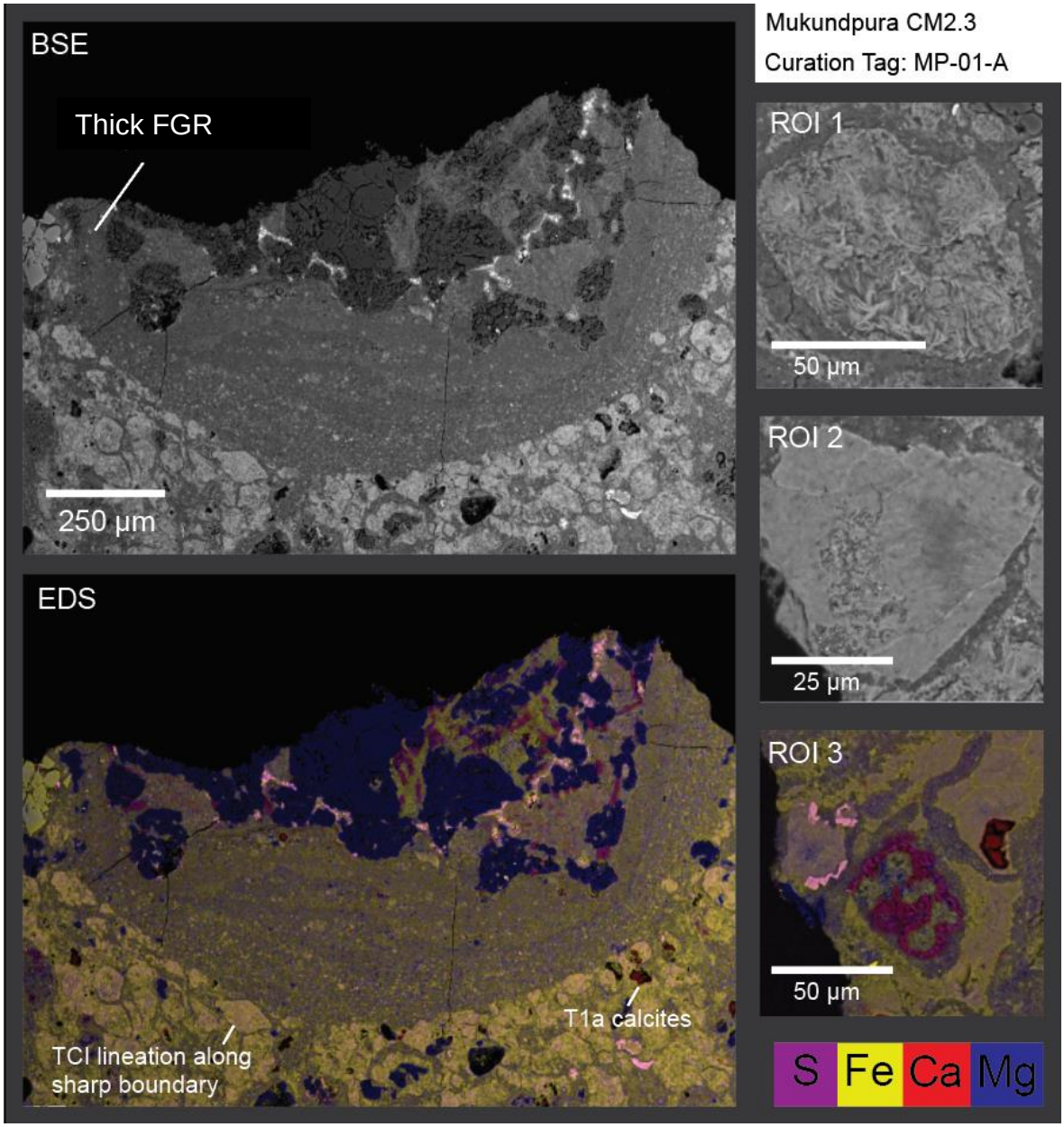

Phyllosilicates	**n**	**Area %**	**'FeO'/ SiO_2**	**S/SiO_2**	**Mg #**	**Totals**
TCI	12	46.56	1.49 ± 0.16	0.32 ± 0.04	46.79 ± 3.83	87.31 ± 0.57
TCI cores	2	47.14	0.73 ± 0.03	0.15 ± 0.03	65.30 ± 0.75	84.17 ± 2.44
Matrix	5		0.77 ± 0.05	0.09 ± 0.1	56.40 ± 2.18	75.41 ± 8.11
Accessory minerals		**Area %**	**Form**			
Surviving precursors[#]		4.11	Fo + Fa fragments			
Carbonates		0.50	Small, T1a			
Sulphides		0.64	Po + Pn + Int			
Chondrules						
Mesostasis	Phyllosilicate					
Phenocryst replacement	Mild – 5-15 %					
Rubin Subtype:	CM2.3					

Plate 4.2 - MP-01-A. Area % = threshold estimates from polished block (void space is not listed). [#]Evenly distributed within matrix (*i.e.*, not large chondrules). Totals are EDS oxide wt %. ROI 1 – TCI with lath texture and rim; ROI 2 – TCI with needle texture and rim; ROI 3 – small, altered CAI with T1a Ca-carbonate and sulphides embedded in TCI. Uncertainties are 2SE.

4.2 ROI 1 & 2), often forming a strong petrofabric. Chondrule accretionary rims are the most prominent observed in this work (Plate 4.2, BSE image), comprising an inner rim of 'welded' appearance with an apparent low porosity, whereas the outer rims constitute a coarser texture of fine-grained matrix and micro-TCI material which is also present as rounded clumps in between chondrules. Each rim surrounds chondrule and chondrule fragments that have been partly altered, with no surviving mesostasis and with 5-15 % aqueous attack of the surviving forsterite crystals. However, occurrences of angular type I and type II chondrule fragments are emplaced within the matrix and exhibit no signs of alteration, despite being juxtaposed next to TCI, indicating alteration conditions were locally heterogeneous (Metzler *et al.*, 1992) and perhaps, anisotropic (Daly *et al.*, 2022). Carbonates are exclusively T1a Ca-carbonates (Lee *et al.*, 2014; Tyra *et al.*, 2007; Tyra *et al.*, 2012; Vacher *et al.*, 2017) in association with TCI. Sulphides are both pyrrhotite of stoichiometric and 'intermediate' Ni/Fe+Ni composition (Chokai *et al.*, 2004); and pentlandite in roughly equal proportions; therefore, in conjunction with the TCI composition this lithology is designated CM2.3.

4.2.3 MP-05-A

MP-05-A is a unique CM lithology and one of the few clasts present at the cm scale (Figs 4.2 and 4.3). Investigation of the Mukundpura pre-rain hand specimen reveal this clast is a featureless, highly fractured inclusion amounting to roughly 20 % of the large, ~8-gram chunk (Figs 4.2 and 4.3), enclosed entirely by the Mukundpura host. It is dominated by total secondary mineral replacement of all primary phases, with pronounced chondrule and chondrule fragment pseudomorphs dictating the petrographic character with a modal surface area of ~75 % (Fig 4.2), exhibiting sharp porphyritic and radial pseudo crystalline habits. In addition, the chondrule pseudomorphs define a pronounced petrofabric. Within and between the chondrule pseudomorphs is a higher contrast, Fe-rich phyllosilicate matrix of homogenous chemical composition (Plate 4.3), more Fe-rich than typical CM interstitial

matrix, but more Fe-poor than typical TCI (Fig 4.4). This material does not petrographically resemble typical TCI morphology as observed in CM2s, in that the majority of occurrences are joined into an interlinked network and lack coherent pseudomorphic shape;

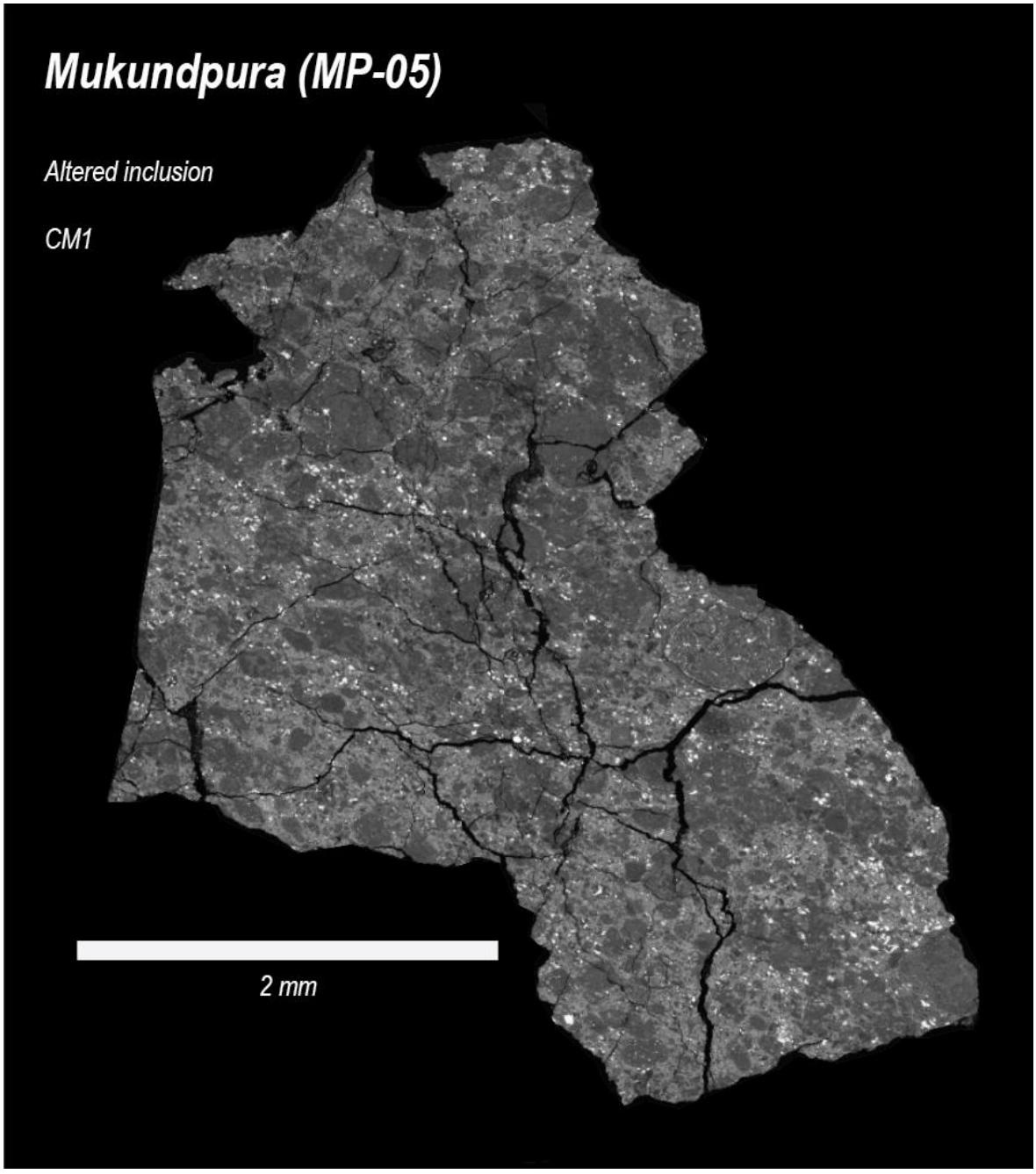

Figure 4.2 – Polished block MP-05. The entire block is one, CM1 lithology (MP-05-A)

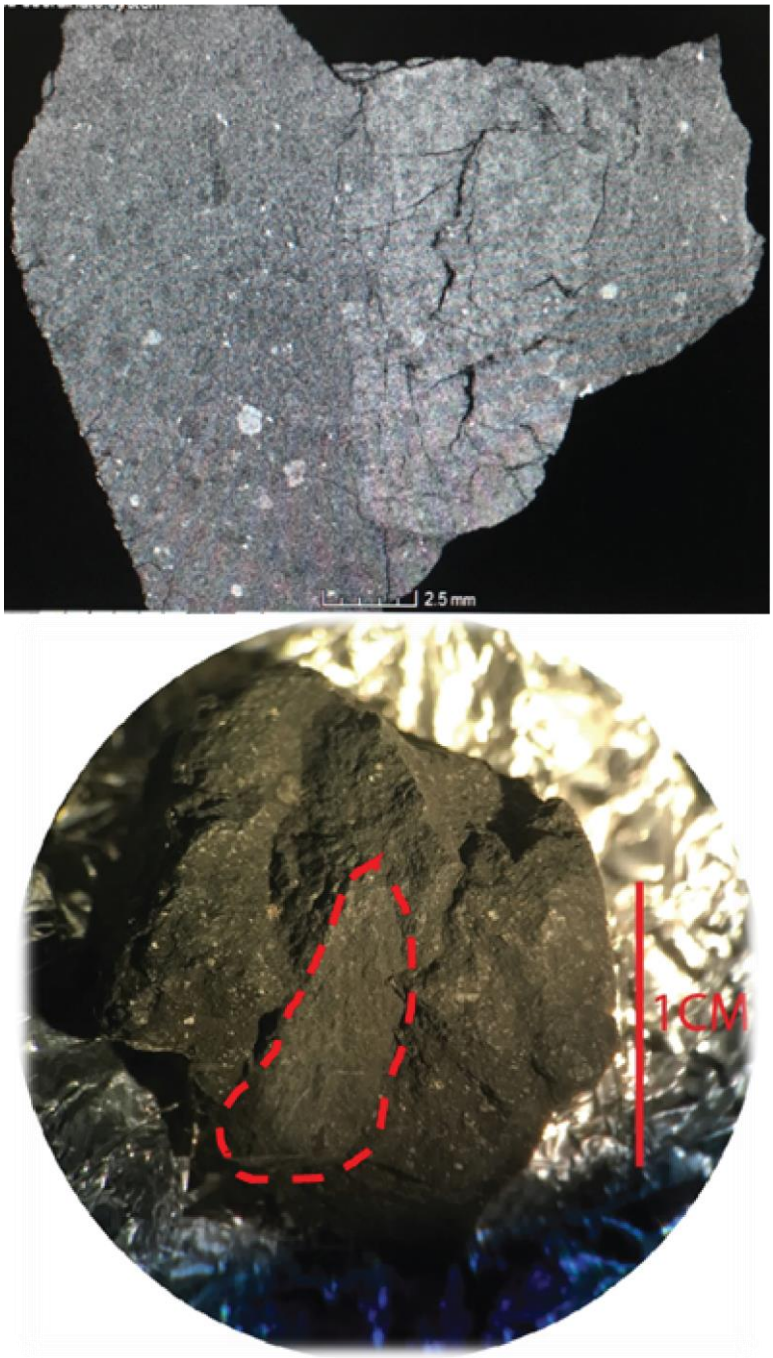

Figure 4.3 – Top: a CT scan of the large, 8 g, inclusion bearing chunk of Mukundpura, courtesy of Dr Sara Russel at the Natural History Museum, London. A cataclastic breccia surrounds a comparatively Fe-rich CM1 inclusion. This inclusion is very large, and therefore the clast is of great scientific interest owed to its potential for coordinated analyses. Bottom: The chunk in hand specimen, the inclusion can be seen as a lighter grey, featureless clast in the centre, outlined in red.

Nevertheless, the chemistry of this phase, specifically the 'FeO' / SiO2 composition is consistent with published TCI compositions from CM1 and CM2.1 lithologies (Rubin, 2015) (Plate 4.3). Accessory phases include pentlandite, 'intermediate' pyrrhotite, magnetite, Ca carbonate and Mg carbonate, plus volumetrically significant occurrences of phosphate

intergrown with sulphide and phyllosilicate. Both dolomite and Ca-carbonate predominantly resemble the T1a and T0 (Vacher *et al.,* 2017) type of carbonate, occurring as monocrystalline grains. Interestingly, accretionary rims surrounding pseudomorphed chondrules are thin or absent.

The texture of this clast is perplexing. The composition of the chondrule pseudomorphs in comparison with the surrounding, Fe-rich material is highly contrasting. Nominally Mg-enrichment of the matrix is expected as alteration progresses, the opposite of what is observed in this material, though the rare 'pockets' of true matrix (either interstitial to the pseudomorphs, or as rims) are indeed significantly Mg-enriched (Fig. 4.4). Chondrule pseudomorphs are all homogenously altered and are compositionally uniform with striking pseudo-phenocryst outlines. If the canonical assumption that the composition of any alteration products is controlled by the altering fluid (Velbel *et al.*, 2012; Velbel *et al.*, 2015), this would suggest extraordinarily different fluid compositions for the Fe-rich material and the matrix + chondrule pseudomorphs. Further evidence for discrete episodes of alteration includes thin bands of phyllosilicate mantling every small pseudomorphic fragment in the order, Fe-rich, Mg-rich, Fe-rich (Plate 4.3, ROI 2), in addition to heterogeneously altered sulphide grains (Plate 4.3, ROI 3). In summary, the extensive pseudomorphic replacement of chondrules, in addition to abundant phosphate and Mg-rich carbonate warrant a CM1 classification.

4.2.4 Mukundpura summary

Mukundpura is dominated by heavily altered ~CM2.3 material except for a very large CM1 clast, MP-05-A, in juxtaposition to cataclastic matrix. This provides strong evidence, though not irrevocably, of a relationship between CM1 and CM2 material and is an indication of the interaction of both within in a single asteroid regolith. The CM1 clast is also rather large (X-ray CT image in figure 4.3), a useful characteristic opening a range of analytical opportunities for further work regarding the CM1-CM2 relationship. The CM2.3 lithology,

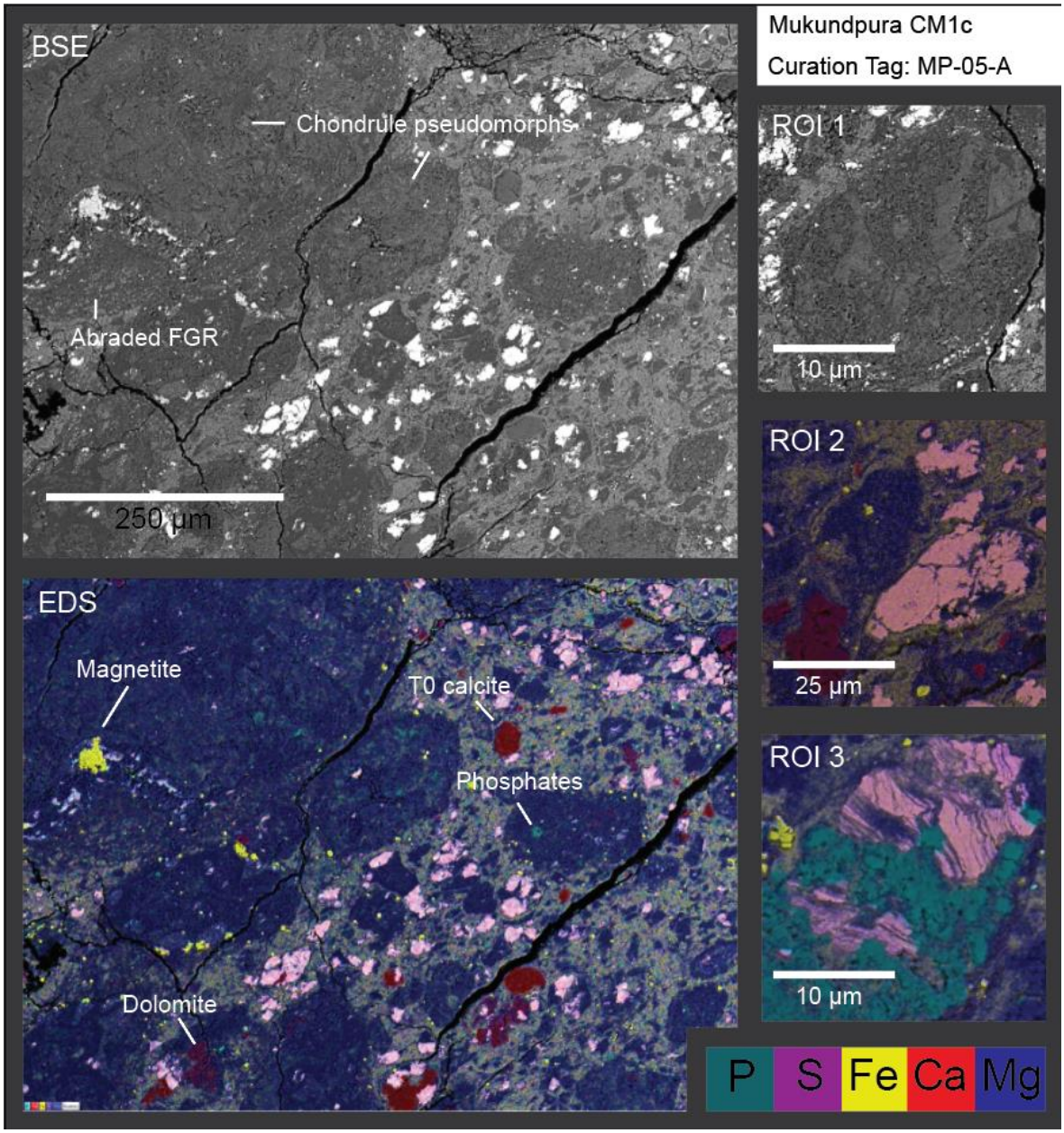

Phyllosilicates	**n**	**Area %**	**'FeO'/ SiO_2**	**S/SiO_2**	**Mg #**	**Totals**
Fe-rich (TCI?)	8	37.75	1.35 ± 0.04	0.13 ± 0.01	43.36 ± 0.85	83.23 ± 0.60
Matrix + Mg phyl	7	49.49	0.53 ± 0.02	0.02 ± 0.02	65.18 ± 4.42	82.09 ± 0.71
Accessory minerals		**Area %**	**Form**			
Phosphate		0.87	Overgrowths of apatite / whitlockite			
Carbonates		2.76	Ca and Mg carbonate, solitary and complex (T0 and T2)			
Sulphides		3.70	Pn + Int			
Magnetite		2.0	Plaquettes			
Chondrules						
Mesostasis	Phyllosilicate					
Phenocryst replacement	100 %					
Rubin Subtype:	CM1					

Plate 4.3 - MP-05-A**.** Area % = threshold estimates from polished block. Totals are EDS oxide wt %. ROI 1 – chondrule pseudomorph with phyllosilicate 'phenocrysts'; ROI 2 – phyllosilicate, dolomite and 'intermediate' sulphide with alternating Mg-Fe-Mg-rich phyllosilicate mantles; ROI 3 – Intermediate sulphide grain replaced by phyllosilicate then phosphate. Uncertainties are 2SE

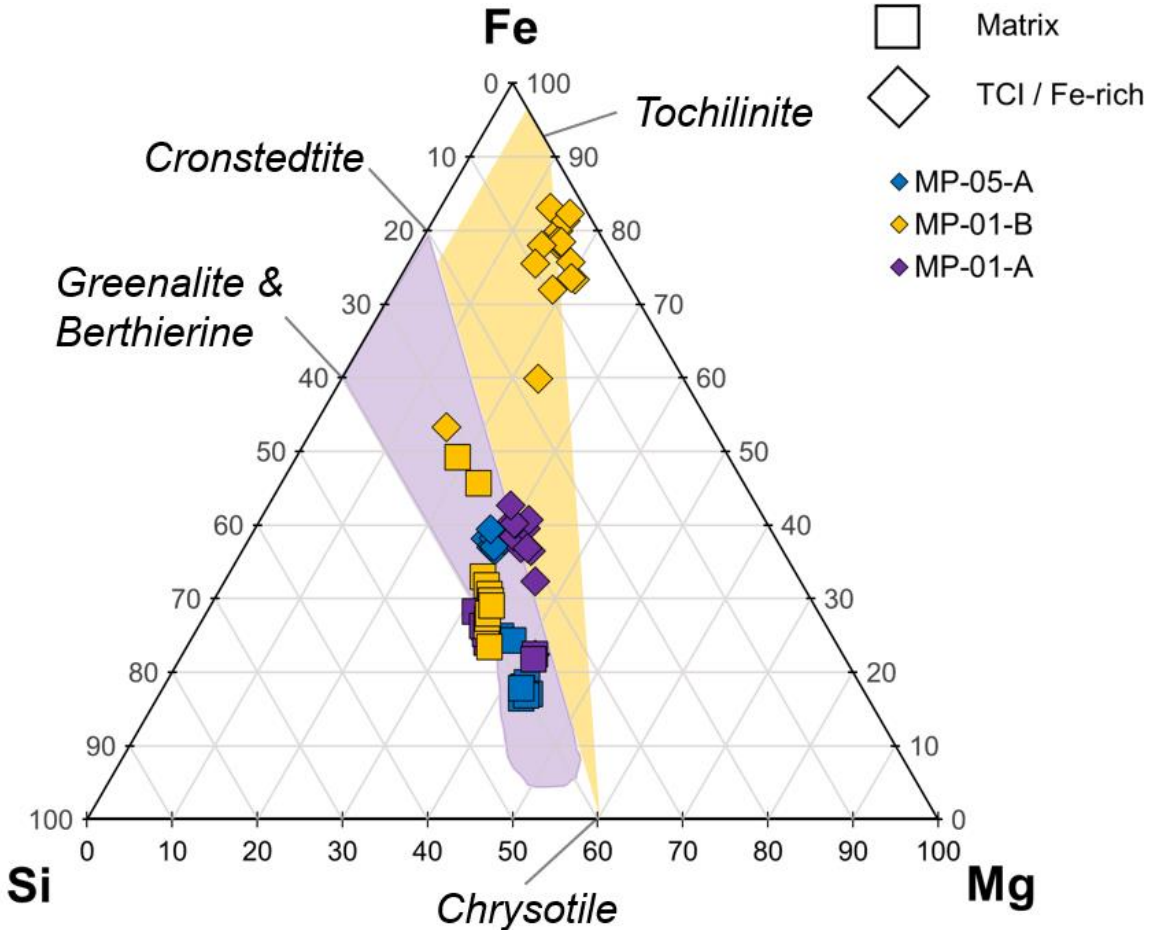

Figure 4.4 - Normalised major element cation ternary diagram for matrix and TCI phases in Mukundpura (at %), with serpentine (purple) and TCI (yellow) fields, heavily modified after Suttle *et al.* (2021), Explanation of the compositional fields are given in Chapter 1, section 1.4.2.2. Of note: TCIs of the incipiently altered lithology, MP-01-B, plot close to the tochilinite endmember but appears to lack cronstedtite, instead intergrown with Mg-serpentine (chrysotile). The 'TCI' phase within both MP-01-B (2.7) and MP-05-A (CM1) are transitional between Mg, Fe and Toch endmembers and appear to contain components from each. Matrix values from all lithologies are consistently at the Mg-rich end of the serpentine field.

MP-01-A preserves an abundance of fine-grained rim and TCI textures, as well as strong petrofabrics, highlighting its suitability as a sample to understand the stages of the CM accretionary process. Inclusion of a 2.7 lithology (MP-01-B) indicates certain localities of the Mukundpura source region had high Fe and S activity, but low levels of alteration, leading to Fe- and S- rich products (TCI and matrix) in-between pristine chondrule phenocrysts. Including literature data (Potin *et al.*, 2020; Ray and Shukla, 2018; Rudraswami *et al.*, 2019) Mukundpura is a fairly typical, heavily altered CM with a petrologic range of 1.0-2.7.

4.3 Aguas Zarcas (2019)

The lithologies described below are from two polished blocks. (Figs 4.6 and 4.6)

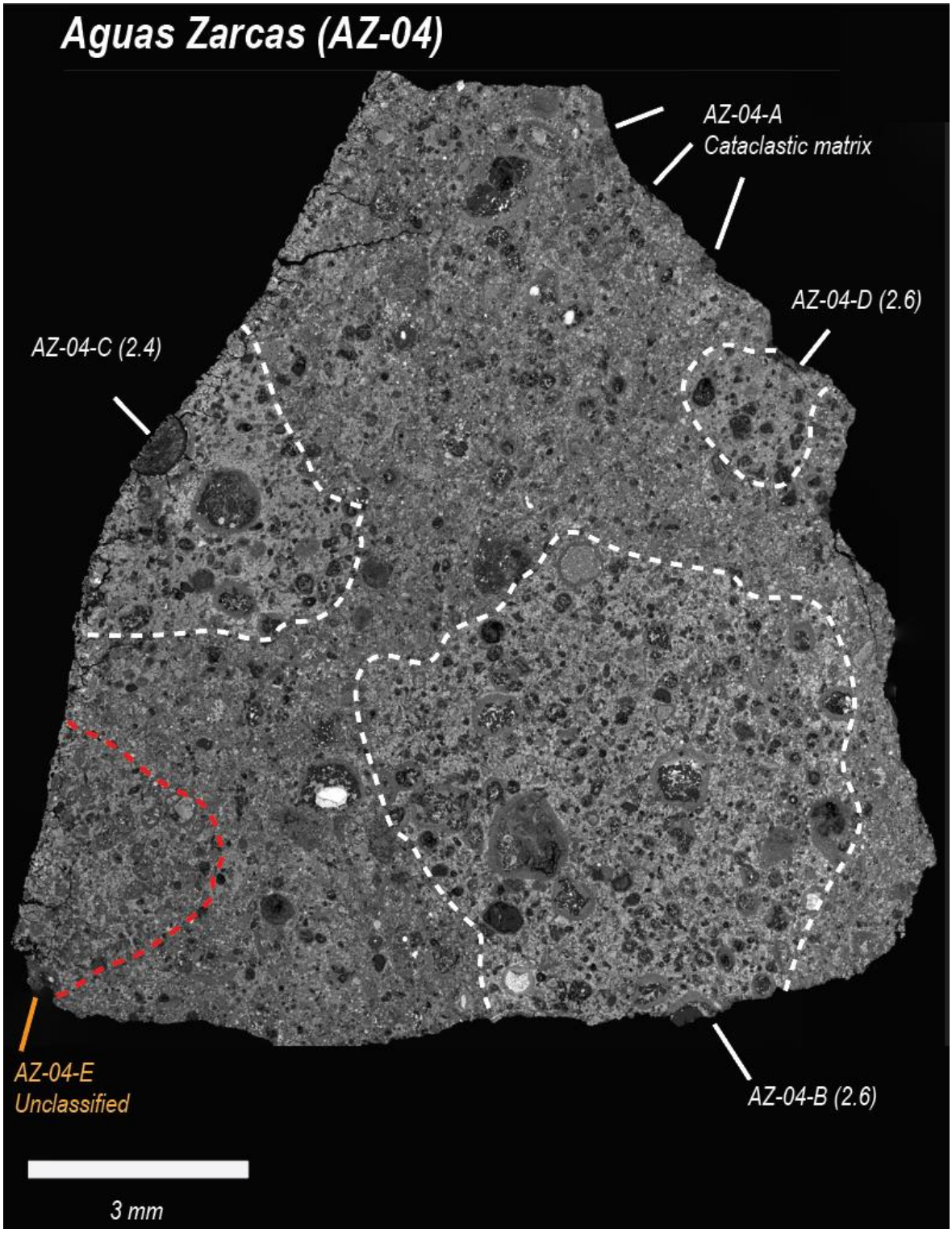

Figure 4.5 – Navigation image for polished block AZ-04

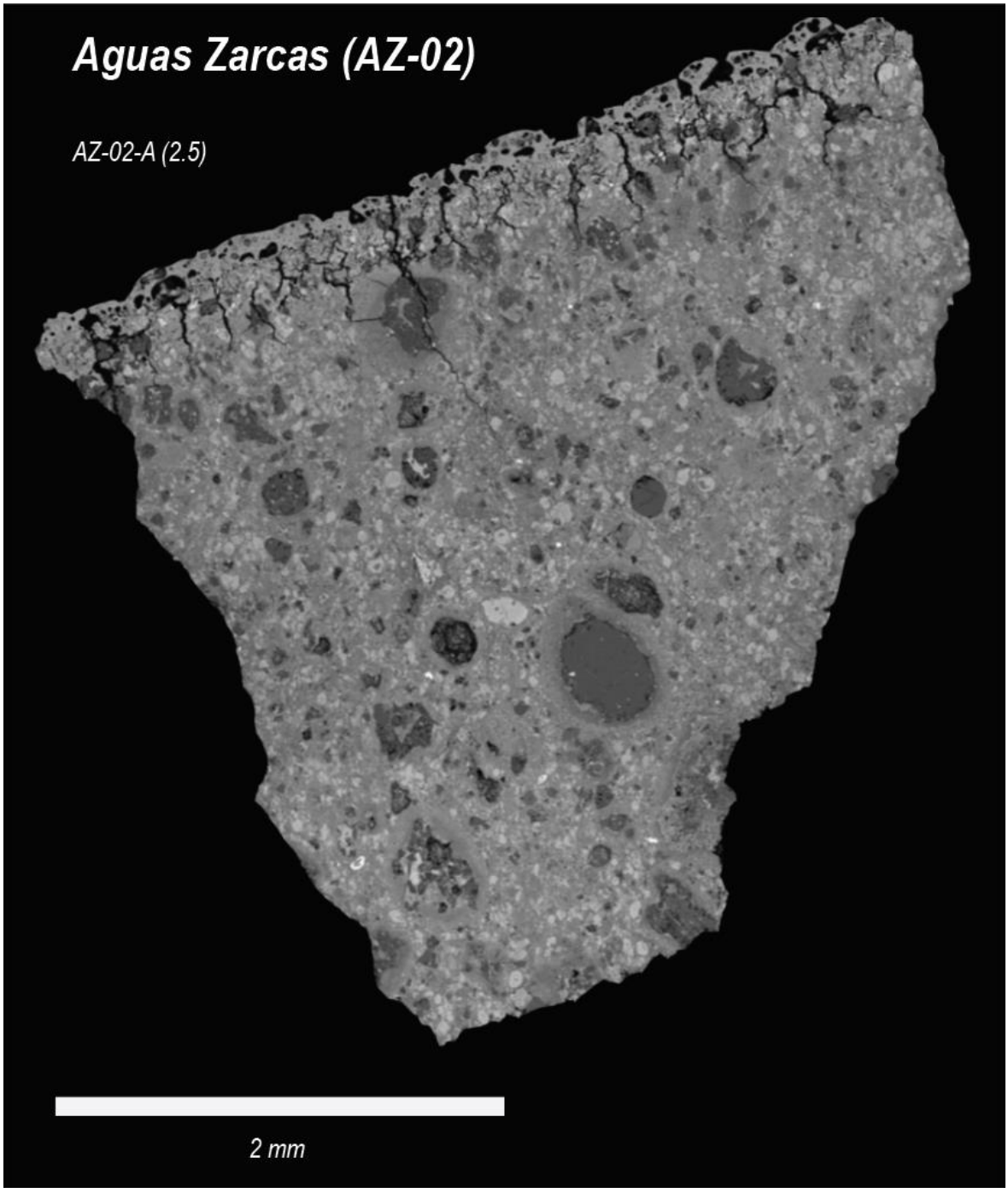

Figure 4.6 - Navigation image for polished block AZ-02

4.3.1 AZ-04-B

A 5 mm wide clast in the longest dimension (Fig 4.5), AZ-04-B is the largest primary accretionary lithology studied in Aguas Zarcas. It is TCI dominant; in fact, the only occurrence of fine-grained matrix is within the accretionary mantles surrounding chondrules — that are weakly altered and often metal-bearing — and the TCIs (Plate 4.4). The TCIs have the highest S/SiO_2 ratio of all Aguas Zarcas lithologies, a characteristic expressed by a

higher brightness-contrast, while the morphology and composition of the TCIs are appreciably heterogeneous with a range of polygonal, smeared and meshwork structures hosting core (phyllosilicate and calcite) and rim structures (Plate 4.4, ROI 1). The phyllosilicate cores are of similar composition to the surrounding matrix. Small chondrules and chondrule fragments are in close association with TCI and accretionary rim material when compared to Mukundpura, Kolang and Winchcombe, rendering it difficult to isolate a suitable domain for micromilling. The population of accreted chondrules and chondrule fragments are quite high, and on close inspection, dominated by smaller particles. Larger chondrules and CAIs, upwards of 200-500 um in width, are also present (Plate 4.4, ROI 2 & 3). Chondrules are commonly fused to one another, adhering via the outer accretionary mantle, which possess two layers as in MP-01-A (Plate 4.2). These characteristics, in tandem with 1 area %, unaltered metal support a CM2.6 classification.

4.3.2 AZ-04-D

Akin to the other lithologies in this section, this one is also mildly to moderately altered. The abundance of anhydrous precursor fragments within the matrix mirror that of AZ-04-B and AZ-04-C at approximately 8 area %. Surviving Fe-Ni metal occurs around chondrules, and the TCIs have high Fe and S content. The TCIs differ when compared to AZ-04-B and AZ-04-C in that they have a meshwork texture of S-rich, Type II TCI structures interspersed with ‘wormy’ cronstedtite-rich domains in and between phyllosilicate clumps (Plate 4.5, ROI 1). Calcium carbonate is in association with TCI and phyllosilicate; hence they are mostly of the T1a variety, however a few lack any obvious alteration and appear solitary as T0 calcites. This lithology is a CM2.6.

4.3.3 AZ-02-A

This is a typical CM2 lithology represented by the entirety of chip AZ-02 (Fig 4.6). The replacement products constitute a 50-50 split of TCI and matrix. TCIs are clearly replacement products but are variable in pseudomorphic geometry, ranging from large, 50

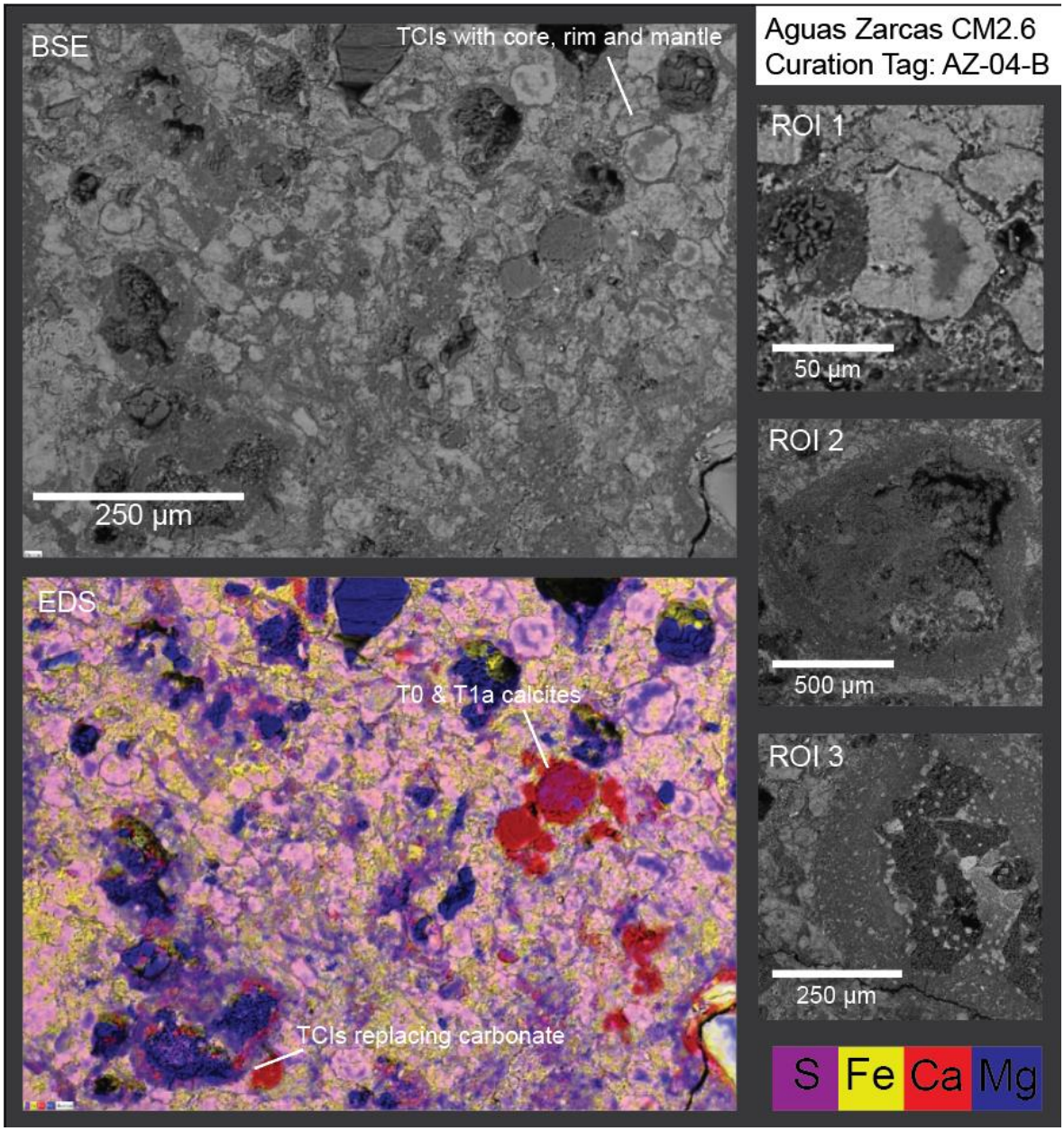

Phyllosilicates	**n**	**Area %**	**'FeO'/ SiO_2**	**S/SiO_2**	**Mg #**	**Totals**
TCI	28	33.8	2.63 ± 0.26	0.59 ± 0.10	34.42 ± 2.37	84.45 ± 0.55
TCI phyllosilicate cores	6	52.6	0.93 ± 0.25	0.21 ± 0.08	62.00 ± 5.61	83.53 ± 2.52
Matrix	12		0.85 ± 0.08	0.12 ± 0.02	54.77 ± 1.92	76.32 ± 2.81
Accessory minerals		**Area %**	**Form**			
Surviving precursors[#]		7.2	Small and medium-grained Fo phenocrysts in matrix			
Carbonates		6.3	T1a and T0			
Sulphides		<1	Pn			
Chondrules						
Mesostasis	Phyllosilicate					
Phenocryst replacement	Negligible - < 5 %					
Rubin Subtype:	CM2.6					

Plate 4.4 AZ-04-B - Area % = threshold estimates from polished block. [#]Evenly distributed within matrix (*i.e.*, not large chondrules). Uncertainties are 2SE. Totals are EDS oxide wt %. ROI 1 - Type II TCI with a Mg-rich phyllosilicate core and a thin accretionary mantle; ROI 2 – Possibly a compound-chondrule CAI with thick accretionary mantle; ROI 3 – Chondrule hosting Type I TCI blebs.

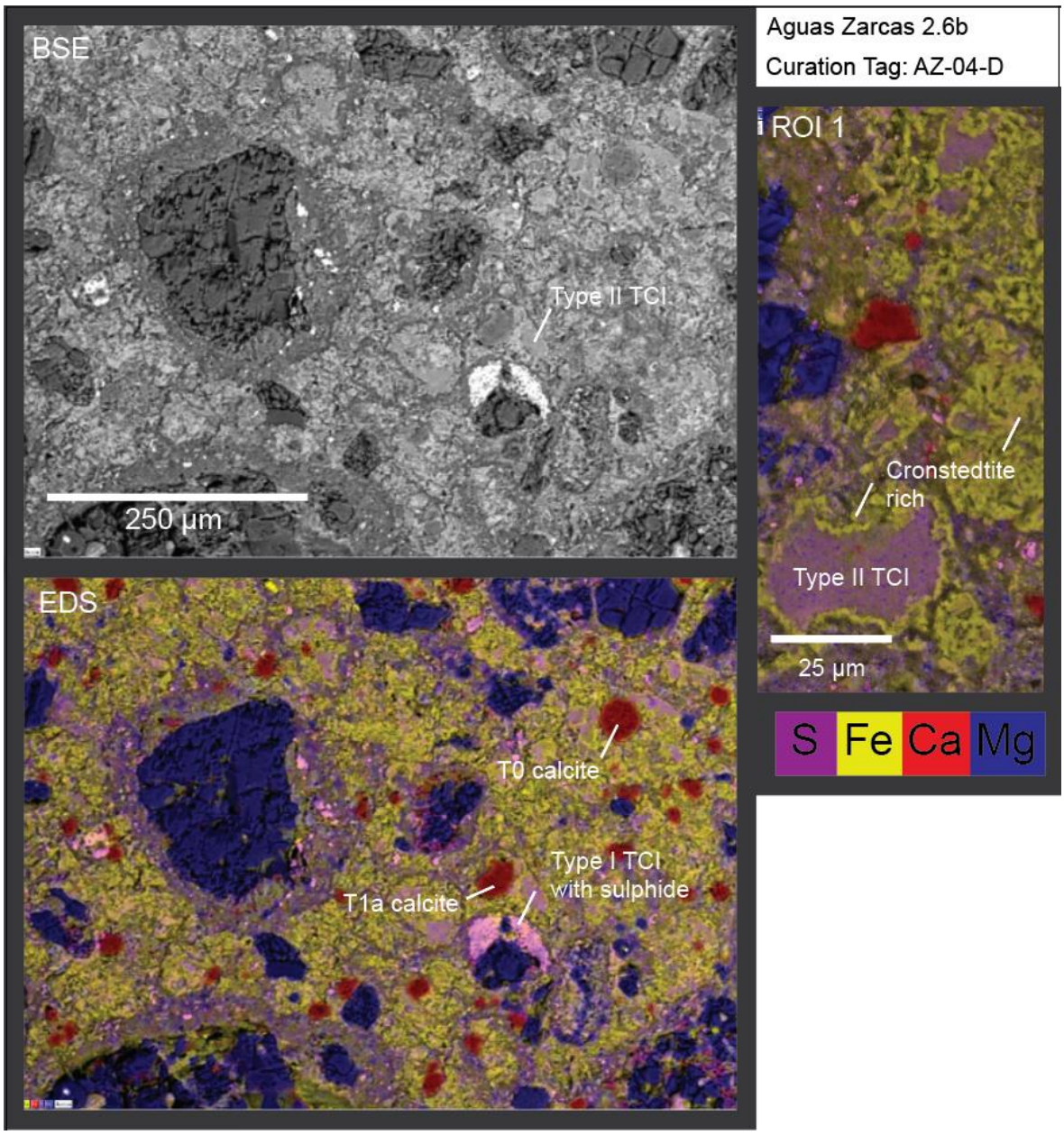

Phyllosilicates	**n**	**Area %**	**'FeO'/ SiO_2**	**S/SiO_2**	**Mg #**	**Totals**
TCI	12	40.3	2.95 ± 0.33	0.69 ± 0.18	34.96 ± 2.49	80.82 ± 0.61
Matrix	5	44.9	0.83 ± 0.11	0.15 ± 0.03	55.51 ± 3.42	74.67 ± 5.34
Accessory minerals		**Area %**	**Form**			
Surviving precursors[#]		8.0	Small chondrules and Fo phenocrysts			
Carbonates		5.5	T0 and T1a calcites			
Sulphides		1.4	Pn + Int			
Chondrules						
Mesostasis	Phyllosilicate					
Phenocryst replacement	Negligible					
Rubin Subtype:	CM2.6					

Plate 4.5 - AZ-04-D**.** Area % = threshold estimates from polished block. [#]Evenly distributed within matrix (*i.e.*, not large chondrules). Uncertainties are 2SE. Totals are EDS oxide wt %. ROI 1 – Higher magnification EDS map showing the 'wormy' texture of cronstedtite-rich regions. Note: the EDS compositions were obtained via averaged hand-drawn regions in AZtec.

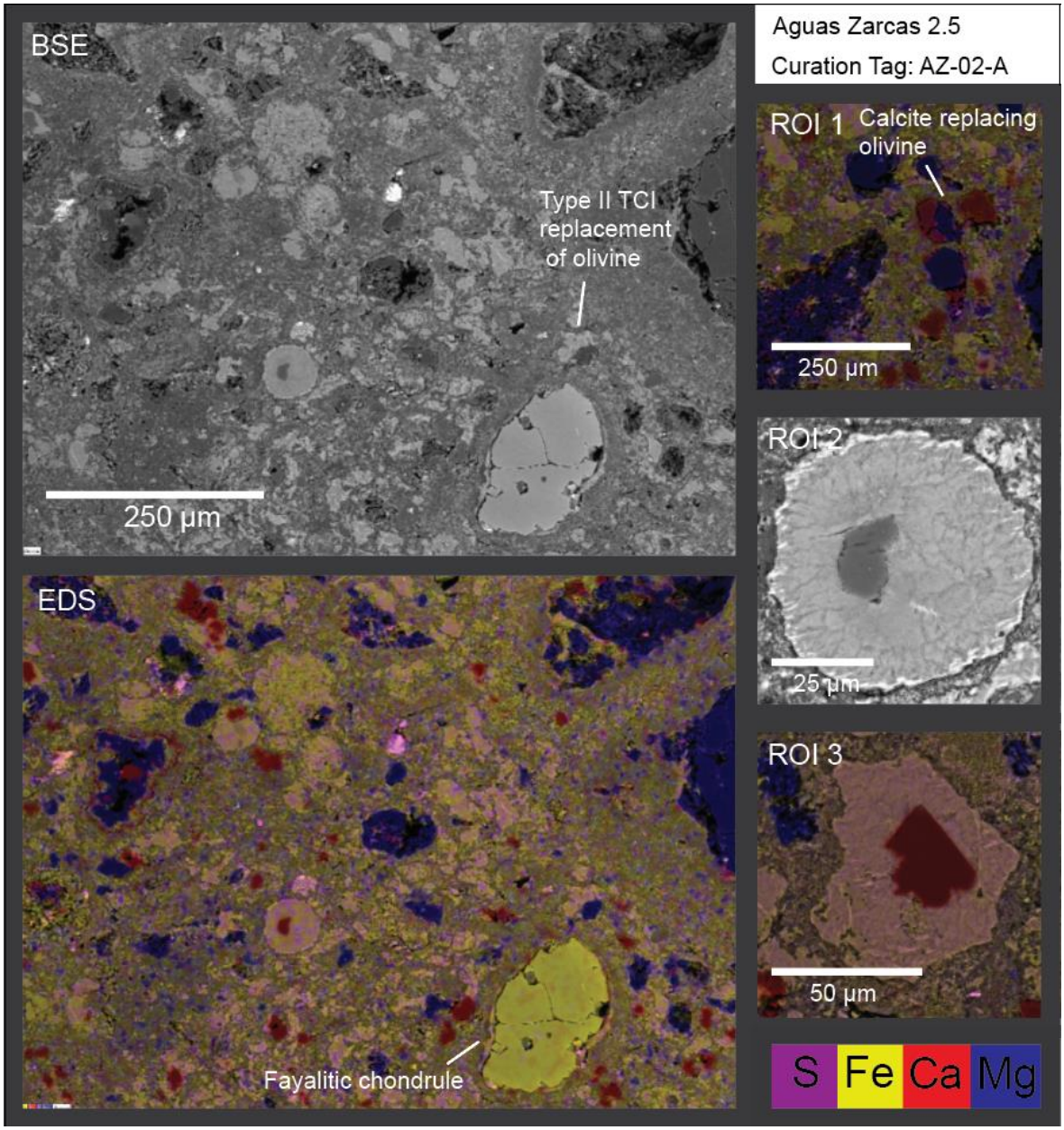

Phyllosilicates	**n**	**Area %**	**'FeO'/ SiO_2**	**S/SiO_2**	**Mg #**	**Totals**
TCI	14	23.5	2.40 ± 0.14	0.52 ± 0.05	32.96 ± 1.88	85.22 ± 0.57
Matrix	6	56.0	0.90 ± 0.14	0.10 ± 0.02	53.00 ± 4.07	79.94 ± 2.00
Accessory minerals		**Area %**	**Form**			
Surviving precursors[#]		13.1	Fo olivine grains < 30 µm			
Carbonates		3.8	T1a and T0 calcites			
Sulphides		1.4	Pn + Int			
Chondrules						
Mesostasis	Phyllosilicate					
Phenocryst replacement	0-5%					
Rubin Subtype:	CM2.6					

Plate 4.6 - AZ-02-A**.** Area % = threshold estimates from polished block. [#]Evenly distributed within matrix (*i.e.*, not large chondrules). Uncertainties are 2SE. Totals are EDS oxide wt %. ROI 1 – T0 Ca-carbonate replacing an olivine crystal; ROI 2 – BSE image of TCI structures including centripetal, tochilinite-rich rim; ROI 3 – Type II TCI replacing a carbonate crystal along ragged edges, indicating a crystallography-controlled preference for replacement of carbonate.

μm featureless, rounded blebs to sharply defined, <10 μm fragments. TCIs host T1a Ca-carbonates (Plate 4.6, ROI 2 & 3), demonstrating centripetal replacement from an outer tochilinite rim, through a more Fe-poor TCI mantle, to a Ca-carbonate core, suggesting carbonates were the immediate precursor phases for the majority of the TCIs in this lithology (*e.g.,* Lee *et al.,* 2013; Pignatelli *et al.,* 2016; Suttle *et al.,* 2023). Olivine is also a TCI precursor, evident by relict olivine grains in the centres of a few TCIs, though the TCI composition remains the same as those with Ca-carbonate cores. Variable degrees of chondrule alteration are confined mostly to the mesostasis and finer-grained phenocrysts, whereas larger phenocrysts and chondrule fragments (of both forsteritic and fayalitic composition) remain largely unaffected by alteration (Plate 4.6). Accretionary rims are present but are noticeably thinner than those observed in other Aguas Zarcas lithologies (*I.e.,* AZ-04-B) and lack any obvious layering. Sulphide generations are predominantly of intermediate Ni/Ni+Fe composition. This lithology is a CM2.5.

4.3.4 AZ-04-C

At first glance, AZ-04-C appears identical to AZ-04-B in that it is TCI dominant and has similar chondrule abundance and degree of alteration (Plate 4.7); however, on closer inspection the TCIs are chemically homogeneous and of lower brightness contrast. The chemical composition of the TCIs, specifically the 'FeO'/SiO_2 ratio are noticeably lower than AZ-04-B, D (Plate 4.7, Fig 4.7), indicating the TCIs of this lithology experienced prolonged interaction and became Fe-depleted over time. A lack of large carbonate and sulphide grains is in support of this. Once again, accretionary mantles are exceptionally well developed/preserved (Plate 4.7, ROI 2) and interestingly, the TCIs are 'squashed' in-between the margins of the chondrules (Plate 4.7, ROI 3), often exhibiting higher contrast. Such petrofabrics are frequently observed within CM chondrites (*e.g.,* Floyd *et al.,* 2023; Hanna *et al.,* 2015; Lindgren *et al.,* 2014; Lindgren *et al.,* 2015; Tomeoka *et al.,* 1999), interpreted to be a result of multiple, low intensity impacts preferentially affecting the

phyllosilicates, which due to their weaker constitution, readily attenuate impact shockwaves and deform preferentially to the chondrules; however, such a texture would be expected section-wide, so it is curious that TCI flattening is heterogeneous in this polished block. Sulphides are predominantly of 'intermediate' composition (Chokai *et al.,* 2004) with a Ni/Ni+Fe composition between 0.10 and 0.40 (Plate 4.7). This lithology is CM2.3.

4.3.5 Aguas Zarcas summary

In contrast to Mukundpura, Aguas Zarcas is a meteorite fall of moderate alteration with a petrologic range of 2.4-2.6. This agrees with the lithologies described elsewhere (Kerraouch *et al.,* 2021; Kerraouch *et al.,* 2022), indicating that multiple accretionary rocks within multiple stones consistently fall within this alteration range. Characteristics unique to this meteorite include a high net abundance of chondrules, potentially compound-chondrule CAIs, and chondrules that preserve a high quantity of Fe-Ni metal. In addition, more exotic clasts have been discovered outside of this study including lithologies with high metal abundance within the matrix, and C1, C1/2 lithologies (Kerraouch *et al.,* 2021; Kerraouch *et al.,* 2022). Unaltered metal in contact with phyllosilicate matrices is a paradox in CM meteoritics that can only be explained by anisotropic alteration through very specific fluid channels, or by heterogeneous, polyphase accretion. The study by Kerraouch *et al.* (2022) supports the latter and the involvement of an exogeneous component, perhaps derived as a xenolith. Aguas Zarcas represents a rich opportunity to deconvolute these different scenarios without the overprinting effects of pervasive alteration.

Early, centripetal replacement (outside-inwards) of both olivine and carbonate grains into TCI (as shown by AZ-02-A) provide proof that both are Type I TCI precursors; indeed, partially altered olivine grains consisting of forsterite and carbonate may represent heterogeneous precursors in themselves (Plate 4.6, ROI 1).

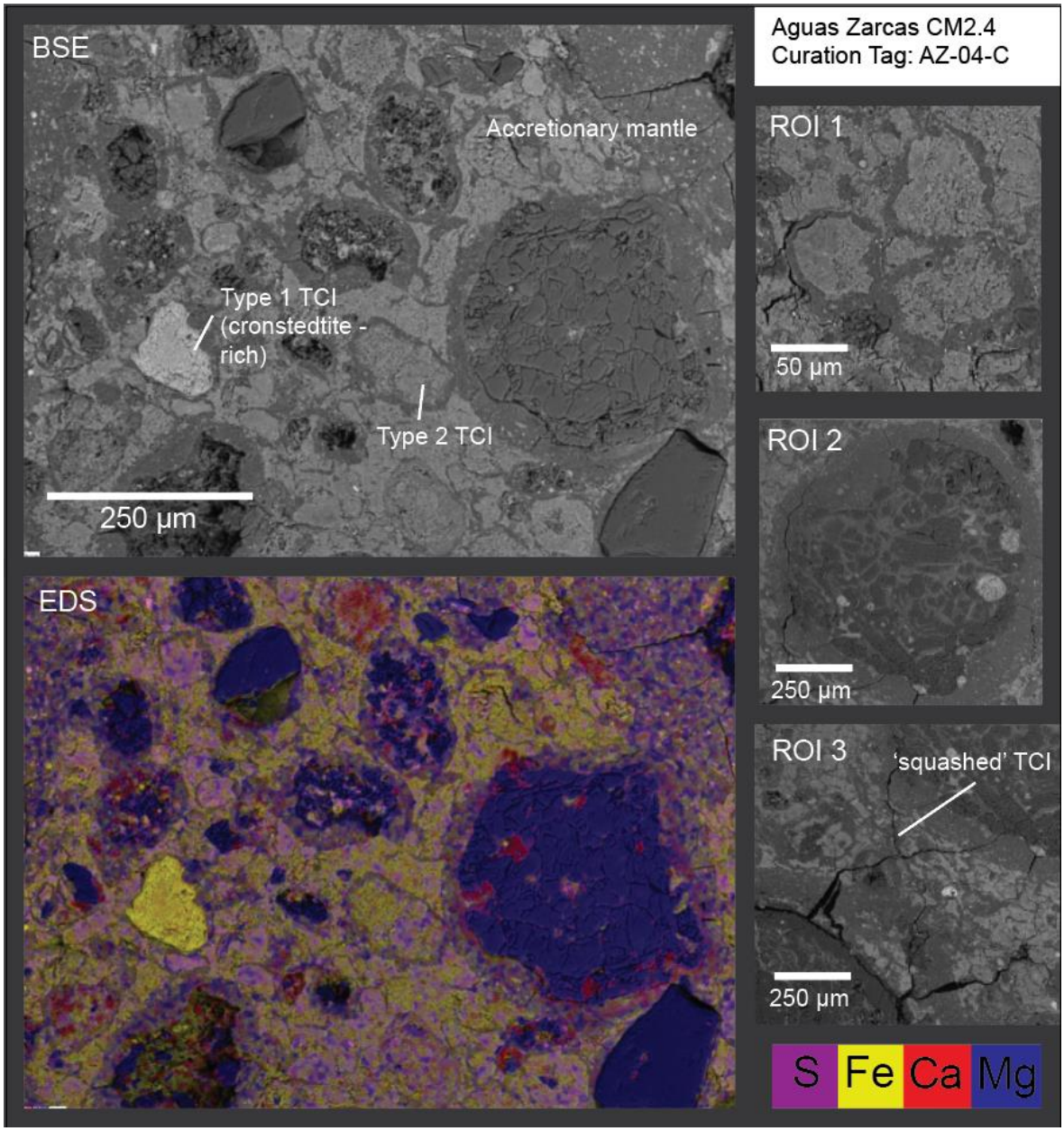

Phyllosilicates	**n**	**Area %**	**'FeO'/ SiO_2**	**S/SiO_2**	**Mg #**	**Totals**
TCI	17	46.1	1.57 ± 0.15	0.31 ± 0.04	47.21 ± 3.98	88.30 ± 3.72
Matrix	9	42.6	0.79 ± 0.05	0.13 ± 0.06	57.04 ± 2.05	79.42 ± 1.84
Accessory minerals		**Area %**	**Form**			
Surviving precursors[#]		7.4	Chondrules <60 µm			
Carbonates		3.0	Ca-carbonate. Sparse, small <10 µm			
Sulphides		<1	Int			
Chondrules						
Mesostasis	Phyllosilicate					
Phenocryst replacement	5-15 %					
Rubin Subtype:	CM2.6					

Plate 4.7 - AZ-04-C. Area % = threshold estimates from polished block. [#]Evenly distributed within matrix (*i.e.*, not large chondrules). Uncertainties are 2SE. Totals are EDS oxide wt %. ROI 1 – a cluster of TCI with accretionary rims; ROI 2 – A POP chondrule with accretionary rim hosting Type I TCI and pyroxene phenocrysts; ROI 3 – 'squashed' Type II TCIs in between two chondrules

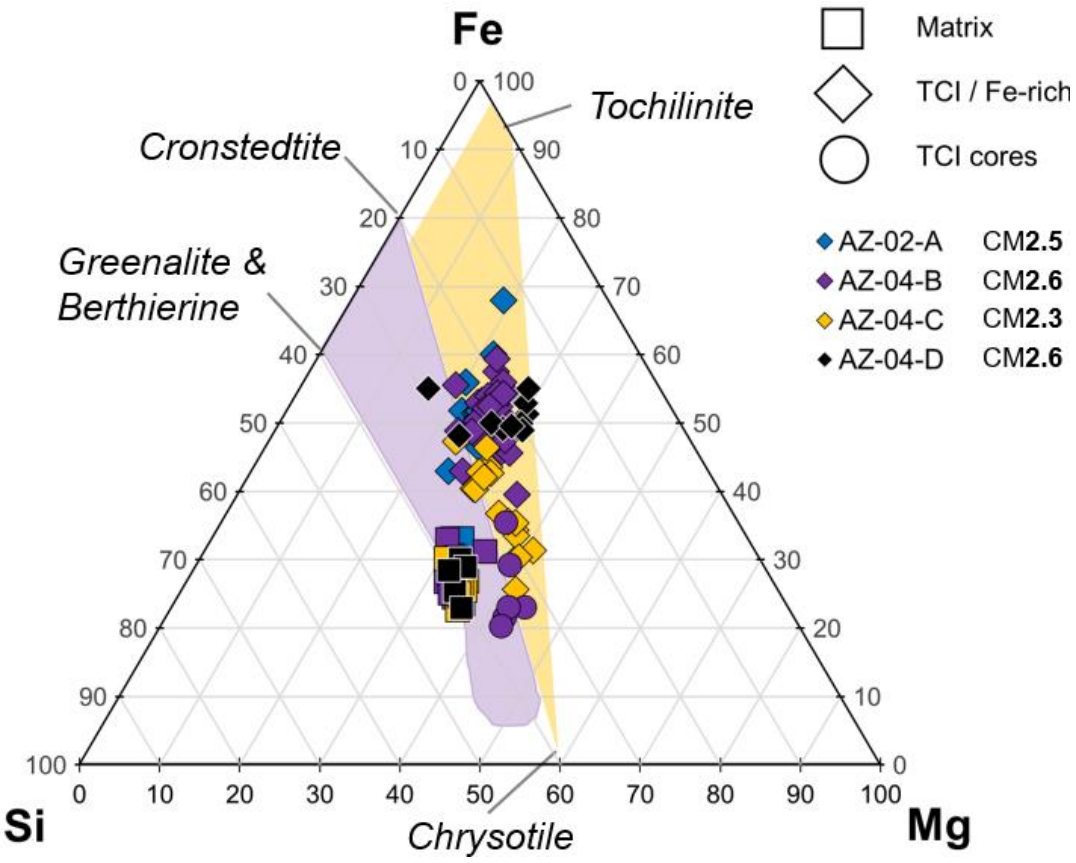

Figure 4.7 - Normalised major element cation ternary diagram for matrix, TCI and TCI cores in Aguas Zarcas (at %), with serpentine (purple) and TCI (yellow) fields, heavily modified after Suttle *et al.* (2021), Explanation of the compositional fields are given in Chapter 1, section 1.4.2.2. Of note: TCIs in all lithologies are Fe-rich and contain a larger proportion of tochilinite and cronstedtite than Mukundpura. Aguas Zarcas matrix compositions are more silica-rich than the TCI 'core', also composed chiefly of Mg-rich serpentine.

4.4 Kolang (2020)

The lithologies described below are from two polished blocks (see Fig 4.8 and 4.9).

4.4.1 KO-01-A

This lithology presents as a sharply delineated chondrule-rich clast in hand specimen. This clast was not easily removed from the surrounding material and so the entire chip, including adjacent material described below, was mounted (Fig 4.8). The clast constitutes ~25 % of the total surface area of the imaged section (Fig 4.8). TCIs are the dominant secondary mineral phase and are small (25 – 50 μm), occasionally hosting cores of either clumpy Mg-phyllosilicate (Plate 4.8, ROI 2 & 3) or T1 Ca-carbonate. Metal is absent and sulphide is very rare,

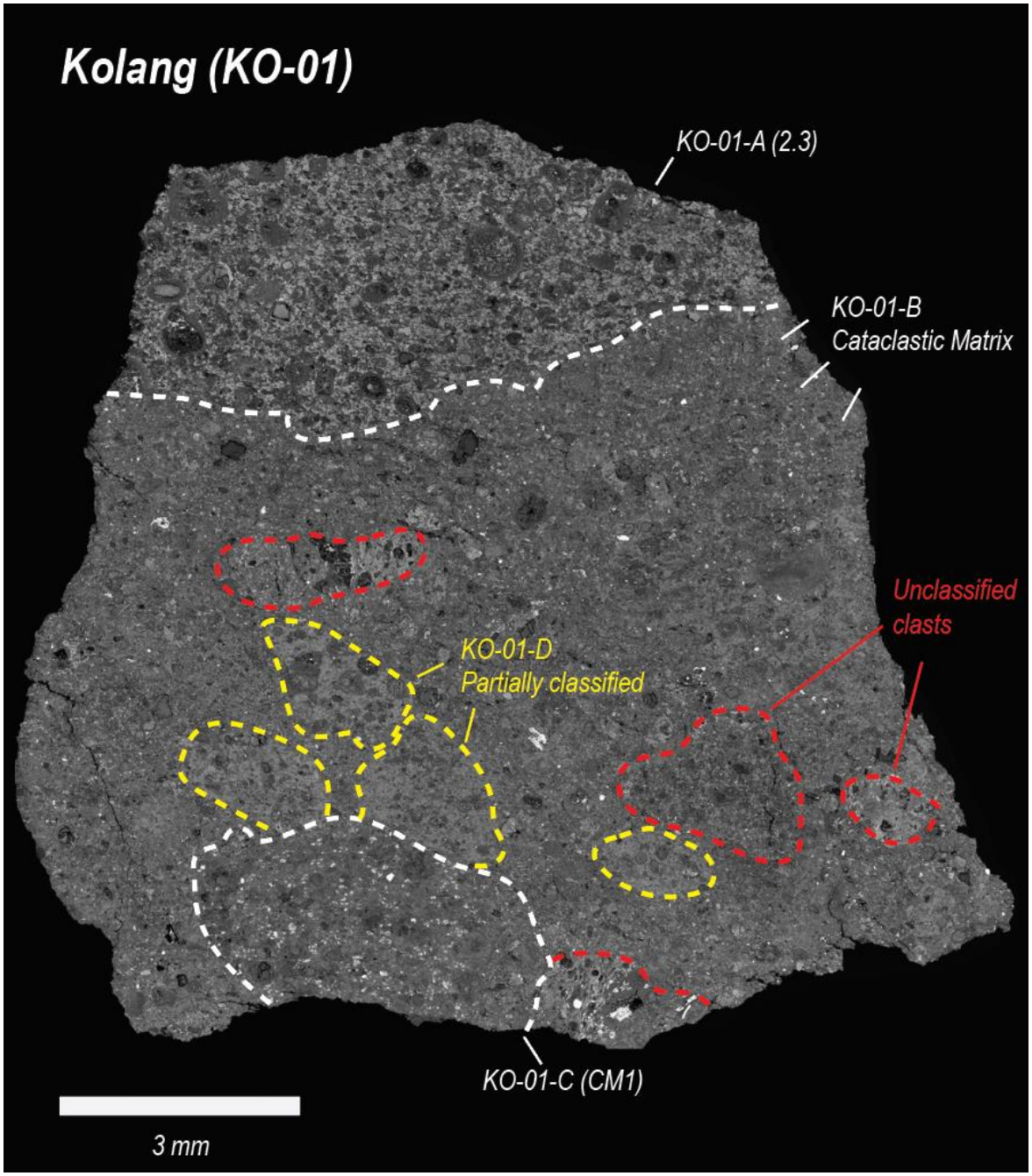

Figure 4.8 – Navigation pane for polished block KO-01

and all chondrules are partially replaced bearing thin, accretionary dust mantles consisting of two layers. The TCI composition (Plate 4.8, Fig 4.10) and degree of chondrule alteration is consistent with a CM2.3 classification, incongruent with the official CM1/2 classification of the type specimen of Kolang on the Meteoritical Bulletin (Gattacceca *et al.*, 2022).

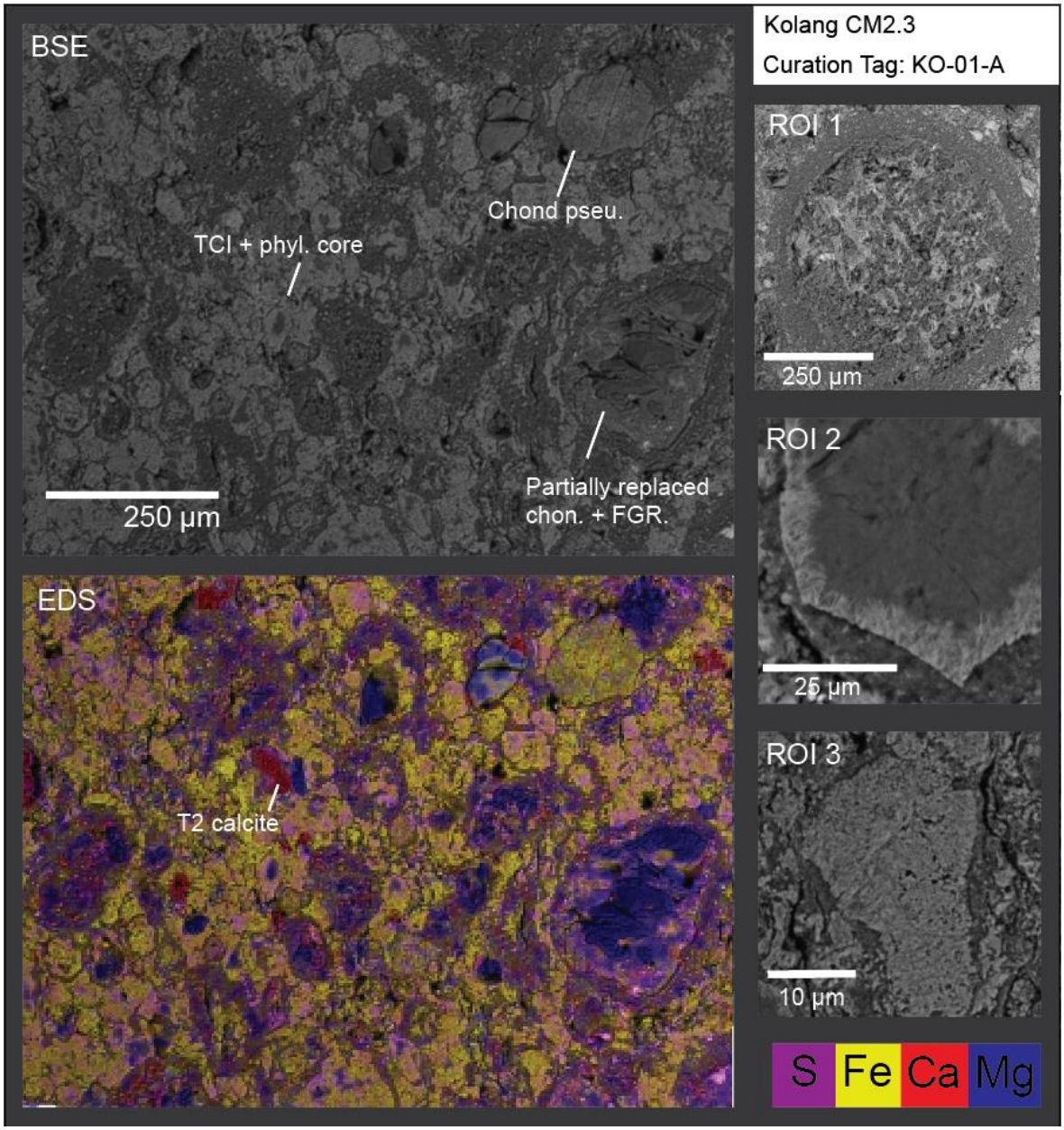

Phyllosilicates	**n**	**Area %**	**'FeO'/ SiO_2**	**S/SiO_2**	**Mg #**	**Totals**
TCI	11	58	1.90 ± 0.17	0.32 ± 0.07	39.19 ± 3.22	83.90 ± 0.96
TCI cores	3	34	0.38 ± 0.01	0.05 ± 0.02	77.54 ± 1.16	80.28 ± 4.03
Matrix	8		0.62 ± 0.04	0.09 ± 0.01	64.57 ± 1.53	74.39 ± 1.97
Accessory minerals		**Area %**	**Form**			
Surviving precursors[#]		3.6	<10 µm Fo grains			
Carbonates		2.6	T1 and T2 Ca-carbonate			
Sulphides		1.3	Po+Pn			
Chondrules						
Mesostasis	Phyllosilicate					
Phenocryst replacement	15-85 %					
Rubin Subtype:	CM2.2					

Plate 4.8 – KO-01-A**.** Area % = threshold estimates from polished block. [#]Evenly distributed within matrix (*i.e.*, not large chondrules). Uncertainties are 2SE. Totals are EDS oxide wt %. ROI 1 – 95 % pseudomorphed chondrule with FGR; ROI 2 – Type II TCI with Mg-serpentine core and TCI rim; ROI 3 – Type II TCI.

4.4.2 KO-01-D

KO-01-D occurs as four clasts in KO-01 (Fig 4.8). Low quality chemical data was obtained on this sample due to a poor polish (Plate 4.9). Partially replaced chondrules are widespread in an Fe-rich matrix, itself interpreted as 'conjoined' TCI material, albeit with a lower contrast than those observed elsewhere in other lithologies (Plate 4.9). Pseudomorphic Mg-rich phyllosilicate clumps are common with exceptionally preserved crystal faces intergrown with T1 Ca-carbonates, which constitute 2 % of the polished block. Minor pentlandite dominates the sulphide budget as massive grains in the matrix and within chondrules. A CM2.1 classification seems appropriate for this lithology, though without reinforcement of quantitative EDS data this is an estimation.

4.4.3 KO-03-A

KO-03-A appeared as a pea-sized, geometric clast standing proud in a Chip A of Kolang (Fig 4.9). Gentle poking with a stainless-steel needle immediately liberated the clast from the host in a 'cast and mould' - like fashion, indicating a sharp, but loose boundary. KO-03-A is unusual and exhibits a number of atypical alteration characteristics. Chondrules are 80 – 90 % replaced (Plate 4.10, ROI 2 & 3), hosting sulphide and type 1 TCI globules in addition to large T2a Ca-carbonate grains constituting ~7 % of the section, themselves occurring as partial to complete pseudomorphic replacement of chondrules. The chondrules are surrounded by compact accretionary rims with a barely discernible, coarse-grained outer layer (Plate 4.10, ROI 2). Aqueous alteration appears to have been arrested at a late stage as forsterite olivine grains survive within chondrule cores (Plate 4.10, ROI 2). The defining characteristic of this lithology is the dendritic veining of a S-free, Fe-rich phyllosilicate, consistent in composition with cronstedtite-rich serpentine (Plate 4.10, Fig 10), which appears to take advantage of an exceptionally high porosity in the matrix. This material crosscuts the base lithology from bottom right to top left in the BSE map in Figure 4.9. The underlying lithology defines a different petrofabric with chondrules

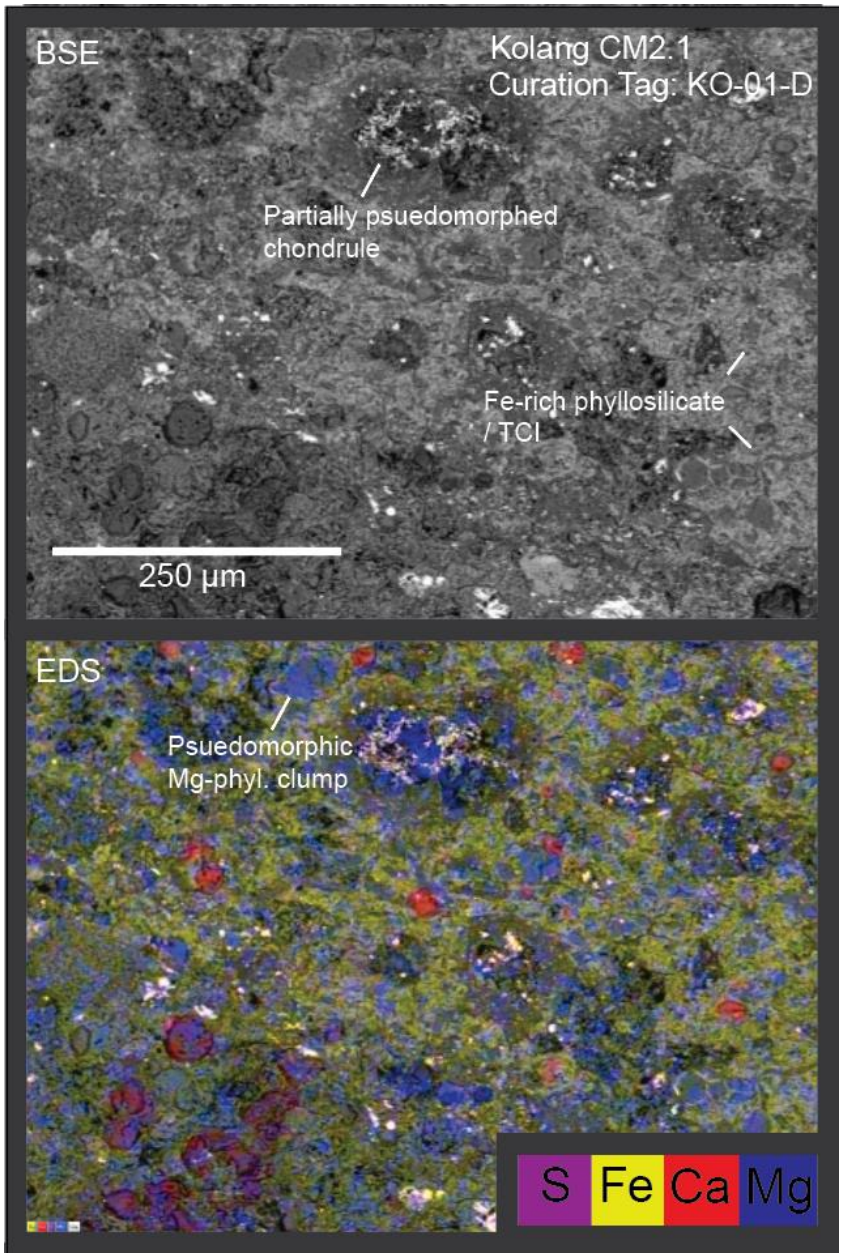

Phyllosilicates	**n**	**Area %**	**'FeO'/ SiO_2**	**S/SiO_2**	**Mg #**	**Totals**
TCI	4	42.2	1.90 ± 0.42	0.16 ± 0.03	47.51 ± 1.81	-
Matrix	7	53.8	0.98 ± 0.29	0.13 ± 0.08	55.16 ± 7.70	-
Accessory minerals		**Area %**	**Form**			
Surviving precursors[#]		0.7	<10 µm Fo phenocrysts in chondrules and matrix			
Carbonates		2.0	T1a and T0 Ca-carbonates			
Sulphides		0.6	Pn			
Chondrules						
Mesostasis	Phyllosilicate					
Phenocryst replacement	>85 %					
Rubin Subtype:	CM2.1					

Plate 4.9 – KO-01-D**.** Area % = threshold estimates from polished block. [#]Evenly distributed within matrix (*i.e.*, not large chondrules). Uncertainties are 2SE. Totals are EDS oxide wt %. EDS data in this section was obtained from normalised data taken from a low-resolution SEM map and is therefore semi-quantitative.

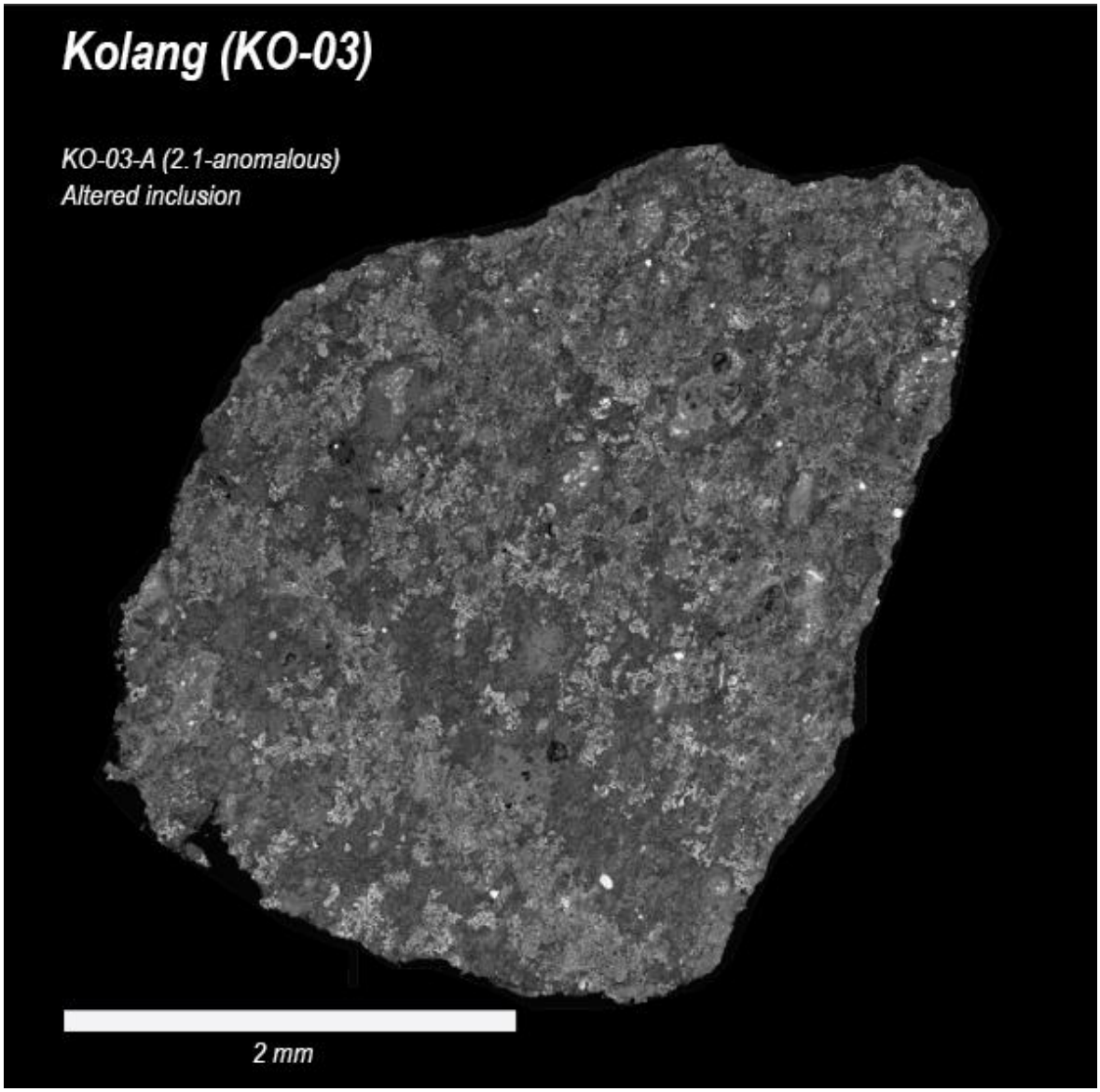

Figure 4.9 - Overview BSE image of KO-03-A. 'Dendritic' cronstedtite crosscuts the lithology.

trending from the bottom left to the top right of the image. Dendritic veining of minerals, *e.g.,* carbonate in terrestrial rocks is indicative of precipitation of minerals from saturated fluids due to a change in environmental conditions (Jones *et al.,* 2005). The dendritic cronstedtite potentially provides evidence of an episode of late fluid mobilisation of an Fe- and Si-saturated fluid, contingent on a short episode of alteration post-dating the main alteration event. Comparison with literature reveals only one other such occurrence of a texturally similar CM1-2 lithology in Aguas Zarcas (Kerraouch *et al.,* 2022). This lithology is best represented by a CM2.1 classification, albeit with anomalous levels of cronstedtite.

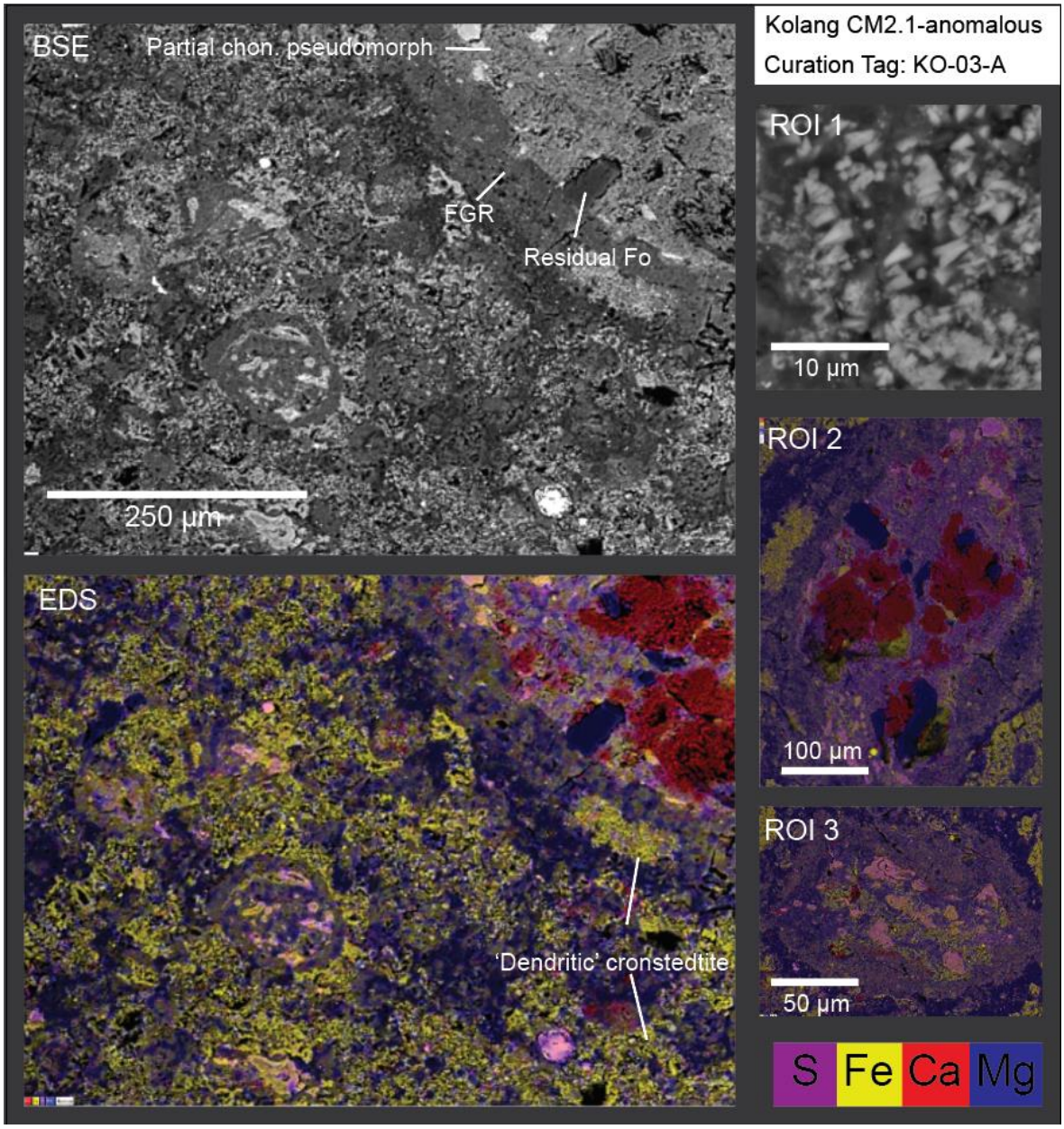

Phyllosilicates	**n**	**Area %**	**'FeO'/ SiO_2**	**S/SiO_2**	**Mg #**	**Totals**
Cronstedtite	8	33.8	2.2 ± 0.24	0	23.4 ± 7.70	76.6 ± 1.36
Matrix	7	52.3	0.42 ± 0.13	0.06 ± 0.02	74.90 ± 5.57	72.65 ± 0.70
Accessory minerals		**Area %**	**Form**			
Surviving precursors[#]		2.0	Small phenocrysts of forsterite in chondrules			
Carbonates		6.7	T2 Ca-carbonates			
Sulphides		2.0	Pn > Po + Int			
Chondrules						
Mesostasis	Phyllosilicate					
Phenocryst replacement	>85 %					
Rubin Subtype:	CM2.1 - anomalous					

Plate 4.10 – KO-03-A**.** Area % = threshold estimates from polished block. [#]Evenly distributed within matrix (*i.e.*, not large chondrules). Uncertainties are 2SE. Totals are EDS oxide wt %. ROI 1 – High magnification image of the cronstedtite, evident by its trigonal, triangular habit; ROI 2- A T2 carbonate grain, pseudomorphic after a chondrule; ROI 3- A chondrule pseudomorph hosting Type I TCI with a homogeneous inner rim and a FGR mantle.

4.4.4 KO-01-C

KO-01-C is found towards the base of the section in opposition to KO-01-A (Fig 4.8). The mineralogy of this clast proved a challenge for polishing and so a smooth surface was not achieved. Boundaries between this clast and the surrounding brecciated host is gradational. The clast is characterised by very large modal % of Mg-rich carbonate and an unusually high-contrast, sulphur-rich TCI-like component scattered throughout (Plate 4.10). These growths exhibit a texture of discrete, small batons under high-magnification and have high S content but appreciable SiO_2 (~10 wt % oxide), so they still fit the loose criteria of TCI. Using the Rubin and Lentfort criteria, the composition of these TCIs would suggest a CM 2.7 classification. This is a clear example where TCI composition does not correlate well with the Rubin method. However, on the bases of the complete replacement of all chondrule silicates, this clast is best classified as a CM1.

4.4.5 Kolang summary

Kolang is a very altered CM chondrite fall. While a large portion of the polished blocks studied constitute a pervasively replaced, cataclastic matrix, numerous primary accretionary clasts can also be identified within (Fig 4.8). Of these clasts, one is a CM2.3 lithology (KO-01-A) and the only one to contain true TCI clumps, hosted within a formally classified CM1/2 meteorite, while another is clearly a CM1 (KO-01-C). The texture of this CM1 lithology is different to the one observed in Mukundpura (MP-05-A, Plate 4.3), in that its carbonate content is exclusively dolomite and the chondrule pseudomorphs are indistinct. Regardless, this is further evidence for the interaction of CM1 and CM2 material in an asteroid regolith. Furthermore, a CM2.1 lithology with anomalous levels of cronstedtite provides evidence for its precipitation within a high porosity matrix (KO-03-A, Fig 4.9) creating a linked network of dendritic-like texture. To date, little has been published on this meteorite, but the Meteoritical Bulletin reports a number of lithologies with strange descriptions, including ‘green-grey breccias’ as well as chondrule-rich and chondrule-poor

clasts (Gattacceca *et al.,* 2022). Akin to Aguas Zarcas (e.g. Kerraouch *et al.,* 2022) and Winchcombe (e.g. Suttle *et al.,* 2023), metal-rich lithologies with atypical oxygen isotopic characteristics are also reported (Gattacceca *et al.,* 2021). The Kolang source material suffered pervasive aqueous alteration (Marrocchi *et al.,* 2023) and provides an opportunity of comparison with less altered CM material.

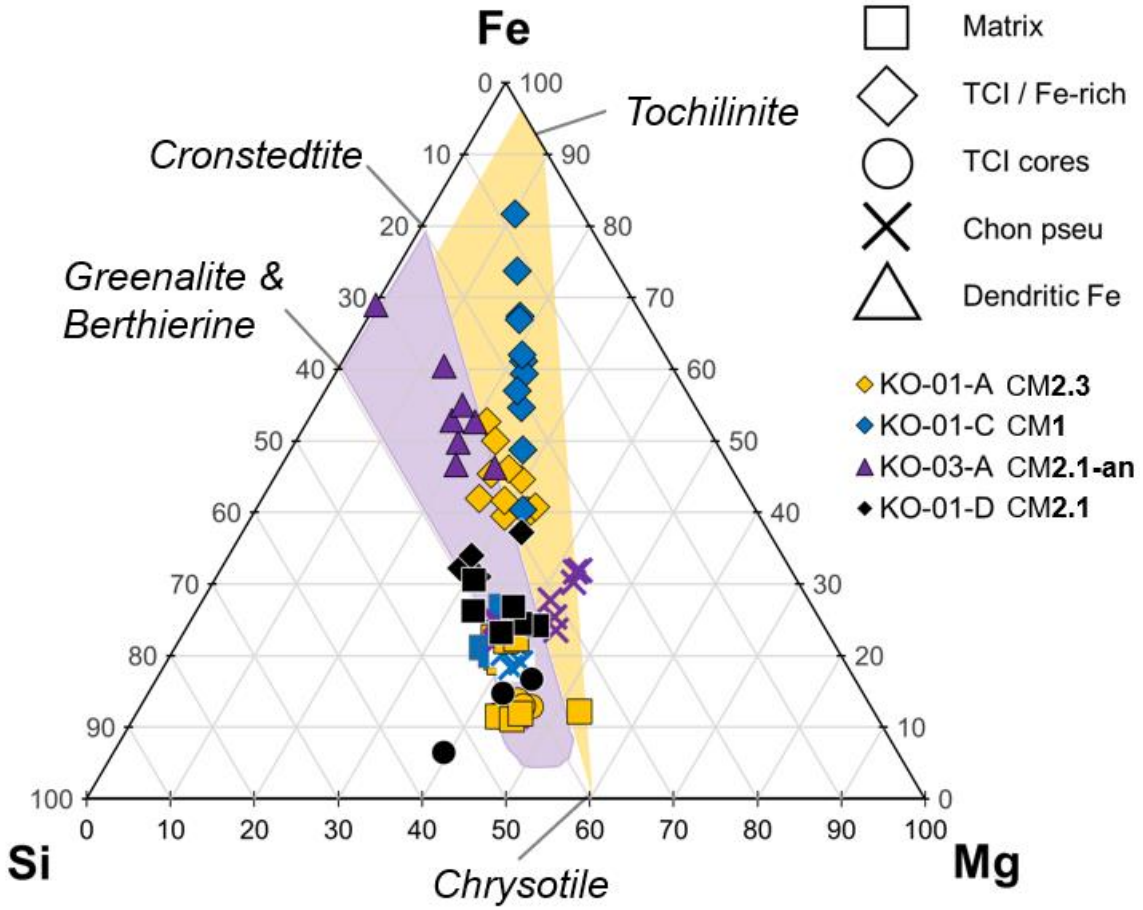

Figure 4.10 - Normalised major element cation ternary diagram for matrix, TCI, TCI cores, chondrule pseudomorphs and dendritic, Fe-rich cronstedtite in Kolang (at %), with serpentine (purple) and TCI (yellow) fields, heavily modified after Suttle *et al.* (2021). Explanation of the compositional fields are given in Chapter 1, section 1.4.2.2. Of note: Dendritic, cronstedtite-rich phases in the CM2.1 anomalous lithology KO-03-A plot towards the cronstedtite end of the cronstedtite – chrysotile solid solution. Tochilinite-rich 'TCI' phases in the CM1 lithology bear towards the tochilinite endmember.

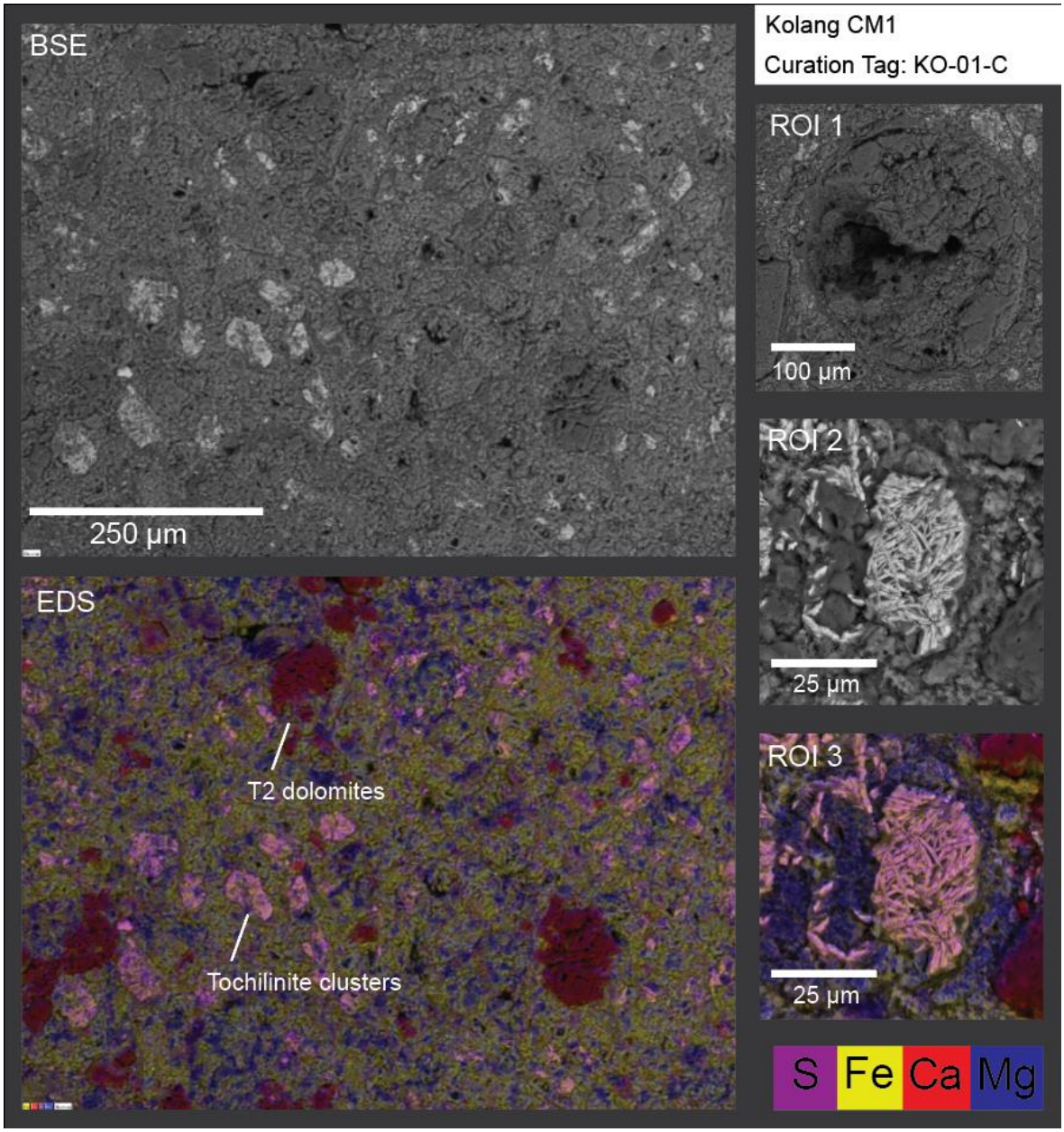

Phyllosilicates	**n**	**Area %**	**'FeO'/ SiO_2**	**S/SiO_2**	**Mg #**	**Totals**
TCI	10	7.7	4.16 ± 1.05	1.65 ± 0.51	27.74 ± 5.04	95.65 ± 1.75
Matrix	6	82.7	0.63 ± 0.10	0.06 ± 0.03	64.52 ± 3.29	80.07 ± 6.72
Accessory minerals		**Area %**	**Form**			
Surviving precursors[#]		0	None			
Carbonates		6.2	T2 Dolomite			
Sulphides		2.0	Pentlandite			
Chondrules						
Mesostasis	Phyllosilicate					
Phenocryst replacement	Complete					
Rubin Subtype:	CM1					

Plate 4.11 – KO-01-C**.** Area % = threshold estimates from polished block. [#]Evenly distributed within matrix (*i.e.*, not large chondrules). Uncertainties are 2SE. Totals are EDS oxide wt %. ROI 1 – Chondrule pseudomorph; ROI 2 – Needles of tochilinite as 'TCI'; ROI 3 – EDS map of ROI 2.

4.5 Winchcombe (2021)

The lithologies described below are from two polished blocks on loan for destructive analysis from the Natural History Museum, London. They are as follows: BM.2022, M1-117 and BM.2022, M1-123. For the purposes of maintaining nomenclature, they shall henceforth be referred to as WC-01 and WC-02 respectively. The results, and some of the associated discussion, presented below are reported in Greenwood *et al.* (2023).

4.5.1 WC-02-A

WC-02-A is a moderately to heavily altered, TCI-rich lithology, present as a large clast (Fig 4.11). The TCIs contain core and rim structures with easily identifiable boundaries, as is common in lithologies of moderate to low petrologic subtype. The cores are either T1a Ca-carbonates or Mg-rich phyllosilicate clumps. The outer rim of Fe- and S-rich phyllosilicate have S/SiO_2 ratios higher than would be expected (0.19 ± 0.03) given the level of alteration in the lithology (Table 4.1), though this is not reflected in the phyllosilicate cores. Chondrules are heterogeneously altered, many completely altered to phyllosilicate and T2 carbonate, while some phenocrysts remain pristine. Sulphides are of the pentlandite and intermediate variety. This lithology is consistent with a CM2.2 classification and appears analogous to Winchcombe 'Lithology A' from King *et al.* (2022) and Suttle *et al.* (2023)

4.5.2 WC-01-A

A very altered lithology. WC-01-A consists of 44.4 %, light grey TCI of similar composition to WC-02-A (Fig 4.12); in fact, the lithology is similar in many aspects, except the distribution of chondrule pseudomorphs and T2 Ca-carbonates constitute a larger proportion. TCIs exhibit similar core and rim structures with high contrast filaments extending into the core (Plate 4.13, ROI 3). While occasional fragments of unaltered chondrules dot the section, the pervasively altered characteristics are in-line with a CM2.1 classification on the Rubin scale. This lithology is analogous to 'Lithology B' from previous works (King *et al.,* 2022; Suttle *et al.,* 2023).

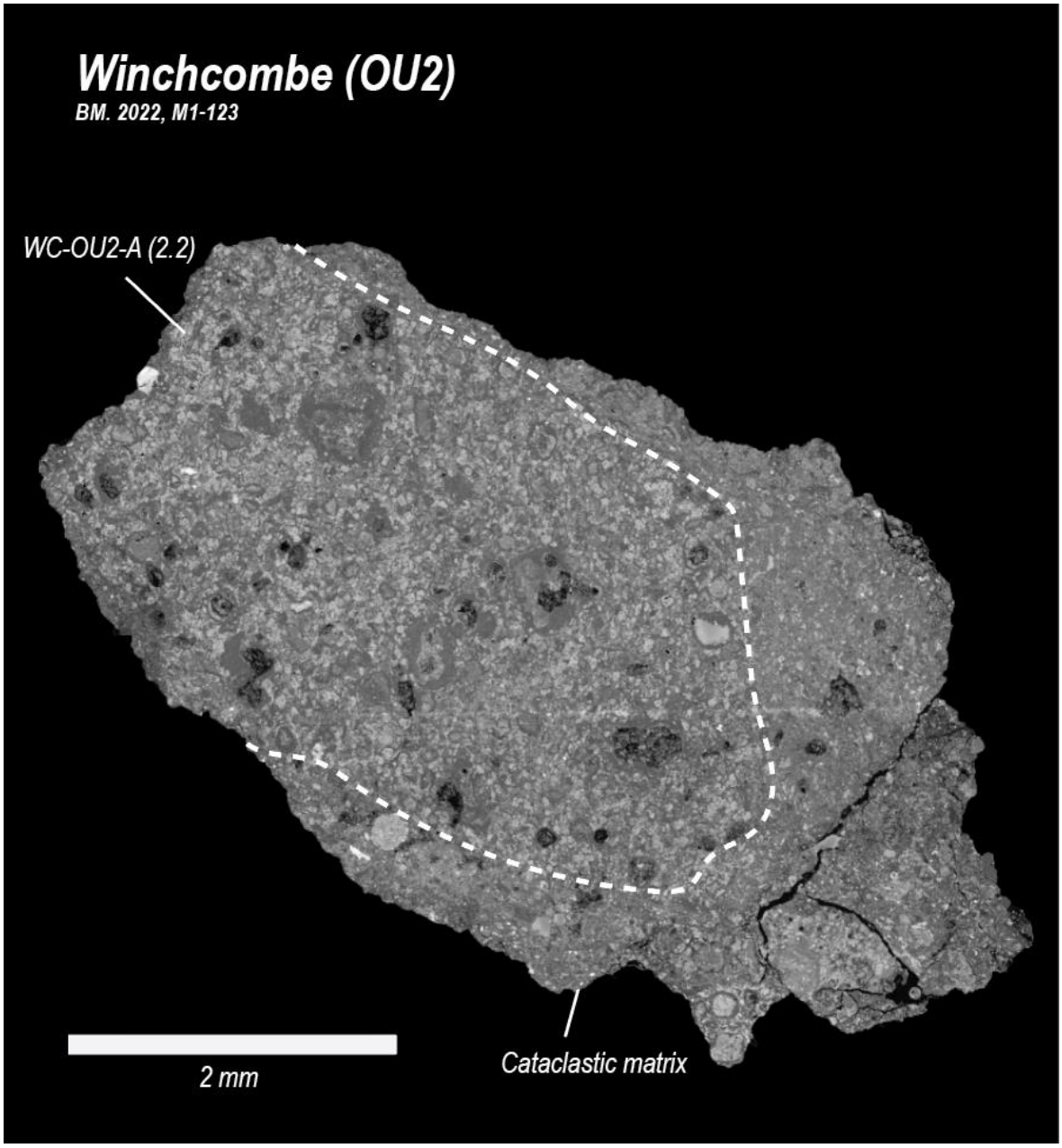

Figure 4.11 – Navigation image for polished block WC-02

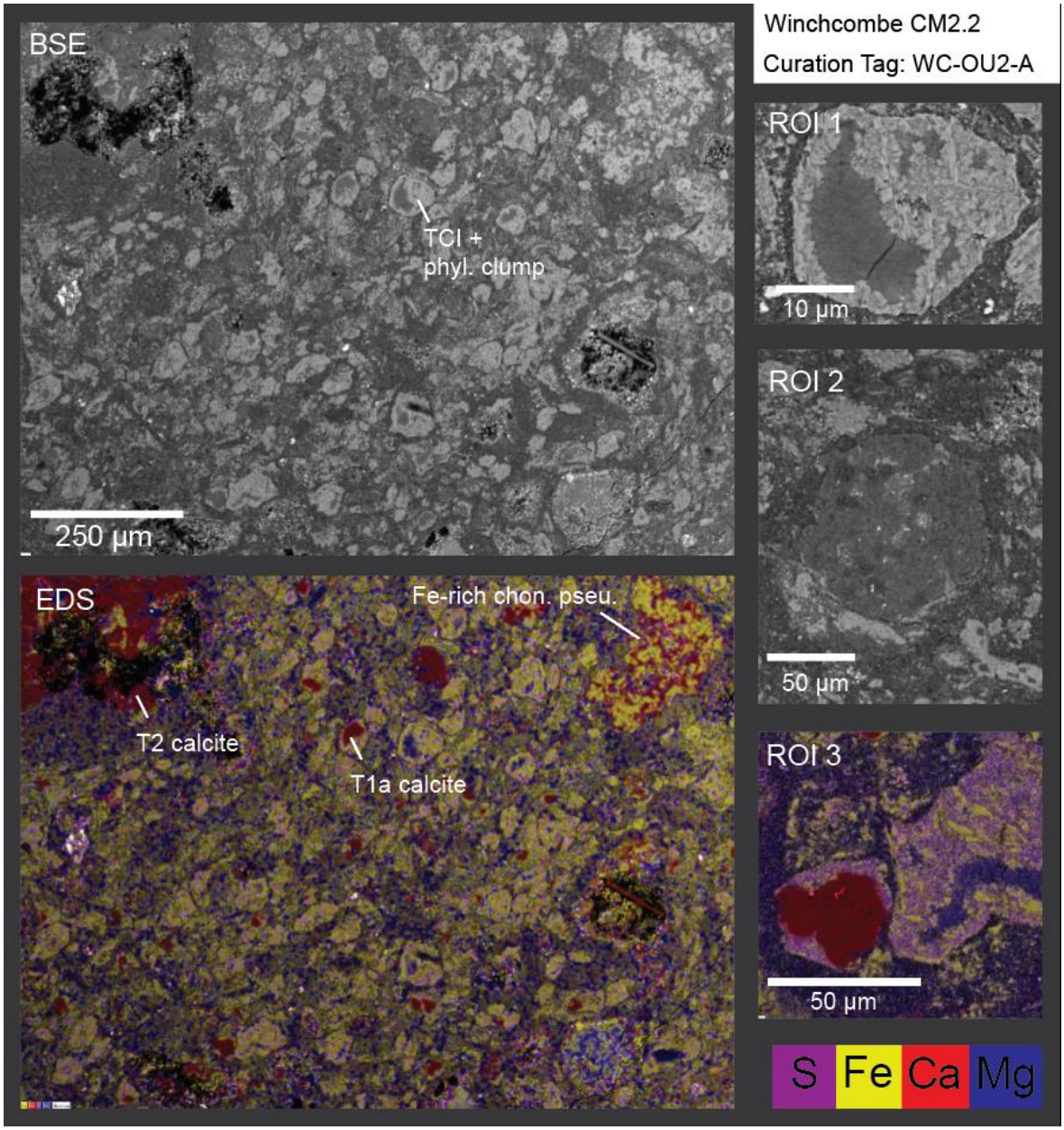

Phyllosilicates	**n**	**Area %**	**'FeO'/ SiO_2**	**S/SiO_2**	**Mg #**	**Totals**
TCI	44	31.2	1.29 ± 0.06	0.19 ± 0.03	48.39 ± 1.83	85.90 ± 0.77
TCI cores	26	58.7	0.41 ± 0.05	0.05 ± 0.01	77.24 ± 1.66	84.04 ± 2.01
Matrix	15		0.62 ± 0.08	0.09 ± 0.02	65.89 ± 3.67	73.49 ± 3.53
Accessory minerals		**Area %**	**Form**			
Surviving precursors[#]		2.6	Rare chondrules			
Carbonates		3.3	T1a and T2 Ca-carbonates			
Sulphides		0.9	Pn + Int			
Chondrules						
Mesostasis	Phyllosilicate					
Phenocryst replacement	>85 %					
Rubin Subtype:	CM2.2					

Plate 4.12 – WC-02-A**.** Area % = threshold estimates from polished block. [#]Evenly distributed within matrix (*i.e.*, not large chondrules). Uncertainties are 2SE. Totals are EDS oxide wt %. ROI 1 TCI core and rim; ROI 2 – T2 carbonate after a chondrule; ROI 3- TCI replacing carbonate and hosting Mg-phyllosilicate.

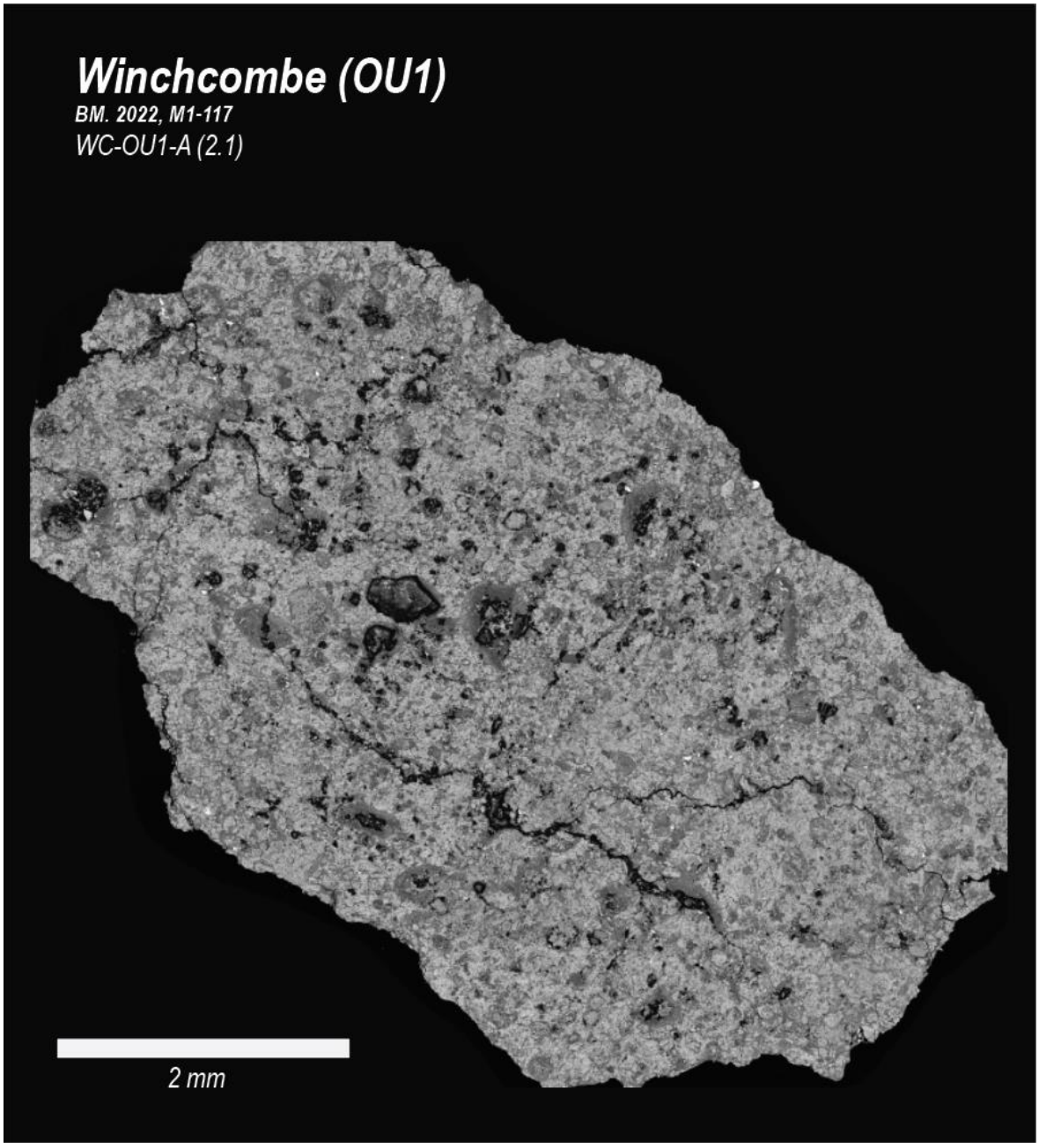

Figure 4.12 - Navigation image for polished block WC-OU1

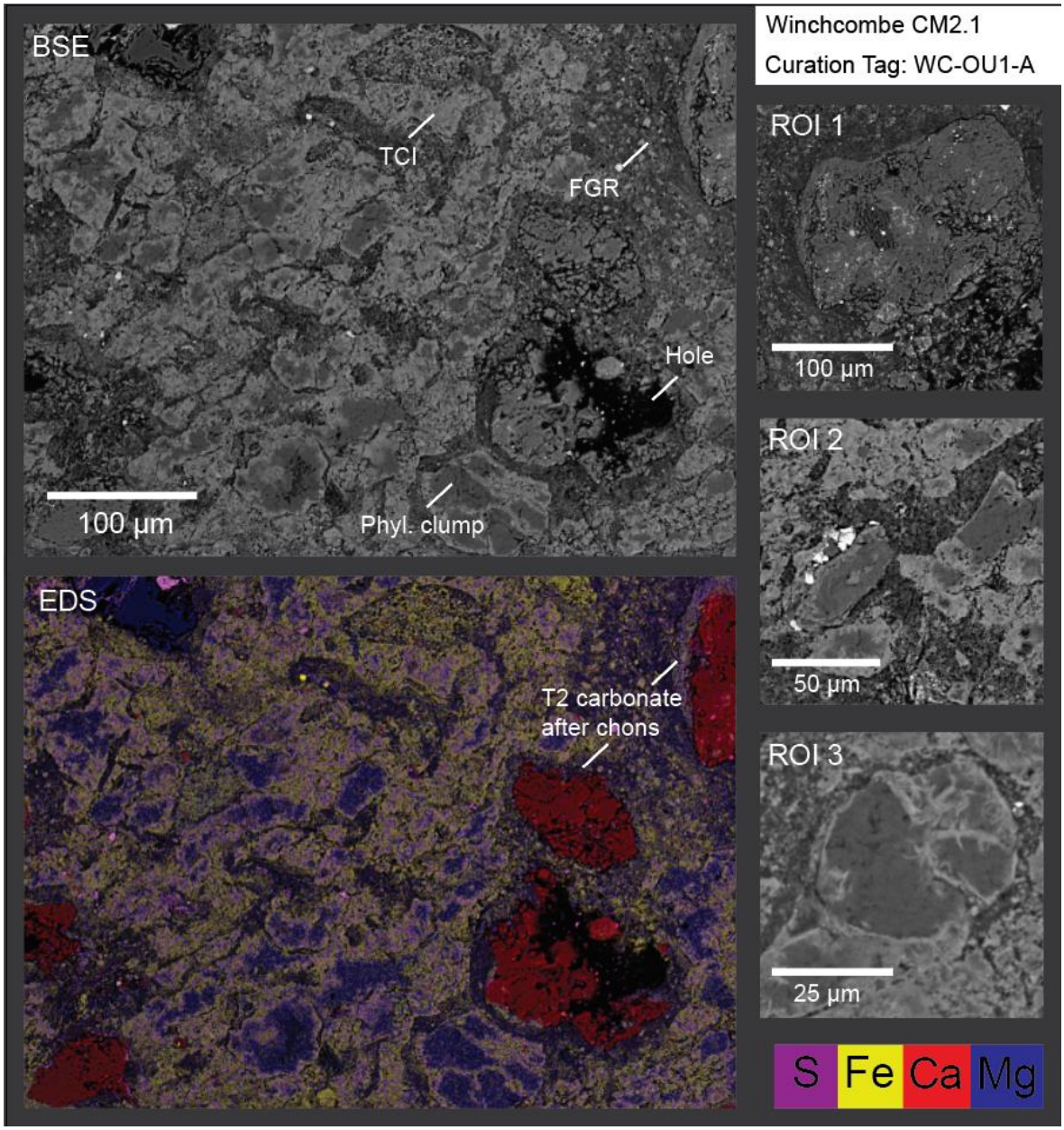

Phyllosilicates	**n**	**Area %**	**'FeO'/ SiO_2**	**S/SiO_2**	**Mg #**	**Totals**
TCI	28	44.4	2.07 ± 0.07	0.25 ± 0.06	33.00 ± 2.96	84.78 ± 0.35
TCI cores	8	41.5	0.63 ± 0.06	0.15 ± 0.03	70.75 ± 1.97	88.57 ± 0.76
Matrix	13		0.56 ± 0.02	0.10 ± 0.01	67.99 ± 1.24	76.81 ± 1.85
Accessory minerals		**Area %**	**Form**			
Surviving precursors[#]		1.4	Rare chondrules			
Carbonates		5.0	T2 Ca-carbonate			
Sulphides		0.2	Po + Int > Po			
Chondrules						
Mesostasis	Phyllosilicate					
Phenocryst replacement	>85 %					
Rubin Subtype:	CM2.1					

Plate 4.13 –Area % = threshold estimates from polished block. [#]Evenly distributed within matrix (*i.e.*, not large chondrules). Uncertainties are 2SE. Totals are EDS oxide wt %. ROI 1 – T2 Ca-carbonate as a chondrule pseudomorph; ROI 2 – Clusters of TCIs mantled by accretionary rims; ROI 3 – TCI replacement texture with filaments protruding into a phyllosilicate core.

4.5.3 Winchcombe summary

Winchcombe is a heavily altered CM chondrite, though it appears to be a transitionary example lying within the narrow region of alteration between Mukundpura and Kolang. The petrologic range of lithologies in Winchcombe is large, from 2.0 (CM1)-2.6 as evidenced by published work (Suttle *et al.,* 2023), though only 2.1 and 2.2 are present in the polished blocks studied here. The mineral chemistry, particularly the TCIs between the two lithologies is slightly offset and reveal the compositional diversity that can be present within a single CM lithology (Fig 4.13).

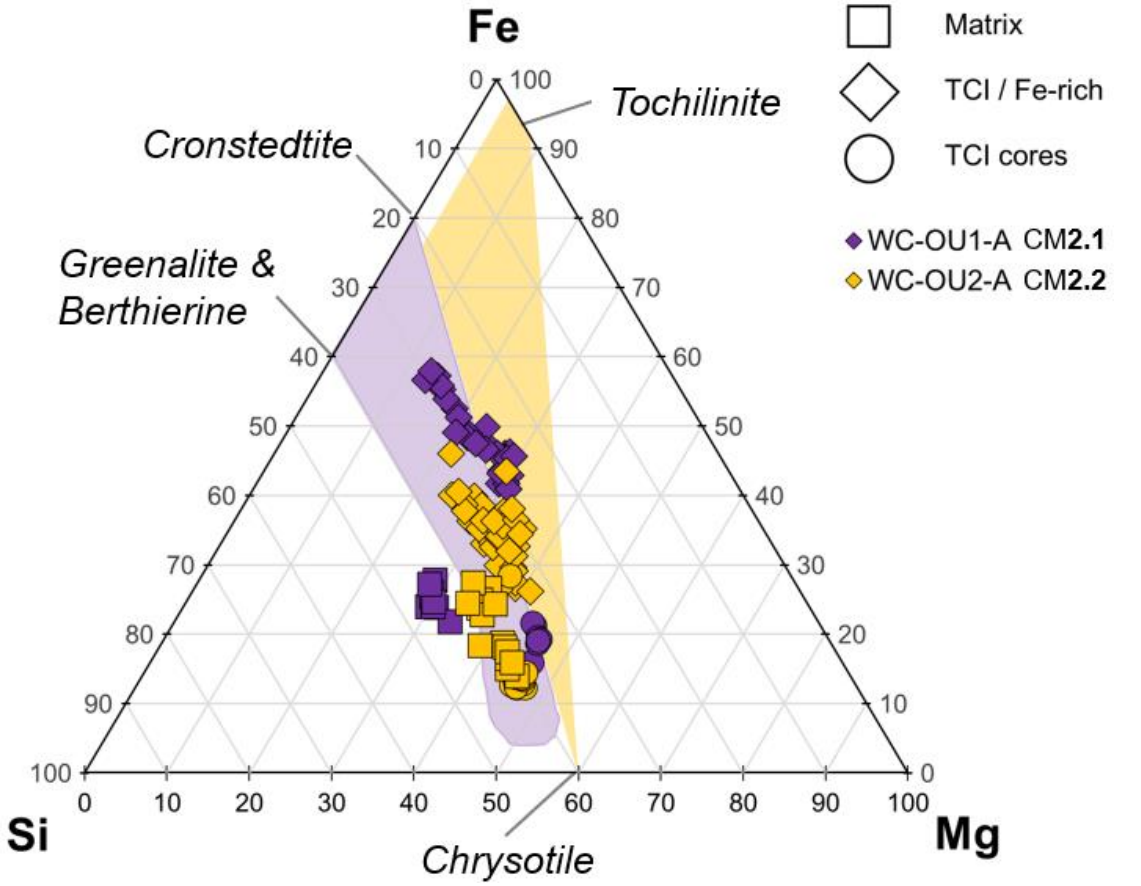

Figure 4.13 - Normalised major element cation ternary diagram for matrix, TCI and TCI cores in Winchcombe (at %), with serpentine (purple) and TCI (yellow) fields, heavily modified after Suttle *et al.* (2021). Explanation of the compositional fields are given in Chapter 1, section 1.4.2.2. Of note: TCI compositions are consistent with mixing between an Fe-rich serpentine and a Mg-rich, Si-depleted phase, perhaps the S-rich serpentines recorded by Bridges *et al.* (2022), with each lithology forming a distinct trend.

4.6 Lonewolf Nunataks 94101

The lithologies described below are from three polished blocks. Figs 4.14 and 4.15 represent LON-01 and LON-03a and are typical, 1-inch resin round blocks. LON-04 is an order of magnitude larger as a polished block measuring 7 cm in the longest dimension. The block represents the sister half to that studied in Gregory *et al*. (2015) and Zolensky *et al*. (2022). Preliminary clasts are outlined in Fig 4.16, whereas clasts dedicated to investigation are outlined in Fig 4.17

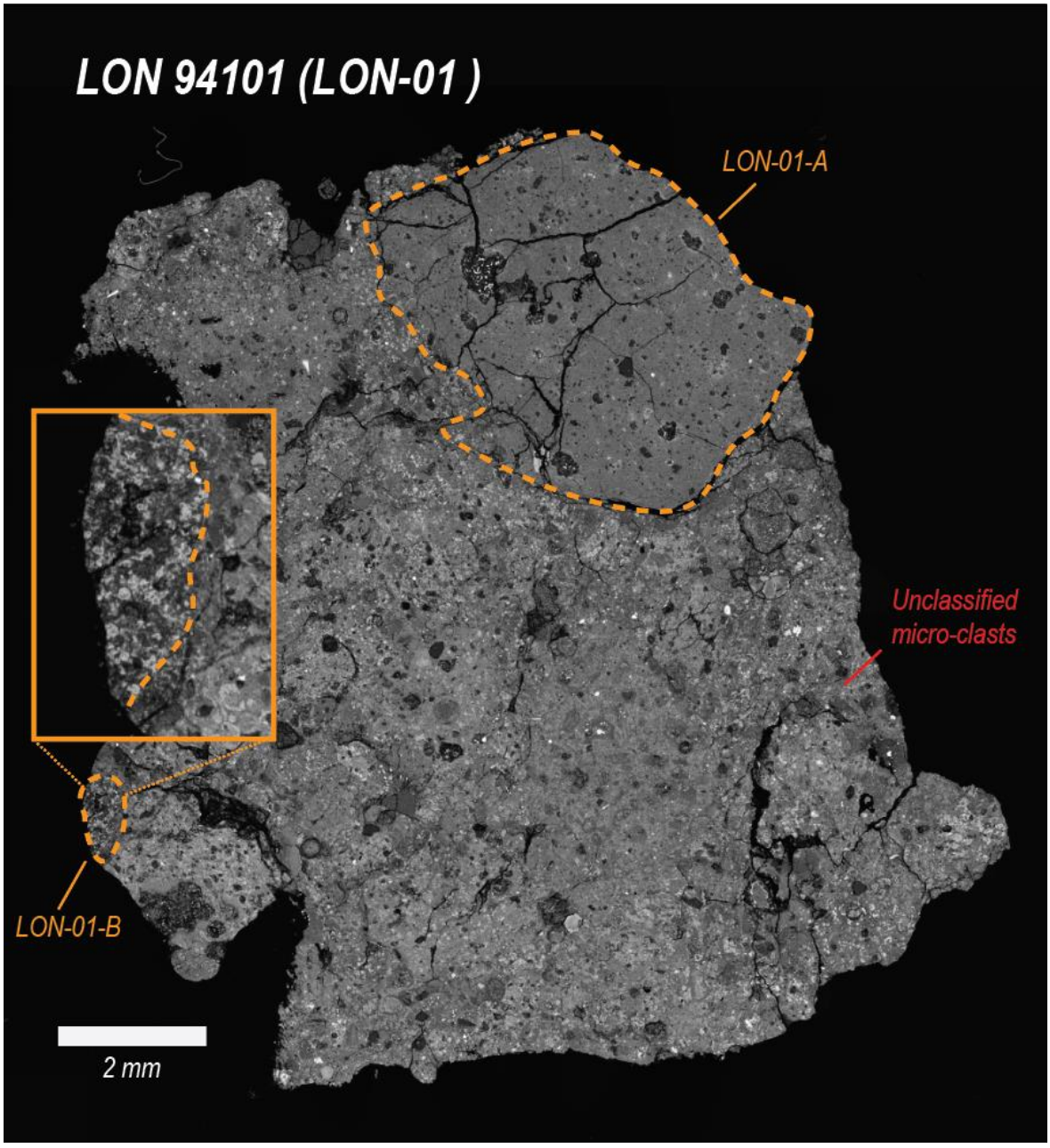

Figure 4.14 – Navigation image for LON-01. Yellow text indicates semi-quantitative classification using normalised data from EDS maps. The bulk of this sample is cataclastic matrix and micro-clasts.

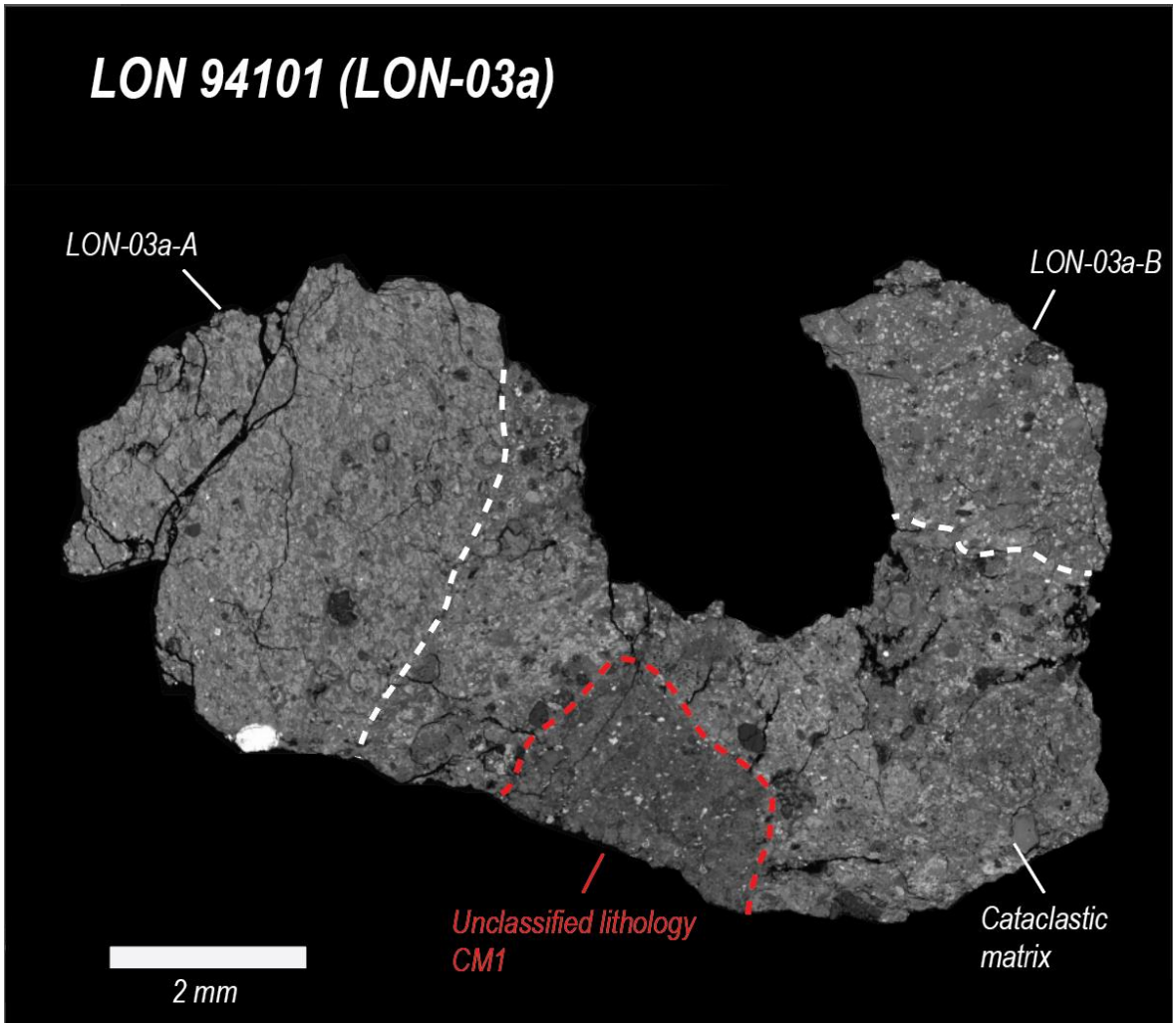

Figure 4.15 - Navigation pane for LON-03a. Red lines indicate an identified clast boundary, however no investigation was undertaken due to time constraints.

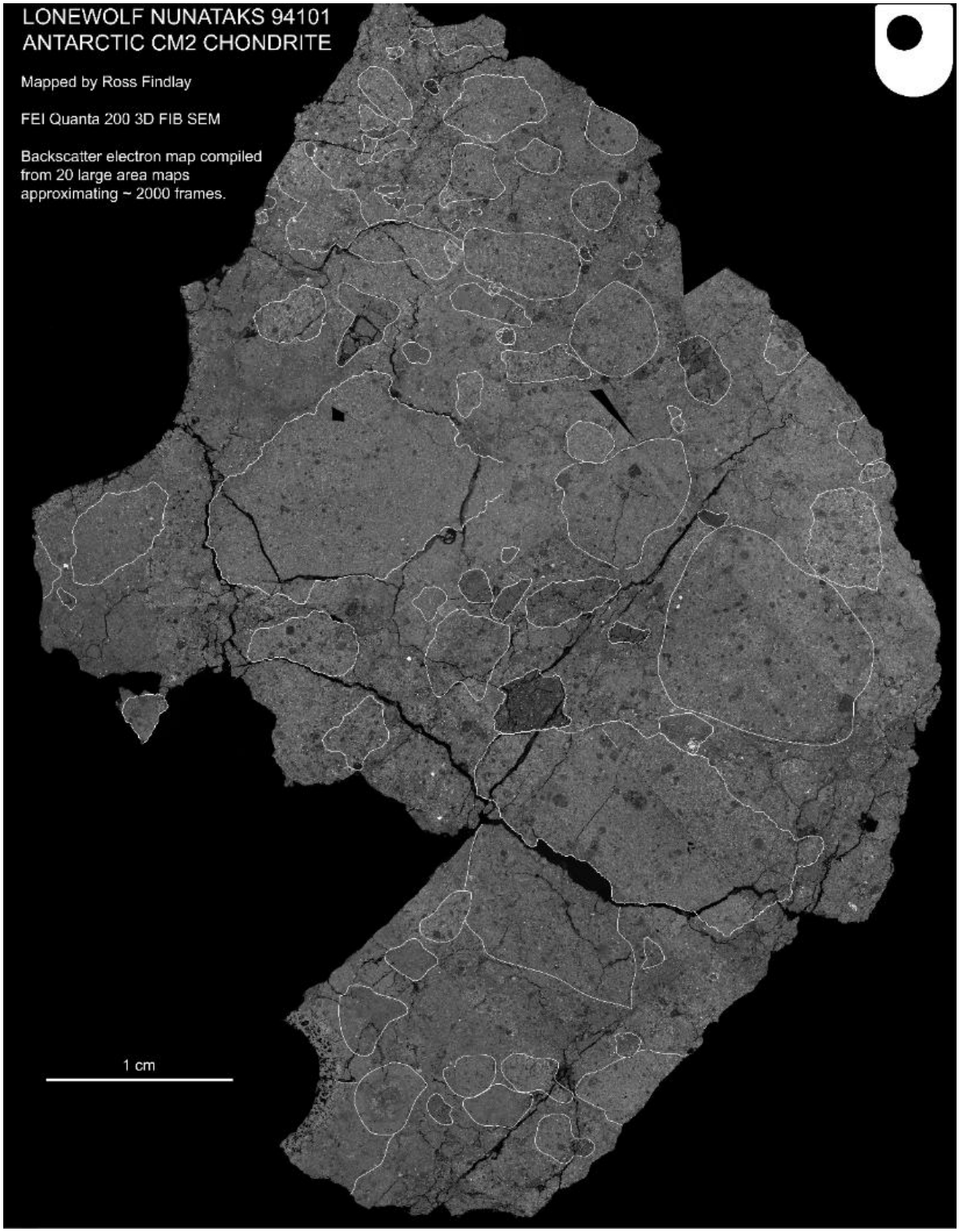

Figure 4.16- Navigation image for LON-04, showing the outline of some of the largest clasts identified in the preliminary examination. The region interstitial to the clasts is a cataclastic breccia composed of disturbed matrix and hundreds of micro-clasts.

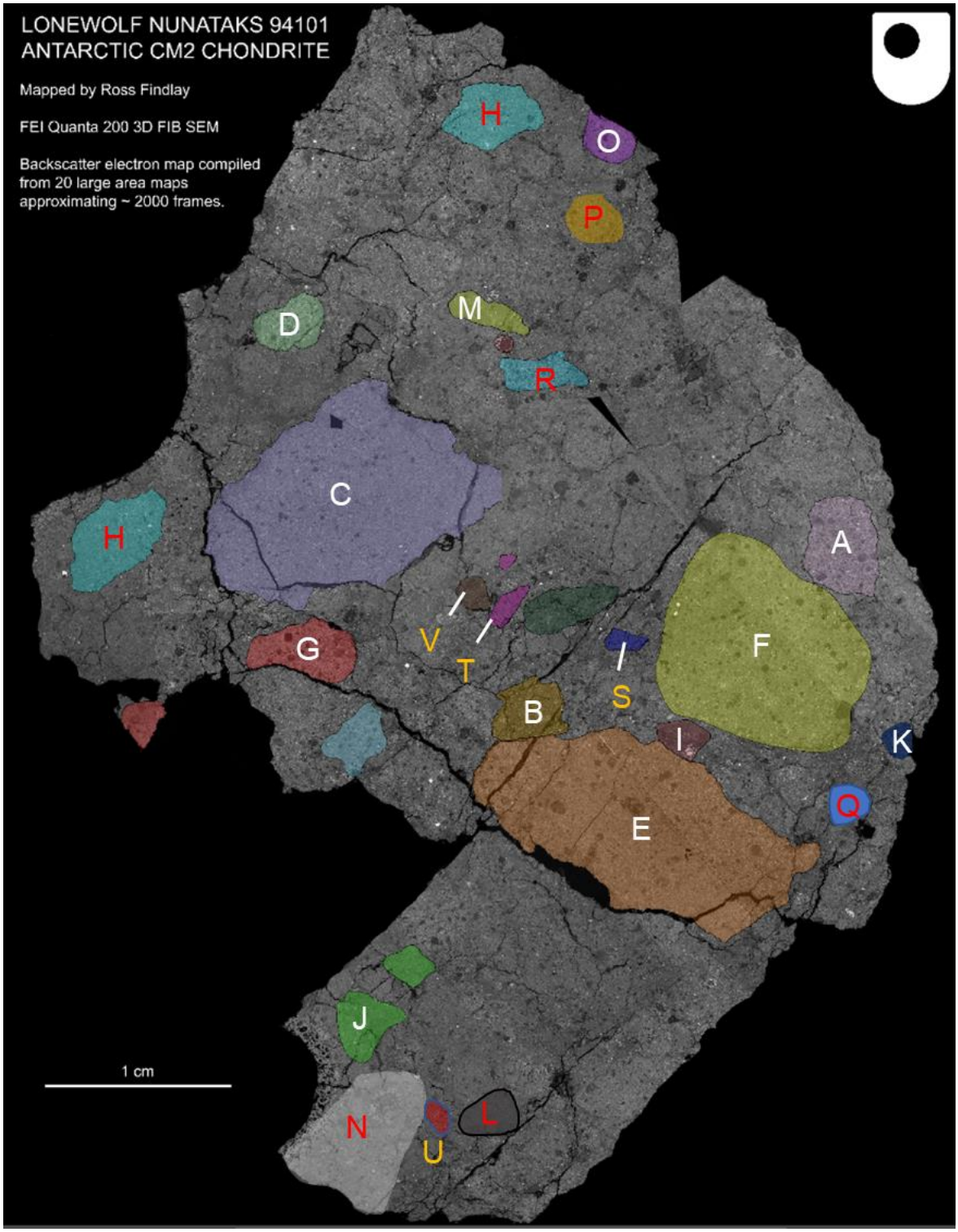

Figure 4.17 – Navigation image of LON-04 with the investigated clasts outlined. The desirable outcome was to select a group of clasts that spanned a large range of aqueous alteration phenomena. Each clast is labelled with a letter. Red letters indicate preliminary mapping. Yellow letters indicate preliminary mapping and detailed EDS investigation. White letters indicate preliminary mapping, detailed EDS investigation and oxygen isotope analysis. Only white and yellow letters are discussed from here on.

4.6.1 LON-04-A

LON-04-A is the least altered CM lithology studied here, occurring as a large, well-polished clast on the surface of the polished block (Fig 4.17, Plate 4.14). On immediate inspection, it is obvious this clast has only suffered incipient alteration as chondrules and chondrule fragments remain intact with sharp edges; and while much of the mesostasis has been converted to phyllosilicate, there are pockets of pyroxene and felspathic glassy material. Beads of kamacite and primary sulphide (troilite and pyrrhotite) are ubiquitously distributed within chondrules and the surrounding matrix (Plate 4.14). Nevertheless, this lithology has not escaped aqueous alteration entirely as S-rich phases, interpreted as tochilinite (type I TCI) are precipitated around chondrules and within the matrix (Plate 4.14, ROI 3). Curiously, the tochilinite also forms lenses, similar to cosmic symplectites in Acfer 094, though this relationship is speculative (Plate 4.14, ROI 2). Veins of Fe-rich material crosscut the section as much as 5-10 % in some areas (Plate 4.14, ROI 1). The EDS composition of the vein mineral is roughly 46 wt.% Fe and 22 wt.% O with only trace signals from other minerals. The totals are therefore low, ~ 77 % consistent with an undetectable component such as OH. An appropriate candidate for this stoichiometry could be goethite. Suspiciously, the 'goethite' exhibits a chlorine peak, suggesting that this may instead be akageneite, a Cl-bearing goethite commonly observed as a terrestrial weathering product in meteorite finds (Bland, 2006; Lee *et al.*, 2020; Lee and Bland, 2004); however, it is worth noting this mineral is not observed anywhere else in LON and does not crosscut the boundaries of the clast into the neighbouring CM2 material. Fractures crosscut the veins opening up voids, indicating the goethite did not take advantage of these pre-existing cracks in Antarctica. A brief circulation of a highly oxidising, Cl-rich fluid in the asteroid may leach Fe and S in a manner akin to terrestrial weathering (*e.g.,* similar in composition to the Ryugu fluid inclusion described in Nakamura *et al*. (2022)). Whether these phases are caused by weathering or processes endemic to the asteroid remains an open question. Spot EDS analyses of the homogenous matrix have slightly higher totals than most CMs (83 ± 10 %, n= 29),

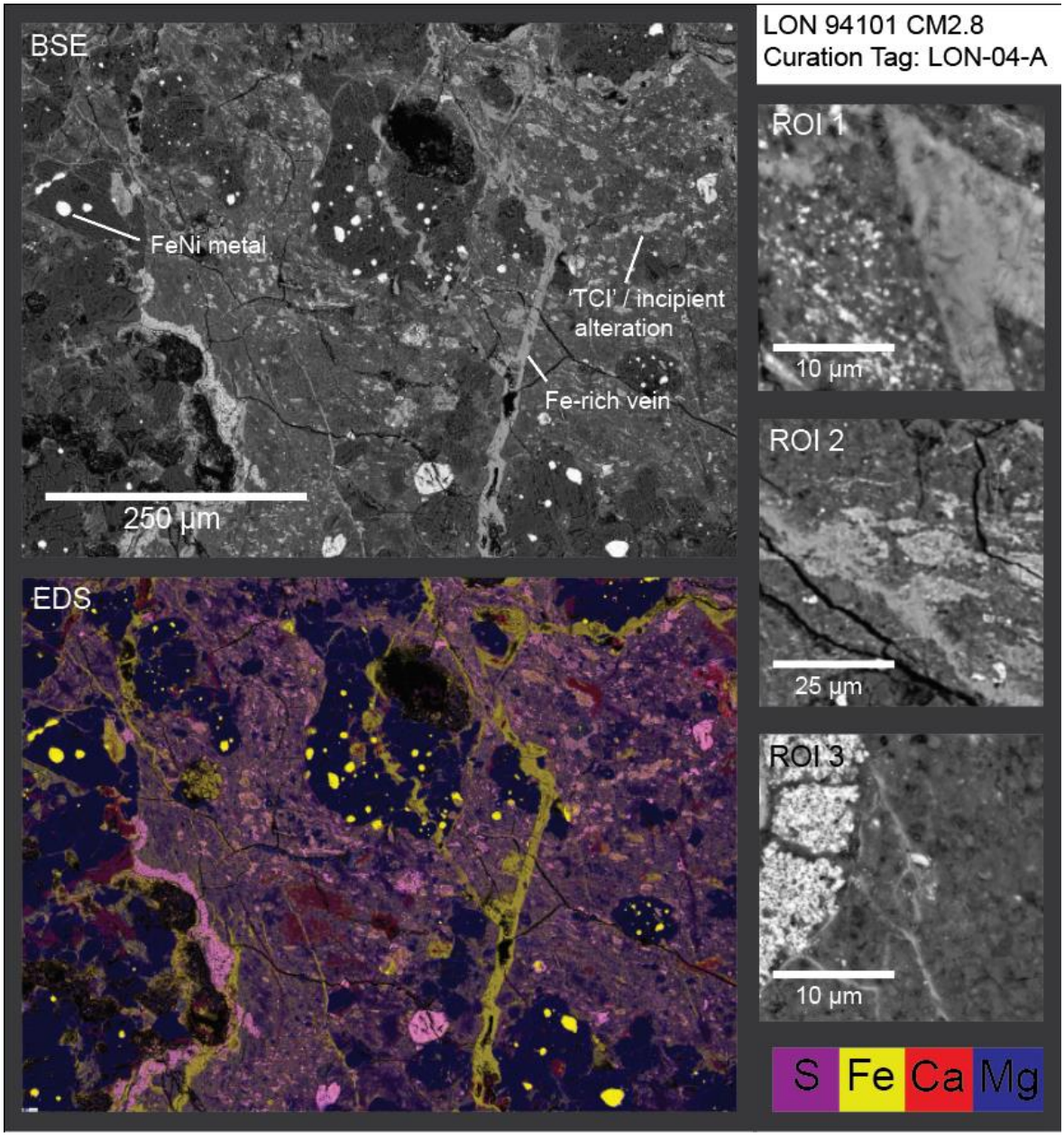

Phyllosilicates	**n**	**Area %**	**'FeO'/ SiO_2**	**S/SiO_2**	**Mg #**	**Totals**
TCI	8	10	15.25 ± 3.77	8.27 ± 2.27	8.82 ± 2.29	85.53 ± 1.48
Matrix	29	49.4	0.83 ± 0.10	**0.18** ± 0.03	52.88 ± 3.49	82.69 ± 1.82
Accessory minerals		**Area %**	**Form**			
Surviving precursors[#]		34.3	Chondrules. Undeterminable amount in fine-grained matrix			
Carbonates		<1	Small veinlets			
Sulphides		5.6	Primary troilite as large euhedral crystals and granular rims			
Chondrules						
Mesostasis	50 % replaced as phyllosilicate					
Phenocryst replacement	Fayalitic phenocrysts attacked. Forsteritic phenocrysts unaffected					
Rubin Subtype:	CM2.8					

Plate 4.14 –Area % = threshold estimates from polished block. [#]Evenly distributed within matrix (*i.e.*, not large chondrules). Uncertainties are 2SE. Totals are EDS oxide wt %.. ROI 1 Veins of Cl-rich iron oxide minerals precipitated within the matrix; ROI 2 – Lenses of S-rich lenses, likely an early form of TCI; ROI 3 – Sulphide rim and small iron-oxide veins within fine grained matrix.

supporting the claim that the matrix may only be partially hydrated. This lithology is not a typical CM, as chondrule abundance is higher than the CM average and interestingly, there are thin or absent accretionary rims surrounding chondrules. Neither does this lithology bear resemblance to the characteristics of CO chondrites (Weisberg *et al.,* 2006) owed to a noticeable phyllosilicate component and a higher matrix to chondrule ratio; rather, it is better classified as a C2-ungrouped. However, its presence within a CM2 dominated meteorite indicates a link to CM material due to the likelihood of re-accumulation during the brecciation process (Michel *et al.,* 2020; Michel and Richardson, 2013). While CM2.9 and CM2.8 subtypes have been reported elsewhere in the literature (*e.g.,* Lentfort *et al.,* 2021), truly incipiently altered lithologies lacking large TCI occurrences together with being confidentially identifiable as CMs are exceptionally rare, having only occurred once in Paris (Hewins *et al.,* 2014) and the Asuka CMs (although many, arguably 'CM-like' C2 and C3 ungrouped meteorites may indeed represent CM3 material, outlined in detail by Ruggiu *et al*. (2022)), the consequence of which is that this type of material has not yet been characterised in detail. This clast is a CM2.8.

4.6.2 LON-01-A

LON-01-A is most curious. It is a large clast, over 5 mm in the longest dimension (Fig 4.14). Uniquely, this is the only lithology observed within LON that shows a low degree of alteration while also being devoid of whole chondrules. It is, uniquely, matrix supported. Chondrule fragments of forsteritic composition are dotted throughout matrix which exhibits the highest 'FeO' content, and lowest Mg# of all meteoritic matrix (Fig 4.19) analysed in this study (the reader is referred to the caption of Plate 4.15 with respect to the accuracy of this data). Micron-grains of Fe-Ni metal, magnetite and sulphide are spread throughout the section alongside slightly larger grains of Ca-carbonate. The lithology is incipiently altered, lacks whole chondrules and is designated CM2.8m.

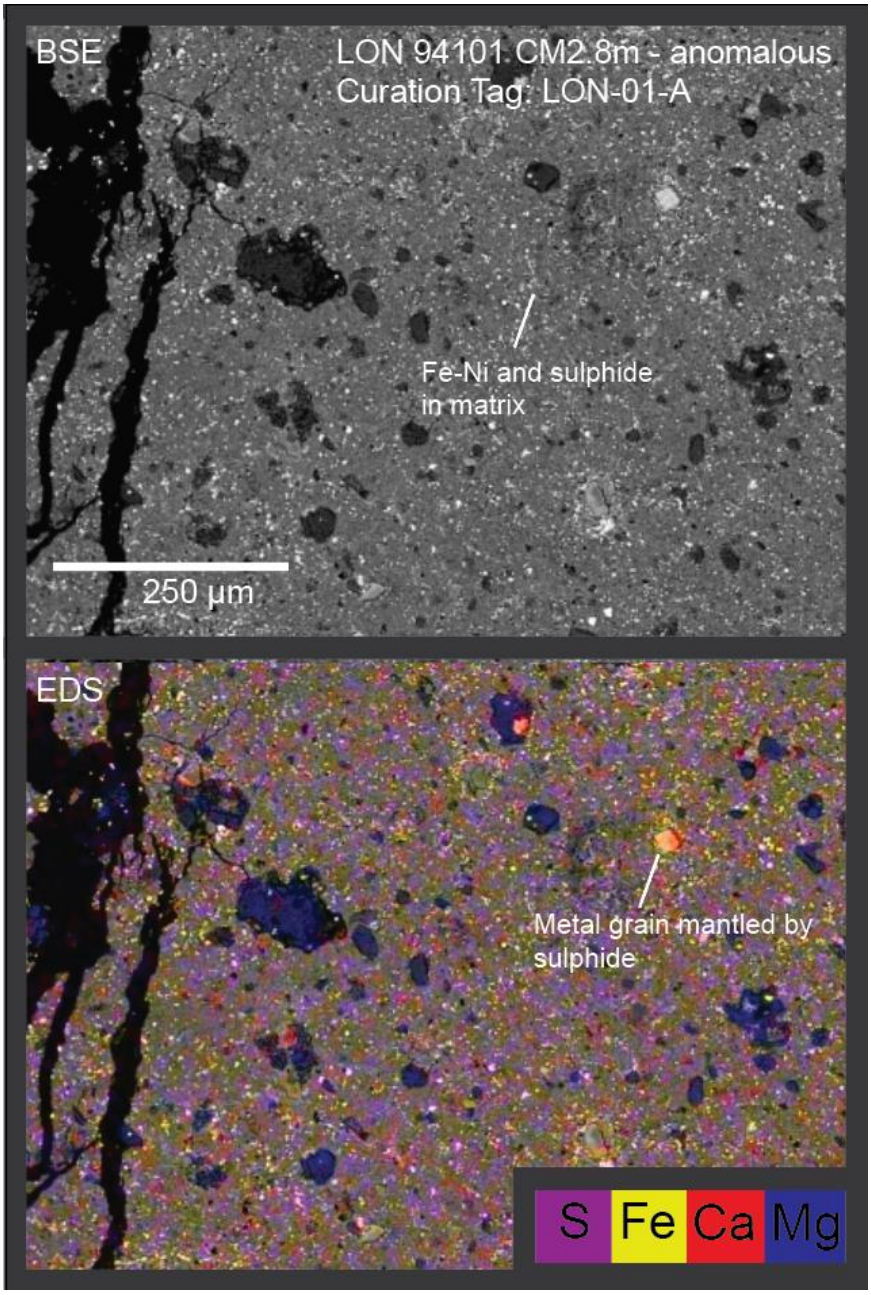

Phyllosilicates	**n**	**Area %**	**'FeO'/ SiO_2**	**S/SiO_2**	**Mg #**	**Totals**
TCI	-	-	-	-	-	-
Matrix	7		1.01 ± 0.17	0.15 ± 0.04	52.67 ± 5.0	-
Accessory minerals		**Area %**	**Form**			
Surviving precursors[#]		10	Mafic chondrule fragments < 150 µm			
Carbonates		2.0	Small <20 µm T0 Ca-carbonates			
Sulphides		1.2	Unknown			
Chondrules						
Mesostasis	Unaltered					
Phenocryst replacement	None					
Rubin Subtype:	CM2.8m - anomalous					

Plate 4.15 –Area % = threshold estimates from polished block. [#]Evenly distributed within matrix (*i.e.*, not large chondrules). Uncertainties are 2SE. Totals are EDS oxide wt %. EDS data in this section was obtained from normalised data taken from a low-resolution SEM map and is therefore semi-quantitative.

4.6.3 LON-04-D

In a similar vein to LON-04-A, LON-04-D has alteration textures that indicate lower levels of aqueous alteration (Plate 4.16). Metal and chondrule mesostasis has been altered to phyllosilicate and early generation, Type I TCI (Nakamura and Nakamuta, 1996; Tomeoka and Buseck, 1985; Vacher *et al.,* 2020), although chondrule phenocrysts of forsteritic and fayalitic composition remain unaltered. Sulphides are pentlandite with occasional pyrrhotite and sparse Ca-carbonate. Fine-grained matrix is present as accretionary rims surrounding chondrules as well as in between other components as a groundmass and has comparatively high abundances of Fe and S compared to more altered CM chondrites. While nominally observed within chondrules and regions of high metal concentration in other CMs, the type I TCIs are also ubiquitously present within the matrix as wormy, elongated grains lacking pseudomorphic shape. These TCIs have an orientation forming an interconnected network in places (Plate 4.16). The TCIs are Fe- and S-rich and comparatively Si poor when compared with other CMs and as such cannot readily be classified using the Rubin *et al.* (2007) criteria. However, providing equal weighting to the other metrics supports a CM2.7 classification.

4.6.4 LON-04-C

LON-04-C is the largest clast in LON-04 (Fig 4.17), at ~2.5cm^2, and offers a rare opportunity to assess the level of lithological homogeneity over a large cross-section. The clast has a relatively low percentage of chondrules (< 10 % by area) for CM2 material, but where present define chondrule-rich and chondrule-poor domains with gradational boundaries. Large porphyritic chondrules over ~500 μm are the most salient outliers to the texture (Fig 4.16), clustering loosely towards the left-hand side of the clast. Thick, homogenous accretionary rims surround each chondrule, proportional to the size of the latter, extending the overall dimension of each chondrule to 1 mm in parts. Complementary to the chondrules

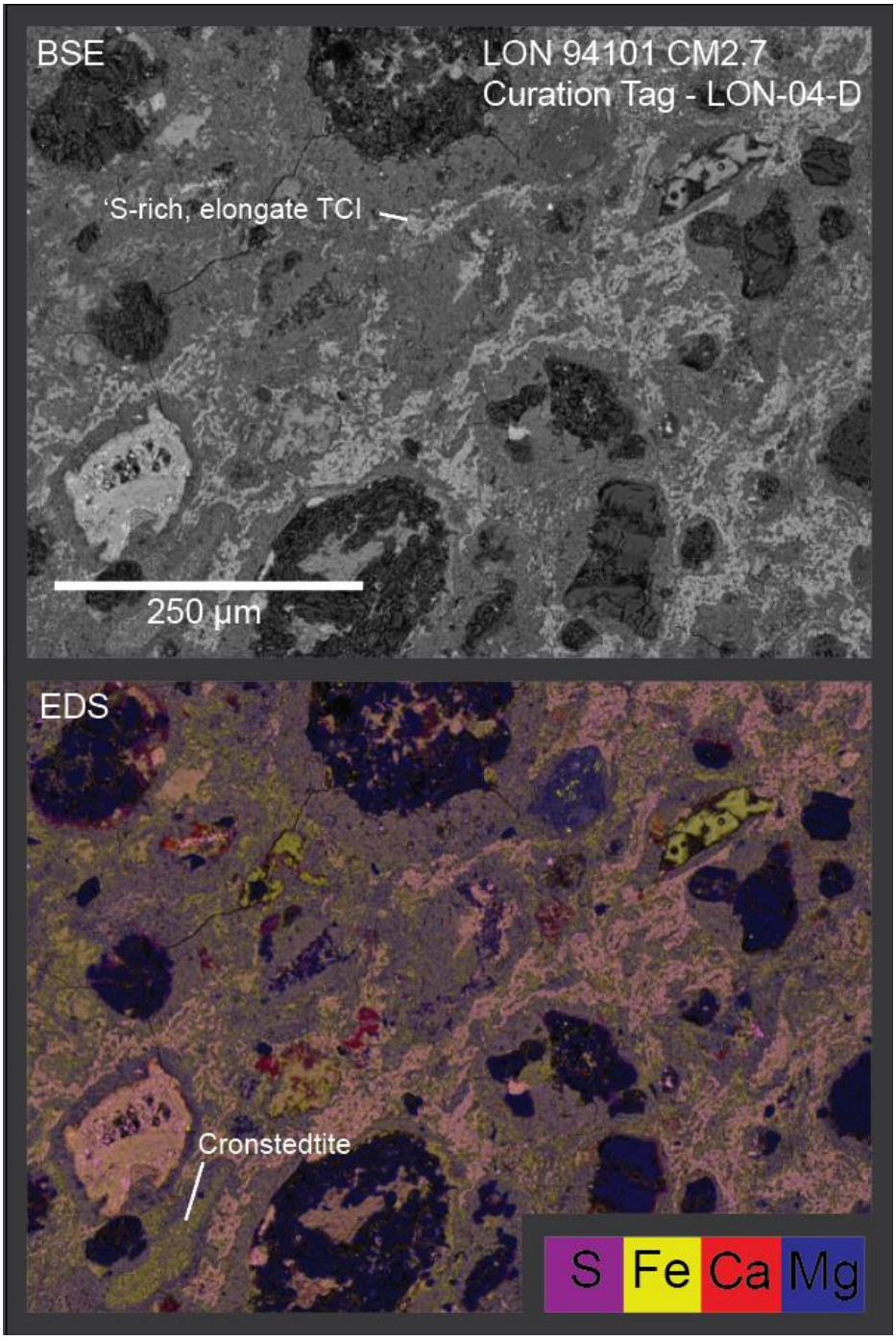

Phyllosilicates	**n**	**Area %**	**'FeO'/ SiO_2**	**S/SiO_2**	**Mg #**	**Totals**
TCI	22	13.6	11.01 ± 1.60	3.21 ± 0.48	23.26 ± 2.55	86.06 ± 1.10
Matrix	20	17.8	1.10 ± 0.08	**0.14** ± 0.01	48.77 ± 1.92	80.14 ± 1.83
Accessory minerals		**Area %**	**Form**			
Surviving precursors[#]		11.5	Small <20 µm Fo phenocrysts			
Carbonates		1.9	Small Ca-carbonates (T1?)			
Sulphides		1.2	Po + Pn			
Chondrules						
Mesostasis	Phyllosilicate					
Phenocryst replacement	None					
Rubin Subtype:	CM2.7					

Plate 4.16 –Area % = threshold estimates from polished block. [#]Evenly distributed within matrix (*i.e.,* not large chondrules). Uncertainties are 2SE. Totals are EDS oxide wt %.

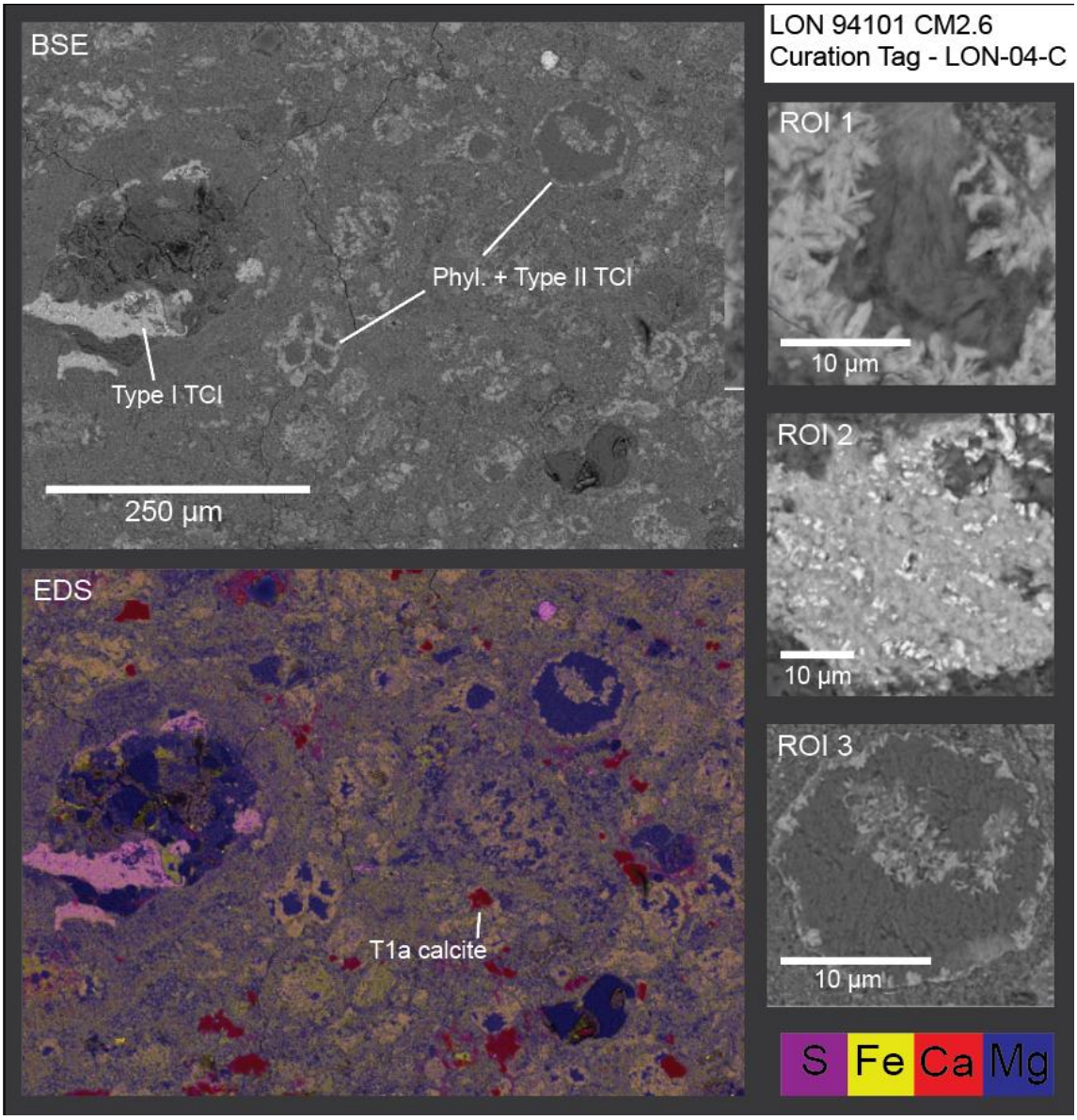

Phyllosilicates	**n**	**Area %**	**'FeO'/ SiO_2**	**S/SiO_2**	**Mg #**	**Totals**
TCI	12	21.0	4.44 ± 0.50	0.88 ± 0.13	21.93 ± 2.38	87.16 ± 1.13
TCI cores	11	72.7	0.38 ± 0.01	0.05 ± 0.00	78.72 ± 0.56	86.98 ± 1.69
Matrix	11		0.84 ± 0.14	0.07 ± 0.01	58.22 ± 5.60	80.56 ± 2.69
Accessory minerals		**Area %**	**Form**			
Surviving precursors[#]		3.1	Rare 50-100 µm Fo phenocrysts			
Carbonates		1.8	T1a Ca-carbonates			
Sulphides		1.4	Po + Pn			
Chondrules						
Mesostasis	Phyllosilicate					
Phenocryst replacement	0-5%					
Rubin Subtype:	CM2.6					

Plate 4.17 –Area % = threshold estimates from polished block. [#]Evenly distributed within matrix (*i.e.*, not large chondrules). Uncertainties are 2SE. Totals are EDS oxide wt %. ROI 1 –Thick needles of tochilinite and cronstedtite protrude into a phyllosilicate core of a type II TCI; ROI 2 – Type I TCI within a chondrule, with grains of sulphide; ROI 3 – Centripetal replacement of a precursor into a Type II TCI.

are clumpy, rounded ‘balls’ of matrix of similar size. Interstitials are TCIs of visually striking bimodal composition (Plate 4.17), also mantled by thin accretionary rims. Within the TCIs a high-contrast, outer rim of type II TCI material protrudes radially — with pointed, lath-like overgrowths — into a fibrous serpentine core, the composition of which is the most magnesium-rich of any serpentine measured in this work (Fig 4.18). The textures of these TCIs are consistent across the section, exhibiting 120° triple junctions internally, indictive of a polycrystalline precursor (Suttle *et al.*, 2023). *In situ* evidence of replacement of carbonate grains (T1a Ca-carbonates) suggest a plausible candidate for some, but not all of the TCIs. While others keep the same replacement texture, they lack such triple junctions (Plate 4.17, ROI 3). The phyllosilicate cores of the TCI indicate a sudden change from Fe- to Mg- controlled activity, and interestingly, pentlandite is present as the dominant sulphide. This clast is ambiguous as it contains components that are congruent with both moderate and high levels of alteration (Table 4.1); nevertheless, the compositional criteria of the TCI and the matrix predominantly support a 2.6 classification, in agreement with the unaltered chondrule phenocrysts.

4.6.5 LON-04-M

An unusual lithology, LON-04-M is made chiefly of fine-grained phyllosilicate matrix (Plate 4.18). Paradoxically, within the matrix are large, 200-300 μm wide, partially altered porphyritic chondrules. Remarkably, chondrule metal has partly survived, closely associated with massive magnetite (Plate 4.18). The small forsteritic olivine phenocrysts appear mostly unaltered, however the inter-crystal Ca-rich mesostasis has been altered into hotspots of Ca-Carbonate. The fine-grained matrix is predominantly featureless with pockets of metal and pyrrhotite ringlets. This clast is not readily classified by current methods as it lacks sufficient petrologic criteria (Rubin *et al.*, 2007), though the matrix composition is anomalously ‘FeO’-rich (Fig 4.19), indicating mild-moderate alteration in line with CM2.6. As this lithology is matrix dominated, it is appropriate to classify this as a CM2.6m-anomalous.

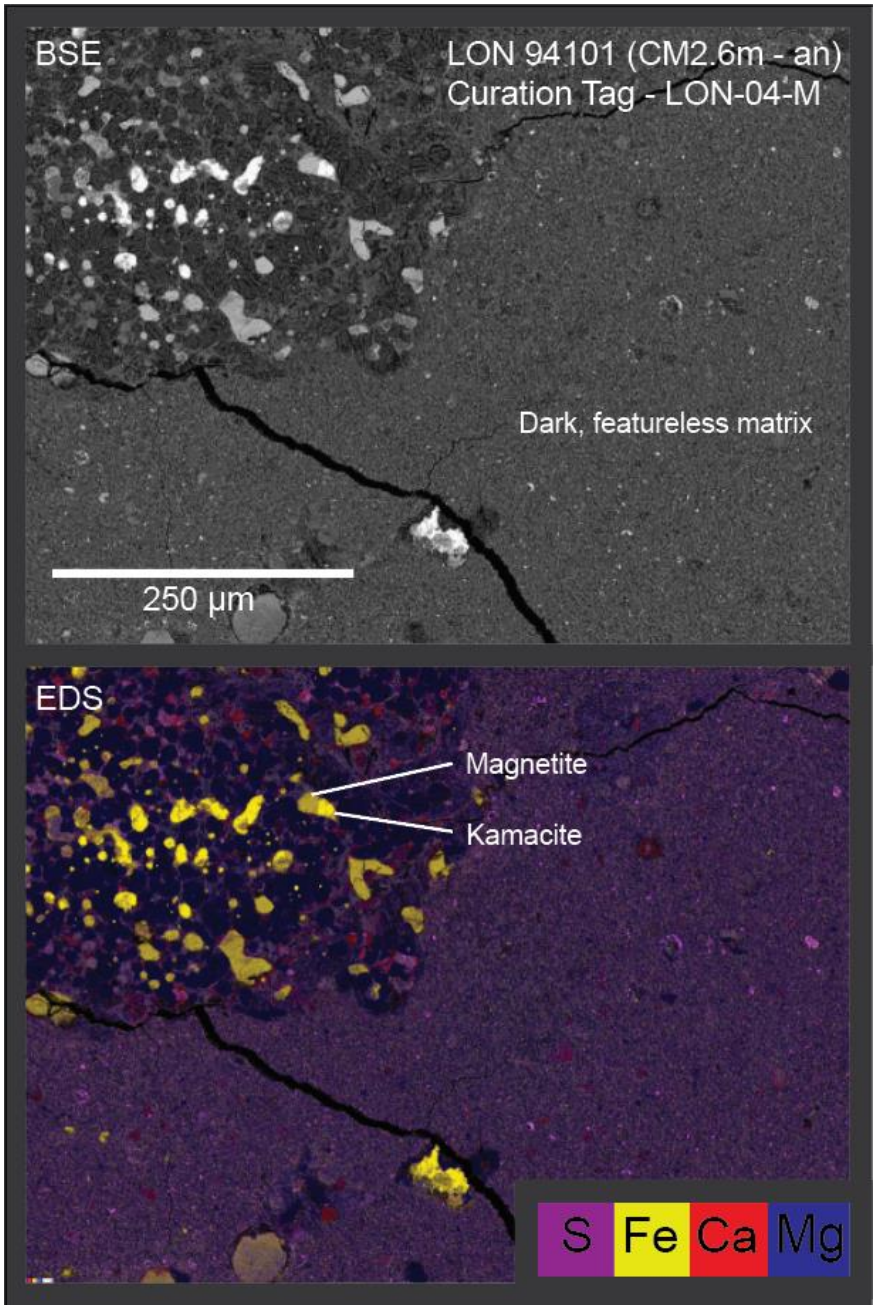

Phyllosilicates	**n**	**Area %**	**'FeO'/ SiO_2**	**S/SiO_2**	**Mg #**	**Totals**
Matrix	25	97.9	0.92 ± 0.08	0.13 ± 0.04	56.43 ±2.95	81.07 ± 1.73
Accessory minerals		**Area %**	**Form**			
Surviving precursors[#]		0.6	Tiny Fo crystals in matrix			
Carbonates		0.5	Small < 10 µm Ca-carbonate			
Sulphides		1.0	Po + Pn			
Chondrules						
Mesostasis	Phyllosilicate					
Phenocryst replacement	0-5 %					
Rubin Subtype:	CM2.6m -anomalous					

Plate 4.18 –Area % = threshold estimates from polished block. [#]Evenly distributed within matrix (*i.e.*, not large chondrules). Uncertainties are 2SE. Totals are EDS oxide wt %. A large, replaced matrix domain contains a partially altered, metal-bearing chondrule in the top left.

4.6.6 LON-04-O

LON-04-O is a rounded clast at the top of LON-04 (Fig 4.17). It contains forsteritic chondrules with little to no evidence of alteration except for the conversion of mesostasis to phyllosilicate. The TCIs are homogenous, with wavy, dendritic and pseudomorphic morphologies (Plate 4.19, ROI 1) and appear to be a transitional example between early type I TCI, such as those found in MP-01-B (Plate 4.1) and LON-04-D (Plate 4.16). Calcium carbonate is rare, and sulphides occur as small grains of stoichiometric pyrrhotite and pentlandite. As no intermediate sulphides are observed, the lithology suitably fits a 2.6 classification when considering its Fe and S-rich matrix (Fig 4.18).

4.6.7 LON-03a-B

LON-03a-B contains a substantial proportion of TCI and chondrule fragments, with the interstitial matrix that makes up the predominant share of the modal abundance at 67%. Small fragments of anhydrous Fo olivine are distributed throughout the section, often juxtaposed directly in contact with TCIs and phyllosilicate matrix. The TCIs are bright and high contrast retains excellent pseudo-crystal faces with 120° triple junctions (Plate 4.20, ROI 1 & 2), indicating replacement of a polycrystalline substrate, possibly carbonate (Suttle *et al.,* 2023). Chondrules are variably altered, some exhibiting partial to full replacement whereas others appear pristine. While the replacement of chondrules indicates pervasive alteration, the low Mg# of the matrix, coupled with the high ‘FeO’/SiO_2 of the TCI phases suggest modest interaction with a fluid on the scale of the section (Fig 4.18), supporting a CM2.5 classification.

4.6.8 LON-04-E

Akin to LON-04-C, LON-04-E is a large clast (Fig 4.17) with similar proportions of components, though subtly of a higher degree of aqueous alteration. Several large, 1-2 mm chondrules are present within the clast, while the remainder are of several hundred μm in size. A trait unique to this lithology is that many of the chondrules have abraded accretionary

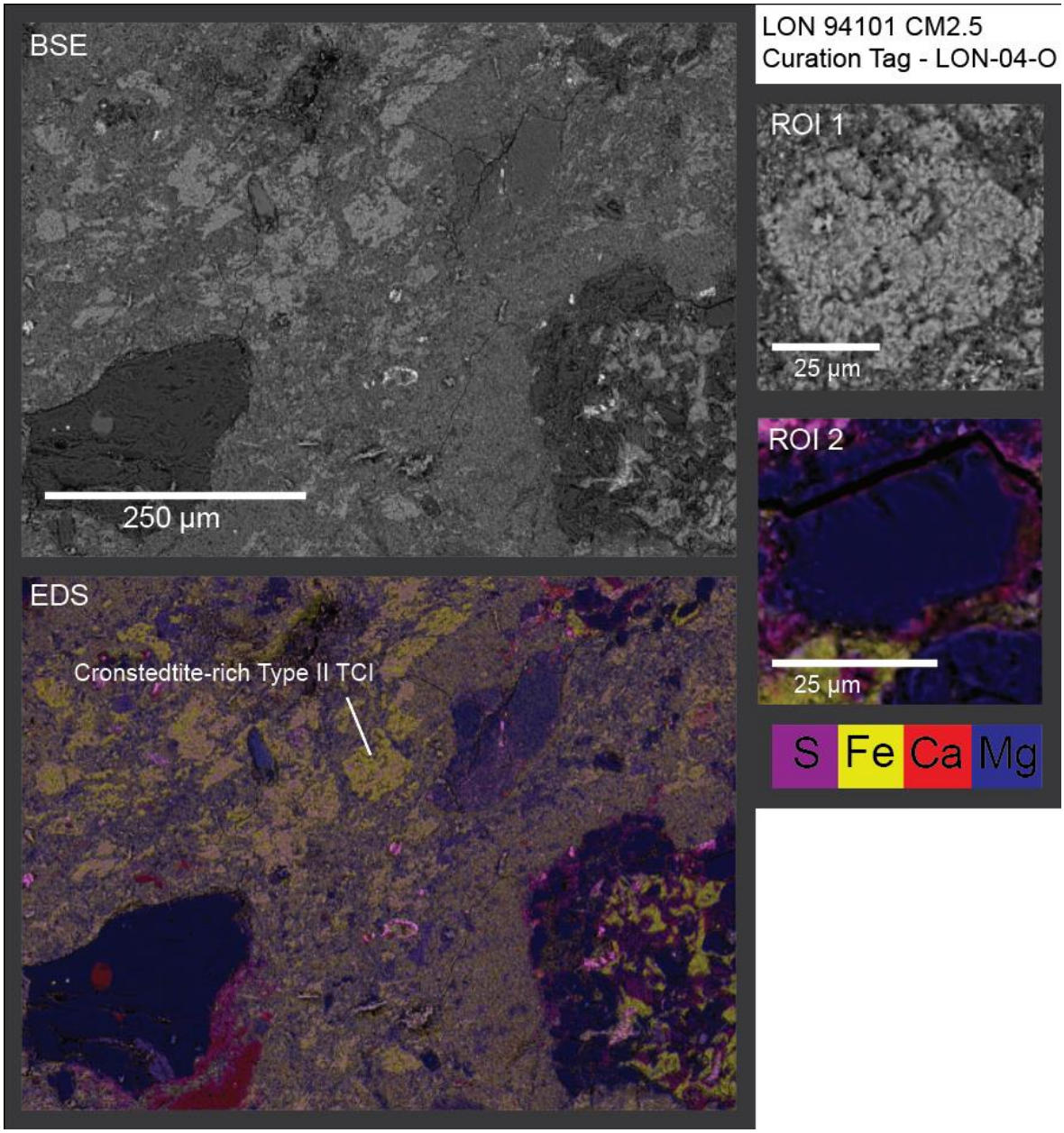

Phyllosilicates	**n**	**Area %**	**'FeO'/ SiO_2**	**S/SiO_2**	**Mg #**	**Totals**
TCI	15	42.1	1.98 ± 0.19	0.10 ± 0.06	30.58 ± 4.99	81.81 ± 1.68
Matrix	9	54.5	0.95 ± 0.08	0.18 ± 0.03	54.04 ± 2.89	82.16 ± 2.46
Accessory minerals		**Area %**	**Form**			
Surviving precursors[#]		1.0	Rare, tiny phenocrysts			
Carbonates		1.5	Ca-carbonate within chondrules			
Sulphides		1.0	Pn			
Chondrules						
Mesostasis	Phyllosilicate					
Phenocryst replacement	Heterogeneous, 5-15 %					
Rubin Subtype:	CM2.6					

Plate 4.19 –Area % = threshold estimates from polished block. [#]Evenly distributed within matrix (*i.e.*, not large chondrules). Uncertainties are 2SE. Totals are EDS oxide wt %. ROI 1 – Type II TCI; ROI 2 – Fo phenocryst with gypsum mantle.

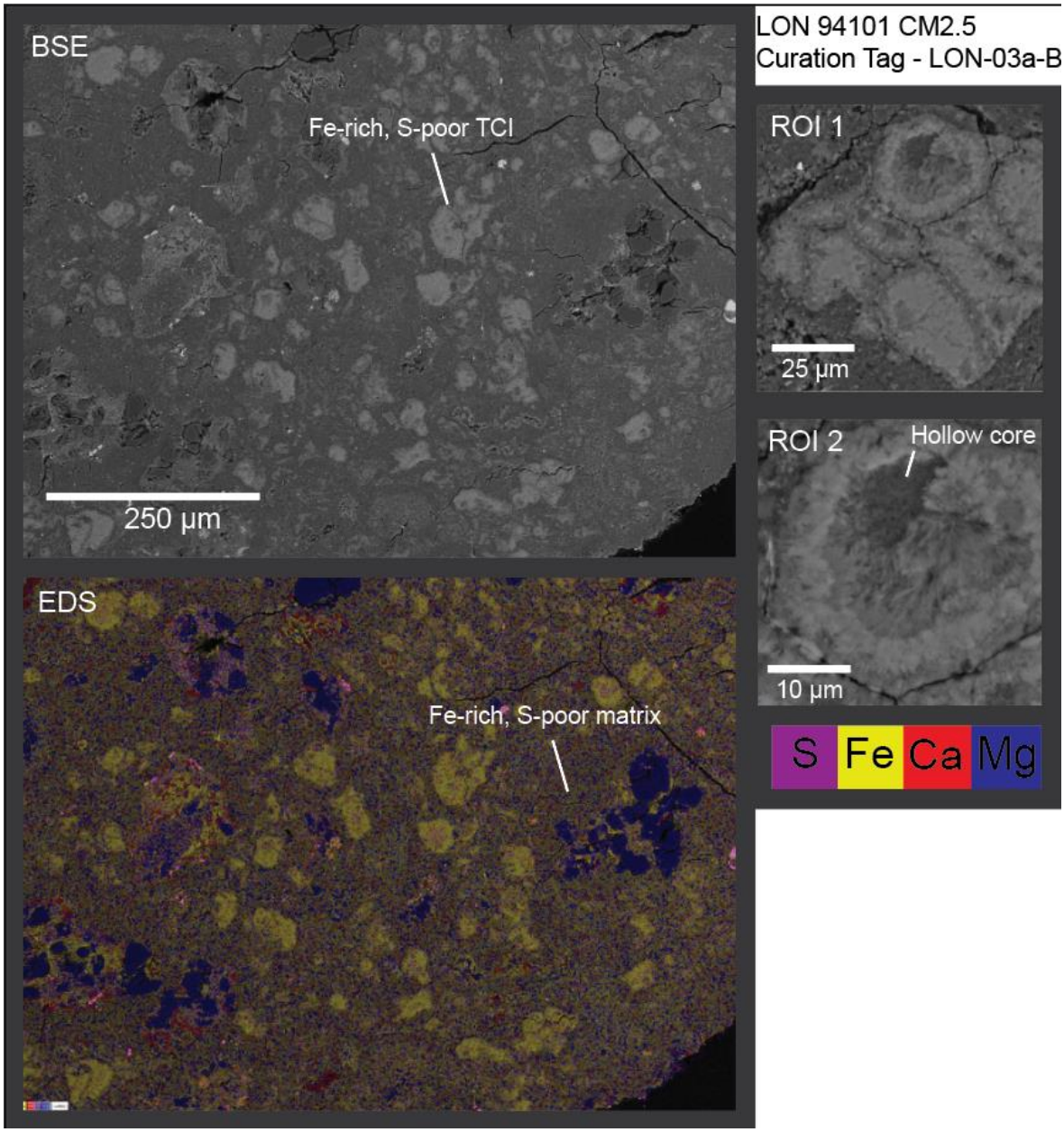

Phyllosilicates	**n**	**Area %**	**'FeO'/ SiO_2**	**S/SiO_2**	**Mg #**	**Totals**
TCI	67	25.2	3.69 ± 0.21	0.34 ± 0.08	29.59 ± 2.57	79.46 ± 0.42
Matrix	41	67.0	0.88 ± 0.09	0.06 ± 0.01	53.63 ± 1.99	71.99 ± 1.52
Accessory minerals		**Area %**	**Form**			
Surviving precursors[#]		2.8	<10 µm Fo phenocrysts			
Carbonates		1.2	Rare, sparse, Ca-carbonate			
Sulphides		1.5	Pn			
Chondrules						
Mesostasis	Phyllosilicate					
Phenocryst replacement	Very heterogeneous. Instances of both 80 % replacement, and unaltered.					
Rubin Subtype:	CM2.5					

Plate 4.20 –Area % = threshold estimates from polished block. [#]Evenly distributed within matrix (*i.e.,* not large chondrules). Uncertainties are 2SE. Totals are EDS oxide wt %.. ROI 1 –Cluster of TCI with 120° triple junctions, indicative of a polycrystalline precursor; ROI 2 – Close up of ROI 1, showing fibrous phyllosilicate and a partially hollow core.

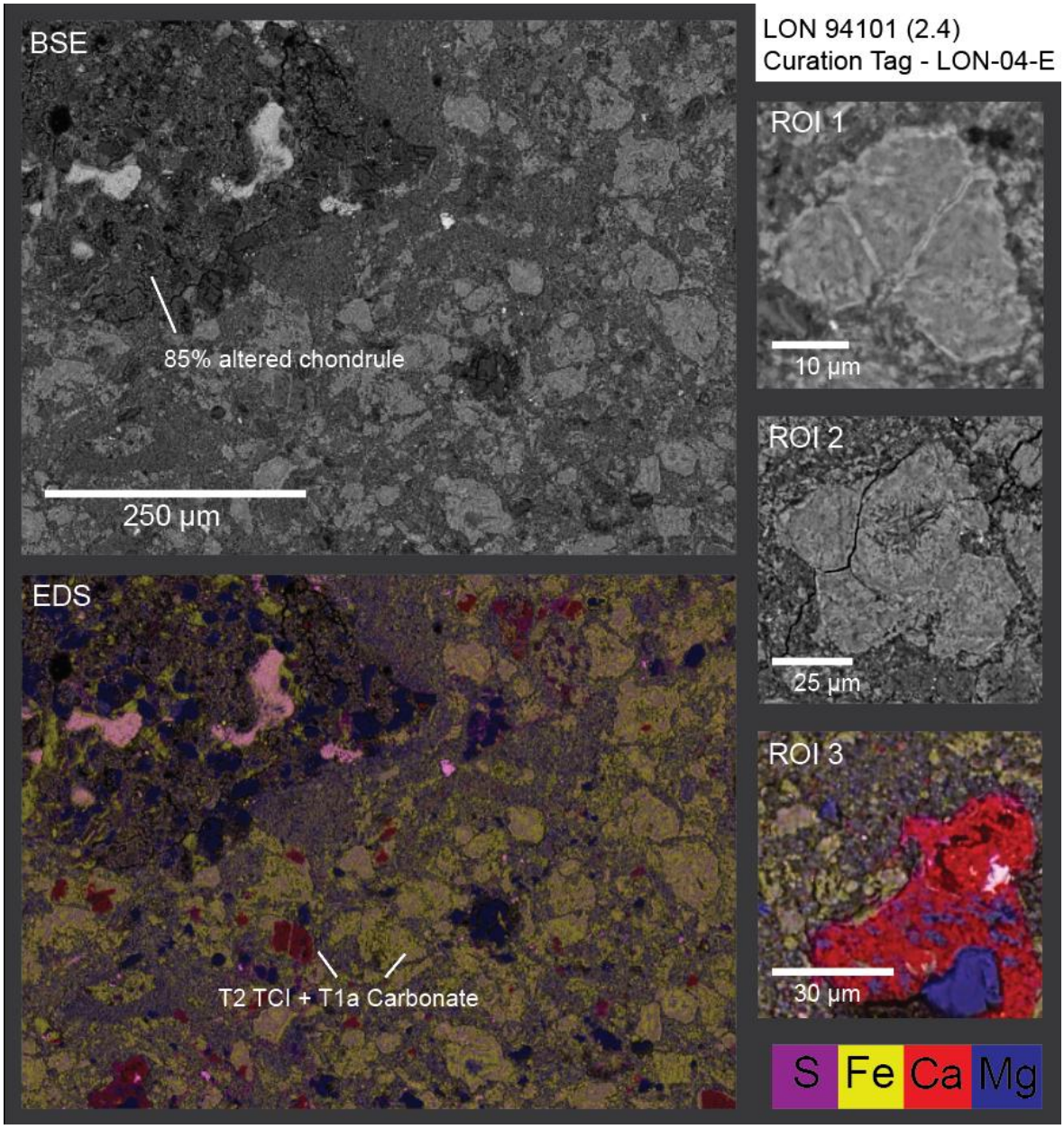

Phyllosilicates	**n**	**Area %**	**'FeO'/ SiO_2**	**S/SiO_2**	**Mg #**	**Totals**
TCI	21	25.3	2.95 ± 0.43	0.41 ± 0.16	26.44 ± 2.22	86.57 ± 1.08
TCI cores	20	68.0	1.60 ± 0.09	0.30 ± 0.02	46.46 ± 1.71	86.99 ± 2.05
Matrix	20		0.64 ± 0.07	0.07 ± 0.01	65.32 ± 2.37	79.57 ± 2.22
Accessory minerals		**Area %**	**Form**			
Surviving precursors[#]		2.2	< 20 µm Fo crystals			
Carbonates		2.7	T1a and rare T2 Ca-carbonates			
Sulphides		1.8	Pn + Int			
Chondrules						
Mesostasis	Phyllosilicate					
Phenocryst replacement	5-15%					
Rubin Subtype:	CM2.4					

Plate 4.21 –Area % = threshold estimates from polished block. [#]Evenly distributed within matrix (*i.e.*, not large chondrules). Uncertainties are 2SE. Totals are EDS oxide wt %.. ROI 1 – TCI with triple junctions; ROI 2 – TCI with hollow core; ROI 3 – Olivine grain replaced by calcium carbonate.

rims on one side, exposing the inner, porphyritic olivine chondrules to the TCI-rich matrix. Paradoxically, the chondrules suffer little alteration with exception of the mesostasis. TCIs are in general, relatively uniform (Plate 4.21, ROI 1 & 2), though clearly sourced from polycrystalline precursors. The TCIs define a core and rim structure, with the outer rim a thin veneer of comparatively higher Fe and S content than the core (Plate 4.21 ROI 1). The inner TCI is quite sulphur rich with a S/SiO_2 ratio of 0.30 and a moderate Mg# of 46, indicating less of a disequilibrium between core and rim than typically observed in TCIs nominally hosting phyllosilicate clumps (Fig 4.18). Very small phenocrysts of forsterite are evenly distributed within the matrix and sulphides are pentlandite plus intermediates. Ca-carbonates are all of the T1a variety. The compositional criterion of this lithology is hard to group, but the level of alteration experienced by the chondrules, the nature of the sulphides, and the composition of the matrix indicate this is a CM2.4 lithology.

4.6.9 LON-04-F

LON-04-F is the third lithology of a triad of larger clasts over 1 cm in the longest dimension (Fig 4.17), the others being LON-04-C and LON-04-E. While the alteration conditions of this lithology are comparable to LON-04-E, it has higher chondrule abundance, though on average the variation in chondrule size is less extreme than the latter two lithologies. Very clear-cut, complete accretionary rims surround the chondrules (Plate 2.22). The TCI structures are limited to a wormy, meshwork-like texture mantling very dark phyllosilicate clumps and T1a Ca-carbonates (Plate 2.22, ROI 3), and as dendritic-like textures in the matrix. The dark phyllosilicate cores are very disequilibrated from their Fe-rich rims, possessing a Mg# of 75, on par with the composition of matrix from the most aqueously altered lithologies studied here (*e.g.*, LON-04-K). The T1a Ca-carbonates are incomplete in some localities and are partially replaced by the phyllosilicate cores. Pentlandite and sulphides of intermediate composition are the main sulphide generations. Like LON-04-E, this lithology is a CM2.4, but with different TCI structures and matrix content.

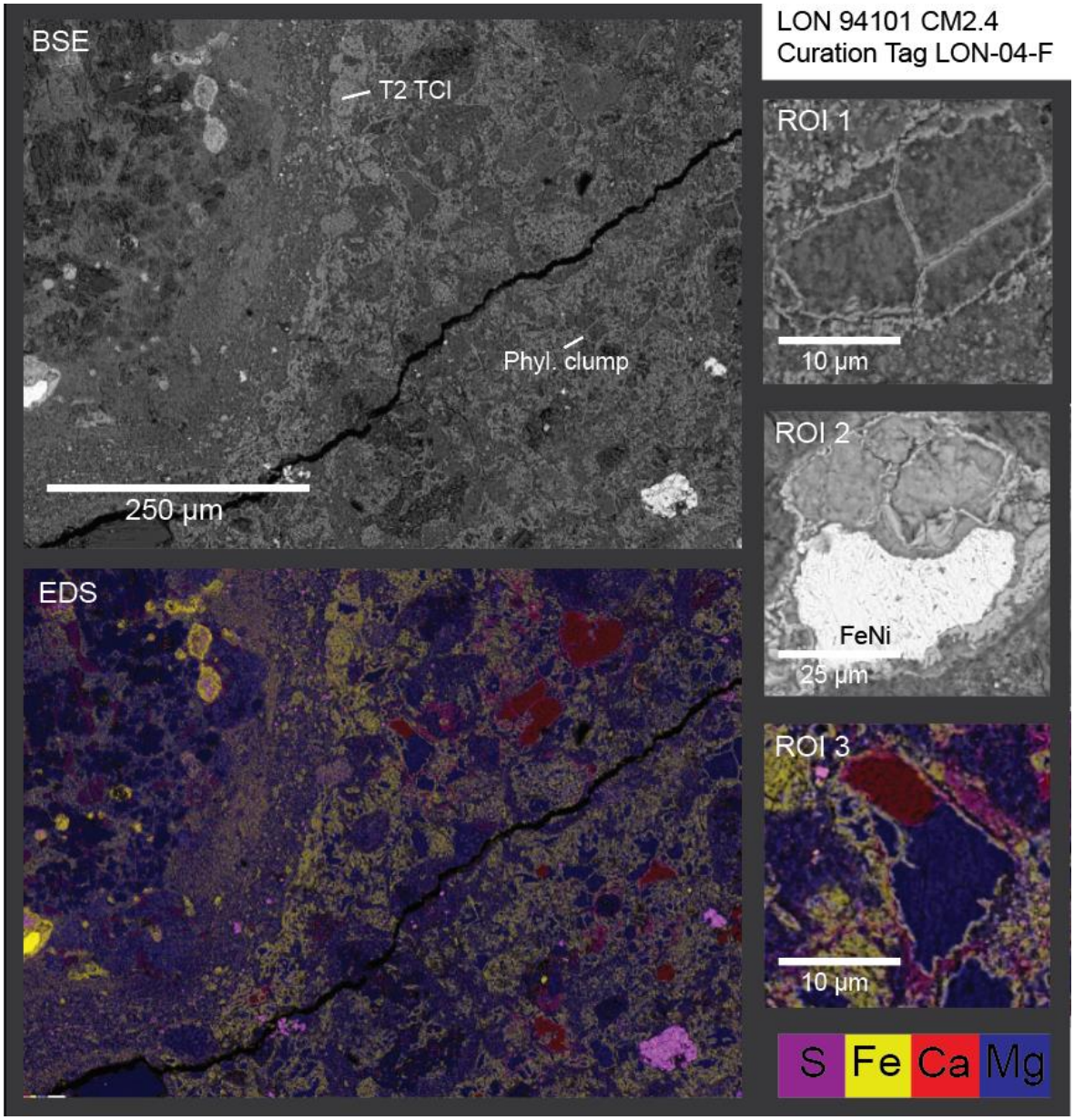

Phyllosilicates	**n**	**Area %**	**'FeO'/ SiO_2**	**S/SiO_2**	**Mg #**	**Totals**
TCI	11	13.2	2.53 ± 0.60	0.09 ± 0.07	25.32 ± 5.87	85.00 ± 0.82
TCI Cores	11	80.2	0.45 ± 0.07	0.07 ± 0.02	75.98 ± 2.44	86.15 ± 2.65
Matrix	11		0.65 ± 0.10	0.10 ± 0.03	64.74 ± 3.82	80.57± 5.33
Accessory minerals		**Area %**	**Form**			
Surviving precursors[#]		2.4	< 30 µm Fo phenocrysts within matrix			
Carbonates		2.2	T1a Ca-carbonate			
Sulphides		2.0	Pn + Int			
Chondrules						
Mesostasis	Phyllosilicate					
Phenocryst replacement	5-15 %					
Rubin Subtype:	CM2.4					

Plate 4.22 –Area % = threshold estimates from polished block. [#]Evenly distributed within matrix (*i.e.*, not large chondrules). Uncertainties are 2SE. Totals are EDS oxide wt %.. ROI 1 – A thin TCI rim hosts a phyllosilicate core; ROI 2 – replacement of a Fe-Ni grain with type I TCI; ROI 3 – a phyllosilicate core replacing a T1a carbonate grain in a type II TCI.

4.6.10 LON-03a-A

This lithology is a textbook example of moderate to severe aqueous alteration (Fig 4.15). Anhydrous fragments are relatively rare, instead occurring as total pseudomorphic replacement products (Plate 4.23, ROI 1). TCIs constitute over 50 % of the surface area; are low contrast; harbour low 'FeO'/SiO_2 and have pronounced, platy/fibrous core and rim structures (Plate 4.23, ROI 1). The TCI cores are compositionally similar to the matrix material surrounding them, except they are enriched in sulphur. Akin to MP-01-A and AZ-04-C, the TCIs exhibit a strong, albeit heterogeneous petrofabric, appearing elongated and squashed in certain areas of the section, yet circular in others. This lithology is a CM2.2.

4.6.11 LON-01-B

LON-01-B outcrops as a lozenge shaped clast in the bottom left of the LON-01. It was selected as a result of its very high contrast (Fig 4.14). Upon close inspection, this lithology shows near-complete alteration with chondrule pseudomorphs retaining a tiny percentage of unaltered forsterite (Plate 4.24). Interestingly, TCIs with sharp pseudomorphic boundaries and accretionary rims are widespread. This is the sole instance of a very altered lithology with TCIs of bright contrast, owed to a very high sulphur content ($S/SiO_2 = 0.49 \pm 0.04$) (the reader is referred to the caption of Plate 4.24 with respect to the accuracy of this data). On the other hand, the compositional data from the matrix agrees with a high level of alteration. Sulphide grains are absent in this section, presumably due to sequestration of the sulphur into TCIs, and carbonates are exclusively T1a Ca-carbonates. The petrologic criteria indicate a CM2.1 classification.

4.6.12 LON-04-G

The surface area of LON-04-G comprises 63.6 % of heterogeneous, variably sized, porous TCI, the most observed in any lithology. The rare chondrules embedded within the TCI-rich matrix are only partially altered, but the compositional criteria strongly suggest a low petrologic subtype; however, the sulphur contents of the matrix are high relative to silicate,

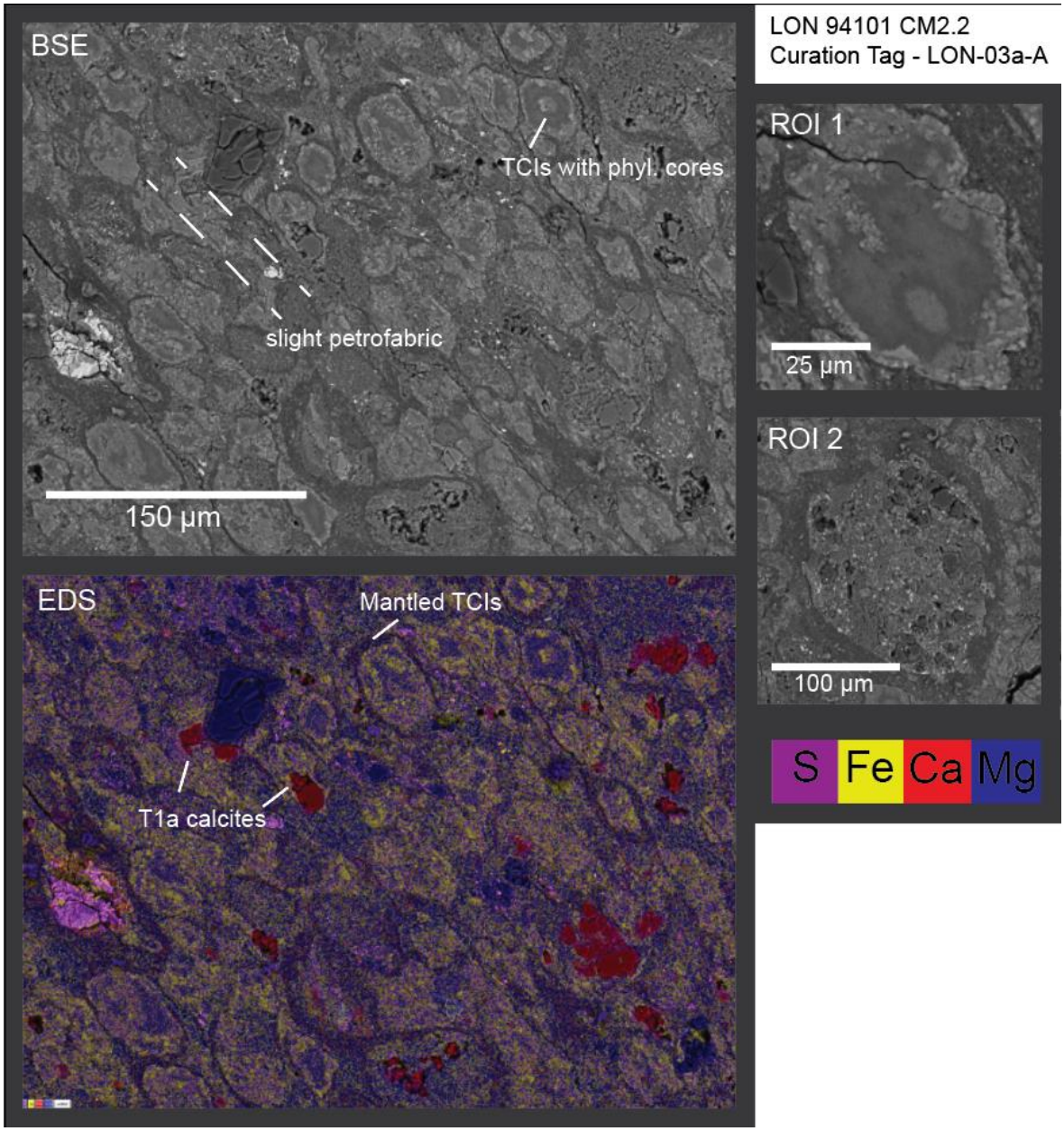

Phyllosilicates	**n**	**Area %**	**'FeO'/ SiO_2**	**S/SiO_2**	**Mg #**	**Totals**
TCI	30	50.4	1.71 ± 0.18	0.12 ± 0.03	36.78 ± 4.78	82.95 ± 0.57
TCI cores	20	39.5	0.84 ± 0.07	0.17 ± 0.02	63.11 ± 1.76	82.25 ± 1.92
Matrix	18		0.65 ± 0.03	0.05 ± 0.01	63.38 ± 1.60	80.51 ± 3.23
Accessory minerals		**Area %**	**Form**			
Surviving precursors[#]		3.0	Very rare Fo phenocrysts			
Carbonates		2.6	T1a Ca-carbonate			
Sulphides		4.5	Pn			
Chondrules						
Mesostasis	Phyllosilicate					
Phenocryst replacement	15 – 85 %					
Rubin Subtype:	CM2.2					

Plate 4.23 –Area % = threshold estimates from polished block. [#]Evenly distributed within matrix (*i.e.*, not large chondrules). Uncertainties are 2SE. Totals are EDS oxide wt %.. ROI 1 – Type II TI with core and rim; ROI 2 – Partial chondrule pseudomorph.

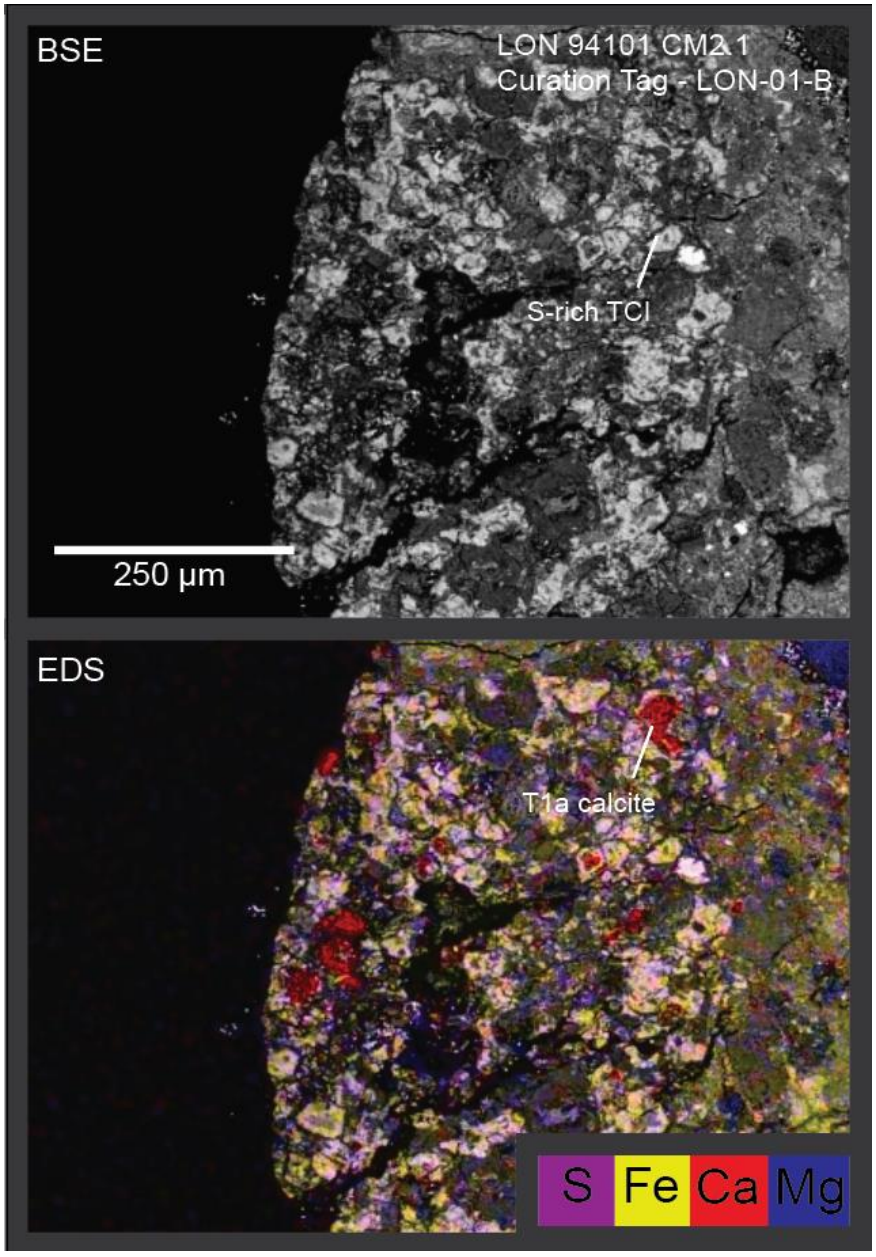

Phyllosilicates	**n**	**Area %**	**'FeO'/ SiO_2**	**S/SiO_2**	**Mg #**	**Totals**
TCI	6	31.4	1.96 ± 0.22	0.49 ± 0.04	25.93 ± 4.14	-
Matrix	5	57.6	0.57 ± 0.10	0.04 ± 0.03	65.04 ± 1.88	-
Accessory minerals		**Area %**	**Form**			
Surviving precursors[#]		2.0	Rare Fo crystals			
Carbonates		1.1	T1a Ca-carbonate			
Sulphides		1.5	Unknown			
Chondrules						
Mesostasis	Replaced					
Phenocryst replacement	> 90 %					
Rubin Subtype:	CM2.1					

Plate 4.24 –Area % = threshold estimates from polished block. [#]Evenly distributed within matrix (*i.e.*, not large chondrules). Uncertainties are 2SE. Totals are EDS oxide wt %. EDS data in this section was obtained from normalised data taken from a low-resolution SEM map and is therefore semi-quantitative.

an anomalous characteristic for a lithology of pervasive alteration. Uniquely, LON-04-G contains a very rare example of a chondrule with a partial inner-rim of TCI material interior to the main accretionary rim (Plate 4.25), lending support to an *in situ* origin for the TCIs in this lithology. Three generations of sulphide are present in pentlandite, pyrrhotite and intermediate sulphides, with pyrrhotite the least abundant. Ca-carbonates are strictly of the T1a variety. This lithology is transitional between CM2.1 and CM2.2 but is classified as the former due to a larger proportion of classification criteria falling within this threshold.

4.6.13 LON-04-I

Another pervasively altered lithology type, LON-04-I contains no TCIs and very few surviving olivine fragments, characterised instead by an assortment of larger chondrule pseudomorphs (up to 500 μm in width) with exceptional preservation of pseudo-crystal faces (Plate 4.26). LON-04-I is unique in that each chondrule is surrounded by an alteration halo of pyrrhotite laths, a texture previously reported once in the C1-ungrouped meteorite Flensburg (Bischoff *et al.*, 2021). Despite the pervasive alteration and the presence of dolomite, the Mg content of the chondrule pseudomorphs matrix are, surprisingly, not among the highest observed (Fig 4.19). LON-04-I therefore represents an area of pervasive and complete alteration with moderate, but not severe, Mg enrichment. Also of note are splotches of Mg-rich sulphate, which may be a weathering product. This clast is a CM1.

4.6.14 LON-04-J

A pervasively altered lithology, LON-04-J is dominated by Mg-rich serpentines; laths of Ni-rich pentlandite spotted throughout the matrix; two striking generations of T2 calcium and magnesium carbonate; and chondrule pseudomorphs (Plate 4.27). No anhydrous precursors remain. Magnetite and sulphide occur as intergrown plaquettes. Closer inspection reveals a range of coarse- and fine-grained phyllosilicate structures with spinach textures (Plate 4.27, ROI 2 & 3), however the range of 'FeO' compositions is quite restricted and only observable at higher magnification. This clast is fully altered and is therefore a CM1.

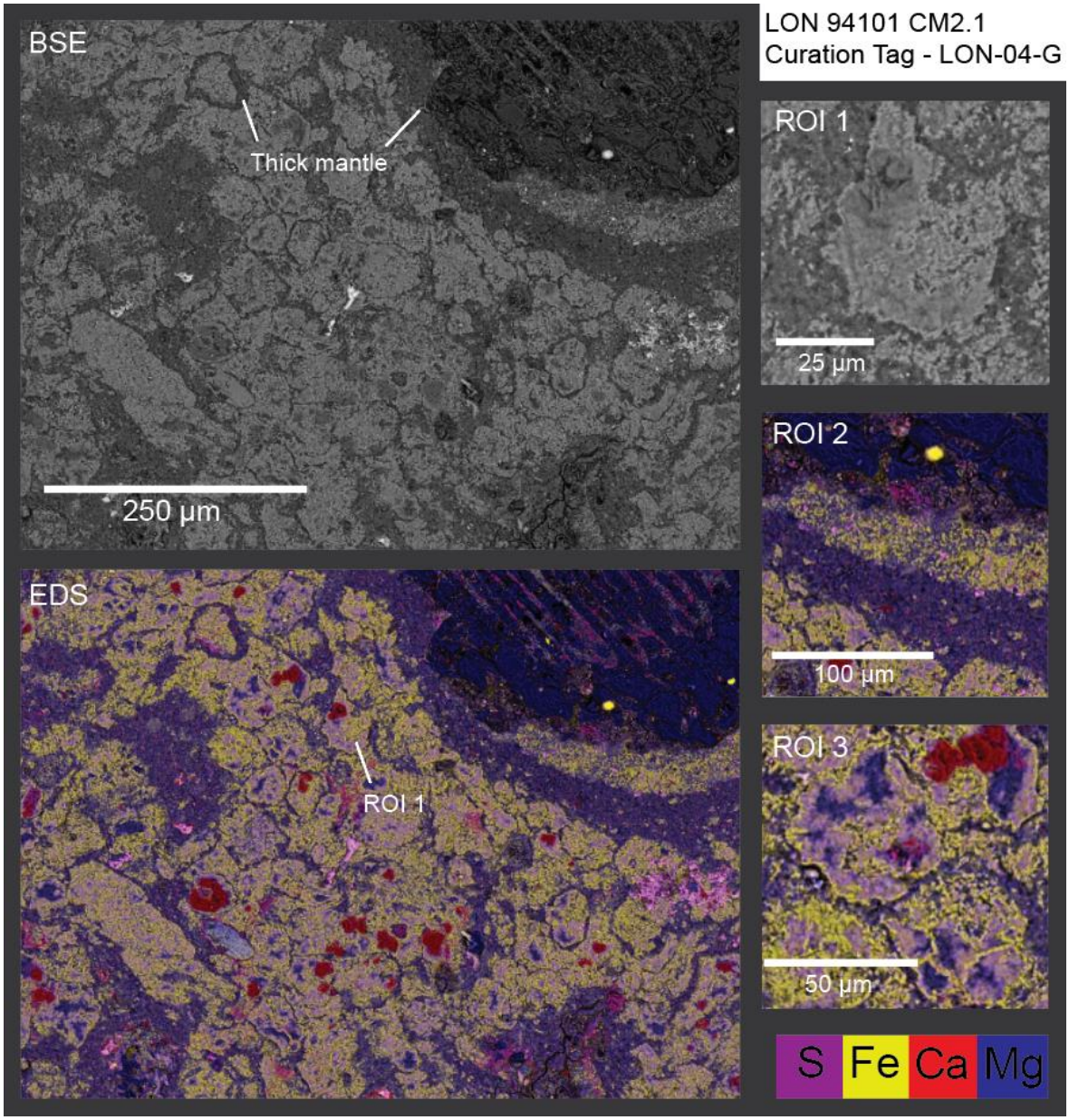

Phyllosilicates	**n**	**Area %**	**'FeO'/ SiO_2**	**S/SiO_2**	**Mg #**	**Totals**
TCI	10	63.6	1.82 ± 0.73	0.07 ± 0.02	32.81 ± 5.94	84.96 ± 0.66
TCI cores	12	34.0	1.68 ± 0.13	0.29 ± 0.04	45.04 ± 1.79	83.93 ± 0.74
Matrix	18		0.89 ± 0.04	0.20 ± 0.02	67.69 ± 1.09	77.83 ± 2.70
Accessory minerals		**Area %**	**Form**			
Surviving precursors[#]		0.2	Very rare Fo fragments			
Carbonates		1.4	T1a Ca-carbonates			
Sulphides		0.8	Pn + Int > Po			
Chondrules						
Mesostasis	Phyllosilicate					
Phenocryst replacement	Variable 5-90 %					
Rubin Subtype:	CM2.1					

Plate 4.25 –Area % = threshold estimates from polished block. [#]Evenly distributed within matrix (*i.e.,* not large chondrules). Uncertainties are 2SE. Totals are EDS oxide wt %.. ROI 1 – A homogenous type II TCI; ROI 2 – Chondrule rim with an inner zone of TCI-rich material; ROI 3 – Polycrystalline TCI structures with hollow, Mg-rich cores.

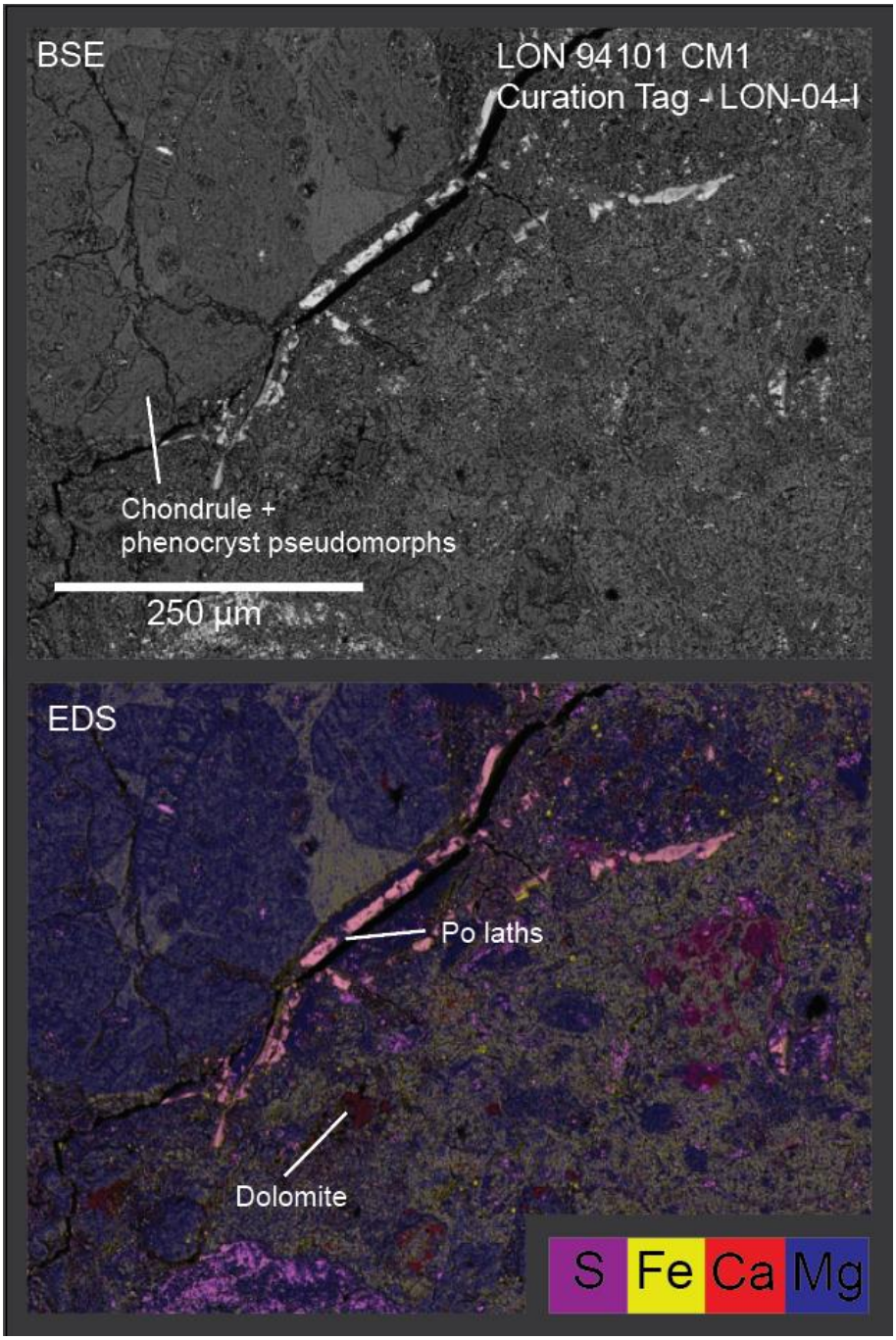

Phyllosilicates	**n**	**Area %**	**'FeO'/ SiO_2**	**S/SiO_2**	**Mg #**	**Totals**
Matrix	10	90.1	0.57 ± 0.09	0.01 ± 0.01	68.64 ± 3.85	85.17 ± 7.13
Accessory minerals		**Area %**	**Form**			
Surviving precursors[#]		0	Absent			
Carbonates		2.0	Euhedral dolomite			
Sulphides		2.5	Po laths (+occasional sulphate (gypsum)			
Chondrules						
Mesostasis	Phyllosilicate					
Phenocryst replacement	100 %					
Rubin Subtype:	CM1					

Plate 4.26 –Area % = threshold estimates from polished block. [#]Evenly distributed within matrix (*i.e.*, not large chondrules). Uncertainties are 2SE. Totals are EDS oxide wt %.

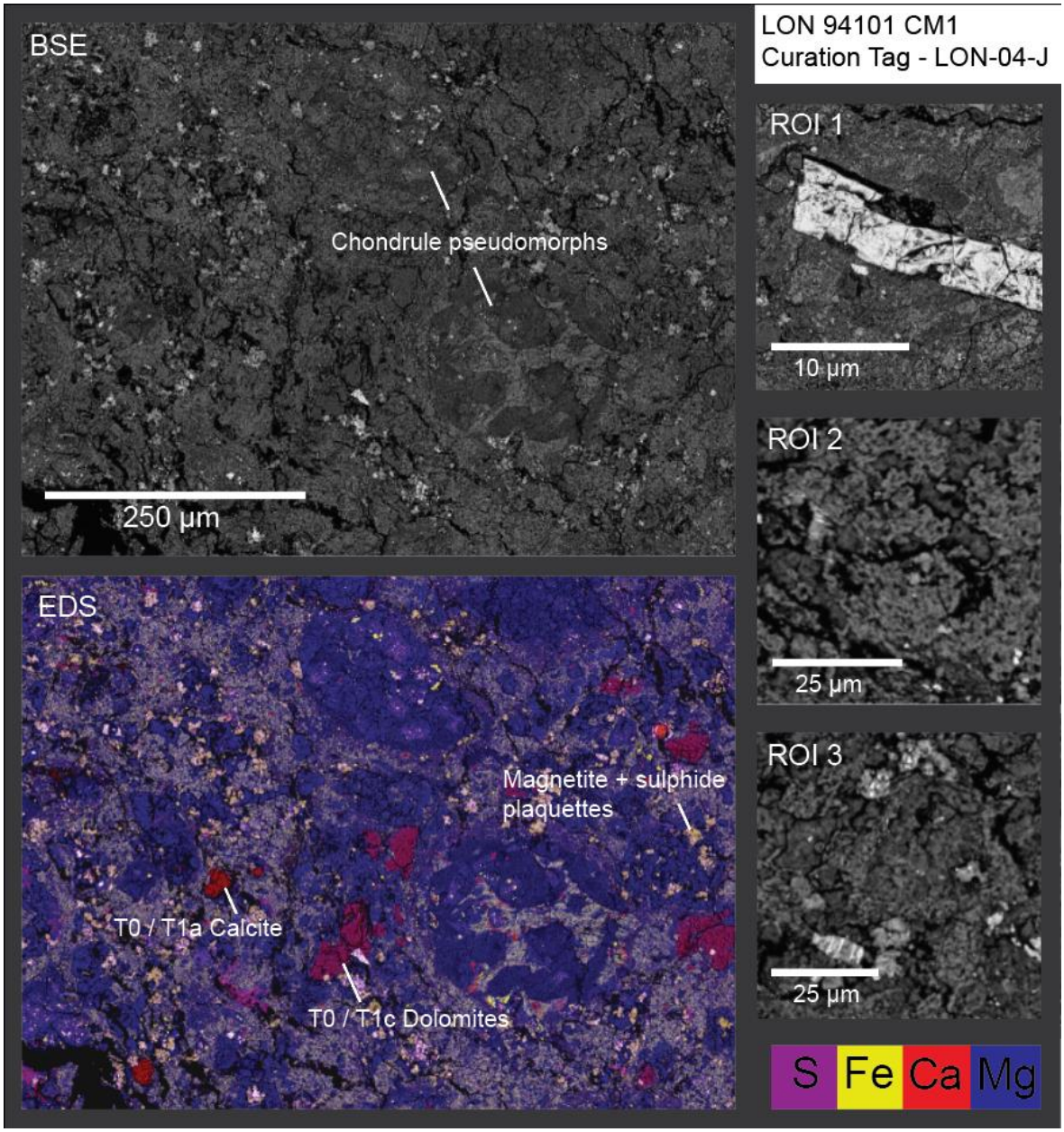

Phyllosilicates	**n**	**Area %**	**'FeO'/ SiO_2**	**S/SiO_2**	**Mg #**	**Totals**
Matrix	8	90	0.55 ± 0.15	0.05 ± 0.05	71.12 ± 5.59	76.38 ± 3.98
Accessory minerals		**Area %**	**Form**			
Surviving precursors[#]		0	Absent			
Carbonates		7.0	Mostly T0 Ca-carbonate and dolomite			
Sulphides		1.6	Po > Pn			
Chondrules						
Mesostasis	Phyllosilicate					
Phenocryst replacement	100 %					
Rubin Subtype:	CM1					

Plate 4.27 –Area % = threshold estimates from polished block. [#]Evenly distributed within matrix (*i.e.*, not large chondrules). Uncertainties are 2SE. Totals are EDS oxide wt %.. ROI 1 – Po lath; ROI 2 – Fe-rich phyllosilicate; ROI 3 – Mg-rich phyllosilicate with small TCI-like intergrowths of sulphide and phyllosilicate .

4.6.15 LON-04-B

Within the kernel of LON-04 is a very low contrast clast 4 mm in the longest dimension (Fig 4.16 & 4.17). The dark colour is its most distinguishing feature, easily spottable in the lowest magnification map of LON-04 (Fig 4.16). It is a highly fractured lithology, comprised chiefly of S- and Fe-depleted matrix dominated by Mg-serpentine with very rare forsterite fragments. Hosted within the matrix is an assortment of replacement products, including an occasional pseudomorphed chondrule. TCIs and phyllosilicate clumps of variable morphology and composition are also included within the matrix (Plate 4.28, ROI 2), containing very dark, S-depleted phyllosilicate cores of close composition to the surrounding matrix. Some TCIs have hollow cores bearing crystals of calcium and sodium-rich sulphate with 3-D structures protruding from the polished surface, presumably a result of interaction with atmospheric moisture post-polishing (Plate 4.28, ROI 3). Carbonates are exclusively dolomite of the solitary T0 and T1c variety, the latter associated with abundant magnetite plaquettes. Other opaque phases are widespread framboidal magnetite (Plate 4.28 ROI 1), and pentlandite.

This clast is clearly a cataclastic regolith breccia, though of sufficiently different composition to typical CM2 material to appear distinct from normal 'cataclastic matrix' (Suttle *et al.,* 2023). Upon analysis of its oxygen isotopic composition, a significant NF_3 problem (Chapter 3) was observed as an isobaric interference and the sample required cryogenic treatment, a characteristic previously only a problem with CI chondrite material. This is tentative evidence that the mineralogy resembles, in part, CI chondrites. For this reason, it is thought appropriate to classify this lithology as a highly brecciated CM1. While perhaps coincidental, the location of this clast within the dead-centre of the block may have protected it from disintegrating during entry. Such chance protection may be requisite for the survival of such material (*e.g.,* Borovička *et al.,* 2019).

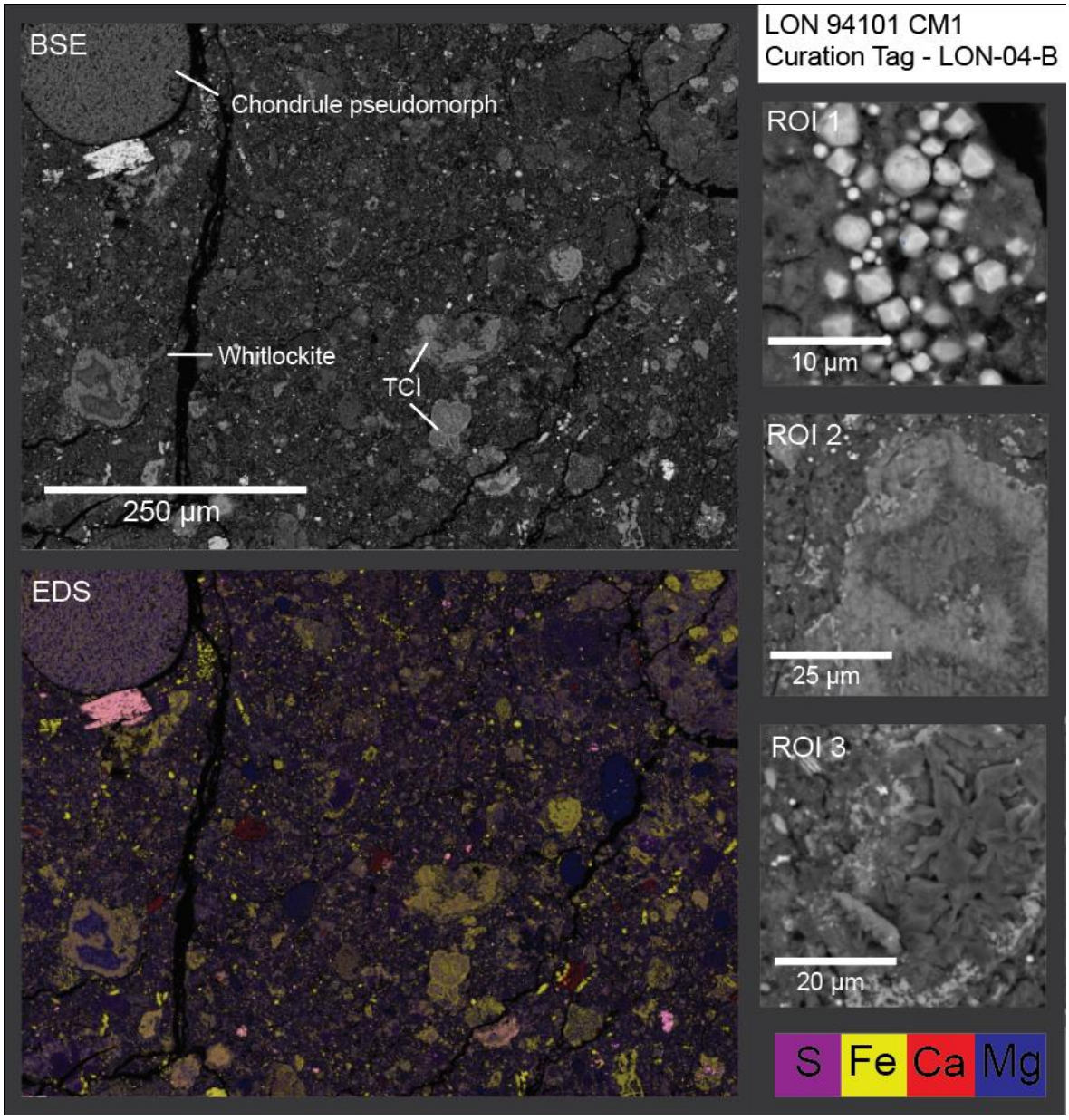

Phyllosilicates	**n**	**Area %**	**'FeO'/ SiO_2**	**S/SiO_2**	**Mg #**	**Totals**
TCI	26	23.1	2.42 ± 0.31	0.46 ± 0.19	31.54 ± 4.66	80.30 ±1.17
TCI Cores		75.1	0.59 ± 0.03	0.41 ± 0.07	73.30 ± 1.55	84.42 ± 1.59
Matrix	6		0.55 ± 0.06	0.10 ± 0.01	67.31 ± 2.07	63.40 ± 1.21
Accessory minerals		**Area %**	**Form**			
Surviving precursors[#]		1.8	Rare < 30 µm Fo grains			
Carbonates		1.1	Grains of magnesium carbonate			
Sulphides		1.3	Po + Pn			
Chondrules						
Mesostasis	Phyllosilicate					
Phenocryst replacement	100 %					
Rubin Subtype:	CM1					

Plate 4.28 –Area % = threshold estimates from polished block. [#]Evenly distributed within matrix (*i.e.*, not large chondrules). Uncertainties are 2SE. Totals are EDS oxide wt %. ROI 1 – Magnetite framboids; ROI 2 – Type II TCI within the matrix; ROI 3 –TCI with gypsum crystals (magnesium sulphate) in the core, presumably due to interaction with atmospheric moisture.

4.6.16 LON-04-V

Of all the highly altered clasts studied in this work, LON-04-V is perhaps the most peculiar of all. While anhydrous fragments are absent, their implied existence is not. Numerous, moderately sized chondrule pseudomorphs dot the section (Plate 4.29), replaced by Mg-rich phyllosilicate, embedded in a similarly Mg-rich fine-grained matrix. The unusual characteristics of this lithology are conveyed by a large modal percentage of stoichiometrically pure pyrrhotite occurring as hexagonal plates and laths, and a total absence of any form of carbonate. Analogous to LON-04-K (Plate 4.32), whitlockite is ubiquitous as small (10 μm) crystals as are rarer grains of ilmenite ($TiFeO_3$). This clast contains a much larger proportion of the unidentifiable (oxy) hydroxide as also found in LON-04-S (Plate 4.30), visible as grey blebs in the EDS map. This clast is a CM1.

4.6.17 LON-04-S

A matrix supported clast; LON-04-S retains a surprisingly large quantity of small forsteritic olivine fragments when compared with other, similar clasts in LON (Plate 4.30). Very small grains of calcium carbonate and sulphide are dotted throughout; however, the most abundant calcium-rich phase is gypsum, which is deposited in clumps in association with the Fe-rich saponite. Interestingly, the surface of the gypsum is flat, and therefore different to the calcium and sodium sulphates sometime seen to protrude outwards from the surfaces of other, similar clasts (LON-04-B), indicating that it may be (at least partially) an indigenous phase. The most puzzling mineral to identify is one that contains approximately equal atomic proportions of Mg^{2+} and Fe^{2+}, that when added together are roughly equal to the measured O content. As little to no Si was detected, this mineral cannot be identified as phyllosilicate. The most sensible match would be an intergrowth of brucite ($Mg(OH)_2$) and amakinite ($Fe^{2+}(OH)_2$), however the wt % oxide totals are very low at 50-60%, indicating a large contribution from unmeasurable elements such as H. An alternative suggestion could be an intergrowth of brucite and ferrihydrite ($(Fe^{3+})_2O_3 \bullet 0.5H_2O$), or an alternative (oxy)-hydroxide

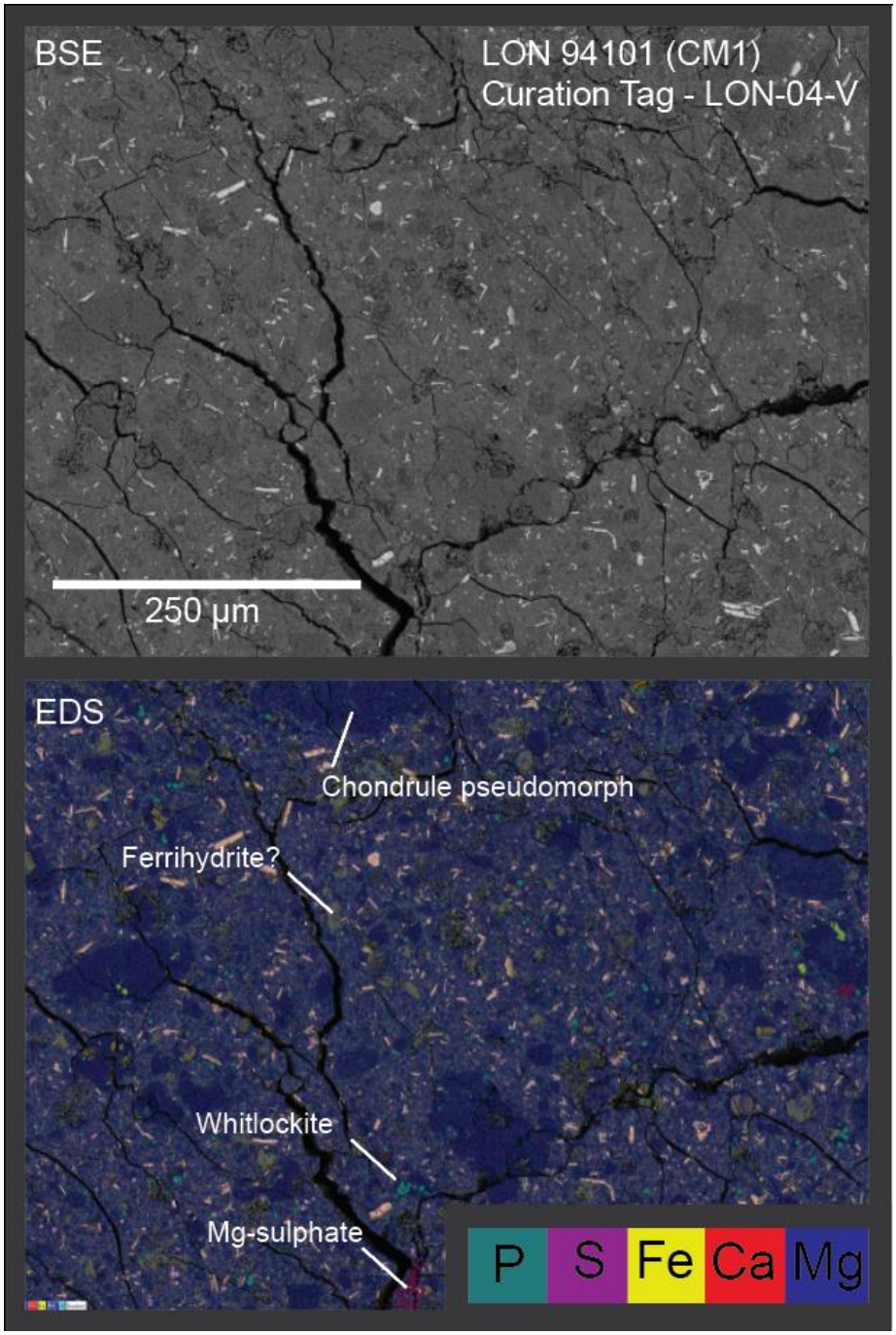

Phyllosilicates	**n**	**Area %**	**'FeO'/ SiO_2**	**S/SiO_2**	**Mg #**	**Totals**
Matrix	10	85.3	0.51 ± 0.02	0.10 ± 0.01	65.98 ± 0.91	76.54 ± 1.21
Accessory minerals		**Area %**	**Form**			
Phosphate		0.6	Whitlockite			
Carbonates		0.1	Small < 20µm dolomites			
Sulphate		0.4	Gypsum in cracks			
Sulphides		2.9	Po			
Chondrules						
Mesostasis	Phyllosilicate					
Phenocryst replacement	100 %					
Rubin Subtype:	CM1					

Plate 4.29 –Area % = threshold estimates from polished block. Uncertainties are 2SE. Totals are EDS oxide wt %.

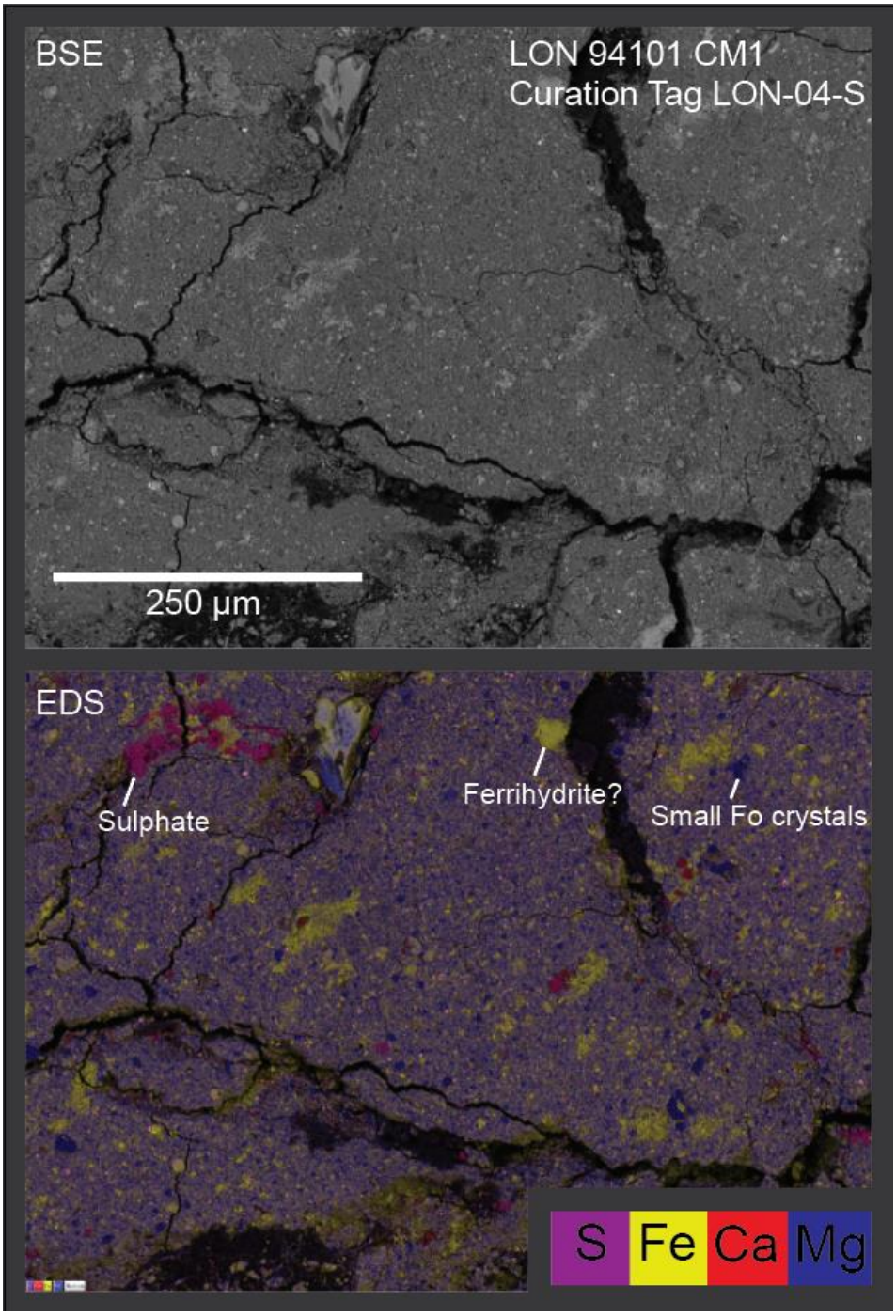

Phyllosilicates	**n**	**Area %**	**'FeO'/ SiO_2**	**S/SiO_2**	**Mg #**	**Totals**
Matrix		82.1				
Accessory minerals		**Area %**	**Form**			
Surviving precursors[#]		3.0				
Sulphate		1.9				
Ferrihyrite?		5.1				
Chondrules						
Mesostasis	N/A					
Phenocryst replacement	N/A					
Rubin Subtype:	CM1m-an					

Plate 4.30 –Area % = threshold estimates from polished block. [#]Evenly distributed within matrix (*i.e.*, not large chondrules). Uncertainties are 2SE. Totals are EDS oxide wt %.

Mineral (Brearley and Jones, 1998), though ultimately the composition of this growth remains enigmatic. The texture and mineralogy of this phase is certainly more akin to CI chondrites (Brearley and Jones, 1998) than CM chondrites, yet both the juxtaposition in a large CM chondrite and the presence of unaltered forsterite is evidence to the contrary with respect to being true CI material. This may be an example of pervasively altered CI-like material, from a CM asteroid, that is just short of the level of alteration observed in classified CIs. Due to the lack of TCIs and chondrules, most Rubin criteria are obsolete; however, when compared to the matrix thresholds, this clast most readily fits CM1m. This clast is therefore classified as a CM1m-anomalous.

4.6.18 LON-04-T

LON-04-T is identical to LON-04-S in terms of olivine, sulphate, sulphide and carbonate content, with one exception in that in place of Fe-rich hydroxide are clusters of magnetite framboids (Plate 4.31). This may represent a different geochemical microenvironment of a similar provenance to LON-04-S, bolstered by the observation that they are found in close proximity to one another in section. This clast is a CM1m-anomalous.

4.6.19 LON-04-K

Occurring as a spherical clast at the edge of the block (Fig 4.17), LON-04-K shares the unusual characteristics of LON-04-B with the exception that it is a primary rock and is unbrecciated (Plate 4.32). It consists of fully altered, low contrast matrix material with only two small chondrule pseudomorphs. As in LON-04-B, carbonates are T0/T1c dolomites and sulphides are pentlandite. Interestingly, composite ‘veins’ of framboidal magnetite and sub-micron pentlandite crosscut the section, perhaps reflecting fluid mobility along a fracture. Uniquely, this clast contains a ubiquitous distribution of small whitlockite grains and small amounts the phosphide schreibersite in close association with all secondary phases. TCIs and phyllosilicate clumps are absent. This clast is a CM1m.

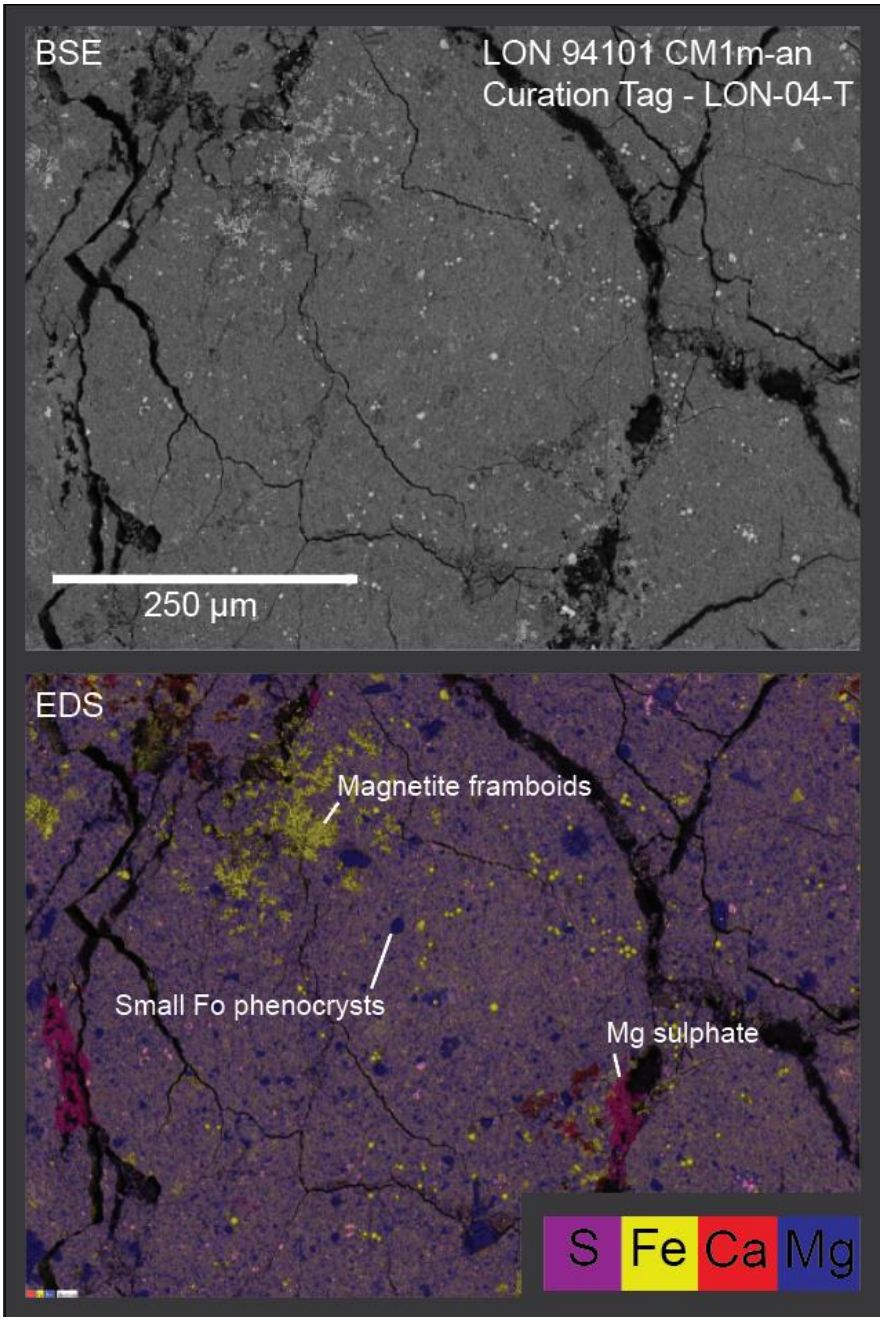

Phyllosilicates	**n**	**Area %**	**'FeO'/ SiO_2**	**S/SiO_2**	**Mg #**	**Totals**
Matrix	10	86.8	0.73 ± 0.02	0.12 ± 0.00	57.58 ± 0.71	72.60 ± 1.42
Accessory minerals		**Area %**	**Form**			
Surviving precursors[#]		1.0	< 20µm Fo crystals			
Carbonates		1.5	< 10µm Ca-carbonates			
Sulphate		1.0	Gypsum as veins along fractures			
Magnetite		4.2	Framboids			
Chondrules						
Mesostasis	N/A					
Phenocryst replacement	N/A					
Rubin Subtype:	CM1m-anomalous					

Plate 4.31 –Area % = threshold estimates from polished block. [#]Evenly distributed within matrix (*i.e.*, not large chondrules). Uncertainties are 2SE. Totals are EDS oxide wt %.

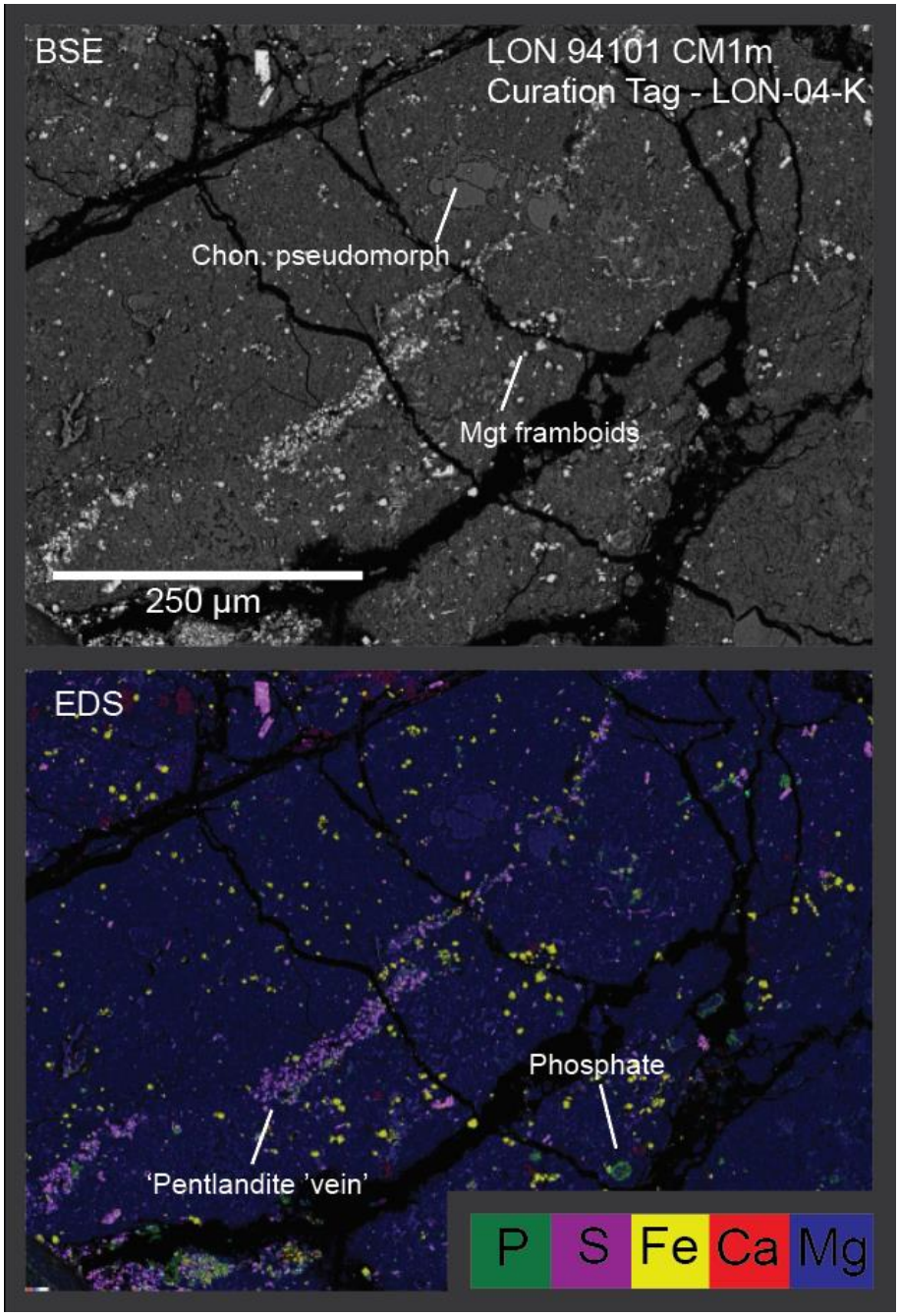

Phyllosilicates	**n**	**Area %**	**'FeO'/ SiO_2**	**S/SiO_2**	**Mg #**	**Totals**
Matrix	10	94.6	0.42 ± 0.04	0.05 ± 0.01	74.46 ± 1.25	74.16 ± 0.96
Accessory minerals		**Area %**	**Form**			
Surviving precursors[#]		0	Absent			
Sulphate		0.9	Gypsum in cracks			
Magnetite		1.6	Framboids			
Phosphate		0.7	Whitlockite			
Sulphides		1.3	Po and Pn as small clusters			
Chondrules						
Mesostasis	N/A					
Phenocryst replacement	100%					
Rubin Subtype:	CM1m					

Plate 4.32 –Area % = threshold estimates from polished block. [#]Evenly distributed within matrix (*i.e.*, not large chondrules). Uncertainties are 2SE. Totals are EDS oxide wt %.

4.6.20 LON-04-U

LON-04-U is a matrix supported clast with striking features when portrayed as an EDS map (Plate 4.33). No anhydrous precursors remain, and the matrix is dotted with up to 6 %, 50-100 µm clusters of µm-scale magnetite framboids. Some anomalous framboids are giant, exceeding 20 µm in diameter (Plate 4.33). Dolomite is widespread and constitutes a large portion of the surface area (6.4 area %), as do hexagonal plates of stoichiometrically pure pyrrhotite (8 %). The remainder comprises featureless, highly S- and Fe- depleted Mg-rich matrix. This clast is analogous to CI material and so is classified as a CM1m.

4.6.21 Lonewolf Nunataks 94101 summary

LON 94101 represents a true cornucopia of CM lithologies with remarkable variety (Gregory *et al.*, 2015; Lindgren *et al.*, 2013; Zolensky *et al.*, 2022), adding an order of magnitude to the available clasts for study. While the petrologic range of this meteorite so far ranges from CM1m – CM2.8, it still appears to be dominated by clasts of a narrow range in alteration conditions, in this case moderately altered, CM2.3-CM2.5 material; indeed, three exceptionally large CM2.3 - CM2.5 clasts (each approximately 10 x 10 mm), designated as lithologies LON-04-C, E and F respectively, constitute 30 % of the exposed surface area alone (Fig 4.17). In-between the moderately altered material are clasts of almost every possible petrologic combination. Some of the most obvious include a large, incipiently altered, CM2.8 lithology (LON-04-A), which appears to be a slightly more altered version of previously reported CM2.8-CM3.0 meteorites such as A-12085, 12169 and 12236 (Kimura *et al.*, 2020) and C2-ungrouped stones such as Acfer 094 (Matsumoto *et al.*, 2019; Newton *et al.*, 1995), and possibly even CO chondrites (Greenwood *et al.*, 2019; Torrano *et al.*, 2021). In addition, the inclusion of incipiently to moderately altered, matrix dominated clasts with peculiar chondrule depletions such as LON-01-A (2.8m-an), LON-04-M (2.6m-an) extend the range of CM textures to include matrix supported lithologies with variable degrees of alteration. Finally, a selection of pervasively altered, chondrule-free CM1

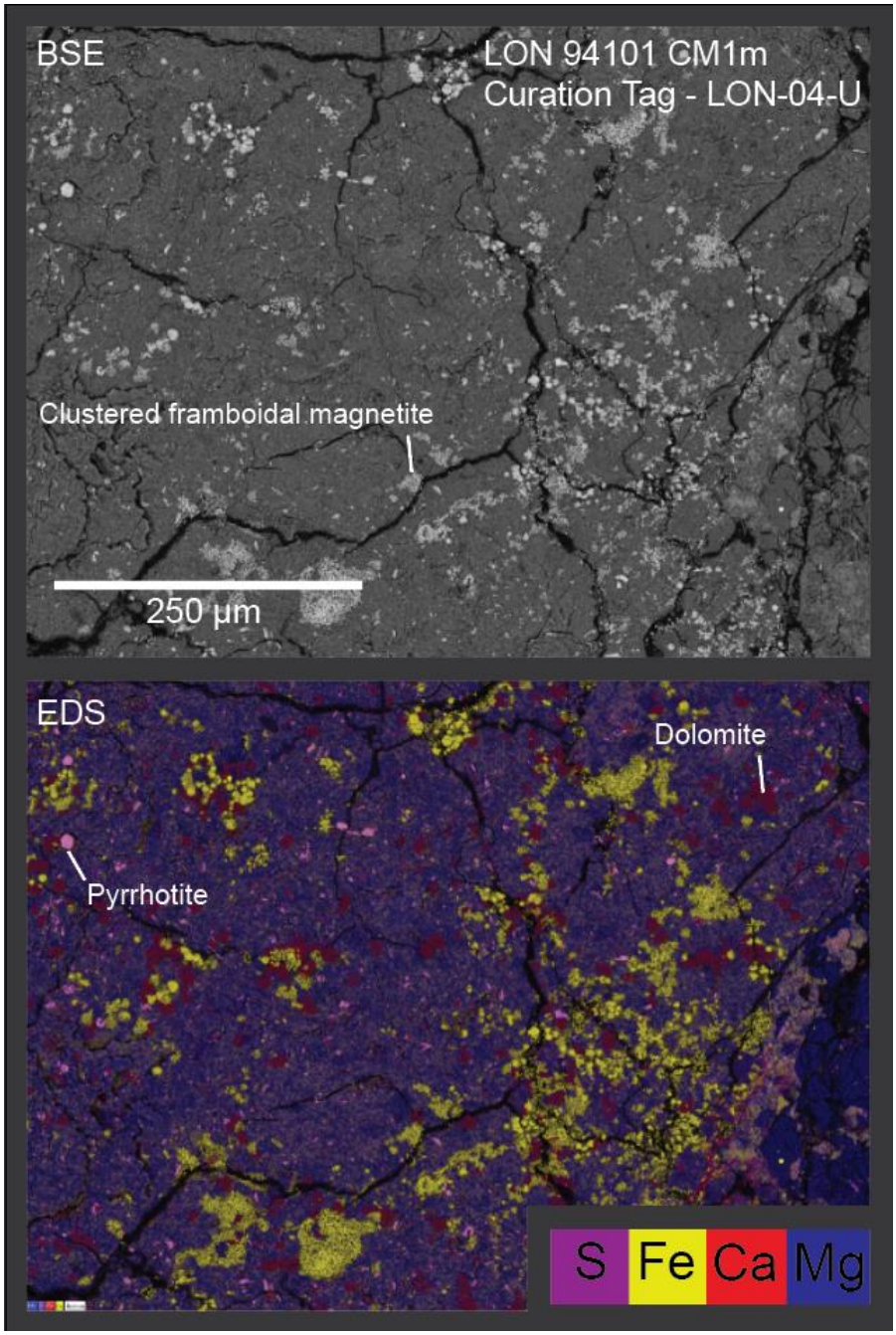

Phyllosilicates	**n**	**Area %**	**'FeO'/ SiO_2**	**S/SiO_2**	**Mg #**	**Totals**
Matrix	6	81	0.57 ± 0.04	0.10 ± 0.01	67.60 ± 2.20	70.99 ± 1.21
Accessory minerals		**Area %**	**Form**			
Magnetite[#]		6.0	Huge clusters of magnetite framboids + plaquettes			
Carbonates		6.4	Dolomite grains			
Sulphides		2.0	Hexagonal pyrrhotite laths			
Sulphate		0.5	Small veins of Mg-sulphaye			
Chondrules						
Mesostasis	N/A					
Phenocryst replacement	N/A					
Rubin Subtype:	CM1m					

Plate 4.33 –Area % = threshold estimates from polished block. [#]Evenly distributed within matrix (*i.e.*, not large chondrules). Uncertainties are 2SE. Totals are EDS oxide wt %.

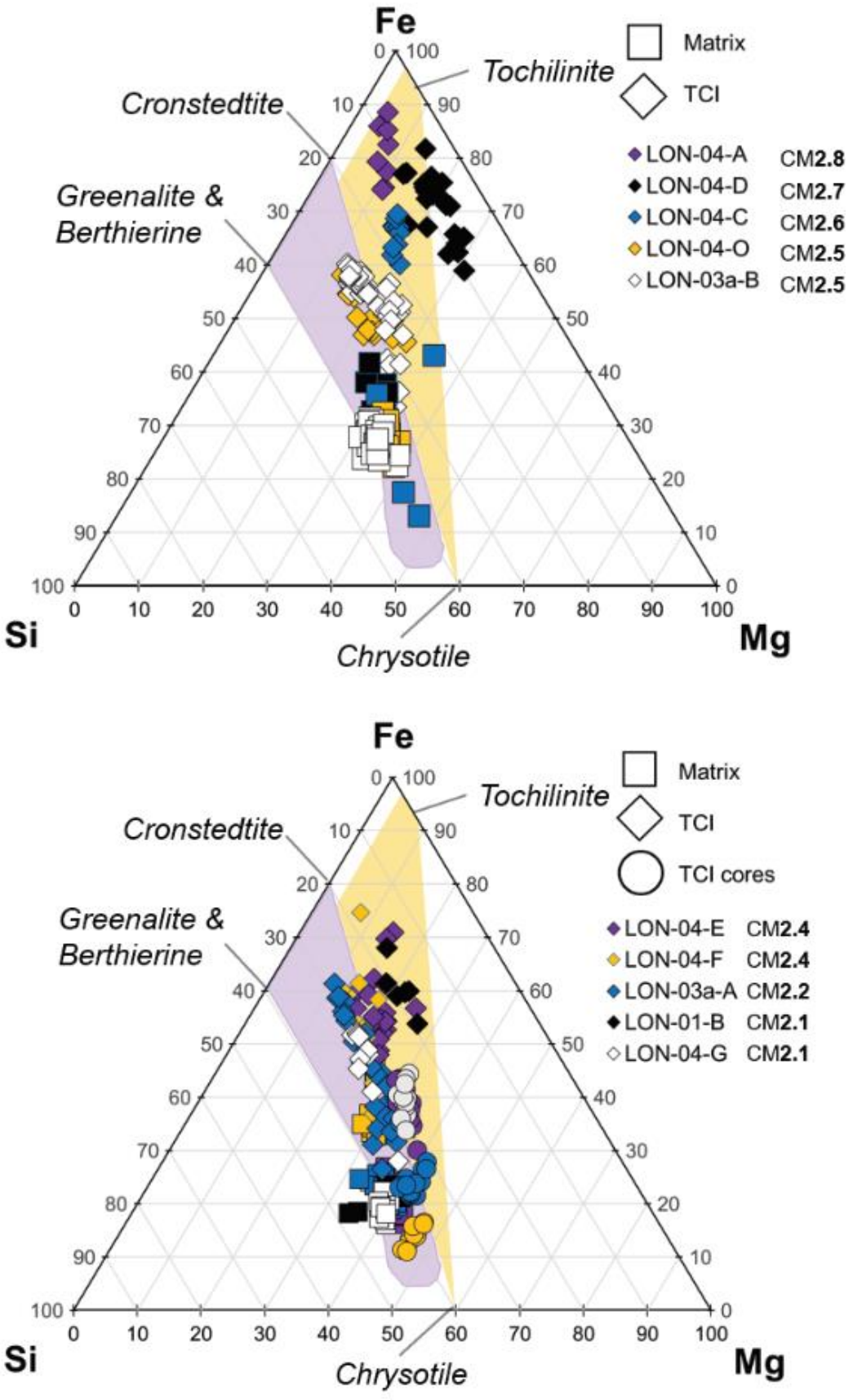

Figure 4.18 - Normalised major element cation ternary diagram for matrix, TCI and TCI cores in LON 94101 (at %). Top: CM2.7 – 2.5. Bottom: CM2.4-2.1)

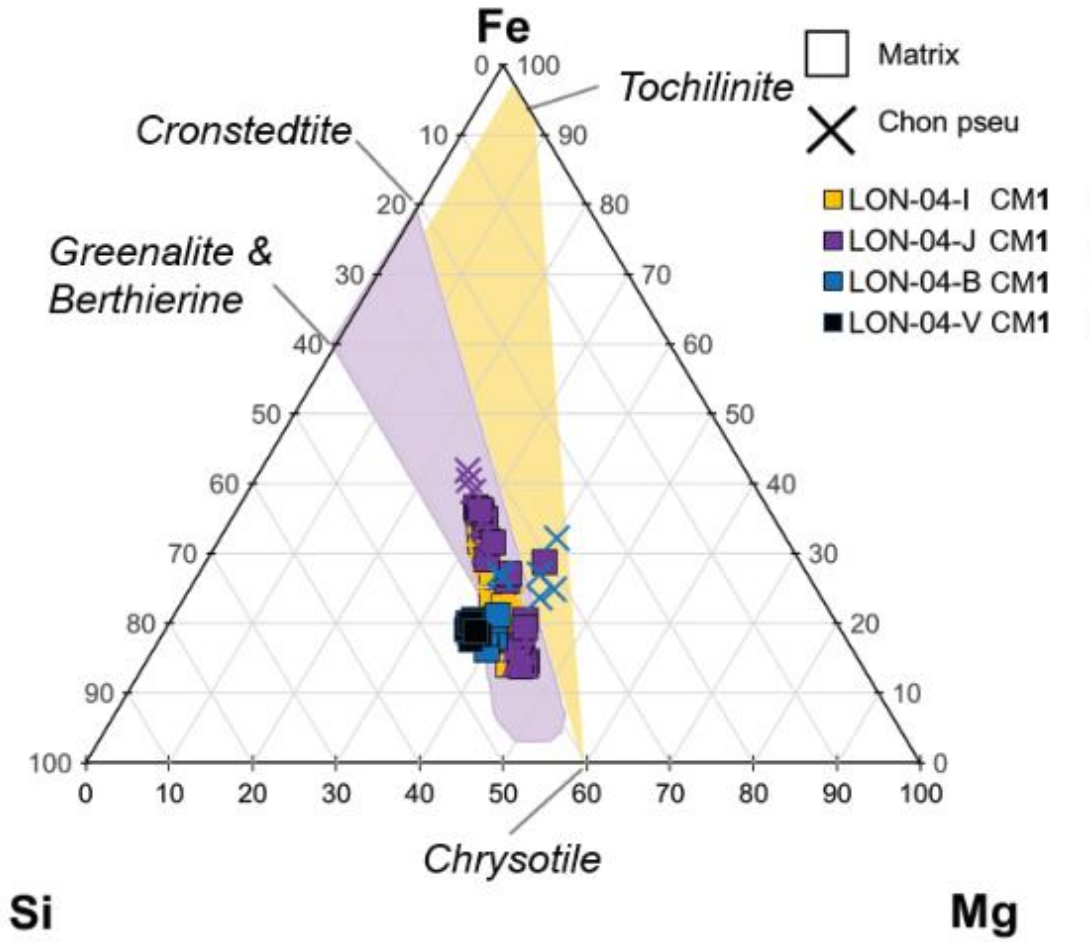

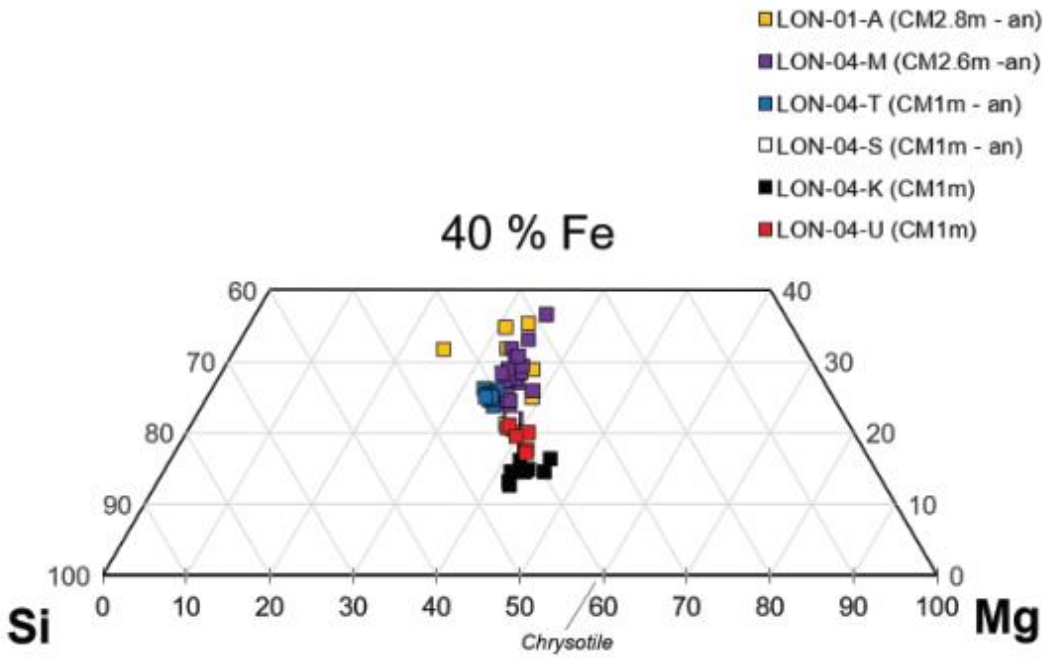

4.19 - Normalised major element cation ternary diagram for matrix and chondrule pseudomorphs in LON 94101 (at %). Top: CM1. Bottom: Matrix compositions of CM1m and anomalous, matrix – rich lithologies.

lithologies (CM1m) bear a rather surprising resemblance to the petrographic characteristics of CI chondrites (Brearley and Jones, 1998; Russell *et al.*, 2022), including a vulnerability to alteration in the terrestrial environment (Lee *et al.*, 2020). However, while the textural properties of these clasts are certainly CI-like, the compositions of the phyllosilicates in these are still predominantly serpentine (Fig 4.19) as opposed to saponite, in line with C1-like clasts observed in HEDs, CRs, CBs, CHs and ureilites (Briani *et al.*, 2012; Herrin *et al.*, 2011; Patzek *et al.*, 2018). This work only touches the surface of the lithological diversity this meteorite has to offer, aiming at the 'low hanging fruit' present as both large and compositionally obvious clasts in BSE. However, a great deal more lithological diversity has yet to be explored here.

4.6.22 Cataclastic matrix

The material interstitial to the primary accretionary lithologies (Metzler *et al.*, 1992) is a highly disturbed, fragmented regolith composed of disaggregated, broken fragments (Figure 4.20). Within the cataclastic matrix (Suttle *et al.*, 2023) are fragmental examples of TCIs, chondrules and micro-clasts from many lithologies. This material is some of the most useful for determining space exposure ages due to its prolonged contact with cosmogenic nuclides via multiple impacts. While it represents an opportunity to examine the diversity of material present in the gardened regolith of an asteroid, this work instead chose to focus on the numerous primary accretionary lithologies that had yet to be classified in detail; therefore, unravelling of the complex nature of the cataclastic matrix was not attempted. In general, the cataclastic matrix of a meteorite is reflective of its dominant form of alteration, usually containing highly broken material and fragments from the meteorite's petrologic range.

4.7 Discussion

More than 85 discrete clasts were initially identified in BSE images from multiple polished blocks in Mukundpura, Aguas Zarcas, Kolang, Winchcombe and LON 94101. From this initial assessment, 38 lithologies were investigated in high resolution using a scanning

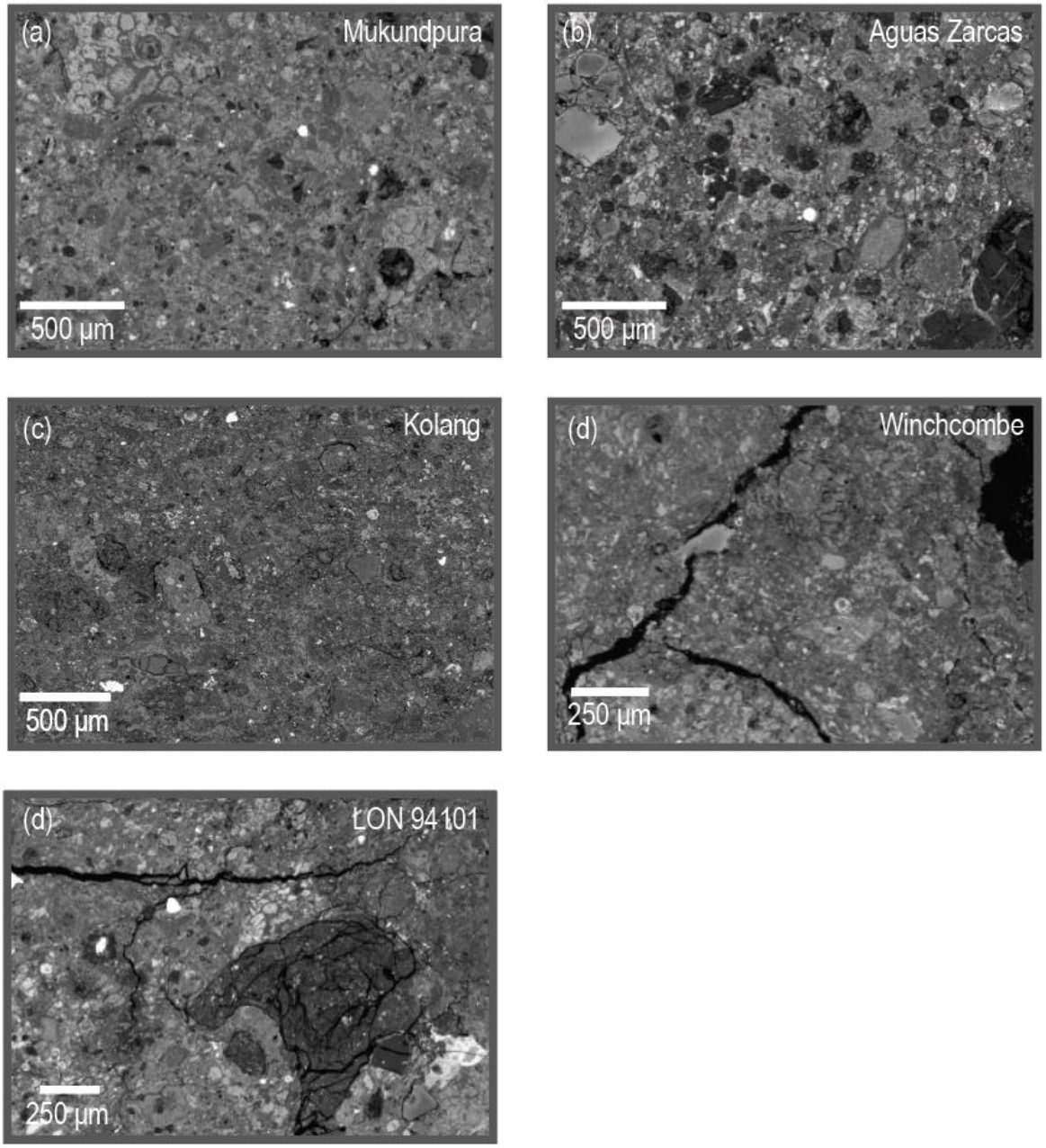

Figure 4.20 – Examples of cataclastic matrix from each meteorite

electron microscope. Twenty-one satisfy the criteria of partial aqueous alteration and are designated as CM2.1-2.9. Eight exhibit complete alteration and are classified as CM1; however, these are divided into two subgroups, CM1 and CM1m, to separate those that are matrix dominated from those that harbour obvious chondrule pseudomorphs. Four lithologies exhibit anomalous characteristics that do not permit confident sub-classification but are nevertheless designated a petrologic subtype according to qualitative investigation. As expected, the extent of this lithological diversity is dominated by the very large sample

of LON (LON-04). Five examples of highly processed cataclastic matrix are represented by a single lithology from each meteorite, though it is duly observed that this material is present across multiple sections of each meteorite, and in abundance (Figure 4.20). From this secondary sub-sample set, 33 lithologies, representing primary accretionary rocks spanning a range of aqueous alteration phenomena were chosen for spot EDS investigation and eventual micro-sampling for oxygen isotope analysis (Tables 4.2, 4.3 and 4.4 below).

A summary of the results, including EDS and thresholding data is presented in Tables 4.2, 4.3 and 4.4. Some lithologies are omitted from certain tables (*e.g.*, TCIs) if the investigated component was missing.

4.7.1 First order observations

Comparing the data from the meteorite falls in accordance with the literature, ~80 % of the lithologies are consistent with a dominant level of alteration *within each* meteorite, in line with, for example, the commonly cited sequence (from least altered to most altered) Paris < Maribo < Murchison < Murray < Mighei < Nogoya < Cold Bokkeveld (*e.g.*, Browning *et al.*, 1996; Haack *et al.*, 2012; Hewins *et al.*, 2014). In the case of this work, this would similarly be: Aguas Zarcas < LON 941010 (broadly) < Mukundpura < Winchcombe < Kolang. Nonetheless, the expression of a dominant petrologic subtype is dependent on both the surface area dedicated for petrographic examination, and the severity of brecciation.

The rewards for analysing a large surface area are revealed by Winchcombe and Aguas Zarcas, some of the more petrographically studied CMs to date. The paper by Suttle *et al.* (2023) covers over 190 mm^2 of exposed thin section surface in Winchcombe, and accordingly permitted the identification of 5 rarer lithologies including CM2.6 material (an observation only possible through extended evaluation). A similar outcome is presented for Aguas Zarcas. Analysis of multiple polished blocks by Kerraouch *et al.* (2022) revealed a CM1, a C1, a CM1/2 and two metal-rich lithologies with anomalous isotopic compositions, whereas the Aguas Zarcas stones in this study contain predominantly chondrule-rich, CM2

Table 4.2 - Modal mineral abundances from representative micromillable domains. Fe phyl includes Fe phyllosilicates from TCI and Fe- S- rich serpentines. Mg phyl includes fine-grained matrix and phyllosilicate clumps within TCIs. Anh = remaining precursors (does not include large chondrules or CAIs). Carb = Ca and Mg carbonate. S-hide = sulphide. Phos = phosphate. S-ate = sulphate. Mag = magnetite. Void = void space. 'FeO' contains FeO from phyllosilicates, Fe^{3+} from cronstedtite and magnetite, and Fe^{2+} from sulphides.

			Modal area %									
Lithology	Desc	Subtype	Fe phyl	Mg phyl	Anh	Carb	S-hide	Phos	S-ate	Mag	Void	Sulph generation
LON 94101												
LON-04-A	CM2	**2.8**	10.7	49.4	34.3		5.6	0.0	0.0	0.0	0.0	Tr+Po
LON-01-A	CM2-an	**2.8**	0.0	85.6	10.0	2.0	1.2	0.0	0.0	1.2		Absent
LON-04-D	CM2	**2.7**	13.6	71.8	11.5	1.9	1.2	0.0	0.0	0.0	0.0	Po + Pn
LON-04-C	CM2	**2.6**	21.0	72.7	3.1	1.8	1.4	0.0	0.0	0.0	0.0	Po-Pn
LON-04-M	CM2- an	**2.6**	0.0	97.9	0.6	0.5	1.0	0.0	0.0	0.0	0.0	Po+Pn
LON-04-O	CM2	**2.5**	42.1	54.5	1.0	1.5	1.0	0.0	0.0	0.0	0.0	Pn
LON03a-B	CM2	**2.5**	25.2	67.0	2.8	1.2	1.5	0.0	0.0	0.0	2.3	Pn
LON-04-E	CM2	**2.4**	25.3	68.0	2.2	2.7	1.8	0.0	0.0	0.0	0.0	Pn + Int
LON-04-F	CM2	**2.4**	13.2	80.2	2.4	2.2	2.0	0.0	0.0	0.0	0.0	Pn + Int
LON-03a-A	CM2	**2.2**	50.4	39.5	3.0	2.6	4.5	0.0	0.0	0.0	0.0	Pn
LON-01-B	CM2	**2.1**	31.4	57.6	2.0	1.1	1.5	0.0	0.0	0.0	6.4	Unknown
LON-04-G	CM2	**2.1**	63.6	34.0	0.2	1.4	0.8	0.0	0.0	0.0	0.0	Pn+Int>Po
LON-04-I	CM1	**2.0**	36.1	54.0	0.0	2.0	2.5	0.0	0.0	1.0	4.4	Po
LON-04-J	CM1	**2.0**	44.6	45.4	0.0	7.0	1.6	0.0	0.0	1.4	0.0	Po+Pn
LON-04-B	CM1	**2.0**	23.1	71.5	1.8	1.1	1.3	0.0	0.0	1.2	0.0	Po+Pn
LON-04-V	CM1	**2.0**	5.1	85.3	0.0	0.1	2.9	0.6	0.4	0.0	5.6	Po
LON-04-S	CM1m - an	**2.0**	5.1	82.1	3.0	0.0	0.0	0.0	1.9	0.0	7.9	Absent
LON-04-T	CM1m - an	**2.0**	0.0	86.8	1.0	1.5	0.0	0.0	1.0	4.2	5.4	Po
LON-04-K	CM1m	**2.0**	0.0	94.6	0.0	0.9	1.3	0.7	0.9	1.6	0.0	Po
LON-04-U	CM1m	**2.0**	0.0	81.0	0.0	6.4	2.0	0.0	0.5	6.0	4.0	Po
Aguas Zarcas												
AZ-04-B	CM2	**2.6**	33.8	52.6	7.2	6.3	0.0	0.0	0.0	0.0	0.0	Pn
AZ-04-D	CM2	**2.6**	40.3	44.9	8.0	5.5	1.4	0.0	0.0	0.0	0.0	Pn+Int
AZ-02-A	CM2	**2.5**	23.5	56.0	13.1	3.8	1.4	0.0	0.0	0.0	2.3	Pn+int
AZ-04-C	CM2	**2.3**	46.1	42.6	7.4	4.0	0.0	0.0	0.0	0.0	0.0	Int
Mukundpura												
MP-01-B	CM2	**2.7**	21.2	63.0	14.0	0.3	1.5	0.0	0.0	0.0	0.0	Pn+Po
MP-01-A	CM2	**2.3**	46.6	47.1	4.1	0.5	0.6	0.0	0.0	0.0	1.0	Po+Pn+Int
MP-05-A	CM1	**2.0**	37.8	49.5	0.0	2.8	3.7	0.9	0.0	2.0	3.4	Po+Int
Winchcombe												
WC-02-A	CM2	**2.2**	31.2	58.7	2.6	3.3	0.9	0.0	0.0	0.0	3.2	Pn+Int
WC-01-A	CM2	**2.1**	44.4	41.5	1.4	5.0	0.2	0.0	0.0	1.0	6.5	Po+Int>Po
Kolang												
KO-01-A	CM2	**2.3**	58.0	34.5	3.6	2.6	1.3	0.0	0.0	0.0	0.0	Po+Pn
KO-01-D	CM2	**2.1**	42.2	53.8	0.7	2.0	0.6	0.0	0.0	0.0	0.7	unknown
KO-03-A	CM2.1 -an	**2.1**	33.8	52.3	2.0	6.7	2.0	0.0	0.0	0.0	3.2	Pn>Po+Int
KO-01-C	CM1	**2.0**	7.7	82.7	0.0	6.2	2.0	0.0	0.0	0.0	1.4	Pn

Table 4.3 - Compositional data for matrix in all lithologies. 'FeO' contains FeO from phyllosilicates, Fe^{3+} from cronstedtite and magnetite, and Fe^{2+} from sulphides.

MATRIX COMPOSITION											
Lithology	**Description**	**Subtype**	**FeO/ SiO_2**	**2SE**	**S/ SiO_2**	**2SE**	**Mg#**	**2SE**	**EDS Total**	**2SE**	**n**
LON 94101											
LON-04-A	CM2	**2.8**	0.8	0.1	0.2	0.0	52.9	3.5	82.7	1.8	29
LON-01-A	CM2-an	**2.8**	1.0	0.2	0.2	0.0	52.7	5.0	-	-	7
LON-04-D	CM2	**2.7**	1.1	0.1	0.1	0.0	48.8	1.9	80.1	1.8	20
LON-04-C	CM2	**2.6**	0.8	0.1	0.1	0.0	58.2	5.6	80.6	2.7	11
LON-04-M	CM2- an	**2.6**	0.9	0.1	0.1	0.0	56.4	2.9	81.1	1.7	25
LON-04-O	CM2	**2.5**	1.0	0.1	0.2	0.0	54.0	2.9	82.2	2.5	9
LON03a-B	CM2	**2.5**	0.9	0.1	0.1	0.0	53.6	2.0	72.0	1.5	41
LON-04-E	CM2	**2.4**	0.6	0.1	0.1	0.0	65.3	2.4	79.6	2.2	20
LON-04-F	CM2	**2.4**	0.7	0.1	0.1	0.0	64.7	3.8	80.6	5.3	11
LON-03a-A	CM2	**2.2**	0.7	0.0	0.1	0.0	63.4	1.6	80.5	3.2	18
LON-01-B	CM2	**2.1**	0.6	0.1	0.0	0.0	65.0	1.9	-	-	5
LON-04-G	CM2	**2.1**	0.9	0.0	0.2	0.0	67.7	1.1	77.8	2.7	18
LON-04-I	CM1	**2.0**	0.6	0.1	0.0	0.0	68.6	3.9	85.2	7.1	10
LON-04-J	CM1	**2.0**	0.5	0.1	0.1	0.0	71.1	5.6	76.4	4.0	8
LON-04-B	CM1	**2.0**	0.6	0.1	0.1	0.0	67.3	2.1	63.4	1.2	6
LON-04-V	CM1	**2.0**	0.5	0.0	0.1	0.0	66.0	0.9	76.5	1.2	10
LON-04-S	CM1m - an	**2.0**	1.1	0.0	0.2	0.0	63.9	0.4	70.6	0.8	6
LON-04-T	CM1m - an	**2.0**	0.7	0.0	0.1	0.0	57.6	0.7	72.6	1.4	10
LON-04-K	CM1m	**2.0**	0.4	0.0	0.0	0.0	74.5	1.2	74.2	1.0	10
LON-04-U	CM1m	**2.0**	0.6	0.0	0.1	0.0	67.6	2.2	71.0	1.2	6
Aguas Zarcas											
AZ-04-B	CM2	**2.6**	0.8	0.1	0.1	0.0	54.8	1.9	76.3	2.8	12
AZ-04-D	CM2	**2.6**	0.8	0.1	0.2	0.0	55.5	3.4	74.7	5.3	5
AZ-02-A	CM2	**2.5**	0.9	0.1	0.1	0.0	53.0	4.1	79.9	2.0	6
AZ-04-C	CM2	**2.3**	0.8	0.1	0.1	0.0	57.0	2.1	79.4	1.8	9
Mukundpura											
MP-01-B	CM2	**2.7**	0.9	0.1	0.1	0.0	53.3	2.5	74.9	2.6	9
MP-01-A	CM2	**2.3**	0.8	0.0	0.1	0.0	56.4	2.2	75.4	8.1	5
MP-05-A	CM1	**2.0**	0.5	0.0	0.0	0.0	65.2	4.4	82.1	0.7	7
Winchcombe											
WC-02-A	CM2	**2.2**	0.6	0.1	0.1	0.0	65.9	3.7	73.5	3.5	15
WC-01-A	CM2	**2.1**	0.6	0.0	0.1	0.0	68.0	1.2	76.8	1.9	13
Kolang											
KO-01-A	CM2	**2.3**	0.6	0.0	0.1	0.0	64.6	1.5	74.4	2.0	8
KO-01-D	CM2	**2.1**	1.0	0.3	0.1	0.1	55.2	7.7	-	-	7
KO-03-A	CM2.1 -an	**2.1**	0.4	0.1	0.1	0.0	74.9	5.6	72.7	0.7	7
KO-01-C	CM1	**2.0**	0.6	0.1	0.1	0.0	64.5	3.3	80.1	6.7	6

Table 4.4 - Compositional data for TCI in all lithologies. 'FeO' contains FeO from phyllosilicates, Fe^{3+} from cronstedtite and magnetite, and Fe^{2+} from sulphides.

TCI COMPOSITION											
Lithology	**Description**	**Subtype**	**FeO/ SiO_2**	**2SE**	**S/ SiO_2**	**2SE**	**Mg#**	**2SE**	**EDS Total**	**2SE**	**n**
LON 94101											
LON-04-A	CM2	**2.8**	15.2	3.8	8.3	2.3	8.8	2.3	85.5	1.5	8
LON-04-D	CM2	**2.7**	11.0	1.6	3.2	0.5	23.3	2.6	86.1	1.1	22
LON-04-C	CM2	**2.6**	4.4	0.5	0.9	0.1	21.9	2.4	87.2	1.1	12
LON-04-O	CM2	**2.5**	2.0	0.2	0.1	0.1	30.6	5.0	81.8	1.7	15
LON03a-B	CM2	**2.5**	3.7	0.2	0.3	0.1	29.6	2.6	79.5	0.4	67
LON-04-E	CM2	**2.4**	3.0	0.4	0.4	0.2	26.4	2.2	86.6	1.1	21
LON-04-F	CM2	**2.4**	2.5	0.6	0.1	0.1	25.3	5.9	85.0	0.8	11
LON-03a-A	CM2	**2.2**	1.7	0.2	0.1	0.0	36.8	4.8	83.0	0.6	30
LON-01-B	CM2	**2.1**	2.0	0.2	0.5	0.0	25.9	4.1	-	-	6
LON-04-G	CM2	**2.1**	1.8	0.2	0.1	0.0	32.8	5.9	85.0	0.7	10
LON-04-B	CM1	**2.0**	2.4	0.3	0.5	0.2	31.5	4.7	80.3	1.2	26
Aguas Zarcas											
AZ-04-B	CM2	**2.6**	2.6	0.3	0.6	0.1	34.4	2.4	84.4	0.6	26
AZ-04-D	CM2	**2.6**	2.9	0.3	0.7	0.2	35.0	2.5	80.8	0.6	12
AZ-02-A	CM2	**2.5**	2.4	0.1	0.5	0.1	33.0	1.9	85.2	0.6	14
AZ-04-C	CM2	**2.3**	1.6	0.1	0.3	0.0	47.2	4.0	88.3	0.9	17
Mukundpura											
MP-01-B	CM2	**2.7**	12.9	7.1	1.8	0.6	21.2	6.6	90.7	5.0	8
MP-01-A	CM2	**2.3**	1.5	0.2	0.3	0.0	46.8	3.8	87.3	0.6	12
MP-05-A	CM1	**2.0**	1.3	0.0	0.1	0.0	43.4	0.9	83.3	0.6	8
Winchcombe											
WC-02-A	CM2	**2.2**	1.3	0.1	0.2	0.0	48.4	1.8	85.9	0.8	44
WC-01-A	CM2	**2.1**	2.1	0.1	0.2	0.1	33.0	3.0	84.8	0.4	28
Kolang											
KO-01-A	CM2	**2.3**	1.9	0.2	0.3	0.1	39.2	3.2	83.9	1.0	11
KO-01-D	CM2	**2.1**	1.8	0.2	0.1	0.0	32.8	5.9	85.0	0.7	10

lithologies of moderate levels of alteration. Collectively, the lithologies in this thesis, together with Kerraouch *et al.* (2022) number 8, on par with Winchcombe. It is clear that the assessment of a dominant form of alteration is only as valid as the number of polished blocks analysed. Analysis of further stones may reveal the dominance of a different lithology in any given meteorite, a fact that is intimately intertwined with the apparent degree of brecciation. More brecciated meteorites would usually be expected to have a greater selection, and dominance, of clasts.

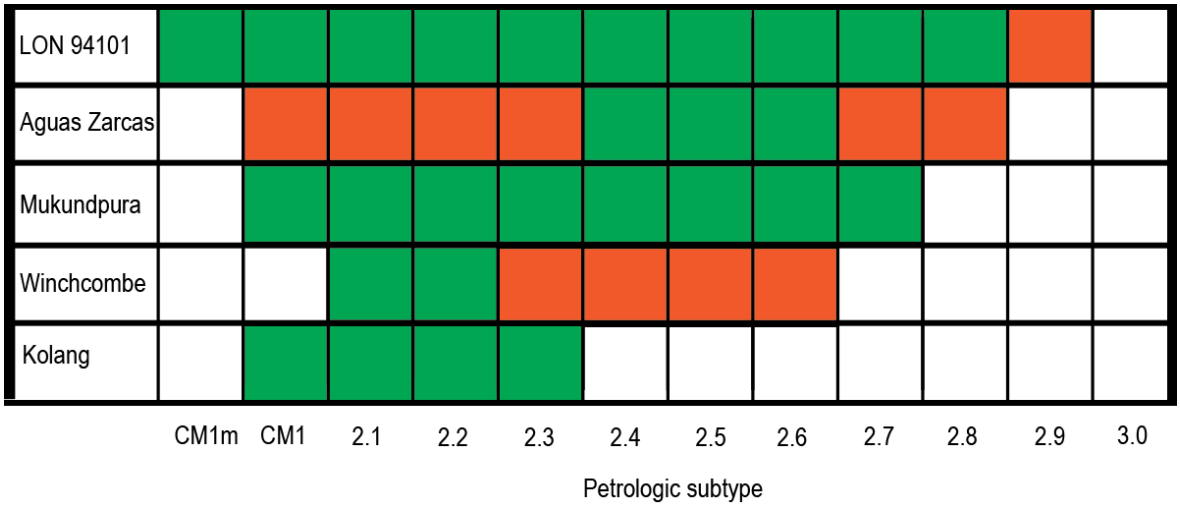

Figure 4.21 - Petrologic ranges determined from this study (green) and literature data (orange). Complementary data from (Gattacceca *et al.,* 2022; Kerraouch *et al.,* 2021; Kerraouch *et al.,* 2019; King *et al.,* 2022; Lentfort *et al.,* 2021; Lindgren *et al.,* 2013; Potin *et al.,* 2020; Ray and Shukla, 2018; Rudraswami *et al.,* 2019; Suttle *et al.,* 2023)

The influence of brecciation (Bischoff *et al.,* 2006; Lentfort *et al.,* 2021) upon the ability to classify a lithology is displayed excellently by LON 94101. Preliminary investigations indicated that every thin section made from this meteorite appeared different and that the exposure of a lithology was a product of chance (Gregory *et al.,* 2015; Zolensky *et al.,* 2022). Measuring approximately 70 x 40 mm, LON-04 offers an unparalleled surface area of 2800 mm^2 (Fig 4.16), an order of magnitude larger than that reported for Winchcombe, further reflected in number of identified clast boundaries at >70, a conservative minimum estimate (Gregory *et al.,* 2015). Many of these clasts exist at the mm - cm scale and could easily be mistaken for different meteorites in their own right if recovered as separate finds, comparable, for example to the recent C1-ung fall, Flensburg at 27 grams (Bischoff *et al.,* 2021) is only ~3 cm across. To extrapolate the diversity found within the ~50 g of LON used to make LON-04 to its total recovered Antarctic mass (2.8 kg), including that of its pairing partner LON 94102 (0.9 kg), it is not unreasonable to postulate that many more CM lithologies may exist across these masses alone given the large number of unique lithologies observed within LON-04. This number will only increase as particularly large meteorite CM

falls of somewhat comparable brecciation, *e.g.,* Aguas Zarcas at ~20 kg, or Boriskino (Vacher *et al.*, 2018) at ~1.3 kg, are subject to further study.

4.7.2 Revisiting the Rubin classification system

The quantitative criteria of the Rubin scale have been plotted below (Figs 4.22, 4.23 and 4.24) to provide rationale for the classification approach in this work. The large amount of data obtained using the same, calibrated microscope offers a unique opportunity to discuss the Rubin classification scheme in light of an expanded dataset. The trends are discussed within the context of partially altered CM2 material. CM1 and CM1m material, while included (and considered) in the plots, are excluded from any apparent trend as they were unable to be subjected to the same level of detailed subclassification. This is shown by a solid grey bar in Figures 4.22-4.24.

4.7.2.1 TCI compositions

To first evaluate the most popular criterion to assess the degree of aqueous alteration, the 'FeO'/SiO_2 composition of Tochilinite-Cronstedtite intergrowths (TCIs) are considered. Figure 4.22 shows the plethora of lithologies plotted. As alteration progresses, the Fe activity of solution, initially highly concentrated due to the dissolution of Fe-Ni metal and FeS, is expected to decrease as alteration proceeds, subsequently lowering the 'FeO'/SiO_2 ratio within the TCI material as the petrologic subtype decreases (Rubin *et al.,* 2007). This relationship is clearly seen in Figure 4.22 (a). Included within the graph are the compositional thresholds outlined in this thesis, Rubin *et al.* (2015) and Lentfort *et al.* (2021) for each subtype, and also the TCI compositions and subtypes from Winchcombe (Suttle *et al.,* 2023). The rationale behind narrowing the thresholds between 2.2 and 2.6, as shown by the yellow polygon, was to provide a more restricted range of compositional criteria to assist the classifier in subdividing the lithologies in this 'ambiguity region' as outlined by the red circle (Table 4.1, Fig 4.22). This was initially established upon assessment of the large range of lithologies within the meteorite falls (*i.e.*, not LON), for which there is an excellent fit.

Unfortunately, TCI material within multiple lithologies in LON fail to fit this trend with a distinct elevation to higher values (Fig 4.22 (b)). While an initial explanation could be Antarctic weathering, this is overruled in consideration of the compositions reported by Suttle *et al.* (2023), who report similar enrichment in Winchcombe, a very pristine fall, to an even higher extreme than LON. This reflects inter-meteorite TCI heterogeneity and reiterates why a single compositional parameter is unsuitable for confidently establishing petrologic subtype. TCIs themselves may also present further problems in the form of their physical appearance biasing the results, as discussed in the next section (4.7.3). The 'FeO'/SiO_2 thresholds established by the falls nevertheless remains within the limits of published trends and are considered acceptable for classification (Table 4.1).

Next to consider is the S/SiO_2 ratio of TCIs (Fig 4.22 (b) and (c)). Sulphur is fluid mobile, and it would be expected that the S/SiO_2 ratio would follow 'FeO'/SiO_2 as primary sulphides are attacked and redistributed during progressive aqueous alteration. Unfortunately, significant heterogeneity among the S/SiO_2 ratio of TCIs has led to the abandonment of this system of measurement since its initial inception by Rubin (2015). As S can exist in several oxidation states, fluid mobility is not the only factor to consider when trying to unravel reasons behind the heterogeneous compositions. Sulphur must be reduced into the S^{2-} to precipitate tochilinite (Vacher *et al.*, 2020). This S activity may be driven by changes in pH and temperature, while the precipitation conditions influenced by the availability of complementary cations. However, it is expected that changes in the oxidation environment will concurrently affect Fe, which can exist in both ferrous (Fe^{2+}) and ferric (Fe^{3+}) forms (Pignatelli *et al.*, 2016). An alternative culprit is the availability of sulphide in the precursor assemblage. Alteration of Fe-Ni metal and FeS will only produce mobile S if the latter is present in significant amounts (Pignatelli *et al.*, 2016). Iron, on the other hand, is a component of both Fe-Ni metal and primary FeS and so will not suffer the same availability issue. Regardless of cause, this sulphur heterogeneity can be observed when comparing the

very strict thresholds outlined by Rubin (2015), with those outlined in this work (Fig 4.22 (b) and (c)). The lithologies in this thesis, particularly the meteorite falls, define much wider thresholds of S/SiO_2 composition in a way which appears useful for subdivision. While it is obvious that the S/SiO_2 ratio alone cannot be used alone to decipher the degree of aqueous alteration, it can be used in tandem with other criteria to provide additional context. It also reveals that different S/SiO_2 trends may be present. In the case of this thesis, the majority of lithologies define a higher trend than Rubin *et al.* (2015), consistent with an exponential relationship as petrologic subtype increases; yet, a few lithologies in LON are anomalously S depleted at higher subtypes, despite having high Fe content, more in line with the Rubin (2015) thresholds, and potentially represents an environment of similar alteration conditions, but with a lower net contribution from sulphur.

Finally, the Mg# of TCIs follows the trend of 'FeO'/SiO_2 ratio, emphasising the increase in Mg content in the TCIs as alteration progresses, and is a useful addition to the classification scheme if desired. No trend is found between the petrologic subtype and the wt % oxide EDS totals of TCIs (Fig 4.23).

Only one CM1 lithology, LON-04-B contains convincing TCI material, though as a cataclastic breccia these TCIs may not be a result of the alteration experienced as a whole by this lithology. MP-05-A contains very obvious matrix of Fe-phyllosilicate that is compositionally identical to highly altered TCIs but lack dominance by common pseudomorphic shapes. Both appear to be congruent with the trends described, within the same degree of scatter as the CM2 material (Figs 4.22-4.23).

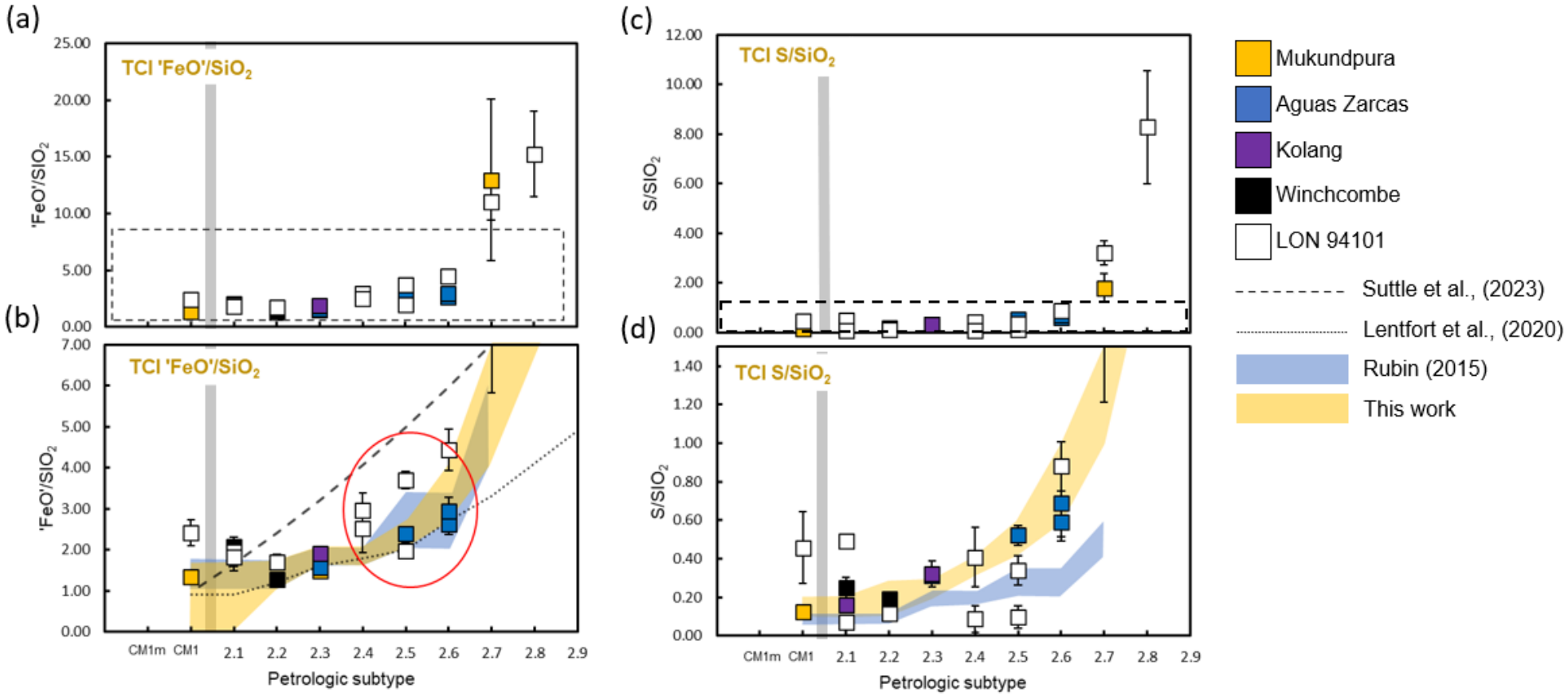

Figure 4.22 - 'FeO'/SiO_2 and S/SiO_2 of TCIs vs petrologic subtype. 'FeO' includes Fe^{2+} and Fe^{3+} in cronstedtite and magnetite. The red circle in (b) highlights the 'ambiguity region' between petrologic subtype 2.4-2.7. The dashed boxes in (a) and (c) represent the areas plotted in (b) and (d), respectively. Yellow thresholds are from Table 4.1. The grey bars separate well characterised CM2 material from the more arbitrary CM1 and CM1m groups. Errors are 2SE.

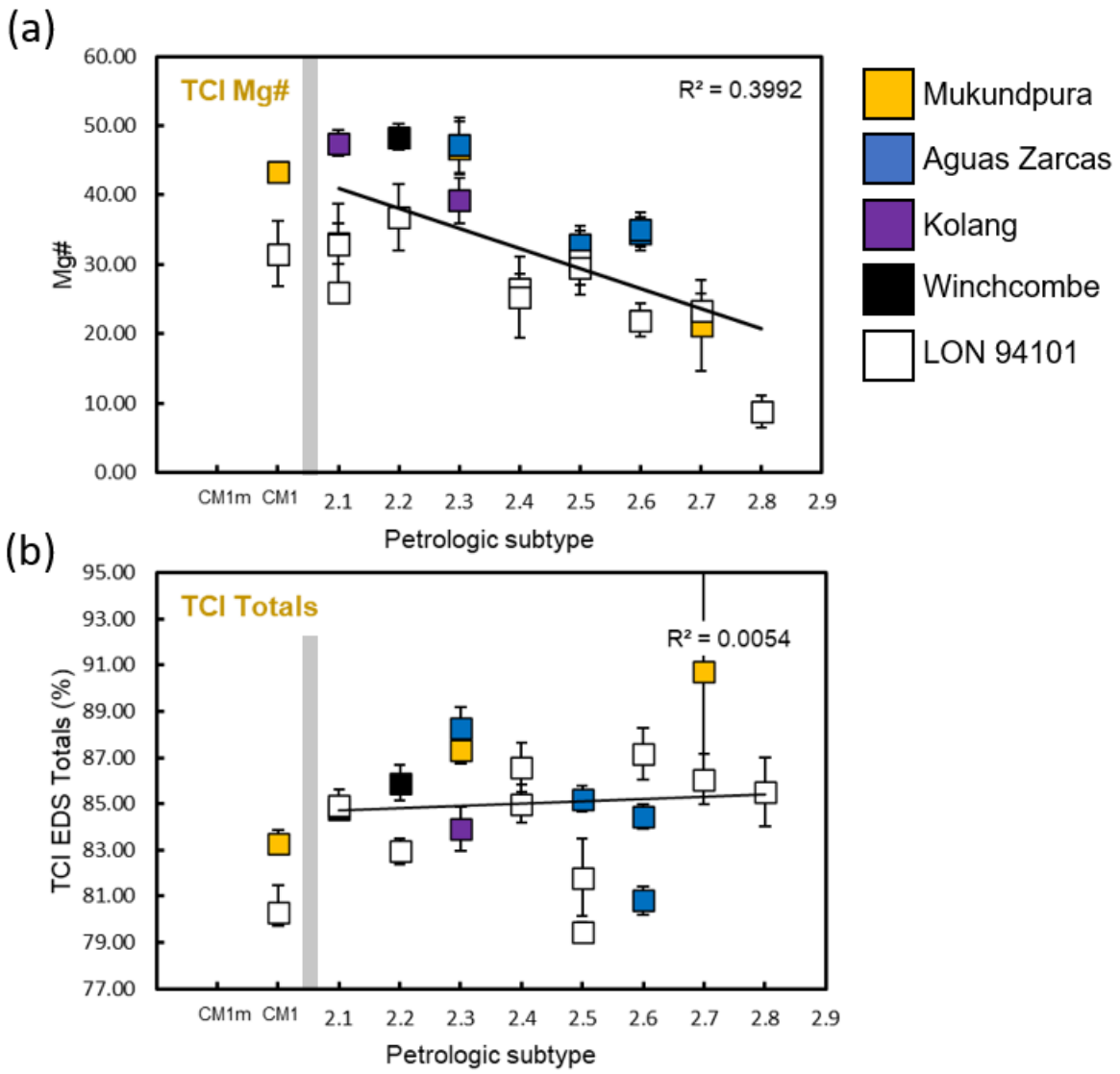

Figure 4.23 – Mg# and EDS totals of TCIs vs petrologic subtype. Mg# exhibits a useful trend with a good correlation of fit. No trend is observed with the EDS totals. The grey bars separate well characterised CM2 material from the more arbitrary CM1 and CM1m groups. Errors are 2SE

4.7.2.2 Matrix compositions

Continuing with the suggestion of appropriate classification metrics, the next obvious choice is the composition of the fine grained, Mg-rich matrix interstitial to the chondrules and TCIs. Due to its omnipresence in all CM lithologies, this component should be a good medium for comparison. In addition, the matrix is the most porous component and therefore the likeliest phase to harbour water during the alteration process (Brearley, 2006), yet rarely is it employed to the same extent as the TCI compositions The matrix 'FeO'/SiO_2 composition in particular has a high apparent trend from subtypes 2.9-2.1 than the complementary trend

exhibited in TCIs, and so this metric was also implemented as a classification threshold (Table 1). This is reflected further in the Mg# of matrix, which has an even tighter trend. Further classification attempts should ideally consider these two tighter-fitting criteria when attempting inter-meteorite comparisons to overcome any potential ambiguity associated with TCI composition alone. A correlation is observed between the petrologic subtype and the matrix EDS totals (Fig 4.24), but this has a high scatter so was not used. It is worth noting that the magnitude of each Rubin increment is undefined as it is an arbitrary scale, therefore using it as a metric to establish trends may be inconsequential. However, as trends are observed in a relatively linear fashion it can be deduced the Rubin scale is at least progressing in a usefully regular manner.

Including matrix compositions of the highly altered, CM1 and CM1m clasts extends the trends to higher / lower values (Fig 4.24). However, the scatter on this data is considerable and quite different between the two subgroups when compared to CM2 material. This is perhaps suggestive of a similar process affecting the CM1 and CM1m clasts as the CM2 to produce such a large range in compositions; however, the lack of a detailed classification system for matrix-supported lithologies, primarily due to the very fine-grained nature of the matrix posing a challenge for identifying any anhydrous precursors, forces these clasts into a limited set of two subgroups.

4.7.2.3 Proportion of Fe phyllosilicate and fine-grained matrix

ImageJ analysis of the surface area of the polished blocks to determine Fe-phyllosilicate content (primarily TCI material) reveals that the abundance of this phase increases as aqueous alteration increases (Table 4.2, Figure 4.25). This matches the increase in TCI abundance from the least altered stages to high up in the moderate stages of alteration. In opposition, the area % of fine-grained matrix decreases as alteration proceeds as a larger modal percentage of the section is taken up by TCIs. However, upon reaching complete alteration, the proportion of Mg-phyllosilicate rapidly increases once more as Mg- enriched,

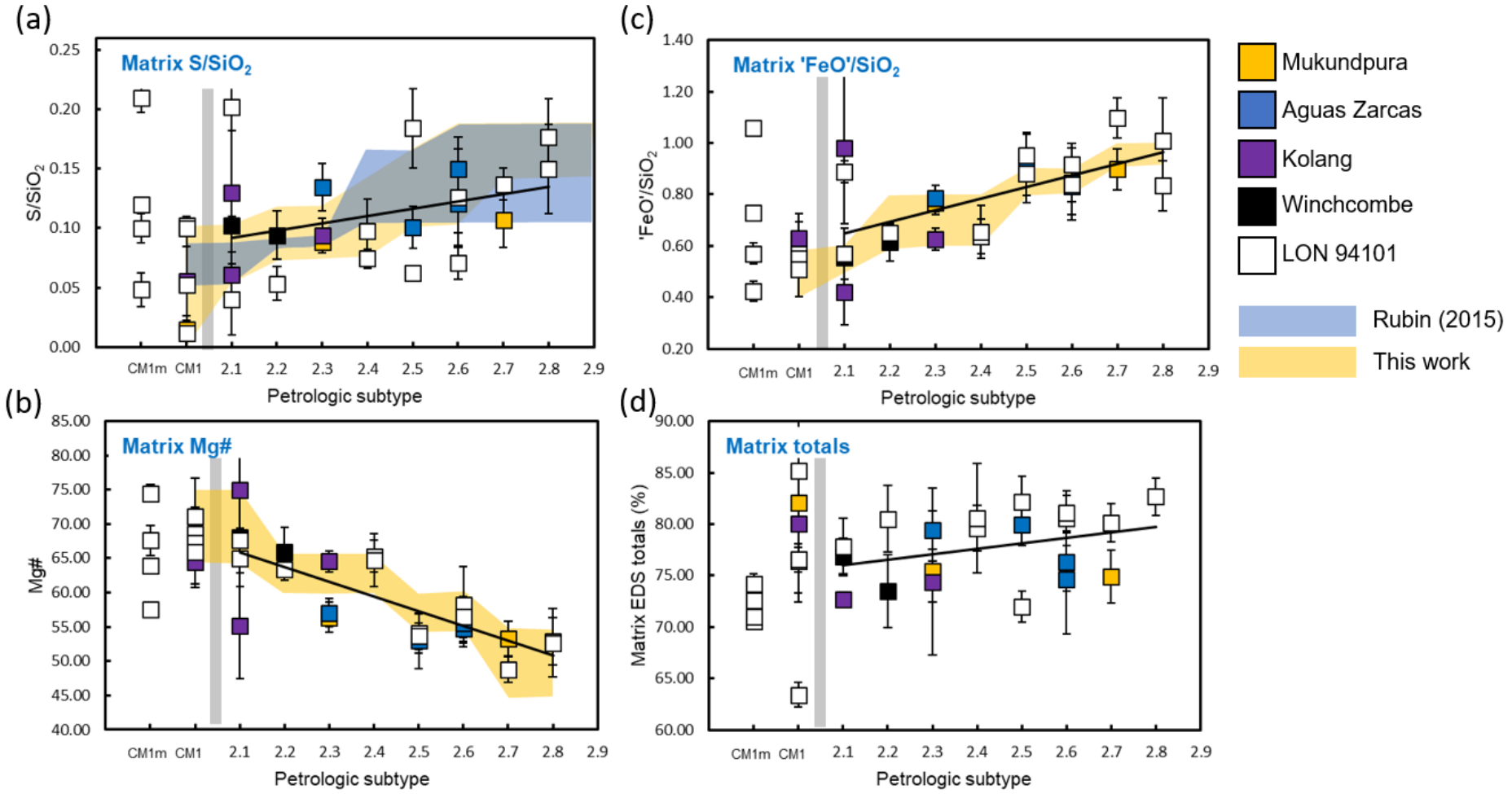

Figure 4.24 – (a) and (b): 'FeO'/SiO_2 and S/SiO_2 of matrix vs petrologic subtype. 'FeO' includes Fe^{2+} and Fe^{3+} in cronstedtite and magnetite. Yellow thresholds are from Table 4.1 (c) and (d) Mg# and EDS totals vs petrologic subtype. Errors are 2SE.

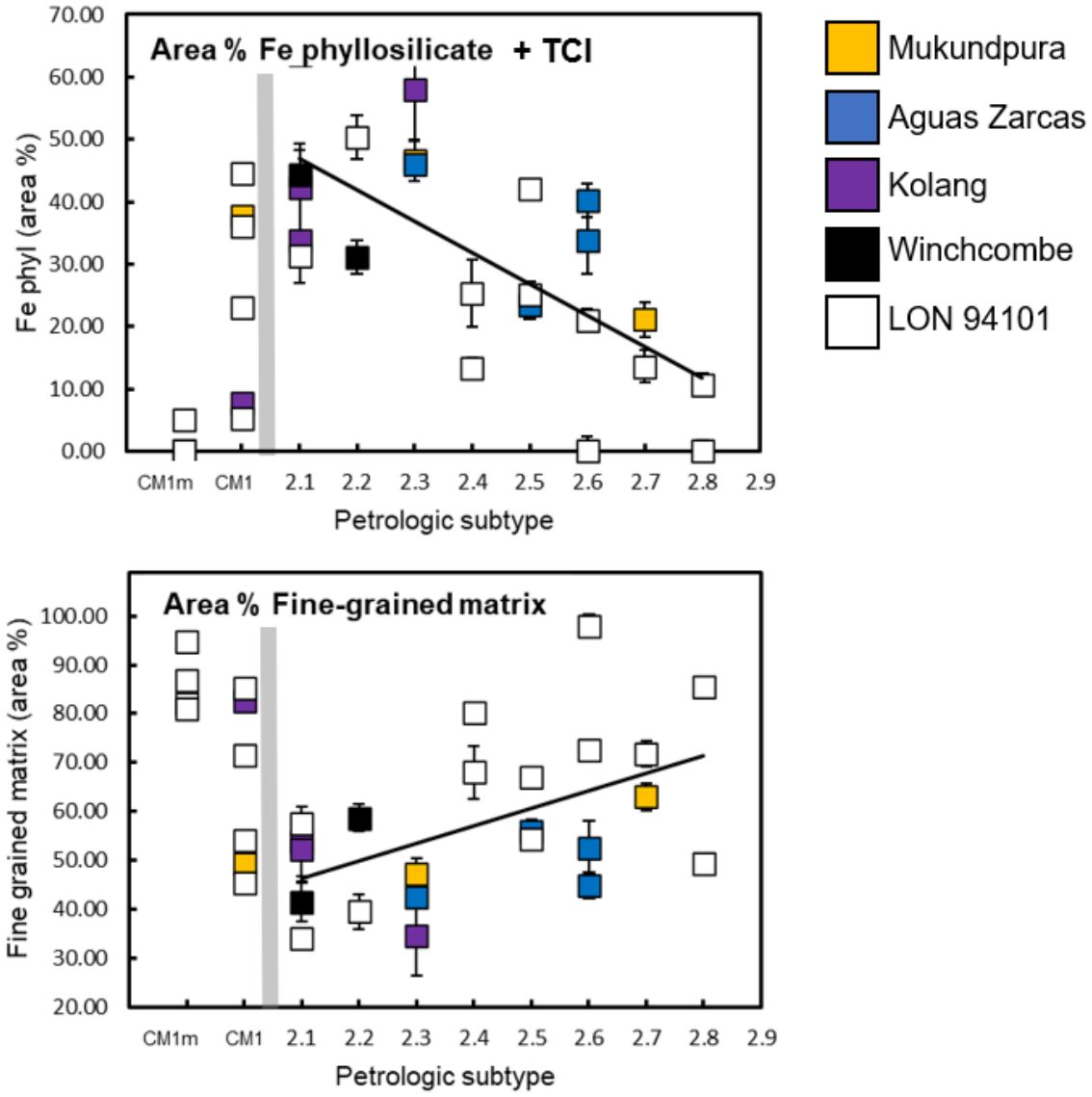

Figure 4.25 - Fe- phyllosilicate (top) and Fine-grained, Mg-rich matrix (bottom) vs petrologic subtype. Trends are observed within the CM2s. CM1 and CM1m material are not included in the trend as shown by the grey bars. Errors are 2SE.

pseudomorphic textures become dominant (Fig 4.25). Both trends have a high degree of scatter but can be used to some effect to bolster the primary classification parameters.

4.7.3 Petrographic evidence for lithological diversity on the CM parent asteroid(s)

4.7.3.1 Juxtaposition of clasts

Aqueous alteration extent, accretionary environment and parent body heritage may be inferred from petrographic relationships (Bischoff *et al.*, 2006). The two largest subdivisions of CM chondrites, the CM2s and CM1s, have often been interpreted as representing two distinct parent bodies based on sufficiently different degrees of aqueous alteration and

variable petrographic and isotopic characteristics (Greenwood *et al.,* 2019; Howard *et al.,* 2011; Howard *et al.,* 2010; King *et al.,* 2018; King *et al.,* 2020; King *et al.,* 2017). This can be challenged in part, if the two materials can be convincingly found next to each other. Juxtaposition of clasts in a polished block, if frequently observed, may imply a degree of petrologic kinship; that is, while it does not prove they formed in the same environment, it does suggest the clasts could sample the same immediate 'secondary' parent body (Greenwood *et al.,* 2020). Three out of the five meteorites: Mukundprua, Kolang and LON 94101 contain large CM1 clasts, adding weight to this suggestion. Furthermore, there is the possibility of a genetic relationship between the CM2 lithologies and the plethora of other clasts, such as CM1m; incipiently altered clasts (CM2.8), and the mystery clasts with unusual transitionary characteristics between canonical CM2 material and CI-like material (*e.g.,* CM2.8m, CM2.6m and two CM1m-anomalous).

4.7.3.2 Heterogeneous accretion

Regardless of stance on the number of CM parent bodies and the nature of alteration, if one is to assume that all the lithologies studied here are from secondary rubble-piles sampling a restricted asteroid-forming region of limited heliocentric distance (*e.g.,* Chaumard *et al.,* 2018), it would be a pre-requisite that a mechanism of heterogeneous accretion, and or material mixing is needed to produce the range of lithologies. This is particularly true for Type II TCIs, which are often mantled by accretionary rims (Haack *et al.,* 2012). Such processes could theoretically occur on a primary precursor asteroid (Bland and Travis, 2017), or in an accretionary environment where chondrules, matrix and TCI-precursors / partially altered TCIs are heterogeneously supplied to the region over time (Marrocchi *et al.,* 2023; Teitler *et al.,* 2010; Wurm and Krauss, 2006). Such a process remains enigmatic but may be natural in a protoplanetary disk full of vortices (Li *et al.,* 2020), settling and streaming instabilities (Johansen *et al.,* 2006), pressure maxima (Brasser and Mojzsis, 2020) and catastrophic disruption (Michel *et al.,* 2020; Michel and Richardson, 2013; Scott *et al.,*

1992), all while being episodically fed from the parental molecular cloud (Piani *et al.*, 2021) and through gravitationally disruptive, planetary migration events (Walsh *et al.*, 2012). For this to occur within a single parent body, however, would require a very specific set of conditions, probably a type of mudball convection (Bland and Travis, 2017).

Chondrites are without question, cosmic sedimentary rocks (Brearley and Jones, 1998). While the microgravity environment of the protoplanetary disk is very different to the sediment transport systems on Earth, the potential for complex processes should nevertheless be just as numerous. The rarity of meteorites has hitherto prevented the suggestion of a chondrite classification system that rivals the detail of those with terrestrial focus, for example, the classification of sandstones and limestones (*e.g.*, Tucker and Jones, 2023); however, armed with an ever-expanding repertoire of CM lithologies and textures, a similar system could theoretically be devised that moves away from the binary system of petrologic type alone. The three major components of a CM lithology are chondrules, TCIs/small fragments <100 μm and matrix, which could represent the apices of a ternary diagram (Fig 4.26) and provide the basis for a renewed classification approach. The modal abundances of these could be established in thin section, regardless of aqueous alteration extent provided that chondrule pseudomorphs can be reliably identified and, therefore the initial accretionary chondrule inventory accurately reconstructed. A suitable variable characteristic would then be aqueous alteration, divided using a classification like, but ideally more detailed than the Rubin scale (Rubin, 2015), to set apart pristine rocks from that have been moderately or totally altered by hydrothermal reactions. A suggestion for how this could be implemented is illustrated in Fig 4.26. Such a classification system applies sedimentological nomenclature to chondrites, including the sorting and accretionary processes that contribute to their formation. Chondrule dominated chondrites such as the ordinary chondrites bear resemblance to arenite sandstones in that 90 % of their composition is dominated by a single component; therefore, ‘chondritic arenite’ is appropriate. Chondrites containing a mixture of

both >100 µm chondrules and a proportion of smaller chondrule fragments, carbonates or TCIs <100 µm in diameter (reflecting that of terrestrial silt), could be named ‘chondritic siltstones’ or ‘chondritic wackes’, depending on the relative proportions of either chondrules or fragments. The matrix dominated chondrites, recorded in the CI chondrites, some dark inclusions and those clasts containing no chondrules could appropriately be called ‘chondritic mudstones’ (Fig 4.26). Such a classification system is juvenile at this point and would require refinement through a meta-analysis of all known chondrite textural data, but theoretically, it would contextualise in full the petrography, which would prove useful in tandem with an additional variable characteristic reflecting aqueous alteration or thermal metamorphism (Fig 4.26).

In summary: within brecciated CMs, the primary accretionary lithologies are clearly separated from highly processed, cataclastic matrix by sharp delineated boundaries. However, this does not preclude the possibility that the primary lithologies are first generation accretionary products. They may themselves be formed by accretionary debris from earlier formed, catastrophically disrupted planetesimals. Mn-Cr dating of T1a calcites, combined with oxygen isotope data on the various concentric, phyllosilicate-rich layers within type II TCIs will be vital in discerning if this hypothesis is correct.

4.7.3.3 Preface to next chapter

In the wake of the large petrographic dataset presented in this chapter, insights into the triple oxygen isotope systematics of bulk phyllosilicate phases from 22 chosen lithologies will now be presented to provide context into the environment and conditions of formation for each lithology.

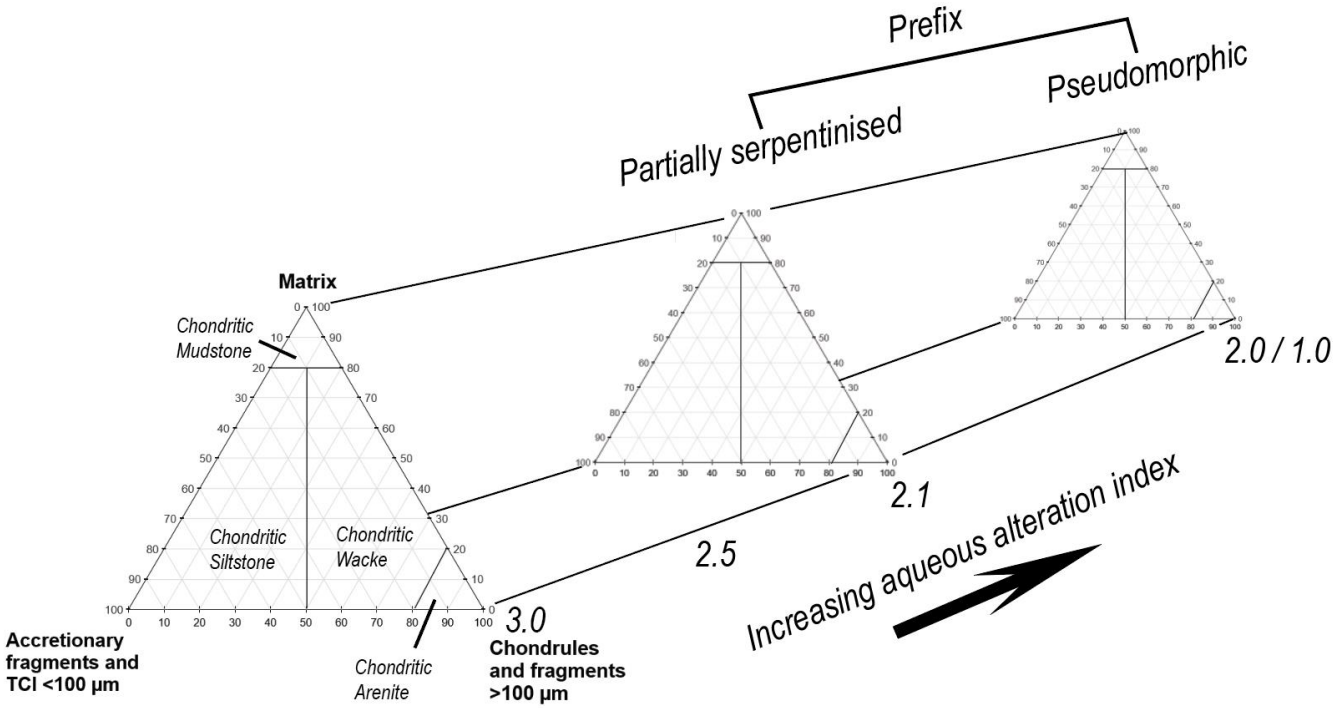

Figure 4.26 - A tentative suggestion for a theoretical classification system for CMs using terminology from sedimentology adding a dimension capable of capturing their accretionary processing history alongside the established criteria for recording aqueous alteration extent (*e.g.*, Tucker and Jones, 2023). The three principal components are matrix, chondrules and fragments over >100 µm, and chondrule fragments / TCIs <100 µm. This diagram does not directly discriminate according to chemical composition or mineralogy, instead offering the variable characteristic of aqueous alteration, attaching the prefix 'partially serpentinised' or 'pseudomorphic' according to severity. As a result, chondrule pseudomorphs or TCIs that exhibit clear pseudomorphic geometry must be counted as accretionary fragments of appropriate size. In this diagram, most CM chondrites that host Type II TCIs would classify as 'partially serpentinised chondritic siltstones'. CM1 material with chondrule pseudomorphs and relict TCIs would be 'pseudomorphic chondritic siltstones', or if lacking smaller grains/TCIs, 'pseudomorphic chondritic wackes'. CM1m and CI material will be 'pseudomorphic mudstones'. This diagram can also classify other chondrites, though they may be better suited to a scale with thermal metamorphism as a variable characteristic. A higher resolution image is provided in Appendix A2

Chapter 5 – Oxygen Isotopic Composition of Clasts in CM Falls

5.1 Introduction

This chapter reports the spatially resolved oxygen isotopic composition of aqueously altered matrix phyllosilicates (hereafter, simply 'matrix') from lithologies in recent meteorite falls Mukundpura, Aguas Zarcas, Kolang, and Winchcombe, as identified in Chapter 4. As meteorite falls are usually very fresh, each sample was recovered and curated days to weeks after falling and stored in a desiccator to prevent curational weathering (*e.g.*, Jenkins *et al.*, 2023; Lee *et al.*, 2020). It is expected that the influence of terrestrial weathering upon the oxygen isotopic composition will be low, and therefore each of these falls will provide an interesting comparison to those measured in LON 94101 — reported in Chapter 6— which has resided on the frozen surface of Antarctica for some extended period of time. Details of the microsampling and analysis procedures are given in Chapters 2 and 3.

Interpretation of the oxygen isotope data of the matrix phyllosilicates, including that reported in the subsequent Chapter 6 (LON 94101), is indeed dependent on previous works and must be compared and contrasted to current paradigms as outlined in Chapter 1 (e.g. Clayton and Mayeda, 1999; Young *et al.*, 1999). A scenario of alteration where a relatively homogenous asteroid is altered *in situ* by water is by and large, the favoured model in the literature (*e.g.*, Clayton and Mayeda, 1984; Clayton and Mayeda, 1999; Franchi *et al.*, 2001; Franchi, 2008; Fujiya, 2018; Schrader *et al.*, 2013). Indeed, bulk CM samples show (broadly) a trend of increasing $\Delta^{17}O$ and $\delta^{18}O$ as the petrologic subtype moves from 3.0 to 2.0 (Greenwood *et al.*, 2023), thought to be reflective of the prolonged interaction of isotopically distinct, ^{16}O-rich anhydrous precursors — likely with a $\Delta^{17}O$ composition of -5.2 ‰ — with a water reservoir enriched in ^{17}O and ^{18}O (Clayton, 2002; Lyons and Young, 2005), manifesting as a slope 0.7 line in oxygen 3-isotope space (Clayton and Mayeda, 1999; Greenwood *et al.*, 2003). However, this relationship falls apart when considering the relatively recent, albeit smaller complementary dataset provided by the CM1 and CM1/2 meteorites that fall along a mixing line that is coincidentally indistinguishable from a mass-dependent fractionation

line (King *et al.*, 2018). Furthermore, the majority of CM1s paradoxically bear intermediate O-isotopic compositions, as opposed to ^{16}O-poor an unexpected outcome considering they are the most altered CM chondrites (Howard *et al.*, 2011a; Howard *et al.*, 2010; King *et al.*, 2018). The nature of the CM1 mixing line (and if it is, indeed, mass-dependent) and its relationship with CM2 material will benefit from the data in this work, as Chapter 4 reports petrographic relationships between CM1 and CM2 materials in Mukundpura, Kolang and LON 94101. However, questions have been raised disputing if CM1 meteorites are contaminated by terrestrial oxygen while residing in Antarctica (Greenwood *et al.*, 2019; King *et al.*, 2018). While fresh falls are not exempt from rapid terrestrial alteration (Jenkins *et al.*, 2023; Lee *et al.*, 2020), weathering is less likely to be a problem if care is taken to ensure minimal atmospheric interaction; thus, this data offers a unique opportunity to discuss the oxygen isotope variations with more confidence.

5.2 Oxygen isotope results

Triple oxygen isotope data are tabulated in Table 5.1 and presented as traditional 3-isotope plots and as Δ^{17}O vs δ^{18}O plots. The graphs include published CM oxygen isotope data sourced from the detailed literature compilation of Greenwood *et al*. (2020), supplemented with additional data published since including the CM1 dataset from King *et al.* (2020). It must be noted that many graphs in the following two chapters will consist of lithology-specific oxygen isotopic compositions of matrix phyllosilicates plotted against the petrologic subtype as determined in Chapter 4; however, any apparent trend or high degree of linearity shown by the data may be inconsequential, as each step of the somewhat arbitrary Rubin alteration index (Rubin, 2015) represents a change in alteration of undetermined magnitude (Howard *et al.*, 2011b). However, strong correlations, irrespective of the linearity, may be linked to tangible phenomena and will be discussed in the context of the petrography reported in Chapter 4. Henceforth, all oxygen isotope measurements refer to the fine-grained

aqueous alteration products ('matrix') unless specified otherwise. A full supply of references of all oxygen and data sources is provided in the relevant figure captions.

Table 5.1 – Triple oxygen isotope compositions of recent CM falls. Some highly altered CM1 / CM2.1 lithlogies were large enough to be removed at the macro scale, providing material for a ~50 mg aliquot of powder for 'bulk' analyses plus a correlated polished block. The three instances in which both bulk and micromilled matrix were analysed display excellent reproducibility, indicating few anhydrous precursors were contaminating the carefully sampled, bulk material. For solitary micromilled samples, the 2σ uncertainty reflects the long-term internal reproducibility of the small sample, single-shot method, as reported in Chapter 3, section 3.3: 0.15 for $\delta^{17}O$, 0.31 ‰ f or $\delta^{18}O$ and 0.03 ‰ for $\Delta^{17}O$ (all in ‰).

Lithology	Desc	Rubin	$\delta^{17}O$	2σ	$\delta^{18}O$	2σ	$\Delta^{17}O$	2σ	n	Analysis
Mukundpura (2017)										
MP-01-B	CM2	2.7	-0.08	0.15	5.31	0.31	-2.85	0.03	1	1 micro
MP-01-A	CM2	2.3	2.14	0.08	9.04	0.12	-2.56	0.05	3	1 micro + 2 bulk
MP-05-A	CM1	1.0	0.70	0.18	6.03	0.20	-2.44	0.09	3	3 bulk
MP – Cata	-	-	1.65	0.60	8.00	1.11	-2.51	0.05	2	2 bulk
Aguas Zarcas (2019)										
AZ-04-B	CM2	2.6	-4.90	0.15	5.09	0.31	-3.14	0.03	1	1 micro
AZ-04-D	CM2	2.6	1.08	0.15	6.83	0.31	-2.48	0.03	1	1 micro
AZ-02-A	CM2	2.5	0.29	0.15	6.45	0.31	-3.06	0.03	1	1 micro
AZ-04-C	CM2	2.3	0.68	0.15	6.54	0.31	-2.72	0.03	1	1 micro
AZ - Cata	-	-	1.14	0.15	7.12	0.31	-2.57	0.03	1	1 micro
Kolang (2020)										
KO-01-A	CM2	2.3	1.88	0.13	8.09	0.39	-2.33	0.07	3	1 micro + 2 bulk
KO-01-D	CM2	2.1	1.30	0.15	6.92	0.31	-2.30	0.03	1	1 micro
KO-03-A	CM2	2.1-an	4.23	0.35	12.17	0.69	-2.10	0.01	3	3 bulk
KO-01-C	CM1	1.0	0.90	0.15	6.38	0.31	-2.42	0.03	1	1 micro
KO - Cata	-	-	1.33	0.33	7.31	0.0	-2.47	0.33	2	1 micro + 1 bulk
Winchcombe (2021)										
'Frag 1'[&]	CM2	2.1	2.75	0.4	9.48	0.5	-2.18	0.02	2	1 bulk
'Frag 2'[&]	CM2	Brec	0.94	0.31	7.29	0.62	-2.85	0.01	2	1 bulk
P30424*[#]	CM2	2.1	2.74	0.15	9.17	0.31	-2.03	0.03	1	1 micro
WC-02-A[*]	CM2	2.2	2.70	0.15	9.59	0.31	-2.28	0.03	1	1 micro
Field stone[*]	CM2	2.2	2.01	0.27	8.21	0.55	-2.25	0.02	2	2 bulk
WC-01-A[*]	CM2	2.1	2.65	0.15	9.05	0.31	-2.13	0.03	1	1 micro
WC – Cata[*]	-	-	1.17	0.15	7.31	0.31	-2.63	0.03	1	1 micro

[&]Data obtained in this work which was reported in Gattececca *et al.* (2022) then published in King *et al.* (2022). [*]Further spatially resolved O-isotope data reported in Greenwood *et al.* (2023). [#]a polished block of Winchcombe containing 'Lithology B' from Suttle *et al.* (2023). Highlighted Winchcombe analyses are one lithology across multiple polished blocks and stones, and have a near identical composition

5.2.1 Mukundpura

Mukundpura hosts three lithologies with quite distinct oxygen isotopic compositions (Fig 5.1). The least altered lithology, MP-01-B (2.7) is the most ^{16}O-rich, consistent with its alteration grade. However, when compared to the CM2 array, the matrix composition appears intermediate, neither lying close to incipiently or highly altered bulk measurements

(Fig 5.1). All matrix appears altered to phyllosilicate at the resolution of the SEM, hosting a modest proportion (21 %) of high-contrast, Fe- and S- enriched TCIs within its matrix (Chapter 4, section 4.2.1). The implications of the oxygen isotopic composition of tochilinite is discussed in detail in Chapter 7, though it is likely to be different to typical Fe- and Mg-matrix serpentines as a result of differences in bond stiffness in its lattice (Schauble, 2004; Zolensky and Mackinnon, 1986). It is possible that early formed tochilinite, in addition to residual precursors with a grain size below the resolution limit at which the samples were

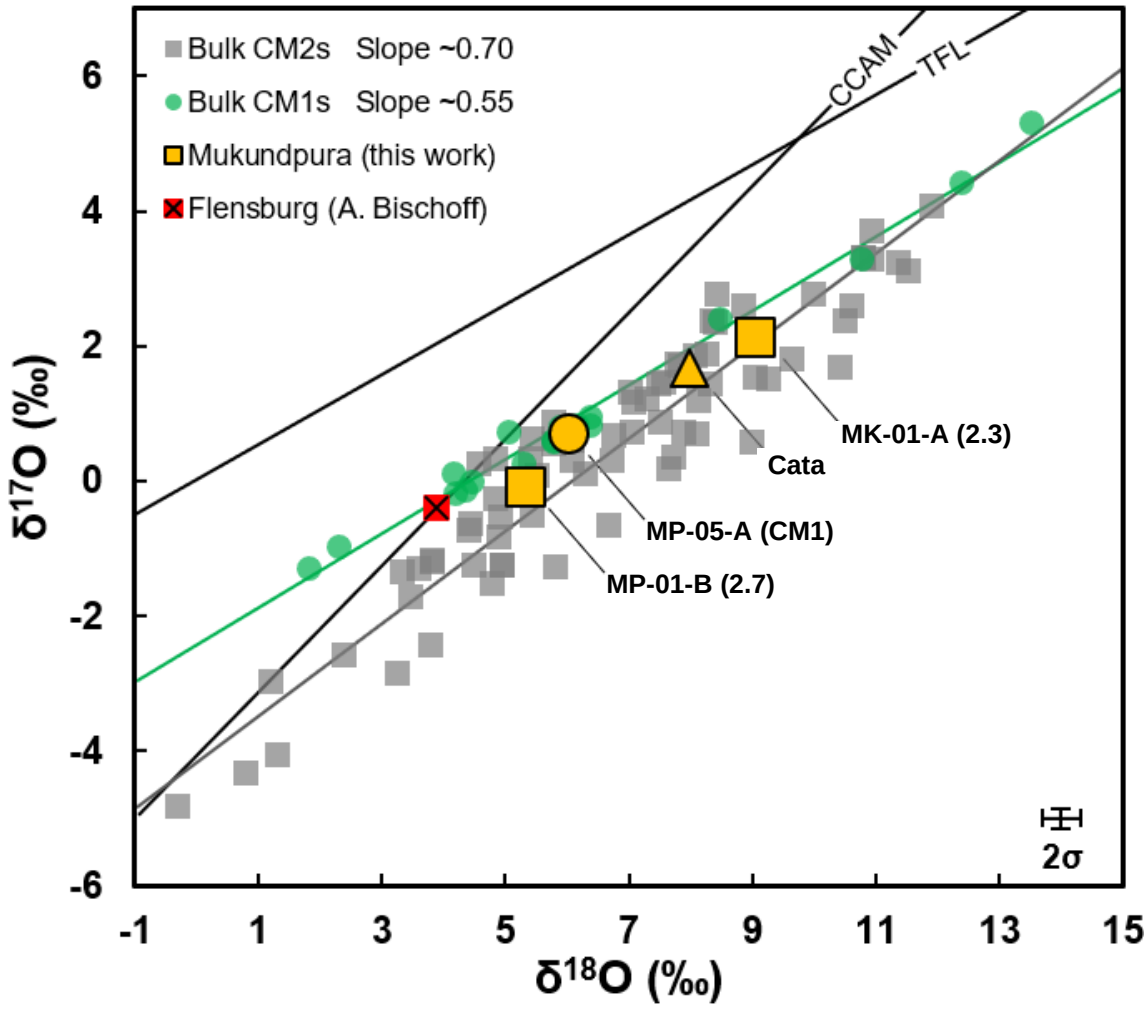

Figure 5.1 - Oxygen 3-isotope plot of spatially resolved matrix from Mukundpura. Most points are congruent with the CM1 array (green line) or intermediate between the CM1 and CM2 array (grey line). The CM1 lithology is isotopically lighter than many CM2 lithologies. Of special mention is the isotopic composition of the C1-ung (possibly CM1) Flensburg (Bischoff *et al.,* 2021) which lies on a slope 0.55 trend with the Mukundpura specimen CM1 lithology MP-05-A. Squares represent CM2 lithologies, circles CM1 lithologies, triangles cataclastic matrix. CM2 data (Clayton and Mayeda, 1999; Fan *et al.*, 2022; Haack *et al.*, 2012; Hewins *et al.*, 2014; Kimura *et al.*, 2020; King *et al.*, 2022; Lee *et al.*, 2019; Lee and Lindgren, 2016; Tyra *et al.*, 2007; Verdier-Paoletti *et al.*, 2019)

studied within the matrix (a possibility given its low alteration grade) are affecting the oxygen isotopic composition of the recovered fraction towards lighter values.

On the other hand, the most common lithology, MP-01-A (2.3), is moderately to highly altered, consistent with lithologies described from Mukundpura elsewhere (Potin *et al.*, 2020; Ray and Shukla, 2018; Rudraswami *et al.*, 2019) and perhaps more reflective of the meteorite as a whole as it lies close to the composition of the cataclastic matrix fraction, which is expected to be more representative of the bulk regolith (Metzler *et al.*, 1992). The microsampled fraction of MP-01-A (2.3) consists mostly of replaced TCI material and FGR matrix. The oxygen isotope data reflects this degree of alteration in being isotopically heavy with a $\delta^{18}O$ of 9.04 ± 0.12 (2σ), plotting just above the CM2 array.

The final lithology, MP-05-A, is certainly a CM1 (Chapter 4.2.3). The oxygen isotopic composition of this clast plots on the CM1 trend (Fig 5.1) within a cluster of CM1 data points and has a near identical $\Delta^{17}O$, -2.44 ‰ to the recent C1-ung fall, Flensburg ($\Delta^{17}O$ = -2.45 ‰), a meteorite that for all intents and purposes in this work is better reclassified as a CM1 (Bischoff *et al.*, 2021). MP-05-A is 3 ‰ lighter in $\delta^{18}O$ compared to MP-01-A (2.3), a paradox if a progressive hydration model (*e.g.*, Clayton and Mayeda, 1984; Clayton and Mayeda, 1999) is assumed, consistent with previous work (Greenwood *et al.*, 2019; Howard *et al.*, 2011a; Howard *et al.*, 2010; King *et al.*, 2018). While the original, Antarctic-dominated dataset of King *et al.* (2018) undoubtedly contains a fraction of isotopically light SLAP weathering products (Greenwood *et al.*, 2019), which may cause an apparent gradient reduction of the CM1 line, MP-05-A as a fresh fall partially vindicates this data as being largely indigenous to the asteroid and CM1s are indeed, dominated by isotopically light compositions. The effect cannot be readily attributed to anhydrous precursors either, as very little, if any anhydrous grains survive at the maximum resolution offered by the SEM. Under current paradigms — which requires CM waters being enriched in both $\delta^{17}O$ and $\delta^{18}O$ — this either requires a separate parent body or a complex process which is able to fractionate

the composition of the phyllosilicates to lighter values. The implication of this data is discussed alongside other CM1-CM2 occurrences in the synthesis chapter.

5.2.2 Aguas Zarcas

Aguas Zarcas proved a challenging meteorite to microsample due to the ubiquitous presence of small grains of forsterite within the matrix, in-between the large chondrules. While every effort was made to target regions dominated by matrix, inevitable contamination by anhydrous precursors was discovered in all lithologies after inspecting the micromilled holes. The most prevalent contamination is within the sample pits of AZ-04-B (2.6) and AZ-02-A (2.5) and as such they are highly concordant with the slope 0.7 array (Fig 5.2), whereas AZ-04-D (2.6) and AZ-04-C (2.3) are less compromised and exhibit transitional $\Delta^{17}O$ between the CM2 and CM1 arrays. Like the 2.7 lithology in Mukundpura, the 2.5-2.6 lithologies in Aguas Zarcas are further complicated by a sizeable proportion of Fe-, S- and tochilinite-rich TCIs with low Mg# which may have distinct oxygen isotopic compositions. In any case, the lithologies in this work, and the cataclastic matrix, occupy a relatively limited region of ~ 1.8 ‰ in $\delta^{18}O$, attesting to the homogeneity and limited degree of alteration in the sample studied here.

Upon inclusion of literature data (Gattacceca *et al.,* 2020; Kerraouch *et al.,* 2021) Aguas Zarcas spans a range of 9 ‰ in $\delta^{18}O$, indicating significant heterogeneity in the lithologies present in this brecciated meteorite (Fig 5.2). A suite of small chips were analysed by Dr Karen Ziegler at the University of New Mexico [MetBul - Gattacceca et al. (2020)] that extends the range of AZ to higher values of 10-13 ‰ $\delta^{18}O$, with all measurements lying below both CM1 and CM2 trendlines (Fig 5.2). Such heavy enrichments suggest distinct petrography compared to that observed in this work, though the unfortunate absence of any petrographic statement precludes any determination of its nature. The comprehensive bulk oxygen isotope study undertaken by Kerraouch *et al.* (2021) retains a much greater degree

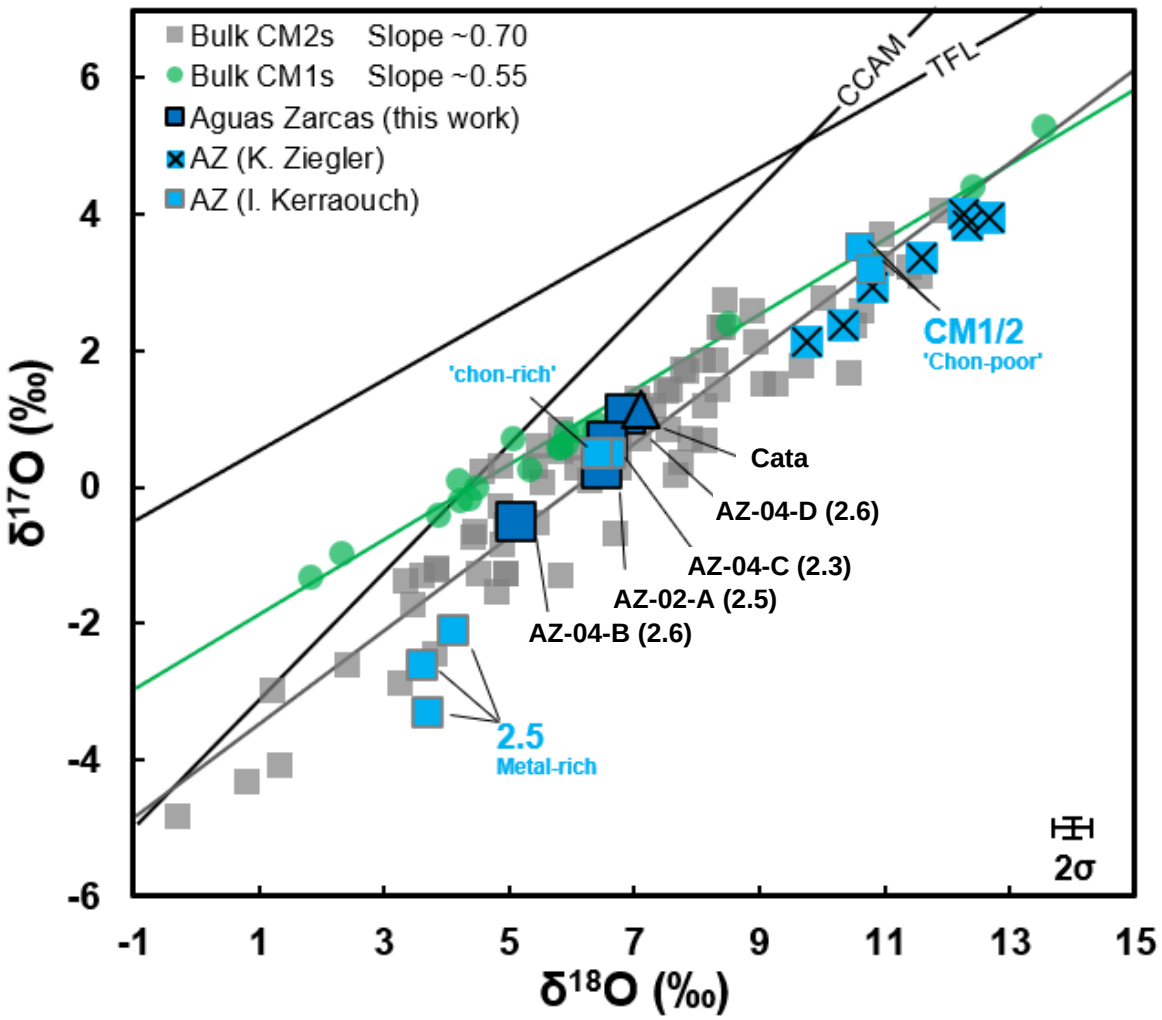

Figure 5.2 – Oxygen 3-isotope plot of Aguas Zarcas including data from Gattacceca *et al.* (2020) and Kerraouch *et al.* (2021). Aguas Zarcas is a very heterogeneous meteorite with a wide range of lithologies lying on or above the slope ~0.7 CM2 array. The metal-rich lithologies are of interest owed to their distinct, light oxygen isotope compositions lying far away from the CCAM line. Chondrule poor lithologies appear to dominate the dataset obtained by Dr Karen Ziegler. Squares represent CM2 lithologies, triangles represent cataclastic matrix. Data sources for CM2 and CM1 chondrites are the same as Fig 5.1. Errors are 2σ uncertainty reproducibility of the small sample method.

of petrographic context. Three lithologies of comparable alteration to this study (2.6-2.8) were measured and found to overlap with the results of this study. Most importantly, Kerraouch *et al.* (2021) analysed chondrule poor lithologies, including one initially designated C1/2 (2.2 later in the text of Kerraouch *et al.* 2021), both of which lie within the range of $\delta^{18}O$ as those measured by the New Mexico group (Fig 5.2). The petrography indicates pervasive alteration, extending the petrographic variability of Aguas Zarcas to

include very altered lithologies. At the other end of the spectrum, Kerraouch *et al.* (2021) also report the oxygen isotopic composition of an unusual metal-rich lithology, Met-1 which lies significantly below the CM2, CM1 and CCAM lines with a $\Delta^{17}O$ value of ~ -3 (Fig 5.2). As this lithology contains 50 % phyllosilicate (Kerraouch *et al.,* 2022), these compositions are not readily explained with a simple hydration model (Clayton and Mayeda, 1999), as the very light isotopic composition and departure from the CM2 mixing line suggests potential variation in the slope ~1 effect amongst its starting materials (Ushikubo *et al.,* 2012; Young and Russell, 1998). Oxygen isotope analysis of the matrix phases would go far in deciphering the nature of this lithology and its alteration history.

5.2.3 Kolang

Petrographic examinations of Kolang point towards this meteorite as being one of the most aqueously altered CM chondrite fall to date (King *et al.*, 2021; Marrocchi *et al.*, 2023; Schrader *et al.,* 2021). The matrix from five lithologies spanning CM1-CM2.3 were analysed, including a CM2.1-anomalous lithology. Each measurement, cataclastic matrix included, lie on or near the CM1 fractionation line (Fig 5.3). The most altered lithology is KO-01-C (CM1), occupying a region of 3-isotope space next to MP-05-A (CM1), further verifying the ^{16}O-rich peculiarity exhibited by CM1 lithologies. The Kolang array then steadily progresses to heavier compositions, starting at a $\delta^{18}O$ value of 6.38 ‰ with KO-01-C (CM1), through to KO-01-D (2.1), then the cataclastic matrix, then KO-01-A (2.3) at 8.09 ‰ before finally jumping significantly to KO-03-A (CM2.1-an) at 12.17 ‰ (Fig 5.3). The degree of fit to the CM1 trend is remarkably tight, but the correlation with alteration index is rather low (Fig 5.5). If the CM1 fractionation line is indeed attributed to mass-dependent processes and the $\Delta^{17}O$ of Kolang is (relatively) fixed, it would indicate that the WR ratio between each lithology is consistent despite the apparent variation of alteration grade, or at the high levels of alteration observed, isotopic equilibrium was achieved with respect to $\Delta^{17}O$. This may offer an explanation as to why CM1 lithologies are isotopically light. Mixing

of reservoirs with distinct compositions would not produce a consistent $\Delta^{17}O$. Instead, a mass-dependent mineral specific, or temperature control is required. The anomalous lithology KO-03-A (CM2.1 -an) offers further insight. This clast is highly altered, albeit not completely, but is ^{18}O-rich, sitting at a value of 12.17 ‰. KO-03-A has a unique mineralogical trait — the clast is highly porous and is 'overprinted' by a modal percent of

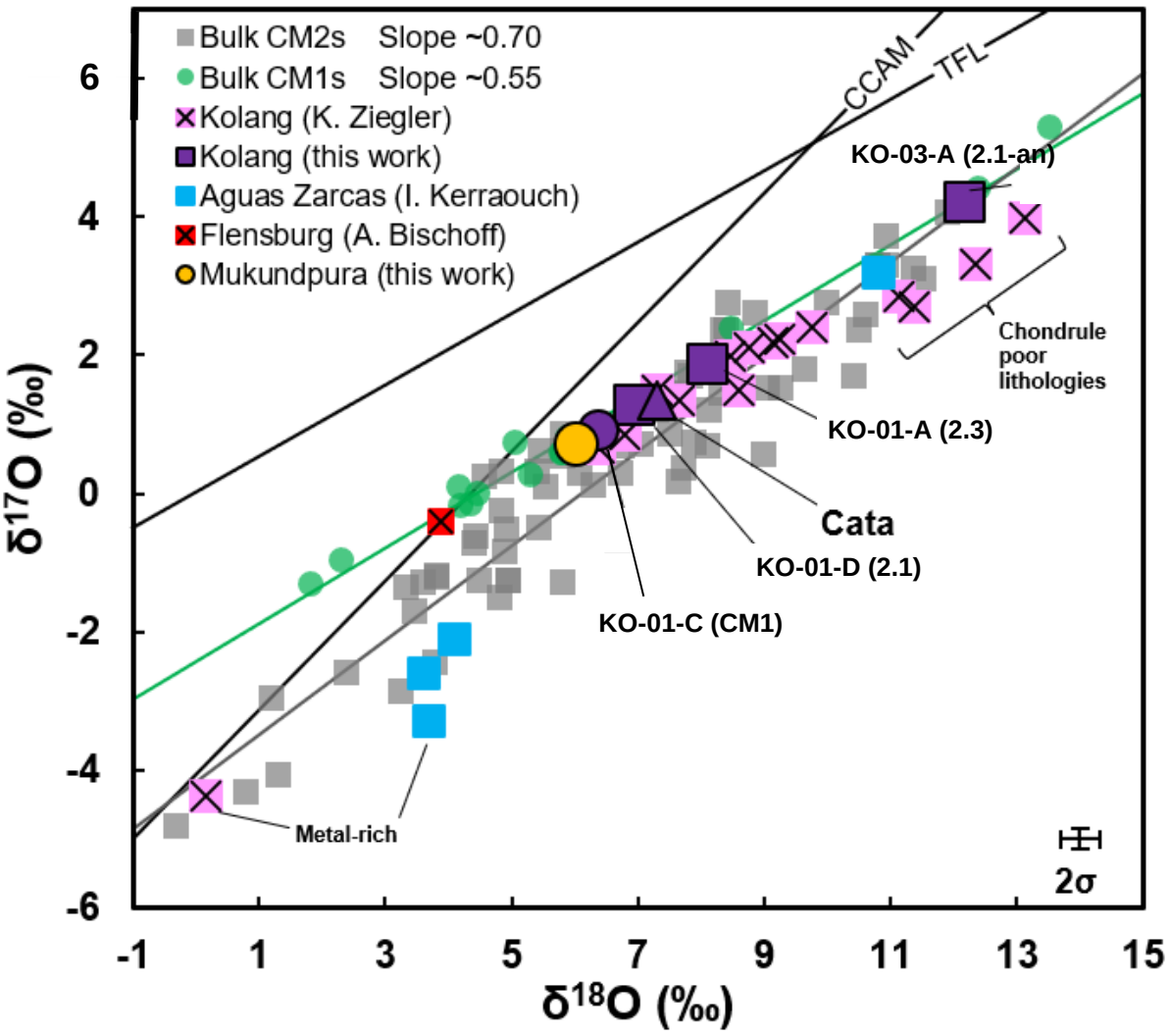

Figure 5.3 - Oxygen 3- isotope plot of Kolang. All points in this work are congruent with the CM1 fractionation line (green line) except for the cataclastic matrix. A CM1 lithology is of identical composition to the CM1 lithology in Mukundpura, both of which have a similar $\Delta^{17}O$ to Flensburg (Bischoff *et al.*, 2021). A highly altered, CM2.1-an lithology is cronstedtite-rich, and appears petrographically similar to the C1/2, chondrule-poor lithology described from Aguas Zarcas (Kerraouch *et al.*, 2021). Other literature points from the MetBul (Gattacceca *et al.*, 2021) show variable compositions. A metal-rich lithology plots very close to the CCAM line, away from the metal-rich lithologies in Aguas Zarcas, possibly indicative of a CM2.9/3.0 precursor provenance. Squares represent CM2 lithologies, circles CM1 lithologies, triangles cataclastic matrix. Data sources for CM2 and CM1 chondrites are the same as Fig 5.1. Errors are 2σ uncertainty reproducibility of the instrument in small sample mode.

33 % Fe-rich, ‘dendritic’ phyllosilicate with the most cronstedtite-like compositions of any other lithology in Kolang (Fig 4.10). The presence of cronstedtite, and the absence of tochilinite, may be exhibiting a control on the oxygen isotopic composition. Lower temperatures could also cause greater degrees of fractionation. This lithology is similar in petrographic composition to the C1/2 lithology previously mentioned in Aguas Zarcas (Kerraouch *et al.,* 2021) and they both have broadly comparable oxygen isotope compositions, indicating similar environments of cronstedtite precipitation are sampled by multiple meteorites. Akin to Aguas Zarcas, bulk O isotope compositions of Kolang were undertaken by Dr K. Ziegler and presented in the Meteoritical Bulletin initial classification report for this sample (Gattacceca *et al.,* 2021). Eight lithologies were subsampled encompassing two average, one chondrule-rich, three chondrule-poor, a ‘green-grey’ breccia and one metal-rich. The analyses were undertaken on small chips removed from each lithology, not spatially resolved matrix. But despite being whole-rock samples they plot along a line much shallower (slope ~0.5) than the whole-rock CM2 slope ~0.7 array. Indeed, the slope is even shallower than the CM1 mixing line and appears entirely consistent with a mass fractionation line (slope ~0.52). It may be that the samples at high $\delta^{18}O$ are contaminated by higher levels of anhydrous precursors, particularly CAIs, dragging them below the normal range of CM2 compositions, but without detailed petrography, this is just speculation. The metal-rich lithology is distinct in isotopic composition from those identified in Aguas Zarcas, plotting in the region occupied by the Asuka CMs close to the CCAM line. This suggests a CM2.8-2.9 provenance and the lithology could present viable evidence for the coexistence of highly altered and incipiently altered material at the Kolang source locality on the asteroid(s).

5.2.4 Winchcombe

All O-isotope data pertaining to the Winchcombe meteorite was obtained by the author during this study). The initial classification data reported on the MetBul (Gattacecca *et al.,*

(2022) was subsequently published in a Science Advances paper (King *et al.,* 2022), and consisted of two O-isotope measurements sourced from two large driveway stones, 'Fragment 1' and 'Fragment 2' (Table 5.1). Approximately 150 mg subsamples from both stones were homogenised (King *et al.,* 2022). Furthermore, two polished blocks, WC-01 and WC-02 were made from each of these fragments respectively and were investigated for lithological variation before microdrilling for further oxygen isotope analyses, published in Greenwood *et al.* (2023). The polished block WC-01 demonstrated that 'Fragment 1' was primarily composed of one CM2.1 lithology (Fig 4.12, Plate 4.13), here named WC-01-A. The polished block WC-02 demonstrated that 'Fragment 2' was predominantly a cataclastic breccia but contained a large inclusion of a CM2.2 lithology (Fig 4.11, Plate 4.12). Correlation of these lithology characteristics with the Winchcombe petrography paper by Suttle *et al.* (2022) indicates that the 2.1 lithology (WC-01-A) and the 2.2 lithology (WC-02-A) are related, or identical to 'Lithology B' and 'Lithology A' as identified in polished blocks made at the Natural History Museum, London.

The identified lithologies were microdrilled for oxygen isotope analysis and the results published in Greenwood *et al.* (2023). WC-01-A (CM2.1) has an identical oxygen isotopic composition to the bulk measurement of 'Fragment 1' (King *et al.,* 2022), as expected, as this stone appeared to constitute one homogenous lithology. As this lithology appeared to correlate with 'Lithology B' in the study of Suttle *et al.* (2023), a polished block containing the lithology from that study (P30424 – Table 5.2) was loaned from the NHM and microsampled. The O-isotopic composition of WC-01-A, P30424, and 'Fragment 1' are complementary / identical (Table 5.2, Fig 5.4), confirming the wide distribution of this lithology among the Winchcombe stones. All three plot on the 'heavy' end of the CM1 fractionation line (Fig 5.4). The O-isotopic composition of WC-02-A is also very similar within error to WC-01-A, attesting to the very altered nature of the Winchcombe meteorite with two lithologies exhibiting differences in petrography yet only small variations in O-

isotopic composition (Fig 5.4). WC-02-A resembled ‘Lithology A’ as reported in Suttle *et al.* 2023, and so a bulk sample of the ‘Field Stone’ — from which five polished blocks were made in Suttle *et al.* 2023 — which appear to be entirely made of ‘Lithology A’, was loaned from the NHM. O-isotope measurements of the Field Stone are in partial agreement with WC-02-A (2.2), in that they have very similar $\Delta^{17}O$ (-2.28 and -2.25 ‰) but variable $\delta^{18}O$ (Greenwood *et al.*, 2023; Fig 5.4). As a homogenised bulk sample, the field stone measurement will have likely contained remnant precursors, albeit at low levels given small shift in $\Delta^{17}O$, but also potentially different proportions of TCI and matrix phyllosilicates. A measurement of the cataclastic matrix from WC-02 confirms this phase, akin to the cataclastic matrix in Aguas Zarcas, Mukundpura and Kolang, has a distinct isotopic signature, possibly made from a combination of all lithologies in each meteorite. ‘Fragment 2’ and by extension, WC-02, contains an appreciable amount of cataclastic matrix, which explains why the O-isotope composition of ‘Fragment 2’ lies very close to the spatially resolved cataclastic matrix measurement.

Winchcombe represents a diverse regolith breccia with a large petrologic range but only a small fraction of the lithologic diversity is explored here for their oxygen isotopic compositions. Of note are two lithologies reported in Suttle *et al.* (2023) that would be interesting to explore in the future, ‘Lithology C’ (2.2/2.3) that contains large areas of tochilinite, and ‘Lithology D’ (2.6) that contains Fe-Ni metal.

5.2.5 Discussion and summary

The spatially resolved matrix data from the meteorite falls Mukundpura, Aguas Zarcas, Kolang and Winchcombe reveal numerous patterns within and between each meteorite. Foremost, their quick recovery and relatively pristine nature permit assessment of the effects

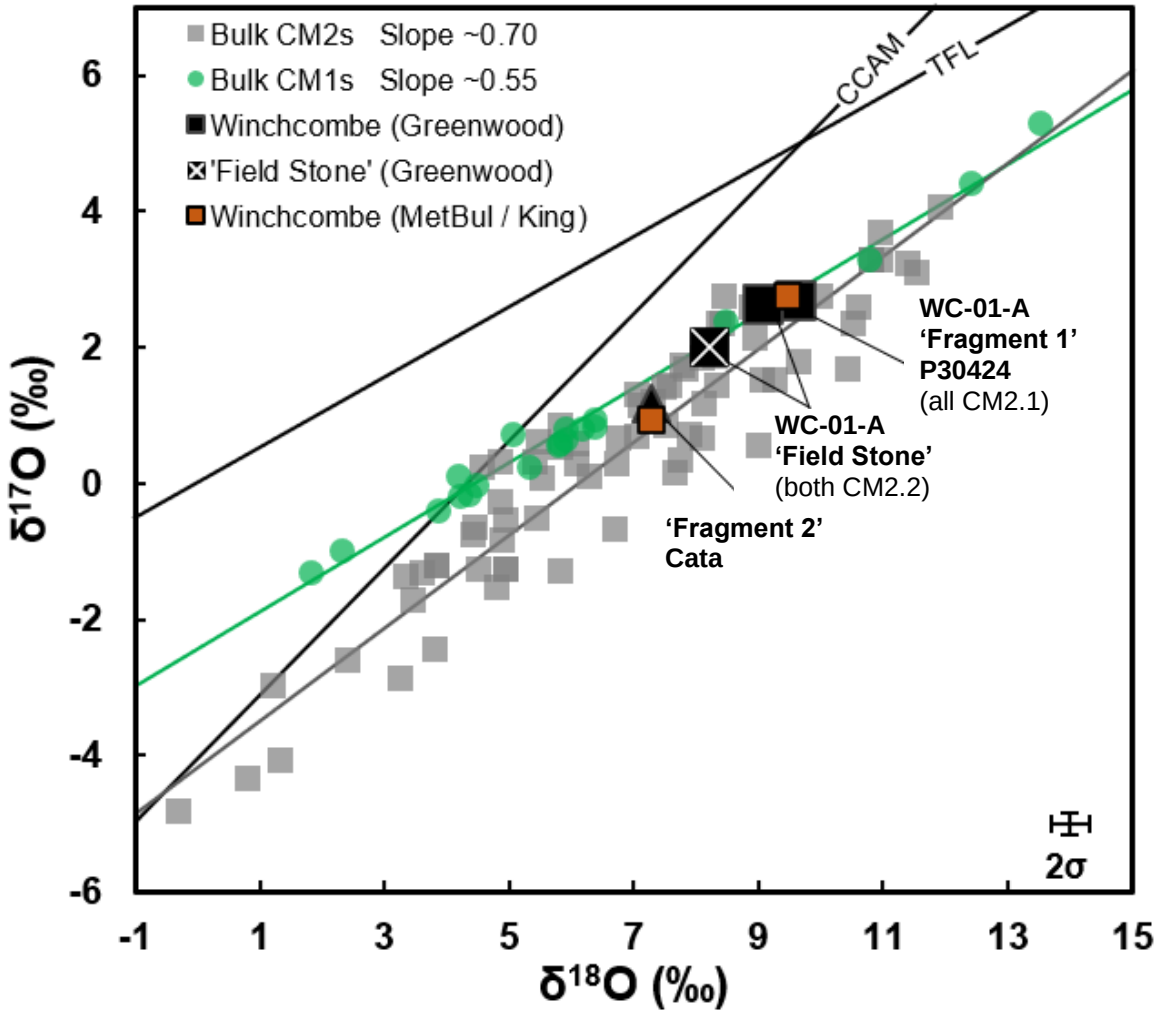

Figure 5.4 - Oxygen 3-isotope plot of Winchcombe. The two highly altered lithologies plot close to the CM1 fractionation line (green line), away from the CM2 array. Analysis of the field stone shows similar compositions. Squares represent CM2 lithologies, triangles cataclastic matrix. Data obtained by the author but published (King *et al.*, 2022; Greenwood *et al.*, 2023, accepted). Data sources for CM2 and CM1 chondrites are the same as Fig 5.1. Errors are 2σ uncertainty reproducibility of the instrument in small sample mode.

of terrestrial weathering. The oxygen isotopic compositions are in line with those recorded from published whole-rock data from falls and finds, especially with respect to the most altered CM1 meteorites recovered in Antarctica, suggesting the slopes of the CM1 and CM2 lines previously reported are not detrimentally affected by terrestrial oxygen as has previously been hypothesised (Greenwood *et al.*, 2019; King *et al.*, 2018). In addition, the CM1 lithologies analysed in Kolang and Mukundpura do indeed have lower $\delta^{18}O$ values compared to less altered CM2 material in the same meteorites (Fig 5.5). The degree of terrestrial weathering upon CM1 chondrites is further questioned upon inclusion of Flensburg, the isotopically lightest C1/CM1 chondrite fall to date (Bischoff *et al.*, 2021). If

it is assumed that CM1 material is an extension of the alteration sequence depicted by CM2s this presents a challenge for existing models used to explain the alteration sequence and isotopic composition of CMs, particularly the hydration model of Clayton and Mayeda (1999) — which would predict the opposite given such pristine compositions and reopens the closed vs open system debate on the nature of CM parent body aqueous alteration.

It is apparent from petrographic observations that the distribution of surviving precursor fragments on the bulk scale is very different from meteorite to meteorite (Chapter 4). This indicates that the lithologies of each meteorite are sampling a region on the parent body(ies) of localised alteration intensity (Greenwood *et al.,* 2023). Kolang and Winchcombe are the most altered, followed by Mukundpura as an intermediate, and finally Aguas Zarcas being least altered. The matrix oxygen isotopic compositions, both $\delta^{18}O$ and $\Delta^{17}O$ are plotted against petrologic subtype in Fig 5.5 and appear to reflect this broad variation in alteration state. Matrix fractions from Kolang have the most ^{17}O-rich signatures, whereas Aguas Zarcas has the most ^{17}O-poor signatures. There is also a trend of increasing $\delta^{18}O$ as alteration index moves from 2.9-2.0. However, both observations are dependent upon the inclusion of matrix from petrologic subtypes 2.6-2.7, for which some have been observed to contain a contaminant anhydrous precursor component, particularly from Aguas Zarcas. If completely altered matrix (*e.g.,* Kolang or the Clayton matrix density separates) is assumed to have a $\Delta^{17}O$ of -2.3 ‰, and the residual anhydrous precursors have a $\Delta^{17}O$ of -5.2 ‰ (Clayton and Mayeda, 1984), approximately 25-30 % of the Aguas Zarcas micromilled fractions are contaminant precursors. If these results are excluded (crosses over symbols in Fig 5.5) the $\delta^{18}O$ trend is weakened and the $\Delta^{17}O$ becomes almost invariant with limited scatter. It might not be prudent to exclude this data entirely, however, as an Aguas Zarcas datapoint, AZ-02-A (2.5), exhibits a ^{16}O-rich composition ($\Delta^{17}O$ = -3.06 ‰) while appearing unaffected by

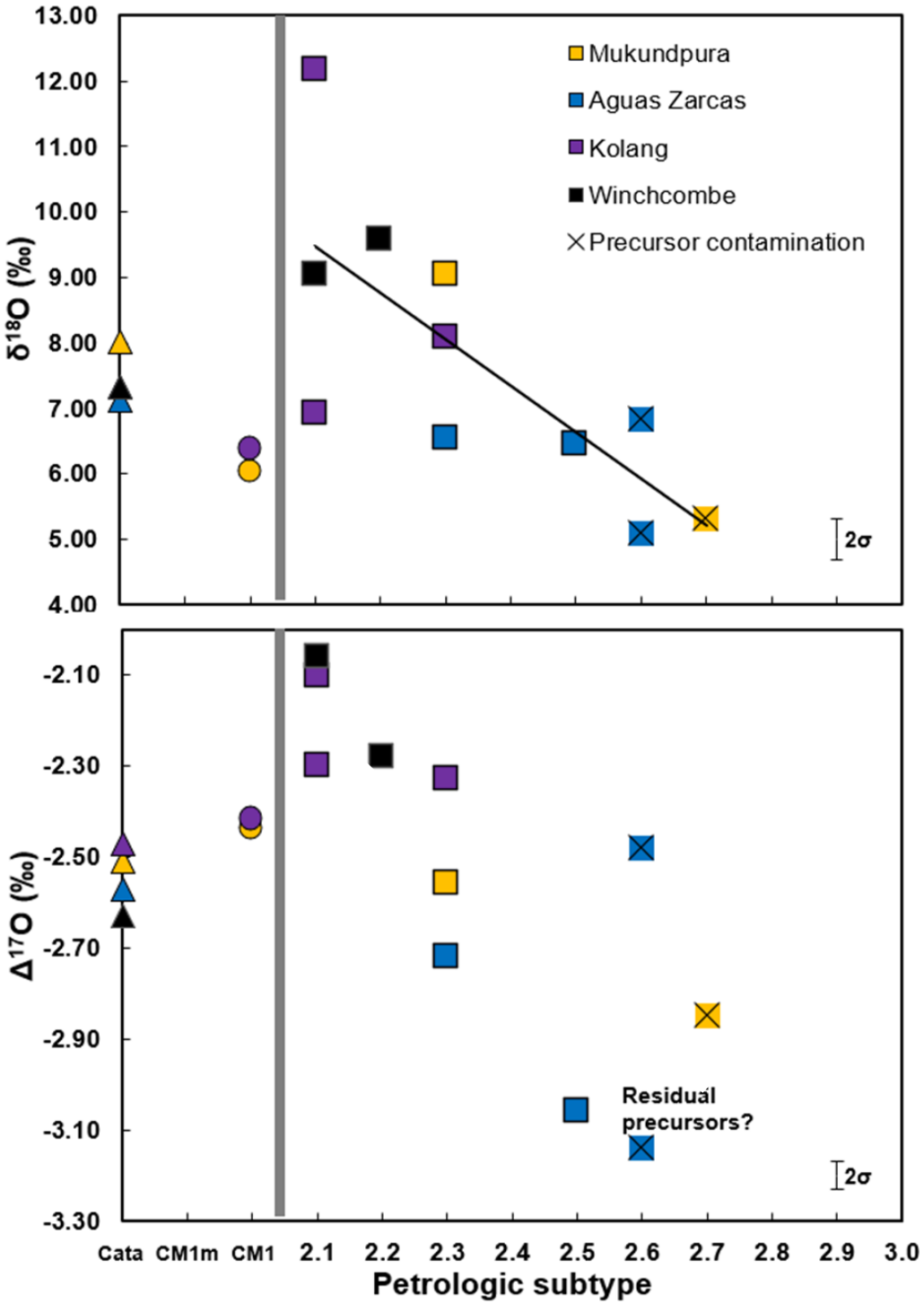

Fig 5.5 – Top: $\delta^{18}O$ vs petrologic subtype. A negative correlation is observed with increasing petrologic grade. Each meteorite appears to occupy a relatively narrow region of $\delta^{18}O$ with occasional outliers. Bottom: $\Delta^{17}O$ vs petrologic subtype. A negative correlation is also observed, with each meteorite occupying a unique region of $\Delta^{17}O$. CM1 lithologies are exempt from both trends. Cataclastic matrix is consistent within 1 ‰ in $\delta^{18}O$ and 0.15 ‰ in $\Delta^{17}O$. Squares represent CM2 lithologies, circles CM1 lithologies, triangles cataclastic matrix The greay line is an arbitrary separation line between the very well characterised CM2 series and the less defined CM1s and CM1ms. 2σ precision is defined by repeat analyses of small obsidian standards after blank correction.

contamination after inspection of the micromilled holes.

Introducing the CM1s and cataclastic matrix points onto the graphs strengthens the invariance of the $\Delta^{17}O$ even further (Fig 5.5). The CM1s are isotopically peculiar and are consistently distinct from CM2s, and explanations as to why the CM1s are mass fractionated to lower $\delta^{18}O$ values are needed to bolster a CM2-CM1 link in a single parent body. In addition, the intermediate $\Delta^{17}O$ values (*i.e.,* not the least negative) do not suggest the highest WR ratios observed, an intriguing observation given their highly altered nature. This may indicate that higher temperatures are also important, facilitating alteration through higher rates of reaction and reducing the degree of $\delta^{18}O$ mass fractionation during serpentine crystallisation.

Cataclastic matrix is quite consistent in O-isotopic composition from meteorite to meteorite (Fig.5.5). While each meteorite contains a cataclastic matrix fraction mostly reflective of the degree of alteration expressed by the meteorite as a whole, the similar oxygen isotopic compositions broadly advocate each is sampling the same range and proportion of materials. This is testament to the regolith gardening process, which would partly homogenise areas of diverse alteration history, combined with a period of post-gardening alteration in line with the rest of the meteorite.

Chapter 6 - Oxygen Isotopic Composition of Clasts in Lonewolf Nunataks 94101

6.1 Introduction

The preceding chapter offered a perspective into the oxygen isotopic evolution during alteration conditions on the CM chondrite parent body(ies) as recorded in pristine falls. A drawback of the falls dataset is that the clasts are spread across four individual stones, so it is not possible to determine if lithologies are genetically linked from meteorite to meteorite as the context of a source body is missing. LON 94101 (hereafter, LON) offers the opportunity to investigate such links through a much broader suite of lithologies. While it is true the spatial location of LON's parent body is similarly unknown, the remarkable plenitude of CM-material — a consequence of its high level of brecciation (Gregory *et al.*, 2015; Lindgren *et al.*, 2013; Zolensky *et al.*, 2022) — covers a collection of lithologies that with some confidence, come from the same immediate parent body, itself the accumulated remains of a catastrophically disrupted planetesimal (Michel *et al.*, 2020; Michel and Richardson, 2013). Therefore, LON provides a unique window into the lithological diversity (*i.e.*, the 'big picture') of at least one CM asteroid.

It has already been established in Chapter 4, section 4.6, that the range of petrographic diversity in LON is greater than what is perceived as 'canonical' CM material, including what is observed within Mukundpura, Aguas Zarcas, Kolang and Winchcombe. O-isotope analysis of spatially resolved, aqueously altered matrix from both typical and atypical clasts in LON offers an opportunity for comparison with the results in Chapter 5. Key aims in this regard are to observe if the lithologies span a similar range of alteration conditions as evidenced in the meteorite falls, and if lithologies from LON can be correlated to them from an oxygen isotope perspective. The composition of the more unusual clasts will also confirm if they are CM related or exogenous.

6.2 LON 94101 oxygen isotope results

Oxygen isotope results from are reported in Table 6.1 and plotted in Figure 6.1.

Table 6.1 – Triple oxygen isotope compositions of LON 94101. The 2σ uncertainty reflects the long-term internal reproducibility of the small sample, single-shot method, as reported in Chapter 3, section 3.3: 0.152 for $\delta^{17}O$, 0.310 ‰ f or $\delta^{18}O$ and 0.03 ‰ for $\Delta^{17}O$ (all in ‰).

Lithology	Desc	Subtype	$\delta^{17}O$	2σ	$\delta^{18}O$	2σ	$\Delta^{17}O$	2σ	n	Analysis
LON 94101										
LON-04-A	CM2	2.8	-4.21	0.15	0.51	0.31	-4.47	0.03	1	Micro
LON-01-A	CM2-an	2.8	-2.72	0.15	2.79	0.31	-4.17	0.03	1	Micro
LON-04-D	CM2	2.7	-0.53	0.15	4.38	0.31	-2.80	0.03	1	Micro
LON-04-C	CM2	2.6	0.31	0.15	5.01	0.31	-2.29	0.03	1	Micro
LON-04-M	CM2-an	2.6	2.54	0.15	9.68	0.31	-2.49	0.03	1	Micro
LON-04-O	CM2	2.5	0.58	0.15	5.44	0.31	-2.25	0.03	1	Micro
LON03a-B	CM2	2.5	1.95	0.15	7.90	0.31	-2.16	0.03	1	Micro
LON-04-E	CM2	2.4	0.58	0.15	5.90	0.31	-2.53	0.03	1	Micro
LON-04-F	CM2	2.4	0.18	0.15	5.09	0.31	-2.47	0.03	1	Micro
LON-03a-A	CM2	2.2	1.08	0.15	6.80	0.31	-2.45	0.03	1	Micro
LON-01-B	CM2	2.1	1.40	0.15	6.25	0.31	-1.85	0.03	1	Micro
LON-04-G	CM2	2.1	2.19	0.15	8.17	0.31	-2.06	0.03	1	Micro
LON-04-I	CM1	1.0 / 2.0	-0.48	0.15	3.91	0.31	-2.51	0.03	1	Micro
LON-04-J	CM1	1.0 / 2.0	-0.51	0.15	3.31	0.31	-2.23	0.03	1	Micro
LON-04-B	CM1	1.0 / 2.0	1.56	0.15	7.80	0.31	-2.50	0.03	1	Micro
LON-04-K	CM1m	1.0 / 2.0	3.68	0.15	11.13	0.31	-2.11	0.03	1	Micro
Cata	-	-	0.81	0.15	6.00	0.31	-2.31	0.03	1	bulk

6.2.1 CM2

Ten CM2 lithologies in total were analysed for their oxygen isotopic composition. Two additional CM2 lithologies have anomalous characteristics and are discussed in 6.2.4. The least altered clast, LON-04-A (2.8) plots within the region occupied by the least altered CM chondrites, LEW 85311 (2.7), Paris (2.7), A-12169 ('3.0' [a disputed classification as mentioned in Suttle *et al.* (2021) as some glass mesostasis has been altered to phyllosilicate]) A-12085 (2.8) and A-12236 (2.9) (Kimura *et al.*, 2020), in line with its incipiently altered petrography (Fig 6.1). Its negative $\Delta^{17}O$ (-4.47 ‰) is within 3σ of the primitive C2-ungrouped chondrite Acfer 094 (Newton *et al.*, 1995), and within 2‰, of the metal-rich lithology reported in Kolang (Gattacceca *et al.*, 2021). The isotopic composition suggests a close relationship to the anhydrous precursor assemblages ($\Delta^{17}O$ = -5.2 ‰) measured in Clayton *et al.* (1999), and that a sizeable precursor component survives. This is backed up by the petrography reported in Chapter 4, section 4.6.1. If the matrix density separates as

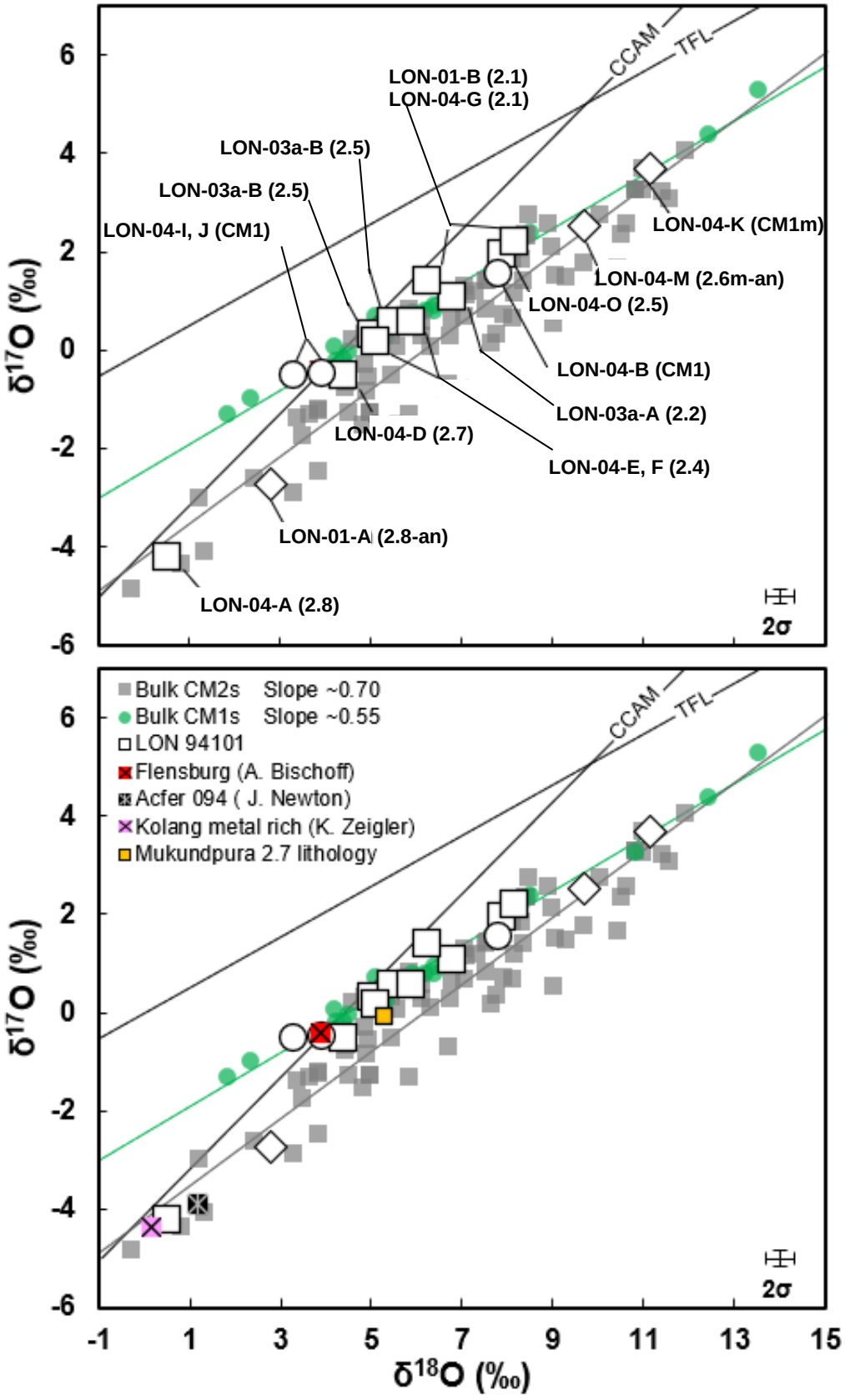

Figure 6.1 - Oxygen isotopic composition of spatially resolved matrix in LON 94101. The lithologies span the majority of known CM compositions. Most lithologies are congruent with the CM1 fractionation line. Squares represent CM2 lithologies, circles CM1 lithologies, diamonds 'matrix-dominated' lithologies, triangles cataclastic matrix. Data sources for CM2 and CM1 chondrites are the same as Fig 5.1. Errors are 2σ uncertainty reproducibility of the instrument in small sample mode.

measured by Clayton and Mayeda (1999) are used as an anchor for the final $\Delta^{17}O$ of the matrix (~2.3 ‰), this clast is ~75 % anhydrous precursor, reasonable given the apparent level of incipient alteration. The hypothetical CM3 precursor, if it exists (Marrocchi *et al.*, 2023; Ruggiu *et al.,* 2022) is a long sought holy grail in CM meteoritics, and clasts like LON-04-A (2.8) are the best link we have to such material. That this clast is found alongside CM2 and CM1 lithologies suggests that material akin to Acfer 094 may be representative of the CM precursor. The second least altered lithology, LON-04-D (2.7), plots closer to the isotopically light end of the CM1 fractionation line than the canonical slope ~0.7 CM2 line (Greenwood *et al.,* 2023), in a region ~ 1‰ from the 2.7 lithology in Mukundpura (Fig 6.1). Assessment of the micromill excavation sites indicates mild contamination by coarse anhydrous precursors; nevertheless, the apparent affinity for the CM1 line corroborates that the phyllosilicate matrix of 2.7 lithologies is close to 100 % alteration and constitutes the majority of the removed fraction.

Seven moderately altered CM2 lithologies, LON-03a-A (2.2), LON-03a-B (2.5); (LON-04-LON-04-C (2.6), LON-04-E (2.4), LON-04-F (2.4), LON-04-G (2.1) and LON-04-O (2.5), occupy a region straddling the CM1 mixing line, which is distinct from the CM2 mixing line (Fig 6.1). Plots of $\delta^{18}O$ and $\Delta^{17}O$ vs petrologic subtype mirror the patterns observed in the meteorite falls (Fig 6.2). No obvious trend can be observed between $\Delta^{17}O$ and petrologic subtype. Indeed, below alteration grade 2.7 the $\Delta^{17}O$ value remains more or less constant at $\Delta^{17}O$ = -2.3 ‰. However, a more apparent correlation is seen in $\delta^{18}O$, which becomes progressively lower as petrologic type increases, with exception of the CM1 clasts.

One of the most altered CM2 clasts, LON-01-B (2.1) has a $\Delta^{17}O$ value that falls approx. 0.4 ‰ above most of the other CM lithologies. In contrast, the petrography does not indicate any characteristics anomalous to what is usually observed in CM2s (section 4.6.10). The $\Delta^{17}O$ of this clast is closer to the heaviest of the matrix density separates in Clayton and

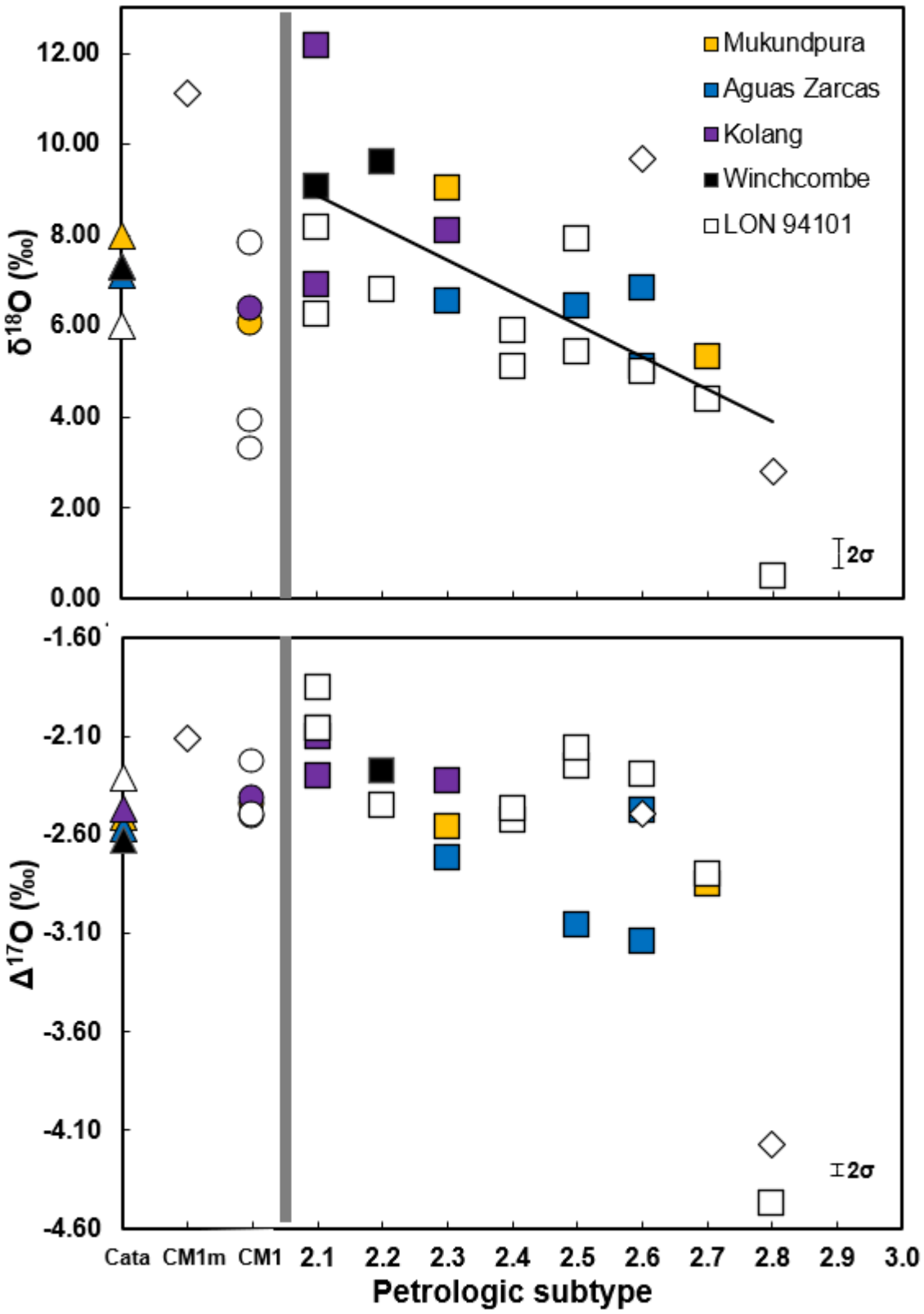

Figure 6.2 – Oxygen isotope composition vs petrologic subtype of matrix from lithologies in LON 94101 plotted alongside falls data. LON supports the correlations reported in Fig 5.5. Top: $\delta^{18}O$ vs petrologic subtype. A negative correlation is observed with increasing petrologic grade. Bottom: $\Delta^{17}O$ vs petrologic subtype where little to no correlation is observed. The grey line represents a division in the alteration index marked by well characterised lithologies to the right, and poorly scaled lithologies of high alteration to the left. Errors are the 2σ uncertainty of the instrument in small sample mode. Squares represent CM2 lithologies, circles CM1 lithologies, diamonds matrix dominated lithologies, triangles cataclastic matrix.

Mayeda (1999), or the C2 ungrouped meteorite Bells at -1.61 ‰ (Rowe *et al.,* 1994) than the other CM2 lithologies present in LON.

6.2.2 CM1

Two CM1 clasts, LON-04-I and LON-04-J, have light oxygen isotopic composition in line with most literature data (King *et al.,* 2017), lying on the CM1 mixing line and corroborating the petrographic link between CM1 and CM2 material that was found in Mukundpura and Kolang. Most interestingly, LON-04-I has a near-identical oxygen isotopic composition to the C1-ung meteorite Flensburg ($\Delta^{17}O$: ~ -2.5, $\delta^{18}O$: ~ 3.5 ‰), and comparable petrography (section 4.6.12). The importance of this similarity cannot be understated as Flensburg is a very unusual meteorite (Bischoff *et al.,* 2021). It's very altered, which occurred under elevated temperatures beyond 200 ℃ (Bischoff *et al.,* 2021). Many isotopic characteristics of Flensburg, as reported by Bischoff *et al.* (2021), are comparable to CM chondrites (such as some noble gases, O, Ti and Cr-isotopic composition), while some are not (H, Te,), prompting the classifiers to group this meteorite into a C1-ung category. While more analysis is needed in addition to the known petrography reported in Bischoff *et al.* (2021) to link LON-04-I to Flensburg, the identical O-isotope composition and similarity in petrography (large, 200 μm wide pseudomorphed chondrules, pyrrhotite laths, dolomite) suggests this material may indeed be related to CM chondrites and is essentially an unusual CM1, sampling a region of the asteroid that is poorly represented by the meteorite collection. The more bizarre isotopic characteristics therefore give insight into the distribution of these elements on the original asteroid.

LON-04-B is also a CM1, but its oxygen isotopic composition and petrography are distinct from the CM1s described above (section 4.6.14). While the $\Delta^{17}O$ remains very congruent (-2.5 ‰) with the other CM1s the $\delta^{18}O$ is heavier than most (7.8 ‰), more in line with what would be canonically expected from a very altered CM2 lithology (Fig 6.2). It is a low contrast, fractured and porous clast (see 4.6.14) with a random assortment of small chondrule

pseudomorphs, in contrast to the larger ones typically observed in CM1s. It also hosts occasional TCIs, which are nominally absent in CM1s. The very fractured appearance suggests this lithology itself may be the result of regolith processing, or it may be a transitional clast between CM2 material and CM1m material such as LON-04-K (CM1m).

6.2.3 CM1m

LON-04-K is the only CM1m analysed out of four identified in Chapter 4. Identification of these dark, featureless clasts occurred late in the project timeline and as such, suffered due to time constraints. Nonetheless, the petrography and oxygen isotopic composition of this clast alone are uniquely insightful into the diversity of CM material. While the identification of such clasts within meteorites is not new (*e.g.,* Patzek *et al.,* 2018; Patzek *et al.,* 2020), the correlated petrography and bulk O-isotopic composition is novel. This clast is enriched in ^{18}O relative to the other lithologies with a $\delta^{18}O$ value of 11.13 ‰ (Fig 6.1 & 6.2) and lies on the CM1 mixing line. This clast is probably not an exogenous clast but more likely an indigenous lithology with CI-like petrography (Patzek *et al.,* 2018). It must be noted that it is not explicitly inferred this is true CI material, rather, its resemblance to CI chondrites is evidence for the formation of CI-like material on, or in a CM asteroid.

A number of CM1 and CM1/2 chondrites from the literature are reported to have similarly heavy $\delta^{18}O$ values. These are NWA 8534 (Ruzicka *et al.,* 2017), NWA 10834, NWA 10853 (Bouvier *et al.,* 2017) and Y 82042 (Grady *et al.,* 1987). The NWA meteorites were recovered from the Sahara and may be influenced by desert weathering (Bland *et al.,* 2006) which can artificially inflate $\delta^{18}O$ (Greenwood *et al.,* 2019; King *et al.,* 2018). This may be an oversight, as again, these meteorites are victim to lack of petrographic study outside of their MetBul classifications. NWA 8534 is described as having no visible chondrules (Ruzicka *et al.,* 2017). NWA 10834 and 10853 are both described as having serpentinised chondrules in a ‘very dark’ matrix (Bouvier *et al.,* 2017). Y 82042, an Antarctic meteorite, has been petrographically studied and is reported to be more like CI chondrites than CM2

(Grady *et al.,* 1987), and contains high $\delta^{18}O$ values that uniquely, as in LON-04-K, cannot be linked to hot desert weathering. Therefore, it is postulated that NWA 8534, 10834, 10853 may be ^{18}O-enriched CM1m lithologies, in contrast to hot-desert weathered CM1s that have obvious chondrule pseudomorphs. King *et al*. (2018) analysed a separate fraction of NWA 8534 and found the oxygen isotopic composition agreed with nominal CM1 chondrites (*i.e.*, 'isotopically light'), indicating sample heterogeneity. NWA 8534 is probably a breccia of CM2, CM1 and CM1m material.

6.2.4 Anomalous clasts

Two anomalous clasts are present. LON-04-M (2.6m-an) and LON-01-A (CM2.8m-an) both have the 'm' suffix designation and are therefore matrix dominated. However, unlike LON-04-K, they are only partially altered, hence their anomalous status.

LON-04-M (2.6m-an) contains abundant phyllosilicate matrix (section 4.6.4). The oxygen isotopic composition of this matrix fraction matches the CM1 mixing line and is of similar $\delta^{18}O$ (9.68 ‰) to LON-04-K (Fig 6.1), indicative of pervasive alteration. Where the clast differs, however, is in its petrography, specifically, it contains partially altered, metal-rich, porphyritic chondrules (section 4.6.4). For a clast of such a high level of alteration this observation is perplexing and raises interesting questions about origin of the matrix. Any degree of significant fluid percolation should cause alteration of the metal. While this has occurred in places, converting the metal to magnetite, it is still far from complete, at odds with the very hydrated matrix. Metal rich lithologies, such as those observed by Kerraouch *et al.* (2021) in Aguas Zarcas display similar paradoxes in that they also contain a large quantity of unaltered metal next to phyllosilicate.

LON-01-A (2.8m-an) represents an unusual category of lithology that has yet to be described in the literature. It is matrix dominated with a ^{18}O- and ^{17}O-poor isotopic composition. With a $\Delta^{17}O$ of -4.17, it is closer to the field of anhydrous precursors than the CM2 lithologies, though it has departed from the CCAM line to the right and has a $\delta^{18}O$ composition of 2.79

‰. (Fig 6.1). Assuming that the anhydrous precursor composition has a $\Delta^{17}O$ of -5.2 ‰ (Clayton and Mayeda, 1999) and the matrix phyllosilicates tend towards a $\Delta^{17}O$ composition of approximately -2.3 ‰, this would suggest 67 % of the sample is anhydrous precursor. A potential example of incipient alteration, this clast may sample the colder, surface regions of the asteroid, akin to LON-04-A (2.8).

6.3 Discussion and summary

The range of $\delta^{18}O$ shown by matrix phyllosilicates from the lithologies in LON 94101 spans 0.51-11.13 ‰ (Fig 6.1), as wide as the majority of known CM $\delta^{18}O$ compositions (*e.g.*, Greenwood *et al.*, 2023) and proof that a single meteorite can contain both the whole alteration range of CM2 material, and the isotopic range (Zolensky *et al.*, 1997). LON provides strong evidence that different CM chondrites come from a common, or remarkably similar source, as the compositions overlap with the matrix analysed from CM falls in Chapter 4 (Fig 6.1 & 6.2). Petrographic correlations between the studied meteorites are more ambiguous, however. The similarity of LON-04-I to Flensburg provides convincing evidence that similar lithologies can be observed within different meteorites, though this is not the case for all. Most CM2 lithologies are different between meteorites, *i.e.*, a CM2.6 in LON is petrographically and isotopically distinct compared to a CM2.6 in Aguas Zarcas. Multiple examples of a single petrologic grade (2.4 in LON) can also differ within the same meteorite. On the other hand, many lithologies, particularly those rich in TCIs, can appear similar to one another – perhaps representing areas of the parent body that have gradational heterogeneity in their abundance of accreted phases. These conclusions may be subjective depending on the approach of the characteriser and if a ‘lumping’ or ‘splitting’ approach is adopted. The former bundles CM lithologies according to broad characteristics, whereas the latter may implement an approach that seeks to subdivide and determine the differences between them. The different approaches are usually driven by different goals. The number of petrographically distinct lithologies found within LON suggest understanding the CM

parent body is better served by the splitting approach, as with such variation it is better to subdivide to resolve petrographic and isotopic characteristics. That CM lithologies are both diverse and occasionally correlated from meteorite to meteorite attests to the degree of petrographic diversity and the many (potentially hundreds?) of lithologies that may exist, demonstrating each meteorite samples an overlapping, or perhaps unique region of the asteroid (s).

Most LON lithologies lie close to, or on the CM1 mixing line, together with most lithologies from the meteorite falls in Chapter 5. In fact, a regression through the LON data produces an identical slope (0.55) to the CM1 mixing line. It is becoming more apparent that a mass-dependent fractionation process, as opposed to a mixing process, is the dominant control on the $\delta^{18}O$ composition as alteration increases (Fig 6.2). This will be discussed in depth with literature data in the next Chapter. The two isotopically distinct lithologies LON-04-A (2.8) and LON-01-A (2.8m-an) are excluded from this regression as anhydrous precursors are undoubtedly contaminating both of them.

6.3.1 Weathering effects

For an Antarctic find, LON has a remarkably low degree of weathering (Zolensky *et al.*, 2022). Even so, it still resided in Antarctica for an indeterminate amount of time, exposed to the contaminating effects of the Earth's atmosphere and potentially transient liquid water when on the ice surface. Despite this, the oxygen isotopic compositions of matrix across all clasts fall in the same region as matrix from the fresh falls from Chapter 5 (Fig 6.1 & 6.2), indicating interaction with Antarctic precipitation, which has a very fractionated isotopic signature ($\delta^{18}O$ = ~-55 ‰), was not pervasive enough to noticeably affect the measured isotopic compositions. The fine grained, CI-like clast LON-04-K (CM1m) does contain gypsum, which may be a weathering product, but as this lithology has the highest $\delta^{18}O$ of any in LON this phase is clearly not abundant enough to provide a significant shift in the oxygen isotopic composition despite Antarctic alteration products typically having very low

$\delta^{18}O$ values (*e.g.,* Alexander et al, 2018). As discussed in section 6.2.3, ^{18}O-enriched meteorite finds from hot deserts may be similar to LON-04-K (CM1m). While weathering has undoubtedly affected a number of hot and cold desert meteorites, the results of this work suggest it is not enough to compromise the indigenous trends to the point of misinterpretation in LON. Recent oxygen isotope analysis of pristine particles from near earth asteroid Ryugu, protected from terrestrial atmosphere at all stages through to analysis, confirm it is analogous to CI chondrites but has a $\Delta^{17}O$ ~0.15 ‰ heavier than that observed in CIs exposed to the terrestrial atmosphere (Greenwood *et al.,* 2022; Nakamura *et al.,* 2022). The difference between Ryugu material and CIs indicates that 15-20% of the oxygen present in CIs may be of terrestrial origin, depending on whether the source is atmospheric O_2 ($\Delta^{17}O$ ~-0.3‰) or meteoric water ($\Delta^{17}O$ ~0‰). CI chondrites, and by extension CI-like clasts in CM chondrites, may be more vulnerable to weathering effects than CM2 clasts. However, the weathering effects observed on some CIs (e.g. Orgueil) are much greater than any observed in the CM1 type clasts reported in LON.

Chapter 7 - Synthesis

7.1 Introduction

A rounded view of the CM-chondrite parent body should accommodate the observations drawn from results Chapters 4, 5 and 6 into a holistic parent body model for the CM chondrites.

- In Chapter 4 a diverse range of CM lithologies were characterised and compared between four meteorite falls: Mukundpura, Aguas Zarcas, Kolang and Winchcombe; and a large Antarctic find, LON 94101. The petrologic range of alteration was quite different between each meteorite fall but in total, broadly comparable to the exceptionally diverse and brecciated find LON 94101.
- In LON, petrographic links were established between CM1, CM2 and incipiently altered material. As LON samples one immediate secondary rubble-pile asteroid, a parent body model should consider the possibility that a lot of these lithologies, and perhaps many CM lithologies across other meteorites, are sampling one asteroid.
- The model should propose an origin for the broad range in petrography between these different CM clasts. Why are some lacking chondrules while others contain 80 % TCI fragments? Why are some heterogeneously altered? If they are from one asteroid, how can they be explained?
- Chapter 5 and 6 established the O isotopic composition of the aqueously altered matrix phyllosilicates from each lithology scatter around a consistent $\Delta^{17}O$. How can this be explained within the context of the complex and variable petrography and the O isotopic data available in the literature?

7.2 Mass-dependence on the CM asteroid

The data from Chapter 5 and 6 is plotted alongside the CM2 and CM1 whole-rock literature dataset and the CM2 matrix density separates from Clayton and Mayeda (1984) in Fig 6.3. One broad, but salient trend is revealed: any phyllosilicate dominated analysis from a CM chondrite lies on or close to the CM1 mixing line. The line is therefore not restricted to CM1

material, but phyllosilicates from all CM lithologies irrespective of host lithology. This line is hereafter called the CM Matrix Fractionation line (CMF). The CMF is defined by the equation $\delta^{17}O = 0.55 * \delta^{18}O - 2.48$ with an average $\Delta^{17}O$ of -2.35 ‰ ± 0.45 ‰ (2σ), consistent with data reported previously for density-separated matrix samples from Clayton and Mayeda (1984). Previously, it had been argued that these matrix results may have been affected by fine-grained anhydrous precursor contamination, and that the density preparations had not fully separated (Baker *et al.*, 2002; Franchi *et al.*, 2001). Given the consistency of the results from the two different approaches it appears that this is not a major contributor to the measured values, although some very low levels of contamination may persist, accounting for some of the scatter in the observed data.

It has long been known that CM2s represent an amalgamation of both mass-independent effects by mixing, and mass-dependent effects caused by mineral crystallisation and temperature (*e.g.*, (Baker *et al.*, 2002; Benedix *et al.*, 2003; Clayton and Mayeda, 1984; Clayton and Mayeda, 1999; Farsang *et al.*, 2021; Franchi *et al.*, 2001; Greenwood *et al.*, 2023; Lindgren *et al.*, 2017; Tyra *et al.*, 2016; Tyra *et al.*, 2012; Vacher *et al.*, 2017; Vacher *et al.*, 2019; Young *et al.*, 1999). However, the magnitude of each has remained enigmatic. From this data, it can be concluded that bulk CM2 oxygen isotopic compositions do not strictly represent binary mixtures of ^{16}O-rich anhydrous precursors and ^{16}O-poor water, rather, the slope ~0.7 line as originally identified by Clayton and Mayeda, (1999), is actually a mixing line between the field of anhydrous precursors and the CMF (which is controlled by mass-dependent fractionation processes occurring during alteration, as shown in Fig 7.1). This adds an extra dimension to the possible location where a bulk measurement may plot, as the phyllosilicates could, in theory, lie anywhere along the CMF (Fig 7.1), explaining the considerable scatter in bulk CM2 measurement. This includes the intermediate compositions of the CM1 and CM1/2 meteorites.

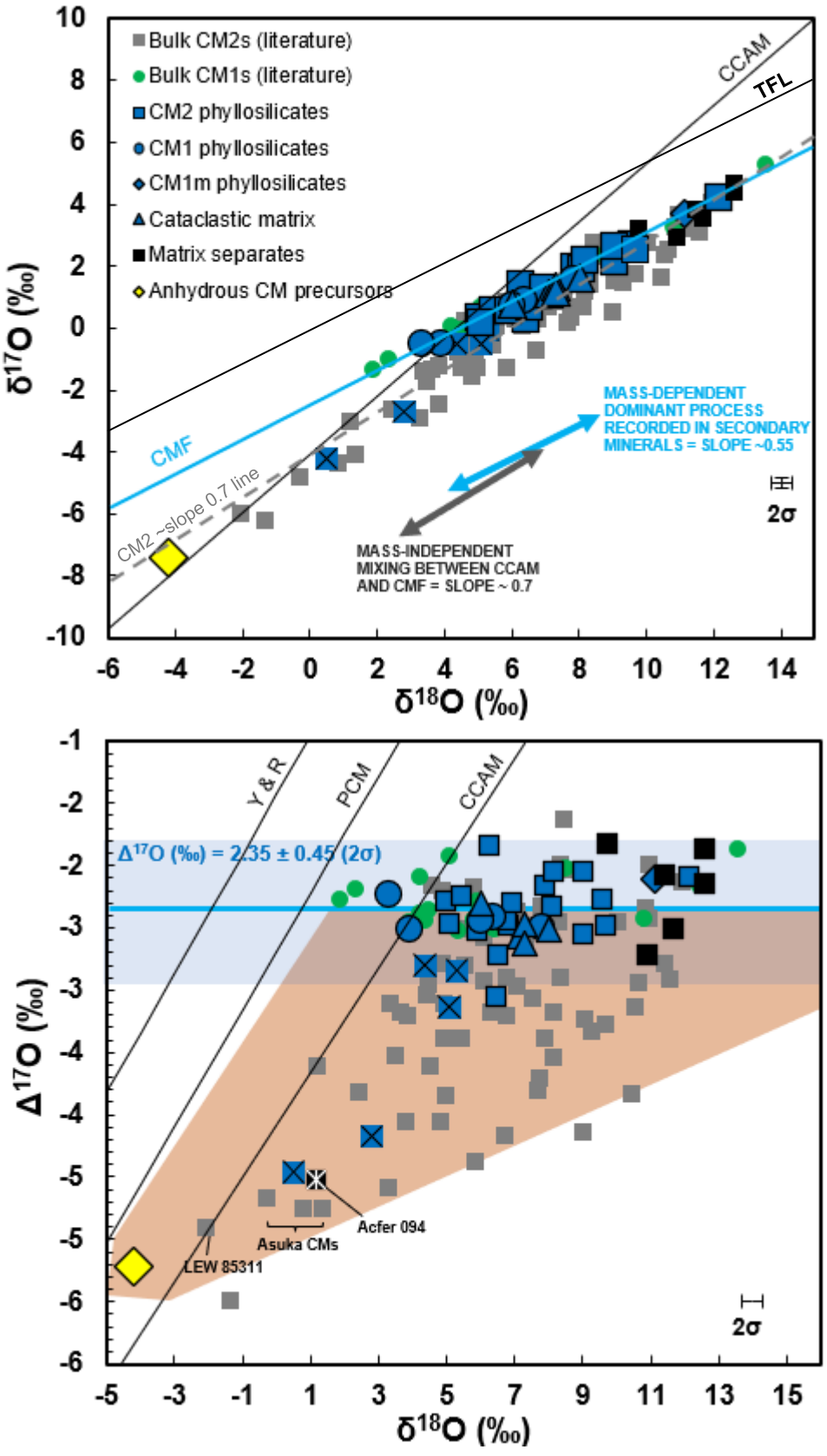

Figure 7.1 - Top: Defining the CM matrix fractionation line (CMF). All CM phyllosilicates from this work (blue) and the literature cluster around a line of slope 0.55. Bottom: the average $\Delta^{17}O$ of all the phyllosilicate fractions is 2.35 ± 0.45 ‰ (2σ), defining the CMF. Bulk measurements represent a non-binary mixing array between the field of anhydrous precursors and the CMF, as shown by the brown triangle. Squares with crosses are discounted from the slope and average calculations due to contaminant anhydrous precursors. Squares represent CM2 lithologies, circles CM1 lithologies, diamonds matrix dominated lithologies, triangles

cataclastic matrix. All the micromilled lithologies are plotted alongside literature data. CM2 data (Clayton and Mayeda, 1999; Fan *et al.,* 2022; Greenwood *et al.,* 2023; Haack *et al.,* 2012; Hewins *et al.,* 2014; Kimura *et al.,* 2020; King *et al.,* 2022; Lee *et al.,* 2019; Lee and Lindgren, 2016; Tyra *et al.,* 2007; Verdier-Paoletti *et al.,* 2019). CM1 data (King *et al.,* 2018) Matrix density separates and CM anhydrous precursors from Clayton and Mayeda (1984). CCAM data is defined by Clayton *et al.* (1973).

Using a traditional mixing model invoking very ^{16}O-poor water, the CM1 meteorites should be very enriched in δ^{18}O. As this is not the case, it can be inferred that the δ^{18}O is not a robust indicator of the intensity of mixing, but instead represents a mass-dependent process such as temperature variations and / or variations in mineral chemistry.

7.2.1 Closed system alteration

The mass-dependence indicates a single dominating process linking the phyllosilicate from lithology to lithology, most certainly aqueous alteration. This implies limited variability in mixing of isotopically distinct water and rock, evidenced by a constant Δ^{17}O (Fu *et al.*, 2017). In fact, the WR ratio, though yet undetermined, could be considered homogenous from the perspective of the whole dataset. However, the reciprocal relationship of WR ratio and water composition remains a hurdle for determining an accurate estimate of either value (Clayton and Mayeda, 1999). There are theoretically lots of combinations that could work to produce this Δ^{17}O value: low WR, $^{17/18}$O-rich water; high WR, $^{17/18}$O-poor water, and any number of combinations in between. With the new data, some constraint on the δ^{17}O and Δ^{17}O of the original water is possible if the system is assumed to be closed.

The stoichiometric requirement for replacement of olivine + pyroxene into serpentine by water demands a WR ratio (by oxygen atoms) of 0.29 (Chapter 1, section 1.7), this represents the lowest minimum estimate of the water contents assuming a simple closed system. The Δ^{17}O of the reacting water, in tandem with an anhydrous starting composition of Δ^{17}O = -5.2 ‰ (Clayton and Mayeda, 1984) would have a Δ^{17}O value of +7.9‰. In reality the WR ratio is likely to be higher than this minimum estimate as the remarkable invariance of the Δ^{17}O among the CM matrix phyllosilicates, alongside the mass-dependently fractionated

$\delta^{18}O$, demands some form of equilibration which would happen more readily at higher WR values. Using an arbitrarily higher WR ratio of 1.2 — the value expected to condense out of a nebula gas of solar composition at <180 K (Lodders, 2003) — the $\Delta^{17}O$ value of the initial water would be +0.13 ‰. Furthermore, the $\delta^{18}O$ values of the matrix phyllosilicates range from +3 to +11 ‰. A possible control on the mass-dependent fractionation (outside of the initial effect of mixing) is temperature through Δ_{sw}, the fractionation factor between serpentine and water. Mg serpentine is the most dominant product in CM matrices, and always fractionates positively from a water reservoir (Zheng, 1993). If the system was truly closed, the O-isotopic composition of the water reservoir must have been as ^{16}-O poor, or more so, than the most ^{16}O-poor chondrite matrix fraction. Within the present literature, ^{16}O-poor CM compositions are occupied by CM1 lithologies or CM1 bulk measurements (Bouvier *et al.*, 2017; Greenwood *et al.*, 2019; Howard *et al.*, 2011a; Howard *et al.*, 2010; King *et al.*, 2018; Ruzicka *et al.*, 2017; Zolensky *et al.*, 1997). Here, the oxygen isotopic composition of Flensburg is used as an anchor for the lightest CM (Bischoff *et al.*, 2021). As a fall, Flensburg is uncontaminated by weathering, and while it is currently classified as a C1-ungrouped, it bears many similarities to CM1 material (Bischoff *et al.*, 2021). In addition, the observation of 'Flensburg-like' clasts in LON with identical oxygen isotopic composition (LON-04-I, J), support a CM-like heritage. Two isotopically lighter bulk CM1 measurements exist in the literature, GRO 95645 and MIL 07689 (King *et al.*, 2018), but as very small Antarctic finds with a high weathering grade (Be / C), it is probable that the extra ^{16}O-enrichment is influenced by interaction with Antarctic water which typically has very low $\delta^{18}O$ values (*e.g.*, Alexander *et al.*, 2018), so these are not used.

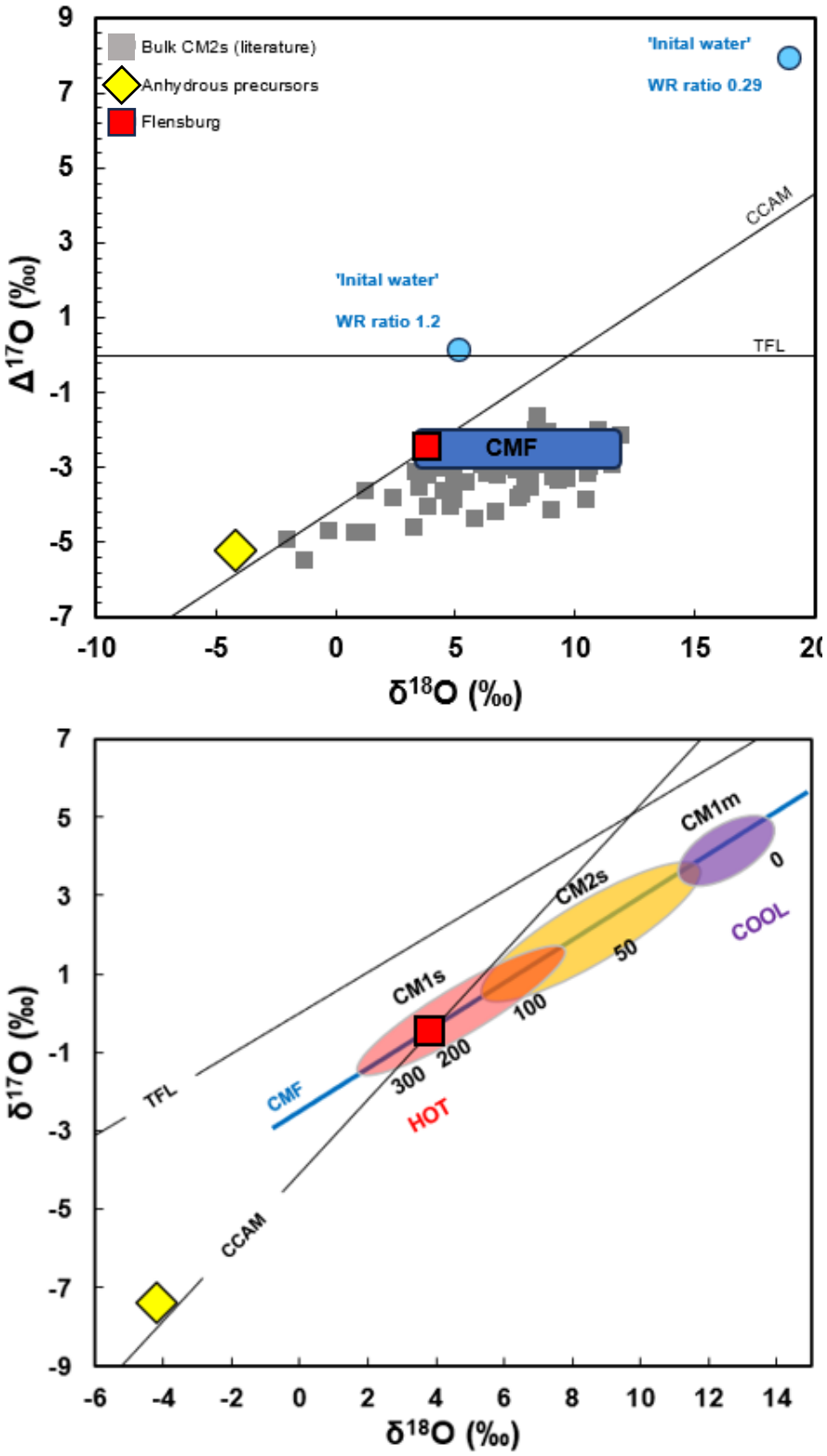

Figure 7.2 – Top: reproduction of the 'initial' CM water assuming WR ratios of 0.29 and 1.2, respectively. Simple modelling of a temperature control of the CMF. A purely temperature effect could, in theory, reproduce the observe variations in O-isotope composition if Flensburg is used as an anchor at approximate 200 °C, using the fractionation factor between water and serpentine (Zheng, 1993).

Bischoff *et al.* (2021) report that the mineralogy of Flensburg, particularly the abundance of recrystallised pyrrhotite and magnetite — coupled with Mn-Cr dating of carbonate suggesting an early alteration age — requires temperatures upward of 200 °C, perhaps as high as 400 °C. While this is on the higher end of alteration temperature in CM2 terms (*e.g.,* Vacher *et al.,* 2019a; Vacher *et al.,* 2019b) most CM1s show evidence of high temperature alteration, perhaps even at least beyond the stability field of tochilinite at 245 °C (Fuchs *et al.,* 1974; King *et al.,* 2017). Taking the $\delta^{18}O$ of Flensburg, which is 3.9 ‰, with 200 °C as a minimum estimate for the high-end of CM aqueous alteration temperature (a lower estimate provided by Bischoff *et al.* (2022)), one can apply the fractionation factor of Zheng (1993) ($\delta^{18}O$) between water and serpentine at 200 °C (3 ‰) to reveal the $\delta^{18}O$ of water in equilibration with a Flensburg-like meteorite on the CMF is ≈ 0.9 ‰. A large range of formation temperatures progressively cooler than the Flensburg region would then facilitate the ~10 ‰ variation of $\delta^{18}O$ shown by the CM matrix phyllosilicates as the serpentine fractionates from a common reservoir of $\delta^{18}O \approx 0.9$ ‰ (Fig 7.2). The CM1s would be formed at the highest temperature, which is more or less in agreement with published statements reporting dolomite, recrystallised sulphide, and no tochilinite, all of which require higher temperatures to promote or inhibit their formation. The TCI-bearing, moderately altered CM2s would occupy a range of temperatures from 200-50 °C. The isotopically heaviest clast measured in this study is the CM1m lithology LON-04-K ($\delta^{18}O$ = ~12 ‰) , which could represent alteration at the lowest temperatures, <50 °C, in line with estimates for CI chondrite material from Ryugu. A very simple model of an internally heated asteroid, sampled from warm core to cold crust, could account for these variations.

An additional implication the CMF is there is no longer a strict requirement for the initial water reservoir to be very enriched in ^{17}O and ^{18}O. In theory it could any number of compositions above the CMF, within the limits of a sensible water/rock (WR) ratio and the

mass-dependent processes that are dominant in the system. Modest WR ratios (*i.e.*, >0.29) invoke compositions that tend towards a $\Delta^{17}O$ value of 0 ‰.

7.2.1.1 Carbonates

With this newfound phyllosilicate data, the large carbonate literature dataset can be revisited (Fig 7.3). Early formed, TCI-associated, T1 calcites are congruent with precipitation from the earliest fluids at $\Delta^{17}O \approx 0$ ‰, coincidentally in agreement with the arbitrary initial water composition calculated using a WR ratio of 1.2. A second generation of polycrystalline T2 calcites have compositions more reflective of the CMF, corroborating evidence that they may be coeval with the formation of the serpentines (Tyra *et al.*, 2012; Vacher *et al.*, 2019a). This is reinforced by petrographic observations as T2 calcites are frequently pseudomorphs after chondrules (Suttle *et al.*, 2023), indicating a later stage of alteration. The reaction progress displayed by the transition from T1 to T2 calcites is not readily identifiable within the bulk O-isotope measurements of phyllosilicates, indicating that while evolution of the water reservoir from $\Delta^{17}O \approx 0$ ‰ to $\Delta^{17}O \approx -2.3$ ‰ occurred early in the alteration regime, it then stayed consistent throughout the serpentinisation process across many lithologies.

The reported O-isotope compositions of carbonate are not always lithology-specific and cannot be directly correlated to any lithology-specific serpentine value reported here; however, the range of $\delta^{18}O$ compositions appears to mimic the serpentines by precipitating along a similar temperature gradient. Work by Vacher *et al.* (2019a) systematically shows that T1 calcites precipitated at lower temperatures than T2 calcites, from 10-100 and 110-245 °C respectively, indicating the alteration was prograde. It's worth noting that SIMS analysis of carbonates represent a snapshot into the aqueous alteration conditions at a very specific point in time owed to their very low levels of oxygen self-diffusion at the temperatures of alteration inferred for CMs. On the other hand, bulk phyllosilicates, as measured in this work, simply represent the average composition of numerous phyllosilicate minerals that likely formed at different times and underwent continued exchange with the

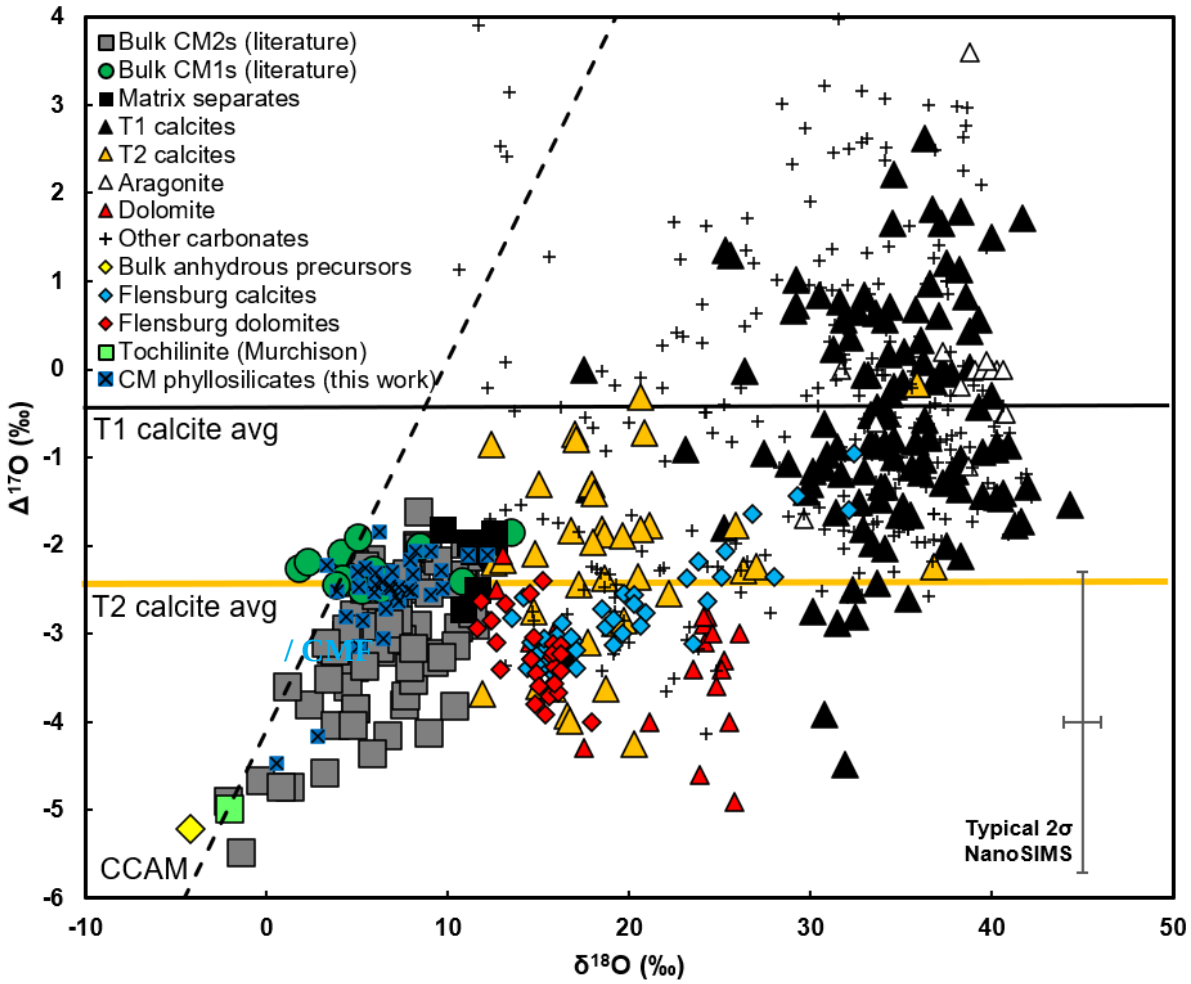

Figure 7.3 – The oxygen isotopic composition of published carbonate data from CMs. T1 carbonates appear to be consistent with precipitating from a water reservoir of terrestrial composition. T2 carbonates appear to be in broad isotopic equilibrium with the matrix density separates from Clayton and Mayeda (1999), the CM1 and CM1/2 chondrites, and the phyllosilicates measured in this work. Please see Figure 1.19 in Chapter 1 for reference sources for carbonates, and Figure 1.20 for CM2 and CM1 data sources.

fluid due to their very fine grain size, poor crystallinity, and high surface area. The fine scale oxygen isotopic systematics of the CM phyllosilicates, potentially obtainable by NanoSIMS, may show a similar spread in data when compared to the T2 calcites.

Carbonate compositions exhibiting a greater oxygen isotopic diversity than T1 and T2 calcites are frequently reported in the literature and most likely represent evolutionary reaction progress or small episodic aqueous alteration events occurring either side of the main serpentinisation event. A more detailed O-isotope examination of matrix phyllosilicates by SIMS may be able to pair the fine-scale carbonate systematics to specific

phyllosilicate generations, although SIMS measurements of fine-grained matrix are very challenging, and subject to greater analytical uncertainties.

7.2.2 Hydration model

The limitation of any closed system model, simple or complex, is the assumption that no water enters or leaves. As such, alteration is expected to be progressive as stagnant pore water exchanges with the rock. The hydration model proposed by Clayton and Mayeda (1999) (outlined in detail in Chapter 1, section 1.7.1) offers a more complete, mass balance solution in a closed system to demonstrate how the O-isotopic composition of any bulk CM chondrite can be explained by *in situ* alteration of the ferromagnesian silicates. In this model, the rock becomes progressively altered depending on the amount of water that is present, the temperature of the system and the duration of alteration. As the pore water equilibrates with the rock, the composition of the secondary products will fall in a region of 3-isotope space in between the composition of the original rock and the original water, the exact location a function of the WR ratio and the intensity of mass-dependent fractionation (Fu *et al.,* 2017). Critical to the model was the determination of degree of alteration, a parameter called 'f', which is usually established in thin section and is the ratio of phyllosilicates to surviving chondrules for a given CM (Clayton and Mayeda, 1999; McSween Jr, 1979). This parameter is directly tied into the mass balance because alteration *in-situ* requires that the anhydrous component contributes towards the composition of the final water (Clayton and Mayeda, 1999). This is correct, but hard to quantify as the proportion of anhydrous precursors in each bulk CM2 chondrite is highly variable. With the increased recognition of CM chondrite brecciation (Bischoff *et al.,* 2006; Lentfort *et al.,* 2021; Metzler *et al.,* 1992) came a considerable CM sampling problem, where variable proportions of anhydrous precursors within different lithologies resulted in a high degree of O-isotope heterogeneity within the same meteorites (Franchi *et al.*, 2001; Franchi, 2008), making it very hard to use the model effectively for its purpose, which was to use bulk compositions to unravel the WR ratio. It

is likely the estimations for parameter ‘f’ were highly inaccurate, unless by chance the thin sections used for deduction came from the precise location the O-isotope sample was extracted, and the sample itself was monomict. This has knock-on consequences for mass balance as improper estimations of the remaining anhydrous fraction will over- or under-compensate for the contribution of this phase to the O-isotopic composition of the equilibrating pore water during alteration (equation 1.3). The result of this unpredictable sampling is the apparent existence of mixing in the modelled results (Chapter 1, Figure 1.23).

As the sampling approach in this thesis removes the greater ambiguity associated with anhydrous precursors by selectively extracting the phyllosilicate fractions, the Clayton, closed system model can be tested. If the model is correct, phyllosilicates formed in different closed systems with different WR ratios should fall on a mixing line with variable $\Delta^{17}O$ (Clayton and Mayeda, 1999); however, the data in this thesis shows the phyllosilicates plot along the mass-dependent fractionation CMF (Fig 6.3), and not a mixing line like the bulk CM2s (Greenwood *et al.,* 2023). In the limitations of the Clayton model, this is only possible if all the lithologies were altered to exactly the same extent, at exactly the same WR ratio. This raises interesting questions as the petrography reported in Chapter 4 is very variable between each lithology, which would intuitively lead to the assumption that WR ratio, and / or degree of alteration ‘f’ must have also been variable (Clayton and Mayeda, 1999). That the phyllosilicates exhibit apparent mass-dependency means that an origin by coeval, static (stagnant) closed-system alteration on multiple, statically altered parent bodies is not possible unless by chance, multiple planetesimals accreted identical WR ratios (Fu *et al.,* 2017) and were altered to the same extent. If the water vapour pressure and material supply to the CM forming region was spatially and temporally homogenous, this may be plausible; however, the variation in petrography suggests that the initial budget of accreted water and rock varied between clasts. A more likely scenario is that this is a complex, single parent body process and that the water was well equilibrated across a large region as sampled by

the CM chondrites. A very useful property of this observation is that the quantity of surviving anhydrous precursor phases in thin section, and/or hand specimen, (previously called ‘degree of alteration’, f) appears little to no effect on the isotopic composition of the measured phyllosilicates. For this reason, the WR ratio, whatever its value, is in fact more accurately described as a water/’aqueous product’, or water/phyllosilicate ratio.

One key question remains: How is it possible for a single asteroid — with such a broad range of petrographic heterogeneity — to maintain an equilibrated water reservoir within itself? This sets the framework for discussion of open system behaviour (Bayron, 2021; Palguta *et al.,* 2010; Young, 2001; Young *et al.,* 1999; Young *et al.,* 2003).

7.3 Further controls on the mass-dependent fractionation

There is a notable paradox within the CM, bulk datasets in the form of a $\delta^{18}O$ dichotomy between lithologies spanning a limited range of alteration index from CM2.2 – CM1 (2.0). The highly altered, CM2.1 lithologies are common in meteorites averaging high levels of alteration such as Winchcombe (Suttle *et al.,* 2023), Kolang, Nogoya (Velbel *et al.,* 2012) and Cold Bokkeveld (Rubin *et al.,* 2007). These lithologies are characterised by the pervasive presence of conjoined, low contrast, heavily altered TCIs (which are probably not ‘real’ TCIs anymore, but clumps of Mg and Fe-rich phyllosilicate replacement products) often amounting to >50 % of the surface area. The $\delta^{18}O$ of these lithologies lies consistently between 8 – 10 ‰. Descending the alteration scale to CM1 (2.0 on the Rubin scale), results in a marked jump to much lighter (comparatively ^{16}O-rich) compositions spanning 3-6 ‰ ($\delta^{18}O$). While the progression of the Rubin scale is arbitrary, it may not be prudent to assume that the mass-dependent fractionation observed over the CMF is exclusively temperature dependent - it is very possible there is also a mineralogical, or fluid evolutionary control on the O-isotopic composition. Once at equilibrium, heavy isotopes of oxygen will be concentrated in minerals where it forms the stiffest bonds (Schauble, 2004). The shortest

(stiffest) bonds are associated with high charge, high oxidation states, strong covalent bonds, and low coordination numbers.

7.3.1 Serpentine diversity

The generalised meteoritic serpentine formula is given by Velbel and Palmer (2011) after Browning *et al.* (1996):

$$((\mathbf{Fe^{2+}},Mg,Mn,Ca,\ldots)_{3-x}(\mathbf{Al,Fe^{3+}})_x)(Si_{2-x}(\mathbf{Al,Fe^{3+}})_x)O_5(OH)_4$$

Octahedral Tetrahedral

Fe-rich serpentine such as greenalite may have Fe^{3+} in its octahedral layer (Browning *et al.*, 1996; Velbel and Palmer, 2011). As Fe^{3+} has a higher oxidation state than Mg, it creates stiffer bonds with O in the lattice, causing greater degrees of heavy isotopic fractionation relative to Mg serpentine (Bayron, 2021). Highly altered, Mg serpentine-rich lithologies with a sizable Fe-serpentine component, such as WC-01-A, B; MP-01-A and LON-04-G, all have ^{18}O-rich compositions on the heavy end of the CMF (Fig 7.4).

Cronstedtite takes this further by having additional Fe^{3+} substitute for Si in the tetrahedral site (Browning *et al.*, 1996; Pignatelli *et al.*, 2017; Vacher *et al.*, 2019b), again, causing stiffer bonds than Si due to its smaller ionic radius and higher charge. Pure, endmember cronstedtite is therefore expected to have the highest affinity for ^{18}O. This may explain why KO-03-A, which has a notable cronstedtite component is the most ^{18}O-rich sample observed (Fig 7.4).

However, with the increasing availability of Al in solution as alteration proceeds, serpentine may begin to undergo coupled substitutions, called Tschermak substitutions (Padrón-Navarta *et al.*, 2013), where Al is swapped in the tetrahedral site in place of Si and/or Fe^{3+} (Browning *et al.*, 1996; Müller *et al.*, 1979; Velbel and Palmer, 2011). Serpentines such as cronstedtite and berthierine may become progressively Al-rich with increased alteration as extensive recrystallisation occurs and the Al is liberated from the coarse grained chondrules.

If this occurs, the affinity for ^{18}O is lessened because oxygen forms weaker bonds with Al than Fe^{3+} or Si (Schauble, 2004). This may provide an additional explanation as to why the most altered CM1 chondrites have an ^{18}O-poor composition (Bayron, 2021). In tandem with higher temperatures and the presence of chondrule pseudomorphs, the prolonged alteration may have caused Al-enrichment in the serpentine, lowering the ^{18}O-affinity in the CM1s (Fig 7.4). The oxygen isotopic systematics of as of yet uncharacterised serpentines, such as the new, S-rich serpentine noted in Winchcombe, may also have unique fractionation factors (Topping *et al.,* 2023; Bridges and Hicks, 2022). However, recent studies have shown that the effect of Tschermak substitutions may not exceed 0.3 ‰ in $\delta^{18}O$, indicating that this process may not be the main controlling factor in determining the $\delta^{18}O$ spread, but may complement the effect of temperature by extending its range (Scicchitano *et al.,* 2023).

7.3.2 Tochilinite

Tochilinite may be very fractionated compared to serpentine (Fig 7.4). As the oxygen budget in this mineral is bonded directly to a H atom as part of the OH group (Zolensky and Mackinnon, 1986), affinity for $\delta^{18}O$ may not be expected (Schauble, 2004). Experiments investigating the fractionation factors of tochilinite relative to water are needed to establish whether tochilinite fractionates negatively or positively ($\delta^{18}O$) in this regard, however there is one, single O-isotope composition of tochilinite — albeit with very high uncertainty — from Murchison reported in the literature (Sakamoto *et al.,* 2007). It has a very light oxygen isotopic composition ($\delta^{17}O$ = -5 ± 2 ‰; $\delta^{18}O$= -2 ± 3 ‰). If this is indeed reflective of the isotopic signature of CM tochilinite, this may explain why tochilinite-rich lithologies appear on the lighter end of the CMF – paradoxically adjacent to the most altered CM1s, which do not contain tochilinite (King *et al.*, 2017). The lithologies MP-01-B, LON-04-D and all the lithologies in Aguas Zarcas appear to have a sizeable tochilinite component and lie adjacent to the CM1s. A good potential analogue to investigate any potential tochilinite fractionation is brucite, $Mg(OH_2)$, as brucite / amakinite-like layers form a part of the tochilinite lattice

(Mackinnon and Zolensky, 1984). Brucite indeed fractionates negatively with respect to water (Zheng, 1998), so an apparent isotopic lightening with increasing tochilinite content may be expected.

Bulk matrix density separates from CM chondrites by Clayton and Mayeda (1999) are remarkably consistent with a $\delta^{18}O$ value of ~12 ‰. However, it must be recognised that the density separation techniques limit their matrix fractions to contain only Mg serpentine (*i.e.,* densities < 2.7 g/cm^3). Denser, Fe-rich phyllosilicate-like minerals, such as cronstedtite, tochilinite and greenalite, have higher bulk densities, typically > 3 g/cm^3. Previous matrix separate studies by Clayton and Mayeda (1984) report the composition of a number of density fractions from Murchison that cover the range of densities between magnesium serpentine and fayalitic olivine, from ~2.6 – 4.4g/cm^3 (Deer *et al.,* 2013), all of which have very variable O-isotopic compositions that range in $\Delta^{17}O$ from -1.8 - -3 ‰, from least dense to most dense, respectively (Clayton and Mayeda 1984). Clayton and Mayeda (1984) attributes this variation to the sequential inclusion of olivine within the fractions denser than 2.7 g/cm^3, which was detected by XRD. However, these fractions will also contain separated cronstedtite and tochilinite. The consistent $\delta^{18}O$ composition of the lower density separate, combined with the large spread of data in this thesis (obtained from micromilled powder, which would not separate according to density, and therefore include cronstedtite and tochilinite), testifies to the potential $\delta^{18}O$ heterogeneity invoked by mineral compositions.

7.3.3 Summary

To conclude, there may be several breaking points during the alteration process where the O-isotope systematics 'see-saw' during aqueous alteration as the environment changes to facilitate the precipitation of different minerals (Bayron, 2021). This will likely happen as temperature rises and falls and (if) fluid flowed. A prediction would be that the formation of tochilinite will result in isotopically lighter phyllosilicate fractions relative to serpentine. As tochilinite is dissolved and reprecipitated as Fe and Mg-rich serpentine, affinity for ^{18}O

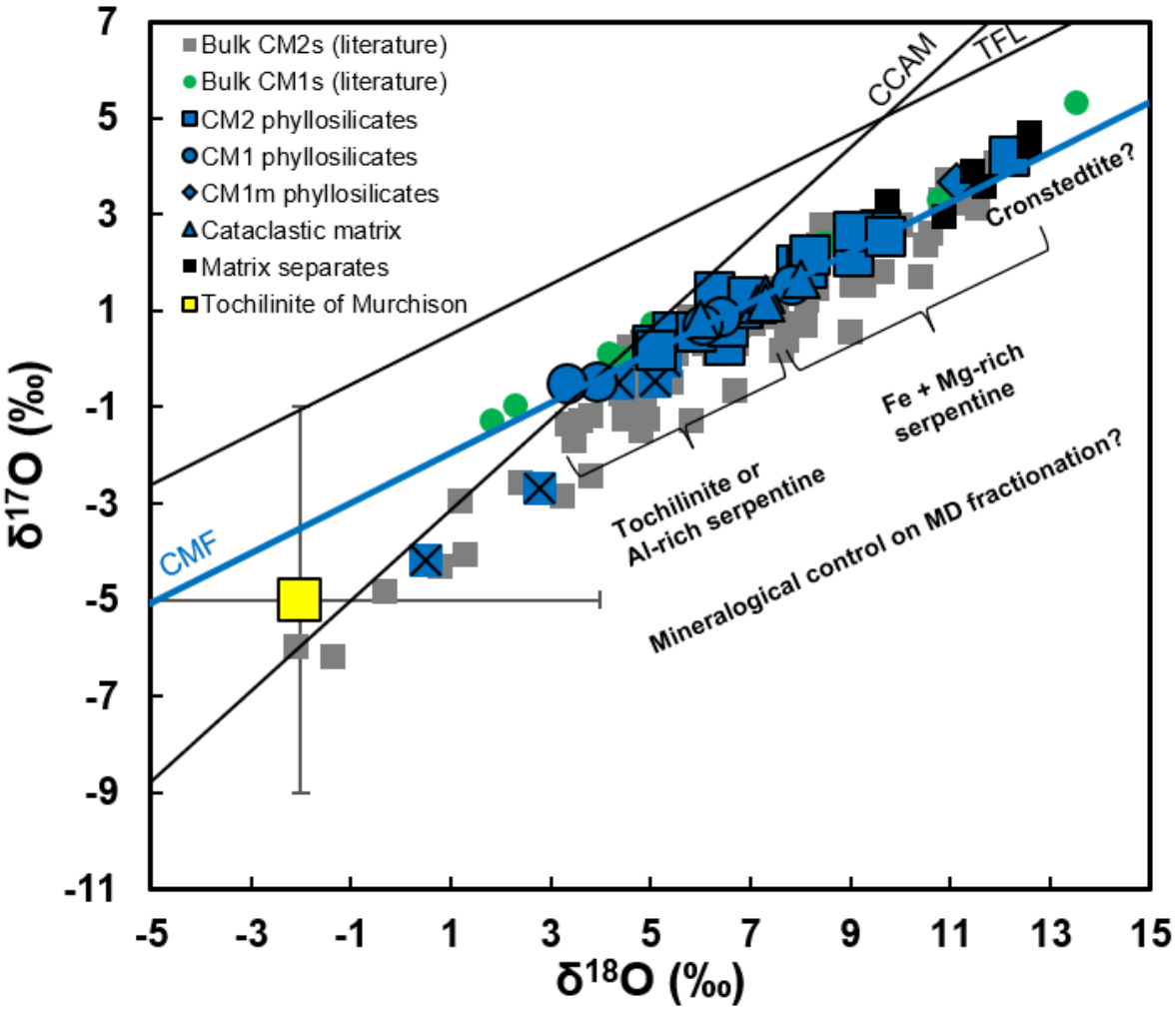

Figure 7.4 - 3-isotope plot with the CMF plotted alongside the sole O-isotope composition of tochilinite from the literature (Sakamoto *et al.*, 2007). A mineralogical control on the mass-dependent fractionation could be explained by the precipitation of different phyllosilicates, including Fe-rich Greenalite and Cronstedtite with tochilinite. Tochilinite is an average isotopographic SIMS measurement and the errors are 2 σ

will increase, with pure Fe-rich serpentines exhibiting the strongest fractionations to heavier values. Accompanying an increase in temperature, the fractionation of serpentine relative to water is reduced due to the inclusion of Al within the serpentine lattice.

In addition, there appears to be a noticeable mineralogical control on the $\delta^{18}O$ that is directly related to the amount of Fe and Mg in the phyllosilicates. These effects are somewhat traceable when plotting the $\delta^{18}O$ vs the Mg# and 'FeO'/ SiO_2 composition of TCIs and matrix from each lithology. As can be seen in Fig 7.5, there are systematic decreases in bulk phyllosilicate $\delta^{18}O$ with increasing 'FeO' content of both components, indicating that a causal link for the location of a phyllosilicate fraction on the CMF is in part, mineralogical.

Particularly, the TCI have a pronounced trend with the bulk O-isotopic composition of the lithology (Fig 7.5). This suggests the removal of tochilinite, and precipitation of serpentine has some influence over the isotopic composition of the rock; however, the scatter is too high to rule out other effects, and temperature clearly plays a role as discussed in section 7.2.

7.4 Open system alteration

It is crucial to remember that the concept of an open or closed systems is scale dependent (Hayes, 2004). Asteroids or asteroid regions may behave as closed systems on the largest scale but operate as an open system internally, with fluid moving from one region and becoming concentrated in another (Castillo-Rogez and Young, 2017; Fu *et al.,* 2017).

7.4.1 Introduction

Within open systems, lines close to mass dependence, such as the CMF, are attainable within regions of consistent fluid flux (Fu *et al.,* 2017; Young, 2001; Young *et al.,* 1999). Depending on the amount of water in any given location the system may become rock dominated or fluid dominated. To decipher which may have been a possible mechanism for reproducing the CMF requires comparison to outputs of various numerical models in the literature.

7.4.2 Rock- or fluid-dominated alteration

A purely rock-dominated open system is an unlikely explanation for the CMF as the phyllosilicates do not lie on a fractionation line with the anhydrous precursors (Fig 7.6). This outcome would be expected if the WR ratio was so low that it buffered the composition of the fluid to near-rock $\Delta^{17}O$, such as that seen in the dark inclusions of Allende (Fu *et al.,* 2017). An exception to this case would be if the CMF is in rock-dominated mass-dependent equilibrium with a precursor phase that is isotopically distinct from the composition of chondrule olivines, intersecting the CCAM at 4 ‰ ($\delta^{18}O$) (Fig 7.6). This might be a plausible scenario as the main medium harbouring the flowing water, if permeating directly through

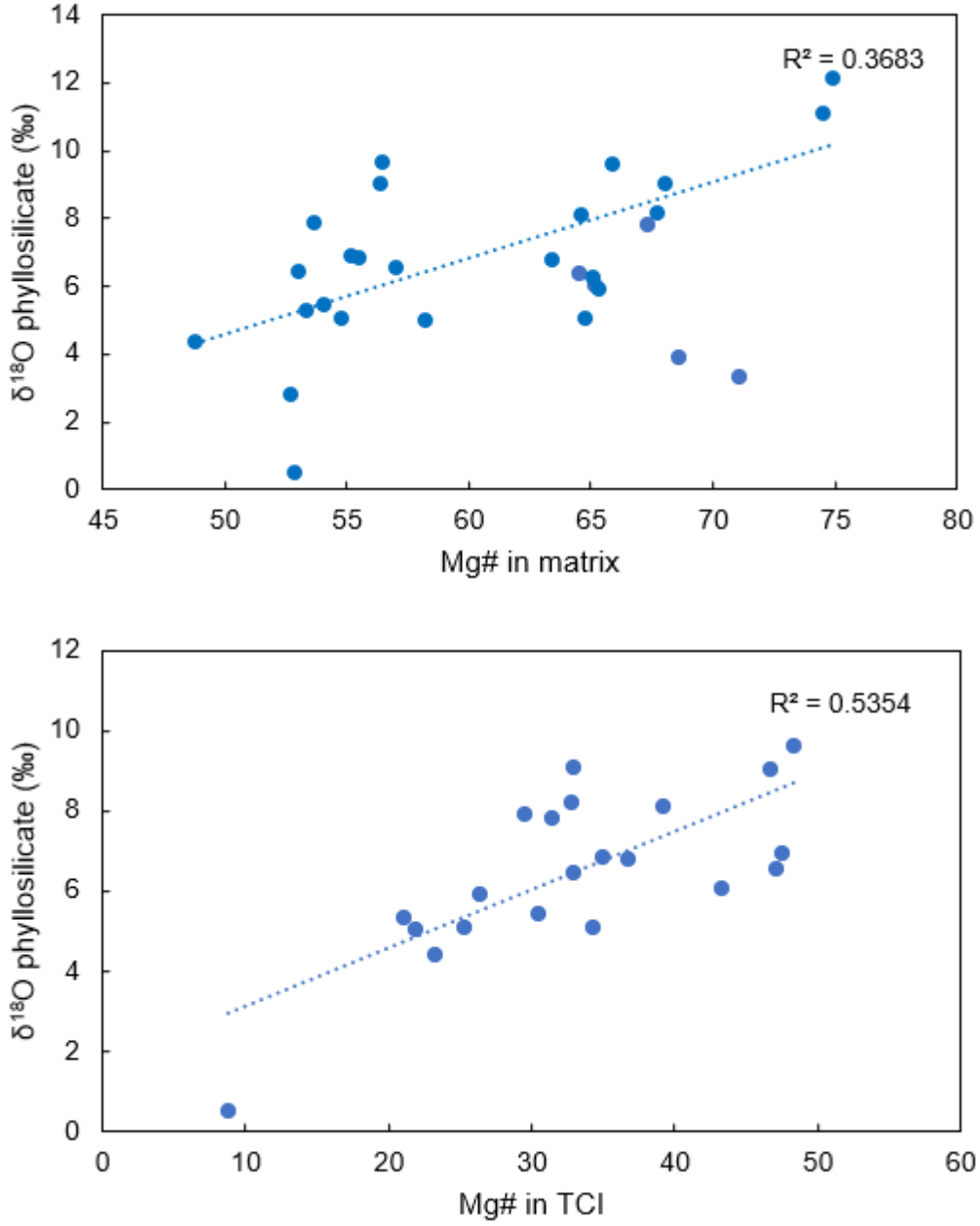

Figure 7.5 – Plots showing the very broad correlations between bulk matrix $\delta^{18}O$ and the Mg# number in TCIs and Matrix dominated (Fu *et al.*, 2017). The reader is referred to the detailed overview on open system behaviour in Chapter 1, section 1.7.2, where the differences between these two regimes are introduced.

the rock, would be the original, fine-grained matrix. Pristine matrix may be isotopically distinct, though unfortunately the bulk O-isotopic composition of such phases are unknown. The only O-isotope measurements of pristine matrix are from Acfer 094, which range from -1 to +3 ‰ ($\Delta^{17}O$) and ~ -2 to + 12 ‰ ($\delta^{18}O$) (Sakamoto *et al.*, 2007; Starkey *et al.*, 2014; Vacher *et al.*, 2020b), which suggests that rock-dominated fluid flow could be a possibility if the original, CM matrix is of a similar composition; however, such an assumption has little

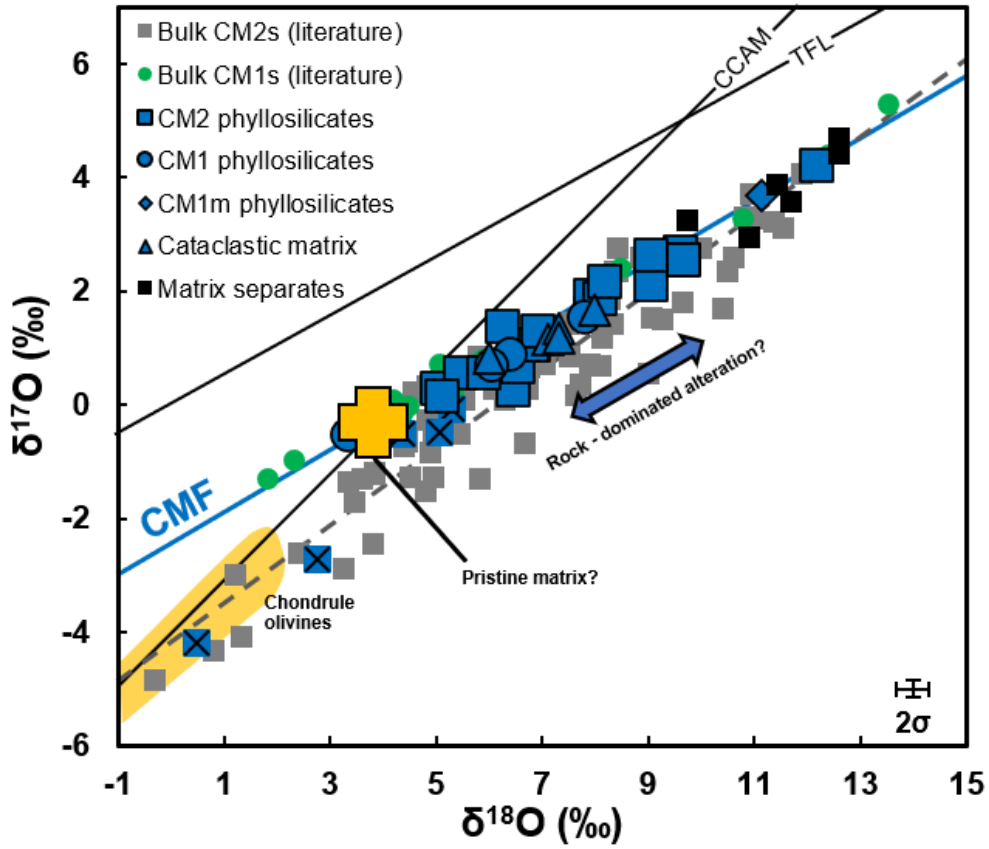

Figure 7.6 – 3 -isotope plot explaining the concept of rock dominated alteration. For this to work, fluid of a composition above the CMF must interact with an anhydrous precursor, with a composition defined where the CMF intersects the CCAM. Diagram inspired from Fu *et al.* (2017).

weight, as pre-solar grains, GEMS, organics and silicate fragments will be present in varying proportions between different meteorite groups (Keller and Messenger, 2011; Leroux *et al.*, 2015; Matsumoto *et al.*, 2019). Coarse-grained olivine within CI chondrite matrix appear to have $\Delta^{17}O$ values ~0 ‰ and $\delta^{18}O$ of ~ 5 ‰ (Piralla *et al.*, 2020), although these compositions may not be appropriate either for a precursor composition if they underwent isotopic exchange during the pervasive, CI chondrite alteration event.

With respect to the CMF, a fluid dominated system is the more likely outcome given the preponderance of high WR ratio estimates for carbonaceous chondrites in the literature (Suttle *et al.*, 2021). During such a regime, the isotopic composition, particularly the $\Delta^{17}O$, is expected to change as it moves from one area to another as fresh, isotopically distinct water is continuously buffered. Once the water reaches a domain of consistent fluid flux, the

$\Delta^{17}O$ may stabilise, producing lines of slope ~0.52. To decipher if the CMF is reflective of a region of variable fluid flux in an open system, it must be compared to existing models.

7.4.4 Single pass flow

The single pass model by Young *et al.* (1999), expanded by Young *et al.* (2001) and (Bayron, 2021), demonstrates a possible trend on a 3-isotope plot if water flowed from the hot centre of an asteroid to the frozen surface. Subject to the input parameters in this model, the trend will progress from low $\Delta^{17}O$ to high $\Delta^{17}O$ from left to right in a stepwise manner on a 3-isotope plot as alteration proceeds (Young, 2001). This is because in the early stages of alteration, the initial, small amount of melted water ice isotopically exchanges with the rock in the warm centre of the asteroid and becomes 'rock dominant'. As the heat radiates outward, more water is added to the regime. As the alteration proceeds to the surface, the rock becomes more 'fluid dominated' as the altered rock loses its capacity to buffer the water to lighter compositions. In Fig 7.7, regions exhibiting mass-dependent fractionation (constant $\Delta^{17}O$) define zones of consistent fluid flux. Regions where the trends deviate from mass-dependency (*i.e.*, the steps or ramps) are where the water moves from one region of fluid flux to another. $\delta^{18}O$ slowly increases from left to right in Fig 7.7, due to the temperature decrease from core to surface and through the addition of more pore water as the alteration front progresses (Brearley, 2006; Young, 2001). The zone of highest fluid flux, and highest alteration, resides just beneath the surface (Young, 2001; Young *et al.*, 1999).

7.4.5 Convection

Alternatively, an asteroid undergoing convection would similarly produce different zones of fluid flux, except this time the system will be 'multi pass' (Palguta *et al.*, 2010; Young *et al.*, 2003). Convection differs from single pass in that the oxygen isotopic composition of the rock is not as strictly coupled to the temperature gradient, as convective cells regulate the heat from the top to the bottom of the asteroid and vice versa, producing large zones of fluid flux within the body as upwellings and downwellings (Palguta *et al.*, 2010; Travis and

Schubert, 2005). The temperature may vary slightly across a convective plume of consistent fluid flux. As the plumes would penetrate in a perpendicular fashion to any potential accretionary layers in the asteroid (Palguta *et al.,* 2010; Travis and Schubert, 2005), convection would produce an opportunity for different accreted lithologies in a layered planetesimal to undergo very different levels of alteration. In addition, vigorous convection could result in more thorough 3-dimensional mixing of mixing and more consistent $\Delta^{17}O$ between different zones of fluid flux (Palguta *et al.,* 2010). If the material moved in addition to the water (mud), then this mixing may be even more apparent (Bland and Travis, 2017). Both single pass flow and convection would produce mass dependent fractionation lines in regions of consistent fluid flux, as shown by Fig 7.8.

7.4.6 Discussion

Is the single pass or convection model suitable to explain the mass-dependency of the CM phyllosilicate data? If the CM asteroid underwent open system behaviour faithful to that modelled by single pass or convective flow, then the CMF would represent an area of constant fluid flux and thus, a very specific region on a potentially diverse parent body. This is because the CMF appears to have invariant $\Delta^{17}O$ within a relatively narrow range of 2σ uncertainty, which is ± 0.45 ‰. Sourcing all CMs from such a specific zone within one asteroid would be a remarkable feat given the plenitude of CM material in the meteorite record (Lee *et al.,* 2020) and the thousands of potential source bodies in the asteroid belt (Greenwood *et al.,* 2020), so perhaps there are further answers hidden in the details. This presents an opportunity to examine the scatter of the CMF to tease out different regions of fluid flux. It is true that the CMF is broadly consistent with a mass-dependent relationship, but it is also true there is a degree of scatter around the line significantly greater than that expected from analytical uncertainty. This may be a weathering or residual precursor effect (Franchi *et al.,* 2001; Lee *et al.,* 2020), but there is also a possibility that it could be caused by open system behaviour. Plotting the $\Delta^{17}O$ of all the CM phyllosilicates in descending

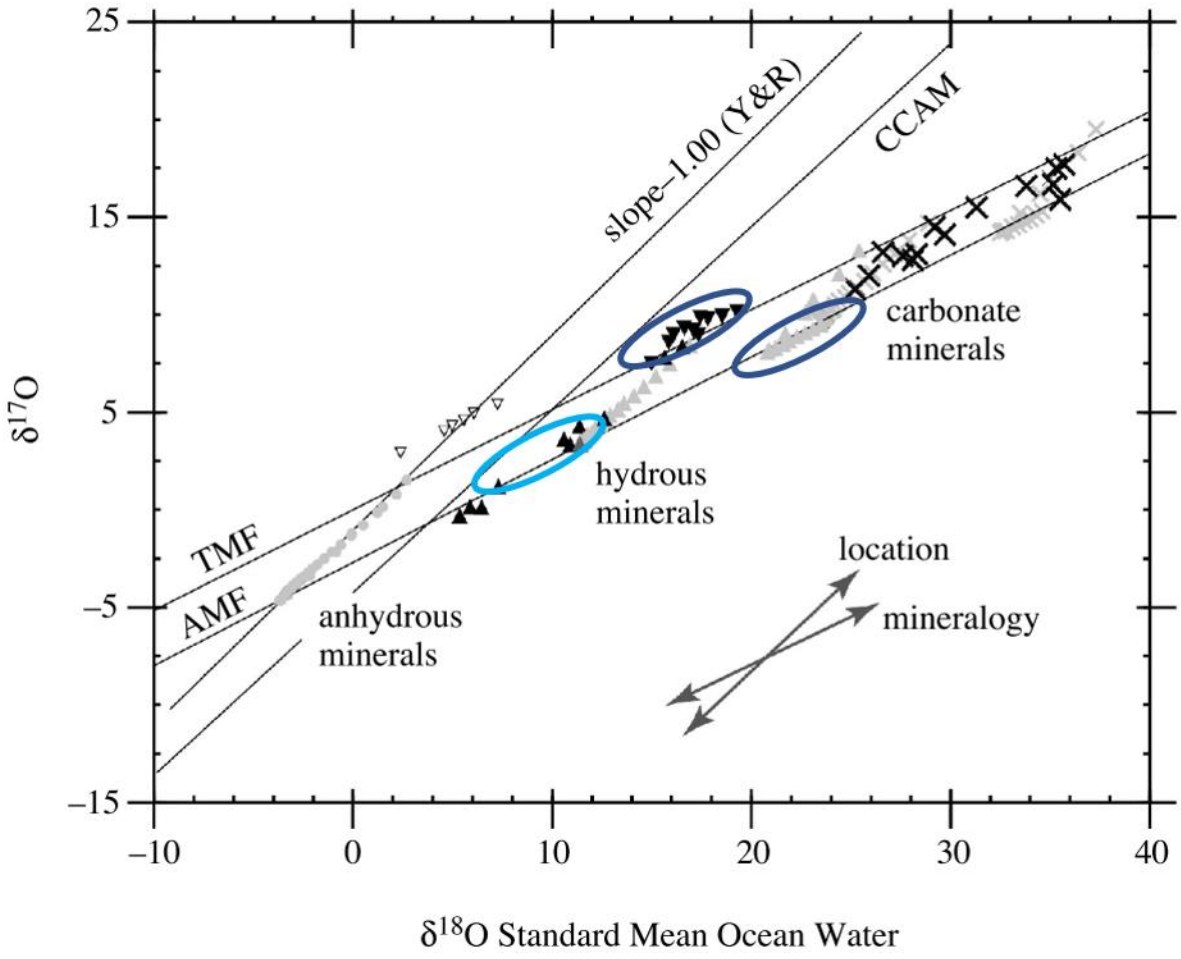

Figure 7.7 – Finite difference model results from Young *et al.* (2001) showing the variety of modelled products (grey triangles and crosses) that could be produced in a 9km radius, parent body within a single-pass flow regime, together with bulk values from the literature (Clayton and Mayeda, 1999; Rowe *et al.*, 1994). The coloured ovals indicate regions where mass-dependent fractionation is occurring, corresponding to domains of constant fluid flux. The light blue oval highlights where the CMF would reside. Mineral compositions in between these areas of constant fluid flux represent a transition in location from one region to another, at varying depths within a parent body.

order reveals several $\Delta^{17}O$ plateaus with transitionary steps in between, which could represent the movement of water from one region of fluid flux to another (Fig 7.9). This interpretation assumes no anhydrous precursor phases are affecting the isotopic compositions of the phyllosilicates. Justification for this assumption is found, in part, within the matrix phyllosilicates of certain lithologies, for example, AZ-02-A ($\Delta^{17}O$ = -3.02). The phyllosilicate in this lithology resides outside of the 2σ

uncertainty of the CMF yet bears no evidence for contaminant anhydrous precursors within the area of sample that was micromilled for O-isotope analysis. Of course, it has been

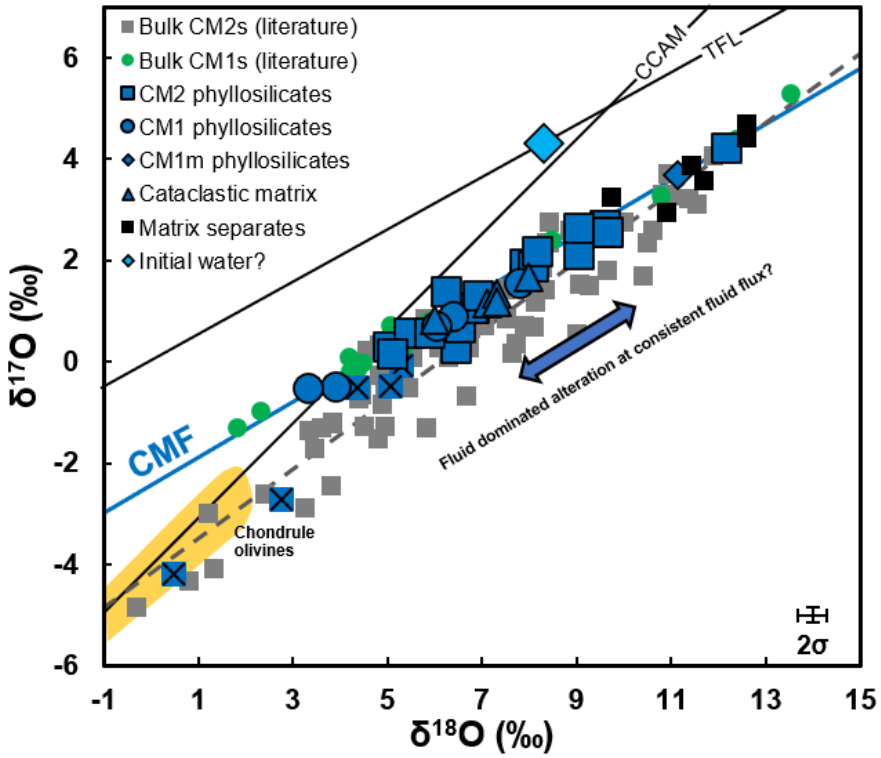

Figure 7.8 – A 3-isotope plot explaining the concept of fluid-dominated alteration. The anhydrous precursors (chondrule olivines) react with the initial water and the oxygen isotopic composition of the secondary products are buffered by the fluid to a composition intermediate between the two end members. Here, a random composition for water is plotted and represents one of many fluid compositions that can exist in an open system.

verified that the matrix in at least some of the lithologies in Aguas Zarcas contain small amounts of olivine, but for the purpose of assessing a parent body model, it is assumed that at low abundance these grains have no effect on the measured isotopic composition and that this therefore reflects the isotopic composition of the phyllosilicates. Aguas Zarcas and the incipiently altered lithologies of petrologic type 2.7-2.5 represent a transition to a plateau at ~2.5 ‰ ($\Delta^{17}O$) consisting of petrologic type 2.5-2.3 and chondrule bearing CM1 material. Two subsequent plateaus are seen, representing groups of the more altered lithologies, the main one at $\Delta^{17}O$ = -2.3 and the other at -2.1 ‰ with many lithologies showing transitional characteristics. This may be a higher resolution version of the $\Delta^{17}O$ variations as reported in Fig 7.7.

Could open system behaviour be a probable cause for such small jumps in $\Delta^{17}O$? Could there be two, maybe three, CMFs? It may be that the feasibility of the single pass model is throttled

by the very high values for initial water that were used in the Young *et al*. (2001) study, $\Delta^{17}O = 16$, $\delta^{18}O = 35$, which were required to model a wide range of O-isotopes exhibited by chondritic material on one body, including CI and CM chondrites. If the water was less enriched, for example, in line with what was calculated for initial water in 7.2.2 ($\Delta^{17}O$ roughly between 0-8 ‰, more likely towards the former), the effects may be more subtle, in line with what is observed in Fig 7.8. In particular the very salient $\delta^{18}O$ increase due to the mass fractionation and mixing of $\delta^{18}O$, as observed in Fig 7.7, may not be so apparent if one considers the diverse mechanisms of potential serpentine fractionation as discussed in section 7.3. However, in any single pass model it is expected that the $\delta^{18}O$ of the phyllosilicates should be correlated towards the composition of the water, and therefore, the $\Delta^{17}O$. Such a correlation is not observed in the CMF otherwise the ramps observed in the modelled data by Young *et al.* (2001) (Fig 7.7) would be readily identifiable in a 3-isotope plot. Therefore, convection may offer a better scenario to explain the variable $\delta^{18}O$ on the CMF due to the possibility of multiple passes. Coincidentally, Palguta *et al.* (2010) chose initial water compositions that are far closer to terrestrial values ($\Delta^{17}O \approx 3.34$ ‰) than Young *et al.* (2001), which makes the results of their model much closer in composition to the phyllosilicates measured in this work. In addition, the starting volume of water ice used by Palguta *et al*. (2010) is very close to one of the inferred WR ratio calculated in section 7.2.1 (1.2, or ~40 volume % water ice).

In any case, it is not possible to use a closed system model (*i.e.*, Clayton and Mayeda, 1999) to accurately determine the initial water parameters if the samples used for the calculation, in reality, come from a discrete area of fluid flux in a complex open system. To do so would only represent the initial composition of the water as it was supplied from one region to another, inaccurately due to time-integrated changes in $\delta^{18}O$ from region to region (Young *et al.,* 1999). The true initial values could be any range of compositions dependent on the location in the parent body, parent body size, heat budget, and the volume of accreted ice

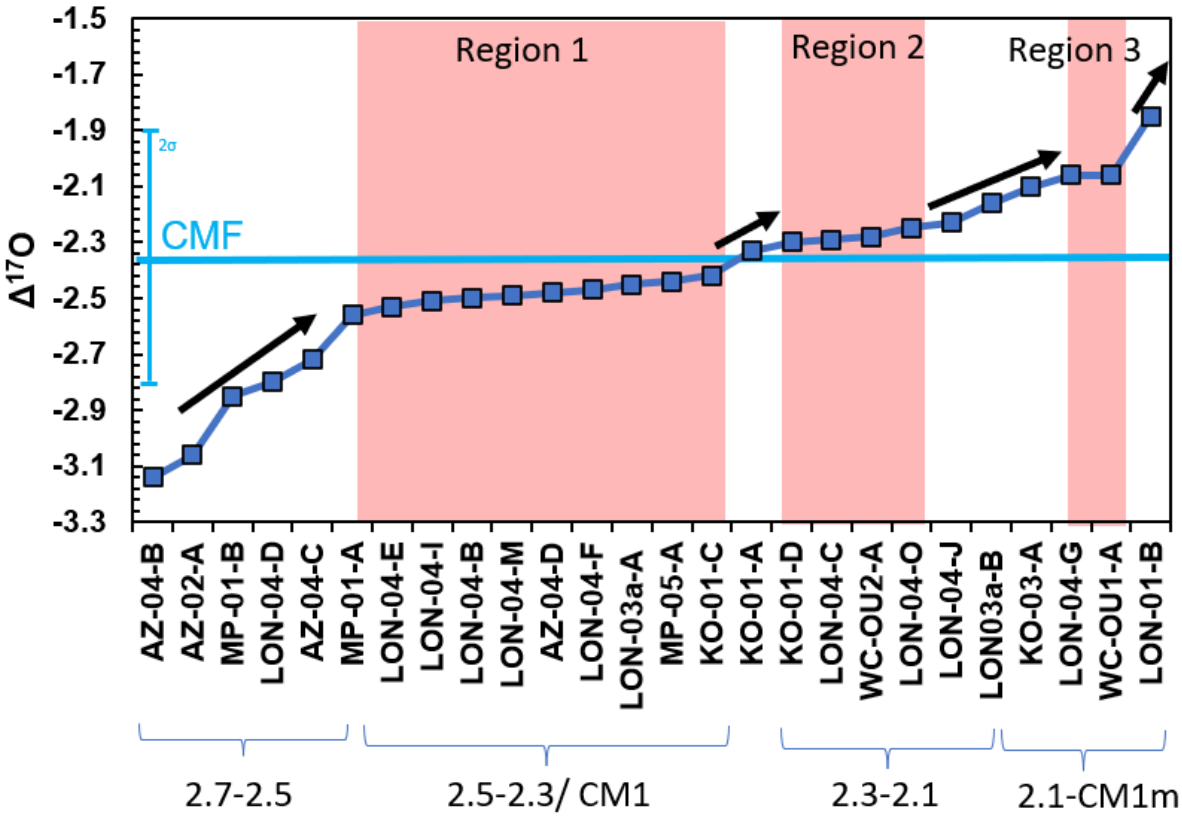

Figure 7.9 – Plotting the $\Delta^{17}O$ of the CM matrix phyllosilicates from this work in descending order. Three plateaus can be observed with intermediate lithologies forming a progressive ramp in between. This may reflect open system behaviour. Note that this is relatively well correlated with alteration extent (alteration index), but not with $\delta^{18}O$, as would be expected with a single-pass model. Alternatively, this is simply an artifact of the scatter on the CMF caused by weathering / anhydrous precursors, however the open system scenario may be valid for some lithologies such as AZ-02-A and LON-01-B, that occupy both ends of the spectrum and do not appear to contain anhydrous precursors (see Chapter 4 for a review of their petrography)

(Castillo-Rogez and Young, 2017). Fortuitously, the fine details of the oxygen isotope data suggest the possibility that CM lithologies represent different areas on a parent body undergoing subtly different degrees of fluid flux and not just a single zone. The very diverse petrography of individual lithologies (Lentfort *et al.*, 2021; Verdier-Paoletti *et al.*, 2019) also supports a spatial variability of material on the parent asteroid. To marry the oxygen isotope data with the petrography either necessitates the water in the asteroid was very well mixed, and / or the initial water was of much lower $\Delta^{17}O$ than the values used in Young *et al*. (2001) and even Palguta *et al.* (2010). This indicates that $\Delta^{17}O$ values close to 0 ‰ for the initial water is reasonable as these would move open system models (Palguta *et al.*, 2010; Young, 2001) in a direction that could produce the oxygen isotope variation on the CMF. In addition,

that these parameters model the data reasonably well with temperature is also testament to its acceptable 'ballpark' accuracy (see 7.2.2).

The duration of aqueous alteration is an additional factor that would contribute to a system being well mixed. Very short alteration duration on the asteroid on the scale of years to thousands of years would require very vigorous convection in a high(er) WR ratio system to produce a mass-dependent line akin to the CMF. Most evidence from Mn-Cr chronometry points towards the CM chondrites experiencing an episodic polyphase alteration history, with many discrete episodes of alteration occurring over a duration of up to 10 million years recorded in carbonates (de Leuw *et al.,* 2009; Lee *et al.,* 2012) The episode of alteration that produced the CMF may have been the largest and most intense episode, but it remains a challenging enigma as to why the CM chondrites are only partially altered if that is the case. Aqueous alteration experiments by Suttle *et al.* (2022) show that the intensity of alteration is linked to higher WR ratios, as opposed to higher duration of alteration. It is a possible outcome that the CM asteroid underwent an intense episode of alteration at a high WR ratio, before the water was suddenly lost from the system before back exchange could occur, for example through a catastrophic impact. Subsequent episodes of alteration may then happen once the body has re-accreted (Lee *et al.,* 2023), but at a lesser intensity than the main event. Precisely dating this duration, however, would require a wide petrographic and correlated isotopic campaign on the carbonates in many lithologies.

Another interesting point is that in Chapter 4 of this thesis, a very large variety of petrographically distinct clasts were identified. Of these a few resembled CI-chondrites in petrography but possessed heavy, CM-like oxygen isotopic compositions (*e.g.*, LON-04-K). CI-like chondrite material may therefore be commonplace among C-complex asteroids (Patzek *et al.,* 2018; Patzek *et al.,* 2020), the texture a product of accretionary history rather than alteration history, exhibiting isotopic variability in line with the heliocentric location in

which it formed. Subtle, open system models may be very applicable to a range of primitive asteroids.

In conclusion, twenty-seven lithologies from Mukundpura, Aguas Zarcas, Kolang, Winchcombe and LON 94101 have bulk phyllosilicate O isotopic compositions that are in broad mass-dependent equilibrium at $\Delta^{17}O$ = -2.35 ‰, defining the CM matrix fractionation line (CMF). This could represent a single, asteroid -wide serpentinisation event, wherein the aqueous alteration environment-maintained equilibrium with the altering water. A convective asteroid operating as one closed system, with internal open system behaviour may have produced the observed variations in $\Delta^{17}O$ and $\delta^{18}O$. It is noted that this does not exclusively constrain the CMs to a single parent body, rather it suggests that these bodies, however many, were complex. LON 94101 as a specific example, however, significantly strengthens the single parent body argument, as its clasts span a very large range of oxygen isotope compositions, including the different groups of samples shown in Fig 7.8.

7.5 The CM parent body(ies)

7.5.1 Accretion and physical structure

The parent bodies of the CM chondrites accreted exterior to the snow line where water could condense. The original anhydrous assemblages resembled incipiently altered chondrites like Acfer 094 (Bischoff and Geiger, 1994), Asuka 12169 (Kimura *et al.*, 2020) or the CM2.8 lithology in LON (LON-04-A), rather than CO chondrites (Greenwood *et al.*, 2023), which probably accreted from a similar reservoir of material to the CM chondrites but interior to the snow line (Torrano *et al.*, 2021).

Mukundpura, Aguas Zarcas, Kolang, Winchcombe and LON 94101 are polymict, regolith breccias containing clasts of diverse accretionary and aqueous history (Chapter 4). Each lithology contains a variable proportion of chondrules, TCI and fine-grained matrix. The coexistence of chondrule-rich and chondrule-poor lithologies requires a mechanism by which to promote heterogeneous accretion, reflecting variability in the supply rate of both

chondrules and matrix in the protoplanetary disk (Hellmann *et al.,* 2023). Streaming instabilities may initially cause preferential incorporation of chondrules over fine-grained matrix, resulting in early-formed chondrule-rich lithologies and later-formed chondrule-poor lithologies (Hellmann *et al.,* 2023). The later accretion of CI-like matrix from the outer Solar System by radial drift may have concentrated near the pressure bump caused by Jupiter (Brasser and Mojzsis, 2020), creating a dust trap and promoting the coagulation of large dust aggregates (Hellmann *et al.,* 2023). van Kooten et al. (2020) speculated that the CM chondrite forming region may have been between Jupiter and Saturn, with fine grained matrix infalling through semi-permeable barrier while Saturn grew.

In addition, the intermittent contribution from disrupted precursor planetesimals would have provided semi-processed fragments to newly accreting bodies. The observation of layered boulders on the surface of asteroid Bennu is evidence that these asteroids were stratified (Ishimaru *et al.,* 2021) (Fig 7.10, 7.11) at least at the metre scale, and likely larger scales given the variability in boulder types observed. The salient cataclastic texture in these meteorites is caused by regolith gardening during the collisional history of the original asteroid (Bischoff *et al.,* 2006) however, this does not preclude the possibility that the 'primary' accretionary lithologies, *i.e.,* the clasts that do not display internal brecciation, are detrital products themselves (Haack *et al.,* 2012; Metzler *et al.,* 1992). CM lithologies of moderate alteration sometimes contain chondrules with sharply abraded accretionary rims (*e.g.,* LON-04-F – Fig 4.29), in addition to anhydrous fragments of fayalitic olivine and metal in juxtaposition to very altered phyllosilicate clumps and tochilinite-cronstedtite intergrowths (TCIs). TCIs surrounded by accretionary mantles may provide evidence that the TCI precursors accreted a fine-grained rim in space (Metzler *et al.,* 1992). As type II TCIs are often radial pseudomorphic replacement products of small, euhedral crystals (often after olivine, pyroxene, and carbonate), and not always rounded chondrules, it is a possibility that their precursors were created through the early, catastrophic disruption of previous

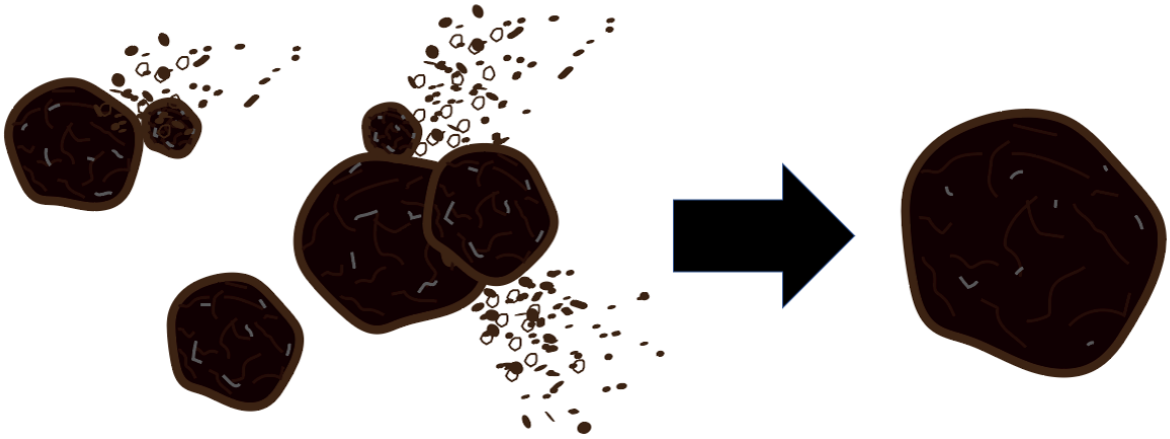

Figure 7.10 – Catastrophic processing of early planetesimals and re-accretion into a next generation parent body.

planetesimals before being incorporated into, and altered on, a next generation CM body (Fig 7.10) (Haack *et al.*, 2012). Shattering of chondrules and early carbonate veins within a precursor planetesimal will have seeded the CM-forming region with coarse angular fragments, similarly to the small CAI fragments reported in Cold Bokkeveld that provide evidence for a greater intensity of fragmentation before incorporation (Greenwood *et al.*, 1994). A mechanism for this disruption could be impacts (Lindgren *et al.*, 2015), or the self-destruction of small bodies through runaway fracturing caused by rapid gas pressurisation of H_2, CO_2, and methane by the aqueous alteration process (Brearley, 2006; Rosenberg *et al.*, 2001; Wilson *et al.*, 1999). Such a process has been observed weakly in active asteroids (Lauretta *et al.*, 2019). Liberation of partially altered matrix from precursor planetesimals would have mixed both phyllosilicate and pristine matrix, resulting in the presence of both in juxtaposition (Fig 7.11) within CM accretionary rims (Daly *et al.*, 2022; Metzler *et al.*, 1992). Subject to the nature of the primordial bodies, these precursors may have experienced alteration on their progenitor asteroids, and a single CM lithology may inherit alteration characteristics from multiple precursor bodies (Fig 7.9). Nebular alteration of the matrix may have also contributed to this budget of phyllosilicates (Bischoff, 1998; Brearley, 2003; Howard *et al.*, 2011b; Marrocchi *et al.*, 2023b; Zanetta *et al.*, 2021).

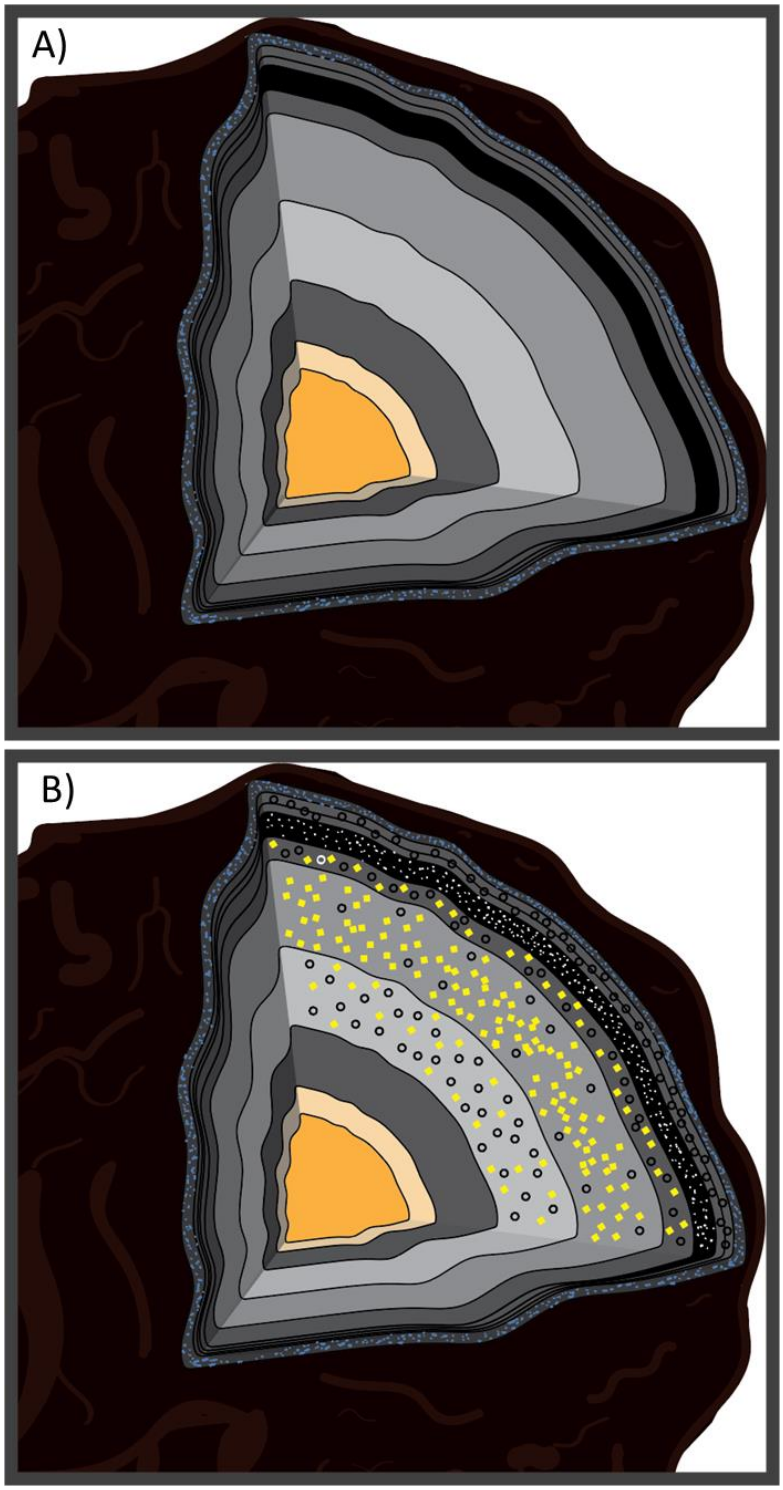

Figure 7.11 – A): A cartoon of a layered planetesimal of 50 – 100 km radius and a frozen surface, each coloured layer represents a temporally accreted deposit B: The same cartoon but with variable accretionary products to illustrate the potential diversity in a C-complex asteroid. Yellow diamonds = TCI material; small circles = chondrules; white dots = fine grained matrix. Note: This is one of many possible CM parent body scenarios and is used for visual demonstration only.

Furthermore, the H isotopic compositions of bulk CMs, if assuming a consistent water component, can be explained by a variable quantity of D-rich organics (Marrocchi *et al.*,

2023b; Piani *et al.*, 2021; Piani *et al.*, 2018; Vacher *et al.*, 2020a). This provides additional evidence for heterogeneous accretion of the CM parent body (Fig 5.6). The CM lithologies with the lowest $\delta^{18}O$ values, which may represent higher temperatures from deeper in a single parent body, coincidentally have the lowest δD. Lithologies with the highest $\delta^{18}O$ values, which may result from lower temperature closer to the surface, have higher δD. The least altered CMs, predicted to come near the frozen surface itself, have the highest δD. This cannot be explained by light H_2 loss by Rayleigh fractionation during aqueous alteration (Piani *et al.*, 2021). It may be better explained by molecular cloud legacy, in which during evolution of the disk, variable quantities of D-rich organics contribute to the accretion region over time (Marrocchi *et al.*, 2023b; Piani *et al.*, 2021). Alternatively, material closer to the frozen surface could become enriched in D through the sublimation of ice into a vacuum (Lécuyer *et al.*, 2017; Mortimer *et al.*, 2018) – the intensity dictated by the length of time between each accreted layer. Several authors have now proposed that a D-rich component accreted later than the bulk and this may explain the D-enrichment in the CM/CR-meteorite Bells (van Kooten *et al.*, 2020), proposed to be a matrix fraction sourced from the outer Solar System (Hellmann *et al.*, 2023). Many CI-like clasts were identified in LON 94101, but regrettably were not analysed for hydrogen due to machine downtime. It would be interesting to observe if these matrix-rich clasts are also enriched in D (LON-04-K, S, T, U, V).

7.5.2 Alteration regime

Many thousands of small planetesimals could have existed in the protoplanetary disk (Greenwood *et al.*, 2020; Weidenschilling, 2011). Over time, it is a likely course that a few larger planetesimals will begin to dominate the disk in the CM forming region (Morbidelli *et al.*, 2009). Twenty-seven lithologies from Mukundpura, Aguas Zarcas, Kolang, Winchcombe and LON 94101 have bulk phyllosilicate O isotopic compositions that are in broad mass-dependent equilibrium at $\Delta^{17}O$ = -2.35 ‰, defining the CM matrix fractionation line (CMF). This is difficult to explain in static alteration terms (Clayton and Mayeda, 1999)

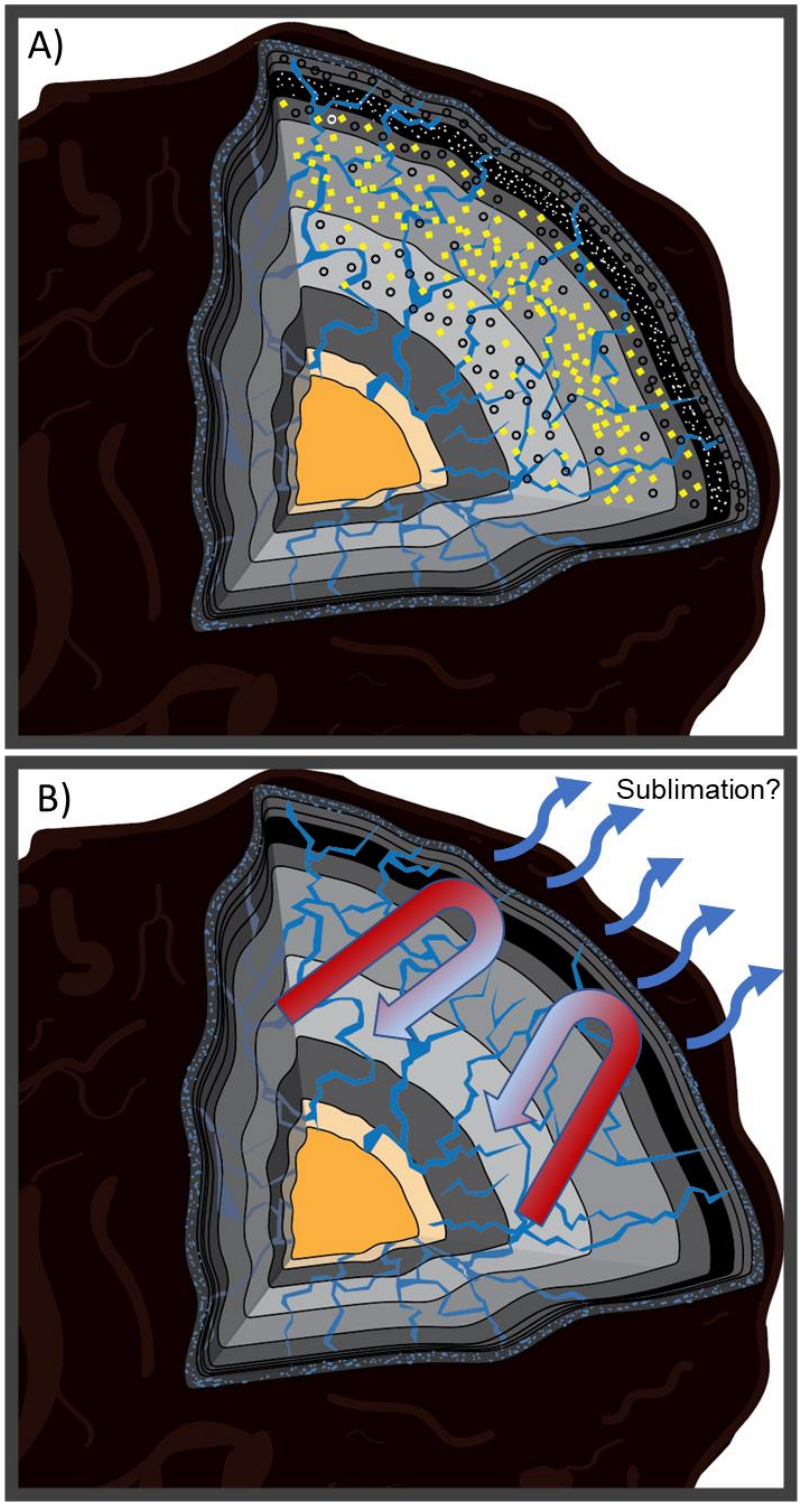

Figure 7.12 - A): A cartoon of a layered planetesimal of 50 – 100 km radius as in Fig 7.9 but this time with a network of fluid channels. Little 'islands' of asteroidal material reside between cracks and may exchange with the fluid but not experience the same degree of flow as that in the fractures; B) a convective scenario where warm water wells up from the core and then cools and falls from the surface. Water frozen at the outermost layer may sublimate into space.

when considering the variable petrography, and instead is interpreted to represent a single, asteroid-wide serpentinisation event wherein the aqueous alteration environment was in

equilibrium with the altering water. Variation in $\delta^{18}O$ along this line occurs due to temperature variations and the precipitation of compositionally diverse serpentines. Variation in $\Delta^{17}O$ could be caused in part by open system behaviour, possibly due to convection, as discussed in section 7.4. However, open system alteration comes with a significant hurdle that will now be discussed.

7.5.2.1 A compromise: channelised 'leaky' flow?

An issue with assuming an open system model is the observation of isochemical alteration in carbonaceous chondrites and the paradox that the most altered chondrites are the most pristine geochemically (Bland *et al.,* 2009). Extensive fluid flow through porosity should fractionate soluble elements from the bulk chondrite and reprecipitate them elsewhere (Brearley, 2006). Measured porosities and permeabilities of extant chondrites are also very low (Corrigan *et al.,* 1997), which if representative of the original porosity, would preclude pervasive fluid flow (Fu *et al.,* 2017). This led Bland and Travis (2017) to suggest that early asteroids were originally giant convecting balls of mud, where rock and water would move together while maintaining isochemical alteration; unfortunately, the lack of any convincing mud flow or shear textures in chondrites argues for rapid lithification of the rock (Bland *et al.,* 2014; Herbst *et al.,* 2021). Evidence of mud flow, if it occurred in the earliest planetesimals, has probably been overprinted by disaggregation, re-accumulation, and protracted alteration.

There is no evidence a of large-scale fracture network in the meteorite record that may promote fluid flow (Bland *et al.,* 2009; Fu *et al.,* 2017), though it is unlikely that a meteorite bearing such a feature would survive the entry through Earth's atmosphere owed to their fragility, unless very fortuitous (Borovička *et al.,* 2019). Carbonate veining within boulders on Bennu indicates that such features may be common on C-complex asteroids (Kaplan *et al.,* 2020). Hydrogen gas released by serpentinisation, and/or water vapour pressures in an environment of 200 °C (consistent with the alteration of some CM1 chondrites) would cause

pressures in the realm of 10s of MPa, which would rapidly overcome the tensile strength of basalts (Schultz, 1993), and most definitely chondritic material (Fu and Elkins-Tanton, 2014). Fracture conduits are a likely consequence (Fig 7.12, A)), increasing permeability by several orders of magnitude compared to what is observed at the thin section scale (Brearley, 2006; Fu *et al.,* 2017). Gas pressure, surface tension and/or convection would cause water (or muddy water) to be transported (Young, 2001).

Convective channelised fluid flow would be a hybrid situation (Fig 7.12 B) that facilitates the mixing of water across a large region without pervasive leaching from the internals of every piece of rock, giving rise to isochemical behaviour on the regional scale if minimal water is lost from the frozen surface, similar to mudball convection. The average WR ratio in this region would remain consistent. Wedged between the fluid bearing fractures would be 'islands' of material with lower permeability that would isotopically exchange with the flowing fluid in the adjacent cracks — *i.e.,* they would 'leak' — but due to the lack of substantial flow through the rock itself, substantial leaching of volatile elements will be

lessened. Initial reports by Daly *et al*. (2022) suggest Winchcombe, which could be analogous to one of these 'islands', possesses an anisotropic fluid network running in a single direction through the sample (Daly *et al.,* 2022). A network like this would limit fluid transfer and preserve mineralogical heterogeneity (GEMS like material within accretionary rims), as has been observed in so many lithologies of moderate alteration in Chapter 4. TCI precursors, which might have been previously altered in a smaller, primordial planetesimal, seem to provide a locus for alteration (Pignatelli *et al.,* 2017; Pignatelli *et al.,* 2016; Suttle *et al.,* 2023). Fluids may make use of existing weaknesses caused by prior aqueous attack, preferentially causing the TCI phases to be replaced relative to the chondrules. The population density of TCIs in some lithologies are high enough that they are continuously contacting at the grain boundaries (see AZ-04-B), which during dissolution, may have provided a smaller network of channels for fluid to flow (Rubin *et al.,* 2007). Dissolution of

tochilinite (Vacher *et al.*, 2019b) and carbonate would have increased porosity and permeability (Zolensky *et al.*, 1997), whereas precipitation of serpentine and occasionally magnetite in hollow TCI cores (Suttle *et al.*, 2023) would result in the opposite. The zoning observed in TCIs, and the complexity of carbonate precipitation (*e.g.*, Farsang *et al.*, 2021) records changes in fluid composition and environment over time.

Observations of boulders on the surface of C-complex asteroid Bennu have revealed a network of high-contrast Ca-rich veins, possibly asteroidal 'caliche' deposits (Zolensky *et al.*, 1997), raising the possibility of fractures and channelised fluid flow in Bennu's parent body (Kaplan *et al.*, 2020). Modal carbonate compositions of the most aqueously altered, chondrule-pseudomorph bearing CM1 chondrites — which were probably altered at higher temperatures — are low (<2 %) compared to CM2s (>2 %), consistent with Ca leaching during retrograde cooling (King *et al.*, 2017; Zolensky *et al.*, 1997). Carbonate, and even salt production may be a natural consequence of leaching and transport under variable pressure-temperature conditions (Castillo-Rogez and Young, 2017; Castillo-Rogez and Kalousová, 2022) and should be a priority for investigation once samples are returned from asteroid Bennu in 2023.

It should also be mentioned that isochemical alteration in itself is not *a priori* evidence for lack of fluid flow (Castillo-Rogez and Young, 2017). In terrestrial systems on Earth, some serpentine massifs have modest - high WR ratios but no visible fractionation of soluble elements (Ehlmann *et al.*, 2012; Li and Lee, 2006). This effect is also dependent on the solute concentration within the altering fluid, as fluid saturation will limit the uptake and transport of soluble ions (Greenwood *et al.*, 2022). The nature of the asteroidal fluid has not yet been precisely determined, but preliminary insights into fluid inclusions trapped within a pyrrhotite grain from asteroid Ryugu indicates the fluids were CO_2-, S-, Na- and halogen-rich brines (Nakamura *et al.*, 2022). Fluid saturation and density will therefore impact the intensity of fluid flow.

It has been shown that the composition of phyllosilicates replacing chondrule olivines in individual CM chondrites are homogenous in a given thin section (Velbel *et al.,* 2012; Velbel *et al.,* 2015). This indicates that the mineralogy of the phyllosilicates is controlled by the composition of the circulating fluid within the rock rather than the phase they are explicitly replacing (Velbel *et al.,* 2012; Velbel *et al.,* 2015). This is congruent with a homogenously distributed fluid, consistent in composition over a wide region. As different lithologies are exposed to variable temperatures — which is dependent on the model of fluid flow and the depth of the rock— the composition of the fluid may change as the stability fields of new minerals are crossed (Vacher *et al.,* 2019b), which explains why serpentines replacing olivines are identical within single meteorites, but different when comparing different meteorites of variable alteration (Velbel *et al.,* 2012; Velbel *et al.,* 2015).

Recent analyses of CM chondrite water using a specialised SIMS approach has shown that most moderately to heavily altered CMs contain a water component with a consistent hydrogen isotopic composition (Marrocchi *et al.,* 2023b; Piani *et al.,* 2021; Piani *et al.,* 2018). A constant δD for CM water is once again congruent with uniformity of the water reservoir across the sampling region of the CM chondrites.

All of the above arguments support the possibility of fluid mobilisation on a CM asteroid. While it does not discount the possibility of static, closed system alteration, there is nevertheless a growing field of evidence that suggests fluid flow is an inevitability. However, one hurdle remains: did the CM parent bodies even grow large enough to support fluid flow?

7.5.3 Parent body size

Determination of the nature of open-system alteration is dependent on its composition and timing of accretion (Castillo-Rogez and Young, 2017). The budget of ^{26}Al at time zero (CAIs), assuming disk-wide ^{26}Al homogeneity (*e.g.,* Gregory *et al.,* 2020), was large enough to cause radiogenic melting of the smallest planetesimals (Zhou *et al.,* 2013) (Fig 7.12). Carbonaceous chondrites must have either formed quite early and small; or late and big.

Accreted water ice fraction is also important as it inhibits radiogenic heating (Castillo-Rogez and Young, 2017). A molar WR of 1.2 would be equivalent to a volumetric WR ratio of 0.63, or ~40% water ice by volume.

Mn-Cr dating of carbonates in CM and CI chondrites suggest late formation ages, 4-6 Myr after CAIs (Fujiya *et al.*, 2012; Fujiya *et al.*, 2013; Jilly *et al.*, 2014; Visser *et al.*, 2020). Late formation ages could accommodate large, ice bearing asteroids upwards of 100 km (Fig 7.12). However, recent measurements of some CM chondrites, Flensburg, and of Ryugu particles using matrix matched SIMS standards suggest the late formation ages may be an artifact of inappropriate standard calibration and the formation ages were in fact, much earlier, from 1.8 to 4.5 Myr after CAIs (Bischoff *et al.*, 2021; Fujiya 2012; McCain *et al.*, 2023). If this is the case for all CMs, the parent body must have either accreted small, or existed as a fragment of a once large asteroid that was disrupted before differentiation (McCain *et al.*, 2023).

However, there is an argument in the literature that asteroids could only form big, with a radius > 100 km (Morbidelli *et al.*, 2009; Schlichting *et al.*, 2012; Weidenschilling, 2011). By definition, this statement would require that the CM parent bodies must have formed late to prevent differentiation. This is particularly true if the accreted ice fraction is low.

However, this is only valid if no heat regulation mechanism occurred. It is noted that even with an accretion age of 2.5 Myr after CAIs, a parent body with a substantial fraction of water ice (50 %) could grow to be quite large (20-100 + km radius) without exceeding 500 °C maximal temperature (Fig 7.13). While this temperature alone is a very high in CM terms, it may be mitigated as accretion is a sequential process and occurs in stages with many periods of impact and reassembly to disrupt internal heating (McCain *et al.*, 2023). In addition, a convective water system may moderate internal temperature to some extent (Bland and Travis, 2017). Furthermore, the existence of a high temperature, metasomatized clast in Murchison provides evidence that the CM parent bodies may have reached much

higher temperatures in their interiors than closer to the surface (Kerraouch *et al.*, 2019) – indicating that the CM parent body must have at least grown to a size large enough to accommodate a moderately hot core. This demands a parent body size of at least 10 km radius to > 100 km radius if considering the early accretion ages of 1.8-2.5 Myr as proposed by McCain *et al.* (2023). Larger asteroids would be more likely to experience convection (Fu *et al.*, 2017), which together with the increasing body of evidence suggesting fluid flow, is supportive of an open system source for the O-isotope data.

7.5.4 Meteorite sampling locations

Figure 7.13 represents a parent body of 50 km radius with convection as the primary mechanism of fluid flow. Overprinting the schematic is the model of Palguta *et al.* (2010) to provide spatial context. Aguas Zarcas is a chondrite that contains lithologies of more negative $\Delta^{17}O$ compared to other CM2s and samples materials that coincide with an upwelling plume of moderate temperature, where the $\Delta^{17}O$ of the water is matched. Kolang and Winchcombe would both sample material associated with a downwelling region of more positive $\Delta^{17}O$ and lower temperature. Mukundpura source regions would straddle a boundary between upwellings and downwellings as it contains lithologies with both relatively positive and negative $\Delta^{17}O$. Both Mukundpura and Kolang have CM1 clasts which must come from a hotter region of the body, within an upwelling plume that has lower $\Delta^{17}O$ to produce their $\Delta^{17}O$ compositions of ~ -2.5. Finally, LON 94101 would sample a range of material from all across the asteroid, including the frozen surface (Fig 7.14).

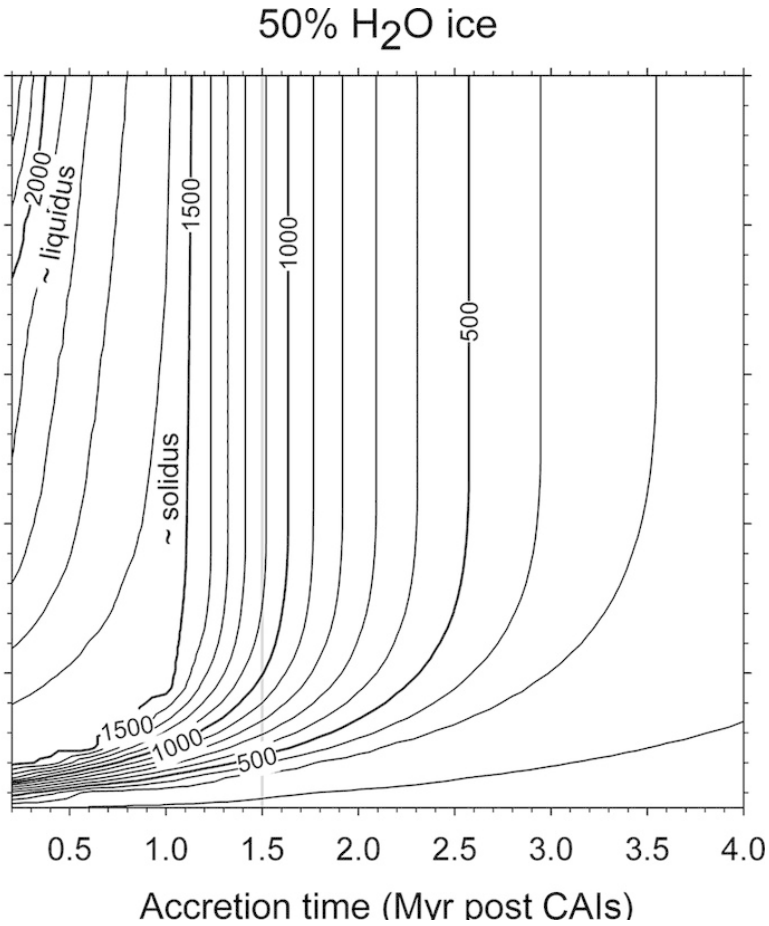

Figure 7.13 – Contours of maximal temperature of planetesimals as a function of terminal radius, accretion time relative to CAIs and water ice. From Fu *et al.* (2017). Details about the models upon which these contours are derived can be found in Zhou *et al.* (2013). Cause of heating is radiogenic decay of ^{16}Al.

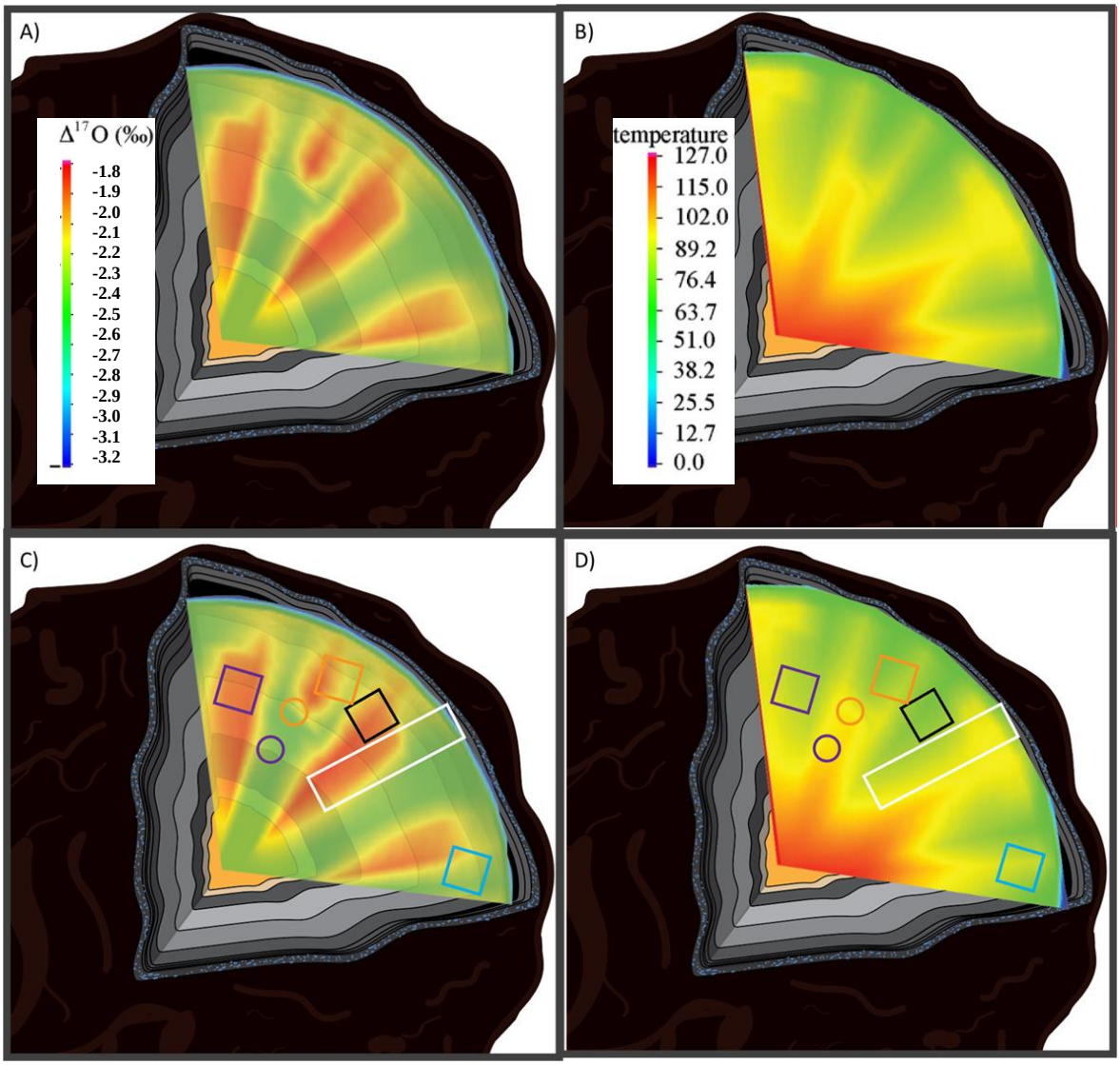

Figure **7.14 –** Cartoon of a CM parent body of 50 km radius and 38 % accreted water ice, undergoing convection with a ^{26}Al weight fraction of 4.5 x 10^{-8}. The visual model results from Palguta *et al.* (2010) are superimposed over the top to provide context. A) A false colour image of the $\Delta^{17}O$ intensity according to upwelling and downwelling regions. The scale has been adjusted to encompass the range of $\Delta^{17}O$ observed in this work. B) A false colour image showing the distribution of temperature across the parent body. Comparison with A shows that the regions of highest temperature are correlated to rock with the lowest $\Delta^{17}O$. C) and D) are the same as A) and B) except for some suggested regions where Aguas Zarcas (blue), Mukundpura (yellow), Kolang (purple), Winchcombe (black) and LON (white) may sample. Parent body is purely schematic but provides a visual aid as to how convection may produce the observed variations in O-isotopic composition.

It must be noted that in this case, a convective scenario is decoupled from the layered structure of the asteroid. Lithologies at any depth could be altered to varying extents dependent on the intersection of the convective plumes. Multiple CM parent bodies may

have existed in this format, but at this stage it is not possible to deconvolve the fine details of the oxygen isotope data to determine how many there were. It is also reiterated that this is one possible interpretation of the data in the context of an open system model from the literature. Numerous other possibilities may exist until the O-isotopic components of CMs are investigated in detail.

7.5.5 Disruption

Disruption of one or more CM asteroids produced a suite of smaller rubble pile asteroids, potentially contributing to the Eulelia, Polana or Sulamitis asteroid families in the main belt (Jenniskens, 2018). The material has been spread widely within the Solar System delivering CM-like clasts to many other asteroidal and planetary bodies, evidenced by their inclusion in ordinary chondrites, HEDs, Ureilites and the Moon (Briani *et al.,* 2012; Patzek *et al.,* 2018; Patzek *et al.,* 2020; Zolensky *et al.,* 1996). CM chondrites also have a large range of young space exposure ages, potentially hinting at a near-Earth asteroid heritage which would indicate the jettisoning of large CM fragments into near-Earth space (Gregory *et al.,* 2015; Suttle *et al.,* 2021; Zolensky *et al.,* 2021). The ages cluster into four groups that appear to correlate well with aqueous alteration, where essentially the youngest ages are the most altered. This has led to the interpretation that continuous disruption of a CM asteroid progressively excavated material towards the more altered core of the body (Vernazza *et al.,* 2016; Zolensky *et al.,* 2021).

During this long period of impact and reassembly, small, isolated episodes of aqueous alteration may be kickstarted due to the heat generated by repeat, low intensity impacts (Floyd *et al.,* 2023; Hanna *et al.,* 2015; Lindgren *et al.,* 2015; Tomeoka *et al.,* 1999). Evidence for episodes of localised alteration overprinting the main serpentinisation event is recorded in complex carbonates (*e.g.,* Farsang *et al.,* 2021); and the radioactive elements thorium and uranium, suggesting liquid water was mobilised within the last million years (Turner *et al.,* 2021). In addition, a disequilibrium has been reported between bulk CM

matrix phyllosilicates and the OH groups within the phyllosilicate lattice, which are enriched in $\Delta^{17}O$ relative to the bulk (Baker *et al.*, 2002; Franchi *et al.*, 2001; Morris, 2008). This may hint at an episode of post-serpentinisation alteration that introduced and / or melted fresh water ice, which circulated and exchanged with the most vulnerable part of the serpentine lattice. Where the impacts were particularly energetic, thermal alteration may have caused dehydration of the phyllosilicates, recrystallisation and light metamorphism (King *et al.*, 2021; Tonui *et al.*, 2014 and references therein).

7.6 Other primitive asteroids

It is difficult to reconcile the number of CC parent bodies using O-isotopes in the context of open system behaviour. This is because any potential evolution of the water phase will obscure its initial composition and abundance as it flows from one region in the asteroid to another. By that logic the water could have any number of starting compositions and could evolve equally complex ways from one region to another, depending on the fluid regime. This is why Young *et al.* (1999) rightly suggested it is possible for all the carbonaceous chondrite groups to be produced on a single asteroid. However, it is unlikely that the meteorite record is dominated by one asteroid alone, considering the number of asteroids that are observed in the main belt (>100,000 exceeding 2 km). This is where links between petrography and other isotope systems are critical to form meaningful interpretations. CR, CI, CM and C2-ung meteorites have very distinct petrography and isotopic characteristics indicating formation at variable heliocentric distances.

7.6.1 CR chondrites

There are other chondrite groups that show evidence of pervasive alteration including the CR, CI chondrites and many ungrouped specimens (Fig 7.15). The asteroid forming process should be fairly universal across the protoplanetary disk, subject to the supply of material (Greenwood *et al.*, 2020; Weidenschilling, 2011), so it could be expected that the trends observed in the CM chondrites are also observed in other groups. All these meteorites, with

the exception of the CI chondrites, suffer from the same problem of anhydrous precursor contamination in their bulk measurements, and necessitate the application of spatially resolved matrix phyllosilicates in a similar fashion to this work and to the same level of coverage. However, some trends may be predicted from the limited compilation of literature matrix data available so far. The CR chondrites constitute the largest dataset of oxygen isotope measurements outside of the CM chondrites (Abreu and Brearley, 2010; Harju *et al.,* 2014; Martins *et al.,* 2007; Schrader *et al.,* 2011; Schrader *et al.,* 2014; Weisberg *et al.,* 1993). Their bulk measurements appear to define a mixing line of a similar slope to that observed in the CM2s, though offset to higher $\Delta^{17}O$, interpreted to be due to the same interaction of isotopically light anhydrous precursors and isotopically heavy water as proposed for the CM chondrites (Franchi, 2008). With the observation that the CM mixing line is actually mixing between anhydrous precursors and mass-dependently fractionated matrix phyllosilicates formed in equilibrium (Fig 6.4), it could be postulated that a similar mass-dependent fractionation line exists for CR matrix phyllosilicates. A select group of CR chondrite matrix measurements (Clayton and Mayeda., 1999; Schrader *et al.,* 2014; Weisberg *et al.,* 1993) are displaced from the whole rock (Schrader et al. 2011) by a comparatively similar amount to that observed in CMs but show a much greater degree of scatter to higher and lower compositions (Fig 7.15), so a possible 'CR matrix fractionation line', if it exists, is hard to accurately plot. This could be due to the variation in sampling protocol: Clayton and Mayeda (1999) utilised a density separation technique, whereas Weisberg *et al.,* (1993) and Schrader *et al.,* (2014) removed matrix manually using dental burs or gentle crushing in mortar and pestles. Crushing uncharacterised chips in a mortar and pestle may introduce a large anhydrous component through accidental incorporation of precursor material. If the matrix compositions are accurate, they clearly show the potential for multiple matrix fractionation lines, one at high $\Delta^{17}O$, and one more, or perhaps two, next to the CM chondrite matrix phyllosilicates and in line with matrix from Bells. This could

mean two separate parent bodies. An approximate location for these parent bodies has been underlain as red lines in Fig 7.14 through the largest clusters of CR matrix measurements.

7.6.2 C2-ungrouped meteorites

In Fig 7.14, the matrix measurements from CR chondrites line up well with matrix density separates from the C2-ung chondrite Essebi (Kallemeyn, 1995; Rowe *et al.,* 1994) and with bulk and matrix measurements from the C2-ung meteorite Tarda (Gattacceca *et al.,* 2021). Both of these ungrouped meteorites have high deuterium enrichments which may indeed suggest a tentative link to CR chondrites, which also have elevated deuterium compositions (Alexander *et al.,* 2013).

Tagish lake is an unusual C2-ung chondrite in that it is thought to be one of the only meteorite samples from a D-type asteroid along with WIS 91600 (Choe *et al.,* 2010; Yabuta *et al.,* 2010). It has a furtive bulk oxygen isotope composition in the literature, with only one full measurement reported (Brown *et al.,* 2000) though there have been reports of oxygen isotopic 'ranges' in numerous abstracts (Clayton and Mayeda, 2001; Engrand *et al.,* 2001). A matrix composition, reported by (Engrand *et al.,* 2001) and averaged by (Baker *et al.,* 2002) from eight SIMS measurements also plots within the region occupied by Essebi matrix, Tarda, and a number of CR chondrite measurements. A potential link between each of these meteorites may suggest a common parent body heritage.

The chondrite Bells has been subject to multiple reclassification attempts. Initially identified a CM chondrite it was subsequently rebranded as a C2-ungrouped (Brearley, 1995; Kallemeyn, 1995; McSween Jr, 1979; Mittlefehldt, 2002). Recently Marrocchi *et al.* (2023a) proposed it is more akin to a CR chondrite than a CM. The matrix separate of Bells is isotopically unique and occupies a region of transitional between CM chondrites and CR chondrites. It represents a very important lithology to bridge the gap between meteorite groups (Fig 7.15), though it is unclear if Bells is directly related to the CMs but if such a relationship could be established through petrologic kinship (*i.e.,* Bells-like clasts within

CMs or vice versa), this would help greatly in better understanding the nature of closed / open system behaviour.

7.6.3 CI, CY and asteroid Ryugu

The pervasively altered CI chondrites define a mass-dependent fractionation line above the TFL to a much tighter precision than the CMF (Clayton and Mayeda, 1999; Greenwood *et al.,* 2022; Rowe *et al.,* 1994), and before this study the CI group was the only one to show such a trend. This is not surprising given their very altered nature. Using the CMF as a reference for comparison, it could be interpreted that the CI chondrite fractionation line is an example of a terminal equilibration point of a C-complex asteroid at a high WR ratio. Alteration may have proceeded to such a level that the rock had lost its ability to buffer the fluid and the entire asteroid becomes an equilibrated, fluid-dominated system (Clayton and Mayeda, 1999; Fu *et al.,* 2017; Greenwood *et al.,* 2022; Rowe *et al.,* 1994). Analyses of asteroid Ryugu particles in 2022 confirmed that it has a CI affinity and that this material is widespread in the Solar System – suggesting its rarity is a function of its fragile nature and general incompatibility with surviving atmospheric entry (Greenwood *et al.,* 2022; Ito *et al.,* 2022; Nakamura *et al.,* 2022). The Ryugu particles are offset by approximately 0.1 ‰ ($\Delta^{17}O$) from the CI chondrites, which has been attributed to significant terrestrial weathering of the latter (Greenwood *et al.,* 2022). The thermally altered CY chondrites (Ikeda, 1992; King *et al.,* 2019) may represent mildly metamorphosed CI chondrites, though their $\Delta^{17}O$ are slightly offset from the CIs which may be evidence for open system behaviour. Further examination of Ryugu particles for thermally metamorphosed clasts would go far in establishing / confirming the CI-CY petrographic link.

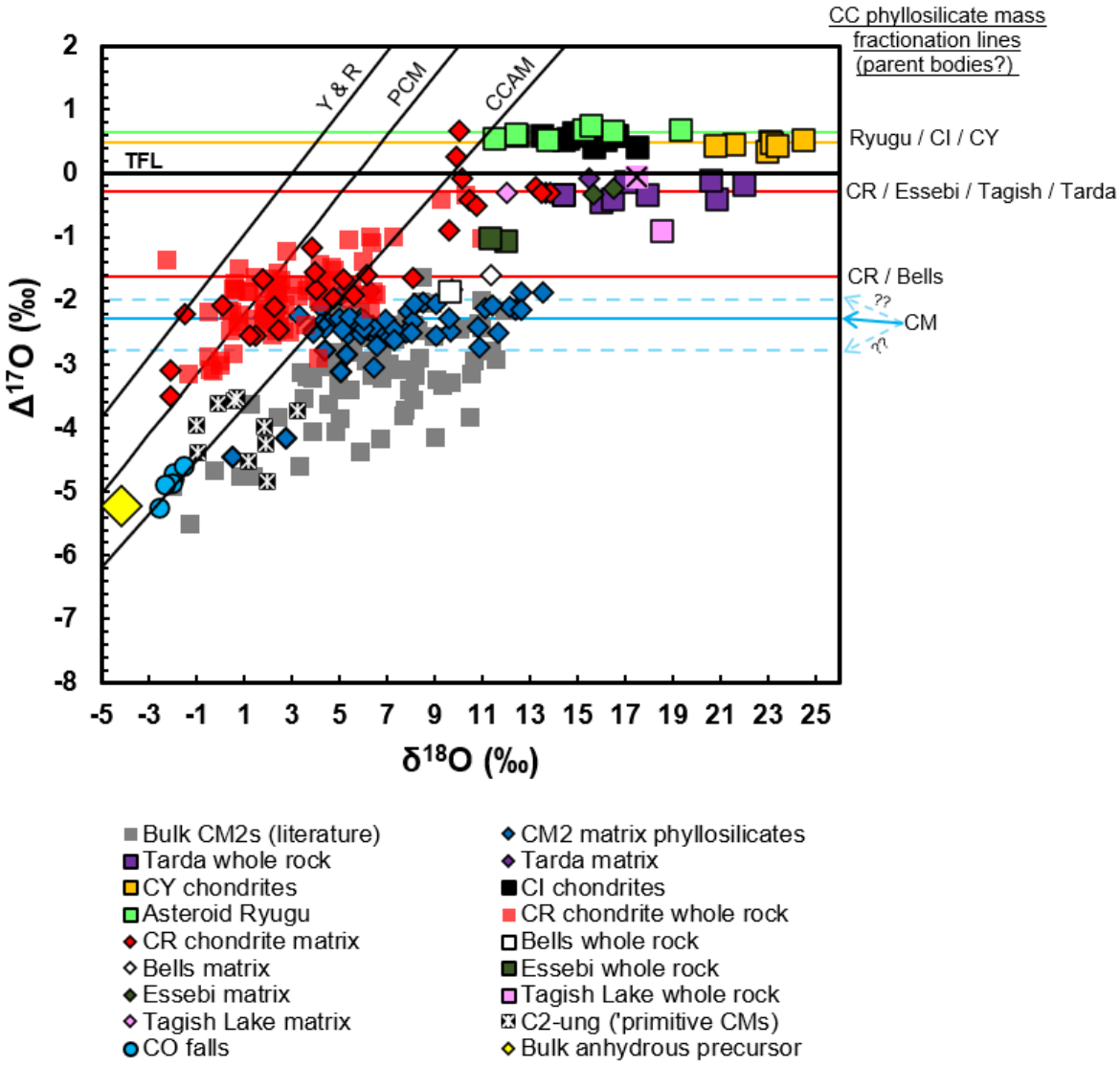

Figure 7.15 – Oxygen isotope plot with the paradigm of aqueously altered chondrite bulk and matrix density separates plotted. The purpose of this exercise is to observe if any comparable mass-dependent trends between other hydrous meteorite groups. Data from a wide range of sources: (Brown *et al.*, 2000; Clayton and Mayeda, 2001; Clayton and Mayeda, 1999; Engrand *et al.*, 2001; Gattacceca *et al.*, 2021; Greenwood *et al.*, 2022; Harju *et al.*, 2014; Martins *et al.*, 2007; Rowe *et al.*, 1994; Schrader *et al.*, 2011; Schrader *et al.*, 2014; Weisberg *et al.*, 1993). Tarda matrix data was obtained during this work.

Chapter 8 - Summary and Future Work

8.1 Summary

CM chondrites are a complex meteorite group that display variable bulk O-isotopic compositions. Their highly unequilibrated, brecciated, and aqueously altered petrography has invoked a number of closed and open system models to explain the spread isotopic data. The aim of this thesis was to unravel the O-isotopic systematics of the CM phyllosilicate matrix in petrographically characterised lithologies from both meteorite falls, and meteorite finds. By removing the layer of ambiguity associated with the poorly defined quantities of isotopically distinct precursors 'contaminating' the bulk measurements, a better understanding of the aqueous alteration process(es) on CM parent bodies would be obtained, garnering insight into whether a closed or open system model is the most feasible. In addition, using both falls and a find permits as assessment of possible terrestrial weathering effects, though it is acknowledged that a single, moderately weathered find alone is unlikely to unravel the extend of weathering that is present across the global collection of hot desert and Antarctic meteorites.

Polished blocks of large surface area were prepared by hand from meteorite falls Mukundpura, Aguas Zarcas, Kolang, and Winchcombe (Chapter 2). A large resin block of the Antarctic find LON 94101, 7 cm in the longest dimension, was provided on the basis that it is one of the most exceptionally brecciated CMs known.

A total of 27 clasts were characterised by SEM across all meteorites (Chapter 4) in addition to 5 examples of highly disturbed cataclastic matrix. All lithologies were characterised using criteria inspired and adapted from widely cited Rubin method (Rubin *et al.*, 2007).

O-isotopic investigation of the aqueous alteration process necessitated extraction of just the phyllosilicate fraction of each characterised clast (Chapter 2). This was achieved using a micromill equipped with a ball point tungsten carbide tip. Challenges associated with the drilling process were investigated and overcome. The most effective method was to gently,

but quickly, drill the samples dry. The micromill was used to extract approximately 200 µg of matrix from each lithology.

The small, volatile-rich CM matrix fractions proved a challenge for laser-assisted fluorination as they are vulnerable to both pre-reaction and blank effects during analysis (Chapter 3). A new protocol was devised to address both of these challenges. Thorough cleaning and minimal exposure of the sample chamber to atmospheric conditions resulted in blanks that were both stable and very low relative to the amounts of O_2 being generated from the samples. As the real blank composition was too small to be measurable, a smaller obsidian standard was run alongside each CM sample to establish the effect of the blank and a correction was subsequently applied to the data, reducing the uncertainty on each measurement to a level comparable to that obtained on larger samples of the internal obsidian standard. In addition, the liberated sample gas underwent an additional phase of cryogenic separation to remove the interfering effects of nitrogen trifluoride. For the first time, accurate and precise O-isotope compositions of small CM matrix samples were determined (Chapter 5 and 6).

8.1.1 Revisiting the thesis aims

The original questions as outlined in the thesis aims in Chapter 1 can now be answered:

What is the nature of the complex alteration in CM chondrites?

The historical, bulk CM O-isotope compositions plot along a line of slope ~0.7 (Clayton *et al.,* 1999; Greenwood *et al.,* 2023). Closed system models have been the favoured paradigm to explain this trend, on the assumption that the complexity of the data is owed to progressive reaction of water and anhydrous precursors under different WR ratios (Clayton *et al.,* 1999). Upon analysis of several phyllosilicate fractions in his work, the trend exhibited purely by the alteration products appears to be much simpler, occupying a fractionation line at a $\Delta^{17}O$ value of -2.35 ± 0.45 ‰ (2σ). Bulk measurements of highly altered CM1s and CM1/2s, in

addition to bulk matrix density separates also plot along this line. This new trend is named the CM Matrix Fractionation line (CMF). These results show the complex spread of bulk CMs measurements along a slope ~0.7 is owed essentially entirely to the variable inclusion of anhydrous precursors. The apparently simple trend of the CMF, exhibited by almost invariant $\Delta^{17}O$, broadly supports the widespread equilibration of a water reservoir at a constant water/rock ratio. The spread in $\delta^{18}O$ across the matrix phyllosilicate is likely controlled primarily by both temperature and mineral specific mass-dependent fractionation, and not solely by mixing.

These oxygen isotope data support a growing body of evidence that water had a consistent composition over the range of material sampled by the CM chondrites (Marrochi et a., 2023; Velbel *et al.,* 2012; Velbel *et al.,* 2015; Piani *et al.,* 2021). To accommodate the paradox of isochemical alteration, the material must be well mixed, with water flowing freely through a fracture network, potentially by convection (*e.g.,* McSween Jr *et al.,* 2002; Palguta *et al.,* 2010; Travis and Schubert, 2005; Young *et al.,* 2003). Convection provides a mechanism to regulate heat on the asteroid, warranting the notion that these asteroids were large, on the scale of 50-100s km radius, supported by relatively late ages for alteration (McCain *et al.,* 2023 and references therein). Alteration by a static, closed system scenario (*e.g.,* Clayton *et al.,* 1999) is an unlikely course unless multiple asteroids, by chance, accreted identical WR ratios, a situation that does not seem probable when considering the very diverse petrography.

Can different lithologies in CMs have a common parent body origin?

The petrologic diversity within the samples studied ranges from CM1.0 – CM2.7 in the meteorite falls, with each meteorite exhibiting a dominant form of alteration in the sequence (from least to most altered) Aguas Zarcas, Mukundpura, Winchcombe, and Kolang. The single most altered example of a CM lithology across the falls was found in Mukundpura, present as a CM1 clast, establishing novel petrographic link between a large CM1 clast and

surrounding CM2 material. Later discovery of a CM1 clast in Kolang corroborated this finding. Together with literature data, the lithologies within the meteorite falls span the entire petrologic range, from CM1-CM2.8. LON 94101 also spans the entire petrologic range, except in this case it is uniquely within one meteorite. This is an important link as the clasts in LON have a high probability of sampling the same parent body and can provide information on the degree of source asteroid diversity. The lithologies within LON consist of rare, incipiently altered, CM2.8 clasts; a full complement of CM2.0-2.7 lithologies that dominate the section, and multiple occurrences of CM1 clasts with pseudomorphed chondrules; furthermore, smaller but still prevalent examples of matrix-rich lithologies, here termed 'CM1m', indicate that the CM parent asteroid accreted lumps of volatile, matrix-rich material, similar in petrographic character to CI chondrites. The petrography of the studied CMs is richly diverse in terms of both primary texture and alteration extent. This suggests heterogeneous accretion of chondrules, matrix, and TCI precursors within the CM forming region, potentially on the same asteroid.

The existence of petrographic kinship does not explicitly imply these lithologies are sampling the same parent body (*e.g.*, Lee *et al.*, 2019) but does imply the probability of such an outcome is more likely than if the material was found only in separate meteorites. CM1 material has consistently appeared in juxtaposition to CM2 material within three meteorites (Mukundpura, Kolang and LON 94101), suggesting a close source region in space, potentially the same parent body. The rarer, more unusual clasts including endmember, incipiently, and heavily altered examples are not correlated between meteorites, and potentially have a stronger petrographic case for being derived from different parent bodies; however, this is not supported by the O-isotopes, which indicate a very similar composition, and that these clasts are sampling a similar range of starting, and secondary materials as regular CM2 chondrites, albeit in different proportions. In summary, it appears that the CM lithologies studied in this work sample lithologically complex parent asteroids. Meteorites

record ancient processes that are not directly measurable; therefore, assuming all clasts are exogeneous xenoliths increases the tendency to overlook the possibility of complex asteroids, which has been extensively modelled to be the more likely outcome (Bland and Travis, 2017; Cohen and Coker, 2000; Grimm and McSween Jr, 1989; McSween Jr *et al.*, 2002; Palguta *et al.*, 2010; Travis and Schubert, 2005; Young, 2001; Young *et al.*, 1999; Young *et al.*, 2003). It is possible that a disruption event of such an asteroid has resulted in specific intercept trajectories with Earth, resulting in the plenitude of CM materials recovered today.

Are the CM chondrites in our meteorite collections representative of the whole CM asteroid(s)?

The answer to this question is probably not. There is a small, but significant proportion of CI-like, 'regolith' clasts in LON 94101, encompassing a range of textures classified herein as CM1 and CM1m material. One in particular, LON-04-B is highly fractured, porous, and fragile, made evident by the pervasive resin contamination within its pore spaces. Coincidentally this clast is also in the centre of the large block. This suggests that LON 94101 preserves CI-like, CM clasts that do not normally survive atmospheric entry owing to their fragility (Borovička *et al.*, 2019), and only by significantly increasing the studied surface area does the probability of finding such clasts increase. By extension, there will be a rubble pile in the Solar System containing a range of fragile, pervasively altered CM lithologies that resemble CI chondrites in addition to more competent boulders resembling CM2 and CM1 material. Return of material from asteroid Ryugu via JAXA's Hayabusa2 mission has confirmed Ryugu has a CI-like affinity (Ito *et al.*, 2022; Nakamura *et al.*, 2022), indicating this material is far more widespread in the Solar System than previously thought, especially considering the rarity of precious CI-chondrite material on Earth (Greenwood *et al.*, 2022). Asteroid Bennu is spectrally similar to CM chondrites (*e.g.*, Hamilton *et al.*, 2019), and this will be confirmed upon the return of material by OSIRIS-REx in the Autumn

of 2023. From the results of this thesis, it is predicted the material sampled by OSIRIS-REx will contain a much higher abundance of fragile regolith resembling lithologies LON-04-B, LON-04-K, LON-04-S, LON-04-T, LON-04-U, LON-04-V, in addition to robust material, that may resemble CM2 and CM1s in texture.

What is the extent of terrestrial weathering?

Using a sample set consisting of both falls and finds has permitted the evaluation of terrestrial weathering effects. Weathering is most certainly a prevalent source of contamination for many isotope systems, including oxygen, in CM lithologies (*e.g.,* Bland *et al.,* 2006a; Bland *et al.,* 2006b; Jenkins *et al.,* 2023; Lee *et al.,* 2020). Nevertheless, comparisons between the meteorite falls in this work with the Antarctic find LON 94101 suggest only mild-moderate terrestrial effects upon the O-isotopic composition of the phyllosilicates, at least when the weathering grades for Antarctic meteorites are low (less than or equal to B/Be, the weathering grade for LON), and are not confidently resolvable from the mass-dependent effects of parent body alteration. Furthermore, the prior statement that the CM1 meteorites are weathered to ^{16}O-rich compositions through the interaction with light Antarctic precipitation (Greenwood *et al.,* 2019; King *et al.,* 2018) is questioned on the observation of ^{16}O-rich CM1 clasts in Mukundpura and Kolang, in addition to the recent, ^{16}O-rich C1-ungrouped chondrite Flensburg (Bischoff *et al.,* 2021), which may be a special CM1 lithology. While Antarctic meteorites have undoubtedly been weathered to lighter values to greater or lesser extents, the compositions of CM1 clasts from LON are not significantly weathered beyond the composition of Flensburg, though they are more ^{16}O-rich than those reported in Kolang and Mukundpura, which may indicate an Antarctic weathering effect. However, it is noted that the petrography is not comparable (Chapter 4) and so could equally represent diverse alteration history. In summary, CM chondrites are not as pervasively weathered as the highly terrestrially altered CI chondrites (*e.g.,* Greenwood *et al.,* 2023; King *et al.,* 2020b), although with this in mind the CM chondrites do contain 'CI-

like' clasts which may have been similarly contaminated. The effects of weathering upon these highly susceptible clasts have not yet been thoroughly investigated, though the single O-isotope analysis of a CM1 lithology, LON-04-K, has a very apparent, ^{18}O-rich signature, perhaps indicating minimal weathering.

8.1.2 Further work

This thesis only touches the surface of the O-isotope complexity in CM chondrites and offers a number of potential avenues for future work.

Further lithological assessment

A simple continuation of this study would suffice to increase our knowledge and understanding of the CMs further. Only 27 of the many potential CM lithologies have been explored for their bulk phyllosilicate O-isotope composition. Particular focus is needed with respect to the unusual clasts, their distribution, prevalence, and O-isotopic composition. CM1m ('CI-like') clasts would greatly benefit from further investigation, as only one was analysed for its bulk O-isotopic composition here. Corroborating the measurements from this thesis will go far in determining if CI-like material can be produced on a CM-parent body. Furthermore, the micromill approach would allow accretionary rim material specifically to be analysed for its O-isotopic composition, permitting a comparison to TCI-rich material. Often the two are found in juxtaposition. This would aid in discerning if the two have a different, or a coeval, accretionary and alteration history.

Other chondrites

The CMF is most certainly not the only fractionation line amongst the aqueously altered meteorites. As highlighted by 7.15, preliminary plotting of phyllosilicate compositions from the literature suggests at least three lines, one exhibited by the CMs and two by the CRs. The more unusual C2-ungrouped chondrites such as Tagish Lake, Tarda, and Essebi have matrix compositions that overlap with these fractionation lines, possibly hinting at similar source region. Furthermore, the CM-like, but ultimately distinct chondrite Bells may occupy a CM-

fractionation line offset from the main CMF to more positive $\Delta^{17}O$ values, encompassing a range of CM lithologies that have more positive $\Delta^{17}O$ than the CMF. Further resolution provided by a similarly forensic approach as adopted in the present study would go far in establishing if these meteorites do indeed occupy their own fractionation lines - and if the process of aqueous alteration in CMs is common amongst the more proximal / distal asteroids in the Solar System that accreted similar quantities of water. The meteorite Tarda is a particularly good choice as it may represent more distal, D-type asteroid material akin to Tagish Lake, and appears to be readily available owed to its large, desert strewn field. A larger volume of material is needed for an exhaustive assessment of any potential lithologies, followed by spatially targeted, destructive micromilling.

In situ work on lithology-specific components

Further *in-situ* work of lithology-specific carbonate generations would pair well with the spatially resolved, bulk phyllosilicate measurements. For now, SIMS analyses of carbonates are usually limited to 'per meteorite' analyses, with little focus on the variable internal heterogeneity. The next step would be to utilise lithology-specific analyses of carbonates to better understand the very large spread in carbonate O-isotope composition, and if it can be correlated to the phyllosilicate compositions within each lithology, which would provide ample room for geothermometry estimates of aqueous alteration per lithology, using the fractionation factors between carbonate and serpentine.

The next obvious course for further investigation would be to use SIMS / NanoSIMS to reveal the O-isotopic composition of phyllosilicates *in-situ*. CM phyllosilicates are complex intergrowths of Mg-serpentine, Fe-serpentine and tochilinite, that have different stability fields and potentially form at different stages of the aqueous alteration process. O-isotope measurements would discern if they formed during different temporal events, or coevally (traced by variable, or constant $\Delta^{17}O$ respectively), and potentially at what temperature through the $\delta^{18}O$ composition. *In-situ* carbonate data has benefitted from increased

petrographic context, permitting resolution of the isotopically distinct T1 calcites from the T2 calcites. T1 calcites in particular are often associated with Type II TCIs, which tend to form the outer edges of the Type II TCI / T1 calcite intergrowths. It would be interesting to see if the TCIs have the same isotopic composition as the carbonates.

If the above aims are achieved, determination of the fractionation factors between cronstedtite and water; and tochilinite and water, would aid in geothermometry and a greater understanding of the conditions of aqueous alteration. Growing both cronstedtite and tochilinite in the laboratory under variable temperatures, using similar techniques to Vacher *et al.* (2019b) and a source of labelled water (Morris, 2008), would be a good first step in determining their respective fractionation factors.

Complementary isotope systems

Pairing O-isotope with H-isotope compositions would be a useful avenue to pursue. Arguments persist in the literature as to whether the significant H-isotopic variations between different chondrite groups are caused by parent body processes or molecular cloud inheritance (*e.g.,* Alexander *et al.,* 2013). While the most recent publications argue for the latter (Marrocchi *et al.,* 2023; Piani *et al.,* 2021), it would be useful to see if there are any systematic variations in H-isotopic compositions with petrologic grade and/or O-isotopic composition within the CM group. Some preliminary observations indicate that the most altered CM lithologies, the CM1s, have the most deuterium- poor compositions (Marrocchi *et al.,* 2023). On the other hand, the least altered CM chondrites have the most deuterium-rich compositions. CM2s of moderate petrologic subtypes have compositions lying in between these two endmembers. These observations are not in line with what would be expected given H_2-loss through Rayleigh type isotope fractionation (essentially, removal of the lightest isotope) from the warm core to the cool surface of an asteroid (Piani *et al.,* 2021). It may instead be an indicator of heterogeneous accretion. This is supported by recent H-isotopic measurement of ‘water’ in CM chondrites, which appears to be invariant, clustering

around -324 ± 30 ‰ (δD), with the variations in bulk CM δD instead being controlled not by parent body alteration, but by the ratio of initial water accreted relative to the amount of insoluble organic matter, with the latter being very enriched in deuterium (Marrocchi *et al.*, 2023; Piani *et al.,* 2021).

The novel stable isotope systems of Li and B may offer insight into the nature of alteration. A long-standing argument for closed system models is that the lack of fractionation amongst the most labile elements in chondrites (Bland *et al.,* 2009). However, if fluid percolation was as extensive as suggested in this thesis, *i.e.,* potentially vigorous convection, heterogeneous distribution of the most fluid-mobile elements may not be so apparent due to remobilisation and thorough mixing. Lithium is an isotope system where the heavier isotope, ^{7}Li, is preferentially removed into solution during weathering on Earth (von Strandmann *et al.*, 2020), and would mimic this during the aqueous alteration process on asteroids (Sephton *et al.,* 20013). Whereas isochemical alteration may be the ultimate outcome, Li is more likely to retain heavy δ^{7}Li compositions in areas of high fluid flux as it is preferentially enriched within phyllosilicates, preserving a record of the aqueous alteration history. Boron on the other hand, is a very sensitive tracer of the pH of solution in marine carbonates (Rasbury and Hemming, 2017; Shearer and Simon, 2017). This could be extended to analysis of the different generations of meteoritic carbonate, to decipher if the events that controlled, for example T1 and T2 carbonate precipitation, fundamentally differed by means of their fluid compositions. Furthermore, the novel, heavy stable isotope systems such as Fe and Zn typically fractionate due to changes in oxidation state, recording the effect of complexation by sulphide and carbonate ligands (*e.g.*, Debret *et al.*, 2016). Both could record, and trace, the formation of multivalent minerals such as cronstedtite and tochilinite, and potentially retain the compositions long after the minerals have been redissolved and destroyed through pervasive alteration.

Deciphering the history of TCIs

TCIs are ambiguous structures and require further investigation to understand their accretionary history. Type II TCIs are particularly perplexing because they are radially replaced alteration structures after olivine, pyroxene, and carbonate, but also contain accretionary rims. While TCI-specific accretionary rims have not been investigated, those surrounding chondrules have been, often described as heterogeneously altered structures hosting surviving GEMS particles. If this is the case for TCIs, then this raises very interesting questions because TCIs are also found in association with unaltered grains, mostly forsterite but some Fe-rich fayalite nearby in the matrix, a paradox given their highly altered nature. If TCIs are a purely *in-situ* product, then this demands very heterogeneous alteration conditions on the scale of 10s μm, preferentially altering the TCIs but not the accretionary rims or the equally vulnerable fayalite, and sometimes surviving metal, surrounding them. Alternatively, TCIs may be accretionary products that were partially altered on a separate parent body, or even within the solar nebula itself, which were then sequentially incorporated into a later planetesimal. Investigation of their O-isotopic composition would aid in discerning which of these outcomes is a greater possibility. Isotopic disequilibrium may indicate a coeval formation with the isotopically distinct T1 calcites they are often found in association with, suggesting they were replacing the calcites during an alteration event on another parent body. Alternatively, equilibration of the TCI structures with the pervasive water reservoir that formed the CMF would lean more towards a more definitive *in-situ* origin.

References

Abe, O. 2008. Isotope fractionation of molecular oxygen during adsorption/desorption by molecular sieve zeolite. *Rapid Communications in Mass Spectrometry,*, 22**,** 2510-2514.

Abreu, N. 2018. Primitive Meteorites and Asteroids : Physical, Chemical, and Spectroscopic Observations Paving the Way to Exploration, *Elsevier*.

Abreu, N. M. & Brearley, A. J. 2010. Early solar system processes recorded in the matrices of two highly pristine CR3 carbonaceous chondrites, MET 00426 and QUE 99177. *Geochimica et Cosmochimica Acta,* 74**,** 1146-1171.

Ahn, I., Kusakabe, M. & Lee, J. I. 2014. Oxygen isotopic fractionation of O2 during adsorption and desorption processes using molecular sieve at low temperatures. *Rapid Communications in Mass Spectrometry,* 28**,** 1321-1328.

Alexander, C. M. D., Howard, K. T., Bowden, R. & Fogel, M. L. 2013. The classification of CM and CR chondrites using bulk H, C and N abundances and isotopic compositions. *Geochimica et Cosmochimica Acta,* 123**,** 244-260.

Alexander, C. M. O. D., Greenwood, R. C., Bowden, R., Gibson, J. M., Howard, K. T. & Franchi, I. A. 2018. A mutli-technique search for the most primitive CO chondrites. *Geochimica et Cosmochimica Acta,* 221**,** 406-420.

Arredondo, A., Campins, H., Pinilla-Alonso, N., De León, J., Lorenzi, V. & Morate, D. 2021. Near-infrared spectroscopy of the Sulamitis asteroid family: Surprising similarities in the inner belt primitive asteroid population. *Icarus,* 358**,** 114210.

Bains-Sahota, S. K. & Thiemens, M. H. 1989. A mass-independent sulfur isotope effect in the nonthermal formation of S2F10. *The Journal of Chemical Physics,* 90**,** 6099-6109.

Baker, L., Franchi, I., Wright, I. & Pillinger, C. 2002. The oxygen isotopic composition of water from Tagish Lake: Its relationship to low-temperature phases and to other carbonaceous chondrites. *Meteoritics & Planetary Science,* 37**,** 977-985.

Ballesteros-Paredes, J., André, P., Hennebelle, P., Klessen, R. S., Kruijssen, J. D., Chevance, M., Nakamura, F., Adamo, A. & Vazquez-Semadeni, E. 2020. From diffuse gas to dense molecular cloud cores. *Space Science Reviews,* 216**,** 1-58.

Bao, H. M. Z., Cao, X. B. & Hayles, J. A. 2016. Triple Oxygen Isotopes: Fundamental Relationships and Applications. *Annual Review of Earth and Planetary Sciences, Vol 44,* 44**,** 463-492.

Barber, D. 1981. Matrix phyllosilicates and associated minerals in C2M carbonaceous chondrites. *Geochimica et Cosmochimica Acta,* 45**,** 945-970.

Barkan, E. & Luz, B. 2005. High precision measurements of 17O/16O and 18O/16O ratios in H2O. *Rapid Communications in Mass Spectrometry,* 19**,** 3737-3742.

Bates, H. C., King, A. J., Hanna, K. L. D., Bowles, N. E. & Russell, S. S. 2020. Linking mineralogy and spectroscopy of highly aqueously altered CM and CI carbonaceous chondrites in preparation for primitive asteroid sample return. *Meteoritics & Planetary Science,* 55**,** 77-101.

Bayron, J. 2021. Frozen in Time: A Numerical Modeling Approach to the Study of Ice Bearing Planetesimals through Carbonaceous Chondrites, *PhD Thesis, City University of New York*.

Beaudoin, G. & Therrien, P. 2009. The updated web stable isotope fractionation calculator. *Handbook of stable isotope analytical techniques,* 2**,** 1120-1122.

Benedix, G., Leshin, L., Farquhar, J., Jackson, T. & Thiemens, M. 2003. Carbonates in CM2 chondrites: Constraints on alteration conditions from oxygen isotopic compositions and petrographic observations. *Geochimica et Cosmochimica Acta,* 67**,** 1577-1588.

Bischoff, A. 1998. Aqueous alteration of carbonaceous chondrites: Evidence for preaccretionary alteration—A review. *Meteoritics & Planetary Science,* 33**,** 1113-1122.

Bischoff, A., Alexander, C. M. D., Barrat, J.-A., Burkhardt, C., Busemann, H., Degering, D., Di Rocco, T., Fischer, M., Fockenberg, T. & Foustoukos, D. I. 2021. The old, unique C1 chondrite Flensburg–insight into the first processes of aqueous alteration, brecciation, and the diversity of water-bearing parent bodies and lithologies. *Geochimica et Cosmochimica Acta,* 293**,** 142-186.

Bischoff, A. & Geiger, T. The unique carbonaceous chondrite Acfer 094: The first CM3 chondrite (?). Lunar and Planetary Science Conference, 1994. 115.

Bischoff, A., Scott, E. R., Metzler, K. & Goodrich, C. A. 2006. Nature and origins of meteoritic breccias. *Meteorites and the early solar system II***,** 679-712.

Bland, P., Collins, G., Davison, T., Abreu, N., Ciesla, F., Muxworthy, A. & Moore, J. 2014. Pressure–temperature evolution of primordial solar system solids during impact-induced compaction. *Nature communications,* 5**,** 5451.

Bland, P., Zolensky, M., Benedix, G. & Sephton, M. 2006a. Weathering of chondritic meteorites. *Meteorites and the early solar system II,* 1**,** 853-867.

Bland, P. A. 2006b. Terrestrial weathering rates defined by extraterrestrial materials. *Journal of Geochemical Exploration,* 88**,** 257-261.

Bland, P. A., Cressey, G. & Menzies, O. N. 2004. Modal mineralogy of carbonaceous chondrites by X-ray diffraction and Mossbauer spectroscopy. *Meteoritics & Planetary Science,* 39**,** 3-16.

Bland, P. A., Jackson, M. D., Coker, R. F., Cohen, B. A., Webber, J. B. W., Lee, M. R., Duffy, C. M., Chater, R. J., Ardakani, M. G. & Mcphail, D. S. 2009. Why aqueous alteration in asteroids was isochemical: High porosity≠ high permeability. *Earth and Planetary Science Letters,* 287**,** 559-568.

Bland, P. A. & Travis, B. J. 2017. Giant convecting mud balls of the early solar system. *Science Advances,* 3.

Blum, J. 2018. Dust evolution in protoplanetary discs and the formation of planetesimals: What have we learned from laboratory experiments? *Space Science Reviews,* 214**,** 52.

Bonato, E. 2020. From protoplanetary dust to asteroidal heating: a mineralogical study of the CO3 chondrites, *PhD Thesis, University of Glasgow.*

Borovička, J., Popova, O. & Spurný, P. 2019. The Maribo CM 2 meteorite fall—Survival of weak material at high entry speed. *Meteoritics & Planetary Science,* 54**,** 1024-1041.

Bottke, W. F. & Norman, M. D. 2017. The late heavy bombardment. *Annual Review of Earth and Planetary Sciences,* 45**,** 619-647.

Bouvier, A., Gattacceca, J., Grossman, J. & Metzler, K. 2017. The meteoritical bulletin, No. 105. *Meteoritics & Planetary Science,* 52**,** 2411.

Brasser, R. & Mojzsis, S. 2020. The partitioning of the inner and outer Solar System by a structured protoplanetary disk. *Nature Astronomy,* 4**,** 492-499.

Braukmüller, N., Wombacher, F., Hezel, D. C., Escoube, R. & Münker, C. 2018. The chemical composition of carbonaceous chondrites: Implications for volatile element depletion, complementarity and alteration. *Geochimica et Cosmochimica Acta,* 239**,** 17-48.

Brearley, A. 2003. Nebular versus parent body processing. *Meteorites and Cosmochemical Processes***,** 309-334.

Brearley, A. J. 1995. Aqueous alteration and brecciation in Bells, an unusual, saponite-bearing, CM chondrite. *Geochimica et Cosmochimica Acta,* 59**,** 2291-2317.

Brearley, A. J. 2006. The action of water. *Meteorites and the early solar system II,* 943**,** 587-624.

Brearley, A. J. & Jones, R. H. 1998. Chondritic meteorites. *In:* Papike J. J., *Planetary Materials.*

Briani, G., Gounelle, M., Bourot-Denise, M. & Zolensky, M. E. 2012. Xenoliths and microxenoliths in H chondrites: Sampling the zodiacal cloud in the asteroid Main Belt. *Meteoritics & Planetary Science,* 47**,** 880-902.

Bridges, J. & Hicks, L. 2022. The Redistribution of Sulphur in Secondary Minerals of Winchcombe and other CM Chondrites *BPSC #3*

Brown, P. G., Hildebrand, A. R., Zolensky, M. E., Grady, M., Clayton, R. N., Mayeda, T. K., Tagliaferri, E., Spalding, R., Macrae, N. D. & Hoffman, E. L. 2000. The fall, recovery, orbit, and composition of the Tagish Lake meteorite: A new type of carbonaceous chondrite. *Science,* 290**,** 320-325.

Browning, L., Zolensky, M. & Barrett, R. 1991. Serpentine and modal compositions of CM chondrites. *Lunar and Planetary Science Conference,* 22, 145-146.

Browning, L. B., Mcsween, H. Y. & Zolensky, M. E. 1996. Correlated alteration effects in CM carbonaceous chondrites. *Geochimica et Cosmochimica Acta,* 60**,** 2621-2633.

Bunch, T. & Chang, S. 1980. Carbonaceous chondrites—II. Carbonaceous chondrite phyllosilicates and light element geochemistry as indicators of parent body processes and surface conditions. *Geochimica et Cosmochimica Acta,* 44**,** 1543-1577.

Burbine, T. H. 2016. Advances in determining asteroid chemistries and mineralogies. *Geochemistry,* 76**,** 181-195.

Carmignano, O. R. D., Vieira, S. S., Brandão, P. R. G., Bertoli, A. C. & Lago, R. M. 2020. Serpentinites: Mineral structure, properties and technological applications. *Journal of the Brazilian Chemical Society,* 31**,** 2-14.

Carmona, A. 2010. Observational diagnostics of gas in protoplanetary disks. *Earth, Moon, and Planets,* 106**,** 71-95.
Caselli, P. & Ceccarelli, C. 2012. Our astrochemical heritage. *The Astronomy and Astrophysics Review,* 20**,** 1-68.
Castillo-Rogez, J. & Young, E. D. 2017. Origin and evolution of volatile-rich asteroids. *Planetesimals: Early Differentiation and Consequences for Planets***,** 92-114.
Castillo-Rogez, J. C. & Kalousová, K. 2022. Ocean worlds in our Solar System. *Elements: An International Magazine of Mineralogy, Geochemistry, and Petrology,* 18**,** 161-166.
Ceccarelli, C. & Du, F. 2022. We drink good 4.5-billion-year-old water. *Elements: An International Magazine of Mineralogy, Geochemistry, and Petrology,* 18**,** 155-160.
Chakraborty, S., Yanchulova, P. & Thiemens, M. H. 2013. Mass-independent oxygen isotopic partitioning during gas-phase SiO2 formation. *Science,* 342**,** 463-466.
Chan, Q. H., Nakato, A., Kebukawa, Y., Zolensky, M. E., Nakamura, T., Maisano, J. A., Colbert, M. W., Martinez, J. E., Kilcoyne, A. D. & Suga, H. 2019. Heating experiments of the Tagish Lake meteorite: Investigation of the effects of short-term heating on chondritic organics. *Meteoritics & Planetary Science,* 54**,** 104-125.
Charlier, B. L. A., Ginibre, C., Morgan, D., Nowell, G. M., Pearson, D. G., Davidson, J. P. & Ottley, C. J. 2006. Methods for the microsampling and high-precision analysis of strontium and rubidium isotopes at single crystal scale for petrological and geochronological applications. *Chemical Geology,* 232**,** 114-133.
Chaumard, N., Defouilloy, C., Hertwig, A. T. & Kita, N. T. 2021. Oxygen isotope systematics of chondrules in the Paris CM2 chondrite: Indication for a single large formation region across snow line. *Geochimica et Cosmochimica Acta,* 299**,** 199-218.
Chaumard, N., Defouilloy, C. & Kita, N. T. 2018. Oxygen isotope systematics of chondrules in the Murchison CM2 chondrite and implications for the CO-CM relationship. *Geochimica et Cosmochimica Acta,* 228**,** 220-242.
Chennaoui Aoudjehane, H., Agee, C., Ziegler, K., Garvie, L., Irving, A., Sheikh, D., Carpenter, P., Zolensky, M., Schmitt-Kopplin, P. & Trif, L. 2021. Tarda (C2-Ung): A New and Unusual Carbonaceous Chondrite Meteorite Fall from Morocco. *Lunar and Planetary Science Conference* 52, #1928.
Choe, W. H., Huber, H., Rubin, A. E., Kallemeyn, G. W. & Wasson, J. T. 2010. Compositions and taxonomy of 15 unusual carbonaceous chondrites. *Meteoritics & Planetary Science,* 45**,** 531-554.
Chokai, J., Zolensky, M., Le, L., Nakamura, K., Mikouchi, T., Monkawa, A., Koizumi, E. & Miyamoto, M. 2004. Aqueous alteration mineralogy in CM carbonaceous chondrites. *Lunar and Planetary Science Conference,* 35, #1506.
Ciesla, F. J. & Cuzzi, J. N. 2006. The evolution of the water distribution in a viscous protoplanetary disk. *Icarus,* 181**,** 178-204.
Clark, B. E., Binzel, R. P., Howell, E. S., Cloutis, E. A., Ockert-Bell, M., Christensen, P., Barucci, M. A., Demeo, F., Lauretta, D. S. & Connolly Jr, H. 2011. Asteroid (101955) 1999 RQ36: Spectroscopy from 0.4 to 2.4 μm and meteorite analogs. *Icarus,* 216**,** 462-475.
Clayton, R. 2003. Oxygen isotopes in meteorites. *Treatise on geochemistry,* 1**,** 711.
Clayton, R. & Mayeda, T. 2001. Oxygen isotopic composition of the Tagish Lake carbonaceous chondrite. *Lunar and Planetary Science Conference,* 32, #1885.
Clayton, R. N. 1955. Variations in oxygen isotope abundances in rock minerals. *PhD Thesis, California Institute of Technology.*
Clayton, R. N. 2002. Self-shielding in the solar nebula. *Nature,* 415**,** 860-861.
Clayton, R. N., Grossman, L. & Mayeda, T. K. 1973. A component of primitive nuclear composition in carbonaceous meteorites. *Science,* 182**,** 485-488.
Clayton, R. N. & Mayeda, T. K. 1963. The use of bromine pentafluoride in the extraction of oxygen from oxides and silicates for isotopic analysis. *Geochimica et Cosmochimica Acta,* 27**,** 43-52.
Clayton, R. N. & Mayeda, T. K. 1983. Oxygen isotopes in Eucrites, Shergottites, Nakhlites, and Chassignites. *Earth and Planetary Science Letters,* 62**,** 1-6.
Clayton, R. N. & Mayeda, T. K. 1984. The oxygen isotope record in murchison and other carbonaceous chondrites. *Earth and Planetary Science Letters,* 67**,** 151-161.

Clayton, R. N. & Mayeda, T. K. 1999. Oxygen isotope studies of carbonaceous chondrites. *Geochimica et Cosmochimica Acta,* 63**,** 2089-2104.
Cloutis, E., Hudon, P., Hiroi, T. & Gaffey, M. 2012. Spectral reflectance properties of carbonaceous chondrites 4: Aqueously altered and thermally metamorphosed meteorites. *Icarus,* 220**,** 586-617.
Cohen, B. A. & Coker, R. F. 2000. Modeling of liquid water on CM meteorite parent bodies and implications for amino acid racemization. *Icarus,* 145**,** 369-381.
Cordier, C., Folco, L., Suavet, C., Sonzogni, C. & Rochette, P. 2011. Major, trace element and oxygen isotope study of glass cosmic spherules of chondritic composition: The record of their source material and atmospheric entry heating. *Geochimica et Cosmochimica Acta,* 75**,** 5203-5218.
Corrigan, C. M., Zolensky, M. E., Dahl, J., Long, M., Weir, J., Sapp, C. & Burkett, P. J. 1997. The porosity and permeability of chondritic meteorites and interplanetary dust particles. *Meteoritics & Planetary Science,* 32**,** 509-515.
Criss, R. E. 1999. Principles of stable isotope distribution, *Oxford University Press.*
Criss, R. E. & Farquhar, J. 2008. Abundance, notation, and fractionation of light stable isotopes. *Oxygen in the Solar System,* 68**,** 15-30.
Daly, L., Mcmullan, S., Rowe, J., Collins, G. S., Suttle, M., Chan, Q. H., Young, J. S., Shaw, C., Mardon, A. G. & Alexander, M. 2020. The UK Fireball Alliance (UKFAll); combining and integrating the diversity of UK camera networks to aim to recover the first UK meteorite fall for 30 years. *Copernicus Meetings.*
Daly, L., Suttle, M., Lee, M., Bridges, J., Hicks, L., Martin, P.-E., Floyd, C., Jenkins, L., Salge, T. & King, A. 2022. A Coordinated Approach to Investigate the Heterogeneity of Aqueous Alteration at the Micro-Scale in the Winchcombe Meteorite, a CM Fall. *LPI Contributions,* 2695**,** 6262.
Dawson, R. I. & Johnson, J. A. 2018. Origins of hot Jupiters. *Annual Review of Astronomy and Astrophysics,* 56**,** 175-221.
Deer, W. A., Frs, Howie, R. A. & Zussman, J. 2013. An Introduction to the Rock-Forming Minerals, *Mineralogical Society of Great Britain and Ireland.*
Dellagiustina, D., Emery, J., Golish, D., Rozitis, B., Bennett, C., Burke, K., Ballouz, R.-L., Becker, K., Christensen, P. & Drouet D'aubigny, C. 2019. Properties of rubble-pile asteroid (101955) Bennu from OSIRIS-REx imaging and thermal analysis. *Nature Astronomy,* 3**,** 341-351.
Demeo, F., Alexander, C., Walsh, K., Chapman, C. & Binzel, R. 2015. The compositional structure of the asteroid belt. *Asteroids iv,* 1**,** 13.
Demeo, F. E., Burt, B. J., Marsset, M., Polishook, D., Burbine, T. H., Carry, B., Binzel, R. P., Vernazza, P., Reddy, V. & Tang, M. 2022. Connecting asteroids and meteorites with visible and near-infrared spectroscopy. *Icarus,* 380**,** 114971.
Demeo, F. E. & Carry, B. 2014. Solar System evolution from compositional mapping of the asteroid belt. *Nature,* 505**,** 629-634.
Desch, S. & Connolly Jr, H. 2002. A model of the thermal processing of particles in solar nebula shocks: Application to the cooling rates of chondrules. *Meteoritics & Planetary Science,* 37**,** 183-207.
Dominik, C. & Tielens, A. 1997. The physics of dust coagulation and the structure of dust aggregates in space. *The Astrophysical Journal,* 480**,** 647.
Drake, M. J. 2005. Origin of water in the terrestrial planets. *Meteoritics & Planetary Science,* 40**,** 519-527.
Drake, M. J. & Righter, K. 2002. Determining the composition of the Earth. *Nature,* 416**,** 39-44.
Ehlmann, B., Bish, D., Ruff, S. & Mustard, J. 2012. Mineralogy and chemistry of altered Icelandic basalts: Application to clay mineral detection and understanding aqueous environments on Mars. *Journal of Geophysical Research: Planets,* 117.
Engrand, C., Gounelle, M., Duprat, J. & Zolensky, M. 2001. *In situ* oxygen isotopic composition of individual minerals in Tagish Lake, a unique type 2 carbonaceous meteorite. Lunar and Planetary Science Conference, 32, #1568.
Fan, Y., Li, S., Liu, S., Yin, Q., Song, G., Xu, R., Zhang, J., Zhang, P., Liu, C. & Wang, R. 2022. Shidian meteorite, a new fall analog of near-Earth asteroid (101955) Bennu. *Meteoritics & Planetary Science.*
Farley, K. A., Vokrouhlický, D., Bottke, W. F. & Nesvorný, D. 2006. A late Miocene dust shower from the break-up of an asteroid in the main belt. *Nature,* 439**,** 295-297.

Farsang, S., Franchi, I. A., Zhao, X., Raub, T. D., Redfern, S. A. & Grady, M. M. 2021. Carbonate assemblages in Cold Bokkeveld CM chondrite reveal complex parent body evolution. *Meteoritics & Planetary Science,* 56**,** 723-741.

Farver, J. R. 1994. Oxygen self-diffusion in calcite: Dependence on temperature and water fugacity. *Earth and Planetary Science Letters,* 121**,** 575-587.

Findlay, R., Greenwood, R., Franchi, I., Anand, M., King, A. & Malley, J. 2022. Assessing the Oxygen Isotope Heterogeneity in Aguas Zarcas, Mukundpura and Kolang. *Lunar and Planetary Science Conference,* 53, #2647.

Fitoussi, C., Bourdon, B. & Wang, X. 2016. The building blocks of Earth and Mars: A close genetic link. *Earth and Planetary Science Letters,* 434**,** 151-160.

Floyd, C., Macante, A., Daly, L. & Lee, M. 2023. Unravelling Petrofabrics in the Brecciated CM Chondrite Cold Bokkeveld. *Lunar and Planetary Science Conference,* 53, #

Fogg, M. J. & Nelson, R. P. 2007. On the formation of terrestrial planets in hot-Jupiter systems. *Astronomy & Astrophysics,* 461**,** 1195-1208.

Forbes, J. C., Alves, J. & Lin, D. N. 2021. A solar system formation analogue in the Ophiuchus star-forming complex. *Nature Astronomy,* 5**,** 1009-1016.

Franchi, I., Akagi, T. & Pillinger, C. 1992. Laser Fluorination of Meteorites--Small Sample Analysis of delta17O and delta18O. *Meteoritics,* 27.

Franchi, I., Baker, L., Bridges, J., Wright, I. & Pillinger, C. 2001. Oxygen isotopes and the early Solar System. *Philosophical Transactions of the Royal Society of London. Series A: Mathematical, Physical and Engineering Sciences,* 359**,** 2019-2035.

Franchi, I. A. 2008. Oxygen isotopes in asteroidal materials. *Reviews in Mineralogy and Geochemistry,* 68**,** 345-397.

Friedrich, J. M., Weisberg, M. K., Ebel, D. S., Biltz, A. E., Corbett, B. M., Iotzov, I. V., Khan, W. S. & Wolman, M. D. 2015. Chondrule size and related physical properties: A compilation and evaluation of current data across all meteorite groups. *Geochemistry,* 75**,** 419-443.

Früh-Green, G. L., Plas, A. & Lécuyer, C. 1996. Petrologic and stable isotope constraints on hydrothermal alteration and serpentinization of the EPR shallow mantle at Hess Deep (site 895). *Proceedings of the ocean drilling program, scientific results,* 255-291.

Fu, R. R. & Elkins-Tanton, L. T. 2014. The fate of magmas in planetesimals and the retention of primitive chondritic crusts. *Earth and Planetary Science Letters,* 390**,** 128-137.

Fu, R. R., Young, E. D., Greenwood, R. C. & Elkins-Tanton, L. 2017. Silicate melting and volatile loss during differentiation in planetesimals. In: Planetesimals: Early differentiation and consequences for planets. *Cambridge University Press.*

Fuchs, L. H., Olsen, E. & Jensen, K. J. 1973. Mineralogy, mineral-chemistry, and composition of the Murchison (C2) meteorite. *Smithsonian contributions to the earth sciences*.

Fujiya, W. 2018. Oxygen isotopic ratios of primordial water in carbonaceous chondrites. *Earth and Planetary Science Letters,* 481**,** 264-272.

Fujiya, W., Sugiura, N., Hotta, H., Ichimura, K. & Sano, Y. 2012. Evidence for the late formation of hydrous asteroids from young meteoritic carbonates. *Nature Communications,* 3**,** 627.

Fujiya, W., Sugiura, N., Marrocchi, Y., Takahata, N., Hoppe, P., Shirai, K., Sano, Y. & Hiyagon, H. 2015. Comprehensive study of carbon and oxygen isotopic compositions, trace element abundances, and cathodoluminescence intensities of calcite in the Murchison CM chondrite. *Geochimica et Cosmochimica Acta,* 161**,** 101-117.

Fujiya, W., Sugiura, N., Sano, Y. & Hiyagon, H. 2013. Mn–Cr ages of dolomites in CI chondrites and the Tagish Lake ungrouped carbonaceous chondrite. *Earth and Planetary Science Letters,* 362**,** 130-142.

Gaches, B. A., Walch, S., Offner, S. S. & Münker, C. 2020. Aluminum-26 enrichment in the surface of protostellar disks due to protostellar cosmic rays. *The Astrophysical Journal,* 898**,** 79.

Gattacceca, J., Mccubbin, F. M., Bouvier, A. & Grossman, J. N. 2020. The Meteoritical Bulletin, no. 108. *Meteoritics & Planetary Science,* 55**,** 1146-1150.

Gattacceca, J., Mccubbin, F. M., Grossman, J., Bouvier, A., Bullock, E., Chennaoui Aoudjehane, H., Debaille, V., D'orazio, M., Komatsu, M. & Miao, B. 2021. The meteoritical bulletin, no. 109. *Meteoritics & Planetary Science,* 56**,** 1626-1630.

Gattacceca, J., Mccubbin, F. M., Grossman, J., Bouvier, A., Chabot, N. L., D'orazio, M., Goodrich, C., Greshake, A., Gross, J. & Komatsu, M. 2022. The Meteoritical Bulletin, No. 110. *Meteoritics & Planetary Science,* 57**,** 2102-2105.

Goderis, S., Soens, B., Huber, M. S., Mckibbin, S., Van Ginneken, M., Van Maldeghem, F., Debaille, V., Greenwood, R. C., Franchi, I. A. & Cnudde, V. 2020. Cosmic spherules from Widerøefjellet, Sør Rondane Mountains (East Antarctica). *Geochimica et Cosmochimica Acta,* 270**,** 112-143.

Gounelle, M. 2015. The abundance of 26Al-rich planetary systems in the Galaxy. *Astronomy & Astrophysics,* 582**,** A26.

Grady, M. M., Graham, A., Barber, D., Aylmer, D., Kurat, G., Ntaflos, T., Ott, U., Palme, H. & Spettel, B. 1987. Yamato-82042: An unusual carbonaceous chondrite with CM affinities.

Greenwood, R., Findlay, R., Martins, R., Steele, R., Shaw, K., Morton, E., Savage, P., Murphy, M., Rehkämper, M. & Franchi, I. 2023. The formation and aqueous alteration of CM2 chondrites and their relationship to CO3 chondrites: A fresh isotopic (O, Cd, Cr, Si, Te, Ti, and Zn) perspective from the Winchcombe CM2 fall. *Meteoritics & Planetary Science*. 13968, 1-26.

Greenwood, R., Howard, K., King, A., Lee, M., Burbine, T., Franchi, I., Anand, M., Findlay, R. & Gibson, M. 2019. Oxygen Isotope Evidence for Multiple CM Parent Bodies: What Will We Learn from the Hayabusa2 and OSIRIS-REx Sample Return Missions? *Lunar and Planetary Science Conference,* 50, #3191.

Greenwood, R., Howard, K., Franchi, I., Zolensky, M., Buchanan, P. & Gibson, J. Oxygen isotope evidence for the relationship between CM and CO chondrites: Could they both coexist on a single asteroid. 2014. *Lunar and Planetary Science Conference,* 45, #2610.

Greenwood, R., Schmitz, B., Bridges, J., Hutchison, R. & Franchi, I. 2007. Disruption of the L chondrite parent body: New oxygen isotope evidence from Ordovician relict chromite grains. *Earth and Planetary Science Letters,* 262**,** 204-213.

Greenwood, R. C., Barrat, J.-A., Miller, M. F., Anand, M., Dauphas, N., Franchi, I. A., Sillard, P. & Starkey, N. A. 2018. Oxygen isotopic evidence for accretion of Earth's water before a high-energy Moon-forming giant impact. *Science advances,* 4, 3.

Greenwood, R. C., Burbine, T. H. & Franchi, I. A. 2020. Linking asteroids and meteorites to the primordial planetesimal population. *Geochimica et Cosmochimica Acta*. 277, 377-406.

Greenwood, R. C., Burbine, T. H., Miller, M. F. & Franchi, I. A. 2017. Melting and differentiation of early-formed asteroids: The perspective from high precision oxygen isotope studies. *Chemie Der Erde-Geochemistry,* 77**,** 1-43.

Greenwood, R. C., Franchi, I. A., Findlay, R., Malley, J. A., Ito, M., Yamaguchi, A., Kimura, M., Tomioka, N., Uesugi, M., Imae, N., Shirai, N., Ohigashi, T., Liu, M.-C., Mccain, K. A., Matsuda, N., Mckeegan, K. D., Uesugi, K., Nakato, A., Yogata, K., Yuzawa, H., Kodama, Y., Tsuchiyama, A., Yasutake, M., Hirahara, K., Tekeuchi, A., Sekimoto, S., Sakurai, I., Okada, I., Karouji, Y., Nakazawa, S., Okada, T., Saiki, T., Tanaka, S., Terui, F., Yoshikawa, M., Miyazaki, A., Nishimura, M., Yada, T., Abe, M., Usui, T., Watanabe, S.-I. & Tsuda, Y. 2022b. Oxygen isotope evidence from Ryugu samples for early water delivery to Earth by CI chondrites. *Nature Astronomy*. 7, 29-38.

Greenwood, R. C., Lee, M. R., Hutchison, R. & Barber, D. J. 1994. Formation and alteration of CAIs in Cold Bokkeveld (CM2). *Geochimica et Cosmochimica Acta,* 58**,** 1913-1935.

Gregory, T., Luu, T.-H., Coath, C. D., Russell, S. S. & Elliott, T. 2020. Primordial formation of major silicates in a protoplanetary disc with homogeneous ^{26}Al. *Science Advances,* 6**.**

Gregory, T., Zolensky, M. E., Trieman, A., Berger, E. L., L., Fagan, A., Takenouchi, A. & Velbel, M. a. N., K. 2015. Lithologies making up CM Carbonaceous Chondrites and their link to space exposure ages. *Lunar and Planetary Science Conference*. 46, #1227.

Greshake, A. 1997. The primitive matrix components of the unique carbonaceous chondrite Acfer 094: A TEM study. *Geochimica et Cosmochimica Acta,* 61**,** 437-452.

Grimm, R. E. & Mcsween Jr, H. Y. 1989. Water and the thermal evolution of carbonaceous chondrite parent bodies. *Icarus,* 82**,** 244-280.

Gritschneder, M., Lin, D., Murray, S., Yin, Q.-Z. & Gong, M.-N. 2011. The supernova triggered formation and enrichment of our solar system. *The Astrophysical Journal,* 745**,** 22.

Guo, W. & Eiler, J. M. 2007. Temperatures of aqueous alteration and evidence for methane generation on the parent bodies of the CM chondrites. *Geochimica et Cosmochimica Acta,* 71**,** 5565-5575.

Haack, H., Grau, T., Bischoff, A., Horstmann, M., Wasson, J., Sørensen, A., Laubenstein, M., Ott, U., Palme, H. & Gellissen, M. 2012. Maribo—A new CM fall from Denmark. *Meteoritics & Planetary Science,* 47**,** 30-50.

Hanna, R. D., Ketcham, R. A., Zolensky, M. & Behr, W. M. 2015. Impact-induced brittle deformation, porosity loss, and aqueous alteration in the Murchison CM chondrite. *Geochimica et Cosmochimica Acta,* 171**,** 256-282.

Hanowski, N. P. & Brearley, A. J. 2001. Aqueous alteration of chondrules in the CM carbonaceous chondrite, Allan Hills 81002: Implications for parent body alteration. *Geochimica et Cosmochimica Acta,* 65**,** 495-518.

Harju, E. R., Rubin, A. E., Ahn, I., Choi, B.-G., Ziegler, K. & Wasson, J. T. 2014. Progressive aqueous alteration of CR carbonaceous chondrites. *Geochimica et Cosmochimica Acta,* 139**,** 267-292.

Harrington, R. & Righter, K. 2017. Carbonaceous Chondrite Thin Section Preparation.

Hatch, C. D., Wiese, J. S., Crane, C. C., Harris, K. J., Kloss, H. G. & Baltrusaitis, J. 2012. Water adsorption on clay minerals as a function of relative humidity: application of BET and Freundlich adsorption models. *Langmuir,* 28**,** 1790-1803.

Hatzes, A. P. 2016. The architecture of exoplanets. *Space Science Reviews,* 205**,** 267-283.

Hayes, J. M. 2004. An introduction to isotopic calculations. *Woods Hole Oceanographic Institution, Woods Hole, MA,* 2543.

Hellmann, J. L., Schneider, J. M., Wölfer, E., Drążkowska, J., Jansen, C. A., Hopp, T., Burkhardt, C. & Kleine, T. 2023. Origin of isotopic diversity among carbonaceous chondrites. *The Astrophysical Journal Letters,* 946**,** L34.

Herbst, W., Greenwood, J. P. & Yap, T. E. 2021. The macroporosity of rubble pile asteroid Ryugu and implications for the origin of chondrules. *The Planetary Science Journal,* 2**,** 110.

Herrin, J., Zolensky, M., Cartwright, J., Mittlefehldt, D. & Ross, D. 2011. Carbonaceous chondrite-rich howardites; the potential for hydrous lithologies on the HED parent. *Lunar and Planetary Science Conference,* 42, #2806.

Hewins, R. H., Bourot-Denise, M., Zanda, B., Leroux, H., Barrat, J. A., Humayun, M., Gopel, C., Greenwood, R. C., Franchi, I. A., Pont, S., Lorand, J. P., Cournede, C., Gattacceca, J., Rochette, P., Kuga, M., Marrocchi, Y. & Marty, B. 2014. The Paris meteorite, the least altered CM chondrite so far. *Geochimica et Cosmochimica Acta,* 124**,** 190-222.

Hiroi, T., Zolensky, M. E., Pieters, C. M. & Lipschutz, M. E. 1996. Thermal metamorphism of the C, G, B, and F asteroids seen from the 0.7 μm, 3 μm, and UV absorption strengths in comparison with carbonaceous chondrites. *Meteoritics & Planetary Science,* 31**,** 321-327.

Howard, K., Benedix, G., Bland, P., Gibson, J., Greenwood, R., Franchi, I. & Cressy, G. 2011a. Mineralogic and O-isotope evolution in CM chondrites: on the non-relationship between bulk O-isotopes and degree of aqueous alteration. *Lunar and Planetary Science Conference*. 42, #2429

Howard, K., Benedix, G., Bland, P., Greenwood, R., Franchi, I. & Cressy, G. 2010. Correlated modal mineralogy, aqueous alteration and oxygen isotope composition of CM Chondrites. *Lunar and Planetary Science Conference,* 41, #1595.

Howard, K. T., Alexander, C. M. O., Schrader, D. L. & Dyl, K. A. 2015. Classification of hydrous meteorites (CR, CM and C2 ungrouped) by phyllosilicate fraction: PSD-XRD modal mineralogy and planetesimal environments. *Geochimica et Cosmochimica Acta,* 149**,** 206-222.

Howard, K. T., Benedix, G. K., Bland, P. A. & Cressey, G. 2009. Modal mineralogy of CM2 chondrites by X-ray diffraction (PSD-XRD). Part 1: Total phyllosilicate abundance and the degree of aqueous alteration. *Geochimica et Cosmochimica Acta,* 73**,** 4576-4589.

Howard, K. T., Benedix, G. K., Bland, P. A. & Cressey, G. 2011b. Modal mineralogy of CM chondrites by X-ray diffraction (PSD-XRD): Part 2. Degree, nature and settings of aqueous alteration. *Geochimica et Cosmochimica Acta,* 75**,** 2735-2751.

Ida, S., Guillot, T. & Morbidelli, A. 2016. The radial dependence of pebble accretion rates: A source of diversity in planetary systems-I. Analytical formulation. *Astronomy & Astrophysics,* 591**,** A72.

Ikeda, Y. 1992. An overview of the research consortium," Antarctic carbonaceous chondrites with CI affinities, Yamato-86720, Yamato-82162, and Belgica-7904". *Antarctic Meteorite Research,* 5**,** 49.

Inoue, T. & Fukui, Y. 2013. Formation of massive molecular cloud cores by cloud–cloud collision. *The Astrophysical Journal Letters,* 774**,** L31.

Irving, A. J., Kuehner, S. M., Rumble, D. I., Korotev, R. L. & Clary, S. 2009. Moapa Valley: A second non-Antarctic CM1 chondrite from Nevada, USA (abstract #5372). *Annual meeting of the Meteoritical Society*.

Ishimaru, K., Lauretta, D., Porter, N., Golish, D., Al Asad, M., Ballouz, R., Barnouin, O., Burke, K., Daly, M. & Dellagiustina, D. 2021. Apparently Layered Boulders with Multiple Textures on Bennu's Surface. *Lunar and Planetary Science Conference*, 52, #1154.

Ito, M., Tomioka, N., Uesugi, M., Yamaguchi, A., Shirai, N., Ohigashi, T., Liu, M.-C., Greenwood, R. C., Kimura, M. & Imae, N. 2022. A pristine record of outer Solar System materials from asteroid Ryugu's returned sample. *Nature Astronomy***,** 1-9.

Izidoro, A., Ogihara, M., Raymond, S. N., Morbidelli, A., Pierens, A., Bitsch, B., Cossou, C. & Hersant, F. 2017. Breaking the chains: hot super-Earth systems from migration and disruption of compact resonant chains. *Monthly Notices of the Royal Astronomical Society,* 470**,** 1750-1770.

Izidoro, A., Raymond, S. N., Morbidelli, A. & Winter, O. C. 2015. Terrestrial planet formation constrained by Mars and the structure of the asteroid belt. *Monthly Notices of the Royal Astronomical Society,* 453**,** 3619-3634.

Jacobsen, S., Yin, Q. & Petaev, M. The oxygen isotope evolution of our Galaxy: implications for the interpretation of early solar system heterogeneities. 2007. *Lunar and Planetary Science Conference,* 38, #1804.

Jenkins, L. E., Lee, M. R., Daly, L., King, A. J., Floyd, C. J., Martin, P. E., Almeida, N. V. & Genge, M. J. 2023. Winchcombe: An example of rapid terrestrial alteration of a CM chondrite. *Meteoritics & Planetary Science*.

Jenniskens, P. Recent documented meteorite falls, a review of meteorite–asteroid links. *Meteoroids 2013: proceedings of the astronomical conference held at AM University*, Poznan, 2013. 57-68.

Jenniskens, P. 2018. Review of asteroid-family and meteorite-type links. *Proceedings of the International Astronomical Union,* 14**,** 9-12.

Jenniskens, P., Fries, M. D., Yin, Q.-Z., Zolensky, M., Krot, A. N., Sandford, S. A., Sears, D., Beauford, R., Ebel, D. S. & Friedrich, J. M. 2012. Radar-enabled recovery of the Sutter's Mill meteorite, a carbonaceous chondrite regolith breccia. *Science,* 338**,** 1583-1587.

Jilly, C. E., Huss, G. R., Krot, A. N., Nagashima, K., Yin, Q.-Z. & Sugiura, N. 2014. 53Mn-53Cr dating of aqueously formed carbonates in the CM2 lithology of the Sutter's Mill carbonaceous chondrite. *Meteoritics & Planetary Science,* 49**,** 2104-2117.

Johansen, A., Henning, T. & Klahr, H. 2006. Dust sedimentation and self-sustained Kelvin-Helmholtz turbulence in protoplanetary disk midplanes. *The Astrophysical Journal,* 643**,** 1219.

Johansen, A. & Lacerda, P. 2010. Prograde rotation of protoplanets by accretion of pebbles in a gaseous environment. *Monthly Notices of the Royal Astronomical Society,* 404**,** 475-485.

Johansen, A. & Lambrechts, M. 2017. Forming planets via pebble accretion. *Annual Review of Earth and Planetary Sciences,* 45**,** 359-387.

Johansen, A. & Youdin, A. 2007. Protoplanetary disk turbulence driven by the streaming instability: nonlinear saturation and particle concentration. *The Astrophysical Journal,* 662**,** 627.

Jones, B., Renaut, R. W., Bernhart Owen, R. & Torfason, H. 2005. Growth patterns and implications of complex dendrites in calcite travertines from Lýsuhóll, Snæfellsnes, Iceland. *Sedimentology,* 52**,** 1277-1301.

Kallemeyn, G. 1995. Bells and Essebi: to be or not to be (CM). *Meteoritics,* 30.

Kaplan, H. H., Lauretta, D. S., Simon, A. A., Hamilton, V. E., Dellagiustina, D. N., Golish, D. R., Reuter, D. C., Bennett, C. A., Burke, K. N., Campins, H., Connolly, H. C., Dworkin, J. P., Emery, J. P., Glavin, D. P., Glotch, T. D., Hanna, R., Ishimaru, K., Jawin, E. R., Mccoy, T. J., Porter, N., Sandford, S. A., Ferrone, S., Clark, B. E., Li, J.-Y., Zou, X.-D., Daly, M. G., Barnouin, O. S., Seabrook, J. A. & Enos, H. L. 2020. Bright carbonate veins on asteroid (101955) Bennu: Implications for aqueous alteration history. *Science,* 370**,** eabc3557.

Keller, L. P. & Messenger, S. 2011. On the origins of GEMS grains. *Geochimica et Cosmochimica Acta,* 75**,** 5336-5365.

Kerraouch, I., Bischoff, A., Zolensky, M. E., Pack, A., Patzek, M., Hanna, R. D., Fries, M. D., Harries, D., Kebukawa, Y. & Le, L. 2021. The polymict carbonaceous breccia Aguas Zarcas: A potential analog to samples being returned by the OSIRIS-REx and Hayabusa2 missions. *Meteoritics & Planetary Science*.

Kerraouch, I., Ebert, S., Patzek, M., Bischoff, A., Zolensky, M. E., Pack, A., Schmitt-Kopplin, P., Belhai, D., Bendaoud, A. & Le, L. 2019. A light, chondritic xenolith in the Murchison (CM) chondrite - Formation by fluid-assisted percolation during metasomatism? *Geochemistry*, 79.

Kerraouch, I., Kebukawa, Y., Bischoff, A., Zolensky, M. E., Wolfer, E., Hellmann, J. L., Ito, M., King, A., Trieloff, M., Barrat, J. A., Schmitt-Kopplin, P., Pack, A., Patzek, M., Hanna, R. D., Fockenberg, T., Marrocchi, Y., Fries, M., Mathurin, J., Dartois, E., Duprat, J., Engrand, C., Deniset, A., Dazzi, A., Kiryu, K., Igisu, M., Shibuya, T., Wakabayashi, D., Yamashita, S., Takeichi, Y., Takahashi, Y., Ohigashi, T., Kodama, Y. & Kondo, M. 2022. Heterogeneous nature of the carbonaceous chondrite breccia Aguas Zarcas - Cosmochemical characterization and origin of new carbonaceous chondrite lithologies. *Geochimica et Cosmochimica Acta*, 334**,** 155-186.

Kimura, M., Imae, N., Komatsu, M., Barrat, J., Greenwood, R., Yamaguchi, A. & Noguchi, T. 2020. The most primitive CM chondrites, Asuka 12085, 12169, and 12236, of subtypes 3.0–2.8: Their characteristic features and classification. *Polar Science***,** 100565.

King, A., Greenwood, R., Gibson, J., Schofield, P. & Franchi, I. 2018. The Oxygen Isotopic Composition of the most Aqueously Altered CM Carbonaceous Chondrites. *Lunar and Planetary Science Conference*, 49, #2201.

King, A., Schofield, P. & Russell, S. 2021a. The Bulk Mineralogy and Water Contents of the Carbonaceous Chondrite Falls Kolang and Tarda (abstract# 1909). *Lunar and Planetary Science Conference* 52, #1909.

King, A., Zulmahilan, N., Schofield, P. & Russell, S. 2020a. CM chondrites from multiple parent bodies: Evidence from correlated mineralogy and cosmic-ray exposure ages. *Lunar and Planetary Science Conference*. 51, #1883.

King, A. J., Bates, H. C., Krietsch, D., Busemann, H., Clay, P. L., Schofield, P. F. & Russell, S. S. 2019. The Yamato-type (CY) carbonaceous chondrite group: Analogues for the surface of asteroid Ryugu? *Geochemistry*, 79.

King, A. J., Daly, L., Rowe, J., Joy, K. H., Greenwood, R. C., Devillepoix, H. a. R., Suttle, M. D., Chan, Q. H. S., Russell, S. S., Bates, H. C., Bryson, J. F. J., Clay, P. L., Vida, D., Lee, M. R., O'brien, Á., Hallis, L. J., Stephen, N. R., Tartèse, R., Sansom, E. K., Towner, M. C., Cupak, M., Shober, P. M., Bland, P. A., Findlay, R., Franchi, I. A., Verchovsky, A. B., Abernethy, F. a. J., Grady, M. M., Floyd, C. J., Van Ginneken, M., Bridges, J., Hicks, L. J., Jones, R. H., Mitchell, J. T., Genge, M. J., Jenkins, L., Martin, P.-E., Sephton, M. A., Watson, J. S., Salge, T., Shirley, K. A., Curtis, R. J., Warren, T. J., Bowles, N. E., Stuart, F. M., Di Nicola, L., Györe, D., Boyce, A. J., Shaw, K. M. M., Elliott, T., Steele, R. C. J., Povinec, P., Laubenstein, M., Sanderson, D., Cresswell, A., Jull, A. J. T., Sýkora, I., Sridhar, S., Harrison, R. J., Willcocks, F. M., Harrison, C. S., Hallatt, D., Wozniakiewicz, P. J., Burchell, M. J., Alesbrook, L. S., Dignam, A., Almeida, N. V., Smith, C. L., Clark, B., Humphreys-Williams, E. R., Schofield, P. F., Cornwell, L. T., Spathis, V., Morgan, G. H., Perkins, M. J., Kacerek, R., Campbell-Burns, P., Colas, F., Zanda, B., Vernazza, P., Bouley, S., Jeanne, S., Hankey, M., Collins, G. S., Young, J. S., Shaw, C., Horak, J., Jones, D., James, N., Bosley, S., Shuttleworth, A., Dickinson, P., Mcmullan, I., Robson, D., Smedley, A. R. D., Stanley, B., Bassom, R., Mcintyre, M., Suttle, A. A., Fleet, R., et al. 2022. The Winchcombe meteorite, a unique and pristine witness from the outer solar system. *Science Advances*, 8**.**

King, A. J., Phillips, K. J. H., Strekopytov, S., Vita-Finzi, C. & Russell, S. S. 2020b. Terrestrial modification of the Ivuna meteorite and a reassessment of the chemical composition of the CI type specimen. *Geochimica et Cosmochimica Acta*, 268**,** 73-89.

King, A. J., Schofield, P. F. & Russell, S. S. 2017. Type 1 aqueous alteration in CM carbonaceous chondrites: Implications for the evolution of water-rich asteroids. *Meteoritics & Planetary Science*, 52**,** 1197-1215.

King, A. J., Schofield, P. F. & Russell, S. S. 2021b. Thermal alteration of CM carbonaceous chondrites: Mineralogical changes and metamorphic temperatures. *Geochimica et Cosmochimica Acta*, 298**,** 167-190.

Kleine, T., Budde, G., Burkhardt, C., Kruijer, T., Worsham, E., Morbidelli, A. & Nimmo, F. 2020. The non-carbonaceous–carbonaceous meteorite dichotomy. *Space Science Reviews*, 216**,** 1-27.

Kohl, I., Warren, P. & Young, E. 2016. State-of-the-Art Laser Fluorination for Oxygen Isotope Ratio Analysis of Extraterrestrial Materials. *Lunar and Planetary Science Conference* ,47, #2775.

Kokubo, E. & Ida, S. 1996. On runaway growth of planetesimals. *Icarus,* 123**,** 180-191.
Kokubo, E. & Ida, S. 1998. Oligarchic growth of protoplanets. *Icarus,* 131**,** 171-178.
Koll, D., Korschinek, G., Faestermann, T., Gómez-Guzmán, J., Kipfstuhl, S., Merchel, S. & Welch, J. M. 2019. Interstellar Fe 60 in Antarctica. *Physical Review Letters,* 123**,** 072701.
Krot, A., Amelin, Y., Bland, P., Ciesla, F., Connelly, J., Davis, A. M., Huss, G., Hutcheon, I. D., Makide, K. & Nagashima, K. 2009. Origin and chronology of chondritic components: A review. *Geochimica et Cosmochimica Acta,* 73**,** 4963-4997.
Krot, A., Keil, K., Scott, E., Goodrich, C. & Weisberg, M. 2014. Classification of meteorites and their genetic relationships. *Meteorites and cosmochemical processes***,** 1-63.
Krot, A. N. & Nagashima, K. 2017. Constraints on mechanisms of chondrule formation from chondrule precursors and chronology of transient heating events in the protoplanetary disk. *Geochemical Journal,* 51**,** 45-68.
Krot, A. N., Yurimoto, H., Mckeegan, K. D., Leshin, L., Chaussidon, M., Libourel, G., Yoshitake, M., Huss, G. R., Guan, Y. & Zanda, B. 2006. Oxygen isotopic compositions of chondrules: Implications for evolution of oxygen isotopic reservoirs in the inner solar nebula. *Geochemistry,* 66**,** 249-276.
Kruijer, T. S., Kleine, T. & Borg, L. E. 2020. The great isotopic dichotomy of the early Solar System. *Nature Astronomy,* 4**,** 32-40.
Kusakabe, M., Maruyama, S., Nakamura, T. & Yada, T. 2004. CO2 laser-BrF5 fluorination technique for analysis of oxygen three isotopes of rocks and minerals. *Journal of the Mass Spectrometry Society of Japan,* 52**,** 205-212.
Lambrechts, M. & Johansen, A. 2012. Rapid growth of gas-giant cores by pebble accretion. *Astronomy & Astrophysics,* 544**,** A32.
Lambrechts, M., Johansen, A. & Morbidelli, A. 2014. Separating gas-giant and ice-giant planets by halting pebble accretion. *Astronomy & Astrophysics,* 572**,** A35.
Lauretta, D., Hergenrother, C., Chesley, S., Leonard, J., Pelgrift, J., Adam, C., Al Asad, M., Antreasian, P., Ballouz, R.-L. & Becker, K. 2019. Episodes of particle ejection from the surface of the active asteroid (101955) Bennu. *Science,* 366**,** eaay3544.
Lauretta, D. S., Kremser, D. T. & Fegley Jr, B. 1996. The rate of iron sulfide formation in the solar nebula. *Icarus,* 122**,** 288-315.
Lecar, M., Podolak, M., Sasselov, D. & Chiang, E. 2006. On the location of the snow line in a protoplanetary disk. *The Astrophysical Journal,* 640**,** 1115.
Lécuyer, C., Royer, A., Fourel, F., Seris, M., Simon, L. & Robert, F. 2017. D/H fractionation during the sublimation of water ice. *Icarus,* 285**,** 1-7.
Lee, M., Daly, L., Floyd, C. & Martin, P.-E. 2020. CM carbonaceous chondrite falls and their terrestrial alteration. *Meteoritics & Planetary Science*.
Lee, M. R. & Bland, P. A. 2004. Mechanisms of weathering of meteorites recovered from hot and cold deserts and the formation of phyllosilicates. *Geochimica et Cosmochimica Acta,* 68**,** 893-916.
Lee, M. R., Cohen, B. E., King, A. J. & Greenwood, R. C. 2019. The diversity of CM carbonaceous chondrite parent bodies explored using Lewis Cliff 85311. *Geochimica et Cosmochimica Acta,* 264**,** 224-244.
Lee, M. R., Floyd, C., Martin, P. E., Zhao, X., Franchi, I. A., Jenkins, L. & Griffin, S. 2023. Extended time scales of carbonaceous chondrite aqueous alteration evidenced by a xenolith in L a P az Icefield 02239 (CM2). *Meteoritics & Planetary Science*.
Lee, M. R. & Lindgren, P. 2016. Aqueous alteration of chondrules from the Murchison CM carbonaceous chondrite: Replacement, pore filling, and the genesis of polyhedral serpentine. *Meteoritics & Planetary Science,* 51**,** 1003-1021.
Lee, M. R., Lindgren, P. & Sofe, M. R. 2014. Aragonite, breunnerite, calcite and dolomite in the CM carbonaceous chondrites: High fidelity recorders of progressive parent body aqueous alteration. *Geochimica et Cosmochimica Acta,* 144**,** 126-156.
Lee, M. R., Sofe, M. R., Lindgren, P., Starkey, N. A. & Franchi, I. A. 2013. The oxygen isotope evolution of parent body aqueous solutions as recorded by multiple carbonate generations in the Lonewolf Nunataks 94101 CM2 carbonaceous chondrite. *Geochimica et Cosmochimica Acta,* 121**,** 452-466.
Lentfort, S., Bischoff, A., Ebert, S. & Patzek, M. 2021. Classification of CM chondrite breccias-Implications for the evaluation of samples from the OSIRIS-REx and Hayabusa 2 missions. *Meteoritics & Planetary Science*.

Leroux, H., Cuvillier, P., Zanda, B. & Hewins, R. H. 2015. GEMS-like material in the matrix of the Paris meteorite and the early stages of alteration of CM chondrites. *Geochimica et Cosmochimica Acta,* 170**,** 247-265.

Levison, H. F., Morbidelli, A., Tsiganis, K., Nesvorný, D. & Gomes, R. 2011. Late orbital instabilities in the outer planets induced by interaction with a self-gravitating planetesimal disk. *The Astronomical Journal,* 142**,** 152.

Levison, H. F., Thommes, E. & Duncan, M. J. 2010. Modeling the formation of giant planet cores. I. Evaluating key processes. *The Astronomical Journal,* 139**,** 1297.

Li, Y.-P., Li, H., Li, S., Birnstiel, T., DrążKowska, J. & Stammler, S. 2020. Planet-induced Vortices with Dust Coagulation in Protoplanetary Disks. *The Astrophysical Journal Letters,* 892**,** L19.

Li, Z.-X. A. & Lee, C.-T. A. 2006. Geochemical investigation of serpentinized oceanic lithospheric mantle in the Feather River Ophiolite, California: implications for the recycling rate of water by subduction. *Chemical Geology,* 235**,** 161-185.

Lindgren, P., Hanna, R. D., Dobson, K. J., Tomkinson, T. & Lee, M. R. 2015. The paradox between low shock-stage and evidence for compaction in CM carbonaceous chondrites explained by multiple low-intensity impacts. *Geochimica et Cosmochimica Acta,* 148**,** 159-178.

Lindgren, P., Lee, M. R., Sofe, M. R. & Zolensky, M. E. 2013. Clasts in the CM2 carbonaceous chondrite Lonewolf Nunataks 94101: Evidence for aqueous alteration prior to complex mixing. *Meteoritics & Planetary Science,* 48**,** 1074-1090.

Lindgren, P., Lee, M. R., Starkey, N. A. & Franchi, I. A. 2017. Fluid evolution in CM carbonaceous chondrites tracked through the oxygen isotopic compositions of carbonates. *Geochimica et Cosmochimica Acta,* 204**,** 240-251.

Liu, M.-C., Mckeegan, K. D., Goswami, J. N., Marhas, K. K., Sahijpal, S., Ireland, T. R. & Davis, A. M. 2009. Isotopic records in CM hibonites: Implications for timescales of mixing of isotope reservoirs in the solar nebula. *Geochimica et Cosmochimica Acta,* 73**,** 5051-5079.

Lodders, K. 2003. Solar system abundances and condensation temperatures of the elements. *The Astrophysical Journal,* 591**,** 1220.

Luz, B. & Barkan, E. 2010. Variations of 17O/16O and 18O/16O in meteoric waters. *Geochimica et Cosmochimica Acta,* 74**,** 6276-6286.

Lyons, J. & Young, E. 2005. CO self-shielding as the origin of oxygen isotope anomalies in the early solar nebula. *Nature,* 435**,** 317-320.

Lyons, J. R., Gharib-Nezhad, E. & Ayres, T. R. 2018. A light carbon isotope composition for the Sun. *Nature Communications,* 9**,** 908.

Macke, R. J., Consolmagno, G. J. & Britt, D. T. 2011. Density, porosity, and magnetic susceptibility of carbonaceous chondrites. *Meteoritics & Planetary Science,* 46**,** 1842-1862.

Mackinnon, I. D. & Zolensky, M. E. 1984. Proposed structures for poorly characterized phases in C2M carbonaceous chondrite meteorites. *Nature,* 309**,** 240-242.

Malvoisin, B., Zhang, C., Müntener, O., Baumgartner, L. P., Kelemen, P. B. & Party, O. D. P. S. 2020. Measurement of volume change and mass transfer during serpentinization: Insights from the Oman Drilling Project. *Journal of Geophysical Research: Solid Earth,* 125**,** e2019JB018877.

Manian, S. H., Urey, H. C. & Bleakney, W. 1934. An investigation of the relative abundance of the oxygen isotopes O16: O18 in stone meteorites. *Journal of the American Chemical Society,* 56**,** 2601-2609.

Marrocchi, Y., Gounelle, M., Blanchard, I., Caste, F. & Kearsley, A. T. 2014. The Paris CM chondrite: Secondary minerals and asteroidal processing. *Meteoritics & Planetary Science,* 49**,** 1232-1249.

Marrocchi, Y., Jacquet, E., Neukampf, J., Villeneuve, J. & Zolensky, M. E. 2023a. From whom Bells tolls: Reclassifying Bells among CR chondrites and implications for the formation conditions of CR parent bodies. *Meteoritics & Planetary Science,* 58**,** 195-206.

Marrocchi, Y., Rigaudier, T., Piralla, M. & Piani, L. 2023b. Hydrogen isotopic evidence for nebular pre-hydration and the limited role of parent-body processes in CM chondrites. *Earth and Planetary Science Letters,* 611**,** 118151.

Martin, R. G. & Livio, M. 2012. On the evolution of the snow line in protoplanetary discs. *Monthly Notices of the Royal Astronomical Society: Letters,* 425**,** L6-L9.

Martins, Z., Hofmann, B., Gnos, E., Greenwood, R., Verchovsky, A., Franchi, I., Jull, A., Botta, O., Glavin, D. & Dworkin, J. 2007. Amino acid composition, petrology, geochemistry, 14C

terrestrial age and oxygen isotopes of the Shişr 033 CR chondrite. *Meteoritics & Planetary Science,* 42**,** 1581-1595.
Marty, B. 2012. The origins and concentrations of water, carbon, nitrogen and noble gases on Earth. *Earth and Planetary Science Letters,* 313**,** 56-66.
Marvin, U. B. 2001. Oral histories in meteoritics and planetary science: II. Robert N. Clayton. *Meteoritics & Planetary Science,* 36**,** A269-A274.
Masiero, J. R., Demeo, F. E., Kasuga, T. & Parker, A. H. 2015. Asteroid family physical properties. *Asteroids IV,* 32**,** 3-340.
Matsuhisa, Y., Goldsmith, J. R. & Clayton, R. N. 1978. Mechanisms of hydrothermal crystallization of quartz at 250 C and 15 kbar. *Geochimica et Cosmochimica Acta,* 42**,** 173-182.
Matsuhisa, Y., Matsubaya, O. & Sakai, H. 1971. BrF5-technique for the oxygen isotopic analysis of silicates and water. *Journal of the Mass Spectrometry Society of Japan,* 19**,** 124-133.
Matsumoto, M., Tsuchiyama, A., Nakato, A., Matsuno, J., Miyake, A., Kataoka, A., Ito, M., Tomioka, N., Kodama, Y. & Uesugi, K. 2019. Discovery of fossil asteroidal ice in primitive meteorite Acfer 094. *Science Advances,* 5**.**
Mccain, K. A., Matsuda, N., Liu, M.-C., Mckeegan, K. D., Yamaguchi, A., Kimura, M., Tomioka, N., Ito, M., Imae, N., Uesugi, M., Shirai, N., Ohigashi, T., Greenwood, R. C., Uesugi, K., Nakato, A., Yogata, K., Yuzawa, H., Kodama, Y., Hirahara, K., Sakurai, I., Okada, I., Karouji, Y., Nakazawa, S., Okada, T., Saiki, T., Tanaka, S., Terui, F., Yoshikawa, M., Miyazaki, A., Nishimura, M., Yada, T., Abe, M., Usui, T., Watanabe, S.-I. & Tsuda, Y. 2023. Early fluid activity on Ryugu inferred by isotopic analyses of carbonates and magnetite. *Nature Astronomy,* 7**,** 309-317.
Mcdermott, K. H. 2013. *A* Geochemical Investigation of Differentiation in the Early Solar System *PhD Thesis, The Open University.*
Mckeegan, K. & Davis, A. 2003. Early solar system chronology. *Treatise on Geochemistry,* 1**,** 711.
Mckeegan, K., Kallio, A., Heber, V., Jarzebinski, G., Mao, P. H., Coath, C., Kunihiro, T., Wiens, R., Nordholt, J. & Moses Jr, R. 2011. The oxygen isotopic composition of the Sun inferred from captured solar wind. *Science,* 332**,** 1528-1532.
Mckinney, C. R., Mccrea, J. M., Epstein, S., Allen, H. & Urey, H. C. 1950. Improvements in mass spectrometers for the measurement of small differences in isotope abundance ratios. *Review of Scientific Instruments,* 21**,** 724-730.
Mcsween Jr, H. Y. 1979. Alteration in CM carbonaceous chondrites inferred from modal and chemical variations in matrix. *Geochimica et Cosmochimica Acta,* 43**,** 1761-1770.
Mcsween Jr, H. Y. 1987. Aqueous alteration in carbonaceous chondrites: Mass balance constraints on matrix mineralogy. *Geochimica et Cosmochimica Acta,* 51**,** 2469-2477.
Mcsween Jr, H. Y., Ghosh, A., Grimm, R. E., Wilson, L. & Young, E. D. 2002. Thermal evolution models of asteroids. *Asteroids III,* 559**,** 559-572.
Melikyan, R. E., Clark, B. E., Hergenrother, C. W., Chesley, S., Nolan, M. C., Ye, Q. Z. & Lauretta, D. 2021. Bennu's natural sample delivery mechanism: Estimating the flux of Bennuid meteors at Earth. *Journal of Geophysical Research: Planets,* 126**.**
Metzler, K. 2004. Formation of accretionary dust mantles in the solar nebula: Evidence from preirradiated olivines in CM chondrites. *Meteoritics & Planetary Science,* 39**,** 1307-1319.
Metzler, K., Bischoff, A. & Stoffler, D. 1992. Accretionary dust mantles in cm chondrites - evidence for solar nebula processes. *Geochimica et Cosmochimica Acta,* 56**,** 2873-2897.
Michel, P., Ballouz, R.-L., Barnouin, O., Jutzi, M., Walsh, K., May, B., Manzoni, C., Richardson, D., Schwartz, S. & Sugita, S. 2020. Collisional formation of top-shaped asteroids and implications for the origins of Ryugu and Bennu. *Nature Communications,* 11**,** 2655.
Michel, P. & Richardson, D. C. 2013. Collision and gravitational reaccumulation: possible formation mechanism of the asteroid Itokawa. *Astronomy & Astrophysics,* 554**,** L1.
Miller, M. Franchi, I. Sexton, A. & Pillinger, C. 1999. High precision δ17O isotope measurements of oxygen from silicates and other oxides: method and applications. *Rapid Communications in Mass Spectrometry,* 13**,** 1211-1217.
Miller, M. F., Franchi, I. A., Thiemens, M. H., Jackson, T. L., Brack, A., Kurat, G. & Pillinger, C. T. 2002. Mass-independent fractionation of oxygen isotopes during thermal decomposition of carbonates. *Proceedings of the National Academy of Sciences,* 99**,** 10988-10993.
Mittlefehldt, D. W. 2002. Geochemistry of the ungrouped carbonaceous chondrite Tagish Lake, the anomalous CM chondrite Bells, and comparison with CI and CM chondrites. *Meteoritics & Planetary Science,* 37**,** 703-712.

Morate, D., De León, J., De Prá, M., Licandro, J., Cabrera-Lavers, A., Campins, H. & Pinilla-Alonso, N. 2018. Visible spectroscopy of the Sulamitis and Clarissa primitive families: a possible link to Erigone and Polana. *Astronomy & Astrophysics,* 610**,** A25.

Morbidelli, A. 2018. Accretion processes.

Morbidelli, A. 2020. Planet formation by pebble accretion in ringed disks. *Astronomy & Astrophysics,* 638**,** A1.

Morbidelli, A., Bitsch, B., Crida, A., Gounelle, M., Guillot, T., Jacobson, S., Johansen, A., Lambrechts, M. & Lega, E. 2016. Fossilized condensation lines in the Solar System protoplanetary disk. *Icarus,* 267**,** 368-376.

Morbidelli, A., Bottke, W. F., Nesvorný, D. & Levison, H. F. 2009. Asteroids were born big. *Icarus,* 204**,** 558-573.

Morbidelli, A., Chambers, J., Lunine, J., Petit, J.-M., Robert, F., Valsecchi, G. B. & Cyr, K. 2000. Source regions and timescales for the delivery of water to the Earth. *Meteoritics & Planetary Science,* 35**,** 1309-1320.

Morbidelli, A., Levison, H. F., Tsiganis, K. & Gomes, R. 2005. Chaotic capture of Jupiter's Trojan asteroids in the early Solar System. *Nature,* 435**,** 462-465.

Morbidelli, A., Lunine, J. I., O'brien, D. P., Raymond, S. N. & Walsh, K. J. 2012. Building terrestrial planets. *Annual Review of Earth and Planetary Sciences,* 40**,** 251-275.

Morbidelli, A. & Nesvorny, D. 2012. Dynamics of pebbles in the vicinity of a growing planetary embryo: hydro-dynamical simulations. *Astronomy & Astrophysics,* 546**,** A18.

Morbidelli, A. & Raymond, S. N. 2016. Challenges in planet formation. *Journal of Geophysical Research: Planets,* 121**,** 1962-1980.

Morbidelli, A., Tsiganis, K., Crida, A., Levison, H. F. & Gomes, R. 2007. Dynamics of the giant planets of the solar system in the gaseous protoplanetary disk and their relationship to the current orbital architecture. *The Astronomical Journal,* 134**,** 1790.

Morbidelli, A., Walsh, K. J., O'brien, D. P., Minton, D. A. & Bottke, W. F. 2015. The dynamical evolution of the asteroid belt. *arXiv preprint arXiv:1501.06204*.

Morbidelli, A. & Wood, B. J. 2015. Late Accretion and the Late Veneer. *In:* BADRO, J. & WALTER, M. (eds.) *Early Earth: Accretion and Differentiation.*

Morris, A. A. 2008. Understanding the origin and evolution of water in the early Solar System. *PhD Thesis, The Open University.*

Mortimer, J., Lécuyer, C., Fourel, F. & Carpenter, J. 2018. D/H fractionation during sublimation of water ice at low temperatures into a vacuum. *Planetary and Space Science,* 158**,** 25-33.

Moynier, F. & Fegley Jr, B. 2015. The Earth's building blocks. *The early Earth: accretion and differentiation***,** 27-47.

Müller, W., Kurat, G. & Kracher, A. 1979. Chemical and crystallographic study of cronstedtite in the matrix of the Cochabamba(CM 2) carbonaceous chondrite. *TMPM Tschermaks Mineralogische Und Petrographische Mitteilungen,* 26**,** 293-304.

Nakamura, T., Matsumoto, M., Amano, K., Enokido, Y., Zolensky, M., Mikouchi, T., Genda, H., Tanaka, S., Zolotov, M. & Kurosawa, K. 2022. Formation and evolution of carbonaceous asteroid Ryugu: Direct evidence from returned samples. *Science***.**

Nakamura, T. & Nakamuta, Y. 1996. X-ray study of PCP from the Murchison CM carbonaceous chondrite. *Antarctic Meteorite Research,* 9**,** 37.

Nakano, H., Kouchi, A., Tachibana, S. & Tsuchiyama, A. 2003. Evaporation of interstellar organic materials in the solar nebula. *The Astrophysical Journal,* 592**,** 1252.

Nesvorný, D., Brož, M. & Carruba, V. 2015. Identification and dynamical properties of asteroid families. *Asteroids IV,* 29**,** 7-321.

Newcombe, M., Nielsen, S., Peterson, L., Wang, J., Alexander, C. O. D., Sarafian, A., Shimizu, K., Nittler, L. & Irving, A. 2023. Degassing of early-formed planetesimals restricted water delivery to Earth. *Nature,* 615**,** 854-857.

Newton, J., Bischoff, A., Arden, J., Franchi, I., Geiger, T., Greshake, A. & Pillinger, C. 1995. Acfer 094, a uniquely primitive carbonaceous chondrite from the Sahara. *Meteoritics,* 30**,** 47-56.

Nishiizumi, K., Caffee, M., Hamajima, Y., Reedy, R. & Welten, K. 2014. Exposure history of the Sutter's Mill carbonaceous chondrite. *Meteoritics & Planetary Science,* 49**,** 2056-2063.

O'brien, D. P., Walsh, K. J., Morbidelli, A., Raymond, S. N. & Mandell, A. M. 2014. Water delivery and giant impacts in the 'Grand Tack'scenario. *Icarus,* 239**,** 74-84.

Ogihara, M. & Ida, S. 2009. N-body simulations of planetary accretion around M dwarf stars. *The Astrophysical Journal,* 699**,** 824.

Ohlsson, K. A. 2013. Uncertainty of blank correction in isotope ratio measurement. *Analytical chemistry,* 85**,** 5326-5329.

Ormel, C. & Klahr, H. 2010. The effect of gas drag on the growth of protoplanets-analytical expressions for the accretion of small bodies in laminar disks. *Astronomy & Astrophysics,* 520**,** A43.

Ormel, C. W. 2017. The emerging paradigm of pebble accretion. *Formation, Evolution, and Dynamics of Young Solar Systems***,** 197-228.

Padrón-Navarta, J. A., Sánchez-Vizcaíno, V. L., Hermann, J., Connolly, J. A., Garrido, C. J., Gómez-Pugnaire, M. T. & Marchesi, C. 2013. Tschermak's substitution in antigorite and consequences for phase relations and water liberation in high-grade serpentinites. *Lithos,* 178**,** 186-196.

Palguta, J., Schubert, G. & Travis, B. J. 2010. Fluid flow and chemical alteration in carbonaceous chondrite parent bodies. *Earth and Planetary Science Letters,* 296**,** 235-243.

Palmer, E. E. & Lauretta, D. S. 2011. Aqueous alteration of kamacite in CM chondrites. *Meteoritics & Planetary Science,* 46**,** 1587-1607.

Pape, J., Mezger, K., Bouvier, A. S. & Baumgartner, L. P. 2019. Time and duration of chondrule formation: Constraints from Al-26-(26) Mg ages of individual chondrules. *Geochimica et Cosmochimica Acta,* 244**,** 416-436.

Patzek, M., Bischoff, A., Visser, R. & John, T. 2018. Mineralogy of volatile-rich clasts in brecciated meteorites. *Meteoritics & Planetary Science***,** 1-22.

Patzek, M., Hoppe, P., Bischoff, A., Visser, R. & John, T. 2020. Hydrogen isotopic composition of CI- and CM-like clasts from meteorite breccias - Sampling unknown sources of carbonaceous chondrite materials. *Geochimica et Cosmochimica Acta,* 272**,** 177-197.

Piani, L., Marrocchi, Y., Rigaudier, T., Vacher, L. G., Thomassin, D. & Marty, B. 2020. Earth's water may have been inherited from material similar to enstatite chondrite meteorites. *Science,* 369**,** 1110-1113.

Piani, L., Marrocchi, Y., Vacher, L. G., Yurimoto, H. & Bizzarro, M. 2021. Origin of hydrogen isotopic variations in chondritic water and organics. *Earth and Planetary Science Letters,* 567**,** 117008.

Piani, L., Yurimoto, H. & Remusat, L. 2018. A dual origin for water in carbonaceous asteroids revealed by CM chondrites. *Nature astronomy,* 2**,** 317-323.

Pignatelli, I., Marrocchi, Y., Mugnaioli, E., Bourdelle, F. & Gounelle, M. 2017. Mineralogical, crystallographic and redox features of the earliest stages of fluid alteration in CM chondrites. *Geochimica et Cosmochimica Acta,* 209**,** 106-122.

Pignatelli, I., Marrocchi, Y., Vacher, L. G., Delon, R. & Gounelle, M. 2016. Multiple precursors of secondary mineralogical assemblages in CM chondrites. *Meteoritics & Planetary Science,* 51**,** 785-805.

Pignatelli, I., Mugnaioli, E. & Marrocchi, Y. 2018. Cronstedtite polytypes in the Paris meteorite. *European Journal of Mineralogy,* 30**,** 349-354.

Piralla, M., Marrocchi, Y., Verdier-Paoletti, M. J., Vacher, L. G., Villeneuve, J., Piani, L., Bekaert, D. V. & Gounelle, M. 2020. Primordial water and dust of the Solar System: Insights from in situ oxygen measurements of CI chondrites. *Geochimica et Cosmochimica Acta,* 269**,** 451-464.

Piralla, M., Villeneuve, J., Schnuriger, N., Bekaert, D. V. & Marrocchi, Y. 2023. A unified chronology of dust formation in the early solar system. *Icarus***,** 115427.

Pollack, J. B., Hubickyj, O., Bodenheimer, P., Lissauer, J. J., Podolak, M. & Greenzweig, Y. 1996. Formation of the giant planets by concurrent accretion of solids and gas. *icarus,* 124**,** 62-85.

Potin, S., Beck, P., Bonal, L., Schmitt, B., Garenne, A., Moynier, F., Agranier, A., Schmitt-Kopplin, P., Malik, A. & Quirico, E. 2020. Mineralogy, chemistry, and composition of organic compounds in the fresh carbonaceous chondrite Mukundpura: CM1 or CM2? *Meteoritics & Planetary Science,* 55**,** 1681-1696.

Railsback, B. 2007. Some Fundamentals of Mineralogy and Geochemistry - Isotope notations: %s, δvalues and ε values [Online]. Available: http://railsback.org/Fundamentals/IsoNotation&MassDiff05P.pdf [Accessed 05/07/23].

Ramdohr, P. 1963. The opaque minerals in stony meteorites. *Journal of Geophysical Research,* 68**,** 2011-2036.

Ray, D. & Shukla, A. D. 2018. The Mukundpura meteorite, a new fall of CM chondrite. *Planetary and Space Science,* 151**,** 149-154.
Raymond, S. N. & Izidoro, A. 2017. Origin of water in the inner Solar System: Planetesimals scattered inward during Jupiter and Saturn's rapid gas accretion. *Icarus,* 297**,** 134-148.
Raymond, S. N., O'brien, D. P., Morbidelli, A. & Kaib, N. A. 2009. Building the terrestrial planets: Constrained accretion in the inner Solar System. *Icarus,* 203**,** 644-662.
Righter, K., Lunning, N., Nakamura-Messenger, K., Snead, C., Mcquillan, J., Calaway, M., Allums, K., Rodriguez, M., Funk, R. & Harrington, R. 2023. Curation planning and facilities for asteroid Bennu samples returned by the OSIRIS-REx mission. *Meteoritics & Planetary Science*.
Robert, F., Tartese, R., Lombardi, G., Reinhardt, P., Roskosz, M., Doisneau, B., Deng, Z. & Chaussidon, M. 2020. Mass-independent fractionation of titanium isotopes and its cosmochemical implications. *Nature Astronomy,* 4**,** 762-768.
Ros, K., Johansen, A., Riipinen, I. & Schlesinger, D. 2019. Effect of nucleation on icy pebble growth in protoplanetary discs. *Astronomy & Astrophysics,* 629**,** A65.
Rosenberg, N. D., Browning, L. & Bourcier, W. L. 2001. Modeling aqueous alteration of CM carbonaceous chondrites. *Meteoritics & Planetary Science,* 36**,** 239-244.
Rowe, M. W., Clayton, R. N. & Mayeda, T. K. 1994. Oxygen isotopes in separated components of CI and CM meteorites. *Geochimica et Cosmochimica Acta,* 58**,** 5341-5347.
Rubin, A. E. 2015. An American on Paris: Extent of aqueous alteration of a CM chondrite and the petrography of its refractory and amoeboid olivine inclusions. *Meteoritics & Planetary Science,* 50**,** 1595-1612.
Rubin, A. E. 2018. Mechanisms accounting for variations in the proportions of carbonaceous and ordinary chondrites in different mass ranges. *Meteoritics & Planetary Science,* 53**,** 2181-2192.
Rubin, A. E., Trigo-Rodriguez, J. M., Huber, H. & Wasson, J. T. 2007. Progressive aqueous alteration of CM carbonaceous chondrites. *Geochimica et Cosmochimica Acta,* 71**,** 2361-2382.
Rudraswami, N. G., Naik, A. K., Tripathi, R. P., Bhandari, N., Karapurkar, S. G., Prasad, M. S., Babu, E. & Sarathi, U. 2019. Chemical, isotopic and amino acid composition of Mukundpura CM2.0 (CM1) chondrite: Evidence of parent body aqueous alteration. *Geoscience Frontiers,* 10**,** 495-504.
Ruggiu, L. K., Devouard, B., Gattacceca, J., Bonal, L., Leroux, H., Eschrig, J., Borschneck, D., King, A., Beck, P. & Marrocchi, Y. 2022. Detection of incipient aqueous alteration in carbonaceous chondrites. *Geochimica et Cosmochimica Acta,* 336**,** 308-331.
Rumble, D., Farquhar, J., Young, E. & Christensen, C. 1997. In situ oxygen isotope analysis with an excimer laser using F2 and BrF5 reagents and O2 gas as analyte. *Geochimica et Cosmochimica Acta,* 61**,** 4229-4234.
Russell, S. S., King, A. J., Bates, H. C., Almeida, N. V., Greenwood, R. C., Daly, L., Joy, K. H., Rowe, J., Salge, T. & Smith, C. L. 2023. Recovery and curation of the Winchcombe (CM2) meteorite. *Meteoritics & Planetary Science*.
Russell, S. S., Suttle, M. & King, A. 2022. Abundance and importance of petrological type 1 chondritic material. *Meteoritics & Planetary Science,* 57**,** 277-301.
Ruzicka, A., Grossman, J., Bouvier, A. & Agee, C. B. 2017. The meteoritical bulletin, No. 103. *Meteoritics & Planetary Science,* 52**,** 1014.
Saccocia, P. J., Seewald, J. S. & Shanks Iii, W. C. 2009. Oxygen and hydrogen isotope fractionation in serpentine–water and talc–water systems from 250 to 450 C, 50 MPa. *Geochimica et Cosmochimica Acta,* 73**,** 6789-6804.
Sakamoto, N., Seto, Y., Itoh, S., Kuramoto, K., Fujino, K., Nagashima, K., Krot, A. N. & Yurimoto, H. 2007. Remnants of the early solar system water enriched in heavy oxygen isotopes. *Science,* 317**,** 231-233.
Sakatani, N., Tanaka, S., Okada, T., Fukuhara, T., Riu, L., Sugita, S., Honda, R., Morota, T., Kameda, S. & Yokota, Y. 2021. Anomalously porous boulders on (162173) Ryugu as primordial materials from its parent body. *Nature Astronomy,* 5**,** 766-774.
Sarafian, A. R., Nielsen, S. G., Marschall, H. R., Mccubbin, F. M. & Monteleone, B. D. 2014a. Early accretion of water in the inner solar system from a carbonaceous chondrite-like source. *Science,* 346**,** 623-626.

Sarafian, A. R., Nielsen, S. G., Marschall, H. R., Mccubbin, F. M. & Monteleone, B. D. 2014b. Early accretion of water in the inner solar system from a carbonaceous chondrite–like source. *Science,* 346**,** 623-626.

Schäfer, U., Johansen, A. & Banerjee, R. 2020. The coexistence of the streaming instability and the vertical shear instability in protoplanetary disks. *Astronomy & Astrophysics,* 635**,** A190.

Schauble, E. A. 2004. Applying stable isotope fractionation theory to new systems. *Reviews in Mineralogy and Geochemistry,* 55**,** 65-111.

Schlichting, H. E., Ofek, E. O., Nelan, E. P., Gal-Yam, A., Wenz, M., Muirhead, P., Javanfar, N. & Livio, M. 2012. Measuring the abundance of sub-kilometer-sized Kuiper belt objects using stellar occultations. *The Astrophysical Journal,* 761**,** 150.

Schmitz, B., Tassinari, M. & Peucker-Ehrenbrink, B. 2001. A rain of ordinary chondritic meteorites in the early Ordovician. *Earth and Planetary Science Letters,* 194**,** 1-15.

Schofield, P., Knight, K., Covey-Crump, S., Cressey, G. & Stretton, I. 2002. Accurate quantification of the modal mineralogy of rocks when image analysis is difficult. *Mineralogical Magazine,* 66**,** 189-200.

Schrader, D. L., Connolly, H. C., Lauretta, D. S., Nagashima, K., Huss, G. R., Davidson, J. & Domanik, K. J. 2013. The formation and alteration of the Renazzo-like carbonaceous chondrites II: Linking O-isotope composition and oxidation state of chondrule olivine. *Geochimica et Cosmochimica Acta,* 101**,** 302-327.

Schrader, D. L. & Davidson, J. 2017. CM and CO chondrites: A common parent body or asteroidal neighbors? Insights from chondrule silicates. *Geochimica et Cosmochimica Acta,* 214**,** 157-171.

Schrader, D. L., Davidson, J., Mccoy, T. J., Zega, T. J., Russell, S. S., Domanik, K. J. & King, A. J. 2021. The Fe/S ratio of pyrrhotite group sulfides in chondrites: An indicator of oxidation and implications for return samples from asteroids Ryugu and Bennu. *Geochimica et Cosmochimica Acta*.

Schrader, D. L., Franchi, I. A., Connolly, H. C., Greenwood, R. C., Lauretta, D. S. & Gibson, J. M. 2011. The formation and alteration of the Renazzo-like carbonaceous chondrites I: Implications of bulk-oxygen isotopic composition. *Geochimica et Cosmochimica Acta,* 75**,** 308-325.

Schultz, R. A. 1993. Brittle strength of basaltic rock masses with applications to Venus. *Journal of Geophysical Research: Planets,* 98**,** 10883-10895.

Scicchitano, M. R., De Obeso, J. C., Blum, T. B., Valley, J. W., Kelemen, P. B., Nachlas, W. O., Schneider, W., Spicuzza, M. J., Wilke, F. D. & Roddatis, V. 2023. An empirical calibration of the serpentine-water oxygen isotope fractionation at T= 25–100° C. *Geochimica et Cosmochimica Acta,* 346**,** 192-206.

Scott, E. R., Keil, K. & Stöffler, D. 1992. Shock metamorphism of carbonaceous chondrites. *Geochimica et Cosmochimica Acta,* 56**,** 4281-4293.

Sears, D. W. 1998. The case for rarity of chondrules and calcium-aluminum-rich inclusions in the early solar system and some implications for astrophysical models. *The Astrophysical Journal,* 498**,** 773.

Sephton, M. A. 2002. Organic compounds in carbonaceous meteorites. *Natural product reports,* 19**,** 292-311.

Singerling, S. A. & Brearley, A. J. 2018. Primary iron sulfides in CM and CR carbonaceous chondrites: Insights into nebular processes. *Meteoritics & Planetary Science,* 53**,** 2078-2106.

Starkey, N., Franchi, I. & Lee, M. 2014. Isotopic diversity in interplanetary dust particles and preservation of extreme 16O-depletion. *Geochimica et Cosmochimica Acta,* 142**,** 115-131.

Starkey, N., Jackson, C., Greenwood, R., Parman, S., Franchi, I., Jackson, M., Fitton, J., Stuart, F., Kurz, M. & Larsen, L. 2016. Triple oxygen isotopic composition of the high-3He/4He mantle. *Geochimica et Cosmochimica Acta,* 176**,** 227-238.

Stockdale, S. C. 2020. Constraining the cooling rates of chondrules, *PhD Thesis, The Open University.*

Sturm, B., Bouwman, J., Henning, T., Evans, N., Waters, L., Van Dishoeck, E., Green, J., Olofsson, J., Meeus, G. & Maaskant, K. 2013. The 69 μm forsterite band in spectra of protoplanetary disks. Results from the Herschel DIGIT programme. *Astronomy & Astrophysics,* 553**,** A5.

Suavet, C., Alexandre, A., Franchi, I. A., Gattacceca, J., Sonzogni, C., Greenwood, R. C., Folco, L. & Rochette, P. 2010. Identification of the parent bodies of micrometeorites with high-precision oxygen isotope ratios. *Earth and Planetary Science Letters,* 293**,** 313-320.

Suttle, M., Daly, L., Jones, R., Jenkins, L., Van Ginneken, M., Mitchell, J., Bridges, J., Hicks, L., Johnson, D. & Rollinson, G. 2023. The Winchcombe meteorite—A regolith breccia from a rubble pile CM chondrite asteroid. *Meteoritics & Planetary Science*.

Suttle, M., Dionnet, Z., Franchi, I., Folco, L., Gibson, J., Greenwood, R., Rotundi, A., King, A. & Russell, S. 2020. Isotopic and textural analysis of giant unmelted micrometeorites–identification of new material from intensely altered 16O-poor water-rich asteroids. *Earth and Planetary Science Letters,* 546**,** 116444.

Suttle, M., King, A., Ramkissoon, N., Bonato, E., Franchi, I., Malley, J., Schofield, P., Najorka, J., Salge, T. & Russell, S. 2022. Alteration conditions on the CM and CV parent bodies–Insights from hydrothermal experiments with the CO chondrite Kainsaz. *Geochimica et Cosmochimica Acta,* 318**,** 83-111.

Suttle, M., King, A., Schofield, P., Bates, H. & Russell, S. 2021. The aqueous alteration of CM chondrites, a review. *Geochimica et Cosmochimica Acta*.

Tartèse, R., Chaussidon, M., Gurenko, A., Delarue, F. & Robert, F. 2018. Insights into the origin of carbonaceous chondrite organics from their triple oxygen isotope composition. *Proceedings of the National Academy of Sciences,* 115**,** 8535-8540.

Taylor Jr, H. P. & Epstein, S. 1962. Relationship between O18/O16 ratios in coexisting minerals of igneous and metamorphic rocks: part 1: principles and experimental results. *Geological Society of America Bulletin,* 73**,** 461-480.

Teitler, S. A., Paque, J. M., Cuzzi, J. N. & Hogan, R. C. 2010. Statistical tests of chondrule sorting. *Meteoritics & Planetary Science,* 45**,** 1124-1135.

Terfelt, F. & Schmitz, B. 2021. Asteroid break-ups and meteorite delivery to Earth the past 500 million years. *Proceedings of the National Academy of Sciences,* 118**,** e2020977118.

Thiemens, M. H. & Heidenreich Iii, J. E. 1983. The mass-independent fractionation of oxygen: A novel isotope effect and its possible cosmochemical implications. *Science,* 219**,** 1073-1075.

Thiemens, M. H. & Lin, M. 2021. Discoveries of mass independent isotope effects in the solar system: Past, present and future. *Reviews in Mineralogy and Geochemistry,* 86**,** 35-95.

Tomeoka, K. & Buseck, P. R. 1985. Indicators of aqueous alteration in cm carbonaceous chondrites - microtextures of a layered mineral containing fe, s, o and ni. *Geochimica et Cosmochimica Acta,* 49**,** 2149-2163.

Tomeoka, K., Mcsween Jr, H. Y. & Buseck, P. R. Mineralogical alteration of CM carbonaceous chondrites: A review. Proc. NIPR Symp. Antarct. Meteorites, 1989. 221-234.

Tomeoka, K., Yamahana, Y. & Sekine, T. 1999. Experimental shock metamorphism of the Murchison CM carbonaceous chondrite. *Geochimica et Cosmochimica Acta,* 63**,** 3683-3703.

Tonui, E., Zolensky, M., Hiroi, T., Nakamura, T., Lipschutz, M. E., Wang, M.-S. & Okudaira, K. 2014. Petrographic, chemical and spectroscopic evidence for thermal metamorphism in carbonaceous chondrites I: CI and CM chondrites. *Geochimica et Cosmochimica Acta,* 126**,** 284-306.

Topping, N., Bridges, J. C., Hicks, L. J. & Noguchi, T. 2023. Correlated Multi-Technique Characterisation of Sulfur-Bearing Serpentine in Carbonaceous Chondrites. *Copernicus Meetings.*

Torrano, Z. A., Schrader, D. L., Davidson, J., Greenwood, R. C., Dunlap, D. R. & Wadhwa, M. 2021. The relationship between CM and CO chondrites: Insights from combined analyses of titanium, chromium, and oxygen isotopes in CM, CO, and ungrouped chondrites. *Geochimica et cosmochimica acta,* 301**,** 70-90.

Travis, B. J. & Schubert, G. 2005. Hydrothermal convection in carbonaceous chondrite parent bodies. *Earth and Planetary Science Letters,* 240**,** 234-250.

Tricarico, P., Scheeres, D., French, A., Mcmahon, J., Brack, D., Leonard, J., Antreasian, P., Chesley, S., Farnocchia, D. & Takahashi, Y. 2021. Internal rubble properties of asteroid (101955) Bennu. *Icarus,* 370**,** 114665.

Tucker, M. E. & Jones, S. J. 2023. *Sedimentary petrology,* John Wiley & Sons.

Turner, S., Mcgee, L., Humayun, M., Creech, J. & Zanda, B. 2021. Carbonaceous chondrite meteorites experienced fluid flow within the past million years. *Science,* 371**,** 164-167.

Tyra, M., Brearley, A. & Guan, Y. B. 2016. Episodic carbonate precipitation in the CM chondrite ALH 84049: An ion microprobe analysis of O and C isotopes. *Geochimica et Cosmochimica Acta,* 175**,** 195-207.

Tyra, M., Farquhar, J., Wing, B., Benedix, G., Jull, A., Jackson, T. & Thiemens, M. 2007. Terrestrial alteration of carbonate in a suite of Antarctic CM chondrites: Evidence from oxygen and carbon isotopes. *Geochimica et Cosmochimica Acta,* 71**,** 782-795.

Tyra, M. A., Farquhar, J., Guan, Y. & Leshin, L. A. 2012. An oxygen isotope dichotomy in CM2 chondritic carbonates-A SIMS approach. *Geochimica et Cosmochimica Acta,* 77**,** 383-395.

Ushikubo, T., Kimura, M., Kita, N. T. & Valley, J. W. 2012. Primordial oxygen isotope reservoirs of the solar nebula recorded in chondrules in Acfer 094 carbonaceous chondrite. *Geochimica et Cosmochimica Acta,* 90**,** 242-264.

Ushikubo, T., Tenner, T. J., Hiyagon, H. & Kita, N. T. 2017. A long duration of the 16O-rich reservoir in the solar nebula, as recorded in fine-grained refractory inclusions from the least metamorphosed carbonaceous chondrites. *Geochimica et Cosmochimica Acta,* 201**,** 103-122.

Vacher, L. G., Marrocchi, Y., Villeneuve, J., Verdier-Paoletti, M. J. & Gounelle, M. 2017. Petrographic and C & O isotopic characteristics of the earliest stages of aqueous alteration of CM chondrites. *Geochimica et Cosmochimica Acta,* 213**,** 271-290.

Vacher, L. G., Marrocchi, Y., Villeneuve, J., Verdier-Paoletti, M. J. & Gounelle, M. 2018. Collisional and alteration history of the CM parent body. *Geochimica et Cosmochimica Acta,* 239**,** 213-234.

Vacher, L. G., Piani, L., Rigaudier, T., Thomassin, D., Florin, G., Piralla, M. & Marrocchi, Y. 2020a. Hydrogen in chondrites: Influence of parent body alteration and atmospheric contamination on primordial components. *Geochimica et Cosmochimica Acta,* 281**,** 53-66.

Vacher, L. G., Piralla, M., Gounelle, M., Bizzarro, M. & Marrocchi, Y. 2019a. Thermal evolution of hydrated asteroids inferred from oxygen isotopes. *The Astrophysical journal letters,* 882**,** L20.

Vacher, L. G., Truche, L., Faure, F., Tissandier, L., Mosser-Ruck, R. & Marrocchi, Y. 2019b. Deciphering the conditions of tochilinite and cronstedtite formation in CM chondrites from low temperature hydrothermal experiments. *Meteoritics & Planetary Science,* 54**,** 1870-1889.

Vacher, R., Liu, N., Nagashima, K. & Huss, G. 2020b. Accretion and circulation of 16O-poor water in the Acfer 094 parent body. *Lunar and Planetary Science Conference,* 51 #2495.

Valdes, M. C., Moreira, M., Foriel, J. & Moynier, F. 2014. The nature of Earth's building blocks as revealed by calcium isotopes. *Earth and Planetary Science Letters,* 394**,** 135-145.

Van Kooten, E., Cavalcante, L., Wielandt, D. & Bizzarro, M. 2020. The role of Bells in the continuous accretion between the CM and CR chondrite reservoirs. *Meteoritics & planetary science,* 55**,** 575-590.

Van Kooten, E. M., Cavalcante, L. L., Nagashima, K., Kasama, T., Balogh, Z. I., Peeters, Z., Hsiao, S. S.-Y., Shang, H., Lee, D.-C. & Lee, T. 2018. Isotope record of mineralogical changes in a spectrum of aqueously altered CM chondrites. *Geochimica et Cosmochimica Acta,* 237**,** 79-102.

Van Schmus, W. & Wood, J. A. 1967. A chemical-petrologic classification for the chondritic meteorites. *Geochimica et Cosmochimica Acta,* 31**,** 747-765.

Vasileiadis, A., Nordlund, Å. & Bizzarro, M. 2013. Abundance of 26Al and 60Fe in evolving giant molecular clouds. *The Astrophysical Journal Letters,* 769**,** L8.

Vattuone, L., Smerieri, M., Savio, L., Asaduzzaman, A. M., Muralidharan, K., Drake, M. J. & Rocca, M. 2013. Accretion disc origin of the Earth's water. *Philosophical Transactions of the Royal Society A: Mathematical, Physical and Engineering Sciences,* 371**,** 20110585.

Velbel, M. A. & Palmer, E. E. 2011. Fine-grained serpentine in CM2 carbonaceous chondrites and its implications for the extent of aqueous alteration on the parent body: A review. *Clays and Clay Minerals,* 59**,** 416-432.

Velbel, M. A., Tonui, E. K. & Zolensky, M. E. 2012. Replacement of olivine by serpentine in the carbonaceous chondrite Nogoya (CM2). *Geochimica et Cosmochimica Acta,* 87**,** 117-135.

Velbel, M. A., Tonui, E. K. & Zolensky, M. E. 2015. Replacement of olivine by serpentine in the Queen Alexandra Range 93005 carbonaceous chondrite (CM2): Reactant-product compositional relations, and isovolumetric constraints on reaction stoichiometry and elemental mobility during aqueous alteration. *Geochimica et Cosmochimica Acta,* 148**,** 402-425.

Verdier-Paoletti, M. J., Marrocchi, Y., Avice, G., Roskosz, M., Gurenko, A. & Gounelle, M. 2017. Oxygen isotope constraints on the alteration temperatures of CM chondrites. *Earth and Planetary Science Letters,* 458**,** 273-281.

Verdier-Paoletti, M. J., Marrocchi, Y., Vacher, L. G., Gattacceca, J., Gurenko, A., Sonzogni, C. & Gounelle, M. 2019. Testing the genetic relationship between fluid alteration and brecciation in CM chondrites. *Meteoritics & Planetary Science,* 54**,** 1692-1709.

Vernazza, P., Castillo-Rogez, J., Beck, P., Emery, J., Brunetto, R., Delbo, M., Marsset, M., Marchis, F., Groussin, O. & Zanda, B. 2017. Different origins or different evolutions? Decoding the spectral diversity among C-type asteroids. *The Astronomical Journal,* 153**,** 72.

Vernazza, P., Marsset, M., Beck, P., Binzel, R., Birlan, M., Cloutis, E., Demeo, F., Dumas, C. & Hiroi, T. 2016. Compositional homogeneity of CM parent bodies. *The Astronomical Journal,* 152**,** 54.

Visser, R., John, T., Whitehouse, M. J., Patzek, M. & Bischoff, A. 2020. A short-lived 26Al induced hydrothermal alteration event in the outer solar system: Constraints from Mn/Cr ages of carbonates. *Earth and Planetary Science Letters,* 547**,** 116440.

Walker, R. J., Bermingham, K., Liu, J., Puchtel, I. S., Touboul, M. & Worsham, E. A. 2015. In search of late-stage planetary building blocks. *Chemical Geology,* 411**,** 125-142.

Walsh, K. J., Delbó, M., Bottke, W. F., Vokrouhlický, D. & Lauretta, D. S. 2013. Introducing the Eulalia and new Polana asteroid families: Re-assessing primitive asteroid families in the inner Main Belt. *Icarus,* 225**,** 283-297.

Walsh, K. J., Morbidelli, A., Raymond, S. N., O'brien, D. P. & Mandell, A. M. 2011. A low mass for Mars from Jupiter's early gas-driven migration. *Nature,* 475**,** 206-209.

Walsh, K. J., Morbidelli, A., Raymond, S. N., O'brien, D. & Mandell, A. 2012. Populating the asteroid belt from two parent source regions due to the migration of giant planets—"The Grand Tack". *Meteoritics & Planetary Science,* 47**,** 1941-1947.

Warren, P. H. 2011. Stable-isotopic anomalies and the accretionary assemblage of the Earth and Mars: A subordinate role for carbonaceous chondrites. *Earth and Planetary Science Letters,* 311**,** 93-100.

Weber, P., Benítez-Llambay, P., Gressel, O., Krapp, L. & Pessah, M. E. 2018. Characterizing the variable dust permeability of planet-induced gaps. *The Astrophysical Journal,* 854**,** 153.

Weidenschilling, S. 1980. Dust to planetesimals: Settling and coagulation in the solar nebula. *Icarus,* 44**,** 172-189.

Weidenschilling, S. 2011. Initial sizes of planetesimals and accretion of the asteroids. *Icarus,* 214**,** 671-684.

Weisberg, M. K., Mccoy, T. J. & Krot, A. N. 2006. Systematics and evaluation of meteorite classification.

Weisberg, M. K., Prinz, M., Clayton, R. N. & Mayeda, T. K. 1993. The CR (Renazzo-type) carbonaceous chondrite group and its implications. *Geochimica et Cosmochimica Acta,* 57**,** 1567-1586.

Wetherill, G. Late heavy bombardment of the moon and terrestrial planets. In: Lunar Science Conference, 6th, Houston, Tex., March 17-21, 1975, Proceedings. Volume 2.(A78-46668 21-91) New York, Pergamon Press, Inc., 1975, p. 1539-1561., 1975. 1539-1561.

White, W. M. 2015. *Isotope geochemistry,* John Wiley & Sons.

Williams, J. P. & Cieza, L. A. 2011. Protoplanetary disks and their evolution. *Annual Review of Astronomy and Astrophysics,* 49**,** 67-117.

Wilson, L., Keil, K. & Love, S. J. 1999. The internal structures and densities of asteroids. *Meteoritics & Planetary Science,* 34**,** 479-483.

Windmill, R. J. 2021. An Isotopic Investigation Of Early Planetesimal Differentiation Processes, *PhD Thesis, The Open University.*

Wu, J., Desch, S. J., Schaefer, L., Elkins-Tanton, L. T., Pahlevan, K. & Buseck, P. R. 2018. Origin of Earth's water: chondritic inheritance plus nebular ingassing and storage of hydrogen in the core. *Journal of Geophysical Research: Planets,* 123**,** 2691-2712.

Wurm, G. & Krauss, O. 2006. Concentration and sorting of chondrules and CAIs in the late solar nebula. *Icarus,* 180**,** 487-495.

Yabuta, H., Alexander, C. M. O. D., Fogel, M. L., Kilcoyne, A. D. & Cody, G. D. 2010. A molecular and isotopic study of the macromolecular organic matter of the ungrouped C2 WIS 91600 and its relationship to Tagish Lake and PCA 91008. *Meteoritics & Planetary Science,* 45**,** 1446-1460.

Yada, T., Abe, M., Okada, T., Nakato, A., Yogata, K., Miyazaki, A., Hatakeda, K., Kumagai, K., Nishimura, M. & Hitomi, Y. 2022. Preliminary analysis of the Hayabusa2 samples returned from C-type asteroid Ryugu. *Nature Astronomy,* 6**,** 214-220.

Yang, C.-C., Johansen, A. & Carrera, D. 2017. Concentrating small particles in protoplanetary disks through the streaming instability. *Astronomy & Astrophysics,* 606**,** A80.
Youdin, A. & Johansen, A. 2007. Protoplanetary disk turbulence driven by the streaming instability: linear evolution and numerical methods. *The Astrophysical Journal,* 662**,** 613.
Young, E. D. 2001. The hydrology of carbonaceous chondrite parent bodies and the evolution of planet progenitors. *Philosophical Transactions of the Royal Society of London Series a-Mathematical Physical and Engineering Sciences,* 359**,** 2095-2109.
Young, E. D., Ash, R. D., England, P. & Rumble, D. 1999. Fluid flow in chondritic parent bodies: Deciphering the compositions of planetesimals. *Science,* 286**,** 1331-1335.
Young, E. D., Ash, R. D., Galy, A. & Belshaw, N. S. 2002a. Mg isotope heterogeneity in the Allende meteorite measured by UV laser ablation-MC-ICPMS and comparisons with O isotopes. *Geochimica et Cosmochimica Acta,* 66**,** 683-698.
Young, E. D., Galy, A. & Nagahara, H. 2002b. Kinetic and equilibrium mass-dependent isotope fractionation laws in nature and their geochemical and cosmochemical significance. *Geochimica et Cosmochimica Acta,* 66**,** 1095-1104.
Young, E. D., Kuramoto, K., Marcus, R. A., Yurimoto, H. & Jacobsen, S. B. 2008. Mass-independent oxygen isotope variation in the solar nebula. *Oxygen in the Solar System,* 68**,** 187-218.
Young, E. D. & Russell, S. S. 1998. Oxygen reservoirs in the early solar nebula inferred from an Allende CAI. *Science,* 282**,** 452-455.
Young, E. D., Zhang, K. K. & Schubert, G. 2003. Conditions for pore water convection within carbonaceous chondrite parent bodies–implications for planetesimal size and heat production. *Earth and Planetary Science Letters,* 213**,** 249-259.
Yurimoto, H., Krot, A. N., Choi, B. G., Aleon, J., Kunihiro, T. & Brearley, A. J. 2008. Oxygen isotopes of chondritic components. *Oxygen in the Solar System,* 68**,** 141-186.
Yurimoto, H. & Kuramoto, K. 2004. Molecular cloud origin for the oxygen isotope heterogeneity in the solar system. *Science,* 305**,** 1763-1766.
Zanetta, P.-M., Leroux, H., Le Guillou, C., Zanda, B. & Hewins, R. 2021. Nebular thermal processing of accretionary fine-grained rims in the Paris CM chondrite. *Geochimica et Cosmochimica Acta,* 295**,** 135-154.
Zanetta, P. M., Le Guillou, C., Leroux, H., Zanda, B., Hewins, R. H., Lewin, E. & Pont, S. 2019. Modal abundance, density and chemistry of micrometer-sized assemblages by advanced electron microscopy: Application to chondrites. *Chemical Geology,* 514**,** 27-41.
Zega, T. J. & Buseck, P. R. 2003. Fine-grained-rim mineralogy of the Cold Bokkeveld CM chondrite. *Geochimica et Cosmochimica Acta,* 67**,** 1711-1721.
Zheng, Y.-F. 1993. Calculation of oxygen isotope fractionation in hydroxyl-bearing silicates. *Earth and Planetary Science Letters,* 120**,** 247-263.
Zheng, Y.-F. 1998. Oxygen isotope fractionation between hydroxide minerals and water. *Physics and Chemistry of Minerals,* 25**,** 213-221.
Zheng, Y.-F. 1999. Oxygen isotope fractionation in carbonate and sulfate minerals. *Geochemical Journal,* 33**,** 109-126.
Zhou, Q., Yin, Q.-Z., Young, E. D., Li, X.-H., Wu, F.-Y., Li, Q.-L., Liu, Y. & Tang, G.-Q. 2013. SIMS Pb–Pb and U–Pb age determination of eucrite zircons at< 5 μm scale and the first 50 Ma of the thermal history of Vesta. *Geochimica et Cosmochimica Acta,* 110**,** 152-175.
Zolensky, M., Barrett, R. & Browning, L. 1993. Mineralogy and composition of matrix and chondrule rims in carbonaceous chondrites. *Geochimica et Cosmochimica Acta,* 57**,** 3123-3148.
Zolensky, M., Mcsween, H., Kerridge, J. & Matthews, M. S. 1988. Meteorites and the early solar system.
Zolensky, M., Nakamura, K., Gounelle, M., Mikouchi, T., Kasama, T., Tachikawa, O. & Tonui, E. 2002. Mineralogy of Tagish Lake: An ungrouped type 2 carbonaceous chondrite. *Meteoritics & Planetary Science,* 37**,** 737-761.
Zolensky, M. E., Le , L., Colbert, M., Maisano, J., Matsuoka, M., Harrington, R. & Ross, D. K. 2022. LON 94101 Provides a Unique Record of C-class Asteroid Regolith Diversity *NIPR 13.*
Zolensky, M. E. & Mackinnon, I. D. 1986. Microstructures of cylindrical tochilinites. *American Mineralogist,* 71**,** 1201-1209.
Zolensky, M. E., Mittlefehldt, D. W., Lipschutz, M. E., Wang, M. S., Clayton, R. N., Mayeda, T. K., Grady, M. M., Pillinger, C. & Barber, D. 1997. CM chondrites exhibit the complete petrologic range from type 2 to 1. *Geochimica et Cosmochimica Acta,* 61**,** 5099-5115.

Zolensky, M. E., Takenouchi, A., Mikouchi, T., Gregory, T., Nishiizumi, K., Caffee, M. W., Velbel, M. A., Ross, D. K., Zolensky, A. & Le, L. 2021. The nature of the CM parent asteroid regolith based on cosmic ray exposure ages. *Meteoritics & Planetary Science,* 56**,** 49-55.

Zolensky, M. E., Weisberg, M. K., Buchanan, P. C. & Mittlefehldt, D. W. 1996. Mineralogy of carbonaceous chondrite clasts in HED achondrites and the Moon. *Meteoritics & Planetary Science,* 31**,** 518-537.

Zsom, A., Ormel, C. W., Güttler, C., Blum, J. & Dullemond, C. 2010. The outcome of protoplanetary dust growth: pebbles, boulders, or planetesimals?-II. Introducing the bouncing barrier. *Astronomy & Astrophysics,* 513**,** A57.

Appendices

Appendix A1 : MicroMill pedantry

Attaching the sample to the stage

The polished blocks were securely attached to the stage with adhesive tape. Ideally the sample should be flat and not wedged but this is not critical as the micromill can drill mildly topographic samples.

Turning on the MicroMill

Once the operating PC has booted, the micromill can be turned on, first by the mains plug socket then the isolator switch on the back on the instrument. After waiting 10 seconds the micromill software loads. Upon activation, the drill calibrates the X, Y and Z stages which will move to their respective maximums. Once complete, the 'calibration' sections of the instrument checklist (Figure 2.7) will be green. After calibration, placement of the X and Y stages at 50 % of their respective scroll bars will centre the microscope to the middle of the stage.

Important: A common glitch causes the instrument to fail calibration of the Z stage, causing the software to freeze. The calibration window must be closed, followed by the software. Restarting the software will resolve this issue. Incorrect shutting down of the instrument (*e.g.,* turning off micromill before closing the software) will also cause this glitch.

First calibration parameter – Drill Tip Position

To be undertaken if a new micro drill bit is loaded.

The micromill requires several calibrations to accurately drill to the desired depth with micron-scale resolution. The first to consider is the calibration of the drill bit position. The length of the shaft may vary from bit to bit and must be calibrated to the stage and sample surface whenever a new one is installed. There may also be discrepancies, through human error, in the placement of the bit and the tightening of the chuck. Loading of the drill bit was

done as follows: *Drill Setup* > *Load a New Drill Bit* > *Follow on-screen instructions*. The stage will be automatically raised until there is sufficient clearance to remove the bit. Replace and proceed with the calibration as per the on-screen instructions.

Critically important: Once the micro drill bit has been loaded, the following statement will appear: "Position the stages so that the drill bit is directly over the top of an empty area on the sample plate". It is imperative that once in 'drill mode', the drill tip is approximately 1 cm above the stage before proceeding by using the Z axis nudge feature to lower the stage to this distance. This is crucial because the initial calibration sets the Z distance to its maximum height. Calibrating from this height causes a timeout error within the software before the tip reaches the stage. Consequently, the drill will plunge into the stage, damaging implements and shocking the Z sensor. In the case of a timeout, the emergency interlock button on the instrument must be pressed (Figure 2.5)

Second calibration parameter – Sample Thickness

To be undertaken for each scan, especially so if the sample is wedged.

In addition to the 'distance of the drill tip from the stage', the instrument requires a value for 'distance to the sample surface' to drill to the desired depth. This is achieved by switching to 'drill mode', and then *Position* > *Define flat sample surface* > *Follow on-screen instructions.* Alternatively, *Sample Thickness* on the Setup Checklist (Figure 2.5)

Critically important: The user MUST ensure that once the system is in 'drill mode' the drill tip is no more than 1 cm above the sample before proceeding, by using the Z axis nudge feature to lower the stage to this distance. As before, this is crucial because the initial calibration sets the Z distance to its maximum height. Calibrating from this height will cause the software to time out before the tip reaches the sample, yet the drill will continue to move downwards. Consequently, the drill will plunge into the sample and shock the Z sensor. In

the case of a timeout, the emergency interlock button on the instrument must be pressed (Figure 2.5)

Third calibration parameter – calibration of the Z sensor

This parameter is factory set and should not need to be changed unless the Z sensor is shocked. Given the likelihood of mishap the recalibration procedure is outlined here.

The electro-optical Z sensor detects when the micro drill bit contacts a solid surface and acts as a sensor probe to determine 'sample thickness' and drill tip position '. The typical distance that the drill must move before it detects the sample surface is about 0.550 mm. Correct calibration of this element is crucial to ensure only a feather touch is registered so the drill will excavate downwards within 1 µm precision to the desired depth. This element therefore has knock on effects for the prior two calibrations and so each must be done in turn after the Z sensor has been recalibrated.

The chuck must be raised using the manual Z axis nudge feature until the micro drill bit can be removed from the chuck. The bit must then be installed the wrong way around, so that the rear of the bit, which is machined flat, is facing downwards. A spare sample stage is placed on top of the installed stage and the drill bit is lowered using the manual Z axis nudge feature until the flat edge is just touching the spare stage. This can be inspected by both moving the spare stage laterally to 'feel' for contact, and by visually inspecting if contact has been made. It is crucial to ensure that the bit is only just touching the spare stage. Then the sensor can be calibrated through *Drill Setup > Calibrate Drill Z Sensor > Follow on-screen instructions*. This step must be repeated until repeat measurements are within 1-2 µm of each other.

Running scans

Live feed and binocular mode can be toggled on and off using the sliding bar by the eyepiece of the microscope. The live feed can be improved by turning the reflected light slider to

maximum and by wrapping foil around the binocular microscope eyepieces to prevent any external light from interfering the with the CCD through the eyepiece. The magnification of is controlled using the magnification dial on the microscope and the focus is set by adjusting the stage position using the Z axis nudge feature.

Before drilling, the desired spots were designated on the sample surface by selecting the single spot geometry from the ‘tools’ dropdown menu, then by clicking on the reflected light image in ‘scope mode’. Each spot then appeared in the defined patterns box wherein the properties of each spot were adjusted to suitable parameters (*e.g.*, for the ball point carbide: 20 % drill speed, 5s dwell time and 3 passes at 100 µm depth) and to reflect the width of the drill tip to ensure no significant over / underlap. The ‘enable drill during scans’ must be toggled as ‘on’ for the drill to activate.

In between analyses, spinning the drill bit in a vial of isopropanol at high drill speed appeared to clean the tip sufficiently. If the drill bit was particularly dirty, a 30 second ultrasonication in isopropanol sufficed.

Appendix A2

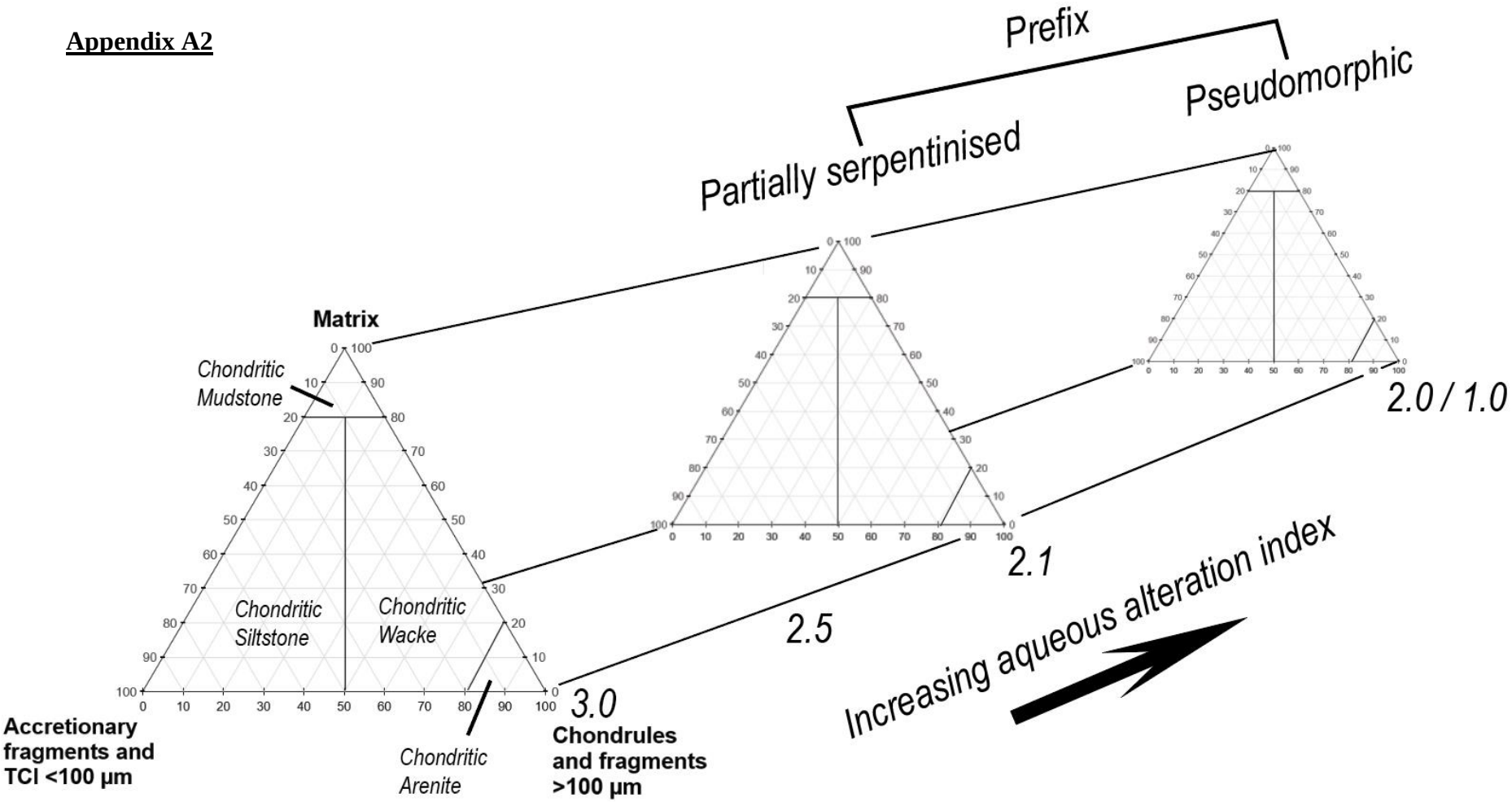
Prefix
Pseudomorphic
Partially serpentinised
Matrix
Chondritic Mudstone
Chondritic Siltstone
Chondritic Wacke
Chondritic Arenite
Accretionary fragments and TCI <100 µm
Chondrules and fragments >100 µm
2.0 / 1.0
2.1
2.5
3.0
Increasing aqueous alteration index

Appendix A3 – finely powdered serpentine and foil container instructions

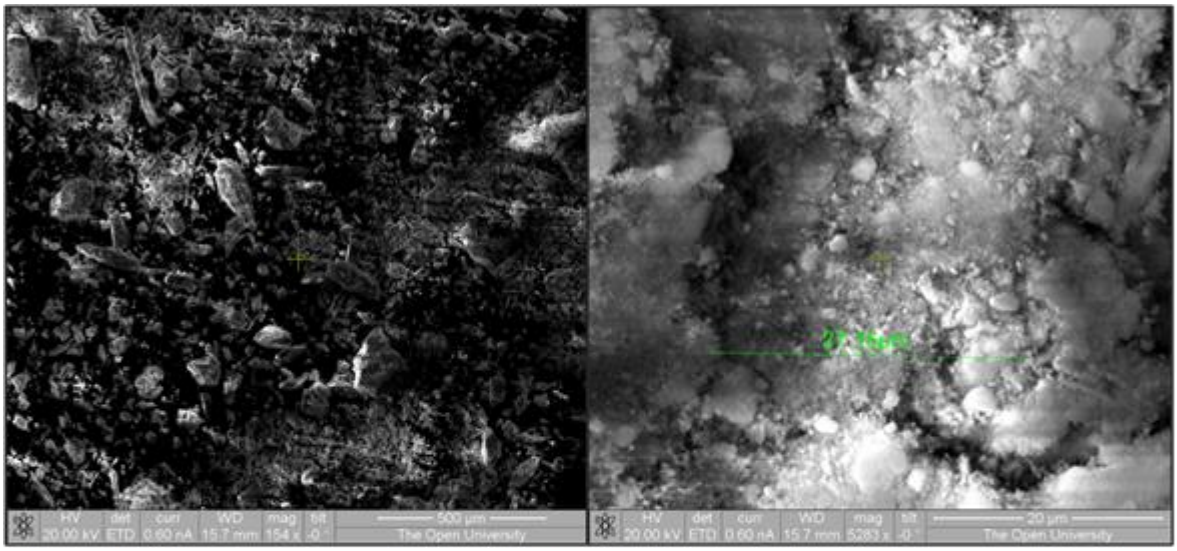

A3.1 – Powdered serpentine. Secondary electron images of hand crushed powder in a mortar and pestle (left) and powder drilled by the micromill (right). The micromilled powder is several orders of magnitude smaller than the hand crushed powder, with clusters of micron-sized particles coagulated together by electrostatic forces.

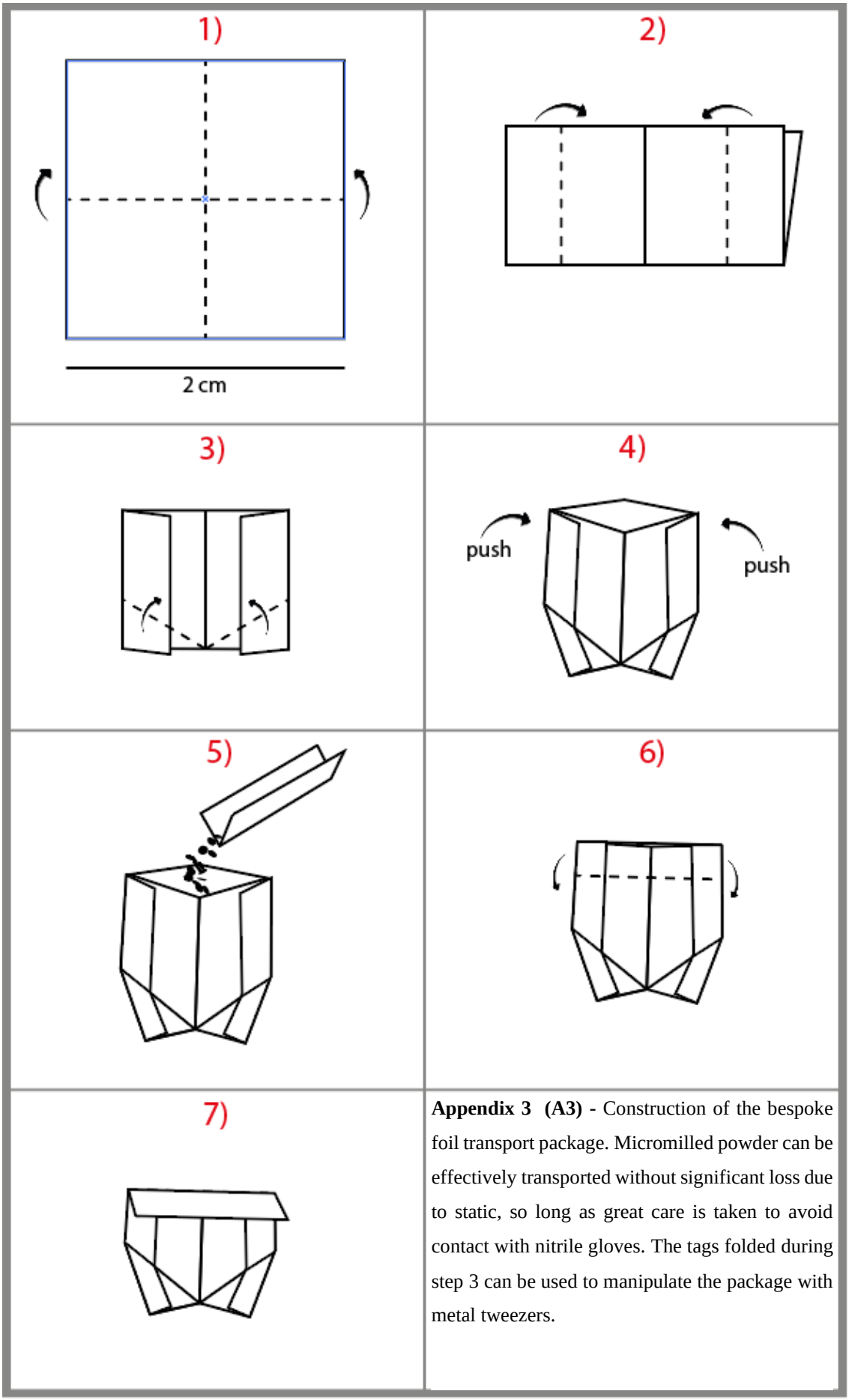

Appendix 3 (A3) - Construction of the bespoke foil transport package. Micromilled powder can be effectively transported without significant loss due to static, so long as great care is taken to avoid contact with nitrile gloves. The tags folded during step 3 can be used to manipulate the package with metal tweezers.

Appendix A4 – Legacy blank data

CM2 *RESULTS FROM OU LOG BOOK*														
SAMPLE NAME	**Supplier**	**Weight (mg)**	**OXYGEN RESULTS (‰)**					**5 min pre-fluorination blank**				**Blank (post-fluorination)**	**DATE RAN**
			µg O_2	**Yield (%)**	**$\delta^{17}O$**	**$\delta^{18}O$**	**$\Delta^{17}O$**	**µg O_2**	**$\delta^{17}O$**	**$\delta^{18}O$**	**$\Delta^{17}O$**	**µg O_2**	
LEW 85311 (an)		2.63	780	30	-4.7	-0.1	-4.65	136	18.1	35.0	-0.09	9	28/11/2018
Cold Bokkeveld	OU	2.25	711	32	1.3	7.2	-2.42	48	2.3	4.5	-0.07	3	24/01/2014
Cold Bokkeveld (replicate)	OU	2.31	779	34	2.0	8.4	-2.35	78	10.2	19.9	-0.15	5	28/01/2014
Cold Bokkeveld	Keiran Howard	2.24	672	30	3.9	12.2	-2.47	104	15.4	30.0	0.22	7	29/01/2014
Cold Bokkeveld (replicate)	Keiran Howard	1.42	449	32	3.7	11.7	-2.37	94	Not recorded			9	30/01/2014
Sutters Mill	Phillip Heck	2.68	740	28	6.3	17.1	-2.59	69	8.9	17.4	-0.12	5	13/03/2014
Murchison	OU	2.49	704	28	1.0	7.4	-2.78	146	16.5	32.0	0.19	13	30/09/2014
LON 94101, 17	Unknown, Lee/ Lingdren? OU?	2.52	880	35	2.3	8.5	-2.16	212	Not recorded			11	09/01/2015
EET 96029	Unknown	2.51	673	27	3.2	10.7	-2.35	102	12.2	23.4	-0.04	3	05/01/2015
EET 96029 (replicate)	Unknown	2.54	678	27	3.4	10.9	-2.33	79	10.3	19.8	0.03	5	05/08/2015
EET 96029 (AK-2)	Unknown	2.53	697	28	-1.0	4.1	-3.15	119	10.0	19.4	-0.14	9	22/06/2015
EET 96029 (AK-2) (replicate)	Unknown	2.52	669	27	-1.4	3.5	-3.25	274	11.9	23.3	0.17	9	23/06/2015
Murchison	OU	2.54	721	28	-0.4	5.2	-3.11	135	Not recorded			5	17/09/2016
Murchison	OU (Mahesh Anand)	2.69	830	31	0.1	6.3	-3.21	32	5.0	9.7	-0.09	2	17/01/2017
Mukundpura post-rain	OU (Mahesh Anand)	2.59	826	32	2.2	9.1	-2.53	47	9.7	19.5	-0.49	4	13/07/2017
Mukundpura post-rain	OU (Mahesh Anand)	2.63	806	31	2.1	9.0	-2.56	51	10.8	21.7	-0.53	4	14/07/2017
Mukundpura pre-rain	OU (Mahesh Anand)	2.63	788	30	1.6	7.9	-2.54	22	9.3	18.6	-0.37	3	18/07/2017
Mukundpura pre-rain	OU (Mahesh Anand)	2.62	769	29	1.4	7.5	-2.49	23	Not recorded			2	20/07/2017
EET 87522	Ashley King	3.12	1144	40	0.1	6.3	-3.17	98	11.7	22.5	0.00	3	Not recorded
Yamato 82054	Ashley King	3.12	1144	40	0.1	6.3	-3.17	Ran in same tray as EET 87522					Not recorded
Sayama	Unknown	2.61	1140	44	2.4	8.0	-1.76	61	8.4	16.2	-0.02	4	15/02/2019
Aguas Zarcas	OU (Ross Findlay and Mahesh Anand)	2.72	796	29	0.9	7.4	-2.90	Not recorded					15/12/2019
Aguas Zarcas	OU (Ross Findlay and Mahesh Anand)	2.59	765	30	0.8	7.1	-2.92	45	7.0	14.3	-0.49	4	15/12/2019

CM1/2 *RESULTS FROM OU LOG BOOK*

SAMPLE NAME	Supplier	Weight (mg)	OXYGEN RESULTS (‰)					5 min pre-fluorination blank				Blank (post-fluorination)	DATE RAN
			µg O_2	Yield (%)	$\delta^{17}O$	$\delta^{18}O$	$\Delta^{17}O$	µg O_2	$\delta^{17}O$	$\delta^{18}O$	$\Delta^{17}O$	µg O_2	
ALH 83100 unheated as chip then powdered	Unknown	2.60	986	38	1.8	7.7	-2.18	149	6.9	13.4	-0.10	9	09/08/2016
ALH 83100 unheated powder (but quite coarse)	Unknown	2.66	1008	38	2.1	8.0	-2.10	150	9.6	18.7	-0.13	11	18/08/2016
LAP 03116 (6?)	Ashley King	2.64	957	36	2.8	8.8	-1.78	229	18.6	36.2	-0.24	12	23/08/2016
NWA 8534	Ashley King	2.65	961	36	3.1	10.4	-2.30	138	18.7	36.6	-0.34	10	30/08/2016
GRO 95645	Ashley King	2.60	1071	41	0.6	5.3	-2.20	106	17.0	33.4	-0.34	8	06/09/2016
GRO 95645 (replicate)	Ashley King	2.64	1113	42	0.8	5.7	-2.21	165	19.3	37.9	-0.37	8	29/09/2016
LAP 031214	Ashley King	2.61	847	32	1.8	8.0	-2.38	232	12.5	24.2	-0.13	9	12/09/2016
MIL 090288	Ashley King	2.56	964	38	2.4	8.4	-1.91	210	18.5	36.1	-0.24	12	14/09/2016
LAP 031214	Ashley King	2.55	818	32	1.7	7.8	-2.40	140	18.9	36.9	-0.33	7	09/06/2016
MCY 05231	Ashley King	2.60	800	31	-0.7	5.1	-3.32	170	20.5	39.8	-0.14	6	18/09/2016
NWA 8534 (replicate)	Ashley King	2.62	875	33	1.7	7.8	-2.32	167	17.8	34.5	-0.19	5	Not recorded
MIL 090288 (replicate)	Ashley King	2.61	897	34	1.0	5.7	-1.99	85	16.6	32.5	-0.25	5	04/11/2016
LAP 03116 (6?) (replicate)	Ashley King	2.56	863	34	1.7	6.9	-1.89	125	16.6	32.5	-0.29	6	08/11/2016
LAP 03116 (6?) (replicate)	Ashley King	2.68	853	32	0.7	5.1	-1.93	19	3.9	7.1	-0.24	3	23/01/2017
LAP 031214 (replicate)	Ashley King	2.51	766	31	0.3	5.4	-2.51	26	7.0	13.9	-0.20	Not recorded	08/02/2017
NWA 8534 (replicate)	Ashley King	2.52	824	33	0.6	5.9	-2.44	20	3.5	7.4	-0.32	Not recorded	10/02/2017
GRO 95645 (replicate)	Ashley King	2.57	970	38	-1.3	1.8	-2.26	23	2.6	5.4	-0.20	Not recorded	15/02/2017
Mukundpura fine grained inclusion	OU (Ross Findlay and Mahesh Anand)	2.61	839	32	0.8	6.1	-2.39	27	4.7	9.1	0.00	3	06/12/2019
Mukundpura fine grained inclusion (replicate)	OU (Ross Findlay and Mahesh Anand)		889	34	1.4	7.3	-2.36	Not recorded					
Mukundpura fine grained inclusion (replicate)	OU (Ross Findlay and Mahesh Anand)	0.84	253	30	0.7	6.1	-2.44	17	6.5	12.7	-0.10	3	26/02/2020

CM1 *RESULTS FROM OU LOG BOOK*

SAMPLE NAME	Supplier	Weight (mg)	OXYGEN RESULTS (‰)					5 min pre-fluorination blank				Blank (post-fluorination)	DATE RAN
			µg O_2	Yield (%)	$\delta^{17}O$	$\delta^{18}O$	$\Delta^{17}O$	µg O_2	$\delta^{17}O$	$\delta^{18}O$	$\Delta^{17}O$	µg O_2	
MET 01070	Keiran Howard	2.46	856	35	1.9	7.9	-2.19	133	13.3	26.0	-0.16	9	22/09/2014
SCO 06043	Keiran Howard	2.49	873	35	1.5	6.9	-2.13	176	Not recorded			Not recorded	24/09/2014

LAP 02277	Ashley King	2.62	988	38	2.4	9.1	-2.36	150	19.5	37.9	-0.22	9	25/08/2016
MIL 07689	Ashley King	1.96	836	43	1.6	7.1	-2.07	136	19.5	37.8	-0.15	6	13/09/2016
MIL 05137	Ashley King	2.57	850	33	2.1	8.3	-2.24	145	18.8	36.8	-0.31	8	16/09/2016
Moapa Valley	Ashley King	2.59	924	36	1.8	8.0	-2.31	107	16.6	32.6	-0.34	7	20/09/2016
MIL 05137	Ashley King	2.61	824	32	-0.4	5.8	-3.40	206	19.2	37.4	-0.24	10	21/09/2016
NWA 4765	Ashley King	2.64	930	35	2.7	9.4	-2.22	238	21.1	41.1	-0.31	17	23/09/2016
MIL 07689 (replicate)	Ashley King	2.66	1033	39	-0.3	3.4	-2.11	70	17.4	34.1	-0.29	6	09/07/2016
MIL 07689 (replicate)	Ashley King	2.51	1307	52	4.9	12.7	-1.65	906	10.2	19.8	-0.08	12	13/09/2016
NWA 4765 (replicate)	Ashley King	2.58	893	35	0.9	6.2	-2.35	110	13.6	26.4	-0.15	6	20/09/2016
MIL 07689 (replicate)	Ashley King	2.36	858	36	-1.0	2.3	-2.19	13	4.3	8.5	-0.09	2	24/01/2017
MIL 090288 (replicate)	Ashley King	2.56	846	33	0.1	4.2	-2.09	15	2.4	4.8	-0.13	Not recorded	27/01/2017
LAP 02277 (replicate)	Ashley King	2.55	834	33	0.2	5.3	-2.52	16	3.7	7.2	-0.04	Not recorded	30/01/2017
MIL 05137 (replicate)	Ashley King	2.57	744	29	-0.2	4.2	-2.38	15	Not recorded			Not recorded	01/02/2017
NWA 4765 (replicate)	Ashley King	2.28	742	33	0.6	5.8	-2.44	24	6.1	12.1	-0.19	Not recorded	02/02/2017
Moapa Valley (replicate)	Ashley King	2.52	854	34	1.2	6.8	-2.38	44	10.3	20.1	-0.21	Not recorded	Not recorded
Moapa Valley (replicate)	Ashley King	2.50	856	34	0.9	6.4	-2.39	24	6.7	13.1	-0.10	Not recorded	07/02/2017
LAP 02277 (replicate)	Ashley King	2.58	873	34	0.4	5.6	-2.49	32	8.6	16.6	-0.07	Not recorded	16/02/2017
MIL 5137	Ashley King	2.54	794	31	0.5	5.6	-2.39	24	4.5	9.2	-0.27	Not recorded	17/02/2017

C-UNGROUPED *RESULTS FROM OU LOG BOOK*

SAMPLE NAME	Supplier	Weight (mg)	OXYGEN RESULTS (‰)					5 min pre-fluorination blank				Blank (post-fluorination)	DATE RAN
			µg O_2	Yield (%)	$\delta^{17}O$	$\delta^{18}O$	$\Delta^{17}O$	µg O_2	$\delta^{17}O$	$\delta^{18}O$	$\Delta^{17}O$	µg O_2	
EET 83226,1 (C2)	Devin Schrader	2.62	883	34	-3.2	0.3	-3.39	40	10.7	20.9	-0.13	4	30/08/2017
EET 83226,1 (replicate) (C2)	Devin Schrader	2.65	842	32	-3.3	0.0	-3.32	33	8.2	15.9	-0.11	3	12/02/2018
LEW 85311 (C2 an)	Unknown	2.63	780	30	-4.7	-0.1	-4.65	136	18.1	35.0	-0.09	9	28/11/2018
NWA 5958 (C2)	Unknown	2.58	907	35	-0.1	6.5	-3.51	106	7.7	15.5	-0.37	3	13/02/2019
MAC 88107 (C3)	Unknown	2.78	819	29	-6.5	-3.2	-4.87					Not recorded	15/02/2019
MAC 87300 (C2)	Unknown	2.79	810	29	-6.7	-3.4	-4.93	Ran in same tray as Sayama, so no results here.				Not recorded	15/02/2019
LEW 85332	Unknown - (OU?)	2.61	806	31	-2.6	-1.6	-1.76					Not recorded	15/02/2019

Appendix A5 – Large obsidian (~2 mg) analyses

Date analysed	$\delta^{17}O$	2SE	$\delta^{18}O$	2SE	$\Delta^{17}O$	2SE
13/07/2017	3.86	0.01	7.35	0.00	0.03	0.01
13/07/2017	3.86	0.00	7.34	0.01	0.04	0.00
14/07/2017	3.89	0.00	7.44	0.01	0.02	0.01
18/07/2017	3.85	0.03	7.40	0.01	0.00	0.02
27/11/2019	3.93	0.03	7.49	0.02	0.03	0.02
03/12/2019	3.82	0.03	7.36	0.01	0.00	0.03
06/12/2019	3.85	0.03	7.39	0.01	0.00	0.02
19/02/2020	3.84	0.01	7.34	0.01	0.02	0.01
26/02/2020	3.84	0.04	7.34	0.00	0.02	0.04
14/10/2020	3.91	0.01	7.47	0.01	0.03	0.01
20/10/2020	3.81	0.02	7.31	0.00	0.01	0.02
06/11/2020	3.86	0.01	7.39	0.01	0.02	0.01
24/11/2020	3.85	0.01	7.38	0.01	0.02	0.01
24/11/2020	3.83	0.01	7.32	0.00	0.02	0.01
26/11/2020	3.87	0.02	7.37	0.01	0.03	0.02
26/11/2020	3.83	0.03	7.34	0.00	0.02	0.03
15/12/2020	3.74	0.02	7.17	0.01	0.01	0.03
15/12/2020	3.74	0.02	7.17	0.01	0.01	0.03
26/01/2021	3.83	0.02	7.35	0.01	0.01	0.02
17/02/2021	3.77	0.01	7.23	0.01	0.01	0.01
23/02/2021	3.79	0.02	7.26	0.01	0.02	0.02
24/02/2021	3.80	0.01	7.25	0.01	0.03	0.01
01/03/2021	3.74	0.02	7.20	0.01	0.00	0.02
02/03/2021	3.79	0.02	7.23	0.00	0.03	0.02
05/03/2021	3.82	0.02	7.27	0.01	0.03	0.02
06/03/2021	3.75	0.01	7.21	0.00	0.00	0.01
07/03/2021	3.74	0.02	7.19	0.01	0.00	0.01
08/03/2021	3.78	0.01	7.22	0.01	0.02	0.01
09/03/2021	3.78	0.02	7.23	0.00	0.02	0.02
10/03/2021	3.80	0.01	7.25	0.01	0.02	0.01
15/03/2021	3.77	0.02	7.22	0.00	0.02	0.02
16/03/2021	3.75	0.02	7.18	0.00	0.01	0.02
09/04/2021	3.76	0.03	7.20	0.01	0.02	0.02
09/04/2021	3.77	0.01	7.21	0.00	0.02	0.01
24/06/2021	3.79	0.02	7.25	0.01	0.02	0.02
25/06/2021	3.84	0.01	7.34	0.00	0.02	0.01
29/06/2021	3.76	0.00	7.19	0.00	0.02	0.00
29/06/2021	3.84	0.00	7.36	0.01	0.01	0.00
30/06/2021	3.76	0.00	7.19	0.00	0.02	0.00
01/07/2021	3.85	0.02	7.34	0.01	0.03	0.03
01/07/2021	3.85	0.02	7.34	0.01	0.03	0.03
21/07/2021	3.85	0.02	7.34	0.01	0.03	0.02
22/07/2021	3.84	0.02	7.32	0.00	0.03	0.02

23/07/2021	3.81	0.02	7.32	0.00	0.00	0.02
04/08/2021	3.95	0.02	7.54	0.01	0.03	0.02
09/08/2021	3.84	0.01	7.36	0.01	0.01	0.01
10/08/2021	3.89	0.01	7.44	0.00	0.01	0.01
23/09/2021	3.72	0.02	7.17	0.00	-0.01	0.02
23/09/2021	3.77	0.03	7.21	0.01	0.02	0.03
19/11/2021	3.83	0.02	7.33	0.01	0.01	0.02
19/11/2021	3.88	0.02	7.43	0.01	0.01	0.02
23/11/2021	3.80	0.01	7.25	0.01	0.03	0.00
07/12/2021	3.79	0.02	7.31	0.01	-0.01	0.01
09/12/2021	3.74	0.02	7.17	0.01	0.01	0.03
17/12/2021	3.83	0.01	7.28	0.00	0.04	0.01
17/01/2022	3.83	0.03	7.36	0.01	0.00	0.02
18/01/2022	3.76	0.02	7.17	0.01	0.03	0.02
19/01/2022	3.85	0.02	7.37	0.01	0.01	0.02
24/06/2022	3.83	0.01	7.35	0.01	0.01	0.01
27/06/2022	3.85	0.01	7.37	0.00	0.02	0.01
28/06/2022	3.82	0.03	7.30	0.01	0.02	0.03
29/06/2022	3.81	0.01	7.30	0.01	0.01	0.01
30/06/2022	3.78	0.02	7.21	0.00	0.03	0.02
01/07/2022	3.84	0.01	7.32	0.01	0.03	0.01
01/07/2022	3.85	0.02	7.33	0.02	0.03	0.02
06/07/2022	3.81	0.02	7.32	0.01	0.01	0.02
07/07/2022	3.80	0.01	7.28	0.02	0.02	0.01
08/07/2022	3.81	0.01	7.30	0.01	0.02	0.01
11/07/2022	3.80	0.01	7.29	0.02	0.01	0.01
12/07/2022	3.83	0.02	7.36	0.01	0.01	0.02
14/07/2022	3.81	0.00	7.29	0.01	0.02	0.01
15/07/2022	3.85	0.02	7.33	0.00	0.04	0.02
22/07/2022	3.81	0.01	7.30	0.00	0.01	0.01
23/07/2022	3.82	0.02	7.29	0.00	0.03	0.02
25/07/2022	3.78	0.03	7.25	0.01	0.01	0.02
26/07/2022	3.76	0.02	7.18	0.00	0.03	0.02
27/07/2022	3.80	0.02	7.26	0.00	0.03	0.02
29/07/2022	3.83	0.03	7.35	0.01	0.01	0.02
06/08/2022	3.88	0.01	7.44	0.01	0.01	0.01
14/12/2022	3.76	0.02	7.19	0.01	0.02	0.02
AVERAGE	**3.81**	**0.09**	**7.30**	**0.17**	**0.02**	**0.02**

Errors are 2SE on individual obsidians

Errors on average are 2σ

Appendix 6 – Rearrangement of the Clayton and Mayeda (1999) equation

This is a due diligence check: Rearranging equations (A1) and substituting (A2) to create (A3) from Clayton and Mayeda (1999)

$$7x\delta_w^i + 7\delta_r^i = (7x - 2f)\delta_w^f + 7(1-f)\delta_r^i + 9f\delta_s^f$$

Substitute

$$\delta_w^f = \delta_s^f - \Delta_{SW}$$

$$7x\delta_w^i + 7\delta_r^i = (7x - 2f)(\delta_s^f - \Delta_{SW}) + 7(1-f)\delta_r^i + 9f\delta_s^f$$

Rearrange to make $(2x - 2f)(\delta_s^f - \Delta_{SW})$ the subject

$$(7x - 2f)(\delta_s^f - \Delta_{sw}) = 7x\delta_w^i + 7\delta_r^i - 7(1-f)\delta_r^i - 9f\delta_s^f$$

Expand brackets on left

$$7x\delta_s^f - 2f\delta_s^f - 7x\Delta_{SW} + 2f\Delta_{SW} = 7x\delta_w^i + 7\delta_r^i - 7(1-f)\delta_r^i - 9f\delta_s^f$$

Add $9f\delta_s^f$

$$7x\delta_s^f + 7f\delta_s^f - 7x\Delta_{SW} + 2f\Delta_{SW} = 7x\delta_w^i + 7\delta_r^i - 7(1-f)\delta_r^i$$

Divide by 7

$$x\delta_s^f + f\delta_s^f - x\Delta_{SW} + \frac{2}{7}f\Delta_{SW} = x\delta_w^i + \delta_r^i + (f-1)\delta_r^i$$

Expand remaining bracket

$$x\delta_s^f + f\delta_s^f - x\Delta_{SW} + \frac{2}{7}f\Delta_{SW} = x\delta_w^i + f\delta_r^i$$

Simplify left

$$(x+f)\delta_s^f + (-x+\frac{2}{7}f)\Delta_{SW} = x\delta_w^i + f\delta_r^i$$

Subtract $\left(-x+\frac{2}{7}f\right)\Delta_{SW}$

$$(x+f)\delta_s^f = -\left(-x+\frac{2}{7}f\right)\Delta_{SW} + x\delta_w^i + f\delta_r^i$$

Divide by x

$$\left(1+\frac{f}{x}\right)\delta_s^f = \left(1-\frac{2}{7}\frac{f}{x}\right)\Delta_{SW} + \delta_w^i + \frac{f}{x}\delta_r^i$$

Divide by $(1+\frac{f}{x})$

$$\delta_s^f = \frac{\left(1-\frac{2}{7}\frac{f}{x}\right)\Delta_{SW} + \delta_w^i + \frac{f}{x}\delta_r^i}{1+\frac{f}{x}}$$

Simplify and tidy top

$$\delta_s^f = \frac{\delta_w^i + \Delta_{SW} + \left(\delta_r^i - \frac{2}{7}\Delta_{SW}\right)\frac{f}{x}}{1+\frac{f}{x}}$$

(As reported in Clayton and Mayeda, 1999, Appendix A, equation (A3))